

Petrological evolution of the Neoproterozoic meta-supracrustal rocks from parts of the Indian shield



*Thesis submitted to Jadavpur University
for the degree of
Doctor of Philosophy (Science)*

By
Sirina Roy Choudhury
Department of Geological Sciences
Jadavpur University

2022



FACULTY OF SCIENCE : DEPARTMENT OF GEOLOGICAL SCIENCES

CERTIFICATE FROM THE SUPERVISORS

This is to certify that the thesis entitled “**PETROLOGICAL EVOLUTION OF THE NEOPROTEROZOIC META-SUPRACRUSTAL ROCKS FROM PARTS OF THE INDIAN SHIELD**” submitted by **Ms. Sirina Roy Choudhury** (registration on **08/10/2015**), for the award of **Ph. D. (Science)** degree of Jadavpur University, is absolutely based upon her own work under the supervision of **Professor Subrata Karmakar** and **Professor Sanjoy Sanyal**, and that neither this thesis, nor any part of it has been submitted for either any degree/ diploma or any other academic award anywhere before.

Subrata Karmakar
22/12/2022

Supervisor

Prof. Subrata Karmakar

Dept. of Geological Sciences

Jadavpur University

Kolkata-700032

Dr. Subrata Karmakar

Professor

Department of Geological Sciences

Jadavpur University

Kolkata-700032, India

Sanjoy Sanyal
22.12.2022

Supervisor

Prof. Sanjoy Sanyal

Dept. of Geological Sciences

Jadavpur University

Kolkata-700032

Dr. Sanjoy Sanyal

Professor

Department of Geological Sciences

Jadavpur University

Kolkata: 700032, India

To my parents

Acknowledgements

At the very beginning, I would like to sincerely thank each and every individual who has been with me all through this journey of my Ph. D work.

It would have been impossible to complete my work without the constant guidance and support of my supervisors, Prof. Subrata Karmakar and Prof. Sanjoy Sanyal. I sincerely wish to thank them for their continuous patience and for providing me constant motivation. I would like to specially thank Prof. Pulak Sengupta, for his relentless efforts, and guidance which has enhanced my work greatly. I am genuinely indebted to him for being a constant source of motivation and inspiration.

I would also like to thank Dr. Shyamal Sengupta for providing valuable guidance.

I would like to acknowledge the Council of Scientific & Industrial Research (CSIR) for their constant financial support, that has made my work easier.

I would like to thank Prof. Dewashish Upadhyay for his support during the analysis of zircon grains presented in this study in IIT Kharagpur. I would also like to thank Dr. Upama Dutta for her immense help during EPMA analysis at ISM Dhanbad, as well as helping me out in many academic aspects in course of this work. I would like to acknowledge the help from Prof. Biswajit Mishra, during the EPMA analysis at IIT Kharagpur. I would also like to express heartfelt thanks to Dr. Aparajita Dutta, Geological Survey of India, Kolkata for always motivating me.

I would like to express my gratitude to Jadavpur University for providing me with all the research facilities, including the Scanning Electron Microscope facilities. Additionally, I would like to express my sincere thanks to all the faculty members, researchers and staff members of the Department of Geological Sciences for their support and co-operation.

I would like express my honest and heartfelt gratitude to Anindita di, for constantly motivating, guiding me in all ways (academically as well as beyond it), and for believing in me from day one. I would also like to thank her for being a

Acknowledgements

wonderful co-worker and for being my constant support and inspiration. I would also like to specially thank Subham da for his constant support, motivation all throughout my Ph. D. work. I would also like to extend my sincere gratitude for him for being a wonderful co-worker and a great senior.

I would like to thank Arimita and Satabdi di for being very helpful co-workers and lab mates. I would like to thank Somdipto, Nivedita di, Sourav, Shreyasi, Mousumi and Nilanjan for being wonderful labmates and juniors. I would also like to thank Prantik da, Swarnali di, Enakshi di, Shreya di, and Hassan da for being wonderful seniors. I would also like to thank Dr. Nandini Chattopadhyay, Dr, Sayan Biswas and Dr Moumita Talukdar for being very supportive seniors.

I would like to express my deepest thanks to my friends: Lisa, Meera, Shreyasi, Swagata, Shabnam, Sangita, Tulika, Anirnita, Bidisha, Payal, Abhishek, Chirantan, Mahesh, Manaska, Dipankar and Dip. I thank them for their constant patience and support.

Most importantly, I would like to thank my parents for their patience, sacrifice and for always believing in me. I would also like to thank my other family members for their constant support.

Sirina Roy Choudhury
Department of Geological Sciences
Jadavpur University, Kolkata

Contents

ABSTRACT	i-ii
1. Introduction	1
1.1 Objectives of this study	6
1.2 Methodologies	7
2. A synthesis of published geological and geochronological information on the Chotanagpur Granite Gneiss Complex and the Granulite Terrane of South India	13
2.1. The Chotanagpur Granite Gneiss Complex (CGGC)	14
2.1.1. Boundary of the CGGC	14
2.1.2. Classification of the CGGC	14
2.2. The Granulite terrane of South India	32
<u>PART-I The Chotanagpur Granite Gneiss Complex</u>	
3. Study area and field relations	61
3.1 Country rock	62
3.2 Enclave suite of rocks	65
3.3 Enclave suite of rocks	70
3.4 Structural relations	71
4. Metamorphic evolution of the calc-silicate granulites	
4.1. Evolution of aluminous clinopyroxene-ilmenite-spinel symplectites in calc-silicate granulite	76
4.1.1 Field Description	78
4.1.2 Petrography	80
4.1.3 Mineral Chemistry	85
4.1.4 Evolution of mineral assemblages and identification of mineral reactions	89
4.1.5 P-T conditions of metamorphism	96
4.1.6 Oxygen Isotope	100

4.1.7 Geochronology	101
4.1.8 Synthesis of information	105
<i>Protolith of the studied rock</i>	105
<i>Formation of symplectites</i>	106
<i>Nature and timing of metamorphism and correlation with other lithounits</i>	108
4.2. Stability of vesuvianite-garnet-epidote bearing calc-silicate granulite	121
4.2.1 Field Description	122
4.2.2 Petrography and mineral compositions	123
4.2.3 Formation of the vesuvianite-garnet-epidote mineral assemblage	138
4.2.4 P-T conditions of formation of vesuvianite-garnet-amphibole- epidote	139
4.2.5 Petrogenetic grid for the studied calc-silicate rock	140
4.3 Factors controlling the incorporation of aluminium within titanites	157
4.3.1 Field Description	159
4.3.2 Mutual relations between mineral phases	162
4.3.3 Mineral Chemistry	167
4.3.4. Discussion	176
5. Metamorphic evolution of pelitic granulite	191
5.1 Field Description	192
5.2 Petrography	194
5.3 Mineral Chemistry	196
5.4 Evolution of mineral assemblages	202
5.5 P-T conditions of metamorphism	203
5.6 Nature and timing of metamorphism	205

Part-II The Granulite Terrane of South India

6. Metamorphic evolution pelitic granulite from Madukkarai	
Supracrustal Unit	210
6.1. Field features	211
6.2. Petrography	213
6.3. Mineral Chemistry	220
6.4. PT conditions and evolution of mineral assemblage	229
6.4.1. <i>Thermobarometry</i>	229
6.4.2. <i>Pseudosection modelling</i>	232
6.5. Geochronology	238
6.5.1. <i>U-Pb Zircon dating</i>	238
6.5.2. <i>Th-U-total-Pb in situ monazite dating</i>	243
6.6. Tectonothermal evolution of the Madukkarai supracrustal Unit	247
6.6.1. <i>Formation of the protoliths of the meta-supracrustal rocks</i>	247
6.6.2. <i>P-T evolution of the Madukkarai supracrustal unit</i>	248
6.6.3. <i>Timing of metamorphism and deformation</i>	248
7. Metamorphic evolution calc-silicate granulite from Madukkarai Supracrustal Unit	255
7.1. Field features	257
7.2. Petrography	258
7.3. Reaction textures and evolution of mineral assemblage	262
7.4. Mineral Chemistry	263
7.5. Petrogenetic grid for the studied calc-silicate granulite	272
8. Discussion	293
8.1. Neoproterozoic evolution of the Indian subcontinent	293
8.1.1. <i>The CGGC</i>	293
8.1.2. <i>The GTSI</i>	299
8.2. The significance of the CGGC and the GTSI in the evolution of the Indian shield	301

8.2.1. <i>Imprints of early Neoproterozoic orogeny in the CGGC and other adjacent terranes: implications for reconstruction of Rodinia</i>	302
8.2.2. <i>Imprints of late Neoproterozoic orogeny in the GTSI and other adjacent terranes: implications for reconstruction of Gondwanaland</i>	309
8.3. Summary	320
8.4. Concluding remarks	321
Appendix	344
Methodology for calculation of effective bulk	344
Analytical techniques for zircon and monazite dating	344
Textural modelling technique	347
Supplementary Material 1	350
Publications	352

ABSTRACT

The metamorphic rocks of the Indian shield record a protracted geological history that span for more than ca.3500 Ma. Tracing the Neoproterozoic tectonothermal pulses in the Indian shield has paramount importance in understanding the formation of the two Neoproterozoic supercontinents (the Rodinia and the Gondwanaland). In view of this, two intercalated calc-silicate and pelitic granulites have been studied from the Chotanagpur Granite Gneissic Complex (CGGC) and the Granulite Terrane of South India (GTSI).

The calc-silicate and pelitic granulites in the CGGC occurs as map scale enclaves within the ca.1450 Ma (protolith age) felsic orthogneisses. Two types of calc-silicate granulite enclaves, having distinct mineralogy are studied. These are: (1) plagioclase+ titanite+ garnet+ clinopyroxene+ amphibole+ ilmenite+ spinel± calcite+ zircon± apatite ± magnetite. The mineral assemblages are asymmetrically distributed in plagioclase, clinopyroxene and garnet-rich bands. This rock develops rare symplectite of highly aluminous clinopyroxene ($Al_2O_3 > 11.5$ wt%), ilmenite and spinel. Interpretation of reaction textures and phase equilibrium modelling in the system Na_2O - CaO - FeO - MgO - Al_2O_3 - SiO_2 - TiO_2 - H_2O - CO_2 - O_2 attest to the reaction: garnet+ titanite+ amphibole= clinopyroxene+ ilmenite+ spinel+ plagioclase (Pl_2)+ vapour, triggered by a steeply decompressive P-T path from ~790-890 °C, ~8.4-9.5 kbar to ~780-860 °C and ~5-5.8 kbar. U-Pb ages of metamorphic zircon overgrowth over the detrital core, dates the timing of the dominant metamorphism at 1060-970 Ma (with a ca.1480 Ma old spot age). The $^{207}Pb/^{206}Pb$ ages of the detrital zircon core suggest that the protolith sediments were sourced from rocks of diverse age populations (~2470 Ma, 2190-2000 Ma and 1790 Ma) from hinterland. The low $\delta^{18}O$ (4 ± 1.2 ‰) values of the whole rock suggest that the protolith sediments were altered via interaction with low $\delta^{18}O$ fluid (meteoric water). (2) This type of calc-silicate granulite comprises clinopyroxene + plagioclase + titanite + amphibole ± apatite. Millimeter thick compositional bands that are rich in clinopyroxene and plagioclase are seen. This rock develops garnet-vesuvianite and epidote bearing veins (clinopyroxene+ plagioclase+ titanite+ vesuvianite+ garnet+ epidote ± apatite ± calcite), proximal to undeformed pegmatite bodies that dissect the host calc silicate granulite. Reaction textures and the activity corrected topologies in P-T-X(fluid) topologies suggest that the infiltration of F-rich aqueous fluid, presumably derived from pegmatites, was responsible for the formation of vesuvianite and garnet by the reactions (a) clinopyroxene+ quartz+ plagioclase± calcite+ fluid ($H_2O + F$) ± $O_2 \rightarrow$ Vesuvianite + CO_2 and (b) clinopyroxene+ plagioclase± quartz± calcite \rightarrow garnet+ CO_2 at ~6kbar and ~600-620°C and $X_{CO_2} \leq 0.40$. Epidote formed later at more H_2O -rich conditions ($\leq 0.1 X_{CO_2}$ and lower X_F) and lower temperatures <600°C. Titanite in some domains is unusually rich in Al_2O_3 (up to 11.5 wt%) and F (up to 3.8 wt%). The dominant substitution that explains the abnormally high Al-F titanite is Ti^{+4}

Abstract

$+O^{2-} \rightarrow Al^{+3} + (F+OH)^-$. f_{F2} in the coexisting fluid controlled the coupled substitution. The mineralogical evolution of the pelitic granulite enclaves show P-T conditions at the culmination of metamorphism (~9.8-10.5 kbar and ~850-880°C) that is similar to the peak P-T conditions recorded from the first type of calc silicate granulite.

The Madukkarai Supracrustal Unit (MSU) within the GTSI is chiefly composed of an interlayered sequence of pelitic granulites (locally with arenaceous components) and calc-silicate granulites. The gneissic fabric of the pelitic granulite of the MSU is defined by centimeter thick laterally discontinuous garnet bearing leucosome. The mineral assemblages of the pelitic granulites include: garnet+ biotite+ sillimanite (locally pseudomorphs after kyanite)+ K-feldspar+ plagioclase+ quartz+ ilmenite ± cordierite± orthopyroxene. Rutile, zircon and monazite occur as accessory minerals. Interpretation of the reaction texture, pseudosection modelling and conventional geothermobarometry recovered maximum temperature and pressure of metamorphism in the realm of ~730–790 °C, ~5.5–7 kbar (relict kyanite indicates pre-peak pressures ≥ 8 kbar). These P-T values correspond to a transient geothermal gradient of ~37°C/km, at crustal depth of ~25 km. Subsequently, the pelitic granulite ascended (corresponding to a shallower crustal depth of ~15km) along a steeply decompressive retrograde P-T path that was followed by cooling up to ~630°C and ~4 kbar. The attainment of high-pressure condition prior to peak metamorphism, and geometry of the retrograde P-T path are consistent with a continent-continent collisional tectonic setting. The calc silicate granulites preserve clinopyroxene+ plagioclase + scapolite (±titanite ±magnetite) as the earliest assemblages. These minerals sequentially develop garnet (up to 75 mol% andradite) + amphibole and epidote through a number of infiltration driven mineral reactions. The observed mineralogical changes are interpreted in the P-T and T-X_{CO2} topologies in the CaO-MgO-Al₂O₃-SiO₂-H₂O-CO₂ (CMASV) system. The effects of Fe²⁺, Fe³⁺ and Na on the CMASV topologies are analysed. Interpretation of the 'frozen in' reaction textures in the activity adjusted CMASV topologies supports the view that the infiltration of an aqueous fluid triggered the metamorphic reactions (X_{CO2}=0.4-0.6, ~440-640°C, ~440°C; at ~4.5-6kbar) in the calc silicate granulites. LA-ICP-MS U–Pb zircon and chemical age of monazite in the pelitic granulite, dates the timing of metamorphism in the range of 550-520 Ma with vestiges of ~600 Ma event. The petro-chronological history of the MSU resembles that of the meta-supracrustal rocks lying north and south of the study area. Observations from this study supports the view that the GTSI behaved as a coherent block during the Ediacaran-Cambrian orogenesis and does not support the view that the Palghat Cauvery Shear Zone is a Neoproterozoic suture zone. The timing and style of tectonothermal events being deduced in this study supports the view that the Indian shield and the Precambrian basements of the east Antarctica and Madagascar behaved as a coherent block in the Rodinia and Gondwanaland supercontinents.

Chapter-1
Introduction

Chapter 1

Introduction

It is well known that the orogenic processes perturb stable geothermal gradient (Thompson and England, 1984), induce fluid rock interaction and consequent chemical alteration of the metamorphic rocks and develop sequence of mineral assemblages in response to the changing physicochemical conditions during orogenesis (Philpotts and Ague, 2009). Pelitic and calcareous rocks, by virtue of its bulk rock compositions are very sensitive to the small variations in the P-T-fluid regime. These properties make these rocks faithful recorder of the changing physicochemical conditions during the evolution of the extinct and extant orogenic belts (Brown, 2008, 2007; Harley et al., 1994; Philpotts and Ague, 2009). Several studies in the past several decades have proposed repeated assembly and break-up of continental blocks, popularly known as the supercontinental cycle (Condie, 2021; Mitchell et al., 2021; Nance and Murphy, 2013). In the Proterozoic Eon, assembly and fragmentation of three major supercontinents, namely Columbia (Meert and Santosh, 2017; Zhao et al., 2015), Rodinia (Li et al., 2008; Pant and Dasgupta, 2017) and Gondwanaland (Meert and Van Der Voo, 1997), have been proposed. It is now clear that the orogenic belts are the loci along which the once disparate crustal segments, were fused together to form the ancient supercontinents (Condie, 2021). Detail studies on the petro-chronological evolution of the orogenic belts and its global correlation are crucial to understand the process of supercontinental cycles that controlled the evolution of the lithosphere-hydrosphere-atmosphere of the Earth (Bradley, 2011; Chowdhury et al., 2017; Hannisdal and Peters, 2011; Hoffman and Schrag, 2002). The ancient orogens in the Indian shield preserve the signals of the dynamics of the earth for more than 3500 Ma (reviewed in Nance et al., 2014). Studies have shown that the roughly WSW-ENE trending orogenic belt, known as Central Indian Tectonic Zone (CITZ), dissected the Indian shield into a northern and a southern Indian block (NIB and SIB respectively, Acharyya, 2003; Bhowmik, 2019). The timing and the process of fusion of NIB and SIB along this composite CITZ belt

remains a matter of intense debate (reviewed in Bhowmik, 2019; Deshmukh and Prabhakar, 2020; Mukherjee et al., 2019).

The Chotanagpur Granite Gneiss Complex (CGGC) (Fig. 1) is considered to be the eastern extension of the CITZ. In the reconstructed Rodinia supercontinent, the CGGC and the Eastern Ghats Mobile Belt (EGMB) are juxtaposed against the Proterozoic mobile belts of east Antarctica (Dalziel, 1995; Dasgupta et al., 2013; Pant and Dasgupta, 2017). Published information from the CGGC, particularly its granulite portion, record extension related felsic magmatism at ~1450-1350 Ma (Mukherjee et al., 2018, 2017; Sequeira et al., 2022) followed by intense high-pressure metamorphism during Grenvillian orogenesis at ~1100-950 Ma (reviewed in Mukherjee et al., 2019). The felsic orthogneisses contains metapelitic, meta-mafic and calc silicate enclaves (reviewed in Mukherjee et al., 2019). Limited studies in metapelites from one area identified (a) Palaeoproterozoic detrital zircon that were presumably derived from the Palaeoproterozoic rocks that are exposed in the lesser Himalaya (Dey et al., 2017) and (b) late Palaeoproterozoic high temperature metamorphism that was superposed by Grenvillian orogenesis (Dey et al., 2019b). Detail petro-chronology on the calc silicate enclaves is lacking although infiltration of F-rich fluids has been documented from a vesuvianite bearing calc silicate rock. (Dey et al., 2019a). Furthermore, the source of sediments for the protoliths of the calc-silicate enclaves and the response of the rocks in different orogenic pulses remain poorly understood. Also, the detail infiltration driven metasomatic process and the products therefrom in the chemically reactive calc-silicate rocks are not worked out. Detail petrochronology of the calc-silicate enclaves, along with the pelitic enclaves is, therefore, expected to provide valuable information about the P-T-Fluid regimes during the orogenic processes that shaped the CGGC from ~1680 Ma (Dey et al., 2019b; Singh et al., 2001) to ~800 Ma (Chatterjee, 2018; Chatterjee et al., 2010; Dey et al., 2019b; Karmakar et al., 2011), with major emphasis on the Neoproterozoic time.

The Granulite Terrain of South India (GTSI) fringes the Meso- to Neoarchaeon Dharwar Craton (Western Dharwar Craton, with both Meso- and Neoarchaeon components, and Eastern Dharwar Craton, with Neoarchaeon

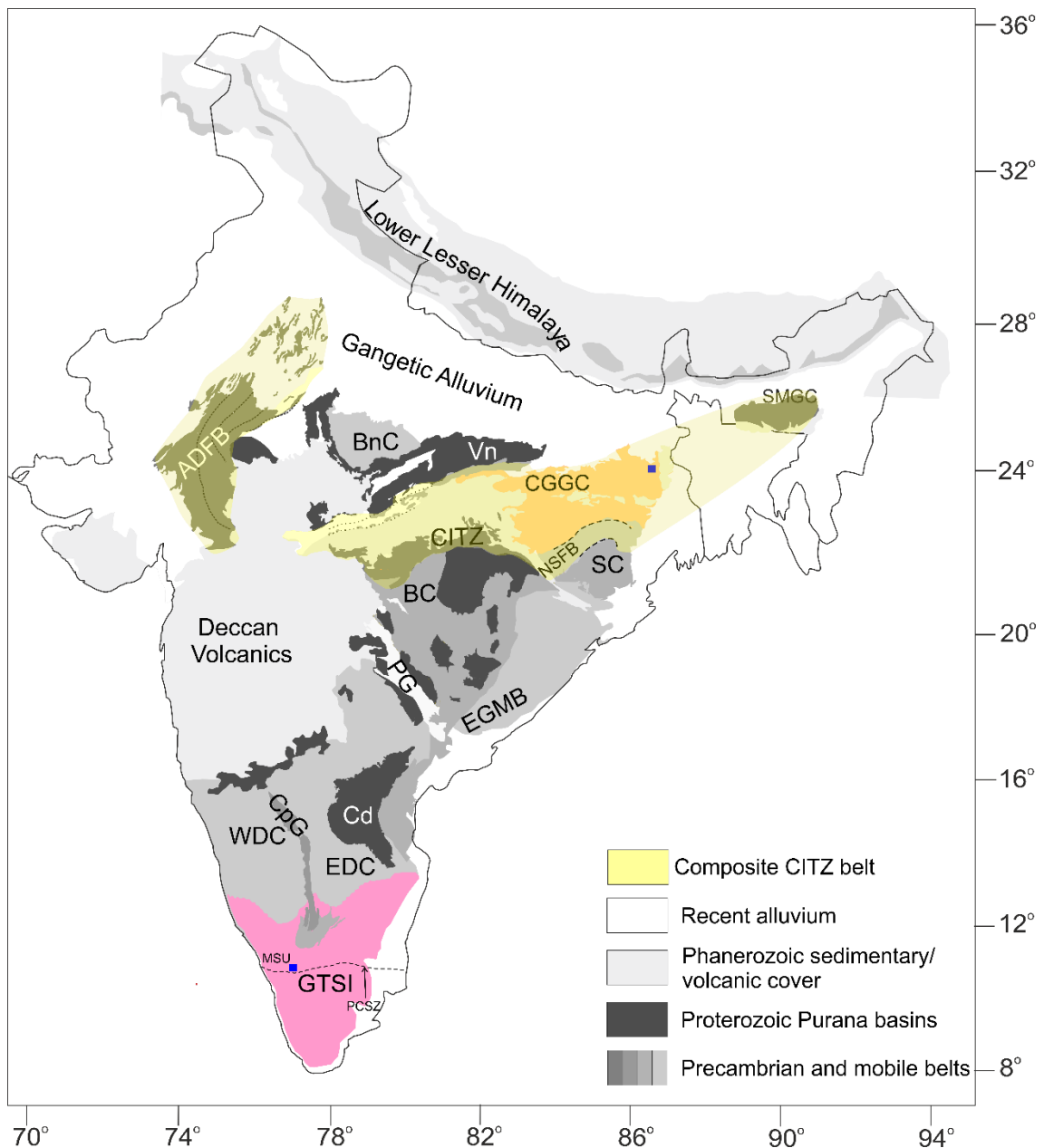


*Fig. 1: Geological map representing the crystalline basement and sedimentary cover of the Indian peninsula. The studied terranes of the CGGC and GTSI have been highlighted in orange and pink respectively (exact study areas marked in blue boxes). The light yellow shaded area represents the possible exposed and subsurface extension of the proposed composite belt of Central Indian Tectonic Zone (CITZ) (Acharya, 2003) that comprises the Proterozoic terranes of MB, SMB, CGGC, NSFB and SMGC. Some considers ADFB to be a distant participant. The perceived Palghat Cauvery Suture Zone within the GTSI has also been marked. The abbreviations are listed below alphabetically:
 AV: Aravalli craton; BC: Bastar craton; BnC: Bundelkhand craton; CB: Chattisgarh basin; CGGC: Chotanagpur Granite Gneiss Complex; CpG: Closepet Granite; Cd: Cudappah basin; DF: Dauki fault; EGMB: Eastern Ghats mobile belt; EDC: Eastern Dharwar craton; MB: Mohakoshal belt; MSRF: Monghyr Saharsa Ridge fault; NSFB: North Singhbhum fold belt; PG: Pranhita Godavari basin; SC: Singhbhum craton; GTSI: Granulite Terrane of South India; SMB: Sausar mobile belt; SMGC: Shillong Meghalaya gneissic complex; SONA: Son Narmada graben faults; Vn: Vindhyan basin; WDC: Western Dharwar craton.*

component) to the south (Fig. 1). The evolution of the GTSI and its relation with the northern Dharwar Craton have paramount importance in understanding the evolution of the Indian shield in specific, and formation and destruction of the Proterozoic supercontinental cycles (reviewed in Talukdar et al., 2022). Studies in the past few decades in the GTSI have identified two chief litho-chronological units. The northern part of the GTSI is constituted by an ultramafic-mafic-anorthosite-chromitite component (~3200-2520 Ma) that are enclosed by Neoproterozoic felsic gneisses with late Archaean protolith (~2840-2500 Ma) (reviewed in Talukdar et al., 2022). The regionally extensive felsic orthogneisses and its enclaves witnessed a high-pressure metamorphism at the earliest phase of the Proterozoic (~2570-2430 Ma, reviewed in Brandt et al., 2014; Talukdar et al., 2022). The other major component is a suite of meta-supracrustal rocks consisting of marble (+calc-silicate rocks)-metapelites-quartzite whose protolith is likely to be limestone-shale-quartzite of stable shelf deposits (reviewed in Sengupta et al., 2015; Talukdar et al., 2022). It is perceived that the Archaean-early Palaeoproterozoic rocks of the northern GTSI is separated from a meta-supracrustal dominated southern part, the 'Madurai Block', by a crustal scale shear zone, the so called Palghat Cauvery Shear Zone (PCSZ; Clark et al., 2009; Santosh, 2020). There exists a strong debate on the very existence, extent and the significance of the PCSZ (reviewed in Brandt et al., 2014; Ghosh et al., 2004; Sengupta et al., 2015; Talukdar et al., 2022). Preponderance of the Ediacaran-Cambrian, high- to ultrahigh temperature metamorphism in the meta-supracrustal rocks south of the PCSZ, and its absence in the areas lying north of it, invoked a number studies to propose that the Madurai block came to juxtaposition with the northern GTSI only during the Ediacaran-Cambrian orogenesis, which mark the closure of the "Mozambique Ocean" along the PCSZ (Collins et al., 2007; Kroener et al., 2000). This contention is contradicted by several studies in the recent times. The main arguments of disclaimers include (a) extension of late Archaean-early Palaeoproterozoic rocks akin to the northern GTSI further south of the PCSZ, (b) lack of field evidence of the laterally continuous shear zones along the propose trend of the PCSZ, and (c) occurrence of vestiges of meta-supracrustal rocks on and further north of the PCSZ (reviewed in Raith et al., 2016; Sengupta et al., 2015; Talukdar et al., 2022). A few studies identified Meso- to Neoproterozoic and early Palaeoproterozoic detrital zircon in the meta-supracrustal

rocks of the Madurai Block, which also speaks against the idea that PCSZ could be an Ediacaran-Cambrian suture zone (reviewed in Kooijman et al., 2011; Sengupta et al., 2015; Talukdar et al., 2022). Limited studies on the meta-supracrustal rocks in the proximity of the PCSZ showed that the grade of metamorphism in this region is distinctly lower (upper amphibolite to transitional granulite or rare granulite, (Raith et al., 2010; Sengupta et al., 2009), relative to the southern part of the Madurai block where the UHT (Ultra-High temperature metamorphism; e.g., Brandt et al., 2011) has been abundantly reported. This leads to the pertinent question as to how the metasupracrustal rocks with UHT metamorphism are related to the meta-supracrustal rocks with distinctly lower grade, compared in terms of their source, timing and the tectonic style of metamorphism? Answer to this question is crucial to understand the growth of GTSI as well as the response of the Indian shield during the formation of the supercontinent Gondwanaland. The petro-chronological evolution of the Madukkarai Supracrustal Unit (MSU) that is situated on the PCSZ is potentially valuable for addressing the status of the PCSZ as well as understanding the reason behind the observed variation of the metamorphic grade in the meta-supracrustal rocks of the GTSI.

In the aforesaid background I have studied the **pelitic granulites and calc-silicate granulites** from two areas, one from the **Deoghar-Jasidih area in the north-eastern part of the CGGC** (Fig. 2.1), and from the **Madukkarai Supracrustal Unit of the GTSI** (Fig. 2.2). The findings of this study is further used to shed new light on the response of the Indian shield during the Neoproterozoic supercontinent cycles.

1.1. Objectives of the present study

1. To establish the status of the pelitic and calc-silicate granulites in the CGGC, with the other lithounits, based on the mutual field relations.
2. To delineate the polymetamorphic P-T-fluid evolutionary history of the calc-silicate granulite and pelitic granulite in the CGGC
3. To trace the processes and conditions of formation of high aluminous clinopyroxene, ilmenite and spinel symplectites, and high aluminous, fluoro titanites stabilised in the calc-silicate granulites.

4. To constrain the timing of sedimentation of these metasedimentary enclave suit in the CGGC, as well as its timing of metamorphism.
5. To establish the mutual field relations of the meta-supracrustal rocks of the MSU with the other lithounits.
6. To understand the fluid regime and style of metamorphism in the MSU and its relation to the other meta-supracrustal rocks from both sides of the PCSZ
7. To constrain the timing of sedimentation and metamorphism of the MSU.
8. To test the hypothesis that the variation of the metamorphic grade in the meta-supracrustal rocks of the GTSI could represent different crustal depth of a unified Ediacaran-Cambrian Orogenesis.
9. To integrate the findings of this study with that of the other adjacent terranes within GTSI, in order to trace the geological evolution of the GTSI in general, and the status of the "PCSZ" in particular.
10. To understand the significance of the geological history of the Early Neoproterozoic metamorphism in the CGGC and the Ediacaran-Cambrian metamorphism in the MSU, in the context of the Indo-Antarctica-Madagascar connection, if there was any.

1.2. Methodologies

To achieve the above-mentioned objectives, the following methods have been applied.

1. Systematic sampling of each rock type from both the study areas.
2. Systematic preparation of thin sections of the samples collected from field for petrographic studies.
4. Detailed petrographic study has been done for each of the sampled rocks for identification of various mineral assemblages, and identification of mutual textural relations in each rock.
5. BSE imaging of various textures have been done to identify and study the opaque phases (wherever present).
6. Detailed and systematic EPMA analysis of each studied rock samples using

Wavelength Dispersive Spectrometry, WDS, to identify the exact mineral compositions and their variations.

7. Mass balance calculations were performed to quantify the observed reaction textures under thin section.

8. Conventional Geothermobarometry and phase equilibria modelling and construction of quantitative petrogenetic grids to constrain the P-T-fluid evolutionary history of the rock.

9. LA-ICP-MS U-Pb isotope dating of zircon and in-situ U-Th-Pb chemical dating of monazite using EPMA to provide an age constraint to the studied rocks.

References

- Acharyya, S.K., 2003. The nature of Mesoproterozoic Central Indian Tectonic Zone with exhumed and reworked older granulites. *Gondwana Res.* 6, 197–214.
- Bhowmik, S.K., 2019. The current status of orogenesis in the Central Indian Tectonic Zone: A view from its Southern Margin. *Geol. J.* 54, 2912–2934.
- Bradley, D.C., 2011. Secular trends in the geologic record and the supercontinent cycle. *Earth-Science Rev.* 108, 16–33.
- Brandt, S., Raith, M.M., Schenk, V., Sengupta, P., Srikantappa, C., Gerdes, A., 2014. Crustal evolution of the Southern Granulite Terrane, south India: New geochronological and geochemical data for felsic orthogneisses and granites. *Precambrian Res.* 246, 91–122. <https://doi.org/10.1016/j.precamres.2014.01.007>
- Brandt, S., Schenk, V., Raith, M.M., Appel, P., Gerdes, A., Srikantappa, C., 2011. Late Neoproterozoic PT evolution of HP-UHT granulites from the Palni Hills (South India): New constraints from phase diagram modelling, LA-ICP-MS zircon dating and in-situ EMP monazite dating. *J. Petrol.* 52, 1813–1856.
- Brown, M., 2008. Characteristic thermal regimes of plate tectonics and their metamorphic imprint throughout Earth history: When did Earth first adopt a plate tectonics mode of behavior? When did plate tectonics begin planet Earth? *J. Metamorphic Geol.* 26, 440, 97.
- Brown, M., 2007. Metamorphic conditions in orogenic belts: a record of secular change. *Int. Geol. Rev.* 49, 193–234.

- Chatterjee, N., 2018. An assembly of the Indian Shield at c. 1.0 Ga and shearing at c. 876–784 Ma in Eastern India: insights from contrasting PT paths, and burial and exhumation rates of metapelitic granulites. *Precambrian Res.* 317, 117–136.
- Chatterjee, N., Banerjee, M., Bhattacharya, A., Maji, A.K., 2010. Monazite chronology, metamorphism–anatexis and tectonic relevance of the mid-Neoproterozoic Eastern Indian Tectonic Zone. *Precambrian Res.* 179, 99–120.
- Chowdhury, P., Gerya, T., Chakraborty, S., 2017. Emergence of silicic continents as the lower crust peels off on a hot plate-tectonic Earth. *Nat. Geosci.* 10, 698–703.
- Clark, C., Collins, A.S., Santosh, M., Taylor, R., Wade, B.P., 2009. The PTt architecture of a Gondwanan suture: REE, U–Pb and Ti-in-zircon thermometric constraints from the Palghat Cauvery shear system, South India. *Precambrian Res.* 174, 129–144.
- Collins, A.S., Clark, C., Sajeev, K., Santosh, M., Kelsey, D.E., Hand, M., 2007. Passage through India: the Mozambique Ocean suture, high-pressure granulites and the Palghat-Cauvery shear zone system. *Terra Nov.* 19, 141–147.
- Condie, K.C., 2021. *Earth as an evolving planetary system.* Academic Press.
- Dalziel, I.W.D., 1995. Earth before Pangea. *Sci. Am.* 272, 58–63.
- Dasgupta, S., Bose, S., Das, K., 2013. Tectonic evolution of the Eastern Ghats belt, India. *Precambrian Res.* 227, 247–258.
- Deshmukh, T., Prabhakar, N., 2020. Linking collision, slab break-off and subduction polarity reversal in the evolution of the Central Indian Tectonic Zone. *Geol. Mag.* 157, 340–350.
- Dey, A., Choudhury, S.R., Mukherjee, S., Sanyal, S., Sengupta, P., 2019a. Origin of vesuvianite-garnet veins in calc-silicate rocks from part of the Chotanagpur Granite Gneiss Complex, East Indian Shield: The quantitative PTX CO₂ topology in parts of the system CaO-MgO-Al₂O₃-SiO₂-H₂O-CO₂ (+ Fe₂O₃, F). *Am. Mineral. J.* 104, 744–760.
- Dey, A., Karmakar, S., Ibanez-Mejia, M., Mukherjee, S., Sanyal, S., Sengupta, P., 2019b. Petrology and geochronology of a suite of pelitic granulites from parts of the Chotanagpur Granite Gneiss Complex, eastern India: Evidence for Stenian-Tonian reworking of a late Paleoproterozoic crust. *Geol. J.*
- Dey, A., Mukherjee, S., Sanyal, S., Ibanez-Mejia, M., Sengupta, P., 2017. Deciphering

- sedimentary provenance and timing of sedimentation from a suite of metapelites from the Chotanagpur Granite Gneissic Complex, India: Implications for Proterozoic Tectonics in the East-Central Part of the Indian Shield, in: *Sediment Provenance*. Elsevier, pp. 453–486.
- Ghosh, J.G., de Wit, M.J., Zartman, R.E., 2004. Age and tectonic evolution of Neoproterozoic ductile shear zones in the Southern Granulite Terrain of India, with implications for Gondwana studies. *Tectonics* 23.
- Hannisdal, B., Peters, S.E., 2011. Phanerozoic Earth system evolution and marine biodiversity. *Science* (80-). 334, 1121–1124.
- Harley, S.L., Fitzsimons, I.C.W., Buick, I.S., 1994. Reactions and textures in wollastonite-scapolite granulites and their significance for pressure-temperature-fluid histories of high-grade terranes. *Precambrian Res.* 66, 309–323.
- Hoffman, P.F., Schrag, D.P., 2002. The snowball Earth hypothesis: testing the limits of global change. *Terra Nov.* 14, 129–155.
- Karmakar, S., Bose, S., Sarbadhikari, A.B., Das, K., 2011. Evolution of granulite enclaves and associated gneisses from Purulia, Chhotanagpur Granite Gneiss Complex, India: evidence for 990–940 Ma tectonothermal event (s) at the eastern India cratonic fringe zone. *J. Asian Earth Sci.* 41, 69–88.
- Kooijman, E., Upadhyay, D., Mezger, K., Raith, M.M., Berndt, J., Srikantappa, C., 2011. Response of the U–Pb chronometer and trace elements in zircon to ultrahigh-temperature metamorphism: the Kadavur anorthosite complex, southern India. *Chem. Geol.* 290, 177–188.
- Kroener, A., Hegner, E., Collins, A.S., Windley, B.F., Brewer, T.S., Razakamanana, T., Pidgeon, R.T., 2000. Age and magmatic history of the Antananarivo Block, central Madagascar, as derived from zircon geochronology and Nd isotopic systematics. *Am. J. Sci.* 300, 251–288.
- Li, Z.-X., Bogdanova, Sv., Collins, A.S., Davidson, A., De Waele, B., Ernst, R.E., Fitzsimons, I.C.W., Fuck, R.A., Gladkochub, D.P., Jacobs, J., 2008. Assembly, configuration, and break-up history of Rodinia: a synthesis. *Precambrian Res.* 160, 179–210.
- Meert, J.G., Santosh, M., 2017. The Columbia supercontinent revisited. *Gondwana*

Res. 50, 67–83.

Meert, J.G., Van Der Voo, R., 1997. The assembly of Gondwana 800-550 Ma. *J. Geodyn.* 23, 223–236.

Mitchell, R.N., Zhang, N., Salminen, J., Liu, Y., Spencer, C.J., Steinberger, B., Murphy, J.B., Li, Z.-X., 2021. The supercontinent cycle. *Nat. Rev. Earth Environ.* 2, 358–374.

Mukherjee, S., Dey, A., Ibanez-Mejia, M., Sanyal, S., Sengupta, P., 2018. Geochemistry, U-Pb geochronology and Lu-Hf isotope systematics of a suite of ferroan (A-type) granitoids from the CGGC: Evidence for Mesoproterozoic crustal extension in the east Indian shield. *Precambrian Res.* 305, 40–63.

Mukherjee, S., Dey, A., Sanyal, S., Ibanez-Mejia, M., Dutta, U., Sengupta, P., 2017. Petrology and U–Pb geochronology of zircon in a suite of charnockitic gneisses from parts of the Chotanagpur Granite Gneiss Complex (CGGC): evidence for the reworking of a Mesoproterozoic basement during the formation of the Rodinia supercontinent. *Geol. Soc. London, Spec. Publ.* 457, 197–231.

Mukherjee, S., Dey, A., Sanyal, S., Sengupta, P., 2019. Proterozoic crustal evolution of the Chotanagpur Granite Gneissic complex, Jharkhand-Bihar-West Bengal, India: current status and future prospect, in: *Tectonics and Structural Geology: Indian Context*. Springer, pp. 7–54.

Nance, R.D., Murphy, J.B., 2013. Origins of the supercontinent cycle. *Geosci. Front.* 4, 439–448.

Nance, R.D., Murphy, J.B., Santosh, M., 2014. The supercontinent cycle: a retrospective essay. *Gondwana Res.* 25, 4–29.

Pant, N.C., Dasgupta, S., 2017. An introduction to the crustal evolution of India and Antarctica: the supercontinent connection. *Geol. Soc. London, Spec. Publ.* 457, 1–6.

Philpotts, A.R., Ague, J.J., 2009. *Principles of Igneous and Metamorphic Petrology*, Cambridge University Press.

Raith, M.M., Brandt, S., Sengupta, P., Berndt, J., John, T., Srikantappa, C., 2016. Element mobility and behaviour of zircon during HT metasomatism of ferroan basic granulite at Ayyarmalai, South India: Evidence for polyphase Neoproterozoic crustal growth and multiple metamorphism in the Northeastern Madurai

- Province. *J. Petrol.* 57, 1729–1774.
- Raith, M.M., Sengupta, P., Kooijman, E., Upadhyay, D., Srikantappa, C., 2010. Corundum–leucosome-bearing aluminous gneiss from Ayyarmalai, Southern Granulite Terrain, India: A textbook example of vapor phase-absent muscovite-melting in silica-undersaturated aluminous rocks. *Am. Mineral.* 95, 897–907.
- Santosh, M., 2020. The Southern Granulite Terrane: A synopsis. *Episodes J. Int. Geosci.* 43, 109–123.
- Sengupta, P., Dutta, U., Bhui, U.K., Mukhopadhyay, D., 2009. Genesis of wollastonite- and grandite-rich skarns in a suite of marble-calc-silicate rocks from Sittampundi, Tamil Nadu: constraints on the P–T–fluid regime in parts of the Pan-African mobile belt of South India. *Mineral. Petrol.* 95, 179.
- Sengupta, P., Raith, M.M., Kooijman, E., Talukdar, M., Chowdhury, P., Sanyal, S., Mezger, K., Mukhopadhyay, D., 2015. Chapter 20 Provenance, timing of sedimentation and metamorphism of metasedimentary rock suites from the Southern Granulite Terrane, India. *Geol. Soc. London, Mem.* 43, 297–308. <https://doi.org/10.1144/m43.20>
- Sequeira, N., Bhattacharya, A., Bell, E., 2022. The ~ 1.4 Ga A-type granitoids in the “Chottanagpur crustal block”(India), and its relocation from Columbia to Rodinia? *Geosci. Front.* 13, 101138.
- Singh, R.N., Thorpe, R., Kristic, D., 2001. Galena Pb isotope data of base metal occurrences in the Hesatu-Belbathan belt, eastern Precambrian shield, Bihar. *J. Geol. Soc. India (Online Arch. from Vol 1 to Vol 78)* 57, 535–538.
- Talukdar, M., Sarkar, T., Sengupta, P., Mukhopadhyay, D., 2022. The Southern Granulite Terrane, India: The saga of over 2 billion years of Earth’s history. *Earth-Science Rev.* 104157.
- Thompson, A.B., England, P.C., 1984. Pressure—temperature—time paths of regional metamorphism II. Their inference and interpretation using mineral assemblages in metamorphic rocks. *J. Petrol.* 25, 929–955.
- Zhao, G., Li, S., Sun, M., Wilde, S.A., 2015. Assembly, accretion , and break-up of the Palaeo- Mesoproterozoic Columbia supercontinent: record in the North China Craton revisited 6814. doi:10.1080/00206814.2010.527631

Chapter-2

**A synthesis of published geological and
geochronological information on the Chotanagpur
Granite Gneiss Complex and the Granulite Terrane
of South India**

Chapter 2

A synthesis of published geological and geochronological information on the Chotanagpur Granite Gneiss Complex and the Granulite Terrane of South India

Before going into detailed case studies, this chapter discusses all the available geological and geochronological information from the CGGC as well as the GTSI, so that the findings of the study can be put into regional context.

2.1. The Chotanagpur Granite Gneiss Complex

2.1.1. Boundary of the CGGC

The CGGC constitutes an integral part of the East Indian shield, covering an area of over 1,00,000 square kilometres. It is arcuate shaped, east-west trending mobile belt, that runs through the states of West Bengal, Bihar, Jharkhand and Chhattisgarh (reviewed in Mahadevan, 2002, Acharya, 2003, Mukherjee et al., 2019). The CGGC is bounded in the east by the Bengal basin sediments, and Phanerozoic Rajmahal traps cover its north-eastern margins. The northern margin is covered by Quaternary Indo-Gangetic sediments, which separates them from the Tertiary rocks of the Himalaya, and the Palaeoproterozoic rocks interweaved with them in the lower part of the Lesser Himalaya. The western of margin of CGGC is shared with the Central Indian Tectonic Zone (*sensu stricto*), consisting of the Mahakoshal supracrustal belt in the north-western part, and the Sausar mobile belt in the south-western part (Acharya and Roy, 2000). However, a major portion of this western boundary is covered by Gondwana sediments of Permian to mid Cretaceous age (Mahadevan, 2002). A part of the north-western boundary is also covered by Vindhyan sediments. The Singhbhum craton in the south is separated from the CGGC

by the Proterozoic mobile belt, the North Singhbhum Fold Belt (NSFB). The boundary of the CGGC and the NSFB is delineated by the Tamar Porapahar Shear Zone (Mahadevan, 2002) or the South Purulia Shear Zone (SPSZ) (Mazumdar, 1988).

2.1.2. Classification of the CGGC

Proper classification of the CGGC have been majorly hindered due to the dearth of proper geological and geochronological studies. This problem has been aggravated by urbanization and tropical weathering, resulting in paucity and scattered distribution of exposures. Earlier, Mahadevan, (2002); Sanyal and Sengupta, (2012) subdivided CGGC in five major blocks, on the basis of Chotanagpur Plateau and Gondwana sediments. However, considering the fact that (i) geomorphic features and/or younger Phanerozoic sediments should not be used for classifying the Precambrian CGGC, (ii) in the last few years, a considerable amount of geological and geochronological information has been published from the various parts of the CGGC, Mukherjee et al., (2019b) re-classified the CGGC into primarily three east-west domains (Domain I, II and III from south to north; Fig. 2.1), based on lithological, metamorphic, and geochronological characteristics. the northern and southern boundaries of the CGGC is bounded by the Monghyr- Saharsa Ridge Fault and South Purulia Shear Zone respectively. Another lineament runs through the middle of Domain I, bounding the Gondwana deposit exposures (Mandal, 2016), termed as Gondwana Boundary Fault (GBF; Mukherjee et al., 2019). The authors subdivided Domain I into two subdomains: Domain IA and IB, based on this GBF marker, but no major lithological or geochronological break is present. Domain II (Bihar Mica Belt: BMB) is distinguished from Domain III by the abundance of mica bearing intrusive pegmatites.

In the following section, salient petrological and geochronological features of the domains have been detailed. Table 2.1 summarises all the geochronological information available from each domain in the CGGC.

Domain IA

This domain is bounded by the GBF and SPSZ in the north and south respectively. It comprises the Raikera-Kunkuri region in the west, Raghunathpur-Adra-Ranchi in the central part and Saltora- Bankura-Bero area in the eastern part. The existing petrological information in the Saltora- Bankura-Bero area identifies a

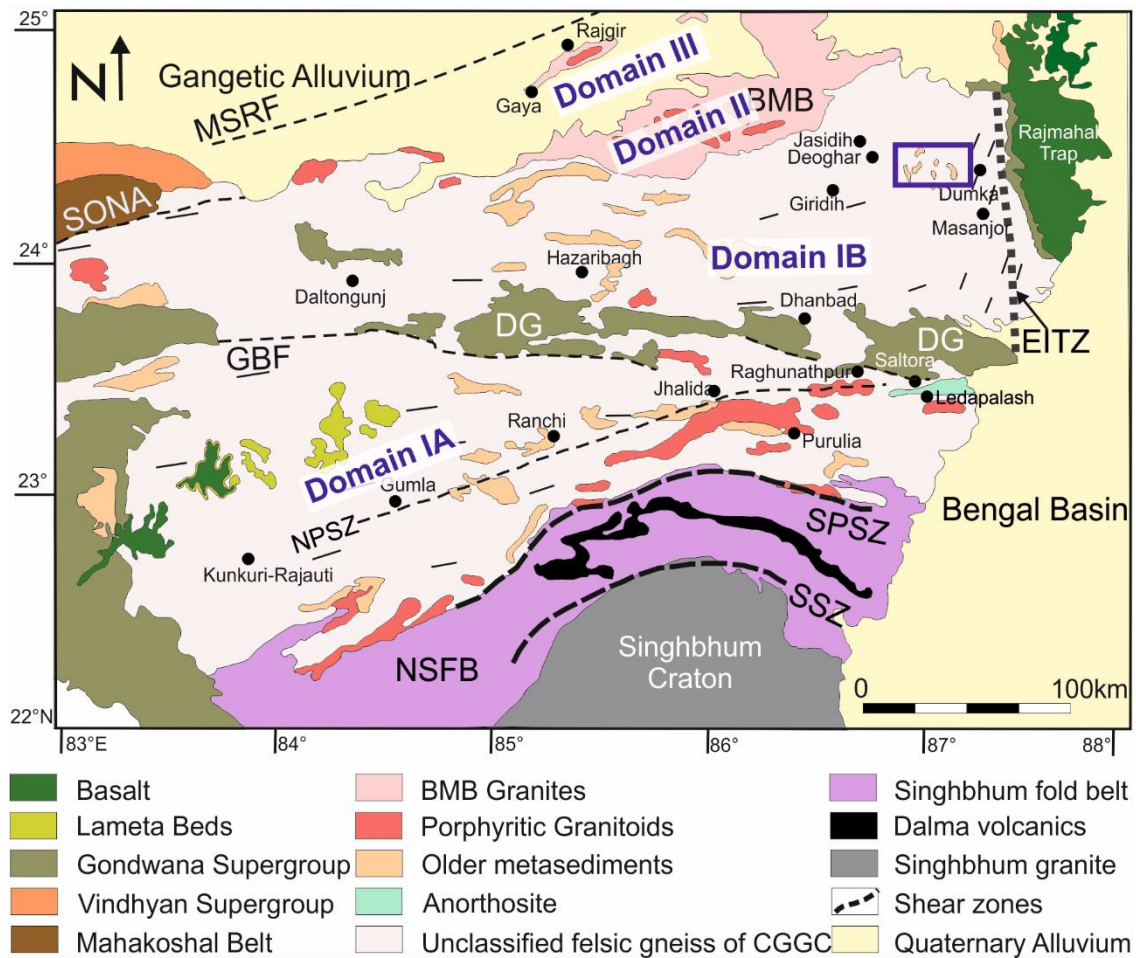


Fig. 2.1: Geological map of the CGGC modified after Mukherjee et al., (2019)) showing the threefold subdivisions. From south to north CGGC is divided into: Domain I, II and III. Domain I is again subdivided into Domain IA and IB.

migmatitic felsic gneissic country rock, which encloses mafic granulites and calc-silicate gneiss (Bhattacharyya and Mukherjee, 1987; Maji et al., 2008; Manna and Sen, 1974; Mukherjee et al., 2005; Roy, 1977; Sen and Bhattacharya, 1993). It is intruded by the massif type 'Bengal anorthosite' rocks. The metamorphic grade in the area varies between amphibolite in the western part, to granulite facies conditions in the eastern part (Chatterjee et al., 2008; Goswami and Bhattacharya, 2013,2010; Karmakar et al., 2011; Maji et al., 2008; Sanyal and Sengupta, 2012), however systematic variation along any geographic direction of metamorphic conditions is not evident. The lithounits of the area show folding, with E-W trending axial planes (Maji et al., 2008).

In the easternmost part, near Saltora-Santuri-Bero, high grade pelitic granulites and quartzo-feldspathic granulites are exposed. Maji et al., (2008) identified four metamorphic and three deformation events in the area. The first

tectonothermal event (M1) has been inferred to be a granulite facies metamorphic event (with a minimum P-T: ~5–6 kbar and ~750–850 °C), that led to the formation of migmatitic banding in the orthogneisses (S1, corresponding to D1) (Sen and Bhattacharya 1993; Maji et al. 2008). Chemical dating of monazite constrains the timing of this event at ~1700 Ma (Chatterjee et al., 2010). Subsequent metamorphism (M2-M3: inferred to be an amphibolite facies event) and deformation events (D2-D3) during ~1300-1100 Ma replaced the early granulite mineral assemblage variably (Maji et al., 2008). Near Saltora, intrusion of massif anorthosite body, termed as “Bengal Anorthosite”, occurred at ~1550 Ma (U-Pb zircon dating; Chatterjee et al., 2008), in between the D1 and D2 deformation events. The fourth metamorphic event (M4: Maji et al., 2008) is the most pervasive metamorphic event, the timing of which has been constrained between 1000-950 Ma (U-Pb zircon dating: Chatterjee et al., 2008; Th-U-Pb monazite dating: Chatterjee et al., 2010). The P-T conditions of this event is slightly controversial. While Chatterjee et al., (2010) constrained high-grade conditions ~850-900°C and 8.5-11 kbar from gabbro-anorthositic rocks, Maji et al., (2008) constrained lower values for peak conditions (650 ± 50 °C at 4–5 kbar). Near (West Bengal), migmatitic, nepheline syenite which intruded the migmatitic felsic gneiss got deformed and metamorphosed (Das et al., 2019; Goswami and Bhattacharyya, 2010). However, timing of this event has not been constrained. Yet, field studies indicate that the intrusion of nepheline syenite occurred post Grenvillian metamorphic event. The metamorphism and deformation occurred subsequently, under amphibolite facies conditions, ~700–750 °C and ~10 kbar (Das et al., 2019). This event may be related to a late Tonian-early Cryogenian tectonothermal event recorded by several workers in the area. Maji et al., 2008; Chatterjee et al., 2010 also recorded late Tonian ages (~900-820 Ma) from overgrowths on older monazites.

In the Raghunathpur area, multiple generations of felsic orthogneisses have been identified (porphyritic as well as deformed granitoids), consisting of calcareous and metapelitic enclaves (Baidya et al., 1989, 1987; Dunn, 1929; Karmakar et al., 2011; Goswami and Bhattacharyya 2013, 2010; Ray Barman et al., 1994). Two major metamorphic events (M1-M2) have been identified, associated with three deformation events (D1-D3). Intrusion of non-porphyritic granite at $\sim 1178 \pm 61$ Ma (Rb–Sr whole rock isochron age, Ray Barman and Bishui, 1994) is

contemporaneous with the development of S1, during first deformation (D1) (Goswami and Bhattacharyya, 2010). Timing of subsequent emplacement of porphyritic granite has been constrained to be 1071 ± 64 Ma (Rb–Sr whole rock age (Goswami and Bhattacharyya, 2010; Ray Barman and Bishui, 1994). Geochemical classification of these porphyritic granites indicates its shoshonitic to high K-calc alkalic nature, and has been inferred to have formed by mingling of crustal melts and mantle-derived mafic magma, which was succeeded by fractional crystallisation, within a continental collisional set up (Goswami and Bhattacharyya, 2013). In the south eastern part, near Adra, Mg–Al granulite and mafic granulites occur as enclaves within the migmatitic felsic gneiss. Monazite dating from the migmatitic felsic gneiss and Mg–Al granulites constrain a ~ 990 – 940 Ma pervasive metamorphic event (Karmakar et al., 2011). The peak conditions of this metamorphism were constrained at ~ 870 °C and 11 kbar, which was followed by a steeply decompressive P–T path (Karmakar et al., 2011). Similar temperatures (~ 800 °C), but lower pressures (6.5–7.5 kbar) were constrained by Goswami and Bhattacharyya, (2010), who suggested that M1 event spanned over both D1 and D2. The younger ages (850–775 Ma) constrained by Karmakar et al., (2011), are also consistent with those obtained by Baidya et al., (1987) (870 ± 40 Ma: K–Ar biotite of porphyritic granite and 810 ± 40 Ma: K–Ar muscovite of leucogranite) from Jaipur, West Bengal, in the western part. Although petrological characterisation of these late Tonian ages is lacking, these youngest age clusters are presumed to be related to the third deformational event D3.

Garnetiferous migmatitic felsic orthogneiss, pelitic schists and minor calc-silicate rocks define the major lithounits exposed in the south-central part of the domain, south of Ranchi, and has been intruded by porphyritic granite (Rekha et al., 2011; Sarkar and Jha, 1985). Zircon and monazite ages from the migmatitic felsic gneiss and metapelites constrain an early Neoproterozoic age (944 ± 9 and 921 ± 18 Ma), and has been interpreted as the timing of metamorphism. Rekha et al., 2011 also constrained emplacement ages of younger granites (928 ± 23 Ma) having older inherited components (1072 ± 17 and 1239 ± 66 Ma).

In the Raikera–Kunkuri region in the south-western part (Chhattisgarh), multiple generations of granites, along with pelitic schists, biotite/ hornblende/

chlorite schists, quartzite and dolerite/ sills (Singh and Krishna, 2009). Two mica-bearing grey granites, also intruded the crust during $\sim 1005 \pm 51$ Ma (Singh and Krishna 2009). However, younger ages (Rb–Sr isochron age of 815 ± 47 Ma) constrained from pink granite has been inferred to be a metasomatic event, related to Y-mineralisation (Singh and Krishna, 2009).

Domain IB

Domain IB is sandwiched between the GBF in the south and Domain II in the north (Fig. 2.1). From west to east, this domain covers the cities of Daltonganj, Jasidih, Deoghar, Dumka and Masanjore. Amongst these, granulite grade rocks are preserved primarily in the eastern part. The country rock of the domain is a felsic orthogneiss, varying in mineral assemblage and compositions. These orthogneisses underwent granulite facies metamorphism, with varying degree of partial melting. This country rock encloses various enclaves of meta-supracrustal, meta-mafic, and meta-igneous rocks. The general strike of the lithounits in the domain varies from E-W to NW-SE, while in the north eastern part, it becomes N-S. a minimum of three sets of deformation has been identified (Ghosh and Sengupta, 1999; Mukherjee et al., 2017; Sanyal and Sengupta, 2012). In the eastern part, near Dumka, Masanjore, the dominant lithounit is a migmatitic felsic gneiss, varying in composition. Compositional variation ranges between amphibolite-biotite gneiss (amphibole \pm biotite + K-feldspar + garnet + plagioclase + quartz + ilmenite) to charnockite gneiss (orthopyroxene + clinopyroxene + garnet + K -feldspar + plagioclase + quartz + ilmenite). Acharyya, (2003) constrained the emplacement ages of this migmatitic charnockite at 1624 ± 5 Ma. This migmatitic felsic gneiss encloses enclaves of Mg-Al granulites, khondalites (garnet-sillimanite gneiss), mafic granulites, and calc-silicate granulite. A porphyritic charnockite intrudes the host felsic gneisses, and contains rafts of the latter within it. Three stages of deformation have been identified for the host gneiss (Sanyal and Sengupta, 2012). The enclave suite of rocks preserves a gneissic banding that predates the foliation of the host felsic gneiss, and has been inferred to have been formed during D1. The E-W foliation of the host migmatitic felsic gneiss, is the pervasive foliation of the area. This foliation was subsequently refolded during

A synthesis of published geological and geochronological information

Table 2.1: Available geochronological information on tectonothermal events in the CGGC.

Domain IA

Age (Ma)	Method	Area	Rocktype	Event	Reference
595	U-Pb monazite	S margin of N-CGGC	Metapelite	hydrothermal alteration	Chatterjee et al. (2010)
784	U-Pb monazite	S margin of N-CGGC	blastoporphyrictic granite	magmatic/metamorphism+anatexis/E-W compression	Chatterjee et al. (2010)
810± 40	K-Ar muscovite	Purulia	alkali feldspar-rich leucogranitoid	magmatism	Baidya et. al. (1987)
815±47	Rb-Sr whole rock	Raikera-Kunkuri region, Jashpur district, Chhattisgarh	granite	age of metasomatism	Singh and Krishna (2009)
825-818	U-Pb monazite	Bero-Saltora	metapelite	metamorphic	Maji et. al. (2008)
850-775	U-Pb monazite	puruliya	migmatitic gneiss	deformation event	Karmakar et. al. (2011)
859	U-Pb monazite	S margin of N-CGGC	Metapelite	metamorphism+anatexis/E-W compression	Chatterjee et al. (2010)
860-830	U-Pb monazite	S margin of N-CGGC	blastoporphyrictic granite	magmatic/metamorphism+anatexis	Chatterjee et al. (2010)
870± 40	K-Ar biotite	Purulia	porphyritic biotite granitoid	magmatism	Baidya et. al. (1987)
921	U-Pb monazite	South of Ranchi	Foliated granite	metamorphism	Rekha et al. (2011)
921	U-Pb monazite	South of Ranchi	metapelite	metamorphism	Rekha et al. (2011)
923	U-Pb zircon	South of Ranchi	quartzofeldspathic gneiss xenolith	metamorphism	Rekha et al. (2011)
928	U-Pb zircon	South of Ranchi	Foliated granite	metamorphism	Rekha et al. (2011)
937	U-Pb monazite	S margin of N-CGGC	Metapelite	older thermal event??	Chatterjee et al. (2010)
944	U-Pb monazite	South of Ranchi	quartzofeldspathic gneiss xenolith	metamorphism	Rekha et al. (2011)
946	U-Pb monazite	S margin of N-CGGC	Metapelite	older thermal event??	Chatterjee et al. (2010)
947±27	U-Pb zircon	Saltora	anorthosite	granulite metamorphism	Chatterjee et. al. (2008)
965	U-Pb monazite	S margin of N-CGGC	blastoporphyrictic granite	older thermal event??	Chatterjee et al. (2010)
990-940 Ma	U-Pb monazite	Purulia	High Mg-Al granulite, migmatitic gneiss	high grade event with decompression	Karmakar et. al. (2011)

A synthesis of published geological and geochronological information

Table 2.1 contd.:

1005±51	Rb–Sr whole rock	Raikera-Kunkuri region, Jashpur district,	granite	emplacement age	Singh and Krishna (2009)
1021-967	U-Pb monazite	Bero-Saltora	metapelite, foliated granite	metamorphic/magmatic	Maji et.al. (2008)
1025	U-Pb zircon	South of Ranchi	quartzofeldspathic gneiss xenolith	metamorphism	Rekha et al. (2011)
1059±104	Rb–Sr whole rock	Kailash nath gufa	Alkali Syenite	magmatism	Krishna et al. (1996)
1065±74	Rb–Sr whole rock	Marne	Pink Granite	magmatism	Krishna et al. (1996)
1071± 64	Rb–Sr whole rock	Murguma-Purulia-Raghunathpur	hypersthene granite	retrogression in amp facies with ITD	Ray Barman et.al.(1994)
1072	U-Pb zircon	south of Ranchi	Foliated granite	metamorphism	Rekha et al. (2011)
1138±193	Rb–Sr whole rock	Kailash nath gufa	Diorite	magmatism	Krishna et al. (1996)
1176	U-Pb monazite	Bero-Saltora	metapelite	metamorphic	Maji et.al. (2008)
1178± 61	Rb–Sr whole rock	Murguma-Purulia-Raghunathpur	migmatite	retrogression in amp facies with ITD	Ray Barman et.al.(1994)
1200-1100	U-Pb monazite	puruliya	migmatitic gneiss	older tectonothermal events	Karmakar et. al. (2011)
1239	U-Pb zircon	south of Ranchi	Foliated granite	metamorphism	Rekha et al (2011)
1331±42	Rb–Sr whole rock	Nagam	granite		Krishna et al. (1996)
1422-1305	U-Pb monazite	S margin of N-CGGC	Metapelite	older thermal event??	Chatterjee et al (2010)
1550±12	U-Pb zircon	Saltora	anorthosite	magmatic	Chatterjee et.al.(2008)
1717-1446	U-Pb monazite	S margin of N-CGGC	blastoporphyratic granite	older thermal event??	Chatterjee et al. (2010)
1737-1664	U-Pb zircon				Saikia et al. (2017)
1800	U-Pb monazite	Purulia	migmatitic gneiss	inherited	Karmakar et. al. (2011)
1870-1691	U-Pb monazite	S margin of N-CGGC	blastoporphyratic granite	older thermal event??	Chatterjee et al. (2010)
1754±116	Rb–Sr whole rock				Dhurandhar et al. (2005)

A synthesis of published geological and geochronological information

Table 2.1 contd.:

<i>Domain IB</i>					
Age	Method	Area	Rocktype	Type of age	Reference
481±18	Bt and K-feldspar Rb–Sr			metamorphism?	Pandey et al.(1986)
560	U–total Pb xenotime	NE CGGC	Biotite–granodiorite gneiss?	metamorphism?	Chatterjee & Ghose (2011)
649	U–Pb monazite	E margin of N-CGGC	quartzofeldspathic gneiss	magmatic/metamorphism+anatexis/E–W compression	Chatterjee et al. (2010)
650–600	Th–U–total Pb monazite	E CGGC	Quartzo-feldspathic gneiss, metapelite	Metamorphism/hydrothermal event	Chatterjee et al. (2010)
850	Monazite	Daltanganj	high-grade gneiss		Kumar et al. (2022)
850–750	U–Pb monazite	Dumka-Deoghar	metapelitic enclave	metamorphism	Sanyal et. al. (2007)
872–838	U–Pb monazite	E margin of N-CGGC	quartzofeldspathic gneiss	magmatic/metamorphism+anatexis/E–W compression	Chatterjee et al. (2010)
876	U–Pb monazite	E margin of N-CGGC	quartzofeldspathic gneiss	magmatic/metamorphism+anatexis/E–W compression	Chatterjee et al. (2010)
876–784	U–Pb monazite		pelitic granulites		Chatterjee et al. (2018)
902	U–Pb zircon	deoghar-Dumka	felsic gneiss	Metamorphism	Mukherjee et al. (2017a)
910	U–Pb monazite	Dumka	Metapelite	Metamorphism	Rekha et al. (2011)
937	U–Pb monazite	E margin of N-CGGC	garnet–sillimanite bearing metapelite	older thermal event??	Chatterjee et al. (2010)
943	U–Pb zircon	deoghar-Dumka	felsic gneiss	Metamorphism	Mukherjee et al. (2017)
945	U–Pb monazite	Dumka	metapelite	Metamorphism	Rekha et al. (2011)
948 ± 22, 951 ± 2.7	U–Pb zircon	deoghar-Dumka	felsic gneiss	Metamorphism	Mukherjee et al. (2018)
950± 20	U–Pb monazite	Dumka	metapelite granulite	retrogression	Chatterjee et al.(2008)
954	U–Pb monazite	E margin of N-CGGC	blastoporphyratic granite	older thermal event??	Chatterjee et al. (2010)
965–930	U–Pb monazite	E margin of N-CGGC	quartzofeldspathic gneiss	older thermal event??	Chatterjee et al. (2010)
974–895	U–Pb monazite		Mica schist and Granitoids	metamorphism	Sequeira and Bhattacharya (2020)
970–950	U–Pb zircon	Dumka	metapelite	high-temperature granulite facies metamorphism	Dey et al. (2019c)
972 ± 28	U–Pb monazite	Daltanganj	granulite rock	metamorphism	Kumar and Diwedi (2019)
975±67 Ma	U–Pb monazite	Daltanganj	granitic gneiss	granulite metamorphism	Chatterjee & Ghosh (2011)
978	Monazite	Daltanganj	high-grade gneiss	metamorphism	Kumar et al. (2022)
979–942	U–Th–Pbmonazite	Dumka- Deoghar	quartzofeldspathic and pelitic gneiss	metamorphism	Sanyal et al. (2007)
995 ± 24	U–Pb monazite	Dumka	metapelite granulite	high grade metamorphism	Chatterjee et al. (2008)
1009	U–Pb zircon	Dumka	metapelite	metamorphic	Rekha et al. (2011)
1045	U–Pb zircon	N CGGC	Granite	Magmatism	Wanjari et. al. (2012)

A synthesis of published geological and geochronological information

Table 2.1 contd.:

1118-1088 1119 Ma,	U-Pb monazite Rb-Sr whole rock	Dumka-Deoghar Chianki	metapelitic enclave gneissic granite	metamorphism	Sanyal et al. (2007) Sarkar et al.(1986)
1183	U-Pb monazite	E margin of N-CGGC	garnet-sillimanite bearing metapelite	older thermal event??	Chatterjee et al. (2010)
1190 ± 26	U-Pb monazite	Dumka	metapelite granulite	high grade metamorphism	Chatterjee et al.(2008)
1270	U-Pb zircon	Dumka	metapelite	?	Rekha et al. (2011)
1272	U-Pb monazite	E margin of N-CGGC	blastoporphyratic granite	older thermal event??	Chatterjee et al. (2010)
1278	U-Pb monazite	E margin of N-CGGC	garnet-sillimanite bearing metapelite	older thermal event??	Chatterjee et al. (2010)
1331± 125	Rb-Sr whole rock	Jamua-Dumka		isobaric cooling age	Ray Barman et al. (1994)
1333	U-Pb zircon	Dumka	metapelite	?	Rekha et al. (2011)
1377	U-Pb zircon	Dumka	metapelite	?	Rekha et al. (2011)
1424 ± 64	U-Pb monazite	Daltanganj	felsic gneiss	emplacement	Kumar and Diwedi (2019)
1434 ±18	U-Pb monazite	Daltanganj	high-grade gneiss	emplacement	Kumar et al. (2022)
1435	U-Pb zircon	Dumka	metapelite	?	Rekha et al (2011)
~1469-1446	U-Pb zircon	Dumka-Deoghar	felsic gneiss	Magmatism	Mukherjee et al. (2018)
1447±11	U-Pb zircon	Dumka-Deoghar	felsic gneiss	Magmatism	Mukherjee et al. (2017)
1450-1350	U-Pb zircon	Dumka-Deoghar	felsic gneiss	emplacement	Sequeira et al. (2022)
~922	U-Pb zircon	Dumka-Deoghar	felsic gneiss	metamorphism	Sequeira et al. (2022)
1457±63	Rb-Sr whole rock	Jamua-Dumka	syenite	high grade meta with partial melting	Ray Barman et.al.(1994)
1462	U-Pb zircon	Dumka	metapelite	?	Rekha et al. (2011)
1480	U-Pb monazite	Dumka	metapelite	?	Rekha et al. (2011)
1515 ±5	U-Pb zircon	mor valley	massive charnockites	Intrusion age	Acharyya (2003)
1522±71 Ma	Rb-Sr whole rock		migmatite	magmatism	Mallik et al.(1991)
1580±33 Ma	Rb-Sr whole rock		migmatite	magmatism	Mallik et al.(1991)
1599±33 Ma	Rb-Sr whole rock		migmatite	magmatism	Mallik et al.(1991)
1624 ±5	U-Pb zircon	mor valley	hypersthene gneiss	crystallization age	Acharyya (2003)
1649	U-Pb zircon	Dumka	metapelite	high grade metamorphism	Rekha et al. (2011)
1628-1518	U-Pb monazite	Dumka-Deoghar	metapelitic enclave	metamorphism	Sanyal et al. (2007)
1629 ± 6	U-Pb zircon	Daltanganj	mafic granulite	emplacement	Kumar et al. (2021)
1638 ± 22	U-Pb zircon	Daltanganj	pelitic granulite	metamorphism	Kumar et al. (2021)
1680-1580	U-Pb zircon	Dumka	metapelite	high-temperature granulite facies metamorphism	Dey et al. (2019c)
1660-1270	U-Pb monazite	Dumka-Deoghar	metapelitic enclave	metamorphism?	Sanyal et al. (2007)
1700-1650	U-Pb zircon	Dumka-Deoghar	metapelitic enclave	sedimentation	Dey et al. (2017)
1710-1635	U-Pb zircon	Dumka-Deoghar	Augen Gneiss	Emplacement	Mukherjee et al. (2019)

Table 2.1 contd.:

1720	U-Pb monazite	E margin of N-CGGC	garnet–sillimanite bearing metapelite	older thermal event??	Chatterjee et al. (2010)
1741±65 Ma	Rb–Sr whole rock	northwest CGC	granite	?	Ray Barman et.al.(1994)
1824-1659	U-Pb monazite	E margin of N-CGGC	quartzofeldspathic gneiss	older thermal event??	Chatterjee et al. (2010)
1870-1720	U-Pb monazite	Dumka-Deoghar	metapelitic enclave	UHT metamorphism	Sanyal et al. (2007)
2600-1900	U-Pb zircon	Dumka	metapelite	detrital	Rekha et al. (2011)

Table 2.1 contd.:

Domain II

Age	Method	Area	Rocktype	Type of age	Reference
590	Apt Fission Track	BMB	Mica Pegmatite	cooling age	Nand Lal (1976)
595	Bt Fission Track	BMB	Mica Pegmatite	cooling age	Nand Lal (1976)
760	mus Fission Track	BMB	Mica Pegmatite	cooling age	Nand Lal (1976)
830	grt Fission Track	BMB	Mica Pegmatite	cooling age	Nand Lal (1976)
855±25	Mica Rb-Sr	Bhallupahari-Nirupahari	Mica Pegmatite	Intrusion age	Pandey et al. (1986b)
910±19	U-Pb, Pb-Pb	Dhajua, jharkhand	Pegmatite Cb-Ta	Intrusion age	Krishna et al. (2003)
960±50	Pb-Pb	Pichili	Pegmatite columbite-tantalite, Samarskite, monazite)	Intrusion age	Vinogradov et al. (1964)
1086-850	K-Ar		Granitoids		Sarkar (1980)
1020±46	Rb–Sr whole rock	BMB	Granite	emplacement	Mallik et. al. (1991)
1100-700 Ma	Fission track mica		Mica Pegmatite	cooling age	Mehta & Nagpal (1971)
1242±34	Rb–Sr whole rock	Binda-Nagnaha	Granite-gneiss		Pandey et al.(1986a)
1238±33	Rb–Sr whole rock	BMB	Granite	emplacement	Mallik et. al. (1991)
1285±108	Rb–Sr whole rock	BMB	Migmatitic Granite gneiss	emplacement	Mallik et. al. (1991)
1300–1100 Ma	Rb–Sr whole rock	BMB	Granite gneiss-Migmatite		Pandey et al.(1986a, b)
1590±30	Rb–Sr whole rock		Granitoids	emplacement	Pandey et al. (1986b)
1700–1650	²¹⁰ Pb age of galena	metasediments		sedimentation age	Singh et. al. (2001)
1717±102	Rb–Sr whole rock	S of BMB	migmatitic granite gneiss		Mallik et. al. (1991)

Table 2.1 contd.:

Domain III

Age (Ma)	Method	Area	Rocktype	Event	Reference
557±99	U-Pb xenotime	Bhagalpur	biotite–granodiorite gneiss	?	Chatterjee and Ghosh (2011)
768±11	U-Pb uraninite	Bhagalpur	biotite–granodiorite gneiss	metamorphism along EITZ	Chatterjee and Ghosh (2011)
929	U-Pb xenotime	Bhagalpur	biotite–granodiorite gneiss	granulite metamorphism	Chatterjee and Ghosh (2011)
1044±35	U-Pb zircon	Bathani	granite	emplacement	Wanjari et al. (2012)
1337±26	Rb–Sr whole rock	Sonbhadra	granite	emplacement	Wanjari et al. (2012)
1583±50	U-Pb xenotime	Gaya	porphyritic granite	cooling of granite	Chatterjee and Ghosh (2011)
1697±17	U-Pb Monazite	Gaya	porphyritic granite	emplacement	Chatterjee and Ghosh (2011)
1737-1664	Rb–Sr whole rock	Gaya	granite	emplacement	Saikia et al. (2017)

D2 and D3 deformation (Sanyal and Sengupta, 2012). The protolith of the porphyritic granite was inferred to have been emplaced during 1515 ± 5 Ma, between D1 and D2 event (Acharyya, 2003). A later generation of mafic dykes intrude the host felsic gneiss, and cuts across its foliation. However, these are also folded by open (D3) folds. Mg-Al granulites, comprising aluminous orthopyroxene, sillimanite, quartz, garnet, hercynite/magnetite, melt, have been inferred to have undergone ultra-high temperature metamorphism (>900 °C, > 8 kbar; Sanyal and Sengupta, 2012). However, Sanyal and Sengupta, 2012 constrained lower pressures from conventional thermobarometry (825 – 850 °C at 8 – 9 kbar), signifying cooling, following the ultra-high temperature metamorphism. Conventional thermobarometry from the porphyritic granite constrains a P-T at 6.5 ± 1 kbar and 700 ± 50 °C and (Sanyal and Sengupta, 2012), and has been correlated with the M3-D3 event.

Most of the geological and geochronological information are available between Deoghar-Dumka (Jharkhand). The country rock of the area is a magmatic felsic orthogneiss, that consists of metre to kilometre scale enclaves of pelitic granulite, mafic granulites, calc-silicate granulites and augen gneiss. Geochemical and isotopic studies by Mukherjee et al., (2018a, 2017) classify the host migmatitic felsic gneiss as a ferroan (A-type) granite. The host rock shows prominent N-S trending migmatitic bandings (S2), defining the regional fabric, which swerves around the enclosed enclaves. The pelitic granulite enclaves contain thick leucosomes, that define the earliest fabric of the area (S1). These S1 foliations are discordant with S2, and become parallel at their contact (Dey et al., 2019b). Dey et al., (2019) characterised this earliest metamorphic event in the area (M1) as a granulite facies metamorphism, which culminated at > 850 °C, medium pressure (~ 8 - 9 kbar), followed by a steep decompression. Subsequently, a second metamorphism (M2) affected the area, resulting in the folding of S1 in the pelitic granulites, and development of migmatitic bandings (S2) in the felsic gneiss, and a second generation of migmatitic foliation in the pelitic granulites (Dey et al., 2019b; Mukherjee et al., 2017). The P-T conditions of this metamorphism (M2) has been constrained to be $\sim 800 \pm 50$ °C and ~ 9 - 14 kbar (Chatterjee et al., 2008; Chatterjee, 2018; Dey et al., 2019b; Mukherjee et al., 2017). The mafic granulites of the area, on

the other hand records even higher pressures (12 ± 1 kbar and 800 ± 50 °C) (Dey et al., 2019c). This high-pressure, moderate temperature metamorphic peak was followed by a steeply decompressive path, defining a clockwise P-T path, corresponding to continent-continent collision (Dey et al., 2019b, 2019c; Mukherjee et al., 2017). A later generation of mafic dykes (now metamorphosed to amphibolites) intrude the S2 foliation of the host felsic gneiss. Subsequent to this, the S2 foliation, along with the mafic dykes are folded by two sets of coaxial folding (with N-S axial plane), corresponding to the third tectonothermal event of the area (Ghosh and Sengupta, 1999; Mukherjee et al., 2018b, 2017; Sanyal and Sengupta, 2012). A N-S trending foliation develops along the axial planes of the folded S2/dykes (S3). Locally, these S3 foliation and folded into open folds, with nearly vertical folds with E-W axial plane (Ghosh and Sengupta, 1999; Mukherjee et al., 2018b, 2017; Sanyal and Sengupta, 2012). The P-T conditions of this third and last tectonothermal event has been constrained to be $\sim 7.3 \pm 0.1$ kbar, 615 ± 15 °C and $\sim 7.7 \pm 0.7$ kbar and $\sim 650 \pm 60$ °C from the felsic orthogneiss and the mafic granulites (Dey et al., 2019b; Mukherjee et al., 2017). Similar P-T conditions have been obtained for M3 event from mafic dykes in the area (~ 700 °C and ~ 7.5 kbar: Mukherjee et al., 2018b; Ray et al., 2011). A gabbro-anorthositic body was reported from the Dumka region (Bhattacharjee et al., 2012), and intruded the felsic country rock, and got metamorphosed together during this M2-D2 event. A wide pressure-temperature range of metamorphism of the anorthosite has been constrained at ~ 511 – 915 °C and 5.0 – 7.5 kbar (Bhattacharjee et al., 2012). Multiple generations of pegmatitic veins cross cut all the lithounits. However, structural data and proper characterisation is not available in the existing database. In the easternmost margin, a highly tectonised, N-NNE trending zone, termed the 'Eastern Indian Tectonic Zone (EITZ)', has been described by Chatterjee et al., (2010). The authors have bracketed the peak P-T of metamorphism for this event at 11.3 kbar and 800°C, followed by an isothermal pressure increase to 12.7 kbar and retrogression to 9 kbar and 730°C which they related with the shearing and anatexis event along EITZ.

The oldest magmatic event is the emplacement of a porphyritic granite (now augen gneiss) between ~ 1710 and 1635 Ma, in a continental arc setting (Mukherjee et al., 2019a). The timing of sedimentation of the protoliths of the metasedimentary enclaves have been constrained from detailed detrital zircon study by Dey et al.,

(2017) between ~1700-1650 Ma (U-Pb zircon ages from Dey et al., 2017 and Pb-Pb isotopic ages from Singh et al., 2001). Additionally, the authors also inferred that these sediments have been sourced from Archaean/ Palaeoproterozoic terranes (Dey et al., 2017; Rekha et al., 2011). U-Pb zircon and monazite age dating from the pelitic granulites constrains the timing of M1 metamorphism between of ~1680–1580 Ma (Dey et al., 2019b). Rekha et al., (2011) obtained similar timing of Palaeoproterozoic metamorphism from metapelites and quartzo-feldspathic gneiss near Dumka. Th-U-total Pb chemical ages from monazites also yield similar ages for the M1 metamorphism (~1684-1659 Ma: Chatterjee et al., 2010; ~1628-1518 Ma: Sanyal and Sengupta, 2012). The emplacement of the protolith of the migmatitic felsic gneiss was constrained to be (during ~1470-1350 Ma) in an extensional tectonic setting, possibly linked with the breakup of Columbia supercontinent (Mukherjee et al., 2018a, 2017; Sequeira et al., 2022). Mukherjee et al., (2018a) inferred that this ~1450 Ma felsic orthogneiss protolith was derived via high temperature partial melting of Paleoproterozoic crustal source (Lu–Hf model age: ~1800–1600 Ma) with limited input from mantle. Mukherjee et al., (2019a) showed that the geochemical characteristics of these felsic orthogneisses resembled that of the melt generated from the ~1700 Ma old porphyritic granite. The workers also showed that extraction of this melt in small pulses, combined with crystal fractionation occurring after emplacement led to the compositional diversity observed in the ~1450 Ma felsic orthogneisses (Mukherjee et al. 2019). Emplacement of a syenitic rock, and a charnockite in the Dumka-Jamua area, Jharkhand, has been inferred to be 1457 ± 63 Ma and 1331 ± 125 Ma (Rb–Sr whole-rock ages) respectively (Ray Barman et al., 1994). The timing of the second metamorphic event M2 has been constrained from zircon and monazite dating at ~1000–930 Ma (Chatterjee et al., 2008, 2010; Dey et al., 2019b; Mukherjee et al., 2017; Rekha et al., 2011). A younger age cluster ~870-650 Ma has been constrained by Chatterjee et al., (2010), and was linked to the tectonothermal event in the EITZ. Zircon and monazite dating constrains the timing of the third (amphibolite facies) metamorphic event (M3) within a time span of ~920-880 Ma (Chatterjee and Ghose, 2011; Mukherjee et al., 2018a; Sanyal and Sengupta, 2012).

In and around Dhanbad and Hazaribag, west of Jasidih, petrological and geochronological information is not available much. In these areas, the general strike of the lithounits varies between E-W to NW-SE. In the Dhanbad district,

amphibolite facies banded gneisses, contain enclaves of olivine-orthopyroxene bearing metanorites, hornblende bearing schists and gneisses and quartzites. Three sets of folding are identified, with development of E-W to NW-SE trending axial planar foliation, corresponding to the second deformation event (Sarangi and Mohanty, 1998).

In Hazaribagh (Jharkhand), amphibolites, calcareous and pelitic rocks contain a E-W trending schistosity. Three generations of folding have been identified, the first two being tight and coaxial, while the third is an open fold (Mahadevan, 2002; Roy Chowdhury, 1979). The youngest age (whole rock Rb–Sr isochron date 481 ± 18 Ma; Pandey et al., 1986b) has been recorded from biotite-K-feldspar from a migmatite.

In the Daltonganj area migmatites and granite gneiss are intercalated with graphite-bearing pelitic schists, quartzites, limestones and are intruded by mafic-ultramafic, anorthositic-komatiitic (Bhattacharya et al., 2010). The ultramafic rocks contain magnetite, fluorite and base metal mineralization (Ghose 1983; Sinha and Bhattacharya, 1995; Soni et al., 1991). High grade conditions (850–800 °C; Chatterjee and Ghose, 2011) corresponding to formation of gneissic foliation have been constrained from granite gneiss. Non-foliated granitic/granodioritic rocks intrude the granite gneisses (Ghose, 1983; Mazumdar, 1988; Rode, 1948). Conditions of partial melting of granulites and metapelites have been constrained between ~2–6 kbar and ~650–800 °C (Srivastava and Ghose, 1992). Ray Barman and Bishui, 1994 dated the timing of granitic magmatism at $\sim 1741 \pm 65$ Ma, which was subsequently metamorphosed during $\sim 975 \pm 67$ Ma (dating of xenotime Chatterjee and Ghose, 2011). Very recent monazite dating by constrained the timing of pre-peak, peak and post-peak (retrograde) metamorphism at ~ 1434 Ma, ~ 978 Ma and ~ 850 Ma respectively from the high-grade metamorphosed island arc granite gneisses in the area (Kumar et al., 2022). The P-T conditions for peak metamorphism has also been constrained to be ~ 8.65 - 9.42 kbar and ~ 772 - 788 °C (Kumar et al., 2022). The age of high-grade metamorphism has also been constrained from granulites near Palamau (~ 972 Ma; Kumar and Dwivedi, 2019). An older Palaeoproterozoic metamorphic age (1638 ± 22 Ma) has been recorded from the pelitic granulites near Daltonganj, while emplacement of protoliths of mafic

granulites have also been constrained at 1629 ± 6 Ma (Kumar et al., 2021). The granite gneiss and metapelites record three deformation events (Lahiri and Das, 1984; Patel, 2007). Mafic dykes and pegmatitic veins intrude the lithounits subsequent to D3. Near Tatapani, the calc-silicate rocks preserve a rare vesuvianite-bearing assemblage. The conditions of vesuvianite formation have been constrained to be 4-6 kbar ~ 590 – 780 °C, under highly aqueous conditions (Dey et al., 2019a; Patel, 2007).

Domain II

This domain, termed as the Bihar Mica belt (BMB) is sandwiched between the GBF in the south, and Domain III in the north. The lithounits include a metasedimentary sequence, comprising hornblende schists, micaceous quartzites, calc-silicate rocks and conglomerates. The calc-silicate rocks are occasionally associated with economic grade, base metal deposits (Ghose, 1992). These metasedimentary units overlie high grade rocks of the CGGC, with local conglomerate base (Ghose and Mukherjee, 2000). Sedimentation ages in the BMB have been constrained to be ~ 1700 – 1650 Ma from Pb-Pb galena ages of base metal deposits (Singh et al., 2001). A migmatitic granite gneissic rock, south of BMB has been dated to be 1717 ± 102 Ma (Rb-Sr whole rock age: Mallik et al., 1991). Three deformational events have been recorded in the metasedimentary units, the first two are the most pervasive and produced the E-W trending prominent foliation. Gabbro anorthosite, dolerite dykes, large granitoid bodies and REE/ rare metal bearing mica pegmatites extensively intrude the whole litho-package. Emplacement of granitoids occurred syn- to post-D2 (1300–1100 Ma). However, oldest emplacement ages dates back to ~ 1600 Ma (Misra and Dey, 2002; Rb–Sr mineral isochron and whole-rock ages; Pandey et al., 1986a). On the other hand, the multiple generations of pegmatites intruded pre-D2 to post-D3 (Mahadevan, 2002). Conditions of emplacement of granite plutons have been estimated at ~ 5 kbar and >1000 °C, under anhydrous conditions during post-collisional extensional setting (Misra and Dey, 2002). Emplacement ages of oldest rare metal/ REE bearing mica pegmatite in the BMB has been estimated to be $\sim 960 \pm 50$ Ma (Pb/Pb age; Vinogradov et al., 1964) and $\sim 910 \pm 20$ Ma (Krishna et al., 2003). Fission track ages of apatite (~ 590 Ma), biotite (~ 590 Ma), garnet (~ 830 Ma) and muscovite (~ 760

Ma) has been correlated with the final timing of exhumation of these mica pegmatites (Lal et al., 1976).

Domain III

This domain lies to the north of BMB, and comprises meta-supracrustals and migmatitic quartzo-feldspathic gneisses. The sedimentary rocks of the Munger Group and the Rajgir Groups overlie the basement gneiss of the CGGC, and their boundary is demarcated by conglomerate horizon (Ghose and Mukherjee, 2000). The supracrustals include low grade quartzites, phyllites, associated with felsic and mafic-ultramafic intrusives.

A porphyritic rock forms the basement of the sedimentary units near Gaya, and a biotite gneiss near Bhagalpur (Chatterjee and Ghose, 2011). The emplacement ages of the granitoids have been constrained at $\sim 1697 \pm 17$ Ma (Chatterjee and Ghose 2011). Cooling ages for the porphyritic granitoids have been estimated as 1583 ± 50 Ma (U-Pb xenotime ages, Chatterjee and Ghose, 2011). These porphyritic granites have been classified geochemically as extensional (A-type) variety (Yadav et al. 2014). Volcano-sedimentary sequence, present in and around Bathani village consists of banded iron formation (BIF), chert bands, garnet-mica schist and mafic-intermediate volcanics (Saikia et al., 2014). Bimodal volcanism (with calc-alkaline trend of the intermediate-felsic magmatism and tholeiitic affinity of the basalt), indicates an island-arc setting (Saikia et al., 2017, 2014). Felsic magmatism has been recorded during ~ 1750 – 1660 Ma, followed by subsequent metamorphism (~ 930 Ma and ~ 768 Ma). This earlier metamorphism has been characterised to be in granulite grade, while the later one has been associated with shearing linked with EITZ (Chatterjee et al., 2010).

The study area falls within the Domain IB, in the north-eastern part of the CGGC, near Deoghar- Dumka (Fig. 2.1). The study area has been described in details in Chapter 3.

2.2. The Granulite Terrane of South India

Situated amidst the Archaean Dharwar Craton (DC) to the north and the Proterozoic Eastern Ghats Belts to the north-east, the GTSI is subdivided into different blocks or units (Fig. 2.2a; Brandt et al., 2014 and references therein): the Northern Granulite terrane (NGT), the Madurai Block (MB) and Cauvery Shear System (CSS). Before going into the details of the published information from these blocks, it is important to clarify the terminology. Different working groups have used different nomenclature for this terrane. Some prefer the term, 'Southern Granulite Terrane' for the whole terrane south of Dharwar Craton, while others (e.g., Braun and Kriegsman, 2003; Janardhan, 1999) refer to the southern part of the granulite terrane (below PCSZ) by this term ('Southern Granulite Terrane'), while portions north of it is termed as NGT (Northern Granulite Terrane). In order to avoid this confusion, the nomenclature 'Granulite Terrane of South India (GTSI)' (Chowdhury et al., 2013; Dutta et al., 2011; Karmakar et al., 2017; Talukdar et al., 2020) has been used to refer to the entire granulite block, starting from the NGT. Table 2.2 summarises all the geochronological information available from the different parts of the GTSI.

The Northern Granulite Terrane

The northernmost unit, known as the NGT or Salem Block, is juxtaposed against the DC, and is dominated by Meso-Neoproterozoic (~3360-2530 Ma emplacement age; Ghosh et al., 2004; Noack et al., 2013; Peucat et al., 2013) felsic orthogneisses with mafic-ultramafic complexes and BIFs occurring as enclaves. All lithologies show imprints of early Palaeoproterozoic (~2570-2470 Ma) HP granulite facies metamorphism (Anderson et al., 2012; Ghosh et al., 2004; Sato et al., 2011).

The Madurai Block

The emplacement ages of the felsic orthogneisses of the MB that constitute the southern part of the GTSI cluster in two groups: While orthogneisses in the western part of the MB were emplaced between ~2700-2440 Ma (Brandt et al., 2014; e.g., Ghosh et al., 2004; Plavsa et al., 2012), orthogneisses of the eastern part (in and around Sirumalai and Alambadi) record ~1740-1620 Ma emplacement ages

(Brandt et al., 2014 and references cited therein). These older Palaeoproterozoic granites have been characterized as subduction related granitoids (Brandt et al., 2014). granites have been characterised The Neoarchaeon/ early Palaeoproterozoic charnockites of MB with rare metapelitic xenoliths bear scarce evidences of high-grade metamorphism at ~2520-2430 Ma (Brandt et al., 2014, 2011, 2010). Rare reports of Archaean alkaline magmatism in the southern part of MB include those in Korangani and Kambamettu (Renjith et al., 2016).

In contrast to the NGT, the MB contains abundant metamorphosed platform sedimentary sequences (metapelites-meta-psammite-marbles-calc silicate-quartzite) that usually overlie the orthogneissic basement. Multiple batholiths of A-type granites and anorthosites intruded the orthogneisses and the metasediments during the mid-Neoproterozoic time (e.g., Brandt et al., 2014). Rare imprints of late Neoproterozoic magmatism include pegmatites (~555 Ma; Plavsa et al., 2015) and alkaline rocks near Sivamalai (~590 Ma; Upadhyay and Raith, 2006). Early Neoproterozoic metamorphic imprints are also preserved in the MB (~1020-700 Ma; Brandt et al., 2014; Kooijman et al., 2011; Plavsa et al., 2014). Late Neoproterozoic to early Cambrian high-grade metamorphic imprints is widely reported within the MB from the metasedimentary assemblages (e.g., Collins et al., 2007; Kooijman et al., 2011; Raith et al., 1997) as well as from the basement orthogneisses (Brandt et al., 2014; Ghosh et al., 2004; Plavsa et al., 2012). The timing of this metamorphism is well-constrained between ~650-500 Ma (Collins et al., 2007; Plavsa et al., 2012; Sengupta et al., 2015). This late Neoproterozoic to early Cambrian imprint, mainly recorded by metapelitic Mg-Al granulites within the MB, bear evidence of HP-Ultra-high temperature (UHT) metamorphism culminating along a clockwise (CW) P-T-t path (e.g., Brandt et al., 2011; Raith et al., 1997; Sajeev et al., 2004). The Mg-Al granulites in the MB occur in a broadly north-south trending zone, termed as the Kambam UHT belt (Brandt et al., 2011).

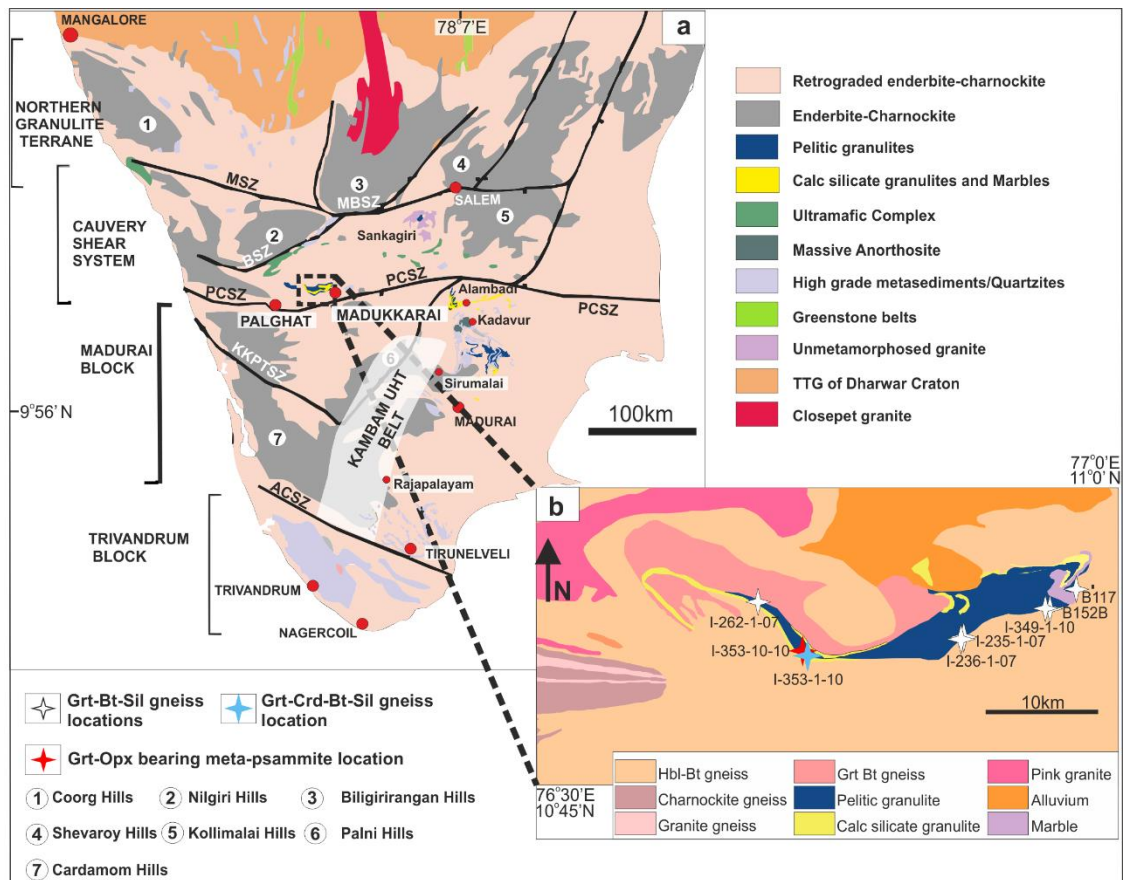


Fig. 2.2(a) Geological map of southern peninsular India showing the different blocks and cross cutting shear zones (modified after Sengupta et al., 2015). The dotted box depicts the studied area. (b) Map showing the sample locations near Madukkarai (modified after Naha et al. (1997) and Geological Quadrangle map (58B) by Geological Survey of India). MSZ: Moyar Shear Zone, MBSZ: Moyar-Bhavani Shear Zone, BSZ: Bhavani Shear Zone, PCSZ: Palghat Cauvery Shear Zone, KKPTSZ: Karur-Kambam-Painavu-Trichur Shear Zone, ACSZ: Achankovil Shear Zone. Mineral abbreviations after (Kretz, 1983).

The Cauvery Shear System

Sandwiched between the NGT and MB, the CSS comprises a network of perceived shear zones (Moyar Shear Zone, Moyar-Bhavani Shear Zone, Bhavani Shear Zone), with the Palghat Cauvery shear Zone (PCSZ) running along its southern margin. It exposes diverse lithologies aging between late Mesoarchean to early Cambrian. Late Neoproterozoic (~2850-2450 Ma) Mg-rich charno-enderbites (Brandt et al., 2014; Ghosh et al., 2004; Raith et al., 2016, 1999; Saitoh et al., 2011; Santosh et al., 2013; Shaji et al., 2014; Yellappa et al., 2012) containing remnants of ~3200-

2520 Ma old BIFs and mafic-ultramafic complexes, interpreted as ancient oceanic crust (Chowdhury et al., 2013; reviewed in Talukdar et al., 2022). These BIFs, mafic-ultramafic and anorthositic bodies are variously exposed in and around PCSZ, near Sittampundi, Mahadevi, Devanur, Kanjamalai, Namakkal, Mettupalyam etc. (reviewed in Talukdar et al., 2022). The anorthosite layers in Sittampundi are associated with metamorphosed counterparts of mafic/ ultramafic and BIFs. The timing of emplacement of these anorthositic body has been constrained at $\sim 2522 \pm 12$ Ma (U-Pb zircon dating; He et al., 2021), that is slightly younger than those constrained by Sm-Nd whole rock ages (2935 ± 60 ; Bhaskar Rao et al., 1996). Interlayered and co-metamorphosed mafic/ultramafic and BIFs, without anorthosite is also reported (e.g., Talukdar et al., 2022; Yellappa et al., 2016). Neoproterozoic magmatic/ emplacement ages (~ 2670 - 2600 Ma; Raith et al., 2016) have also been constrained recently from charnockite with enclaves of mafic dykes from Ayyarmalai, associated with a rare aluminous corundum bearing rock (Karmakar et al., 2020; Raith et al., 2016, 2010). The felsic orthogneisses with its enclaves underwent HP granulite facies metamorphism (~ 750 - 830 °C, ~ 11 - 14 kbar; Chowdhury and Chakraborty, 2019; Talukdar et al., 2020) during the early Palaeoproterozoic (~ 2526 - 2430 Ma; Brandt et al., 2014; George et al., 2019; Ghosh et al., 2004; Mohan et al., 2013; Raith et al., 2016; Saitoh et al., 2011; Samuel et al., 2018; Santosh et al., 2013; Shaji et al., 2014). Mid Neoproterozoic magmatic ages (~ 820 - 740 Ma) are dominantly from granite and plagiogranites, and few mafic rocks (Ghosh et al., 2004; Santosh et al., 2012; Sato et al., 2011). Rare mid-Neoproterozoic metamorphic imprints are also documented in a few areas (~ 900 - 715 Ma; Brandt et al., 2014; Mohan et al., 2013; Rao et al., 1996; Yellappa et al., 2012). Late Neoproterozoic HP-UHT metamorphism has been reported from Mg-Al granulites at several localities near PCSZ and has been linked with the Kambam UHT belt of the MB (Brandt et al., 2014). CW P-T-t paths have been reconstructed for most occurrences of these Mg-Al granulites (Clark et al., 2009; Shimpo et al., 2006 etc.). Counter-clockwise P-T-t paths were postulated as well for some occurrences (e.g., Sajeev et al., 2009). However, the existence of UHT metamorphism in the PCSZ has been questioned by Raith et al., (2010) and Sengupta et al., (2009), who estimated lower temperatures (~ 700 - 800 °C) from corundum-bearing aluminous paragneisses and wollastonite-grandite rich skarn rocks respectively.

Geochronological studies estimate the timing of this metamorphism at ~633-455 Ma (Brandt et al., 2014; Collins et al., 2007a; Sengupta et al., 2015 and some others).

The Madukkarai Supracrustal Unit

Meta-supracrustal packages are rare in the PCSZ and usually occur only in small stretches (Raith et al., 2010; Sengupta et al., 2009). The Madukkarai Supracrustal Unit (MSU), exposed in the western part of the PCSZ, represents, by far the largest occurrence (stretching ~40 km) of meta-supracrustal sequences in and around the PCSZ (Fig. 2.2). The MSU comprises broad sequences of interlayered metapelites, meta-psammites, quartzites, marbles and calc silicate rocks (Fig. 2.2a & b) that were possibly deposited in a platform environment (Raith et al., 2016; Sengupta et al., 2015). These meta-supracrustals overlie migmatitic enderbitic gneisses that were widely retrogressed to hornblende-biotite gneisses. Field relationships and preliminary geochronological data from the immediate orthogneiss basement (LA-ICPMS U-Pb zircon emplacement ages of ~2700-2500 Ma, S. Brandt, unpublished data) indicate that it is a part of the late Neoproterozoic felsic country rock of the PCSZ. Naha et al., (1997) identified two main sets of deformation (D1-D2) in the MSU, where isoclinal D1 folds have been superimposed by another set of coaxial D2 folds in the metapelites and associated calc silicate rocks. In a preliminary study, peak-metamorphic P-T conditions of ~5-6 kbar and ~650-700°C were constrained for rocks of the MSU (Srikantappa and Jagannathappa, 1990) Sm-Nd garnet whole rock age data for garnet-sillimanite gneisses and calc silicate rocks indicate deposition of the sedimentary protoliths between ~1900-610 Ma and peak metamorphism at ~610-490 Ma (Meißner et al., 2002). Similar depositional ages, spanning between mid-Palaeoproterozoic to Neoproterozoic, have also been constrained from other areas in and around the PCSZ (Raith et al., 2010; Sengupta et al., 2015) as well as from the MB (e.g., Kooijman et al., 2011; Plavsa et al., 2014).

Table 2.2: Available geochronological information on tectonothermal events in the GTSI. Cauvery Shear System

	Age (Ma)	Method	Area	Rocktype	Reference
Archaean to Palaeoproterozoic metamorphism	2526±38		Kolli massif	garnet pyroxenite	George et al., 2019
	2525±6	LA-ICP-MS Zircon U-Pb	Nilambur, E of Nilgiri, Kerala	Amphibolite	Shaji et al. 2014
	2524±6	LA-ICP-MS Zircon U-Pb	Nilambur, E of Nilgiri, Kerala	TTG	Shaji et al. 2014
	2520±27	LA-ICP-MS zircon U-Pb	Nilgiri block	Garnet pyroxenite	Samuel et al., (2018)
	2508±16	LA-ICP-MS Zircon U-Pb	Nilambur, E of Nilgiri, Kerala	Amphibolite	Shaji et al. 2014
	2503±28	LA-ICP-MS Zircon U-Pb	Nilambur, E of Nilgiri, Kerala	Meta gabbro	Shaji et al. 2014
	2501 ± 13	LA-ICP-MS zircon U-Pb	Nainarmalai	Granodiorite gneiss	Plavsa et al. (2015)
	2491 ± 11	LA-ICP-MS zircon U-Pb	Near Trichengodu	Grt-Opx tonalites	Brandt et al. (2014)
	2490-2470	LA-ICP-MS-Zircon, U-Pb	Near Kanjamalai	Gt-Ky±Bt bearing Felsic gneiss	Anderson et al. 2012
	2486 ± 16	LA-ICP-MS zircon U-Pb	Kanvayapatti	Enderbite	Brandt et al. (2014)
	2484 ± 4	SHRIMP U-Pb zircon	Kanjamalai	Quartzo-feldspathic gneiss	Saitoh et al., 2011
	2480 ± 20	ID-TIMS zircon U-Pb	Mettupalyam	Amphibolite and mafic granulite	Ghosh et al. (2004)
	2480	LA-ICP-MS zircon U-Pb	Ayarmalai	charnockite	Raith et al., 2016
	~2479	LA-ICP-MS zircon U-Pb	Mahadevi Layered Complex	Felsic orthogneiss	Talukdar et al., 2020
	2478±28	LA-ICP-MS zircon U-Pb	Nilgiri block	Garnet pyroxenite	Samuel et al., (2018)
	2478 ± 3	SHRIMP U-Pb zircon	Kanjamalai	Charnockite	Saitoh et al. (2011)
	2471 ± 69	SHRIMP U-Pb zircon	Agali Hills	Meta granite	Santosh et al. (2013)
	2461 ± 15	LA-ICP-MS zircon U-Pb	Sittampundi	Anorthosite	Ram Mohan et al. (2013)
	2442 ± 20	LA-ICP-MS zircon U-Pb	Kanjamalai	Granite	Sato et al. (2011b)
	2434 ± 17	Lu-Hf isotope of whole-rock	Kanjamalai	Metabasite	Noack et al. (2013)
2355 ± 22	Sm-Nd garnet	Moyar Shear Zone	Basic granulite	Meißner et al. (2002)	
Tonian metamorphism/thermal imprint??	899 ± 270, 807 ± 210	SHRIMP U-Pb zircon	Devanur	Trondhjemite	Yellappa et al. (2012)
	839 ± 8	LA-ICP-MS zircon U-Pb	Near Paramati	Migmatitic Bt gneiss	Brandt et al. (2014)
	804 ± 15	LA-ICP-MS zircon U-Pb	Kanvayapatti	Enderbite	Brandt et al. (2014)
	794 ± 5	LA-ICP-MS zircon U-Pb	Paramati	Migmatitic Bt gneiss	Brandt et al. (2014)
	726 ± 9	Sm-Nd whole-rock	Cauvery ShearZone	Metabasite	Bhaskar Rao et al.(1996)
	722 ± 13	SHRIMP U-Pb zircon	Namakkal	Mafic granulite	Ghosh et al. (2004)
	715 ± 189	LA-ICP-MS zircon U-Pb	Sittampundi	Meta anorthosite	Ram Mohan et al.(2012)
Ediacaran metamorphism	633-487	LA-ICP-MS zircon U-Pb	Sankagiri	Metapelite	Sengupta et al., 2015
	615+/-11		Ayyarmalai	corrundum bearing leucosome	Raith et al., 2010
	614 ± 160	Sm-Nd garnet	Moyar Shear Zone	Enderbitic gneiss	Meißner et al. (2002)
	610-520		Ayarmalai	Mafic granulite	Raith et al., 2016
	604 ± 15, 540 ± 13	Rb-Sr biotite	Moyar Shear Zone	Retrogressed enderbite	Meissner et al. (2002)
	594 ± 25	Rb-Sr muscovite	Moyar Shear Zone	Retrogressed enderbite	Meißner et al. (2002)
	567-525	LA-ICP-MS zircon U-Pb	Namakkal	Psammitic paragneiss	Sengupta et al., 2015

Table 2.2contd.:

Ediacaran metamorphism	560 ± 17, 610	Sm–Nd garnet	Madukarai	Sillimanite–garnet schist	Meißner et al. (2002)
	556 ± 14	LA-ICP-MS zircon U–Pb	South of Aniyapuram	Migmatitic leucosome	Plavsa et al. (2015)
	552 ± 13	Sm–Nd garnet	Bhavani Shear Zone	Meta dolerite	Meisner et al. (2002)
	549 ± 28	LA-ICP-MS zircon U–Pb	Manamedu	Plagiogranite	Sato et al. (2011a)
	541 ± 3	ID-TIMS zircon U–Pb	Namakkal	Migmatitic Bt gneiss (neosome)	Ghosh et al. (2004)
	539 ± 8	LA-ICP-MS zircon U–Pb	Paramati	Migmatitic Bt gneiss	Brandt et al. (2014)
	537 ± 9	SHRIMP U–Pb monazite	Panangad	Grt–Ky–Crd–Sapp–Bt gneiss	Collins et al. (2007)
	535		Panangad	Mg–Al rich granulite	Clark et al 2009a
	535 ± 4.9	SHRIMP U–Pb zircon	Panangad	Grt–Ky–Crd–Sapp–Bt gneiss	Collins et al. (2007)
	532 ± 10	SHRIMP U–Pb monazite	Sevitturanganpatti	Sill–Musc–Qtz gneiss	Collins et al. (2007)
	Ir int. 532±63	LA ICP MS Zircon, U Pb	Ayyarmalai	High Al migmatites	Raith et al. 2010
	529+/-9	LA ICP MS Zircon, U Pb	Ayyarmalai	corrundum bearing leucosome	Raith et al., 2010
	525 ± 10	SHRIMP U–Pb monazite	Sevitturanganpatti	Ky–Grt–Ged–Sapp–Crn gneiss	Collins et al. (2007)
	522 ± 3	ID-TIMS zircon U–Pb	Palghat	Granite gneiss	Ghosh et al. (2004)
	521 ± 8	Sm–Nd garnet	Palghat	Garnet-biotite gneiss	Meißner et al. (2002)
	521 ± 13	Rb–Sr biotite	Bhawani Shear Zone	Mylonitic gneiss	Meißner et al. (2002)
	514 ± 5	SHRIMP U–Pb zircon	Manamedu	Metamorphosed plagiogranite	Santosh et al. (2012)
	502 ± 7	SHRIMP U–Pb zircon	Manamedu	Metagabbro	Santosh et al. (2012)
	491 ± 52	Sm–Nd garnet	Madukarai	Calc–silicate	Meißner et al. (2002)
485 ± 12	Rb–Sr biotite	Palghat	Garnet–biotite gneiss	Meißner et al. (2002)	
455 ± 124	ID-TIMS zircon U–Pb	Mettupalyam	Granite gneiss	Ghosh et al. (2004)	
Mesozoic–Neozoic mafic magmatism	3200–2800	Sm–Nd whole rock	Kollimalai	Charnockite	Tomson, et al (2013)
	3045 ± 170	SHRIMP, zircon, U–Pb	Namakkal	Mafic granulite	Ghosh et al. (2004)
	2935 ± 60	Sm–Nd wholerock	Sittampundi	Mafic granulite	Bhaskar Rao et al. (1996)
	2898 ± 52	Sm–Nd whole	Bhawanisagar	Metabasite	Bhaskar Rao et al. (1996)
	2644 ± 30	LA-ICP-MS zircon U–Pb	Nilambur	Metagabbro	Shaji et al. (2014)
	2661 ± 59, 2659 ± 21	LA-ICP-MS zircon U–Pb	Nilambur	Amphibolite	Shaji et al. (2014)
	2547 ± 17	SHRIMP, zircon,	Agali Hills	Metagabbro	Santosh et al. (2013)
	2541 ± 13	LA-ICP-MS zircon	Sittampundi	Anorthosite	Ram Mohan et al. (2013)
	2536 ± 300	Lu–Hf isotope of whole- rock	Kanjamalai	Metabasite	Noack et al. (2013)
	2530–2500		Mettupalyam	Amphibolite/mafic granulite	Ghosh et al. (2004)
	2522 ± 12	ID-TIMS zircon U–SIMS U–Pb zircon	Sittampundi	Anorthosite	He et al. (2021)
Mesozoic–Neozoic felsic magmatism	2852 ± 76	LA-ICP-MS zircon U–Pb	Trichengodu	Grt–opx tonalites	Brandt et al. (2014)
	2800	SHRIMP, zircon, U–Pb	Palghat	Biotite gneiss	Ghosh et al. (2004)
	2670	LA-ICP-MS zircon U–Pb	Ayyarmalai	Ferroan dyke, syenite	Raith et al., 2016
	2661±59	LA-ICP-MS Zircon U-Pb	Nilambur, E of Nilgiri, Kerala	Amphibolite	Shaji et al. 2014

Table 2.2contd.:

Mesoarchean–Neoproterozoic felsic magmatism	2647 ± 11	LA-ICP-MS zircon U–Pb	Kanjamalai	Granite	Sato et al. (2011b)
	2644±30	LA-ICP-MS Zircon U-Pb	Nilambur, E of Nilgiri, Kerala	Meta gabbro	Shaji et al. 2014
	2619±21	LA-ICP-MS Zircon U-Pb	Nilambur, E of Nilgiri, Kerala	TTG	Shaji et al. 2014
	2619 ± 6	LA-ICP-MS zircon U–Pb	Nilambur	TTG	Shaji et al. (2014)
	2605	LA-ICP-MS zircon U–Pb	Kanjamalai	Bt-bearing felsic gneiss	Anderson et al. (2012)
	2600	LA-ICP-MS zircon U–Pb	Ayarmalai	charnockite	Raith et al., 2016
	2600, 2,502 ± 81	LA-ICP-MS zircon U–Pb	Namakkal	Enderbite	Brandt et al. (2014)
	2569±21	LA-ICP-MS Zircon U-Pb	Nilambur, E of Nilgiri, Kerala	Amphibolite	Shaji et al. 2014
	2547 ± 7	SHRIMP, zircon	Agali Hills	Trondhjemite	Santosh et al. (2013)
	2545 ± 56	SHRIMP, zircon, U–Pb	Devanur	Trondhjemite	Yellappa et al. (2012)
	2542±249	LA-ICP-MS Zircon U-Pb	Nilambur, E of Nilgiri, Kerala	Amphibolite	Shaji et al. 2014
	2537 ± 34, 2530 ± 2	LA-ICP-MS zircon U–Pb	Mahadevi Layered Complex	Felsic orthogneiss	Talukdar et al., 2020
	2537 ± 0.7	ID-TIMS zircon U–	Namakkal	Syntectonic	Ghosh et al. (2004)
	2536 ± 1	SHRIMP U–Pb	Kanjamalai	Charnockite	Saitoh et al. (2011)
	2534 ± 17	LA-ICP-MS zircon	Nainarmalai	Granodiorite gneiss	Plavsa et al. (2015)
	2532 ± 9	SHRIMP, zircon,	Agali Hills	Meta granite	Santosh et al. (2013)
	2532 ± 4	SHRIMP U–Pb	Kanjamalai	Garnet gneiss	Saitoh et al. (2011)
	2528 ± 61	SHRIMP, zircon,	Devanur	Trondhjemite	Yellappa et al. (2012)
	2517 ± 25	ID-TIMS zircon U–	Mettupalyam	Granite gneiss	Ghosh et al. (2004)
	2515 ± 9	ID-TIMS zircon U–	Mettupalyam	Tonalite	Ghosh et al. (2004)
	2512 ± 2	ID-TIMS zircon U–	Namakkal	Biotite gneiss	Ghosh et al. (2004)
	2507 ± 1.2	ID-TIMS zircon U–	Namakkal	Syntectonic	Ghosh et al. (2004)
	2504 ± 2	ID-TIMS zircon U–	Namakkal	Biotite gneiss	Ghosh et al. (2004)
	2502 ± 81	LA-ICP-MS zircon	Namakkal	Enderbite	Brandt et al. (2014)
2460 ± 81	Rb–Sr whole rock	Nilgiri Massifs	Garnetiferous enderbite	Raith et al. (1999)	
2445±38	LA-ICP-MS Zircon U-Pb	Nilambur, E of Nilgiri, Kerala	Amphibolite	Shaji et al. (2014)	
Tonian magmatism	817 ± 16	LA-ICP-MS zircon	Manamedu	Plagiogranite	Sato et al. (2011a)
	791 ± 50	ID-TIMS zircon U–	Palghat	Granite	Ghosh et al. (2004)
	786 ± 7	SIMS U–Pb zircon	Manamedu	Gabbro	Santosh et al. (2012)
	782 ± 24	SIMS U–Pb zircon	Manamedu	Plagiogranite	Santosh et al. (2012)
	774 ± 11	SIMS U–Pb zircon	Manamedu	Gabbro	Santosh et al. (2012)
	737 ± 23	SIMS U–Pb zircon	Manamedu	Plagiogranite	Santosh et al. (2012)
Ediacaran granitic magmatism	623 ± 21	Rb–Sr whole-rock	Sivamalai	Nepheline Syenite	Subba Rao et al. (1994)
	601 ± 1	ID-TIMS zircon U–Pb	Mettupalayam	Vein Quartz	Ghosh et al. (2004)
	590 ± 1.3	ID-TIMS zircon U–	Sivamalai	Nepheline Syenite	Upadhyay et al. (2006)
	559 ± 3.5	LA-ICP-(SF)-MS, zircon, U/Pb	Shankari	Pegmatoidal granite	Glorie et al. (2014)
	556 ± 3	LA-ICP-MS zircon	Shankari	Pegmatoidal granite	Brandt et al. (2014)
	554 ± 9	LA-ICP-MS zircon	Namakkal	Pegmatite	Plavsa et al. (2015)
	522 ± 3	ID-TIMS zircon U–	Palghat	Granite	Ghosh et al. (2004)
	504 ± 13	Rb–Sr muscovite	Bhavani Shear Zone	Pegmatitic dyke	Meißner et al. (2002)
	497 ± 12	Rb–Sr biotite	Bhavani Shear Zone	Pegmatitic dyke	Meißner, Det al (2002)
	513	Sm–Nd garnet	Bhavani Shear Zone	Pegmatitic dyke	Meißner et al. (2002)

Table 2.2contd.:
Madurai Block

	Age (Ma)	Method	Area	Rocktype	Reference
Archaean to Palaeoproterozoic metamorphism	2472±15	LA-ICP-MS Zircon U-Pb	near Kangayam	Migmatitic Grt-Opx Gneiss	Brandt et al. 2014
	2469±13	LA-ICP-MS Zircon	Palni hill	Felsic orthogneiss	Brandt et al. 2011
	2451 ± 91	monazite	Palni hill	Grt-Crd migmatites	Brandt et al. 2010
	2434 ± 24		Palni hill	Grt-Crd migmatites	Brandt et al. 2010
	2060±23	LA-ICP-MS Zircon U-Pb	Palni hill	Leucosome of Meta pelite	Brandt et al. 2011
	2520±25	LA-ICP-MS Zircon U-Pb	EMD	Porphyritic charnockite	Brandt et al. 2014
	2480		Palni hill	Grt-Crd migmatites	Brandt et al. 2010
	2430	monazite	WMB	Migmatitic Grt- Opx gneiss	Brandt et al. 2014
Tonian to Ediacaran metamorphism	1500-850	Monazite EPMA	Mottamala, near	Sapp+Grt+	Braun 2006
	955±16	LA-ICP-MS-Zircon, U-Pb	Kadavur	Quartzite	Kooijman et al. 2011
	950-850	Monazite EPMA	Mottamala, near Rajapalayam	Sapp+Grt+ Opx+Sill+Crd metasediments	Braun 2006
	950-550	LA-ICP-MS-Zircon, U-Pb	Southern MB	Quartzite	Li et al 2017
	860±21	LA-ICP-MS-Zircon, U-Pb	Kadavur	Quartzite	Plavsa et al. 2014
	843±23	LA-ICP-MS-Zircon, U-Pb	Kadavur	Quartzite	Teale et al. 2011
	821-611	LA-ICP-MS-Zircon, U-Pb	Ganguvarpatti	Quartzite	Plavsa et al. 2014
	821±33	LA-ICP-MS Zircon U-Pb	Alambari	Migmatitic Hbl-Bt gneiss	Brandt et al. 2014
	810±16	LA-ICP-MS-Zircon, U-Pb	Kadavur	Quartzite	Kooijman et al. 2011
	810±13	LA-ICP-MS Zircon U-Pb	Sirumalai	Meta rhyolite	Brandt et al. 2014
	1020	LA-ICP-MS-Zircon, U-Pb	Sirumalai	Quartzite	Kooijman et al.2011
810	LA-ICP-MS-Zircon, U-Pb	Alambari	Metapelite	Kooijman et al. 2011	

Table 2.2contd.:

Tonian to Ediacaran metamorphism	810	LA-ICP-MS-Zircon, U-Pb	Sirumalai	Quartzite	Kooijman et al. 2011
	786	LA-ICP-MS Zircon U-Pb	Raja Palayam	Grt-granite	George et al. 2015
	770			Quartzite	Plavsa et al. 2014
	798 ± 22			granodiorite	Plavsa et al. 2012
	793±7	LA-ICP-MS Zircon U-Pb	W of Sirumalai	Migmatitic charnokite	Brandt et al. 2014
	790±11	LA-ICP-MS-Zircon, U-Pb	N of Sivagiri	Grt-Sill-Bt Gneiss	Plavsa et al. 2014
	785±4	LA-ICP-MS Zircon U-Pb	Sirumalai	Leuco gabbro	Brandt et al. 2014
	784±6	LA-ICP-MS Zircon U-Pb	Varamalai	Porphyritic charnokite	Brandt et al. 2014
	768±69	LA-ICP-MS Zircon U-Pb	Sirumalai	Porphyritic charnokite	Brandt et al. 2014
	736±55	LA-ICP-MS Zircon U-Pb	near Kangayam	Migmatitic Grt-Opx Gneiss	Brandt et al. 2014
	696±9	LA-ICP-MS-Zircon, U-Pb	Sivagiri	Felsic	Plavsa et al. 2014
	696±10	LA-ICP-MS-Zircon, U-Pb	N of Sivagiri	Grt-Sill-Bt Gneiss	Plavsa et al. 2014
	662±46	LA-ICP-MS Zircon U-Pb	Sirumalai	Porphyritic charnokite	Brandt et al. 2014
	650±46	LA-ICP-MS Zircon U-Pb	Sirumalai	Porphyritic charnokite	Brandt et al. 2014
	630-530	Monazite EPMA	Mottamala, near Rajapalayam	Sapp+Grt+ Opx+Sill+Crd metasediments	Braun 2006
	624-529	LA-ICP-MS-Zircon, U-Pb	Ganguvarpatti	Quartzite	Plavsa et al. 2014
	622±9	LA-ICP-MS Zircon U-Pb	near Varusandhu	Migmatitic charnokite	Brandt et al. 2014
	600-500	Monazite EPMA	Mottamala, near Rajapalayam	Sapp+Grt+ Opx+Sill+Crd metasediments	Braun 2006
	590-490	LA-ICP-MS-Zircon, U-Pb	Alambari	metapelite	Kooijman et al. 2011
	590 Ma	LA-ICP-MS-Zircon, U-Pb	Sirumalai	Quartzite	Kooijman et al. 2011

Table 2.2contd.:

Ediacaran metamorphism	588±36	LA-ICP-MS Zircon U-Pb	Ayyarmalai	A-type granite, charnokite	Sato et al. 2011a
	586±8 to 532±7		Madurai	Sapphirine- bearing pelite	Tiwari and Sarkar, 2020
	580-500	LA-ICP-MS-Zircon, U-Pb	near Tirunelveli	Quartzite	Li et al 2017
	578±7	LA-ICP-MS Zircon U-Pb	near Varusandhu	Migmatitic charnokite	Brandt et al. 2014
	576±48	LA-ICP-MS-Zircon, U-Pb	E of Dindigul	Quartzite	Plavsa et al. 2014
	576±9	LA-ICP-MS-Zircon, U-Pb	Sivagiri	Granodiorite	Plavsa et al. 2012
	571±114	TIMS U-Pb zircon		Granite gneiss	Ghosh et al., 2004
	570±19	LA-ICP-MS Zircon U-Pb	Alambari	Porphyritic granite	Sengupta et al. 2015
	563±33	LA-ICP-MS Zircon	Varamalai	porphyritic	Brandt et al. 2014
	561	LA-ICP-MS-Zircon, U-Pb	N of Sivagiri	Mg-Al granulite	George et al. 2015
	557±3	LA-ICP-MS Zircon U-Pb	W of Sirumalai	Migmatitic charnokite	Brandt et al. 2014
	556±4			Enderbitic gneiss	Brandt et al. 2011
	556±4	LA-ICP-MS Zircon U-Pb	near Polachi	Migmatitic charnokite	Brandt et al. 2014
	556±12	LA-ICP-MS-Zircon, U-Pb		Felsic gneiss	Plavsa et al. 2014
	553±4.5	LA-ICP-MS Zircon U-Pb	Palni hill	Leucosome of Meta pelite	Brandt et al. 2011
	550-500	LA-ICP-MS Zircon U-Pb	near Munnar	Granite and charnockite	Bhattacharya et al., 2014
	550±3	LA-ICP-MS Zircon U-Pb	cardamom hill??	Migmatitic Charnokite	Brandt et al. 2014
	530±15, 530±5	SHRIMP Zircon U-Pb age	Perumalmai	Sapp bearing granulite	Prakash et al. 2010
	549±10	LA-ICP-MS Zircon U-Pb	Munnar	Hbl-Bt gneiss	Brandt et al. 2014
	547±17	Evaporation of Zircon,Pb-Th age	Kodaikanal	Meta granite	Bartlett et al. 1998
544±8	La-ICP-MS, Zircon, U/Pb	Kodaikanal	Monzodiorite	Plavsa et al. 2012	
542±8	LA-ICP-MS-Zircon, U-Pb	Sivagiri	Felsic gneiss	Plavsa et al. 2014	

Table 2.2contd.:

Ediacaran metamorphism	544±8	La-ICP-MS, Zircon, U/Pb	Kodaikanal	Monzodiorite	Plavsa et al. 2012
	542±8	LA-ICP-MS-Zircon, U-Pb	Sivagiri	Felsic gneiss	Plavsa et al. 2014
	541±8	LA-ICP-MS Zircon U-Pb	Palayam (near Alambadi)	Granodiorite	Plavsa et al. 2015
	540±8	La-ICP-MS, Zircon, U/Pb	Munnar	Granodiorite	Plavsa et al. 2012
	553±3.4	LA-ICP-MS Zircon U-Pb	Palni hill	Restite of Meta pelite	Brandt et al. 2011
	550	LA-ICP-MS Zircon U-Pb	Sirumalai	Leuco gabbro	Brandt et al. 2014
	550	LA-ICP-MS Zircon U-Pb	N of Sivagiri	Incipient Charnokite	George et al. 2015
	535	LA-ICP-MS-Zircon, U-Pb	Sivagiri	Qtz monzodiorite	Plavsa et al. 2012
	538±7	LA-ICP-MS Zircon U-Pb	NW of Karur	Migmatitic felsic gneiss	Plavsa et al. 2015
	533±56	SHRIMP U/Pb Zircon	Theni	Granite	Plavsa et al. 2012
	529±5		Ganguvarpatti	Quartzite	Plavsa et al. 2014
	525±7	SHRIMP U/Pb Zircon	Kodaikanal	Granodiorite	Plavsa et al. 2012
	523±6	LA-ICP-MS Zircon U-Pb	Near Karur	Pegmatite, Kfs bearing melt	Plavsa et al. 2015
	522±160	LA-ICP-MS Zircon U-Pb	Alambari	Migmatitic Hbl-Bt gneiss	Brandt et al. 2014
	518±11	LA-ICP-MS-Zircon, U-Pb	Theni	Qtz monzodiorite	Plavsa et al. 2012
	514±10	SHRIMP U-Pb Zircon	Ganguvarpatti	Quartzite	Collins et al. 2007b
	512±13/ 508.3 ± 9.0/ 513±6Ma	SHRIMP U/Pb Zircon	Kodaikanal	Granodiorite	Plavsa et al. 2012
	500-550	LA-ICP-MS Zircon U-Pb	N of Sivagiri	Charnokite	George et al. 2015
	500	LA-ICP-MS-Zircon, U-Pb	Kadavur	BIF	Sato et al. 2011
	rim 502±4; lr int.497±29	U-Pb Zircon	Palayam (near Palayam)	undeformed Hbl bearing pegmatite	Plavsa et al. 2015
499±50	U-Pb Zircon	Sivagiri	Qtz monzodiorite	Plavsa et al. 2012	
448±59	U-Pb Zircon	Karur	Granodiorite	Plavsa et al. 2012	

Table 2.2contd.:

Madurai Block

	Age (Ma)	Method	Area	Rocktype	Reference
Archaean to Palaeoproterozoic Magmatism	3010-2510	Sm-Nd whole rock	Munnar	Granodiorite	Plavsa et al. 2012
	2700	LA-ICP-MS Zircon U-Pb	Varamalai	Porphyritic Charnokite	Brandt et al. 2014
	2689±26	SHRIMP, Zircon, U-Pb	Kodaikanal	Granodiorite	Plavsa et al. 2012
	2534±9	LA-ICP-MS Zircon U-Pb	Palni hill	Felsic orthogneiss	Brandt et al. 2011
	2527±8	LA-ICP-MS Zircon U-Pb	Munnar	Granodiorite	Plavsa et al. 2012
	2525±25	LA-ICP-MS-Zircon, U-Pb	Theni	Qtz monzodiorite	Plavsa et al. 2012
	2520±25	LA-ICP-MS Zircon U-Pb	Varamalai	Porphyritic Charnokite	Brandt et al 2015
	2520±17	LA-ICP-MS Zircon U-Pb	Karur	Granodiorite	Plavsa et al. 2012
	2504±20	SHRIMP, Zircon, U-Pb	Kodaikanal	Granodiorite	Plavsa et al. 2012
	2501±19	LA-ICP-MS Zircon U-Pb	Kodaikanal	Granodiorite	Plavsa et al. 2012
	2493±10	LA-ICP-MS Zircon U-Pb	near Kangayam	Migmatitic Grt-Opx Gneiss	Brandt et al. 2014
	2464±69	LA-ICP-MS Zircon U-Pb	cardamom hill	Migmatitic Charnokite	Brandt et al. 2014
	2464+/-23	LA-ICP-MS Zircon U-Pb	near Kangayam	Migmatitic charnockite	Brandt et al. 2014
	2442±13	ID-TIMS Zircon U-Pb	Karur	granite gneiss	Ghosh et al. 2004
	2436+/-4	Evaporation of Zircon,Pb-Th age	Kodaikanal	Meta granite	Bartlett et al. 1998
	Mesoproterozoic to Tonian/ Cambrian magmatism	2190±27	SHRIMP U-Pb Zircon	Ganguvarpatti	Quartzite
2287		Sm-Nd whole rock, TIMS	Kadavur	Gabbro anorthosite	Teal et al. 2011
1905±28		SHRIMP U-Pb Zircon	Ganguvarpatti	Quartzite	Collins et al. 2007b
1761±28		LA-ICP-MS Zircon U-Pb	Sirumalai	Porphyritic charnokite	Brandt et al. 2014
1690-1380		Sm/Nd whole rock	Sivagiri	Qtz monzodiorite	Plavsa et al. 2012
1660±29 (core)		LA-ICP-MS Zircon U-Pb	Sirumalai	Leuco gabbro	Brandt et al. 2014
1619±8		LA-ICP-MS Zircon U-Pb	W of Sirumalai	Migmatitic charnokite	Brandt et al. 2014
1560±41		LA-ICP-MS Zircon U-Pb	Sirumalai	Meta rhyolite	Brandt et al. 2014
1060±8		LA-ICP-MS Zircon U-Pb	N of Sivagiri	Charnokite	George et al. 2015
1007±23					Plavsa et al. 2012

Table 2.2contd.:

Mesoproterozoic to Tonian/ Cambrian magmatism	1007 ±23	LA-ICP-MS-Zircon, U-Pb	Sivagiri	Qtz monzodiorite	Plavsa et al. 2012
	900-1100	Evaporation of Zircon,Pb-Th age	Kodaikanal	Meta granite	Bartlett et al. 1998
	836±73	LA-ICP-MS Zircon U-Pb	Raja Palayam	Grt-granite	George et al. 2015
	831±31	LA-ICP-MS Zircon U-Pb	N of Sivagiri	Charnokite	George et al. 2015
	829±14	LA-ICP-MS Zircon U-Pb	Kadavur	Gabbro anorthosite	Teal et al. 2011
	829±14	LA-ICP-MS U-Pb zircon	Kadavur	Gabbro anorthosite	Teale et al. (2011)
	826±50	LA-ICP-MS Zircon U-Pb	Palni hill	Meta pelite	Brandt et al. 2011
	821±9	LA-ICP-MS Zircon U-Pb	Sirumalai	Meta rhyolite	Brandt et al. 2014
	819±26	LA-ICP-MS Zircon U-Pb	near Kadavur	Rapakivi granite	Sato et al. 2011a
	818±51	LA-ICP-MS Zircon U-Pb	near Varusandhu	Migmatitic charnokite	Brandt et al. 2014
	815-803	LA-ICP-MS Zircon U-Pb	Alambari	Porphyritic granite	Sengupta et al. 2015
	811±4	LA-ICP-MS Zircon U-Pb	Sirumalai	Leuco gabbro	Brandt et al. 2014
	804±6	LA-ICP-MS Zircon U-Pb	Munnar	Hbl-Bt gneiss	Brandt et al. 2014
	798±22	LA-ICP-MS-Zircon, U-Pb	Sivagiri	Granodiorite	Plavsa et al. 2012
	796±1	ID-TIMS Zircon U-Pb	Rangamalai	Charnokite	Ghosh et al. 2004
	795±13	SHRIMP U/Pb Zircon	Theni	Granite	Plavsa et al. 2012
	794±6	LA-ICP-MS Zircon U-Pb	Polachi	Migmatitic charnokite	Brandt et al. 2014
	794±3	LA-ICP-MS Zircon U-Pb	Sirumalai	Porphyritic charnokite	Brandt et al. 2014
	789±5	LA-ICP-MS Zircon U-Pb	Alambadi	Granodiorite	Plavsa et al. 2015
	788±4	LA-ICP-MS Zircon U-Pb	Varamalai	porphyritic charnokite	Brandt et al. 2014
	784 ±18	LA-ICP-MS-Zircon, U-Pb	Sivagiri	Qtz monzodiorite	Plavsa et al. 2012
	781±8	LA-ICP-MS-Zircon, U-Pb	Sivagiri	Monzodiorite	Plavsa et al. 2012
	772±49	LA-ICP-MS Zircon U-Pb	N of Sivagiri	Charnokite	George et al. 2015
	768±3	LA-ICP-MS Zircon U-Pb	Alambadi	Porphyritic granite	Sengupta et al. 2015
	766±8	LA-ICP-MS Zircon U-Pb	Kadavur	felsic gneiss	Teal et al. 2011
	766±8	LA-ICP-MS U-Pb zircon	Kadavur	Granitoid	Teale et al. (2011)
	762±7			Undeformed	
	(core), up int. 810±60	LA-ICP-MS Zircon U-Pb	Palayam	Hbl bearing pegmatite	Plavsa et al. 2015
	563±9	SHRIMP, Zircon, U-Pb	Odenchatram	Anorthosite	Ghosh et al. 2004

References

- Acharyya, S.K., 2003. The nature of Mesoproterozoic Central Indian Tectonic Zone with exhumed and reworked older granulites. *Gondwana Res.* 6, 197–214.
- Acharyya, S.K., Roy, A., 2000. Tectonothermal History of the Central Indian Tectonic Zone and Reactivation of Major Faults/Shear Zones. *Geol. Soc. India* 55, 239–256.
- Anderson, J.R., Payne, J.L., Kelsey, D.E., Hand, M., Collins, A.S., Santosh, M., 2012. High-pressure granulites at the dawn of the Proterozoic. *Geology* 40, 431–434.
- Baidya, T.K., Chakravorty, P.S., Drubetskoy, E., Khiltova, V.J., 1987. New geochronologic data on some granitic phases of the Chhotanagpur granite gneiss complex in the north-western Purulia district, West Bengal. *Indian J. earth Sci.* 14, 136–141.
- Baidya, T.K., Maity, N., Biswas, P., 1989. Tectonic phases and crustal evolution in a part of the Eastern Chotanagpur Gneissic Complex. *Geol. Soc. India* 34, 318–324.
- Bhattacharjee, N., Ray, J., Ganguly, S., Saha, A., 2012. Mineralogical study of gabbro-anorthosite from Dumka, Chhotanagpur Gneissic Complex, Eastern Indian Shield. *J. Geol. Soc. India* 80, 481–492.
- Bhattacharya, D.K., Mukherjee, D., Barla, V.C., 2010. Komatiite within Chhotanagpur Gneissic Complex at Semra, Palamau district, Jharkhand: petrological and geochemical fingerprints. *J. Geol. Soc. India* 76, 589–606.
- Bhattacharyya, P.K., Mukherjee, S., 1987. Granulites in and around the Bengal anorthosite, eastern India: genesis of coronal garnet and evolution of the granulite–anorthosite complex. *Geol. Mag.* 124,
- Brandt, S., Raith, M.M., Schenk, V., Sengupta, P., Srikantappa, C., Gerdes, A., 2014. Crustal evolution of the Southern Granulite Terrane , south India : New geochronological and geochemical data for felsic orthogneisses and granites. *Precambrian Res.* 246, 91–122.

<https://doi.org/10.1016/j.precamres.2014.01.007>

- Brandt, S., Schenk, V., Raith, M.M., Appel, P., Gerdes, A., Srikantappa, C., 2011. Late Neoproterozoic PT evolution of HP-UHT granulites from the Palni Hills (South India): New constraints from phase diagram modelling, LA-ICP-MS zircon dating and in-situ EMP monazite dating. *J. Petrol.* 52, 1813–1856.
- Brandt, S., Schenk, V., Raith, M.M., Gerdes, A., Srikantappa, C., 2010. Pan-African reworking of late Archean-early Paleoproterozoic crust in the Madurai Block of South India, and implications for Gondwana reconstructions, in: Proceedings of the 88th Annual Meeting of the Deutsche Mineralogische Gesellschaft (DMG).
- Braun, I., Kriegsman, L.M., 2003. Proterozoic crustal evolution of southernmost India and Sri Lanka. *Geol. Soc. London, Spec. Publ.* 206, 169–202.
- Chatterjee, N., 2018. An assembly of the Indian Shield at c. 1.0 Ga and shearing at c. 876–784 Ma in Eastern India: insights from contrasting PT paths, and burial and exhumation rates of metapelitic granulites. *Precambrian Res.* 317, 117–136.
- Chatterjee, N., Banerjee, M., Bhattacharya, A., Maji, A.K., 2010. Monazite chronology, metamorphism–anatexis and tectonic relevance of the mid-Neoproterozoic Eastern Indian Tectonic Zone. *Precambrian Res.* 179, 99–120.
- Chatterjee, N., Crowley, J.L., Ghose, N.C., 2008. Geochronology of the 1.55 Ga Bengal anorthosite and Grenvillian metamorphism in the Chotanagpur gneissic complex, eastern India. *Precambrian Res.* 161, 303–316.
- Chatterjee, N., Ghose, N.C., 2011. Extensive early Neoproterozoic high-grade metamorphism in north Chotanagpur gneissic complex of the Central Indian tectonic zone. *Gondwana Res.* 20, 362–379.
- Chowdhury, P., Chakraborty, S., 2019. Slow Cooling at Higher Temperatures Recorded within High-P Mafic Granulites from the Southern Granulite Terrain, India: Implications for the Presence and Style of Plate Tectonics near the Archean–Proterozoic Boundary. *J. Petrol.* 60, 441–486.
- Chowdhury, P., Talukdar, M., Sengupta, P., Sanyal, S., Mukhopadhyay, D., 2013.

- Controls of PT path and element mobility on the formation of corundum pseudomorphs in Paleoproterozoic high-pressure anorthosite from Sittampundi, Tamil Nadu, India. *Am. Mineral.* 98, 1725–1737.
- Clark, C., Collins, A.S., Santosh, M., Taylor, R., Wade, B.P., 2009. The PTt architecture of a Gondwanan suture: REE, U–Pb and Ti-in-zircon thermometric constraints from the Palghat Cauvery shear system, South India. *Precambrian Res.* 174, 129–144.
- Collins, A.S., Santosh, M., Braun, I., Clark, C., 2007. Age and sedimentary provenance of the Southern Granulites, South India: U–Th–Pb SHRIMP secondary ion mass spectrometry. *Precambrian Res.* 155, 125–138.
- Das, S., Sanyal, S., Karmakar, S., Sengupta, S., Sengupta, P., 2019. Do the deformed alkaline rocks always serve as a marker of continental suture zone? A case study from parts of the Chotanagpur Granite Gneissic complex, India. *J. Geodyn.* 129, 59–79.
- Dey, A., Choudhury, S.R., Mukherjee, S., Sanyal, S., Sengupta, P., 2019a. Origin of vesuvianite-garnet veins in calc-silicate rocks from part of the Chotanagpur Granite Gneiss Complex, East Indian Shield: The quantitative PTX CO₂ topology in parts of the system CaO–MgO–Al₂O₃–SiO₂–H₂O–CO₂ (+ Fe₂O₃, F). *Am. Mineral. J.* 104, 744–760.
- Dey, A., Karmakar, S., Ibanez-Mejia, M., Mukherjee, S., Sanyal, S., Sengupta, P., 2019b. Petrology and geochronology of a suite of pelitic granulites from parts of the Chotanagpur Granite Gneiss Complex, eastern India: Evidence for Stenian–Tonian reworking of a late Paleoproterozoic crust. *Geol. J.*
- Dey, A., Karmakar, S., Mukherjee, S., Sanyal, S., Dutta, U., Sengupta, P., 2019c. High pressure metamorphism of mafic granulites from the Chotanagpur Granite Gneiss Complex, India: Evidence for collisional tectonics during assembly of Rodinia. *J. Geodyn.* 129, 24–43.
- Dey, A., Mukherjee, S., Sanyal, S., Ibanez-Mejia, M., Sengupta, P., 2017. Deciphering sedimentary provenance and timing of sedimentation from a suite of

- metapelites from the Chotanagpur Granite Gneissic Complex, India: Implications for Proterozoic Tectonics in the East-Central Part of the Indian Shield, in: *Sediment Provenance*. Elsevier, pp. 453–486.
- Dunn, J.A., 1929. The geology of north Singhbhum including parts of Ranchi and Singhbhum districts. *Geol. Surv. India Mem.* 54, 1–280
- Dutta, U., Bhui, U.K., Sengupta, P., Sanyal, S., Mukhopadhyay, D., 2011. Magmatic and metamorphic imprints in 2.9 Ga chromitites from the Sittampundi layered complex, Tamil Nadu, India. *Ore Geol. Rev.* 40, 90–107.
- George, P.M., Sajeev, K., Santosh, M., Zhai, M., 2019. Granulite-grade garnet pyroxenite from the Kolli-massif, southern India: Implications for Archean crustal evolution. *Lithos* 342, 499–512.
- Ghose, N.C., 1983. Geology, tectonics and evolution of the Chhotanagpur granite-gneiss complex, Eastern India. *Recent Res. Geol.* 10, 211–247.
- Ghose, N.C., 1992. Chhotanagpur gneiss-granulite complex, Eastern India: Present status and future prospect. *Indian Jour. Geol.* 64, 100–121.
- Ghose, N.C., Mukherjee, D., 2000. Chotanagpur gneiss–granulite complex, Eastern India — akaleidoscope of global events, in: A.N. Trivedi, B.C. Sarkar, N.C. Ghose, Y.R.D. (Ed.), *Geology*
- Ghosh, J.G., de Wit, M.J., Zartman, R.E., 2004. Age and tectonic evolution of Neoproterozoic ductile shear zones in the Southern Granulite Terrain of India, with implications for Gondwana studies. *Tectonics* 23.
- Ghosh, S.K., Sengupta, S., 1999. Boudinage and composite boudinage in superposed deformations and syntectonic migmatization. *J. Struct. Geol.* 21, 97–110.
- Goswami, B., Bhattacharyya, C., 2010. Tectonothermal Evolution of Chhotanagpur Granite Gneiss Complex From Northeastern Part of Puruliya District, West Bengal, Eastern India. *Indian J.*
- Goswami, B., Bhattacharyya, C., 2013. Petrogenesis of shoshonitic granitoids,

- Eastern India: Implications for the late Grenvillian post-collisional magmatism. *Geosci. Front.* 5, 821–843. doi:10.1016/j.gsf.2013.09.003
- He, H.-L., Wang, Y.-Q., George, P.M., Sajeev, K., Guo, J.-H., Lai, C.-K., Zhai, M.-G., 2021. Formation of ~ 2.5 Ga Sittampundi anorthosite complex in southern India: Implications to lower crustal stabilization of the Dharwar Craton. *Precambrian Res.* 354, 106012.
- Janardhan, A.S., 1999. Southern granulite terrain, south of the Palghat-Cauvery shear zone: implications for India-Madagascar connection. *Gondwana Res.* 2, 463–469.
- Karmakar, S., Bose, S., Sarbadhikari, A.B., Das, K., 2011. Evolution of granulite enclaves and associated gneisses from Purulia, Chhotanagpur Granite Gneiss Complex, India: evidence for 990–940 Ma tectonothermal event (s) at the eastern India cratonic fringe zone. *J. Asian Earth Sci.* 41, 69–88.
- Karmakar, S., Mukherjee, S., Dutta, U., 2020. Origin of corundum within anorthite megacrysts from anorthositic amphibolites, Granulite Terrane, Southern India. *Am. Mineral. J. Earth Planet. Mater.* 105, 1161–1174.
- Karmakar, S., Mukherjee, S., Sanyal, S., Sengupta, P., 2017. Origin of peraluminous minerals (corundum, spinel, and sapphirine) in a highly calcic anorthosite from the Sittampundi Layered Complex, Tamil Nadu, India. *Contrib. to Mineral. Petrol.* 172, 1–23.
- Kooijman, E., Upadhyay, D., Mezger, K., Raith, M.M., Berndt, J., Srikantappa, C., 2011. Response of the U–Pb chronometer and trace elements in zircon to ultrahigh-temperature metamorphism: the Kadavur anorthosite complex, southern India. *Chem. Geol.* 290, 177–188.
- Krishna, V., Sastry, D., Pandey, B.K., Sinha, R.P., 2003. U–Pb and Pb–Pb ages on columbite-tantalite minerals from pegmatites of Bihar Mica Belt, Jharkhand, India, in: *ISMAS Silver Jubilee Symposium on Mass Spectrometry. V. 2: Contributed Papers.*

- Kumar, R.R., Dwivedi, S.B., 2019. EPMA monazite geochronology of the granulites from Daltonganj, eastern India and its correlation with the Rodinia supercontinent. *J. Earth Syst. Sci.* 128, 1–22.
- Kumar, R.R., Dwivedi, S.B., Pathak, P., 2022. Phase equilibria modelling and geochemistry of high-grade gneiss from the Chhotanagpur Granite Gneiss Complex, eastern India: Implications for tectono-metamorphic evolution. *Geosystems and Geoenvironment* 100082.
- Kumar, R.R., Kawaguchi, K., Dwivedi, S.B., Das, K., 2021. Metamorphic evolution of the pelitic and mafic granulites from Daltonganj, Chhotanagpur Granite Gneiss Complex, India: Constraints from zircon U–Pb age and phase equilibria modelling. *Geol. J.* 57, 1284–1310.
- Lahiri, G., Das, S., 1984. Petrology of the area east of Daltonganj, Palamau district, Bihar. *Geol. Soc. India* 25, 490–504.
- Lal, N., Saini, H.S., Nagpaul, K.K., Sharma, K.K., 1976. Tectonic and cooling history of the Bihar Mica Belt, India, as revealed by fission-track analysis. *Tectonophysics* 34, 163–180.
- Mahadevan, T.M., 2002. *Geology of Bihar & Jharkhand*. Geological Society of India, Bangalore.
- Mandal, P., 2016. Shear-wave splitting in Eastern Indian Shield: Detection of a Pan-African suture separating Archean and Meso-Proterozoic terrains. *Precambrian Res.* 275, 278–285.
- Maji, A.K., Goon, S., Bhattacharya, A., Mishra, B., Mahato, S., Bernhardt, H.-J., 2008. Proterozoic polyphase metamorphism in the Chhotanagpur Gneissic Complex (India), and implication for trans-continental Gondwanaland correlation. *Precambrian Res.* 162, 385–402.
- Mallik, A.K., Gupta, S.N., Ray Barman, T., 1991. Dating of early Precambrian granite-greenstone complex of the eastern Indian Precambrian shield with special reference to the Chotanagpur granite gneiss complex. *Rec. Geol. Surv. India*

125(2), 25–27.

Manna, S.S., Sen, S.K., 1974. Origin of garnet in basic granulites around Saltora, West Bengal, India. *Contrib. to Mineral. Petrol.* 44, 195–218.

Meißner, B., Deters, P., Srikantappa, C., Köhler, H., 2002. Geochronological evolution of the Moyar, Bhavani and Palghat shear zones of southern India: implications for east Gondwana correlations. *Precambrian Res.* 114, 149–175.

Misra, S., Dey, S., 2002. Bihar Mica Belt plutons-an example of post-orogenic granite from eastern Indian shield. *Geol. Soc. India* 59, 363–377.

Mohan, M.R., Satyanarayanan, M., Santosh, M., Sylvester, P.J., Tubrett, M., Lam, R., 2013. Neoproterozoic suprasubduction zone arc magmatism in southern India: Geochemistry, zircon U-Pb geochronology and Hf isotopes of the Sittampundi Anorthosite Complex. *Gondwana Res.* 23, 539–557.

Mukherjee, S., Dey, A., Ibanez-Mejia, M., Sanyal, S., Sengupta, P., 2018a. Geochemistry, U-Pb geochronology and Lu-Hf isotope systematics of a suite of ferroan (A-type) granitoids from the CGGC: Evidence for Mesoproterozoic crustal extension in the east Indian shield. *Precambrian Res.* 305, 40–63.

Mukherjee, S., Dey, A., Sanyal, S., Ibanez-Mejia, M., Dutta, U., Sengupta, P., 2017. Petrology and U-Pb geochronology of zircon in a suite of charnockitic gneisses from parts of the Chotanagpur Granite Gneiss Complex (CGGC): evidence for the reworking of a Mesoproterozoic basement during the formation of the Rodinia supercontinent. *Geol. Soc. London, Spec. Publ.* 457, 197–231.

Mukherjee, S., Dey, A., Sanyal, S., Ibanez-Mejia, M., Sengupta, P., 2019a. Bulk rock and zircon geochemistry of granitoids from the Chotanagpur Granite Gneissic Complex (CGGC): implications for the late Paleoproterozoic continental arc magmatism in the East Indian Shield. *Contrib. to Mineral. Petrol.* 174, 1–17.

Mukherjee, S., Dey, A., Sanyal, S., Sengupta, P., 2019b. Proterozoic crustal evolution of the Chotanagpur Granite Gneissic complex, Jharkhand-Bihar-West Bengal, India: current status and future prospect, in: *Tectonics and Structural Geology:*

Indian Context. Springer, pp. 7–54.

Mukherjee, S., Dey, A., Sanyal, S., Sengupta, P., 2018b. Tectonothermal imprints in a suite of mafic dykes from the Chotanagpur Granite Gneissic complex (CGGC), Jharkhand, India: Evidence for late Tonian reworking of an early Tonian continental crust. *Lithos* 320–321. <https://doi.org/10.1016/j.lithos.2018.09.014>

Mukherjee, D., Ghose, N.C., Chatterjee, N., 2005. Crystallization history of a massif anorthosite in the eastern Indian shield margin based on borehole lithology 25, 77–94. doi:10.1016/j.jseaes.2004.01.012

Mazumdar, S.K., 1988. Crustal evolution of the Chotanagpur gneissic complex and the Mica Belt of Bihar, in: Mukhopadhyay, D. (Ed.), *Precambrian of the Eastern Indian Shield*. Geological Society of India

Naha, K., Srinivasan, R., Deb, G.K., 1997. Structural geometry of the early Precambrian terrane south of Coimbatore in the “Palghat Gap”, southern India. *Proc. Indian Acad. Sci. Planet. Sci.* 106, 237–247.

Noack, N.M., Kleinschrodt, R., Kirchenbaur, M., Fonseca, R.O.C., Münker, C., 2013. Lu–Hf isotope evidence for Paleoproterozoic metamorphism and deformation of Archean oceanic crust along the Dharwar Craton margin, southern India. *Precambrian Res.* 233, 206–222.

Pandey, B.K., Gupta, J.N., Lall, Y., 1986a. Whole rock and mineral Rb–Sr isochron ages for the granites from Bihar mica belt of Hazaribagh, Bihar, India. *Indian J. earth Sci.* 13, 157–162.

Pandey, B.K., Upadhyay, D.L., Sinha, K.K., 1986b. Geochronology of Jajawal-Binda-Nagnaha granitoids in relation to uranium mineralisation. *Indian J. earth Sci.* 13, 163–168.

Patel, S.C., 2007. Vesuvianite-wollastonite-grossular-bearing calc-silicate rock near Tatapani, Surguja district, Chhattisgarh. *J. earth Syst. Sci.* 116, 143–147.

Peucat, J.-J., Jayananda, M., Chardon, D., Capdevila, R., Fanning, C.M., Paquette, J.-L.,

2013. The lower crust of the Dharwar Craton, Southern India: Patchwork of Archean granulitic domains. *Precambrian Res.* 227, 4–28.
- Plavsa, D., Collins, A.S., Foden, J.D., Clark, C., 2015. The evolution of a Gondwanan collisional orogen: A structural and geochronological appraisal from the Southern Granulite Terrane, South India. *Tectonics* 34, 820–857.
- Plavsa, D., Collins, A.S., Foden, J.F., Kropinski, L., Santosh, M., Chetty, T.R.K., Clark, C., 2012. Delineating crustal domains in Peninsular India: age and chemistry of orthopyroxene-bearing felsic gneisses in the Madurai Block. *Precambrian Res.* 198, 77–93.
- Plavsa, D., Collins, A.S., Payne, J.L., Foden, J.D., Clark, C., Santosh, M., 2014. Detrital zircons in basement metasedimentary protoliths unveil the origins of southern India. *GSA Bull.* 126, 791–811.
- Raith, M.M., Brandt, S., Sengupta, P., Berndt, J., John, T., Srikantappa, C., 2016. Element mobility and behaviour of zircon during HT metasomatism of ferroan basic granulite at Ayyarmalai, South India: Evidence for polyphase Neoproterozoic crustal growth and multiple metamorphism in the Northeastern Madurai Province. *J. Petrol.* 57, 1729–1774.
- Raith, M.M., Karmakar, S., Brown, M., 1997. Ultra-high-temperature metamorphism and multistage decompressional evolution of sapphirine granulites from the Palni Hill Ranges, southern India. *J. Metamorph. Geol.* 15, 379–399.
- Raith, M.M., Sengupta, P., Kooijman, E., Upadhyay, D., Srikantappa, C., 2010. Corundum–leucosome-bearing aluminous gneiss from Ayyarmalai, Southern Granulite Terrain, India: A textbook example of vapor phase-absent muscovite-melting in silica-undersaturated aluminous rocks. *Am. Mineral.* 95, 897–907.
- Raith, M.M., Srikantappa, C., Buhl, D., Koehler, H., 1999. The Nilgiri enderbites, South India: nature and age constraints on protolith formation, high-grade metamorphism and cooling history. *Precambrian Res.* 98, 129–150.
- Rao, Y.J.B., Chetty, T.R.K., Janardhan, A.S., Gopalan, K., 1996. Sm-Nd and Rb-Sr ages

- and PT history of the Archean Sittampundi and Bhavani layered meta-anorthosite complexes in Cauvery shear zone, South India: evidence for Neoproterozoic reworking of Archean crust. *Contrib. to Mineral. Petrol.* 125, 237–250.
- Ray Barman, T., Bishui, P.K., Mukhopadhyay, K., Ray, J.N., 1994. Rb-Sr geochronology of the high-grade rocks from Purulia, West Bengal and Jamua-Dumka sector, Bihar. *Indian Miner.* 48, 45–60.
- Ray, S., Sanyal, S., Sengupta, P., 2011. Mineralogical control on rheological inversion of a suite of deformed mafic dykes from parts of the Chottanagpur Granite Gneiss Complex of eastern India, in: *Dyke Swarms: Keys for Geodynamic Interpretation*. Springer, pp. 263–276.
- Rekha, S., Upadhyay, D., Bhattacharya, A., Kooijman, E., Goon, S., Mahato, S., Pant, N.C., 2011. Lithostructural and chronological constraints for tectonic restoration of Proterozoic accretion in the Eastern Indian Precambrian shield. *Precambrian Res.* 187, 313–333.
- Renjith, M.L., Santosh, M., Satyanarayanan, M., Rao, D.V.S., Tang, L., 2016. Multiple rifting and alkaline magmatism in southern India during Paleoproterozoic and Neoproterozoic. *Tectonophysics* 680, 233–253.
- Rode, K.P., 1948. On charnockitic rocks of Palamau, Bihar, India. *Schweiz. Min. Petr. Mitt* 28, 288–307.
- Roy, A.K., 1977. Structure and metamorphic evolution of the Bengal anorthosite and associated rocks. *J. Geol. Soc. India* 18, 203–223.
- Roy Chowdhury, 1979. Annual general report of the Geological survey of India, for the year 1972-73. *Rec. Geol. Surv. India* 107, 147–151.
- Saikia, A., Gogoi, B., Ahmad, M., Ahmad, T., 2014. Geochemical constraints on the evolution of mafic and felsic rocks in the Bathani volcanic and volcano-sedimentary sequence of Chotanagpur Granite Gneiss Complex. *J. Earth Syst. Sci.* 123, 959–987.

- Saikia, A., Gogoi, B., Kaulina, T., Lialina, L., Bayanova, T., Ahmad, M., 2017. Geochemical and U–Pb zircon age characterization of granites of the Bathani Volcano Sedimentary sequence, Chotanagpur Granite Gneiss Complex, eastern India: vestiges of the Nuna supercontinent in the Central Indian Tectonic Zone. *Geol. Soc. London, Spec. Publ.* 457, 233–252.
- Saitoh, Y., Tsunogae, T., Santosh, M., Chetty, T.R.K., Horie, K., 2011. Neoproterozoic high-pressure metamorphism from the northern margin of the Palghat–Cauvery Suture Zone, southern India: Petrology and zircon SHRIMP geochronology. *J. Asian Earth Sci.* 42, 268–285.
- Sajeev, K., Osanai, Y., Santosh, M., 2004. Ultrahigh-temperature metamorphism followed by two-stage decompression of garnet–orthopyroxene–sillimanite granulites from Ganguvarpatti, Madurai block, southern India. *Contrib. to Mineral. Petrol.* 148, 29–46.
- Sajeev, K., Windley, B.F., Connolly, J.A.D., Kon, Y., 2009. Retrogressed eclogite (20 kbar, 1020 C) from the Neoproterozoic Palghat–Cauvery suture zone, southern India. *Precambrian Res.* 171, 23–36.
- Samuel, V.O., Kwon, S., Santosh, M., Sajeev, K., 2018. Garnet pyroxenite from Nilgiri Block, southern India: Vestiges of a Neoproterozoic volcanic arc. *Lithos* 310, 120–135.
- Santosh, M., Shaji, E., Tsunogae, T., Mohan, M.R., Satyanarayanan, M., Horie, K., 2013. Suprasubduction zone ophiolite from Agali hill: petrology, zircon SHRIMP U–Pb geochronology, geochemistry and implications for Neoproterozoic plate tectonics in southern India. *Precambrian Res.* 231, 301–324.
- Santosh, M., Xiao, W.J., Tsunogae, T., Chetty, T.R.K., Yellappa, T., 2012. The Neoproterozoic subduction complex in southern India: SIMS zircon U–Pb ages and implications for Gondwana assembly. *Precambrian Res.* 192, 190–208.
- Sanyal, S., Sengupta, P., 2012. Metamorphic evolution of the Chotanagpur granite gneiss complex of the east Indian shield: current status. *Geol. Soc. London, Spec. Publ.* 365, 117–145.

- Sarangi, S., Mohanty, S., 1998. Structural studies in the Chhotanagpur gneissic complex near Gomoh, Dhanbad district, Bihar. *Indian J. Geol.* 70, 73–80.
- Sarkar, A.N., Jha, B.N., 1985. Structure, metamorphism and and granite evolution of the Chottanagpur granite gneissic complex. *Geol. Surv. India Rec.* 113, 1–12.
- Sato, K., Santosh, M., Tsunogae, T., Chetty, T.R.K., Hirata, T., 2011. Laser ablation ICP mass spectrometry for zircon U-Pb geochronology of metamorphosed granite from the Salem Block: Implication for Neoproterozoic crustal evolution in southern India. *J. Mineral. Petrol. Sci.* 106, 1–12.
- Sen, S.K., Bhattacharya, A., 1993. Post-peak pressure– temperature–fluid history of the granulites around Saltora, West Bengal., in: *Proceedings of the National Academy of Sciences of India*, 63(A). pp. 282–306
- Sengupta, P., Dutta, U., Bhui, U.K., Mukhopadhyay, D., 2009. Genesis of wollastonite- and grandite-rich skarns in a suite of marble-calc-silicate rocks from Sittampundi, Tamil Nadu: constraints on the P–T–fluid regime in parts of the Pan-African mobile belt of South India. *Mineral. Petrol.* 95, 179.
- Sengupta, P., Raith, M.M., Kooijman, E., Talukdar, M., Chowdhury, P., Sanyal, S., Mezger, K., Mukhopadhyay, D., 2015. Chapter 20 Provenance, timing of sedimentation and metamorphism of metasedimentary rock suites from the Southern Granulite Terrane, India. *Geol. Soc. London, Mem.* 43, 297–308. <https://doi.org/10.1144/m43.20>
- Sequeira, N., Bhattacharya, A., Bell, E., 2022. The ~ 1.4 Ga A-type granitoids in the “Chottanagpur crustal block”(India), and its relocation from Columbia to Rodinia? *Geosci. Front.* 13, 101138.
- Shaji, E., Santosh, M., He, X.-F., Fan, H.-R., Dev, S.G.D., Yang, K.-F., Thangal, M.K., Pradeepkumar, A.P., 2014. Convergent margin processes during Archean–Proterozoic transition in southern India: Geochemistry and zircon U–Pb geochronology of gold-bearing amphibolites, associated metagabbros, and TTG gneisses from Nilambur. *Precambrian Res.* 250, 68–96.

- Shimpo, M., Tsunogae, T., Santosh, M., 2006. First report of garnet–corundum rocks from southern India: implications for prograde high-pressure (eclogite-facies?) metamorphism. *Earth Planet. Sci. Lett.* 242, 111–129.
- Singh, R.N., Thorpe, R., Kristic, D., 2001. Galena Pb isotope data of base metal occurrences in the Hesatu-Belbathan belt, eastern Precambrian shield, Bihar. *J. Geol. Soc. India (Online Arch. from Vol 1 to Vol 78)* 57, 535–538.
- Singh, Y., Krishna, V., 2009. Rb-Sr geochronology and petrogenesis of granitoids from the Chhotanagpur granite gneiss complex of Raikera-Kunkuri region, Central India. *J. Geol. Soc. India* 74, 200–208.
- Sinha, A.K., Bhattacharya, D.K., 1995. Geochemistry of the magnetite deposits around Sua, Palamau district, Bihar. *Geol. Soc. India* 46, 313–316.
- Soni, S., Mukherjee, A.B., Sengupta, D.K., 1991. A new fluorite deposit in the Palamau District, Bihar and the associated iron-fluorine-tungsten skarns and hornfelses. *J. Geol. Soc. India* 38, 504–510.
- Srikantappa, C., Jagannathappa, S.P.N., 1990. P–T– Xf-condition during granulite facies metamorphism around Madukkarai, Tamil Nadu, in: *Abs. Indian Geological Congress*. p. 167.
- Srivastava, S.C., Ghose, N.C., 1992. Petrology of the highgrade gneisses and granites around Chianki, south of daltonganj, district Palamau, Bihar. *Indian Jour. Geol* 64, 122–142.
- Talukdar, M., Mukhopadhyay, D., Sanyal, S., Sengupta, P., 2020. Early Palaeoproterozoic structural reconstitution of a suite of rocks from the Mahadevi Layered Complex, Tamil Nadu, India. *Geol. J.*
- Talukdar, M., Sarkar, T., Sengupta, P., Mukhopadhyay, D., 2022. The Southern Granulite Terrane, India: The saga of over 2 billion years of Earth’s history. *Earth-Science Rev.* 104157.
- Upadhyay, D., Raith, M.M., 2006. Intrusion age, geochemistry and metamorphic conditions of a quartz-monzosyenite intrusion at the craton–Eastern Ghats Belt contact near Jojuru, India. *Gondwana Res.* 10, 267–276.

Vinogradov, A., Tugarinov, A.L., Zhykov, C., Stapnikova, N., Bibikova, E., Khorre, K., 1964. Geochronology of Indian Precambrian, in: Report of the 22nd International Geological Congress, New Delhi. pp. 553–567.

Yellappa, T., Chetty, T.R.K., Santosh, M., 2016. Precambrian iron formations from the Cauvery Suture Zone, Southern India: Implications for sub-marine hydrothermal origin in Neoproterozoic convergent margin settings. *Ore Geol. Rev.* 72, 1177–1196.

Yellappa, T., Santosh, M., Chetty, T.R.K., Kwon, S., Park, C., Nagesh, P., Mohanty, D.P., Venkatasivappa, V., 2012. A Neoproterozoic dismembered ophiolite complex from southern India: geochemical and geochronological constraints on its suprasubduction origin. *Gondwana Res.* 21, 246–265.

PART-I

The Chotanagpur Granite Gneiss Complex

Chapter-3

Study area and field relations

Chapter 3

Study area and field relations

As discussed in the previous chapter, the CGGC is dominated majorly by voluminous felsic orthogneiss. The supracrustal rocks are mainly exposed in the north-eastern part of the CGGC near Deoghar-Dumka, and hence this area has been chosen for detail study. The country rock of the study area is the migmatitic felsic gneiss, which hosts several enclaves. The enclave suite of rocks can be subdivided into orthogneissic ones (now deformed and/or metamorphosed to 'augen gneiss' and 'mafic granulite'), and paragneissic enclaves (now metamorphosed to pelitic granulites, calc-silicate granulites and quartzites). The country rock and the enclave suite of rocks are later intruded by a suite of mafic dykes and pegmatites.

Fig. 3.1 represents disposition of different lithounits in the study area, modified after Mukherjee et al., (2018a). The different lithounits have been described briefly below.

3.1. Country rock

As evident from Fig. 3.1, the dominant rock type in the CGGC is a felsic orthogneiss. It is non-porphyrific in nature, but depending upon slight variations in appearance and modal variation of constituting minerals, a few subvarieties are recognised in the study area.

The first is a migmatitic variety, and is exposed in the eastern part of the study area, between the Deoghar-Dumka stretch. This variety is constituted by biotite+ amphibole+ garnet+ K-feldspar+ plagioclase and quartz, and shows distinct leucosomal and melanosomal bandings. Hence, this variety has been termed as 'migmatitic felsic gneiss' (MFG). However, proportion of biotite and amphibole (hornblende) varies in different outcrops of the MFG, and hence been variously named as biotite-amphibole gneiss or amphibole-biotite gneiss (Fig. 3.1, 3.2a-b). The

leucosomal segregations are defined by alkali feldspar, plagioclase and quartz, while melanosomes comprise biotite and amphibole. Garnet is associated with both leucosomes and melanosomes. Two types of leucosomal segregations are observed: (i) thick, laterally continuous leucosomes, comprising ~15 vol% of the rock (Fig. 3.2a-b), and are inferred to have formed during the second metamorphic event (M2). Feldspar, quartz, garnet and rare biotite/ amphibole constitute these leucosomes. These leucosomes are commonly folded, with the development of an axial planar foliation (S3). (ii) Thin leucosomes, associated with the axial planar foliation (Fig. 3.2c). Amphibole and biotite constitute the melanosomes. This foliation defined by these thin leucosomes and melanosomes constitute the pervasive foliation of the rock.

Locally within the migmatitic felsic gneiss outcrops, patches of greasy charnockite are observed (Fig. 3.2d). These charnockite patches consists of orthopyroxene, clinopyroxene, garnet, biotite, amphibole, alkali feldspar, plagioclase and quartz. In this variety, the pyroxene and garnet define the melanosomes, while quartz, feldspar and garnet define the leucosomes, that are parallel and continuous with the S2 foliation of the enclosing migmatitic felsic gneiss. The boundary between these two are always diffused, and the weathered surface of the charnockite patches resemble the migmatitic felsic gneiss. Hence, all these signify that the latter represents the retrogressed counterpart of the charnockite.

However, in the western part of the study area, near Jasidih, a third variety of this host rock is exposed. In this part, the migmatitic nature is not prominent (Fig. 3.2e). However, the rock shows gneissic banding, with alternate melanocratic (dominated by biotite, and rare amphibole and garnet) and leucocratic (defined by quartzo-feldspathic minerals) bands. This unit also intrudes into the augen gneiss enclave (Fig. 3.2f).

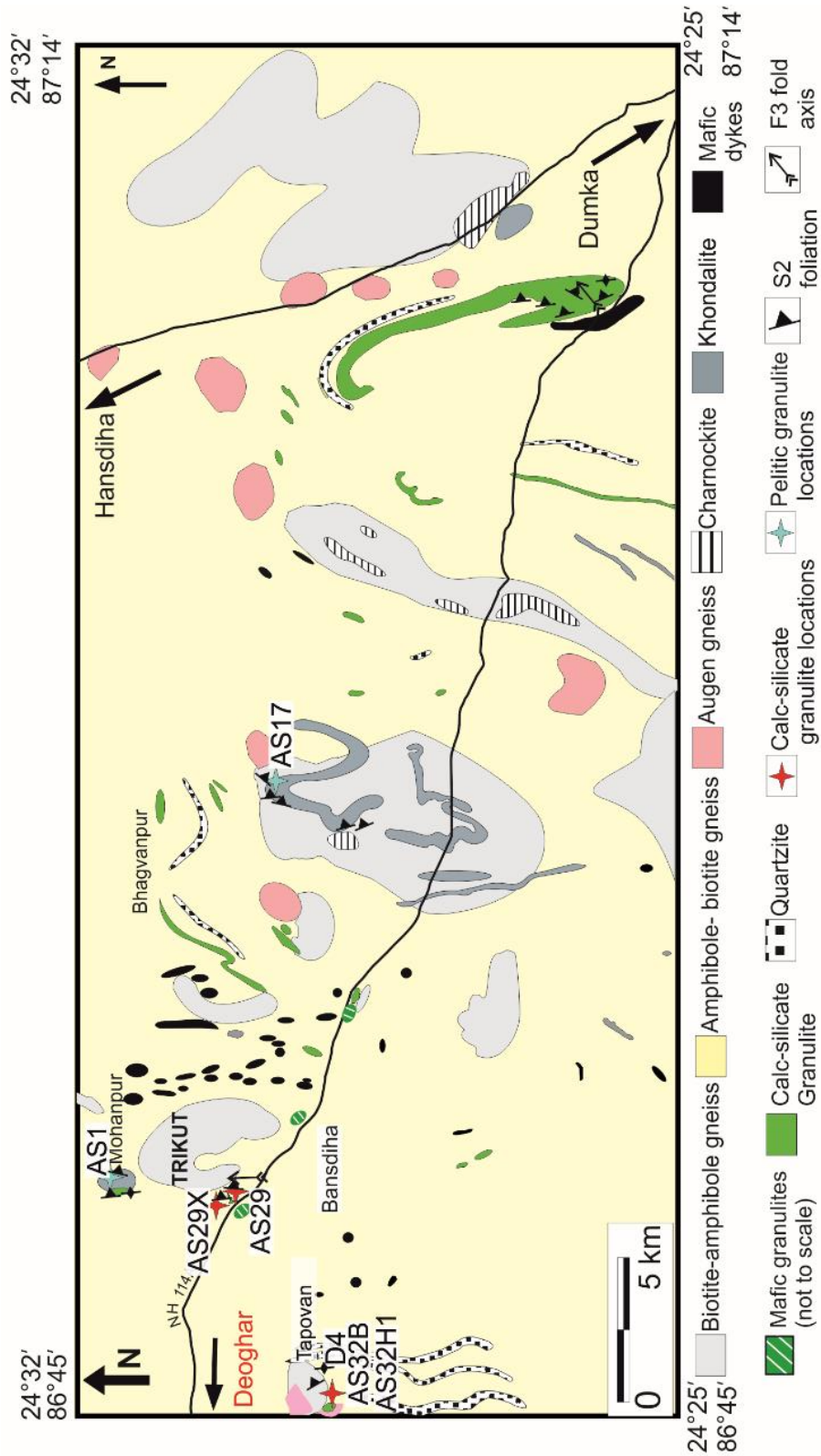


Fig. 3.1: Map showing major lithological distributions, of the studied area (modified after Mukherjee et al., 2018), in addition with representative structural information near the studied locations. The stars indicate the sample locations for the calc-silicate and pelitic granulites.

3.2. Enclave suite of rocks

3.2.1. Orthogneissic enclaves:

Augen Gneiss

This unit occurs as small hillocks in the western part of the study area, near Deoghar-Jasidih. Augen gneiss outcrops are surrounded by granite gneiss (which is fine-medium grained, and is not migmatitic in nature in the western part). However, locally this fine-grained granite gneiss (migmatitic in the eastern part) intrudes the augen gneiss, as small, centimeter thick, veins (Fig. 3.2f) (Mukherjee et al., 2019). The overall mineralogy of the augen gneiss includes alkali feldspar, plagioclase, quartz, as well as biotite and amphibole (biotite being slightly more abundant than amphibole). Large clasts (varying between a few millimetres) of alkali feldspar and plagioclase, and clots of quartz are present, which are now deformed into elliptical/stretched grains, forming augen shape, that impart a porphyritic nature to the rocks (Fig. 3.2g). Commonly, granular aggregates of alkali feldspar only, constitute the clasts. These stretched clasts, along with biotite and amphibole foliation, define the alternate leucocratic and melanocratic fabric of the rock. The biotite-amphibole foliation serves around these porphyroclasts. The amount of deformation of the feldspar clasts varies in outcrop scale. In a few outcrops, these clasts are extremely stretched, such that they appear to be nearly continuous bands (Fig. 3.2h). Garnet is scarcely observed in the rock. Local nebulitic patches comprising quartzo-feldspathic minerals are present in the outcrops.

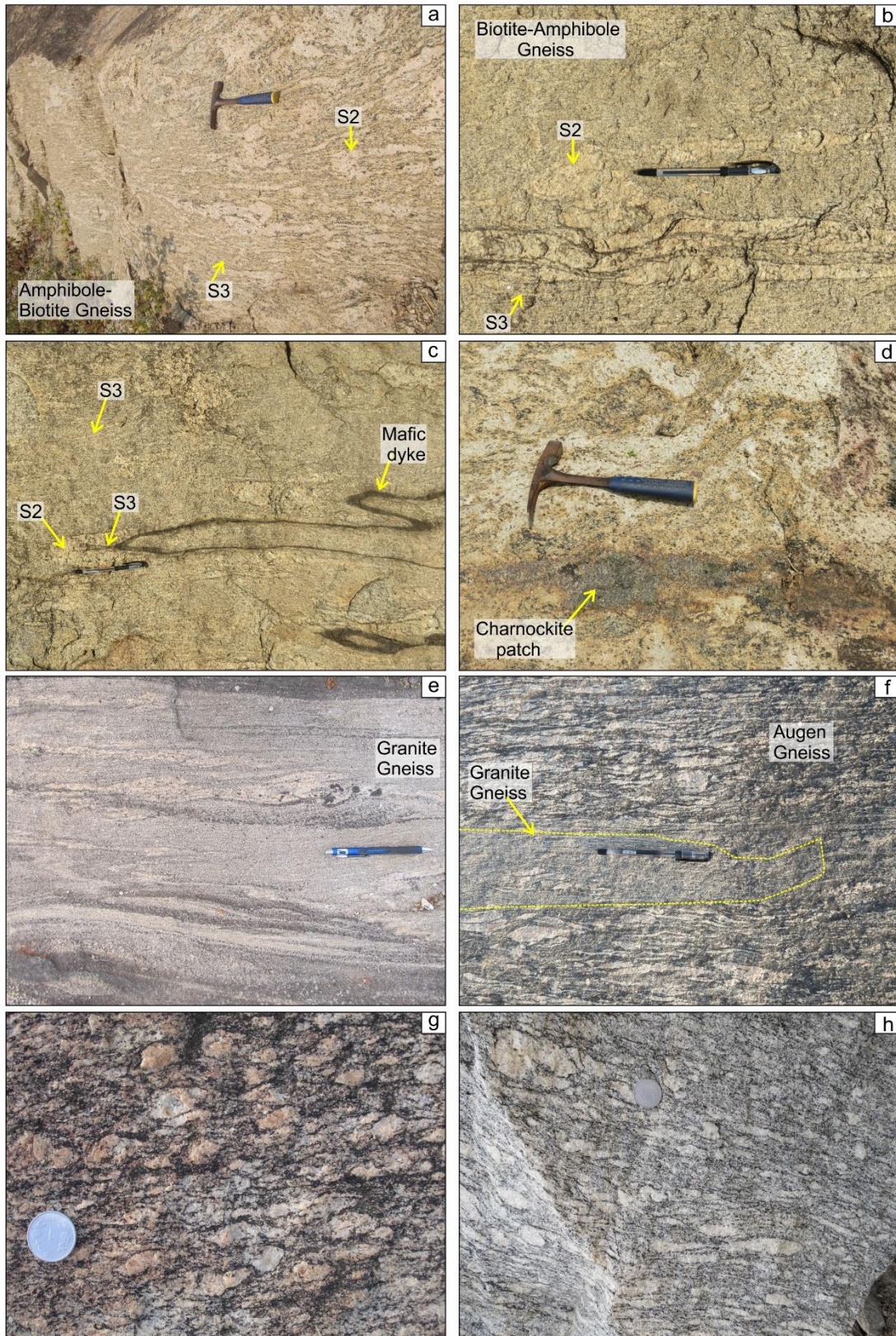


Fig. 3.2: Figure showing the different field features of all the lithounits of the study area. (a) Amphibole-biotite gneiss and (b-c) Biotite-amphibole gneiss varieties of the MFG, showing thick S2 leucosomes. S3 foliation associated with thin leucosomes develop axial planar to the folded S2 leucosomes. Note the mafic dykes that are co-folded with the S2 fabric of the host MFG. Also note the thin biotite and amphibole selvages at the margins of the leucosomes. (d) Charnockite patches within the MFG, with diffused boundaries. (e) Fine-grained, non migmatitic variety (granite gneiss) of the country rock. (f) Thin apophyses of granite gneiss intruding the augen gneiss. (g-h) Augen gneiss with porphyroclasts of alkali feldspar and plagioclase. Note in 'f' and 'h' that these porphyroclasts are stretched, resembling discontinuous bands.

Mafic Granulite

The second enclave variety of metamorphosed igneous rock include a suite of mafic rocks. These mafic granulites mostly occur as decimetre scale pods, directly within the migmatitic felsic gneiss country rock. In these outcrops, the foliation of host MFG swerve around the mafic granulite enclaves (Fig. 3.2i). In most of the outcrops they are slightly elongated/ stretched along the foliation of the host rock. These enclaves are mostly massive in nature. Locally these also depict crude N-S foliation, parallel to that of the host gneiss. The overall mineral assemblage of the mafic granulites include amphibole, plagioclase, pyroxene \pm garnet (Dey et al., 2019b).

3.2.2. Paragneissic enclaves:

The migmatitic felsic gneiss hosts a variety of paragneissic enclaves: pelitic granulite, calc-silicate granulite and quartzites.

Pelitic Granulites

The pelitic granulite enclaves are abundant, and occur mainly as metre to kilometre scale, bouldary outcrops. However, small, a few centimetres to decimetre scale pods, although rare, are enclosed directly within the host migmatitic felsic gneiss. Although rare, this unit preserves the initial, or earliest foliation, defined by thick garnetiferous leucosomes (~20-30 vol% of rock) (Fig. 3.2j) (Dey et al., 2019a). In few outcrops where the pelitic granulite occur as pods directly within the host MFG, the foliation of the MFG swerves around these pods (Fig. 3.2k). This internal fabric of the enclave is at high angles to the outer foliation of the MFG, at the centre

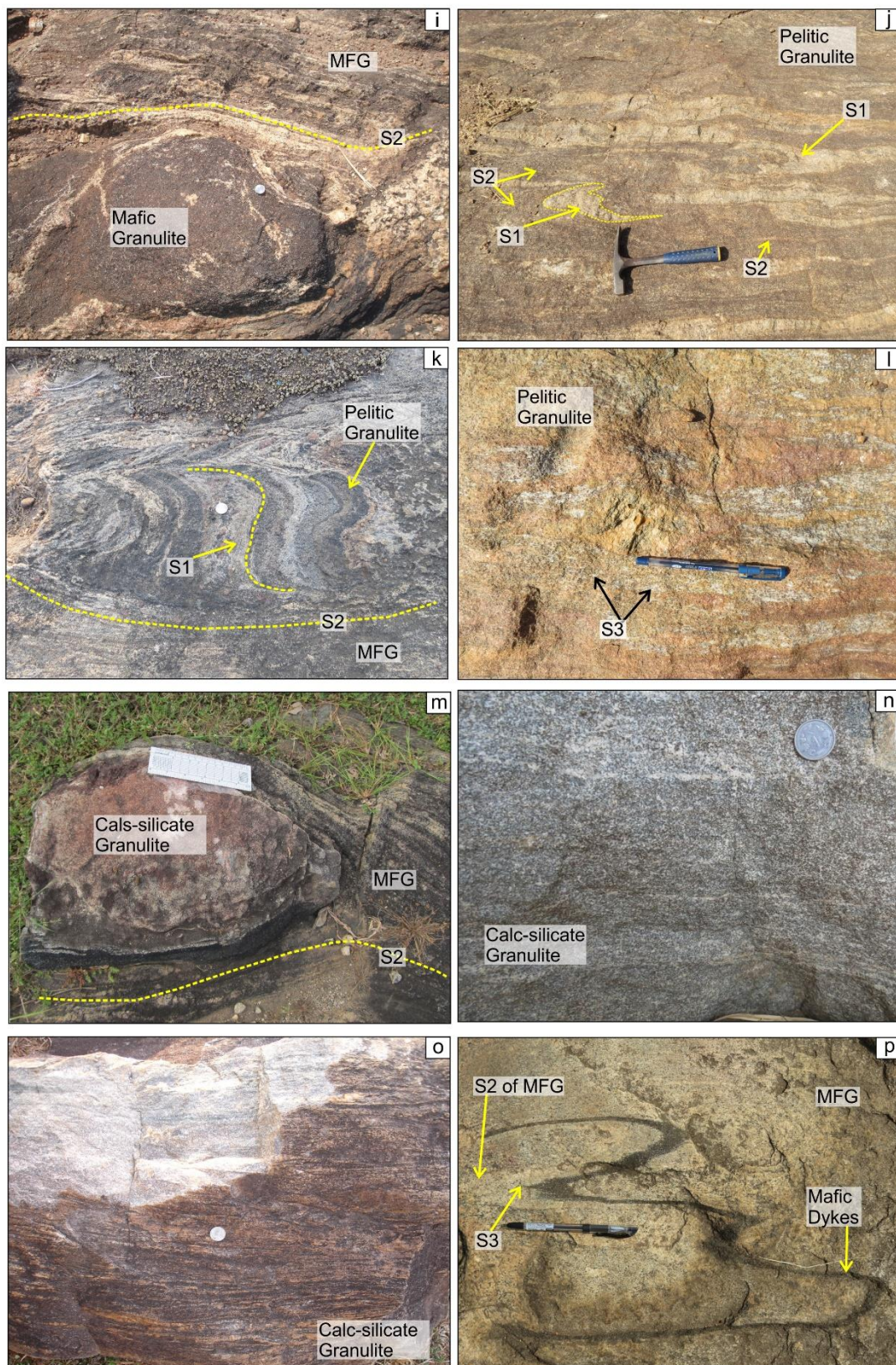


Fig. 3.2contd.: (i) S2 foliation of the MFG swerves around the mafic granulite enclaves. (j) Folded, thick S1 leucosomes in the pelitic granulites, having N-S axial planar trend. S2 foliations develop axial planar to these folds, and are associated with thin migmatitic bandings. (k) S1 foliation preserved in the pelitic granulite enclaves, discordant to the S2 foliation of the MFG at the center, and transposed along S2 near the margins. (l) Sillimanite grains defining the S3 foliation of the pelites. (m) S2 foliation of the host MFG, swerving around the calc-silicate granulite enclaves. (n) Alternate light and dark coloured compositional banding, commonly observed in most of the calc-silicate granulites of the area. (o) Prominent ridge and groove structures evident in highly weathered calc-silicate outcrops. (p) Mafic dykes that are co-folded with the S2 fabric of the host MFG, with development of axial planar S3 foliation.

of the pod, while at the boundary of the two units, they are dragged into parallelism. Hence, field relations suggest the formation of this earliest fabric prior to the emplacement of the protolith of the MFG. The mineral assemblage in the leucosomes includes K-feldspar, quartz and some plagioclase, along with garnet, while the melanosomes are defined by garnet, biotite and sillimanite (Fig. 3.2l). The thick leucosomes show tight folding, with the development of axial planar thin leucosomal/ melanosomal fabric (Fig. 3.2j, l).

Calc-silicate granulites

The calc-silicates are relatively less abundant than pelitic granulites. These occur mostly as metre scale boulders. The host MFG is disposed near the vicinity of these outcrops. However, small, slightly elliptical pods are also infrequently found directly within the MFG (Fig. 3.2m). In these outcrops, the foliation of the host gneiss swerve around the calc-silicate granulite pods. Apart from a very few outcrops, where the calc-silicate rocks are massive, most of the outcrops are banded in nature (Fig. 3.2n). These rocks show alternate leucocratic and melanocratic compositional bandings, which define the pervasive N-S foliation of the rock. As early generation of foliation, or folding of the foliations are not evident from these calc-silicates, it is inferred the last deformation event (D3) overprinted imprints of all early deformations. Hence the pervasive bandings are related to the third metamorphic, and deformation event (M3-D3) in the CGGC. The overall mineralogy of the all the calc-silicate granulites in the study area include clinopyroxene+ plagioclase+ titanite+ garnet± amphibole ± quartz. The compositional bandings of these rocks are mostly defined alternately by plagioclase, and clinopyroxene± amphibole. However, the calc-silicate granulites show a wide mineralogical variation in outcrop scale (as

well as within single outcrops) with respect to certain minerals like: vesuvianite, epidote/ zoisite, scapolite, spinel, ilmenite, as well as with respect to the modal proportions of these minerals. Highly weathered outcrops show prominent ridge and groove structures also (Fig. 3.2o).

3.3. Later intrusives

Mafic dykes

A swarm of mafic dykes, varying in thickness from about a few millimetres to several decimetres, even a metre, intrudes the MFG. They also intrude and cross cut the foliation of granite gneiss (host rock in the western part) and locally, the augen gneiss. The mafic dykes, along with the S2 foliations were deformed and folded in the subsequent D3 deformation, with N-S axial plane (Fig. 3.2p). The general mineral assemblage includes clinopyroxene, orthopyroxene, amphibole and plagioclase, with a small amount of biotite, ilmenite, titanite and quartz (Mukherjee et al., 2018b). Amphibole and stretched feldspar occur along the axial plane of the folded dykes, defining a N-S foliation (Fig. 3.2p).

Pegmatitic veins

Pegmatites of several generations are present in the study area. The mineral assemblage includes quartz, plagioclase± alkali feldspar, along with small proportions of amphibole or biotite, varying in different outcrops. Some of the pegmatites are deformed, and locally also show folding (having N-S axial planes). Another generation of pegmatites (having amphibole) are undeformed, and intrude parallel to the foliation of the rocks.

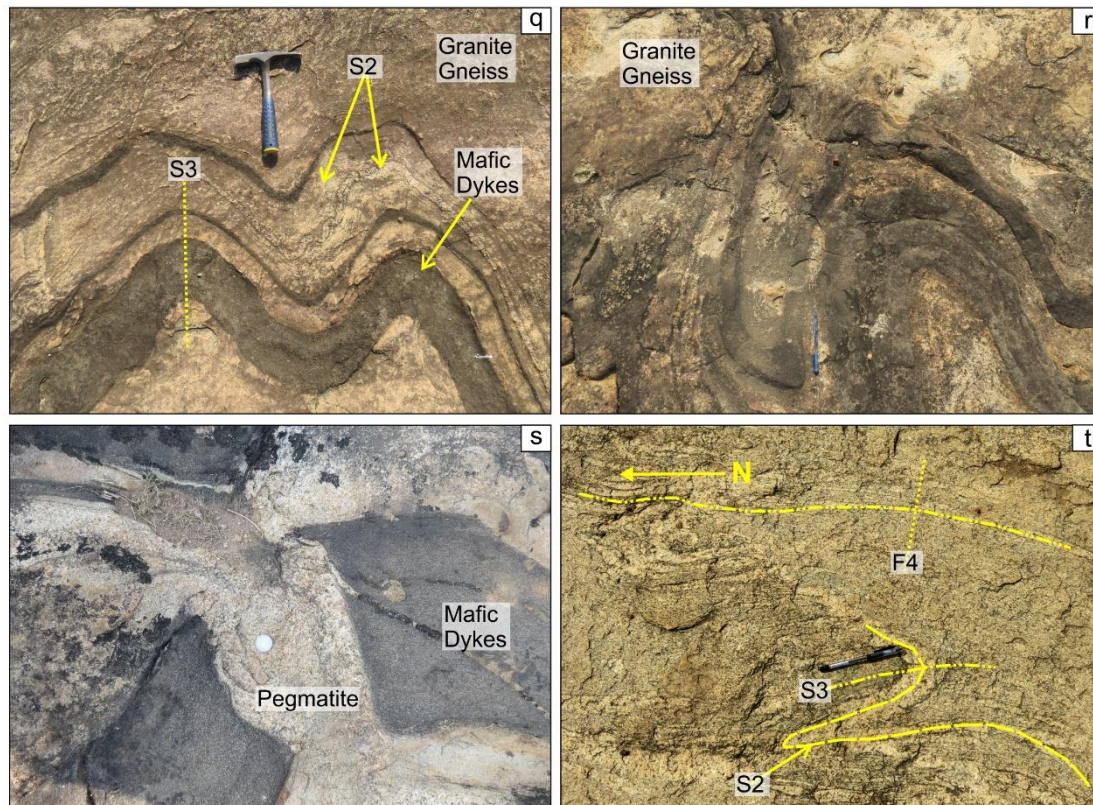


Fig. 3.2contd.: (q) Mafic dykes that are co-folded with the S2 fabric of the host MFG, with development of axial planar S3 foliation. (r) Hook shaped folds formed by two sets of coaxial folding in the dykes. (s) limbs of the folded dykes become stretched and boudinaged. Pegmatites intrude along these boudinaged zones. (t) Open folds with E-W axial planes (F4) resulting from the last phase of deformation.

3.4. Structural relations

Field observations indicate multiple deformational events suffered by the lithounits of the study area. A total of three major deformational events (D1-D3) are evident. The earliest deformation fabric (S1) is preserved in the pelitic granulite enclaves. The S1 foliations are defined by thick leucosomal segregations. S1 trends east-west at the center of the enclaves, where it is discordant with the foliation of the enclosing host rock (MFG) (Fig. 3.2k). But at the margins, it gets transposed along the host gneiss foliation (Fig. 3.2k). The foliation of the MFG is defined by thick leucosomal and melanosomal segregations. This foliation swerves around the pelitic, mafic and the calc-silicate granulite enclaves (where the latter are directly enclosed within the MFG) (Fig. 3.2k, i, m), signifying that the S1 foliation in the pelitic granulite enclaves formed before the intrusion of the protoliths of the MFG.

Therefore, the migmatitic foliation of the host MFG subsequently formed during a later deformation event (D2), and hence designated as S2 (Fig. 3.2b). The D2 deformation is therefore manifested by formation of S2 leucosomal/ melanosomal segregations in the MFG, transposition of S1 foliation in the pelitic granulite pods along S2, as well as folding of the thick S1 leucosomes in the pelitic granulites (Fig. 3.2j), and development of axial planar S2 foliation.

The general strike of S2 is N-S (Fig. 3.1). However, the strike slightly varies in outcrops scale, between NNW-SSE. S2 foliations are generally steeply dipping with the dip amount varying as: 70°-78° towards east. Some of the foliations show nearly vertical dip amounts (~82-88°). At few outcrops, shallower dip amounts have also been recorded (40-52° → E).

The third deformation event (D3), is the last major deformational event experienced by the lithounits of the area. D3 is evident from the folding of the S2 leucosomes in the MFG and the pelitic granulites, and development of N-S S3 foliation, axial planar to the D3 folds (Fig. 3.2c). The pervasive N-S foliation preserved in all the lithounits of the study area, including the metasedimentary enclaves and host MFG is a consequence of this last major/ dominant deformation, D3. The mafic dykes, that intrudes the host granite gneiss, (locally cross cutting relation with S2 foliation is preserved) also show folding. Hence this signifies that the intrusion of mafic dykes is post-D2, but pre-D3. These mafic dykes are co-deformed with the S2 fabric of other lithounits during D3 (Fig. 3.2p-q). The S3 fabric of the mafic dykes form axial planar to the D3 folds of the mafic dykes, as well as folded S2 foliations of the host rock (Fig. 3.2p). These S3 fabric/ F3 fold axis trend varies from mostly N-S to NNW-SSE, and are moderately plunging (32°→ 003°; 38°→ 350°). Although most of the plunge directions are towards north, few F3 axis also plunges towards south (159-170°).

Three sets of folding were identified from the mafic dykes (DKF1, DKF2 and DKF3; Mukherjee et al., 2018b). The first two of which are coaxial, and isoclinal, with N-S axial plane. Rare presence of hook shaped folds (Fig. 3.2r) defined by mafic dykes and granite gneiss foliation, attests to this coaxial folding. As a result of strong E-W compression (possibly related to the coaxial folding: DKF1 and DKF2; see

Mukherjee et al., 2018b), the limbs of the folded dykes become stretched and boudinaged (Fig. 3.2s). Pegmatitic veins intrude along the boudinaged zones. The third folding (DKF3) is open to close in nature, with an E-W axial plane, which results in an open warping of the limbs of the mafic dykes and felsic gneisses (Fig. 3.2t). These fold axis (F4) have moderately steep plunge amount (62-65°) mostly plunging towards east.

Therefore, it is evident that the three major deformational events (D1-D3) affected the study area, corresponding to the three metamorphic events (M1-M3). The third deformation event was however prolonged, during which the three subordinate deformations (DKF1, DKF2 and DKF3) occurred in the rocks.

References

- Dey, A., Karmakar, S., Ibanez-Mejia, M., Mukherjee, S., Sanyal, S., Sengupta, P., 2019a. Petrology and geochronology of a suite of pelitic granulites from parts of the Chotanagpur Granite Gneiss Complex, eastern India: Evidence for Stenian-Tonian reworking of a late Paleoproterozoic crust. *Geol. J.*
- Dey, A., Karmakar, S., Mukherjee, S., Sanyal, S., Dutta, U., Sengupta, P., 2019b. High pressure metamorphism of mafic granulites from the Chotanagpur Granite Gneiss Complex, India: Evidence for collisional tectonics during assembly of Rodinia. *J. Geodyn.* 129, 24–43.
- Mukherjee, S., Dey, A., Ibanez-Mejia, M., Sanyal, S., Sengupta, P., 2018a. Geochemistry, U-Pb geochronology and Lu-Hf isotope systematics of a suite of ferroan (A-type) granitoids from the CGGC: Evidence for Mesoproterozoic crustal extension in the east Indian shield. *Precambrian Res.* 305, 40–63.
- Mukherjee, S., Dey, A., Sanyal, S., Ibanez-Mejia, M., Sengupta, P., 2019. Bulk rock and zircon geochemistry of granitoids from the Chotanagpur Granite Gneissic Complex (CGGC): implications for the late Paleoproterozoic continental arc magmatism in the East Indian Shield. *Contrib. to Mineral. Petrol.* 174, 1–17.

Mukherjee, S., Dey, A., Sanyal, S., Sengupta, P., 2018b. Tectonothermal imprints in a suite of mafic dykes from the Chotanagpur Granite Gneissic complex (CGGC), Jharkhand, India: Evidence for late Tonian reworking of an early Tonian continental crust. *Lithos* 320–321. <https://doi.org/10.1016/j.lithos.2018.09.014>

Chapter-4

Metamorphic evolution of the calc-silicate granulites

Chapter-4.1

Evolution of aluminous clinopyroxene- ilmenite-spinel symplectites in calc-silicate granulite

Chapter 4.1

Evolution of aluminous clinopyroxene-ilmenite-spinel symplectites in calc-silicate granulite

Symplectic intergrowth of clinopyroxene-ilmenite-spinel has been commonly reported from intrusive igneous rocks of mafic-ultramafic compositions and as xenoliths in kimberlites (Barton et al., 1991; Garrison and Taylor, 1981; Schulze et al., 1978). A number of processes have been proposed to explain this intergrowth, which includes: exsolution from pre-existing clinopyroxene due to decreased solubility of the Cr-Al components (CrMgTs) in pyroxenes (Garrison and Taylor, 1981; Secchiari et al., 2019 and references therein), eutectic co-precipitation of pyroxene and spinel and/or ilmenite (Dawson and Reid, 1970; Schulze et al., 1978), or crystallization from a melt phase (e.g., Seyler et al., 2007; Suhr et al., 2008), discontinuous precipitation (Field, 2008; Field and Haggerty, 1994), and breakdown of chromium bearing garnet due to decompression during ascent of mantle peridotites (Secchiari et al., 2019; Shimizu et al., 2008).

Clinopyroxene-ilmenite-spinel bearing symplectic or coarser assemblages, are less common in metamorphic rocks. The reported occurrences of the symplectites are commonly restricted in high to ultra-high pressure mafic granulites and retrogressed eclogites (Faryad et al., 2006; Marsh and Kelly, 2017; Zhang and Liou, 2003). Decomposition of garnet and primary ultra-high pressure clinopyroxene with or without participation of titanite and amphibole along a steeply decompressive retrograde P-T path has been invoked as a common mechanism for the formation of clinopyroxene-ilmenite-spinel bearing assemblage (Cruciani et al., 2008; Marsh and Kelly, 2017; Ringwood and Lovering, 1970; Tam et al., 2012 and references therein; Zhang and Liou, 2003). Within this assemblage, only a few reported occurrence show high aluminous ($\text{Al}_2\text{O}_3 = 3\text{-}14.6$ wt%) clinopyroxenes in regionally metamorphosed mafic or ultramafic granulites (Curtis and Gittins, 1979; Dasgupta et al., 1993; Faryad et al., 2006; Petrakakis et al., 2018;

Yoshino et al., 1998), that formed via breakdown of garnet and titanite, or olivine and plagioclase (Dasgupta et al., 1993; Faryad et al., 2006).

Al-rich clinopyroxenes ($\text{Al}_2\text{O}_3=4\text{-}27$ wt%) and spinel bearing assemblages in calcareous rocks are described from a few infiltration driven skarns (Moine et al., 1985; e.g., Pascal et al., 2005, 2001), and in the calc silicate rocks that are formed by interaction of basaltic magma and metasedimentary rocks (Owens, 2000; Reato et al., 2022). Occurrence of clinopyroxene (low- and/ or high-aluminous)-ilmenite± spinel association is extremely rare in the regionally metamorphosed calcareous granulites (Bouregghda et al., 2016; Janardhan et al., 2001; Le Bas et al., 2002; Maki et al., 2009). In only one study this rare assemblage is shown to have formed by the break down of garnet + titanite (Bouregghda et al., 2016).

The present study reports and interprets the occurrence of high aluminous clinopyroxene-ilmenite-spinel symplectites from regionally metamorphosed calc-silicate granulite, exposed in the north-eastern part of the Chotanagpur Granite Gneiss Complex (Fig. 2.1). Detailed field and textural study, phase equilibria modelling, combined with LA-ICP-MS U–Pb zircon dating and stable oxygen isotope composition of whole rock are presented to: (i) explore the factors that triggered the formation of clinopyroxene-ilmenite-spinel symplectites; (ii) identify the plausible protolith of the studied rocks; and (iii) put a constraint on the timing of high-grade metamorphism that led to the formation of the Al-rich clinopyroxene-ilmenite-spinel symplectites.

4.1.1. Field description

The studied rock (AS29, Fig. 3.1) is exposed at the southern foothills of the Trikut hill, ~20 km south-east of Deoghar. It is 3-5 metres in width, and ~10 metres in length, and occur as enclaves within the migmatitic felsic gneiss (now extensively retrogressed to amphibole-biotite gneiss). The host migmatitic felsic gneiss also contains pods, lenses and laterally discontinuous bands of typical calc-silicate granulite (nearest outcrop (AS29X) exposed within ~50 meter of the studied rock, primarily comprises clinopyroxene, plagioclase, garnet and titanite; Fig. 3.1). This calc-silicate granulite in AS29X also shows millimetre to centimetre thick alternate

layers, rich in clinopyroxene and plagioclase respectively (Fig. 4.1.1a), that are similar in appearance and mineralogy with the other calc-silicate granulites in the region (Fig. 2a; Dey et al., 2019a).

Owing to tropical weathering, direct contact between the studied rock and the migmatitic felsic gneiss could not be seen. However, relative position in field indicates that the migmatitic felsic gneiss encloses the studied rock. The studied rock shows three types of mineralogical bandings (Fig. 4.1.1b-c) namely, (i) leucocratic band (rich in plagioclase with minor garnet, clinopyroxene and amphibole), (ii) melanocratic band (rich in clinopyroxene, ilmenite, spinel and amphibole), and (iii) garnet rich band (~70 vol% garnet with minor plagioclase and clinopyroxene).

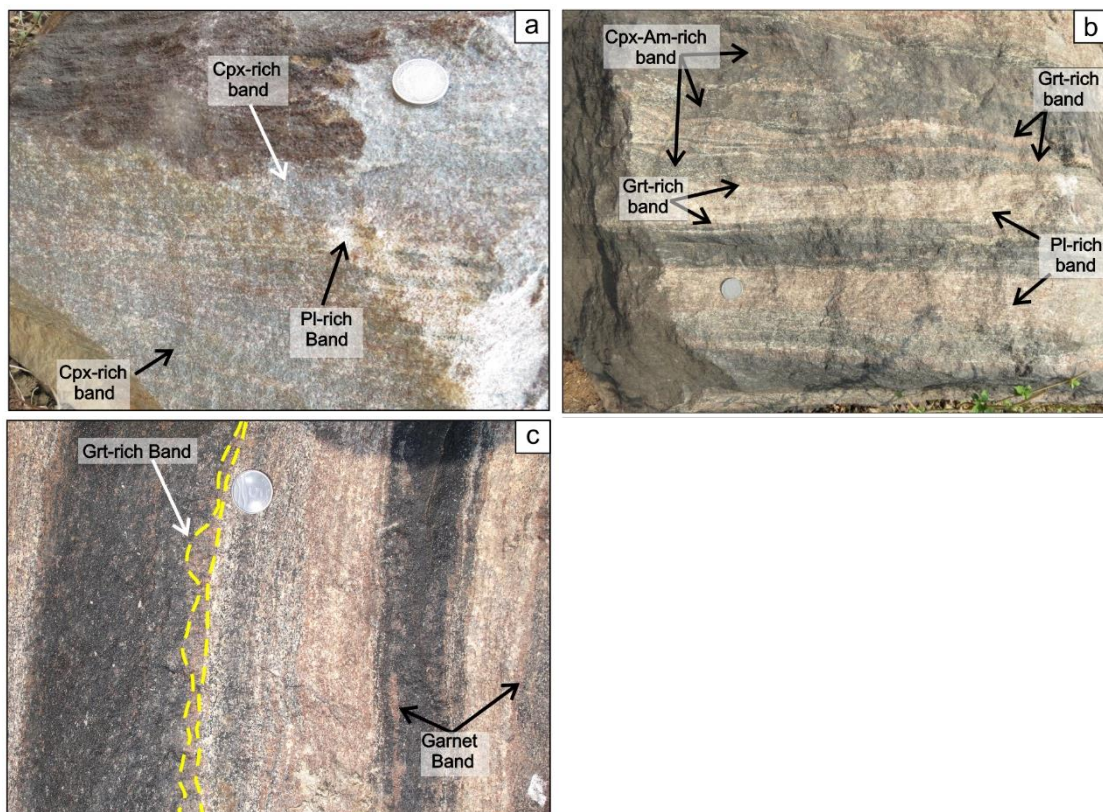
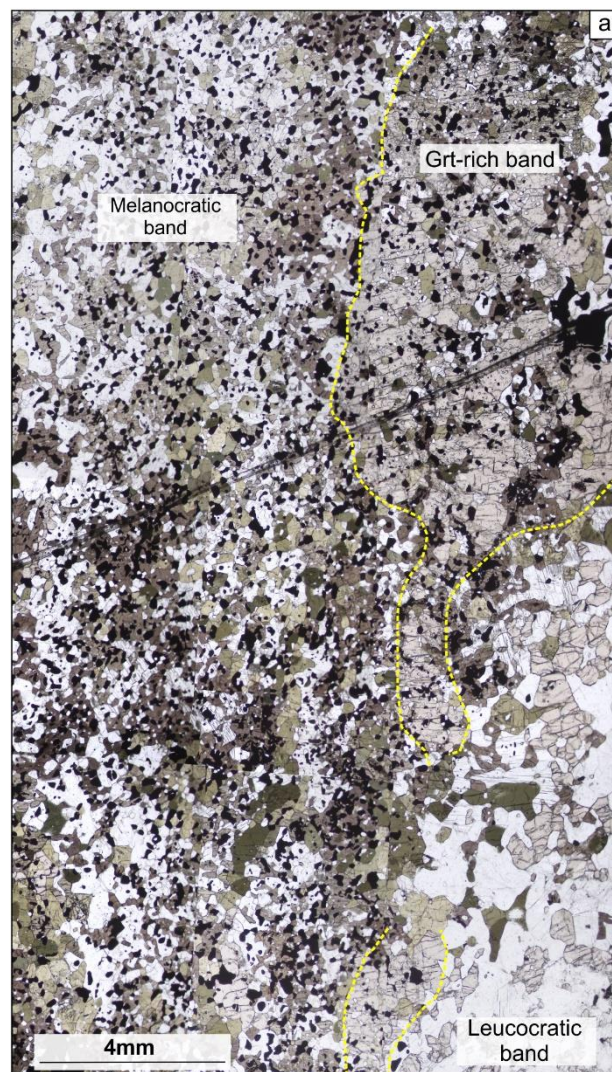


Fig. 4.1.1: (a) Alternate pyroxene rich and plagioclase rich bands in the adjacent calc-silicate granulite (location no.: AS29X). (b) Alternate leuco- and melanocratic bands of varying thickness, dominated by plagioclase and pyroxene-spinel-ilmenite-amphibole respectively, in the studied rock (location no.: AS29). Note that the contacts between the two bands are gradational, and thin garnet bands are present at their interface. (c) Zoomed in image of garnet-rich bands forming along the boundary of leucocratic and melanocratic bands. Mineral abbreviations are after Kretz (1983).

Millimetre thin garnet-rich bands separate the leucocratic and melanocratic bands. Mineralogical gradation across the compositional banding is a characteristic feature of the rock. The compositional banding of the studied rock is parallel with the gneissic banding of the enclosing migmatitic felsic gneiss and the compositional banding of the typical calc-silicate granulites. Together, these planar structures define the regional N-S fabric (Fig. 4.1.1b-c).

4.1.2. Petrography

The major mineralogy of the studied rock consists of plagioclase, garnet, amphibole, clinopyroxene, ilmenite and spinel. Other accessory minerals include titanite, apatite, zircon and rare magnetite and calcite. A number of thin sections from each of the three bands identified in the field (melanocratic, leucocratic and garnet bands) have been studied (AS29i, AS29ii, AS29iii). Variation of modal mineralogy, particularly the relative proportion of garnet, plagioclase, clinopyroxene, spinel and ilmenite has been noted in the three bands (Table 4.1.1). Fig. 4.1.2a depicts the different bands evident under thin section. The



back scattered electron images have been taken in the Scanning Electron Microscope Laboratory, Department of Geological Sciences, Jadavpur University. Salient petrographic features in each of the three bands are presented below:

4.1.2.1. Leucocratic band

This band is dominated by plagioclase (~40% vol%), followed by garnet (c.a. 20% vol%) + clinopyroxene (~15% vol%) + ilmenite (~10% vol%) + spinel (~5% vol%) + amphibole (~10% vol%). Plagioclase (Pl₁) grains are large, and define a polygonal granoblastic mosaic along with amphibole (Am₁), garnet and rare matrix ilmenite (Fig. 4.1.2b-d). Medium sized (~500-1000 micrometre) subhedral garnet grains contain inclusions of amphibole (Am_{inc}), plagioclase (Pl_{inc}) and rare ilmenite (Fig. 4.1.2b, e). Volumetrically small titanite, is dispersed in the granoblastic matrix as an accessory phase. Texturally, two distinct varieties of clinopyroxenes are identified. Small to medium sized, subidioblastic to xenoblastic clinopyroxene (Cpx₁), pleochroic in shades of brown, are present along the grain margins of Pl₁ (Fig. 4.1.2d). Cpx₁ grains show sharp, planar, boundaries with garnet, Pl₁ and Am₁, in the granoblastic mosaic. In a few places, symplectic intergrowths of brown clinopyroxenes (Cpx₂) and plagioclase (Pl₂), with vermicular blebs of ilmenite + spinel is formed (Figs. 4.1.2f-j). These symplectites form at high angles to garnet and in contact with amphibole (Am₁; Figs. 4.1.2f-i). The symplectites also protrude into the garnet grains, making the boundaries between the two, irregular and gradational (Fig. 4.1.2h-i, k). Locally the symplectite partially or completely engulfs the garnet grains (Fig. 4.1.2k). Relict amphibole (Am₁) and rare titanite are present within the symplectites (Figs. 4.1.2f, h). These textural features are consistent with the formation of symplectite after garnet, Am₁ and titanite.

4.1.2.2. Melanocratic band:

This band is dominated by brown clinopyroxene (~25 vol %), spinel (~15 vol %) ilmenite (~15 vol %), followed by amphibole (~20 vol %), plagioclase (~20 vol %) and rare titanite (Fig. 4.1.2i). Although, mutual textural relations between the minerals are similar to the leucocratic band, this band shows a few distinctive features. Compared to the leucocratic and garnet-rich bands, the modal proportion of the symplectites is much higher in this band. The symplectic assemblage are also coarser, with Cpx₂ containing larger blebs of ilmenite-spinel (Figs. 4.1.2l-n). Garnet in this band occupies smaller modal volume, and occurs as a relict sharing irregular grain boundary with the large symplectites of Cpx₂-ilmenite-spinel-Pl₂ (Fig. 4.1.2l-

m). Amphibole (Am_1) mostly shows equilibrium relations with garnet. Inclusions of amphiboles within symplectites are common (Fig. 4.1.2n). Rare magnetite is also present in the matrix.

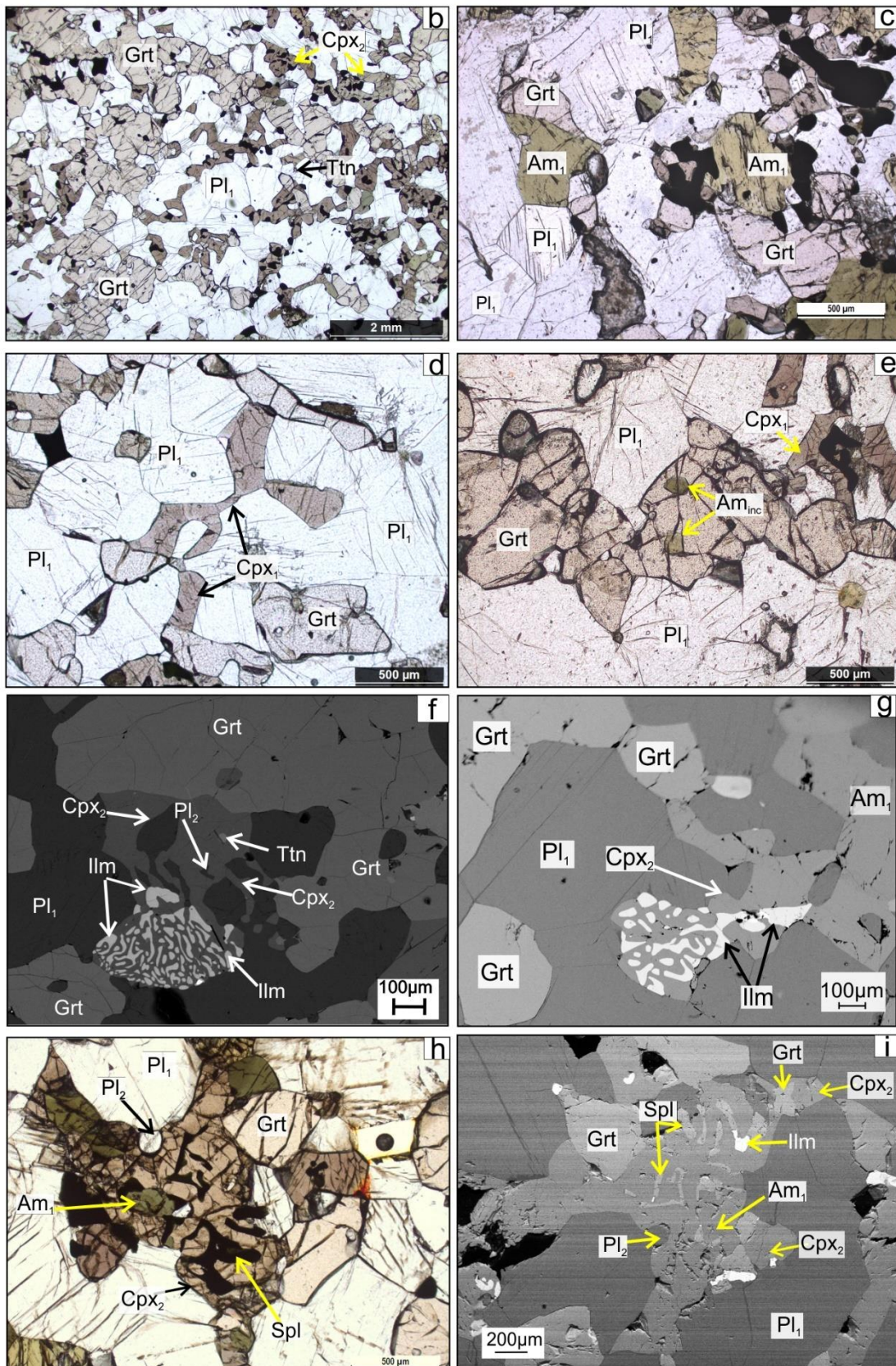


Fig. 4.1.2: Petrographic features of the studied rocks: (a) The leucocratic, melanocratic and garnet-rich bands, visible in thin section scale. Leucocratic band (b-k), Melanocratic band (l-n), Garnet-rich band (o). (b) Granoblastic mosaic defined by garnet, clinopyroxene (Cpx₁) and plagioclase (Pl₁). (c) Straight equilibrium boundaries between amphibole (Am₁) and garnet, as well as Pl₁. (d) Cpx₁ having sharp, prominent boundaries with garnet and Pl₁, together defining a recrystallised granoblastic mosaic. (e) Inclusions of amphibole (Am_{inc}) in garnet. (f) BSE image of titanite inclusion present within Cpx₂-Ilm-Pl₂ symplectite. Note the clinopyroxenes growing at high angles to garnet margin. Also note that small plagioclases (Pl₂) are present with these symplectites. (g) BSE image showing symplectites of Cpx₂ and vermicular blebs of ilmenite forming at high angles to the margins of garnet and Am₁. (h-i) Spinel blebs are also associated with these symplectites. Note that amphiboles are partially to fully engulfed by the symplectic Cpx₂-spinel-ilmenite. Also, irregular margins shared by garnet and the symplectite in g-h. Am_{inc}: Inclusion of prograde amphibole, Am₁: peak amphibole, Am₂: replacing amphibole, Cpx₁: peak clinopyroxene, Cpx₂: symplectic clinopyroxene, Pl₁: peak plagioclase, Pl₂: symplectic plagioclase. All mineral abbreviations are after Kretz, (1983).

4.1.2.3. Garnet rich band:

The garnet-rich bands comprise almost c.a. 60 vol% garnet. The rest are occupied by plagioclase, brown clinopyroxene, amphibole, ilmenite, spinel and few titanites (Fig. 4.1.2o; Table 4.1.1). Medium to large grains of garnet occurs as aggregates. Inclusions of amphibole (Am_{inc}) are present within garnet (Fig. 4.1.2n). The modal proportion of the symplectites are least in this band. The symplectic assemblage Cpx₂-ilmenite-spinel is concentrated at the boundary/contact with the melanocratic and leucocratic bands, though patches of the symplectites are also found to replace garnet within the bands (Fig. 4.1.2o). The proportion of symplectite in the garnet-rich band is lower than the adjoining leucocratic as well as the melanocratic bands. In contrast to the other two bands, here plagioclase is rare, and present only as small islands within the band (Fig. 4.1.2o).

Some additional features are common to all the three bands. Another textural variant of amphibole (Am₂) is found to replace garnet and the symplectic assemblage (Cpx₂-Ilm-Spl-Pl₂) (Fig. 4.1.2p-q) in all the bands. In contrast to Am₁, which is part of the granoblastic fabric, Am₂ locally displays crude orientation. Rare calcite is present adjacent to clinopyroxene, plagioclase and amphibole in the matrix (Fig. 4.1.2r). However, it does not replace any minerals, implying that it is not a secondary mineral. Zircon is mostly dispersed as matrix grains, and as rare

inclusions in garnets. None of the bands contain segregations of quartz and alkali-feldspar suggesting that the studied rock did not undergo any partial melting.

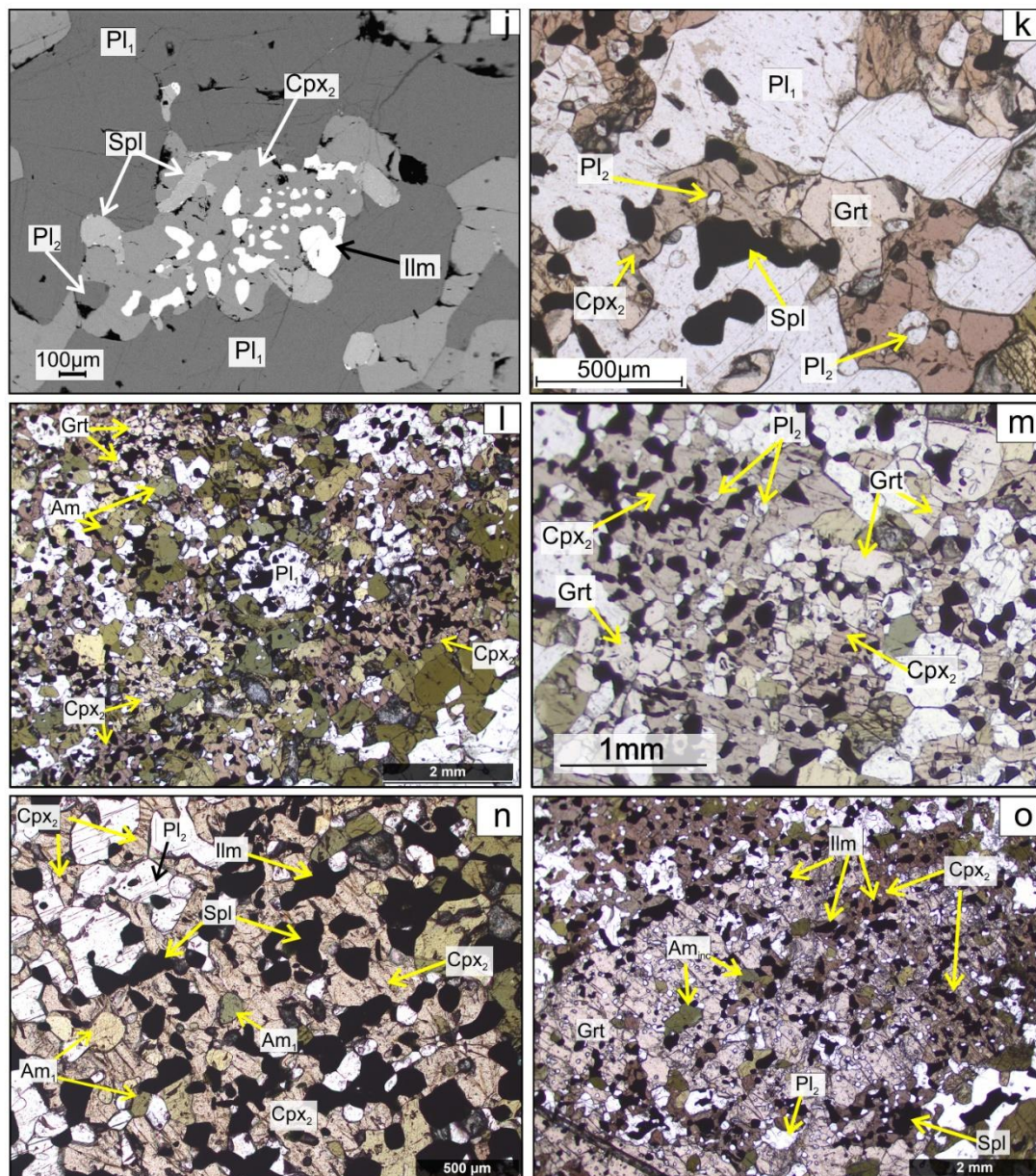


Fig. 4.1.2 contd.:(j) Spinel blebs associated with these symplectites. (k) Symplectites engulfing garnet grains. (l-m) Coarse Cpx₂-ilmenite-spinel-Pl₂ assemblage dominate the melanocratic band. Relict garnets occur sporadically in this band (see 'k-l'). Note the corroded margins of garnet at the interface of symplectites in 'l-m'. (n) These coarse Cpx₂-ilmenite-spinel-Pl₂ assemblage enclose Am₁ within them. (o) Garnet-rich band comprising aggregates of garnets, along with amphibole. Cpx₂-ilmenite-spinel symplectites form both at the margins as well as within these garnet-rich bands. Plagioclase occurs as small islands within this band. Am₁: peak amphibole, Am₂: replacing amphibole, Cpx₁: peak clinopyroxene, Cpx₂: symplectic clinopyroxene, Pl₁: peak plagioclase, Pl₂: symplectic plagioclase. All mineral abbreviations are after Kretz, (1983).

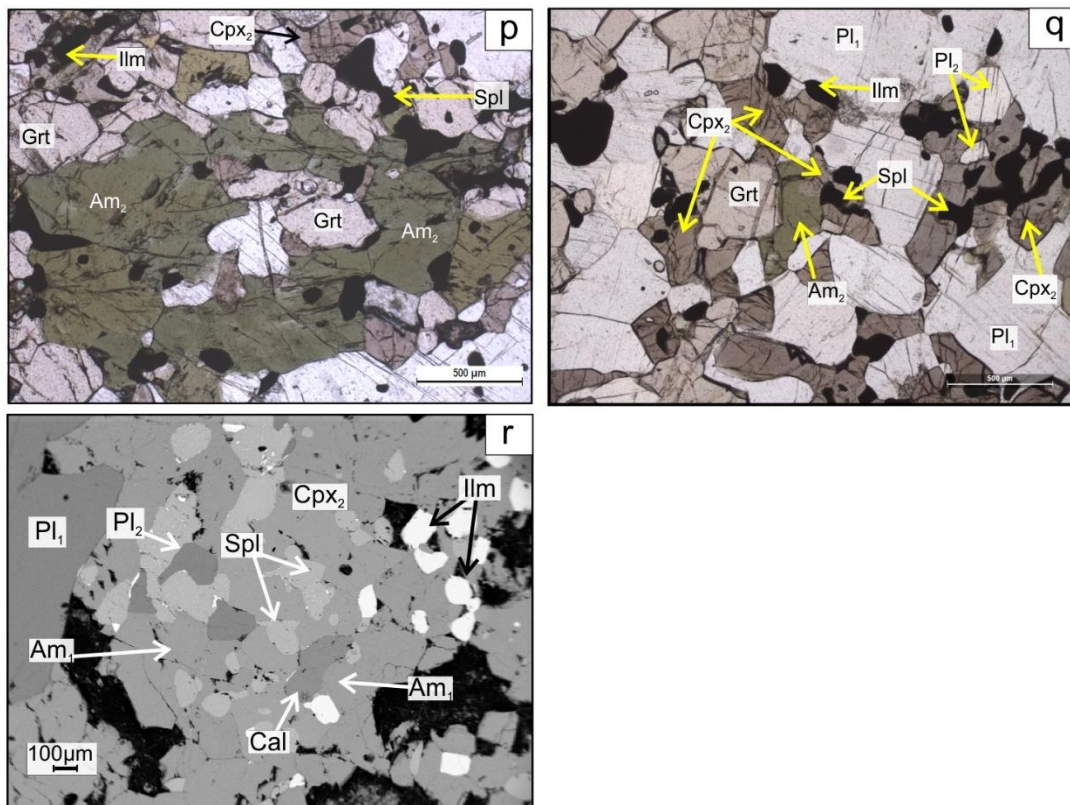


Fig. 4.1.2 contd.:(p-q) Later generation of amphiboles (Am_2) replacing garnet and the symplectites. (r) Calcite disposed in the matrix amongst clinopyroxene and amphibole. Am_{inc} : Inclusion of prograde amphibole, Am_1 : peak amphibole, Am_2 : replacing amphibole, Cpx_1 : peak clinopyroxene, Cpx_2 : symplectitic clinopyroxene, Pl_1 : peak plagioclase, Pl_2 : symplectitic plagioclase. All mineral abbreviations are after Kretz, (1983).

4.1.3. Mineral Chemistry

Mineral compositions were analysed at the Central Research Facility of the Indian Institute of Technology (Indian School of Mines), Dhanbad, India using CAMECA SX5 electron microprobe. The analytical details have been provided in Appendix. Mineral compositions were measured from a number of thin sections of the different samples. Fe^{+3} was calculated using the scheme of Droop, (1987) and Grew et al., (2013), during cation recalculation. Cation recalculation of amphibole was done using the scheme of Hawthorne et al., (2012). No compositional differences have been observed amongst the different bands for any of the minerals in the three samples. Therefore, compositions of the minerals from across the

Table 4.1.1: Summary of the mineral assemblages, along with their respective modal proportions in the studied calc-silicate granulite.

Sample	Studied calc-silicate granulite		
	AS29i	AS29ii	AS29iii
Minerals			
Plagioclase	10	20	35
Garnet	55	5	20
Clinopyroxene (aluminous)	17	25	15
Ilmenite	5	15	12
Spinel	5	15	8
Amphibole	8	20	10
Titanite	a.m.	a.m.	a.m.
Quartz	-	-	-
Calcite	a.m.	a.m.	a.m.
Magnetite	a.m.	a.m.	a.m.
Apatite	a.m.	a.m.	a.m.

a.m.: Accessory mineral

"-": not present

different bands have been described together below, and their representative data provided in Table 4.1.2a-f. Mineral abbreviations used are after Kretz, (1983).

Clinopyroxene:

Clinopyroxenes are highly aluminous, with Al_2O_3 content varying from ~7.9 to 11.5 wt % (0.4-0.5 apfu; Table 4.1.2a). However, no zoning was observed within individual grains. These clinopyroxenes are dominantly magnesian, with X_{Mg} [$Mg/(Mg+Fe^{+2})$] values ranging between ~0.67-0.81. However, no compositional zoning was observed within individual grains. Essentite ($CaFe^{+3}Si_2O_6$) and Ca-Tschermak ($CaAl^{+3}Si_2O_6$) components vary between ~5-15 mol% and ~6-14 mol% respectively. The measured mineral data are plotted in the composition plots for aluminous clinopyroxenes (Fig. 4.1.3a; Cosca and Peacor, 1987). An inverse relation

between $(Al(VI)+Fe)^{+3}$ vs $(Mg+Fe)^{+2}$ and $Al(IV)$ vs Si prominently demonstrates the substitution in octahedral and tetrahedral sites (Fig. 4.1.3b). Acmite and jadeite components together add up to ~ 1 mol% (Table 4.1.2a). However, the compositions of Cpx_1 and Cpx_2 are overlapping in all the bands.

Garnet:

Garnets are dominantly a solid solution of grossular and almandine with small and variable proportion of andradite ($\sim 1-7$ mol% Fig. 4.1.3c, Table 4.1.2b). Core of garnet ($Py_{0.09-0.11}Grs_{0.48-0.52}Alm_{0.32-0.37}Sps_{0.02}Adr_{0.02-0.07}$; X_{Mg} : 0.21-0.25) is grossular rich and almandine poor than the rims ($Py_{0.09-0.10}Grs_{0.43-0.46}Alm_{0.40-0.44}Sps_{0.01}Adr_{0.01-0.05}$; X_{Mg} : 0.17-0.20).

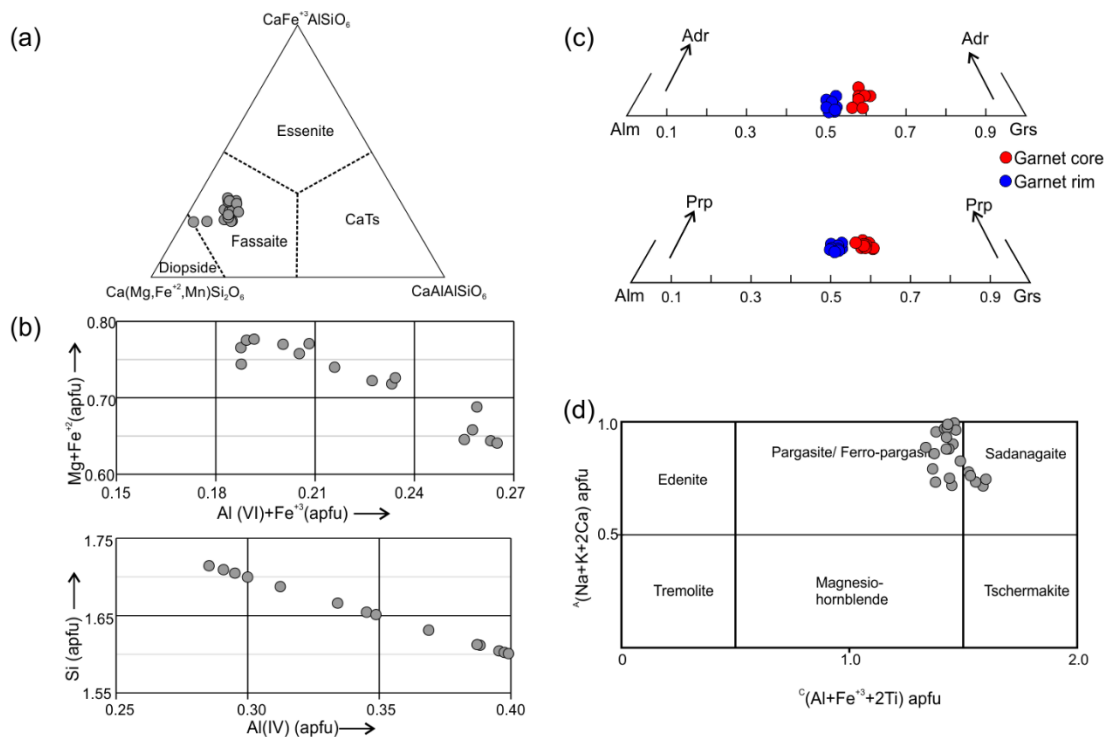


Fig. 4.1.3: Compositional plots of aluminous clinopyroxene in the studied rock: (a) on the basis of substitution in M1 site (Cosca and Peacor, 1987). (b) $Al(VI)+Fe^{+3}$ (apfu) vs $Mg + Fe^{+2}$ (apfu) and $Al(IV)$ (apfu) vs Si (apfu) plot demonstrating substitution in the octahedral and tetrahedral sites respectively. Compositions of peak and symplectitic clinopyroxenes overlap with each other. (c) Composition of garnet plotted in andradite-almandine-grossular and pyrope-almandine-grossular triangles. Note that the end members for the respective triangular plots have been recalculated to 100 for presentation. (d) Composition of amphiboles presented in a $A(Na+K+2Ca)$ vs $C(Al+Fe^{+3}+2Ti)$ (apfu) plot for calcic amphiboles after the classification scheme of Hawthorne et al., (2012). All mineral abbreviations are after Kretz, (1983).

Plagioclase:

Plagioclases are almost purely anorthitic ($\text{An}_{0.98-0.99}\text{Ab}_{0.01-0.02}\text{Or}_0$) in composition (Table 4.1.2c). The compositions of both large matrix plagioclases (Pl_1) and small ones, associated with the symplectites (Pl_2), are identical in all the bands.

Ilmenite:

All ilmenites (both matrix grains and those within symplectites) have almost pure composition with negligible amounts of MgO (~0.5-1.2 wt%) and MnO (~0.1-0.5 wt%). They contain some amount of Fe^{+3} component (up to ~0.10 apfu) as calculated from ideal stoichiometry (Table 4.1.2c).

Amphibole:

Amphiboles range between pargasite to sadanagaite variety (Hawthorne et al., 2012); Fig. 4.1.3d). These are slightly magnesian, with X_{Mg} varying between ~0.57-0.64. Al_2O_3 content varies between ~16.9-18.5 wt% (Table 4.1.2d). No compositional zoning was observed in the individual amphibole grains. The compositions of Am_{inc} , Am_1 and Am_2 are overlapping and fall within the above limits.

Spinel:

Spinel is primarily hercynitic, but also consists of considerable amount of spinel and magnetite components ($\text{Herc}_{0.61-0.68}\text{Spl}_{0.25-0.31}\text{Mt}_{0.05-0.11}\text{Chr}_{0-0.01}$). Chromite content never exceeds ~1 mol%. Their X_{Mg} values range between ~0.25-0.31. The spinel contains low concentration of zinc in their composition (<0.01 wt%; Table 4.1.2e).

Titanite:

Titanites contain a small proportion of aluminium in their structure (~2.7-2.9 wt% Al_2O_3). These titanites does not contain fluorine and chlorine in detectable amount (Table 4.1.2e). The slightly low totals indicate that these titanites might contain some amount of rare earth elements (Table 4.1.2e).

Other phases:

Apatite contains considerable amount of fluorine (~3.1-4.4 wt%), along with minor amounts of chlorine (~0.8-0.9 wt%; Table 4.1.2f). Magnetite contains around ~4.6-9.7 wt% TiO₂ in its structure (Table 4.1.2f). Calcite is essentially CaCO₃ with minor amount of MgO (~0.5 wt%; Table 4.1.2f).

4.1.4. Evolution of mineral assemblages and identification of mineral reactions

Detailed petrographic observations suggest nearly similar mineralogical evolution in all the three bands, though the extent of the mineralogical changes varies in the three bands. The presence of granoblastic fabric among amphibole (Am₁), garnet, clinopyroxene (Cpx₁) and plagioclase (Pl₁) suggest that these phases stabilised during the culmination of metamorphism. Titanite and rare matrix ilmenite, that constitute part of the granoblastic assemblage, are also considered to have been stable during peak metamorphic conditions. Owing to the formation of the granoblastic fabric at the culmination of metamorphism, the prograde metamorphic path can be constrained from the inclusions in the peak mineral assemblage. Presence of inclusions of amphibole (Am_{inc}), plagioclase (Pl_{inc}) and rare ilmenite within garnet suggests that these minerals were stable prior to development of garnet. Very rare occurrence of calcite (where present) suggests it to be possibly a part of the prograde assemblage, that reacted to form the peak minerals. Therefore, the following prograde dehydration reaction is proposed for the formation of the peak minerals: Am_{inc} + Pl_{inc} ± Ilm ± Cal = Grt + Cpx₁ + Ttn + vapour ... (A). Absence of quartz-alkali feldspar segregations suggest that this prograde reaction that develops this granoblastic fabric, did not involve partial melting.

Textural relations suggest that the symplectic assemblage involving aluminous clinopyroxene-ilmenite-spinel-plagioclase (Cpx₂-Ilm-Spl-Pl₂) were formed after the garnet- Cpx₁ bearing granoblastic assemblage by the following reaction: Grt + Am₁ + Ttn = Cpx₂ + Ilm ± Spl + Pl₂ + vapor ... (B). Secondary amphibole (Am₂) replaces garnet and the symplectic assemblage (Cpx₂-Ilm-Spl-Pl₂), suggesting limited ingress of fluid during retrogression, after symplectite formation.

Table 4.1.2a: Representative electron microprobe analysis of clinopyroxene (stoichiometry calculated on the basis of 6 oxygens, oxide data are given in weight%).

Point No.	13 / 1 .	19 / 1 .	45 / 1 .	27 / 1 .	9 / 1 .	43 / 1 .
Texture	Cpx1	Cpx1	Cpx1	Cpx2	Cpx2	Cpx2
SiO ₂	42.30	42.83	44.62	45.02	44.43	42.06
TiO ₂	2.49	2.51	1.91	1.72	1.85	2.43
Al ₂ O ₃	11.53	11.51	9.61	7.93	9.46	10.90
Cr ₂ O ₃	0.00	0.02	0.06	0.20	0.02	0.00
FeO	10.07	9.32	9.16	8.21	9.62	9.24
MnO	0.00	0.02	0.00	0.00	0.00	0.00
MgO	8.74	8.92	9.38	10.55	9.07	9.01
CaO	23.73	23.69	23.78	24.66	23.54	24.45
Na ₂ O	0.18	0.12	0.07	0.09	0.11	0.12
K ₂ O	<d.l.	<d.l.	0.01	0.01	<d.l.	0.03
Total	99.04	98.94	98.60	98.39	98.10	98.23
Si	1.61	1.63	1.70	1.71	1.71	1.61
Ti	0.07	0.07	0.05	0.05	0.05	0.07
Al	0.52	0.52	0.43	0.36	0.43	0.49
Cr ⁺³	0.00	0.00	0.00	0.01	0.00	0.00
Fe ⁺³	0.13	0.09	0.05	0.12	0.05	0.15
Fe ⁺²	0.19	0.21	0.24	0.14	0.26	0.14
Mn	0.00	0.00	0.00	0.00	0.00	0.00
Mg	0.50	0.51	0.53	0.60	0.52	0.51
Ca	0.97	0.97	0.97	1.01	0.97	1.00
Na	0.01	0.01	0.01	0.01	0.01	0.01
K	0.00	0.00	0.00	0.00	0.00	0.00
Total	4.00	4.00	4.00	4.00	4.00	4.00
X _{Mg}	0.72	0.71	0.69	0.81	0.67	0.78
Al(IV)	0.39	0.37	0.30	0.29	0.29	0.39
Al(VI)	0.13	0.15	0.14	0.07	0.14	0.10
Di	0.52	0.53	0.55	0.64	0.54	0.56
Hd	0.20	0.22	0.25	0.15	0.26	0.16
Ac	0.00	0.00	0.00	0.00	0.00	0.00
Jd	0.01	0.01	0.01	0.01	0.01	0.01
Ess	0.13	0.09	0.05	0.12	0.05	0.15
CrTs	0.00	0.00	0.00	0.01	0.00	0.00
CaTs	0.12	0.14	0.13	0.06	0.13	0.10
Wo	0.97	0.97	0.97	1.01	0.97	1.00
En	0.50	0.51	0.53	0.60	0.52	0.51
Fs	0.19	0.21	0.24	0.14	0.26	0.14
Don	0.00	0.00	0.00	0.00	0.00	0.00

<d.l.: below detection limit

Table 4.1.2b: Representative electron microprobe analysis of garnet (stoichiometry calculated on the basis of 12 oxygens, oxide data are given in weight%).

Point No.	36 / 1 .	20 / 1 .	50 / 1 .	6 / 1 .	21 / 1 .	5 / 1 .	35 / 1 .
Texture	core				rim		
SiO ₂	38.19	38.63	37.91	38.76	38.14	37.99	38.20
TiO ₂	0.19	0.15	0.17	0.14	0.09	0.12	0.15
Al ₂ O ₃	20.42	21.27	20.05	20.83	21.02	20.50	21.46
Cr ₂ O ₃	0.00	0.00	0.00	0.00	0.04	0.00	0.00
FeO	17.07	17.54	17.51	17.13	20.67	19.90	20.20
MnO	0.86	0.78	0.78	0.87	0.49	0.63	0.53
MgO	2.46	2.88	2.84	2.52	2.54	2.60	2.32
CaO	19.48	18.08	18.74	19.26	16.13	16.82	16.42
Na ₂ O	0.03	0.03	0.02	<d.l.	0.07	0.04	<d.l.
K ₂ O	0.03	0.01	<d.l.	<d.l.	0.04	<d.l.	0.03
Total	98.72	99.38	98.01	99.50	99.23	98.61	99.35
Si	2.99	3.00	2.99	3.01	2.99	3.00	2.99
Ti	0.01	0.01	0.01	0.01	0.01	0.01	0.01
Al	1.89	1.95	1.87	1.91	1.94	1.91	1.98
Cr ⁺³	0.00	0.00	0.00	0.00	0.00	0.00	0.00
Fe ⁺³	0.11	0.03	0.13	0.05	0.07	0.09	0.01
Fe ⁺²	1.01	1.11	1.03	1.07	1.28	1.22	1.31
Mn	0.06	0.05	0.05	0.06	0.03	0.04	0.04
Mg	0.29	0.33	0.33	0.29	0.30	0.31	0.27
Ca	1.64	1.51	1.59	1.60	1.36	1.42	1.38
Na	0.00	0.00	0.00	0.00	0.01	0.01	0.00
K	0.00	0.00	0.00	0.00	0.00	0.00	0.00
Total	8.00	8.00	8.00	8.00	8.00	8.00	8.00
X _{Adr}	0.05	0.02	0.07	0.02	0.04	0.05	0.01
X _{Py}	0.09	0.11	0.11	0.10	0.10	0.10	0.09
X _{Alm}	0.32	0.37	0.33	0.35	0.42	0.40	0.44
X _{Grs}	0.51	0.49	0.48	0.52	0.43	0.45	0.46
X _{Sps}	0.02	0.02	0.02	0.02	0.01	0.01	0.01
X _{Mg}	0.22	0.23	0.25	0.21	0.19	0.20	0.17

<d.l.: below detection limit

Table 4.1.2c: Representative electron microprobe analysis of plagioclase and ilmenite (stoichiometry calculated on the basis of 8 and 3 oxygens respectively, oxide data are given in weight %).

Mineral	Plagioclase			Ilmenite		
	Point No.	8 / 1 .	14 / 1 .	37 / 1 .	56 / 1 .	53 / 1 .
Texture	Pl1	Pl1	Pl2	matrix	symplectite	
SiO ₂	43.20	43.34	42.92	0.00	0.04	0.05
TiO ₂	0.01	0.00	0.02	49.96	50.71	49.70
Al ₂ O ₃	36.49	36.17	36.65	0.11	0.12	0.00
FeO	0.22	0.12	0.14	48.15	46.40	47.58
MnO	0.07	0.00	0.00	0.14	0.50	0.08
MgO	0.00	0.01	0.00	0.50	1.24	0.91
CaO	19.80	19.66	19.98	0.06	0.01	0.06
Na ₂ O	0.08	0.16	0.10	0.04	<d.l.	0.01
K ₂ O	0.02	0.01	<d.l.	<d.l.	0.01	<d.l.
Total	99.89	99.47	99.81	98.98	99.02	98.42
Si	2.00	2.02	1.99	0.00	0.00	0.00
Ti	0.00	0.00	0.00	0.95	0.96	0.95
Al	1.99	1.98	2.00	0.00	0.00	0.00
Fe ⁺³	0.01	0.00	0.01	0.10	0.07	0.10
Fe ⁺²	0.00	0.01	0.00	0.92	0.90	0.91
Mn	0.00	0.00	0.00	0.00	0.01	0.00
Mg	0.00	0.00	0.00	0.02	0.05	0.03
Ca	0.98	0.98	0.99	0.00	0.00	0.00
Na	0.01	0.01	0.01	0.00	0.00	0.00
K	0.00	0.00	0.00	0.00	0.00	0.00
Total	5.00	5.00	5.00	2.00	2.00	2.00
X _{An}	0.99	0.98	0.99			
X _{Ab}	0.01	0.02	0.01			
X _{Or}	0.00	0.00	0.00			

<d.l.: below detection limit

Table 4.1.2d: Representative electron microprobe analysis of amphibole(after Hawthorne et al., 2012; stoichiometry calculated on the basis of 23 oxygens, oxide data are given in weight%).

Point No.	17/ 1	20/1	15/1	24 / 1 .	27 / 1 .	14/ 1
Texture	Am _{inc}	Am ₁	Am ₁	Am ₁	Am ₂	Am ₂
SiO ₂	37.98	37.87	38.02	38.05	37.91	38.89
TiO ₂	1.10	1.02	1.03	1.22	1.23	1.12
Al ₂ O ₃	18.18	17.87	18.12	18.51	18.01	16.99
Cr ₂ O ₃	0.01	0.00	0.00	0.00	0.00	0.00
FeO	14.45	14.42	14.84	13.79	14.91	15.29
MnO	0.05	0.04	0.06	0.06	0.10	0.03
MgO	10.12	10.07	10.19	10.07	9.92	9.35
CaO	12.00	11.92	11.90	12.65	12.37	12.29
Na ₂ O	2.41	2.67	2.62	2.37	2.26	1.80
K ₂ O	0.50	0.49	0.55	0.59	0.60	1.03
F	<d.l.	<d.l.	<d.l.	0.05	<d.l.	<d.l.
Cl	0.09	0.10	0.09	0.69	0.79	0.19
Total	96.89	96.48	97.41	98.01	97.84	96.99
Si	5.66	5.69	5.65	5.66	5.64	5.85
Al	2.34	2.31	2.35	2.34	2.36	2.15
Ti	0.00	0.00	0.00	0.00	0.00	0.00
Fe ³⁺	0.00	0.00	0.00	0.00	0.00	0.00
T subtotal	8.00	8.00	8.00	8.00	8.00	8.00
Ti	0.12	0.12	0.12	0.14	0.14	0.13
Al	0.86	0.85	0.82	0.90	0.80	0.86
Cr	0.00	0.00	0.00	0.00	0.00	0.00
Fe ³⁺	0.53	0.45	0.55	0.36	0.54	0.34
Mn ²⁺	0.00	0.00	0.00	0.01	0.00	0.00
Fe ²⁺	1.24	1.33	1.26	1.36	1.32	1.58
Mg	2.25	2.26	2.26	2.23	2.20	2.10
C subtotal	5.00	5.00	5.00	4.99	5.00	5.00
Mn ²⁺	0.01	0.01	0.01	0.00	0.01	0.00
Fe ²⁺	0.03	0.03	0.04	0.00	0.00	0.01
Mg	0.00	0.00	0.00	0.00	0.00	0.00
Ca	1.92	1.92	1.90	2.00	1.97	1.98
Na	0.04	0.04	0.06	0.00	0.01	0.01
B subtotal	2.00	2.00	2.00	2.00	2.00	2.00
Ca	0.00	0.00	0.00	0.02	0.00	0.00
Na	0.65	0.73	0.70	0.68	0.64	0.51
K	0.09	0.09	0.10	0.11	0.11	0.20
A subtotal	0.75	0.83	0.80	0.81	0.75	0.71
O (non-W)	22.00	22.00	22.00	22.00	22.00	22.00
OH	1.98	1.97	1.98	1.80	1.80	1.95
F	0.00	0.00	0.00	0.02	0.00	0.00
Cl	0.02	0.03	0.02	0.17	0.20	0.05
O	0.00	0.00	0.00	0.00	0.00	0.00
W subtotal	2.00	2.00	2.00	2.00	2.00	2.00
Sum T,C,B,A	15.75	15.83	15.80	15.80	15.75	15.71
		sadanagaite			sadanagaite pargasite	
X _{Mg}	0.64	0.62	0.64	0.62	0.63	0.57

T: Tetrahedral site; B,C: Octahedral sites; A: Alkali site; <d.l.: below detection limit

Table 4.1.2e: Representative electron microprobe analysis of spinel and titanite (stoichiometry calculated on the basis of 4 and 5 oxygens, oxide data are given in weight%).

Mineral	Spinel				Titanite		
	Point No.	40 / 1	43 / 1 .	50 / 1 .	7 / 1 .	20 / 1 .	42 / 1 .
SiO ₂		0.01	0.03	0.15	0.01	30.12	30.31
TiO ₂		0.00	0.04	0.03	0.00	37.14	37.11
Al ₂ O ₃		55.40	54.98	55.47	57.94	2.73	2.90
Cr ₂ O ₃		0.71	0.00	1.03	0.00	0.00	0.01
FeO		36.65	36.62	37.09	35.43	0.51	0.36
MnO		0.08	0.25	0.12	0.19	0.00	0.02
MgO		7.06	7.24	5.93	6.48	0.01	0.01
ZnO		0.01	0.00	0.00	0.00	0.00	0.00
CaO		0.00	0.04	0.03	0.00	28.01	28.15
Na ₂ O		0.00	0.00	0.05	0.04	0.01	0.04
K ₂ O		0.00	0.00	0.03	0.00	0.00	0.00
F		n.m.	n.m.	n.m.	n.m.	<d.l.	<d.l.
Cl		n.m.	n.m.	n.m.	n.m.	<d.l.	<d.l.
Total		99.98	99.25	99.96	100.09	98.53	98.91
Si		0.00	0.00	0.00	0.00	0.98	0.99
Ti		0.00	0.00	0.00	0.00	0.91	0.91
Al		1.83	1.82	1.84	1.90	0.11	0.11
Cr ⁺³		0.02	0.00	0.02	0.00	0.00	0.00
Fe ^{+3*}		0.16	0.17	0.13	0.10	0.02	0.01
Fe ⁺²		0.70	0.69	0.74	0.72	0.00	0.00
Mn		0.00	0.01	0.00	0.00	0.00	0.00
Mg		0.29	0.30	0.25	0.27	0.00	0.00
Zn		0.00	0.00	0.00	0.00		
Ca		0.00	0.00	0.00	0.00	0.98	0.98
Na		0.00	0.00	0.00	0.00	0.00	0.00
K		0.00	0.00	0.00	0.00	0.00	0.00
Total		3.00	3.00	3.00	3.00	3.00	3.00
X _{Mt}		0.08	0.09	0.07	0.05		
X _{SpI}		0.27	0.31	0.25	0.27		
X _{Herc}		0.64	0.61	0.67	0.68		
X _{Gah}		0.00	0.00	0.00	0.00		
X _{Chr}		0.01	0.00	0.01	0.00		
X _{Mg}		0.30	0.31	0.25	0.27		

n.m.: not measured

<d.l.: below detection limit

Table 4.1.2f: Representative electron microprobe analysis of apatite, magnetite and calcite (stoichiometry of apatite, magnetite and calcite calculated on the basis of 25, 4 and 3 oxygens respectively, oxide data are given in weight%).

Mineral Point No.	Apatite		Magnetite		Calcite
	10 / 1 .	11 / 1 .	62 / 1 .	6 / 1 .	25 / 1 .
SiO ₂	0.06	0.08	2.11	0.51	<d.l.
TiO ₂	0.03	0.01	9.31	4.33	<d.l.
Al ₂ O ₃	0.02	<d.l.	2.37	1.11	<d.l.
Cr ₂ O ₃	<d.l.	<d.l.	<d.l.	0.26	<d.l.
Fe ₂ O ₃			37.09	53.67	
FeO	0.13	<d.l.	35.58	33.29	0.73
MnO	0.03	0.00	0.18	0.06	0.09
MgO	0.03	0.03	2.18	0.18	0.53
CaO	54.45	54.89	0.23	0.19	62.92
Na ₂ O	<d.l.	<d.l.	<d.l.	0.02	0.01
K ₂ O	<d.l.	<d.l.	0.06	<d.l.	<d.l.
F	4.39	3.14	n.m.	n.m.	0.10
Cl	0.86	0.77	n.m.	n.m.	<d.l.
P ₂ O ₅	41.89	41.86	n.m.	n.m.	<d.l.
Total	101.87	100.73	89.11	93.62	64.24
Si	0.01	0.01	0.09	0.02	0.00
Ti	0.00	0.00	0.29	0.13	0.00
Al	0.00	0.00	0.11	0.05	0.00
Cr ⁺³	0.00	0.00	0.00	0.01	
Fe ^{+3*}	0.00	0.00	1.14	1.64	0.01
Fe ⁺²	0.02	0.00	1.22	1.13	0.00
Mn	0.00	0.00	0.01	0.00	0.00
Mg	0.00	0.00	0.13	0.01	0.01
Ca	9.41	9.60	0.01	0.01	0.98
Na	0.00	0.00	0.00	0.00	0.00
K	0.00	0.00	0.00	0.00	0.00
P	5.72	5.78			0.00
Cl	0.24	0.21			
F	2.24	1.62			
OH	0.00	0.17			
Total	17.17	17.40	3.00	3.00	1.00

n.m.: not measured

<d.l.: below detection limit

The composition of minerals, both prograde and symplectic, remains nearly uniform across the three bands. Hence, variation of the modal abundance of the symplectic assemblage could be controlled by the proportion of reactant minerals (in reaction B) stabilised during peak conditions in each band. Development of the symplectic assemblage to different extents renders estimation of the exact proportion of the peak metamorphic minerals difficult in the different bands. Nevertheless, abundance of symplectic ilmenite (highest being in the melanocratic band) suggest that the initial proportion of titanite (the source of Ti for ilmenite), was higher in the melanocratic band than in the leucocratic, and garnet-rich bands. However, textural features do not support any significant Ti metasomatism. Moreover, in view of the absence of secondary carbonate minerals, limited formation of amphibole, and preservation of symplectites, it seems unlikely that infiltration driven process was responsible for the large progress of reaction B in the melanocratic band, relative to the leucocratic and the garnet-rich bands. Combining all the features it stands to reason that the large progress of the reaction B, and hence the abundance of the $\text{Cpx}_2 + \text{Ilm} \pm \text{Spl} + \text{Pl}_2$ symplectic assemblage in the melanocratic band was caused by a higher proportion of titanite relative to the other two bands. Owing to low abundance of titanite, the garnet +Am₁ could not break extensively through reaction B in the leucocratic band (relative to the melanocratic band), as well as in the garnet-rich band (where the least breakdown is observed).

4.1.5. P-T conditions of metamorphism:

The mineral assemblage (garnet-clinopyroxene-plagioclase-quartz-amphibole) of the studied rocks is apparently suitable for mineralogical thermobarometry. However, the presence of significant Fe³⁺ in garnet and clinopyroxene, (2) very grossular-rich composition of garnet (Ellis and Green, 1979; Ganguly, 1979), and (3) highly calcic plagioclase (An_{0.98-0.99}; (Holland and Blundy, 1994), (4) Fe-poor (X_{Fe}<0.4) amphiboles (Anderson and Smith, 1995), introduces large errors in the application of the conventional geothermobarometers on the studied assemblage (e.g., garnet-clinopyroxene, garnet-amphibole and amphibole-plagioclase geothermometers and garnet-

clinopyroxene-plagioclase-quartz barometers). This is because the extant geothermobarometers are not calibrated for the phase compositions observed in the studied assemblages (Reviewed in Essene, 1989; Holland and Blundy, 1994). For this reason, the P-T estimates at the culmination of metamorphism and during the symplectite formation have been estimated from the intersecting isopleths in the P-T pseudosection computed for the representative bulk composition of the studied rock, using the *Perple_X* program, version 6.9.1 (Connolly, 2005 updated February, 2021). Owing to the presence of calcite and amphibole, the pseudosection has been computed in the system NCFMASHTO-H₂O-CO₂ (Na₂O-CaO-FeO-MgO-Al₂O₃-SiO₂-TiO₂-O₂-H₂O-CO₂), using the internally consistent thermodynamic dataset of Holland and Powell (2011). The activity-compositions (a-X) relations used for the solid solution minerals include Holland et al. (2018) (garnet, clinopyroxene, orthopyroxene, spinel, olivine and melt), Green et al. (2016) (amphibole), Holland and Powell (2003) (plagioclase), White et al. (2014) (chlorite), White et al. (2000) (ilmenite), Holland and Powell (2011) (epidote). Titanite is considered as a pure phase. Due to the absence of any K₂O and MnO bearing phases (negligible amounts present only in garnet), these have not been considered as system components. The studied rock is dominated by silicates with few oxide phases (spinel, ilmenite and magnetite, Table 4.1.1). Frost, (1991) opined that for oxide-poor silicate rocks f_{O_2} cannot be an independent variable and is buffered by mineral reactions. As the garnet, clinopyroxene and amphibole of the studied rock contain both Fe²⁺ and Fe³⁺, and are associated with ilmenite (in leuco-, melano- and garnet-rich bands) and magnetite (melanocratic band), the pseudosection has been calculated for the quartz-fayalite-magnetite (FMQ) buffer (reviewed in Spear, 1993).

Presence of compositional banding in meso- to microscopic scale point towards the large mineralogical heterogeneity (even within a single thin section; Fig. 4.1.2a) of the studied rocks. In such heterogeneous rocks, the choice of the actual equilibration volume, plays a very important role in determining the bulk composition, and in turn, the phase relationships of the constructed pseudosection (Palin et al., 2016). The large mineralogical heterogeneity across the three bands in the studied rock suggest an equilibrium volume, that is not

more than the width of each of the three bands. This follows that bulk compositions obtained from whole rock X-Ray Fluorescence (XRF) methods should lead to estimation of a much larger volume than the actual equilibrated one. In view of these, the use of effective bulk compositions for the phase equilibria modelling of the studied rock seems logical (Palin et al., 2016).

Effective bulk composition of the garnet-rich band was chosen for the pseudosection since it shows extensive formation of peak garnet, and its least breakdown. Effective bulk was calculated by combining the chemical compositions of minerals, with their respective representative modal proportions. The modal proportion of the minerals were calculated by the ImageJ software (Fan et al., 2022), by compilation from several grids (of equal size and magnification within the garnet band) under plane polarized light. Estimation of concentration of fluid for the pseudosection is not straight forward. Under mid to lower crustal conditions, porosity is greatly reduced ($\sim 0.1\text{vol}\%$; Clemens and Vielzeuf, 1987), which suggest that fluids are only present within the hydrous (amphibole) and carbonate (calcite) phases, and not as a free phase (Clemens and Vielzeuf, 1987). The exact proportion of fluid bearing phases that were present before the formation of the ilmenite-spinel-clinopyroxene symplectite cannot be measured. To overcome this problem, and considering the absence of any partial melting in the studied rock (i.e., absence of quartz-alkali feldspar segregation) the pseudosection is calculated using fluid (H_2O and CO_2) as saturated components (Connolly, 2005). X_{CO_2} of the system is fixed at 0.3, as beyond this X_{CO_2} value, scapolite, which is completely absent in the studied rock, becomes preponderant in the chosen P-T field.

Results of pseudosection modelling:

In the constructed pseudosection, the field representing the peak mineral assemblage: clinopyroxene + amphibole + garnet + plagioclase + titanite + ilmenite, spans over a large P-T range. Although the different textural varieties of clinopyroxene and plagioclase have similar/overlapping compositions, garnet core and rim compositions are different (Fig. 4.1.3c, Table 4.1.2b). We had therefore used garnet core compositions (X_{Mg} , X_{Grs} , X_{Py} , X_{Adr}) to constrain the peak pressure-

temperatures. These isopleths further refine the peak P-T conditions between ~790-890°C and ~8.4-9.5 kbar (Fig. 4.1.4a).

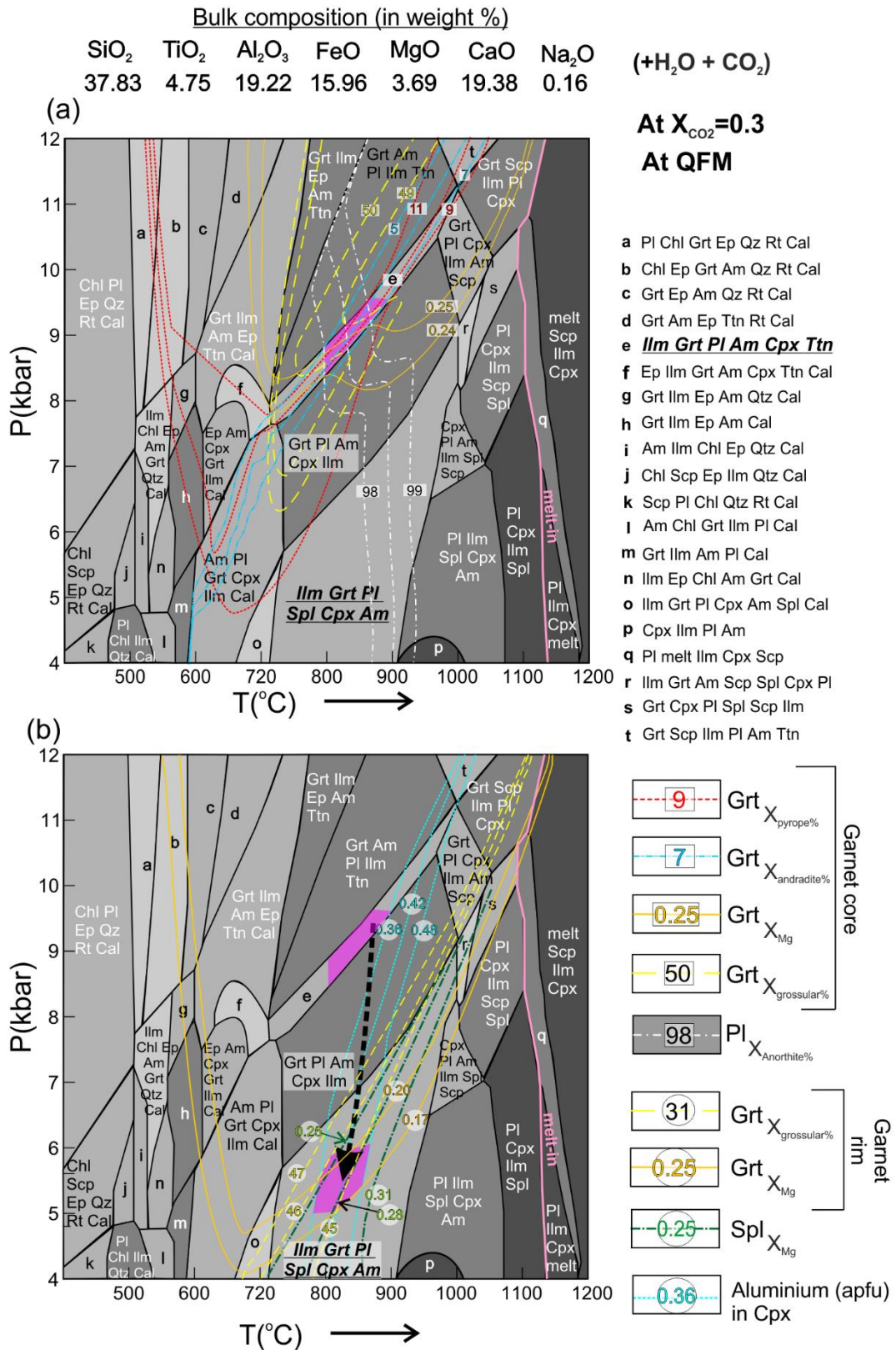


Fig. 4.1.4: P-T pseudosection constructed in the system NCFMASHTO-H₂O-CO₂, at 'QFM' oxygen buffer. The peak and post-peak symplectite fields are marked in bold italics and underlined. Intersecting isopleths shown by solid, dashed and dotted lines, constrain the peak (pink; in a) and post-peak symplectite (pink; in b) P-T conditions. The index of the lines has been given the figure itself. The overall P-T path is shown in black dashed arrow. The used bulk composition has been given at the top of the pseudosection. All mineral abbreviations are after Kretz, (1983).

Post peak condition, manifested by the formation of Cpx₂-ilmenite-spinel-Pl₂ symplectites, is defined by the field amphibole + garnet + clinopyroxene + plagioclase + ilmenite + spinel. The formation of symplectites at high angles to the margins of garnet, indicate that the garnet rim was in equilibrium with the symplectic assemblage. Therefore, isopleths defining compositions of garnet rim, aluminium content of symplectic clinopyroxenes (Cpx₂) and X_{Mg} content of spinel were used to constrain the conditions of symplectite formation between ~780-860°C and ~5-5.8 kbar in this domain (Fig. 4.1.4b).

Fig. 4.1.4 indicates that the studied rocks experienced a high pressure, moderate to high temperature peak, followed by a near isothermal decompression up to 5 kbar, during which the symplectic assemblage stabilised. The temperature sensitive isopleths (aluminium content in clinopyroxenes, X_{An} in plagioclase; Fig. 4.1.3), pass through both peak, and post-peak fields suggesting that their composition remained insensitive to P-T change from peak to post-peak symplectite forming condition. Additionally, they are also parallel to the deduced near isothermal decompressive path, which justifies the development of minerals (Cpx₁ and Cpx₂, Pl₁ and Pl₂) in different textural varieties having similar and/or overlapping compositions.

4.1.6. Oxygen Isotope:

4.1.6.1. Analytical techniques and methodology:

Oxygen isotopic analysis was done at the University of Göttingen, Germany, using Thermo Scientific MAT 253 gas isotope ratio mass spectrometer. The bulk oxygen isotope compositions of five different samples of the studied rock were measured. The data is reported here as δ¹⁸O (definition of δ¹⁸O provided in McKinney et al., 1950) relative to the VSMOW scale. Representative sample aliquots

were selected and ground to a homogenous powder. ~2 mg of sample powders was subjected to laser fluorination (Sharp, 1990), and the released oxygen gas was analysed by gas chromatography isotope ratio monitoring gas mass spectrometry in continuous flow mode (Pack et al., 2013, details of the procedure has been described in existing literature, e.g., 2007).

4.1.6.2. Results:

The measured oxygen isotope compositions of the five samples are presented in Table 4.1.3. The samples were found to have $\delta^{18}\text{O}$ values ranging between $2.9 \pm 0.2\text{‰}$ to $5.6 \pm 0.2\text{‰}$ (averaging to $4 \pm 1.2 \text{‰}$ (Table 4.1.3).

Table 4.1.3: Oxygen isotope results.

Sample	$d_{18}\text{O}$ (per mil)
AS29A	3.24
AS29A1	5.56
AS29A2	5.20
AS29A3	2.88
AS29A4	3.02

4.1.7. Geochronology

Zircon grains from the studied rock weres analysed in-situ at the Department of Geology and Geophysics, Indian Institute of Technology, Kharagpur, using LA-ICPMS method. Details of the analytical techniques have been provided in Appendix. In-situ zircons were analysed from multiple thin sections (AS29i, AS29ii, AS29iii) of the studied rock. Both detrital and metamorphic zircons were analysed by this method.

4.1.7.1. Morphology

Detrital zircons:

Majority of the zircons occur in the matrix, while a very few are also present as inclusions in garnet. Fig. 4.1.5a-d represents the cathodoluminescence (CL) image of the morphology of these zircons. These zircons are mostly sub-elliptical with their lengths varying from ~60 μm to ~120 μm (Fig. 4.1.5a-d; length: width ratio varying from 7:4 to 5:4). However, few smaller, subhedral grains are also present. All these

grains preserve a distinct rounded to sub-rounded core. The cores have irregular, resorbed boundaries, indicating that the margins probably got abraded during transportation and deposition (Corfu et al., 2003). The cores preserve distinct oscillatory zoning (Fig. 4.1.5a-d). All these features point towards their detrital nature. These large detrital cores are generally overgrown by thin (Fig. 4.1.5a, d) to slightly thick (Fig. 4.1.5b-c), moderately luminescent overgrowths. These features indicate development of these overgrowths on detrital cores during subsequent tectonothermal events.

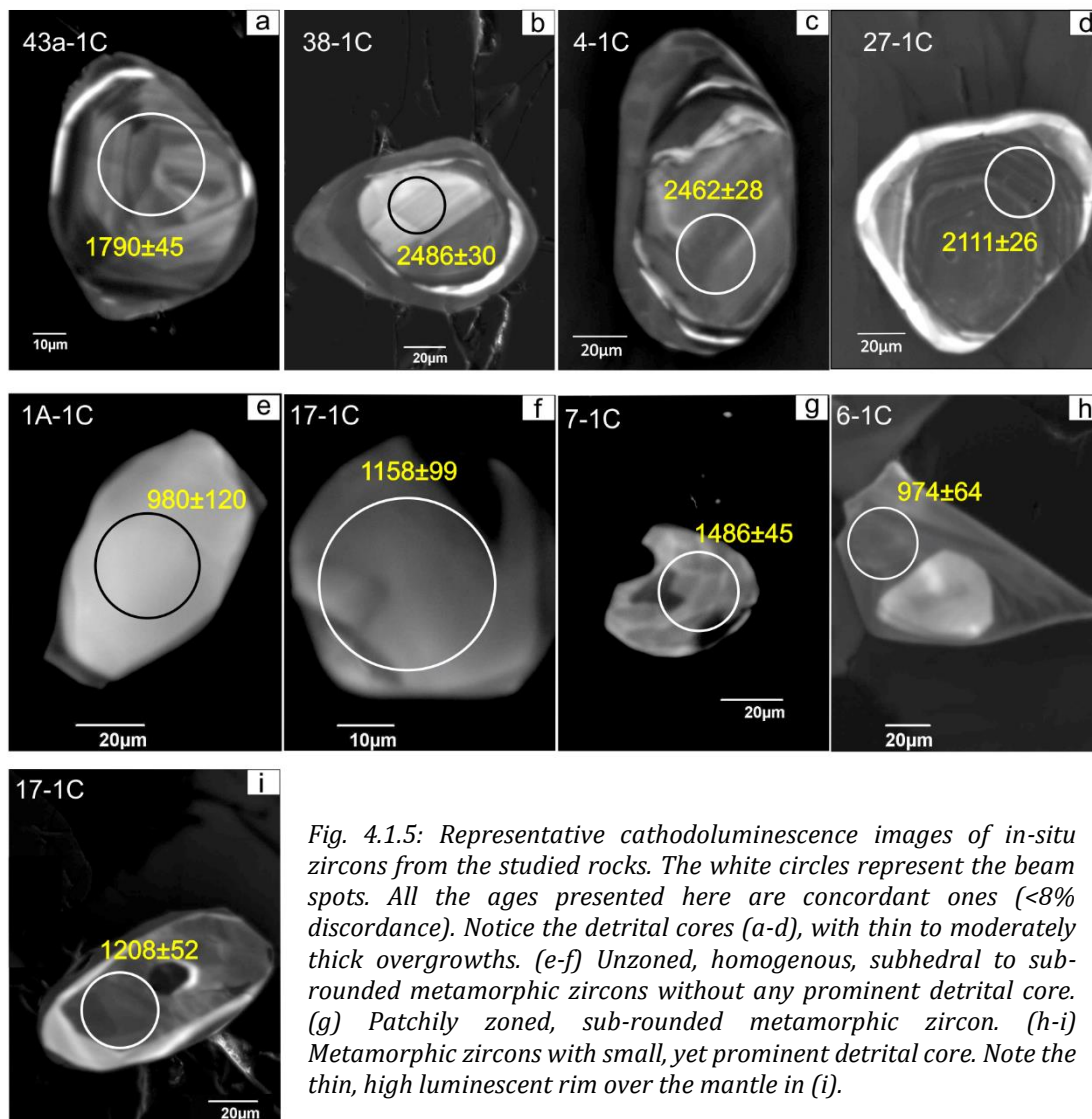


Fig. 4.1.5: Representative cathodoluminescence images of in-situ zircons from the studied rocks. The white circles represent the beam spots. All the ages presented here are concordant ones (<8% discordance). Notice the detrital cores (a-d), with thin to moderately thick overgrowths. (e-f) Unzoned, homogenous, subhedral to sub-rounded metamorphic zircons without any prominent detrital core. (g) Patchily zoned, sub-rounded metamorphic zircon. (h-i) Metamorphic zircons with small, yet prominent detrital core. Note the thin, high luminescent rim over the mantle in (i).

Metamorphic zircons

Most of the analysed in-situ metamorphic grains occur in the matrix. The metamorphic zircons have a wide variety of structure and morphological features. Fig. 4.1.5e-i represents the cathodoluminescence images of these zircons. Majority of the grains are small, subhedral (Fig. 4.1.5e, h-i) to sub-rounded (Fig. 4.1.5f-g) in shape, varying mostly from 40 μ m to 80 μ m in length. These are homogenous and unzoned (Fig. 4.1.5e-f), or less commonly patchily zoned (Fig. 4.1.5g), without any prominent core, attesting to their metamorphic origin (Corfu et al., 2003). In few zircons, the broad, low luminescent, patchy zoned mantle overgrowths, which surround the small, but prominent detrital cores (Fig. 4.1.5h-i), are also presumed to be metamorphically grown (Corfu et al., 2003). Additionally, in few zircons the mantle is surrounded by another thin, highly luminescent overgrowth (Fig. 4.1.5i). No metamorphic zircon exhibits oscillatory zoning which further supports the growth of metamorphic zircon in absence of a melt phase.

4.1.7.2. Results

A total of 42 spots were analysed from 39 zircon grains from the different thin sections of the studied rock, consisting of both detrital and metamorphic ones.

Detrital zircons:

25 spot dates were analysed from detrital cores amongst which, eleven spot dates yield concordant (<8% discordance) data, with the $^{207}\text{Pb}/^{206}\text{Pb}$ ages ranging between 1790 Ma to 2486 Ma (Table 4.1.4a). Probability density curve (Fig. 4.1.6a) using these concordant dates from detrital cores depict prominent age clusters at ~2470 Ma, 2000-2190 Ma and 1790 Ma. The Th/U ratio of these ages show a wide span from 0.12-0.86, with >73% data showing ratio higher than 0.35. However, the detrital cores present within a few metamorphic grains (Fig. 4.1.5i) are too small to be analysed.

Metamorphic zircons

A total of 17 spots were analysed from the metamorphic grains and overgrowths. Amongst these, fifteen spot dates show less than ~7% discordance,

and yield $^{207}\text{Pb}/^{206}\text{Pb}$ ages ranging between ~ 970 Ma to ~ 1330 Ma (Table 4.1.4b). These dates define three distinct concordia ages of 972 ± 13 Ma ($n=4$, $\text{MSWD}_{\text{C+E}}(\text{concordance+equivalence}) = 0.012$), 1056 ± 15 Ma ($n=4$, $\text{MSWD}_{\text{C+E}} = 0.091$) and 1267 ± 14 Ma ($n=3$, $\text{MSWD}_{\text{C+E}} = 2.0$) (Fig. 4.1.7a-c). Apart from these, one individual spot age (with 100% concordance), analysed from a patchy zoned grain yield a slightly older spot age of 1486 ± 45 Ma (Fig. 4.1.5g, Table 4.1.4b). The metamorphic zircons have very low Th/U ratio ~ 0.01 - 0.09 (with $\sim 93\%$ of the data having the ratio ~ 0.01 , Table 4.1.4b).

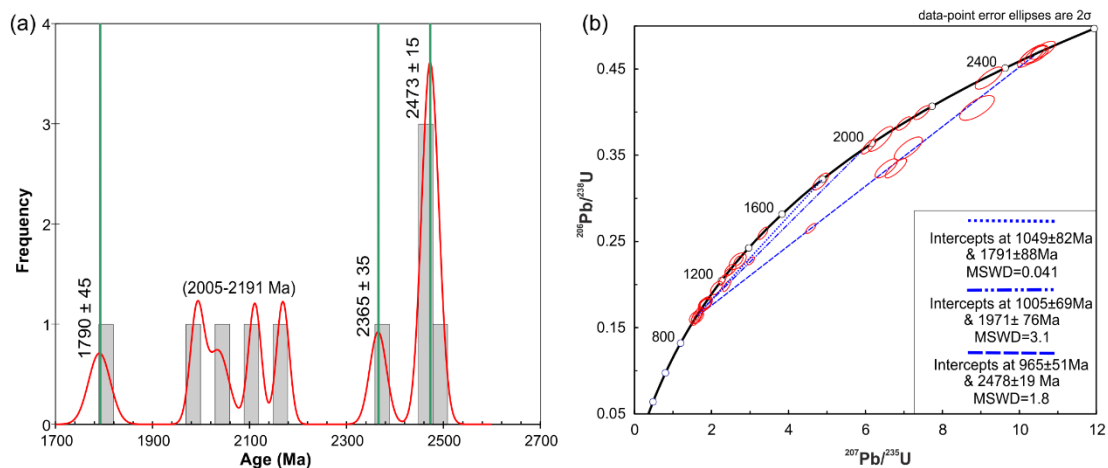


Fig. 4.1.6: (a) Probability density curve depicting the different age clusters obtained from the concordant detrital cores. (b) U–Pb discordia diagram defining different upper-intercept ages (~ 2470 - 1790 Ma; implying multiple sources from which the detrital zircons were derived), and lower-intercept ages (~ 1050 - 960 Ma), during which the zircon grains experienced partial Pb loss.

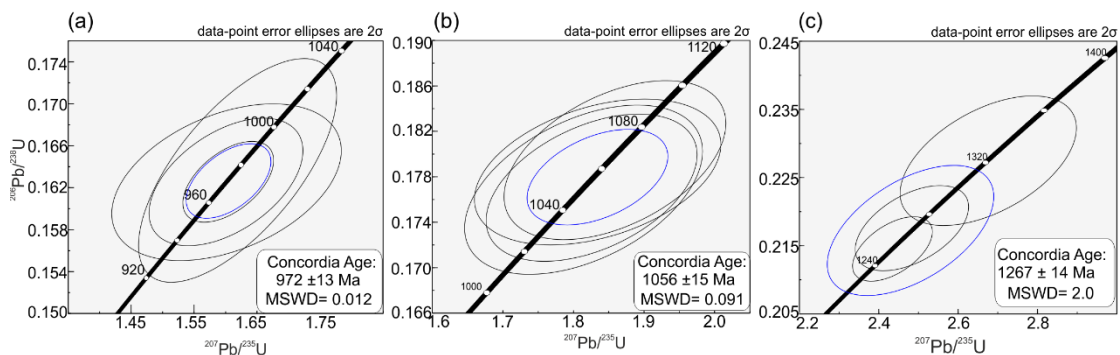


Fig. 4.1.7: (a-b) Concordia age clusters obtained from homogenous metamorphic zircons and overgrowths. (c) Concordia age clusters obtained from mantles of few homogenous metamorphic zircon grains.

In a discordia diagram (Fig. 4.1.6b), constructed with both concordant and discordant data from the detrital cores, metamorphic grains and overgrowths, the discordant dates fall along multiple discordia lines (Fig. 4.1.6b). The upper intercept ages are distinct (2478 ± 19 Ma, 1971 ± 76 Ma and 1791 ± 88 Ma) and corroborate well with the age peaks obtained from detrital zircons (Fig. 4.1.6a). The lower intercept ages are within the uncertainty limit of each other (965 ± 51 Ma, 1005 ± 69 Ma and 1049 ± 82 Ma), and matches well with the concordia ages obtained from the metamorphic zircons (Fig. 4.1.7a-b). This indicate that the detrital zircons in the studied rock were derived from multiple sources and experienced partial Pb loss during a pervasive metamorphic event at ca. 1050-960 Ma.

4.1.8. Synthesis of information

4.1.8.1. Protolith of the studied rock:

Detailed analyses of the protolith of the studied rock are beyond the scope of this work. Nevertheless, based on mineralogy, zircon morphology, bulk rock chemistry and preliminary oxygen isotope data, an attempt is made to obtain some information about the likely protoliths of the studied rock. Presence of detrital zircon suggests that the progenitor of the studied rock were terrigenous sediments. The abundant grossular-rich garnet with variable andradite, highly calcic plagioclase, clinopyroxene along with variable titanite and rare calcite points towards a calcareous source. The assemblage garnet + clinopyroxene + calcic plagioclase + amphibole + titanite that developed during the culmination of metamorphism in the studied rocks, also developed in the typical calc-silicate granulites from the studied area (Dey et al., 2019a). However, relative to the other calc silicate granulites of the area, the studied rock has higher proportion of Al_2O_3 , FeO and lesser amount of CaO (see Supplementary Material 1). This characteristic bulk composition stabilised the highly Al-rich clinopyroxene, ilmenite and spinel in the studied rock, that are not found in the adjoining calc-silicate granulites. The observed mineralogy is also not found in the majority of the calc-silicate rocks reported elsewhere (Dasgupta, 1993; Groppo et al., 2017; Harley and Buick, 1992). A mixture of (1) argillaceous material and limestone (Le Bas et al., 2002), (2) sediments derived from mafic and calcareous sources (Johnson et al., 2008) have

been suggested as a suitable protolith for the development of Al-rich clinopyroxene ± spinel ± ilmenite in calc-silicate rocks having terrigenous components. While a mixed source (either possibility (1) or (2) described above) can be the likely protolith for the studied rock, the low $\delta^{18}\text{O}$ values ($4 \pm 1.2\text{‰}$) of the studied rock is in marked contrast with the terrigenous sediments ($\delta^{18}\text{O} = \sim 15\text{-}25\text{‰}$; Valley, 2018) and igneous rocks ($\delta^{18}\text{O} = \sim 6\text{-}10\text{‰}$; Taylor Jr, 1978). Integrating all the evidence, it seems likely that the protolith sediments of the studied rock interacted with low $\delta^{18}\text{O}$ meteoric water (Luz and Barkan, 2010). Extensive fluid rock interaction lowered the high $\delta^{18}\text{O}$ values of the terrigenous sediments prior to the onset of metamorphism. This intense interaction with meteoric water might have made the protolith sediments Al-rich, and relatively rich in Fe and depleted in Ca (with respect to the other calc-silicate granulites of the area). Similar processes have also been inferred to explain the low oxygen isotopic values in eclogites, felsic gneisses and meta-carbonates (Rehman et al., 2014; Zheng et al., 2003).

4.1.8.2. Formation of symplectites:

Extant geological studies show that the clinopyroxene-ilmenite-spinel bearing association have a very restricted occurrence in regionally metamorphosed rocks, and is rarer in calc-silicates. The formation of these symplectites has been variously ascribed to the breakdown of garnet + titanite, or olivine + plagioclase (Dasgupta et al., 1993; Faryad et al., 2006) during medium-high pressure granulite to amphibolite facies metamorphism ($\sim 8\text{-}11$ kbar, $\sim 800\text{-}1000^\circ\text{C}$; Curtis and Gittins, 1979; Dasgupta et al., 1993) along clockwise P-T paths in regionally metamorphosed meta-mafic rocks. In regionally metamorphosed calc-silicates, their formation has been ascribed to the breakdown of garnet and rutile in the process of isobaric heating during medium-pressure granulite facies metamorphism (Maki et al., 2009).

Now, as discussed earlier, the lack of evidence of any large-scale fluid infiltration in the studied rocks (e.g., absence of veining features and carbonate-bearing phases, preservation of symplectites, limited proportion of amphibole) contradict any imprints of metasomatism during the peak or post peak symplectite forming phase). As manifested from the textural relations and mineral evolutionary

history, the studied calc-silicate granulite experienced peak pressure-temperature conditions that culminated at ($\sim 790\text{-}890^\circ\text{C}$ and $\sim 8.4\text{-}9.5$ kbar). This moderate to high pressure, moderate temperature granulite facies metamorphism stabilised the peak mineral assemblage: garnet, clinopyroxene (Cpx_1), amphibole (Am_1), plagioclase (Pl_1) and titanite. Phase equilibria modelling indicates that the symplectites formed due to a decompression of ~ 4 kbar, subsequent to this peak

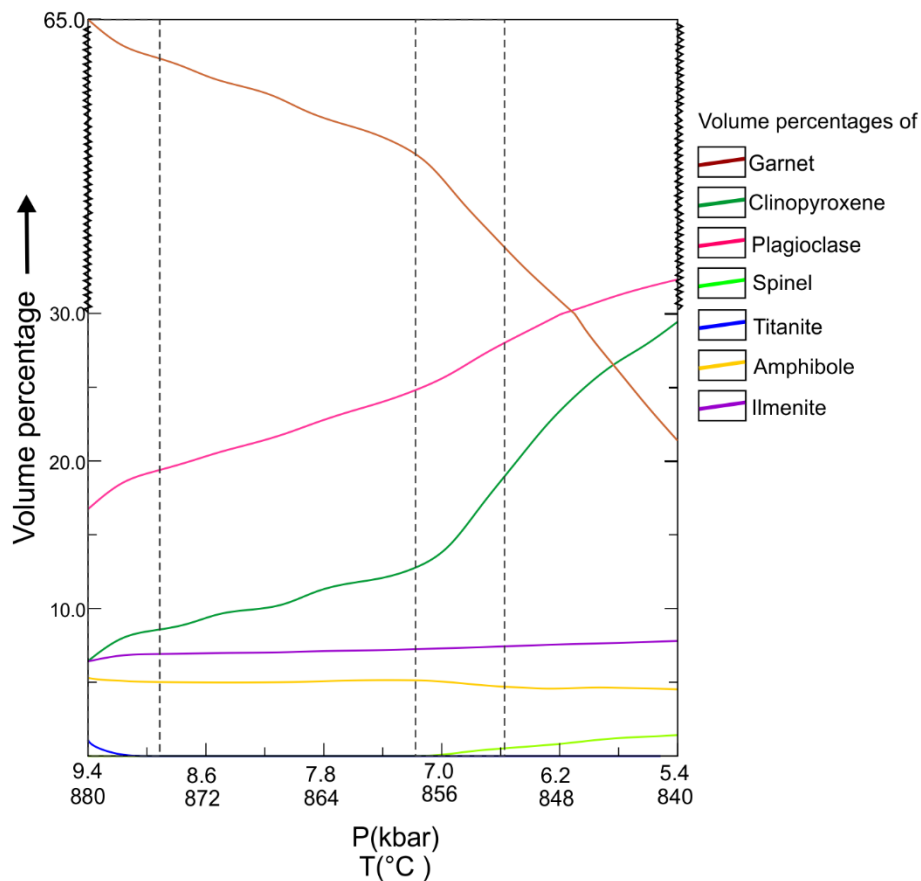


Fig. 4.1.8: Volume change (in percentage) of the minerals in the studied calc-silicate granulite. The X-axis corresponds to the constrained P-T path, from peak conditions (left margin) to the conditions of post-peak, symplectite formation (right margin) at constant temperature. The dashed areas represent zones of breakdown of garnet amphibole and titanite, and corresponding sharp increase in volume percentage of ilmenite, spinel, clinopyroxene and plagioclase.

metamorphism, via breakdown of garnet, amphibole and titanite. A volume vs pressure-temperature graph (Fig. 4.1.8) demonstrates the observed symplectite forming reaction textures. From $\sim 9.4\text{-}8.9$ kbar pressure, a prominent decrease in garnet, titanite and amphibole volume is evident, which corresponds to an increase in ilmenite, clinopyroxene and plagioclase volume percentage, suggesting the

reaction: $\text{Grt} + \text{Ttn} + \text{Am}_1 = \text{Cpx}_2 + \text{Pl}_2 + \text{Ilm}$. Also, between ~ 7.2 - 6.6 kbar, another decline in garnet and amphibole volume percentage, corresponds to increase in volume of spinel, plagioclase and clinopyroxene, indicating the reaction: $\text{Grt} + \text{Am}_1 = \text{Cpx}_2 + \text{Pl}_2 + \text{Spl}$. Therefore, Fig. 4.1.8 demonstrates the participation of garnet, amphibole and titanite in the formation of the symplectic assemblage in the studied calc-silicate granulite.

The isotopic data, additionally validates that the protolith of the studied calc-silicates were altered to an aluminium-rich, and relatively iron-rich, calcium-poor (with respect to the other calc-silicate granulites) bulk, via interaction with meteoric fluid at surficial conditions. Integrating the above information, it is inferred that these altered sediments were later metamorphosed under high pressure, moderate to high temperature granulite facies conditions, followed by a near isothermal decompression, during which this unique clinopyroxene-ilmenite-spinel-plagioclase symplectite developed.

4.1.8.3. Nature and timing of metamorphism and correlation with other lithounits:

The studied calc-silicate granulite is a part of the meta-sedimentary enclave suite of rocks exposed throughout the study area. These calc-silicate granulites and the associated enclaves of pelitic granulites and quartzites represent the metamorphosed counterpart of an old sandstone-shale-limestone sequence. From the analysed detrital zircon population in the studied sample, the time span of sedimentation can broadly be confined between ~ 1790 Ma (youngest detrital spot age) and ~ 1486 Ma (oldest thermal/ metamorphic imprint). This timing falls well within the timing of basin formation (~ 1700 - 1650 Ma) constrained by Dey et al. (2017), through an exhaustive detrital zircon study from the associated pelitic granulites of the area.

The studied calc-silicates record peak conditions at ~ 790 - 890°C and ~ 8.4 - 9.5 kbar, followed by a near-isothermal decompression up to ~ 750 - 830°C and ~ 4.6 - 5.6 kbar. Although the prograde path could not be constrained from the existing mineral assemblage, this moderate to high pressure, moderate temperature peak,

followed by a steeply decompressive P-T path, point towards the clockwise nature of the P-T path (England and Thompson, 1984; Harley, 1989). Similar clockwise P-T paths (with high pressure, moderate temperature peak: $\sim 750\text{-}870^\circ\text{C}$ and $\sim 9\text{-}12$ kbar, succeeded by a steep decompressive path) have also been recorded from the adjacent pelitic and mafic granulite enclaves (Dey et al., 2019b, 2019c), and the host migmatitic felsic gneiss (Dey et al., 2019b; Mukherjee et al., 2017) of the study area; as well as from other parts of the CGGC (Chatterjee, 2018; Karmakar et al., 2011). This metamorphic event has been related to the second major tectonothermal event (M2) recorded from the CGGC. The peak P-T conditions as constrained from the studied calc-silicate granulite define an apparent geothermal gradient of $\sim 28^\circ\text{C}/\text{km}$. Comparable gradients ($\sim 20\text{-}26^\circ\text{C}/\text{km}$) have also been constrained from the other lithounits (Dey et al., 2019b, 2019c; Karmakar et al., 2011; Kumar et al., 2022; Mukherjee et al., 2017). Hence, the clockwise P-T path, combined with the apparent geothermal gradient, all point towards a continental collisional setting (Brown, 2008; Harley, 1989) prevalent during M2 (e.g., Dey et al., 2019b; Mukherjee et al., 2017; Sanyal and Sengupta, 2012).

Early Neoproterozoic / late Stenian-early Tonian ages (~ 970 Ma and ~ 1060 Ma) are the predominant concordia age clusters preserved in the zircons from the studied calc-silicate granulite. These ages were obtained from unzoned metamorphic grains, or few overgrowths on small detrital cores, and hence constrain the timing of peak metamorphism (and symplectite formation), during which new zircons (new grains and overgrowth) formed in the studied calc-silicate granulite.

References

- Anderson, J.L., Smith, D.R., 1995. The effects of temperature and $f\text{O}_2$ on the Al-in-hornblende barometer. *Am. Mineral.* 80, 549–559.
- Bhowmik, S.K., Wilde, S.A., Bhandari, A., Pal, T., Pant, N.C., 2012. Growth of the Greater Indian Landmass and its assembly in Rodinia: geochronological evidence from the Central Indian Tectonic Zone. *Gondwana Res.* 22, 54–72.

- Bouregghda, N., Ouzegane, K., Bendaoud, A., Aït-Djafer, S., Kienast, J.-R., 2016. Petrology, mineralogy, and P–T path of calc-silicate granulites and fassaite-marbles from the Paleoproterozoic Gour Oumelalen area (Central Hoggar, Algeria). *Arab. J. Geosci.* 9, 1–17.
- Brown, M., 2008. Characteristic thermal regimes of plate tectonics and their metamorphic imprint throughout Earth history: When did Earth first adopt a plate tectonics mode of behavior? When did plate tectonics begin planet Earth? 440, 97.
- Chatterjee, N., 2018. An assembly of the Indian Shield at c. 1.0 Ga and shearing at c. 876–784 Ma in Eastern India: insights from contrasting PT paths, and burial and exhumation rates of metapelitic granulites. *Precambrian Res.* 317, 117–136.
- Chatterjee, N., Banerjee, M., Bhattacharya, A., Maji, A.K., 2010. Monazite chronology, metamorphism–anatexis and tectonic relevance of the mid-Neoproterozoic Eastern Indian Tectonic Zone. *Precambrian Res.* 179, 99–120.
- Chatterjee, N., Crowley, J.L., Ghose, N.C., 2008. Geochronology of the 1.55 Ga Bengal anorthosite and Grenvillian metamorphism in the Chotanagpur gneissic complex, eastern India. *Precambrian Res.* 161, 303–316.
- Chatterjee, N., Ghose, N.C., 2011. Extensive early Neoproterozoic high-grade metamorphism in north Chotanagpur gneissic complex of the Central Indian tectonic zone. *Gondwana Res.* 20, 362–379.
- Chattopadhyay, A., Chatterjee, A., Das, K., Sarkar, A., 2017. Neoproterozoic transpression and granite magmatism in the Gavilgarh-Tan Shear Zone, central India: Tectonic significance of U-Pb zircon and U-Th-total Pb monazite ages. *J. Asian Earth Sci.* 147, 485–501.
- Clemens, J.D., Vielzeuf, D., 1987. Constraints on melting and magma production in the crust. *Earth Planet. Sci. Lett.* 86, 287–306.
- Connolly, J.A.D., 2005. Computation of phase equilibria by linear programming: A

tool for geodynamic modeling and its application to subduction zone decarbonation. <https://doi.org/10.1016/j.epsl.2005.04.033>

Corfu, F., Hanchar, J.M., Hoskin, P.W.O., Kinny, P., 2003. Atlas of zircon textures. *Rev. Mineral. geochemistry* 53, 469–500.

Cosca, M.A., Peacor, D.R., 1987. Chemistry and structure of esseneite (CaFe (super 3+) AlSiO 6), a new pyroxene produced by pyrometamorphism. *Am. Mineral.* 72, 148–156.

Cruciani, G., Franceschelli, M., Groppo, C., Brogioni, N., Vaselli, O., 2008. Formation of clinopyroxene+ spinel and amphibole+ spinel symplectites in coronitic gabbros from the Sierra de San Luis (Argentina): a key to post-magmatic evolution. *J. Metamorph. Geol.* 26, 759–774.

Curtis, L.W., Gittins, J., 1979. Aluminous and titaniferous clinopyroxenes from regionally metamorphosed agpaitic rocks in central Labrador. *J. Petrol.* 20, 165–186.

Das, E., Karmakar, Subrata, Dey, A., Karmakar, Shreya, Sengupta, P., 2017. Reaction textures, pressure–temperature paths and chemical dates of monazite from a new suite of sapphirine–spinel granulites from parts of the Eastern Ghats Province, India: insights into the final amalgamation of India and East Antarctica during the for. *Geol. Soc. London, Spec. Publ.* 457, 141–170.

Dasgupta, S., 1993. Contrasting mineral parageneses in high-temperature calc-silicate granulites: examples from the Eastern Ghats, India. *J. Metamorph. Geol.* 11, 193–202.

Dasgupta, S., Bose, S., Bhowmik, S.K., Sengupta, P., 2017. The Eastern Ghats Belt, India, in the context of supercontinent assembly. *Geol. Soc. London, Spec. Publ.* 457, 87–104.

Dasgupta, S., Sengupta, P., Mondal, A., Fukuoka, M., 1993. Mineral chemistry and reaction textures in metabasites from the Eastern Ghats belt, India and their implications. *Mineral. Mag.* 57, 113–120.

- Dawson, J.B., Reid, A., 1970. A pyroxene-ilmenite intergrowth from the Monastery Mine, South Africa. *Contrib. to Mineral. Petrol.* 26, 296–301.
- Dey, A., Choudhury, S.R., Mukherjee, S., Sanyal, S., Sengupta, P., 2019a. Origin of vesuvianite-garnet veins in calc-silicate rocks from part of the Chotanagpur Granite Gneiss Complex, East Indian Shield: The quantitative PTX CO₂ topology in parts of the system CaO-MgO-Al₂O₃-SiO₂-H₂O-CO₂ (+ Fe₂O₃, F). *Am. Mineral. J.* 104, 744–760.
- Dey, A., Karmakar, S., Ibanez-Mejia, M., Mukherjee, S., Sanyal, S., Sengupta, P., 2019b. Petrology and geochronology of a suite of pelitic granulites from parts of the Chotanagpur Granite Gneiss Complex, eastern India: Evidence for Stenian-Tonian reworking of a late Paleoproterozoic crust. *Geol. J.*
- Dey, A., Karmakar, S., Mukherjee, S., Sanyal, S., Dutta, U., Sengupta, P., 2019c. High pressure metamorphism of mafic granulites from the Chotanagpur Granite Gneiss Complex, India: Evidence for collisional tectonics during assembly of Rodinia. *J. Geodyn.* 129, 24–43.
- Dey, A., Mukherjee, S., Sanyal, S., Ibanez-Mejia, M., Sengupta, P., 2017. Deciphering sedimentary provenance and timing of sedimentation from a suite of metapelites from the Chotanagpur Granite Gneissic Complex, India: Implications for Proterozoic Tectonics in the East-Central Part of the Indian Shield, in: *Sediment Provenance*. Elsevier, pp. 453–486.
- Droop, G.T.R., 1987. A General Equation for Estimating Fe³⁺ Concentrations in Ferromagnesian Silicates and Oxides from Microprobe Analyses, Using Stoichiometric Criteria. *Mineral. Mag.* 51, 431–435. <https://doi.org/10.1180/minmag.1987.051.361.10>
- Ellis, D.J., Green, D.H., 1979. An experimental study of the effect of Ca upon garnet-clinopyroxene Fe-Mg exchange equilibria. *Contrib. to Mineral. Petrol.* 71, 13–22.

- England, P.C., Thompson, A.B., 1984. Pressure—temperature—time paths of regional metamorphism I. Heat transfer during the evolution of regions of thickened continental crust. *J. Petrol.* 25, 894–928.
- Essene, E.J., 1989. The current status of thermobarometry in metamorphic rocks. *Geol. Soc. London, Spec. Publ.* 43, 1–44.
- Fan, L., Xiao, C., Guan, P., Zou, Y., Wen, H., Liu, C., Luo, Y., Tan, G., Wang, Q., Li, Y., 2022. Extracellular Matrix-Based Conductive Interpenetrating Network Hydrogels with Enhanced Neurovascular Regeneration Properties for Diabetic Wounds Repair. *Adv. Healthc. Mater.* 11, 2101556.
- Faryad, S.W., Perraki, M., Vrána, S., 2006. P–T evolution and reaction textures in retrogressed eclogites from Svetlik, the Moldanubian Zone (Czech Republic). *Mineral. Petrol.* 88, 297–319.
- Field, S.W., 2008. Diffusion, discontinuous precipitation, metamorphism, and metasomatism: The complex history of South African upper-mantle symplectites. *Am. Mineral.* 93, 618–631.
- Field, S.W., Haggerty, S.E., 1994. Symplectites in upper mantle peridotites: development and implications for the growth of subsolidus garnet, pyroxene and spinel. *Contrib. to Mineral. Petrol.* 118, 138–156.
- Frost, B.R., 1991. Introduction to oxygen fugacity and its petrologic importance. *Rev. Mineral. Geochemistry* 25, 1–9.
- Ganguly, J., 1979. Garnet and clinopyroxene solid solutions, and geothermometry based on Fe-Mg distribution coefficient. *Geochim. Cosmochim. Acta* 43, 1021–1029.
- Garrison, J.R., Taylor, L.A., 1981. Petrogenesis of pyroxene–oxide intergrowths from kimberlite and cumulate rocks: co-precipitation or exsolution? *Am. Mineral.* 66, 723–740.

- Green, E.C.R., White, R.W., Diener, J.F.A., Powell, R., Holland, T.J.B., Palin, R.M., 2016. Activity–composition relations for the calculation of partial melting equilibria in metabasic rocks. *J. Metamorph. Geol.* 34, 845–869.
- Grew, E.S., Locock, A.J., Mills, S.J., Galuskina, I.O., Galuskin, E. V, Hålenius, U., 2013. Nomenclature of the garnet supergroup. *Am. Mineral.* 98, 785–811.
- Groppo, C., Rolfo, F., Castelli, D., Mosca, P., 2017. Metamorphic CO₂ production in collisional orogens: Petrological constraints from phase diagram modeling of Himalayan, scapolite-bearing, calc-silicate rocks in the NKC (F) MAS (T)-HC system. *J. Petrol.* 58, 53–83.
- Harley, S.L., 1989. The origins of granulites: a metamorphic perspective. *Geol. Mag.* 126, 215–247.
- Harley, S.L., Buick, I.A.N.S., 1992. Wollastonite—Scapolite assemblages as indicators of granulite pressure-temperature-fluid histories: The Rauer group, East Antarctica. *J. Petrol.* 33, 693–728.
- Hawthorne, F.C., Oberti, R., Harlow, G.E., Maresch, W. V, Martin, R.F., Schumacher, J.C., Welch, M.D., 2012. Nomenclature of the amphibole supergroup. *Am. Mineral.* 97, 2031–2048.
- Holland, T., Blundy, J., 1994. Non-ideal interactions in calcic amphiboles and their bearing on amphibole-plagioclase thermometry. *Contrib. to Mineral. Petrol.* 116, 433–447.
- Holland, T., Powell, R., 2003. Activity–composition relations for phases in petrological calculations: an asymmetric multicomponent formulation. *Contrib. to Mineral. Petrol.* 145, 492–501.
- Holland, T.J.B., Green, E.C.R., Powell, R., 2018. Melting of peridotites through to granites: a simple thermodynamic model in the system KNCFMASHTOCr. *J. Petrol.* 59, 881–900.

- Holland, T.J.B., Powell, R., 2011. An improved and extended internally consistent thermodynamic dataset for phases of petrological interest, involving a new equation of state for solids. *J. Metamorph. Geol.* 29, 333–383.
- Janardhan, A.S., Sriramguru, K., Basava, S., Shankara, M.A., 2001. Geikielite-Mg. Al. spinel-titanoclinohumite association from a marble quarry near Rajapalayam area, part of the 550 Ma old Southern Granulite Terrain, southern India. *Gondwana Res.* 4, 359–366.
- Johnson, T.E., White, R.W., Powell, R., 2008. Partial melting of metagreywacke: a calculated mineral equilibria study. *J. Metamorph. Geol.* 26, 837–853.
- Karmakar, S., Bose, S., Sarbadhikari, A.B., Das, K., 2011. Evolution of granulite enclaves and associated gneisses from Purulia, Chhotanagpur Granite Gneiss Complex, India: evidence for 990–940 Ma tectonothermal event (s) at the eastern India cratonic fringe zone. *J. Asian Earth Sci.* 41, 69–88.
- Kohn, M.J., Corrie, S.L., Markley, C., 2015. The fall and rise of metamorphic zircon. *Am. Mineral.* 100, 897–908.
- Kretz, R., 1983. Symbols for rock-forming minerals. *Am. Mineral.* 68, 277–279. [https://doi.org/10.1016/0016-7037\(83\)90220-X](https://doi.org/10.1016/0016-7037(83)90220-X)
- Kumar, R.R., Kawaguchi, K., Dwivedi, S.B., Das, K., 2022. Metamorphic evolution of the pelitic and mafic granulites from Daltonganj, Chhotanagpur Granite Gneiss Complex, India: Constraints from zircon U–Pb age and phase equilibria modelling. *Geol. J.* 57, 1284–1310.
- Le Bas, M.J., Subbarao, K. V, Walsh, J.N., 2002. Metacarbonatite or marble?—the case of the carbonate, pyroxenite, calcite–apatite rock complex at Borra, Eastern Ghats, India. *J. Asian Earth Sci.* 20, 127–140.
- Luz, B., Barkan, E., 2010. Variations of 17O/16O and 18O/16O in meteoric waters. *Geochim. Cosmochim. Acta* 74, 6276–6286.

- Maji, A.K., Goon, S., Bhattacharya, A., Mishra, B., Mahato, S., Bernhardt, H.-J., 2008. Proterozoic polyphase metamorphism in the Chhotanagpur Gneissic Complex (India), and implication for trans-continental Gondwanaland correlation. *Precambrian Res.* 162, 385–402.
- Maki, K., Fukunaga, Y., Nishiyama, T., Mori, Y., 2009. Prograde P–T path of medium-pressure granulite facies calc-silicate rocks, Higo metamorphic terrane, central Kyushu, Japan. *J. Metamorph. Geol.* 27, 107–124.
- Marsh, J.H., Kelly, E.D., 2017. Petrogenetic relations among titanium-rich minerals in an anatectic high-P mafic granulite. *J. Metamorph. Geol.* 35, 717–738.
- McKinney, C.R., McCrea, J.M., Epstein, S., Allen, H.A., Urey, H.C., 1950. Improvements in mass spectrometers for the measurement of small differences in isotope abundance ratios. *Rev. Sci. Instrum.* 21, 724–730.
- Mitchell, R.J., Johnson, T.E., Clark, C., Gupta, S., Brown, M., Harley, S.L., Taylor, R., 2019. Neoproterozoic evolution and Cambrian reworking of ultrahigh temperature granulites in the Eastern Ghats Province, India. *J. Metamorph. Geol.* 37, 977–1006.
- Moine, B., Rakotondratsima, C., Cuney, M., 1985. Les pyroxénites à urano-thorianite du Sud-Est de Madagascar: conditions physico-chimiques de la métasomatose. *Bull. minéralogie* 108, 325–340.
- Mukherjee, S., Dey, A., Sanyal, S., Ibanez-Mejia, M., Dutta, U., Sengupta, P., 2017. Petrology and U–Pb geochronology of zircon in a suite of charnockitic gneisses from parts of the Chotanagpur Granite Gneiss Complex (CGGC): evidence for the reworking of a Mesoproterozoic basement during the formation of the Rodinia supercontinent. *Geol. Soc. London, Spec. Publ.* 457, 197–231.
- Mukherjee, S., Dey, A., Sanyal, S., Sengupta, P., 2019. Proterozoic crustal evolution of the Chotanagpur Granite Gneissic complex, Jharkhand-Bihar-West Bengal, India: current status and future prospect, in: *Tectonics and Structural Geology: Indian Context*. Springer, pp. 7–54.

- Owens, B.E., 2000. High-temperature contact metamorphism of calc-silicate xenoliths in the Kiglapait Intrusion, Labrador. *Am. Mineral.* 85, 1595–1605.
- Pack, A., Gehler, A., Süssenberger, A., 2013. Exploring the usability of isotopically anomalous oxygen in bones and teeth as paleo-CO₂-barometer. *Geochim. Cosmochim. Acta* 102, 306–317.
- Pack, A., Toulouse, C., Przybilla, R., 2007. Determination of oxygen triple isotope ratios of silicates without cryogenic separation of NF₃–technique with application to analyses of technical O₂ gas and meteorite classification. *Rapid Commun. Mass Spectrom. An Int. J. Devoted to Rapid Dissem. Up-to-the-Minute Res. Mass Spectrom.* 21, 3721–3728.
- Palin, R.M., Weller, O.M., Waters, D.J., Dyck, B., 2016. Quantifying geological uncertainty in metamorphic phase equilibria modelling; a Monte Carlo assessment and implications for tectonic interpretations. *Geosci. Front.* 7, 591–607.
- Pascal, M.-L., Fonteilles, M., Verkaeren, J., Piret, R., Marincea, S., 2001. The melilite-bearing high-temperature skarns of the Apuseni Mountains, Carpathians, Romania. *Can. Mineral.* 39, 1405–1434.
- Pascal, M.-L., Katona, I., Fonteilles, M., Verkaeren, J., 2005. Relics of high-temperature clinopyroxene on the join di-cats with up to 72 mol.% Ca (Al, Fe³⁺) AlSiO₆ in the skarns of Ciclova and Magureaua Vatei, Carpathians, Romania. *Can. Mineral.* 43, 857–881.
- Petrakakis, K., Schuster-Bourgin, N., Habler, G., Abart, R., 2018. Ca-rich garnets and associated symplectites in mafic peraluminous granulites from the Gföhl Nappe System, Austria. *Solid Earth* 9, 797–819.
- Raith, M.M., Brandt, S., Sengupta, P., Berndt, J., John, T., Srikantappa, C., 2016. Element mobility and behaviour of zircon during HT metasomatism of ferroan basic granulite at Ayyarmalai, South India: Evidence for polyphase Neoproterozoic crustal growth and multiple metamorphism in the Northeastern

- Madurai Province. *J. Petrol.* 57, 1729–1774.
- Reato, L., Huraiová, M., Konečný, P., Marko, F., Hurai, V., 2022. Formation of esseneite and kushiroite in tschermakite-bearing calc-silicate xenoliths ejected in alkali basalt. *Minerals* 12, 156.
- Rehman, H.U., Tanaka, R., O'Brien, P.J., Kobayashi, K., Tsujimori, T., Nakamura, E., Yamamoto, H., Khan, T., Kaneko, Y., 2014. Oxygen isotopes in Indian Plate eclogites (Kaghan Valley, Pakistan): Negative $\delta^{18}\text{O}$ values from a high latitude protolith reset by Himalayan metamorphism. *Lithos* 208, 471–483.
- Rekha, S., Upadhyay, D., Bhattacharya, A., Kooijman, E., Goon, S., Mahato, S., Pant, N.C., 2011. Lithostructural and chronological constraints for tectonic restoration of Proterozoic accretion in the Eastern Indian Precambrian shield. *Precambrian Res.* 187, 313–333.
- Ringwood, A.E., Lovering, J.F., 1970. Significance of pyroxene-ilmenite intergrowths among kimberlite xenoliths. *Earth Planet. Sci. Lett.* 7, 371–375.
- Sanyal, S., Sengupta, P., 2012. Metamorphic evolution of the Chotanagpur granite gneiss complex of the east Indian shield: current status. *Geol. Soc. London, Spec. Publ.* 365, 117–145.
- Schulze, D.J., Helmstaedt, H., Cassie, R.M., 1978. Pyroxene-ilmenite intergrowths in garnet pyroxenite xenoliths from a New York kimberlite and Arizona latites. *Am. Mineral.* 63, 258–265.
- Secchiari, A., Montanini, A., Bosch, D., Macera, P., Cluzel, D., 2019. Origin of the spinel-pyroxene symplectites in the harzburgites from the New Caledonia peridotite. *Ophioliti* 44, 31–42.
- Seyler, M., Lorand, J.-P., Dick, H.J.B., Drouin, M., 2007. Pervasive melt percolation reactions in ultra-depleted refractory harzburgites at the Mid-Atlantic Ridge, 15 20' N: ODP Hole 1274A. *Contrib. to Mineral. Petrol.* 153, 303–319.

- Sharp, Z.D., 1990. A laser-based microanalytical method for the in situ determination of oxygen isotope ratios of silicates and oxides. *Geochim. Cosmochim. Acta* 54, 1353–1357.
- Shimizu, Y., Arai, S., Morishita, T., Ishida, Y., 2008. Origin and significance of spinel–pyroxene symplectite in lherzolite xenoliths from Tallante, SE Spain. *Mineral. Petrol.* 94, 27–43.
- Sláma, J., Košler, J., Pedersen, R.B., 2007. Behaviour of zircon in high-grade metamorphic rocks: evidence from Hf isotopes, trace elements and textural studies. *Contrib. to Mineral. Petrol.* 154, 335–356.
- Spear, F.S., 1993. Metamorphic phase equilibria and pressure-temperature-time paths.
- Suhr, G., Kelemen, P., Paulick, H., 2008. Microstructures in Hole 1274A peridotites, ODP Leg 209, Mid-Atlantic Ridge: Tracking the fate of melts percolating in peridotite as the lithosphere is intercepted. *Geochemistry, Geophys. Geosystems* 9.
- Tam, P.Y., Zhao, G., Sun, M., Li, S., Wu, M., Yin, C., 2012. Petrology and metamorphic P–T path of high-pressure mafic granulites from the Jiaobei massif in the Jiao-Liao-Ji Belt, North China Craton. *Lithos* 155, 94–109.
- Taylor Jr, H.P., 1978. Oxygen and hydrogen isotope studies of plutonic granitic rocks. *Earth Planet. Sci. Lett.* 38, 177–210.
- Valley, J.W., 2018. Stable isotope geochemistry of metamorphic rocks, in: *Stable Isotopes in High Temperature Geological Processes*. De Gruyter, pp. 445–490.
- White, R., Powell, R., Holland, T.J.B., Worley, B.A., 2000. The effect of TiO₂ and Fe₂O₃ on metapelitic assemblages at greenschist and amphibolite facies conditions: mineral equilibria calculations in the system K₂O-FeO-MgO-Al₂O₃-SiO₂-H₂O-TiO₂-Fe₂O₃. *J. Metamorph. Geol.* 18, 497–511.

- White, R.W., Powell, R., Holland, T.J.B., Johnson, T.E., Green, E.C.R., 2014. New mineral activity–composition relations for thermodynamic calculations in metapelitic systems. *J. Metamorph. Geol.* 32, 261–286.
- Yoshino, T., Yamamoto, H., Okudaira, T., Toriumi, M., 1998. Crustal thickening of the lower crust of the Kohistan arc (N. Pakistan) deduced from Al zoning in clinopyroxene and plagioclase. *J. Metamorph. Geol.* 16, 729–748.
- Zhang, R.Y., Liou, J.G., 2003. Clinopyroxenite from the Sulu ultrahigh-pressure terrane, eastern China: Origin and evolution of garnet exsolution in clinopyroxene. *Am. Mineral.* 88, 1591–1600.
- Zheng, Y.-F., Fu, B., Gong, B., Li, L., 2003. Stable isotope geochemistry of ultrahigh pressure metamorphic rocks from the Dabie–Sulu orogen in China: implications for geodynamics and fluid regime. *Earth-Science Rev.* 62, 105–161.

Chapter-4.2

Stability of vesuvianite-garnet- epidote bearing calc-silicate

Chapter 4.2

Stability of vesuvianite-garnet-epidote bearing calc-silicate granulite

The studied calc-silicate enclaves preserve a unique assemblage of vesuvianite-garnet and epidote variously developed in a clinopyroxene-plagioclase-titanite bearing calc-silicate rock. Detailed field and textural relations, combined with quantitative petrogenetic grids have been used to trace the evolution of this association.

4.2.1. Field description

The studied calc-silicate granulites occur as enclaves within the migmatitic felsic gneiss (Fig. 3.1). Owing to tropical weathering the contact

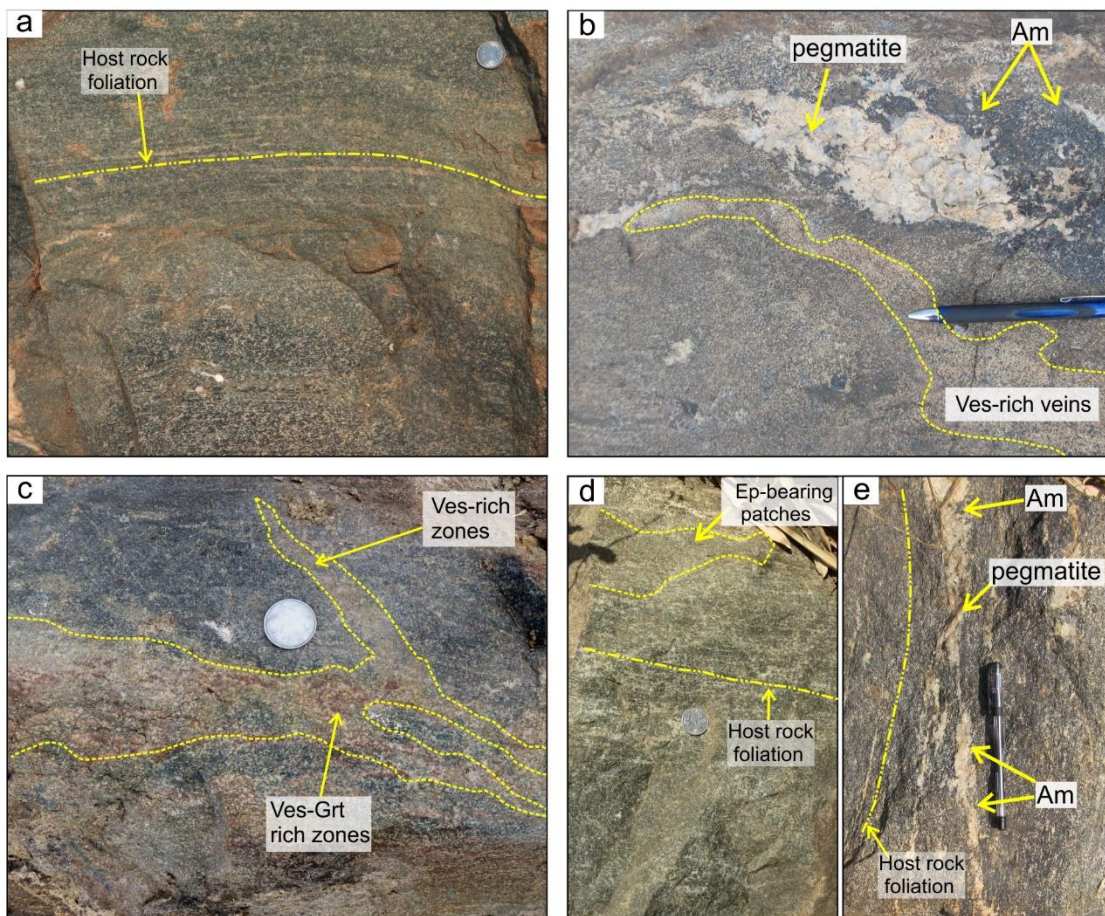


Fig. 4.2.1: Field features of the studied calc-silicate rocks. (a) Host calc-silicate showing N-S foliation. (b-c) Vesuvianite-garnet veins intruding the host calc-silicates. Note the pegmatites with prominent amphibole selvages at the interface of the host calc-silicate. (d) Epidote-bearing patches present within the host calc-silicate. (e) Pegmatitic veins intruding parallel, as well as at low angles to the host calc-silicate foliation. All mineral abbreviations are after Kretz, (1983).

between the studied calc-silicate granulites and the enclosing migmatitic felsic gneiss could not be found. The latter is exposed a few tens of meters away from the outcrop of the studied rocks. The studied calc-silicate rocks (referred to as the “host calc-silicate”) depict prominent, alternate leuco- and melanocratic bandings, dominated by plagioclase and clinopyroxene respectively (Fig.4.2.1a). These bands define a pervasive N-S foliation, which parallel that of the migmatitic felsic gneiss, as well as other enclaves.

Within the host calc-silicate rock, vesuvianite-garnet-epidote bearing zones, occur as centimeter thick, light green-coloured veins or patches (Fig.4.2.1b-d). The mineralogy of the veins include: clinopyroxene, plagioclase, vesuvianite, garnet \pm epidote. The proportion of vesuvianite, garnet and epidote, varies gradually within the veins. These veins mostly develop parallel to the foliation of the host calc-silicates, but also crosscut the latter locally (Fig.4.2.1b-c). These veins are always associated with pegmatitic veins which intrude the host calc-silicates, parallel to its foliation, but also locally intersect them at low angles (Fig.4.2.1b, e). The pegmatitic veins are dominated by quartzo-feldspathic minerals, with a few scattered amphibole grains (Fig.4.2.1e). Amphibole-rich selvage develop at the contact of the pegmatitic veins and the host calc-silicate (Fig.4.2.1b).

4.2.2. Petrography and mineral compositions:

Detailed petrographic study from multiple thin sections of the host calc-silicate, vesuvianite-garnet-epidote- bearing veins, as well as pegmatites has been done, which are delineated below.

Mineral compositions were analysed by CAMECA SX5 microprobe at the Central Research Facility in the Indian Institute of Technology (Indian School of Mines), Dhanbad, India. The diameter of the electron beam was 2–3 μm , and operating voltage and beam current were 15 kV and 15 nA respectively. Except for Mn and Ti (for which synthetic standards were used), natural standards were used for all other major elements (Si, Al, Cr, Fe, Mg, Ca, Na, K). Fe^{+3} was calculated using

the scheme of Droop, (1987) and Grew et al., (2013), during cation recalculation, except for vesuvianite, where all Fe was considered as Fe⁺³. Cation recalculation of amphibole was done using the scheme of Hawthorne et al., (2012). Cation calculation of vesuvianite was done following the method described in Dey et al., (2019). Anions in vesuvianite were calculated following the procedure in Ketchum, (2015). All mineral abbreviations used are after Kretz, (1983). Representative compositions of the minerals have been provided in Table 4.2.1-4.2.7. Characteristic compositional features of the minerals have been described along with their petrographic features below.

4.2.2.1. Host calc-silicate (AS32H1)

The overall mineralogy of the host calc-silicate includes clinopyroxene + plagioclase + titanite + amphibole ± apatite. Similar to its field appearance, millimeter-thick compositional bands, alternately rich in clinopyroxene and plagioclase (Fig.4.2.2a), together add up to 70% volume of the rock. Clinopyroxenes and plagioclase occur as medium to large sized, subidioblastic grains that share straight equilibrium boundaries amongst them, defining a granoblastic texture. Locally, clinopyroxenes are slightly elongated and stretched, defining a crude foliation (Fig.4.2.2b). Clinopyroxene and plagioclase contain inclusions of quartz. Titanite (~10%) is dispersed in the matrix in association with the above minerals. Locally, titanites also occur as inclusions in clinopyroxene. Plagioclase also shows patchy zoning, with the darker shades (Pl₁), surrounded by another generation plagioclase (showing lighter shade: Pl₂) (Fig.4.2.2c). Medium sized amphiboles (up to ~20% by volume) replace clinopyroxenes and plagioclase (Pl₁) along their grain boundaries (Fig.4.2.2d). Proportion of amphibole increases proximal to the pegmatite veins.

The *clinopyroxene* is magnesian, with X_{Mg} (Mg⁺²/Mg⁺²+Fe⁺²) varying between 0.58-0.63 (Fig.4.2.3a). Clinopyroxenes are low aluminous (Al₂O₃: ~0.9-1.7 wt%). The Al-Tschermak and essonite components vary within the range of ~2-3 mol%. Acmite (NaFe⁺³Si₂O₆), jadeite (NaAl⁺³Si₂O₆), and donpeacorite [(Mn,Mg)⁺²MgSi₂O₆] components add up to a maximum of ~3 mol% (Table 4.2.1).

The **plagioclase** occurs in textural varieties, which differ slightly in composition. Pl₁ is slightly more anorthitic (An_{0.79-0.91}Ab_{0.09-0.20}Or_{0-0.01}), than Pl₂ (An_{0.59-0.70}Ab_{0.29-0.40}Or_{0.01}) (Table 4.2.2; Fig.4.2.3b).

The **amphibole** mainly belongs to the potassic-pargasite category (Hawthorne et al., 2012 and references therein; Fig.4.2.3c). X_{Mg} of amphiboles range between: 0.53-0.57. Amphiboles also contain a considerable amount of F (~0.9-1 wt%) in their structure (Table 4.2.3).

The **titanite** grains have a considerable amount of aluminium (Al₂O₃: ~6.8-9.6 wt%, X_{Al} [Al⁺³/(Al⁺³+Fe⁺³+Ti⁺⁴)= 0.26-0.36) and F in their (~1.7-2.5 wt%) and recalculated OH (~0.01-0.15 apfu) (Table 4.2.4).

4.2.2.2. Quartzo-feldspathic pegmatitic veins (AS32Di, ii, iii)

The pegmatites consist of plagioclase, quartz, and amphibole. These minerals are coarse-grained and show interlocking texture (Fig.4.2.2e). However, these minerals do not show any recrystallisation features. Amphiboles are large-sized, subhedral, and are dispersed within the matrix of plagioclase and quartz. At the contact with the host calc-silicate, these amphiboles replace clinopyroxenes. Patchy veins of a second generation of plagioclase variably replace the Pl₁ (Fig.4.2.2f) and develop around amphibole grains.

The **plagioclase** shows patchy zoning, with Pl₁ (An_{0.62-0.78} Ab_{0.22-0.37} Or_{<0.01}; Table 4.2.2; Fig. 4.2.3b) is distinctly more anorthite rich than Pl₂ (An_{0.16-0.58} Ab_{0.42-0.82} Or_{<0.01}).

The **amphibole** compositions range between the fields of pargasite to potassic pargasite and ferro-pargasite (Table 4.2.3; Fig. 4.2.3c). The X_{Mg} content varies between 0.46-0.52. Na content varies up to ~0.4 apfu (Table 4.2.3). However, they do not show any variation within individual grains. F contents vary between 0.4-0.6 wt%.

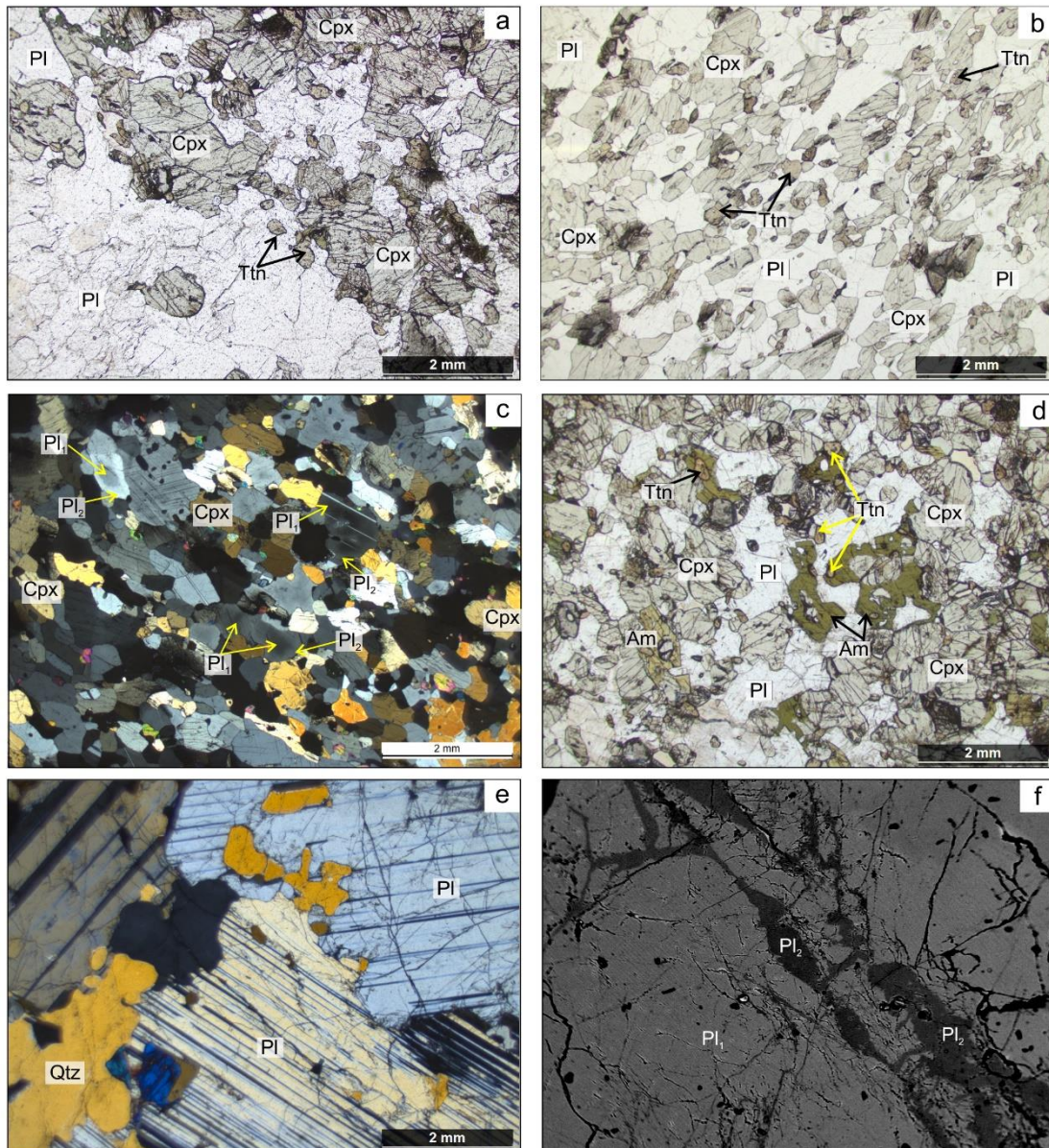


Fig.4.2.2: Petrographic features of the host calc-silicate (a-d), quartzo-feldspathic veins (e-f) and vesuvianite-garnet-epidote veins (g-o). (a) Alternate clinopyroxene and plagioclase rich domains in the host calc-silicate. (b) Stretched clinopyroxenes slightly elongated defining a crude foliation. (c) Plagioclase showing patchy zoning, with darker shades of plagioclase (Pl₁) replaced by Pl₂. (d) Amphibole growing along the margins of clinopyroxene and plagioclase. (e) Quartz and plagioclase showing interlocking boundaries in pegmatites. (f) Albitic plagioclase (Pl₂) replacing early plagioclase (Pl₁). All mineral abbreviations are after Kretz, (1983).

4.2.2.3. Vesuvianite-garnet- epidote veins

The overall mineral association include clinopyroxene, plagioclase, titanite, vesuvianite, garnet, epidote ± apatite ± calcite. These veins consist of different

microdomains, dominated alternately by vesuvianite or garnet or epidote within them. Vesuvianite and coronal garnets preferentially grow on the plagioclase-and clinopyroxene-rich bands respectively (Fig.4.2.2g). The modal proportions of plagioclase: clinopyroxene: vesuvianite: garnet in the vesuvianite (or plagioclase-rich) domain is 50:15:25:10, and that in the garnet-rich domain is 10:25:5:60. In the vesuvianite-rich domains, vesuvianite forms subidioblastic grains, consisting of inclusions of clinopyroxene, plagioclase and quartz, and rare apatite and calcite (Fig.4.2.2h). Plagioclase, clinopyroxene and minor titanite define a granoblastic mosaic. Small coronal garnet develops along the margins of clinopyroxene, plagioclase and vesuvianite (Fig.4.2.2i).

In the garnet-rich domains, aggregates of medium-sized coronal garnet form an interconnected network surrounding clinopyroxene, titanite, quartz (Fig.4.2.2j) and rare calcite. Here also, vesuvianite contains inclusions of clinopyroxene, calcite, quartz, titanite, and occurs as subidioblastic grains within this matrix.

Epidote (~40 vol%) occurs in a few microdomains along with vesuvianite and coronal garnet. These domains comprise all the above minerals (clinopyroxene, vesuvianite, garnet and plagioclase; Fig.4.2.2k). Vesuvianite occurs as medium-sized grains in the matrix. Small, subrounded garnets grow along the margins of clinopyroxene, plagioclase and vesuvianite (Fig.4.2.2l-n). Titanite occurs as medium-sized, locally euhedral grains in the matrix (Fig.4.2.2k-l). Epidote is dispersed as medium to large sized grains, having sharp margins. Some of the grains occur as aggregates also, without any visible distinct boundary. Epidote extensively replaces clinopyroxene, plagioclase, vesuvianite and coronal garnets (Fig.4.2.2m-o).

Compositions of the minerals constituting the veins, do not show any significant differences in different domains (vesuvianite/ garnet/ epidote). The *clinopyroxene* is magnesian ($X_{Mg} = 0.54-0.61$). They are also low aluminous (0.7-2.2 wt%) and acmite, jadeite, donpeacorite, Al-Tschermak and essenite components together add up to ~9 mol% (Table 4.2.1; Fig.4.2.2a).

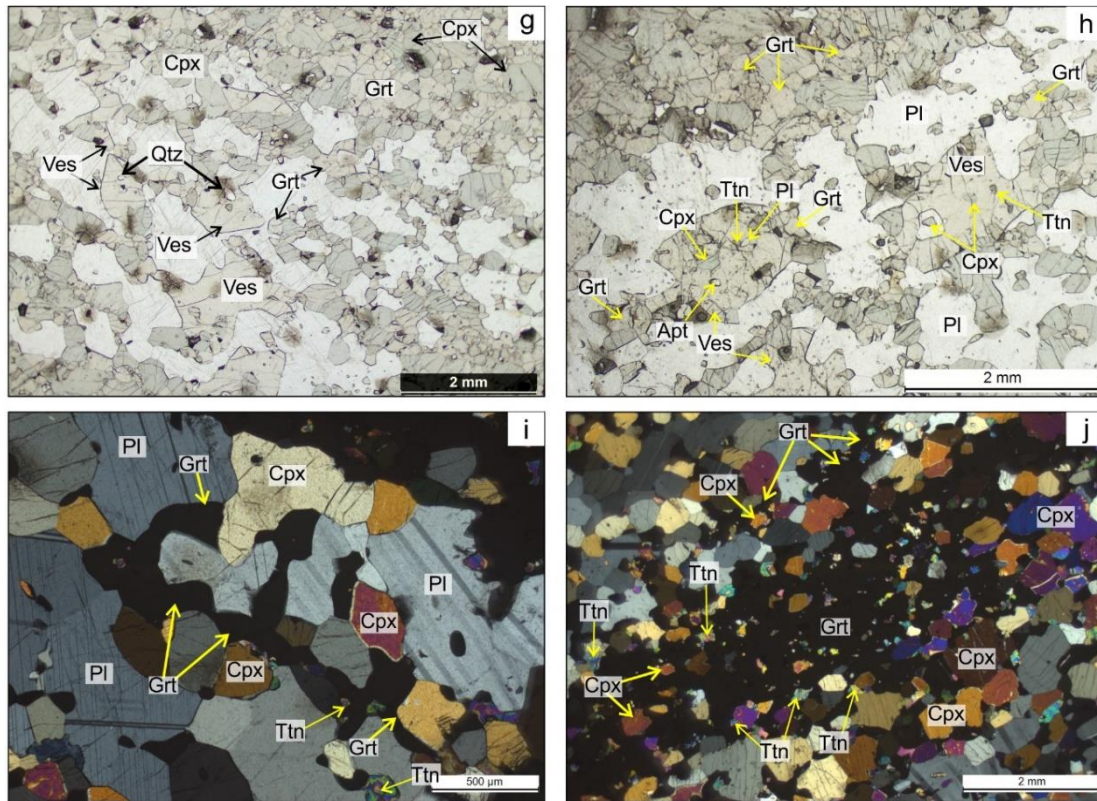


Fig.4.2.2 contd.:(g-h) Subidioblastic vesuvianite preferentially growing on plagioclase-rich bands. Note the inclusions of clinopyroxene, titanite, plagioclase and apatite within vesuvianites. Also note small coronal garnets growing over vesuvianite, clinopyroxene and plagioclase margins. (i) Coronal garnets growing along plagioclase and clinopyroxene. (j) Aggregates of coronal garnets join to form a network, and enclose numerous small grains of clinopyroxene, plagioclase, and titanite. All mineral abbreviations are after Kretz, (1983).

The **plagioclase** is highly anorthitic, and has a very restricted composition of $An_{0.92-0.98}Ab_{0.02-0.08}$ (Table 4.2.2; Fig.4.2.2b).

The **titanite** grains are highly aluminous (Al_2O_3 : ~8-11.5 wt%; $X_{Al} = 0.31-0.46$), and consists of a considerable amount of F (~1.7-3.8 wt%) and OH (~0.01-0.18 apfu) in epidote-free domains (Table 4.2.4). However, in epidote bearing domains, titanites are less aluminous (Al_2O_3 : ~7.5-8.1 wt%), and are OH rich and contain very small amount of fluorine (0.02).

The **vesuvianite** composition has been recalculated on the basis of 50 cations. Si content is >17.5 apfu suggesting that very little Al in its T site (Groat et al., 1992a). The Al content (15.7-17.5 wt% Al_2O_3 , ~9-10 apfu Al) indicates that all the Fe is in Fe^{+3} state to balance the charge (Table 4.2.5). Presence of 1.3-1.5 apfu Mg (1.8-2 wt%) indicates that the bivalent Y1 site (occupancy 1 apfu) does not contain any Fe^{+2} . The excess Mg fills the Y3 site along with Mn, Fe^{+3} , Al^{+3} and Ti^{+4} . Presence

of 33.5-37 wt% CaO (17.7-19 apfu Ca) implies that the X site is incompletely filled (Ca site with occupancy 19 apfu). Na content in any case does not exceed 0.2 apfu.

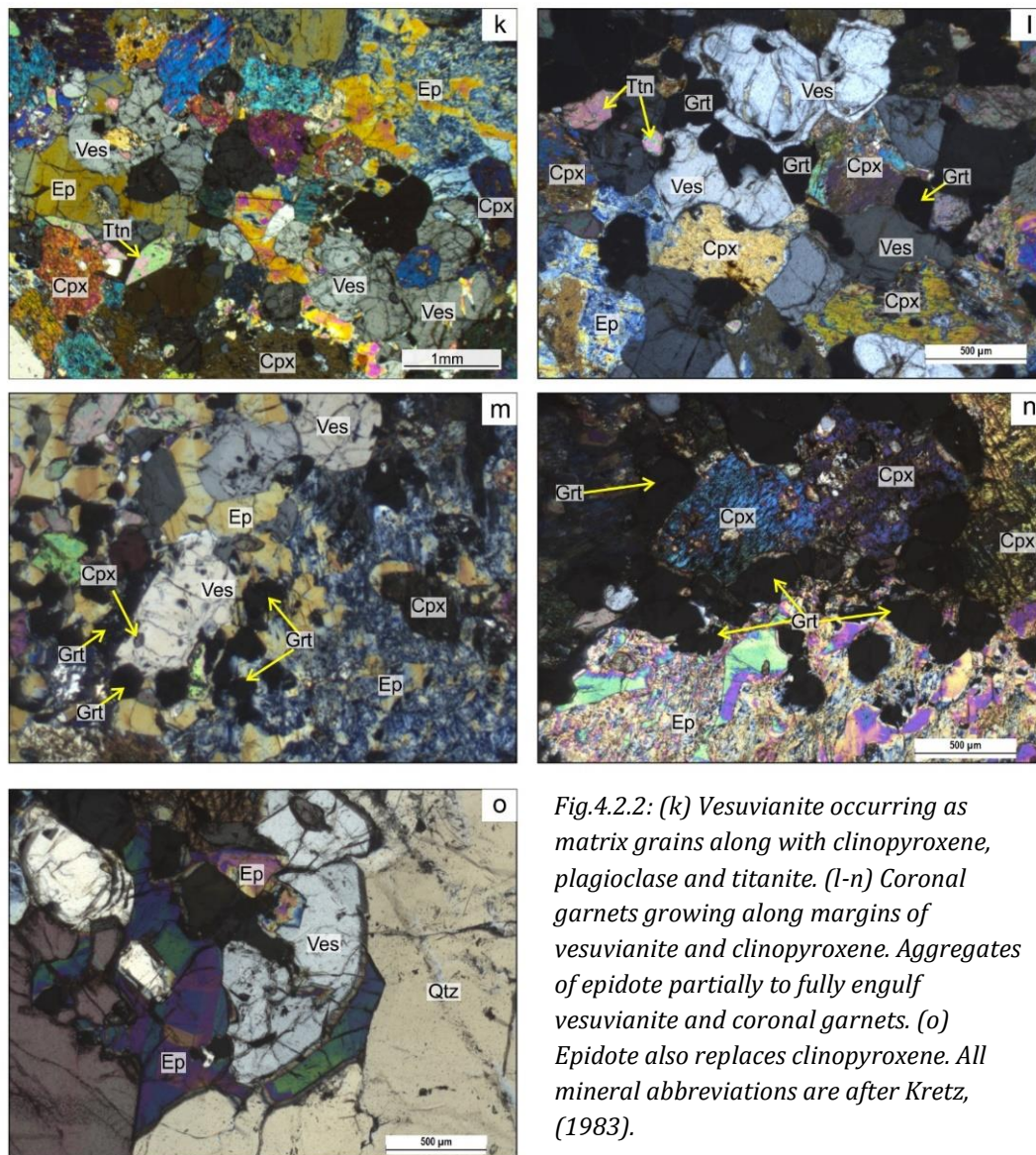


Fig.4.2.2: (k) Vesuvianite occurring as matrix grains along with clinopyroxene, plagioclase and titanite. (l-n) Coronal garnets growing along margins of vesuvianite and clinopyroxene. Aggregates of epidote partially to fully engulf vesuvianite and coronal garnets. (o) Epidote also replaces clinopyroxene. All mineral abbreviations are after Kretz, (1983).

Compositionally homogeneous vesuvianite shows significant F (1.5-2.5 wt%; up to ~3.7 apfu) and insignificant Cl content (up to 0.09 wt%) in its structure (Table 4.2.5). In the epidote-bearing micro-domains, however, vesuvianites do not have F in their structure. All the vesuvianites are boron-free. No compositional zoning was observed within individual grains.

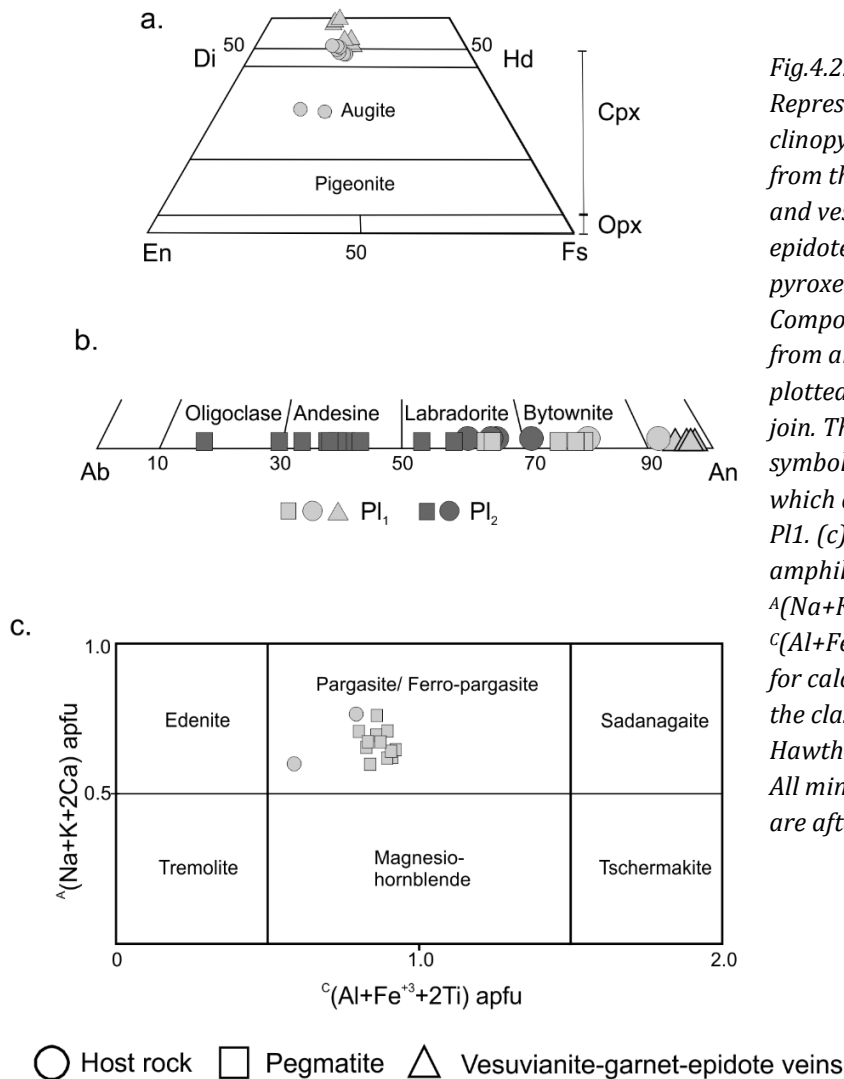


Fig.4.2.3: (a) Representative clinopyroxene compositions from the host calc-silicate, and vesuvianite-garnet-epidote veins plotted in pyroxene quadrilateral. (b) Composition of plagioclase from all associations plotted on albite-anorthite join. The darker shaded symbols represent Pl₂, which are relatively than Pl₁. (c) Composition of amphiboles presented in a $^a(\text{Na}+\text{K}+2\text{Ca})$ vs. $^c(\text{Al}+\text{Fe}^{+3}+2\text{Ti})$ (apfu) plot for calcic amphiboles after the classification scheme of Hawthorne et al., (2012). All mineral abbreviations are after Kretz, (1983).

The coronal garnets are highly grossular rich, along with subordinate amounts of almandine and andradite components. Garnets are primarily a solid solution of grossular and almandine ($\text{Grs}_{0.73-0.80} \text{Alm}_{0.12-0.17} \text{Adr}_{0.01-0.07} \text{Sps}_{0.02-0.04}$, $X_{\text{Mg}}:0.07-0.13$). However, some garnets also contain andradite component in solid solution with grossular, instead of almandine ($\text{Grs}_{0.80} \text{Alm}_{0.06-0.07} \text{Adr}_{0.07-0.08}$, $X_{\text{Mg}}:0.10-0.11$). A considerable amount of F (0.4 -1 wt%) is also present within their structure. Garnets do not show any compositional zoning within individual grains (Table 4.2.6).

The epidote shows restricted compositional ranges. No compositional variation is observed from core to rim. Pistacite $[\text{Fe}^{+3}/(\text{Fe}+\text{Al})^{+3}]$ component of epidote varies between 0.09-0.19 (Table 4.2.7).

Table 4.2.1.: Representative electron microprobe analysis of clinopyroxene (stoichiometry calculated on the basis of 6 oxygens, oxide data are given in weight %).

Point	Host Rock							Vesuvianite-epidote veins				
	32/1	12/1 [#]	24/1	6/1	8/1	9/1	10/1	12/1	1/1	44/1	61/1	73/1
SiO ₂	52.94	52.64	52.79	51.93	51.24	51.24	51.24	50.89	51.88	49.45	51.50	51.85
TiO ₂	0.01	0.08	0.03	0.24	0.18	0.2	0.13	0.05	0.18	0.14	0.00	0.00
Al ₂ O ₃	0.86	1.27	1.28	1.41	1.73	1.28	1.27	0.98	1.89	2.17	0.15	0.66
Cr ₂ O ₃	0.11	0.19	0.18	0	0.15	0.01	0.04	0.09	<d.l.	0.04	0.00	0.00
FeO	12.03	11.87	12.46	13.36	13.23	13.17	12.96	12.91	13.71	13.25	19.80	16.71
MnO	0.28	0.37	0.36	0.42	0.3	0.34	0.4	0.34	0.42	0.40	0.81	0.60
MgO	10.63	10.78	9.80	10.13	9.88	10.06	10.3	10.16	9.04	9.05	12.55	14.39
CaO	23.93	24.22	23.87	22.97	22.49	22.91	22.93	23.39	23.77	23.49	13.52	13.88
Na ₂ O	0.20	0.23	0.24	0.27	0.33	0.21	0.24	0.24	0.19	0.22	0.00	0.08
K ₂ O	<d.l.	<d.l.	<d.l.	0.01	<d.l.	<d.l.	<d.l.	<d.l.	<d.l.	<d.l.	0.05	0.00
Total	101.00	101.67	101.04	100.75	99.59	99.45	99.62	99.1	101.11	98.22	98.39	98.17
Si	1.99	1.97	1.99	1.97	1.96	1.97	1.96	1.96	1.97	1.93	2.02	2.00
Ti	0.00	0.00	0.00	0.01	0.01	0.01	0.00	0.00	0.01	0.00	0.00	0.00
Al	0.04	0.06	0.06	0.06	0.08	0.06	0.06	0.04	0.08	0.10	0.01	0.03
Cr ⁺³	0.00	0.01	0.01	0.00	0.00	0.00	0.00	0.00	0.00	0.00	0.00	0.00
Fe ⁺³	0.00	0.02	0.00	0.01	0.00	0.01	0.03	0.05	0.00	0.05	0.00	0.00
Fe ⁺²	0.38	0.35	0.39	0.42	0.42	0.41	0.39	0.37	0.44	0.38	0.65	0.54
Mn	0.01	0.01	0.01	0.01	0.01	0.01	0.01	0.01	0.01	0.01	0.03	0.02
Mg	0.60	0.60	0.55	0.57	0.56	0.58	0.59	0.58	0.51	0.53	0.73	0.83
Ca	0.97	0.97	0.97	0.93	0.92	0.94	0.94	0.96	0.97	0.98	0.57	0.57
Na	0.01	0.02	0.02	0.02	0.02	0.02	0.02	0.02	0.01	0.02	0.00	0.01
K	0.00	0.00	0.00	0.00	0.00	0.00	0.00	0.00	0.00	0.00	0.00	0.00
Total	4.00	4.00	4.00	4.00	4.00	4.00	4.00	4.00	4.00	4.00	4.00	4.00
Di	0.59	0.60	0.55	0.56	0.55	0.56	0.58	0.58	0.51	0.53	0.52	0.59
Hd	0.39	0.35	0.43	0.40	0.41	0.40	0.38	0.37	0.45	0.39	0.46	0.39
Ac	0.00	0.00	0.00	0.00	0.00	0.00	0.00	0.02	0.00	0.00	0.00	0.00
Jd	0.01	0.02	0.02	0.02	0.02	0.02	0.02	0.00	0.01	0.02	0.00	0.01
Ess	0.00	0.02	0.00	0.01	0.00	0.01	0.03	0.03	0.00	0.05	0.00	0.00
crTs	0.00	0.01	0.01	0.00	0.00	0.00	0.00	0.00	0.00	0.00	0.00	0.00
AlTs	0.02	0.01	0.03	0.01	0.02	0.01	0.00	0.00	0.04	0.01	0.02	0.03
Wo	0.97	0.97	0.97	0.93	0.92	0.94	0.94	0.96	0.97	0.98	0.57	0.57
En	0.60	0.60	0.55	0.57	0.56	0.58	0.59	0.58	0.51	0.53	0.73	0.83
Fs	0.39	0.35	0.43	0.42	0.42	0.41	0.39	0.37	0.45	0.38	0.65	0.54
Don	0.01	0.01	0.01	0.01	0.01	0.01	0.01	0.01	0.01	0.01	0.03	0.02
X _{Mg}	0.61	0.63	0.58	0.58	0.57	0.58	0.60	0.61	0.54	0.58	0.53	0.61

Don: Donpeacorite; [#] Dey et al. (2019a); d.l.= detection limit;

Table 4.2.2: Representative electron microprobe analysis of plagioclase (stoichiometry calculated on the basis of 8 oxygen, oxide data are given in weight %).

Point	Host Rock						Quartzo-feldspathic veins						Ves-Ep veins		
	2/1	25	27	10/1	15/1.		48/1.	8/1.	41/1.	34/1.	32/1.	10/1.	37/1.	13/1	10/1
	Pl ₁	Pl ₁	Pl ₂	Pl ₂	Pl ₂		Pl ₁	Pl ₁	Pl ₂	Pl ₂	Pl ₂	Pl ₂	Pl ₂	Pl ₁	Pl ₁
SiO ₂	48.93	45.82	54.10	51.27	51.80		48.20	52.48	62.96	58.69	57.81	54.39	53.56	42.90	44.16
TiO ₂	<d.l.	<d.l.	<d.l.	0.06	0.02		0.00	0.01	0.03	0.00	0.00	0.01	0.00	<d.l.	0.08
Al ₂ O ₃	32.70	34.72	29.36	31.66	29.79		32.77	29.53	21.73	25.02	26.10	27.35	28.23	35.42	35.98
FeO	<d.l.	<d.l.	<d.l.	<d.l.	0.17		0.09	0.00	0.62	0.00	0.05	0.13	0.05	<d.l.	<d.l.
MnO	<d.l.	<d.l.	<d.l.	<d.l.	0.01		0.00	0.12	0.10	0.04	0.07	0.02	0.01	<d.l.	<d.l.
MgO	<d.l.	<d.l.	<d.l.	<d.l.	<d.l.		0.00	0.00	0.37	0.01	0.00	0.01	0.01	<d.l.	<d.l.
CaO	16.14	18.75	12.18	14.58	13.40		16.54	12.92	3.27	7.93	8.87	10.62	11.76	21.23	19.40
Na ₂ O	2.28	1.01	4.48	3.30	4.00		2.53	4.23	9.41	7.21	7.00	5.27	4.75	0.70	0.37
K ₂ O	0.09	<d.l.	0.18	0.14	0.13		0.04	0.16	0.38	0.11	0.09	0.09	0.07	<d.l.	<d.l.
Total	100.41	100.35	100.44	101.16	99.32		100.22	99.45	98.87	99.09	99.99	97.93	98.44	100.44	100.03
Si	2.23	2.10	2.44	2.31	2.37		2.20	2.39	2.81	2.65	2.58	2.51	2.46	1.97	2.04
Ti	0.00	0.00	0.00	0.00	0.00		0.00	0.00	0.00	0.00	0.00	0.00	0.00	0.00	0.00
Al	1.76	1.88	1.56	1.68	1.61		1.76	1.59	1.14	1.33	1.37	1.49	1.53	1.92	1.96
Fe ⁺³	0.00	0.00	0.00	0.00	0.00		0.00	0.00	0.00	0.00	0.00	0.00	0.00	0.00	0.00
Fe ⁺²	0.00	0.00	0.00	0.00	0.00		0.00	0.00	0.00	0.00	0.00	0.00	0.00	0.00	0.00
Mn	0.00	0.00	0.00	0.00	0.00		0.00	0.00	0.00	0.00	0.00	0.00	0.00	0.00	0.00
Mg	0.00	0.00	0.00	0.00	0.00		0.00	0.00	0.02	0.00	0.00	0.00	0.00	0.00	0.00
Ca	0.79	0.92	0.59	0.70	0.66		0.81	0.63	0.16	0.38	0.42	0.52	0.58	1.04	0.96
Na	0.20	0.09	0.39	0.29	0.35		0.22	0.37	0.81	0.63	0.61	0.47	0.42	0.06	0.03
K	0.01	0.00	0.01	0.01	0.01		0.00	0.01	0.02	0.01	0.01	0.01	0.00	0.00	0.00
Total	5.00	5.00	5.00	5.00	5.00		5.00	5.00	5.00	5.00	5.00	5.00	5.00	5.00	5.00
X _{An}	0.79	0.91	0.59	0.70	0.64		0.78	0.62	0.16	0.38	0.41	0.52	0.58	0.94	0.97
X _{Ab}	0.20	0.09	0.40	0.29	0.35		0.22	0.37	0.82	0.62	0.59	0.47	0.42	0.06	0.03
X _{Or}	0.01	0.00	0.01	0.01	0.01		0.00	0.01	0.02	0.01	0.00	0.01	0.00	0.00	0.00

d.l.: detection limit

Table 4.2.3: Representative electron microprobe analysis of amphibole (calculated after Hawthorne et. al. 2012 and references therein; oxide data are given in weight %).

Point	Host Rock		Quartzo-feldspathic veins								
	Potassic-pargasite		pargasi	potassic-ferro-pargasite					Potassic-pargasite		
	11/1 [#]	13/1 [#]		2/1.	1/1.	5/1.	18/1.	12/1.	25/1.	3/1.	22/1.
SiO ₂	42.37	44.65	42.34	42.07	42.42	42.74	42.07	42.73	42.89	42.93	
TiO ₂	0.50	0.68	0.92	1.65	1.58	0.96	1.30	1.34	1.30	1.05	
Al ₂ O ₃	12.68	10.02	11.08	11.15	10.87	10.52	11.22	11.04	11.05	10.45	
Cr ₂ O ₃	1.35	1.48	0.13	0.15	0.14	0.07	0.14	0.10	0.19	0.09	
FeO	14.73	14.63	17.63	17.48	18.23	17.75	18.60	17.61	17.43	18.10	
MnO	0.29	0.27	0.30	0.33	0.31	0.22	0.22	0.10	0.11	0.03	
MgO	9.48	11.05	9.60	8.87	8.45	9.19	9.20	9.55	9.51	9.60	
CaO	12.24	12.29	12.10	11.65	11.61	11.94	12.11	12.48	11.90	12.01	
Na ₂ O	1.18	0.97	1.24	1.23	1.18	1.06	1.35	1.01	1.22	1.17	
K ₂ O	2.24	1.84	1.77	1.71	1.68	1.53	1.97	1.71	1.81	1.71	
F	1.06	0.88	<d.l.	0.39	0.63	0.40	<d.l.	<d.l.	<d.l.	<d.l.	
Cl	<d.l.	<d.l.	<d.l.	0.05	0.04	0.01	<d.l.	<d.l.	<d.l.	<d.l.	
Total	98.13	98.75	97.25	96.78	97.15	96.45	98.31	97.88	97.79	97.28	
Si	6.42	6.67	6.44	6.47	6.53	6.57	6.38	6.46	6.51	6.53	
Al	1.58	1.33	1.56	1.53	1.47	1.43	1.62	1.54	1.49	1.47	
Ti	0.00	0.00	0.00	0.00	0.00	0.00	0.00	0.00	0.00	0.00	
Fe ³⁺	0.00	0.00	0.00	0.00	0.00	0.00	0.00	0.00	0.00	0.00	
T	8.00	8.00	8.00	8.00	8.00	8.00	8.00	8.00	8.00	8.00	
Ti	0.06	0.08	0.11	0.19	0.18	0.11	0.15	0.15	0.15	0.12	
Al	0.68	0.43	0.43	0.49	0.50	0.48	0.38	0.43	0.48	0.41	
Cr	0.16	0.18	0.02	0.02	0.02	0.01	0.02	0.01	0.02	0.01	
Fe ³⁺	0.00	0.00	0.22	0.05	0.04	0.14	0.18	0.14	0.05	0.18	
Mn ²⁺	0.04	0.03	0.03	0.02	0.02	0.01	0.01	0.01	0.00	0.00	
Fe ²⁺	1.87	1.83	2.03	2.20	2.31	2.14	2.18	2.09	2.14	2.11	
Mg	2.14	2.46	2.18	2.03	1.94	2.11	2.08	2.15	2.15	2.18	
C	4.94	5.00	5.00	5.00	5.00	5.00	5.00	4.99	5.00	5.00	
Mn ²⁺	0.00	0.00	0.01	0.03	0.02	0.02	0.02	0.00	0.01	0.00	
Fe ²⁺	0.00	0.00	0.00	0.00	0.00	0.00	0.00	0.00	0.02	0.02	
Mg	0.00	0.00	0.00	0.00	0.00	0.00	0.00	0.00	0.00	0.00	
Ca	1.99	1.97	1.97	1.92	1.91	1.97	1.97	2.00	1.93	1.96	
Na	0.01	0.03	0.01	0.06	0.06	0.02	0.02	0.00	0.04	0.02	
B	2.00	2.00	2.00	2.00	2.00	2.00	2.00	2.00	2.00	2.00	
Ca	0.00	0.00	0.00	0.00	0.00	0.00	0.00	0.02	0.00	0.00	
Na	0.33	0.25	0.35	0.31	0.29	0.30	0.38	0.30	0.32	0.32	
K	0.43	0.35	0.34	0.34	0.33	0.30	0.38	0.33	0.35	0.33	
A	0.77	0.60	0.70	0.65	0.62	0.60	0.76	0.65	0.67	0.65	
O (non-	22.00	22.00	22.00	22.00	22.00	22.00	22.00	22.00	22.00	22.00	
OH	1.49	1.58	2.00	1.80	1.68	1.80	2.00	2.00	2.00	2.00	
F	0.51	0.42	0.00	0.19	0.31	0.20	0.00	0.00	0.00	0.00	
Cl	0.00	0.00	0.00	0.01	0.01	0.00	0.00	0.00	0.00	0.00	
W	2.00	2.00	2.00	2.00	2.00	2.00	2.00	2.00	2.00	2.00	
Sum	15.71	15.60	15.69	15.65	15.62	15.60	15.76	15.64	15.67	15.66	
T,C,B,A											
X _{Mg}	0.53	0.57	0.52	0.48	0.46	0.50	0.49	0.51	0.50	0.51	

Table 4.2.4: Representative electron microprobe analysis of titanite (stoichiometry calculated on the basis of 5 oxygens, oxide data are given in weight %).

Point	Host Rock			Vesuvianite-epidote veins							
	4	22	26 / 1	epidote-free					epidote-bearing		
				2 / 1	2 / 26	4 / 1	24 / 1	49 / 1	71 / 1 .	72 / 1 .	
SiO ₂	31.45	31.54	31.18	30.49	30.23	31.80	30.34	29.95	30.17	30.70	
TiO ₂	30.28	26.49	27.83	27.72	22.37	27.87	21.32	22.66	28.39	27.82	
Al ₂ O ₃	6.77	9.55	8.31	8.33	10.74	8.27	11.53	11.29	7.56	8.10	
Cr ₂ O ₃	0.22	0.43	0.30	<d.l.	<d.l.	<d.l.	0.05	0.04	0.00	0.00	
Fe ₂ O ₃	0.50	0.21	0.29	0.38	0.30	0.44	0.24	0.23	0.48	0.32	
MnO	<d.l.	<d.l.	<d.l.	<d.l.	<d.l.	<d.l.	<d.l.	0.04	0.00	0.01	
MgO	0.09	0.09	0.08	<d.l.	<d.l.	<d.l.	<d.l.	0.03	0.01	0.05	
CaO	28.91	29.14	28.94	28.98	29.24	29.14	28.81	28.05	29.52	29.75	
Na ₂ O	<d.l.	<d.l.	<d.l.	<d.l.	<d.l.	<d.l.	<d.l.	0.07	0.00	0.02	
K ₂ O	<d.l.	<d.l.	<d.l.	<d.l.	<d.l.	<d.l.	<d.l.	0.01	0.00	0.01	
F	2.49	2.08	1.65	1.73	3.75	2.11	3.50	2.52	0.02	0.00	
Cl	<d.l.	<d.l.	<d.l.	<d.l.	<d.l.	0.04	<d.l.	0.00	0.01	0.01	
Total	100.84	99.58	98.68	97.78	96.69	99.85	95.87	95.10	96.13	96.84	
Si	1.00	1.00	1.00	0.99	0.99	1.01	1.00	0.99	0.98	0.99	
Ti	0.73	0.63	0.67	0.68	0.55	0.67	0.53	0.56	0.69	0.67	
Al	0.25	0.36	0.31	0.32	0.42	0.31	0.45	0.44	0.29	0.31	
Cr ⁺³	0.01	0.01	0.01	0.00	0.00	0.00	0.00	0.00	0.00	0.00	
Fe ^{+3*}	0.01	0.00	0.01	0.01	0.01	0.01	0.01	0.01	0.01	0.01	
Fe ⁺²	0.00	0.00	0.00	0.00	0.00	0.00	0.00	0.00	0.00	0.00	
Mn	0.00	0.00	0.00	0.00	0.00	0.00	0.00	0.00	0.00	0.00	
Mg	0.00	0.00	0.00	0.00	0.00	0.00	0.00	0.00	0.00	0.00	
Ca	0.99	0.99	0.99	1.01	1.03	0.99	1.02	0.99	1.03	1.02	
Na	0.00	0.00	0.00	0.00	0.00	0.00	0.00	0.00	0.00	0.00	
K	0.00	0.00	0.00	0.00	0.00	0.00	0.00	0.00	0.00	0.00	
Total	3.00	3.00	3.00	3.00	3.00	3.00	3.00	3.00	3.00	3.00	
F	0.25	0.21	0.17	0.18	0.39	0.21	0.37	0.27	0.00	0.00	
Cl	0.00	0.00	0.00	0.00	0.00	0.002	0.00	0.00	0.00	0.00	
OH	0.01	0.15	0.15	0.15	0.03	0.11	0.08	0.18	0.29	0.31	
X _{Al}	0.26	0.36	0.32	0.32	0.43	0.31	0.46	0.60	0.29	0.31	
X _F	0.94	0.59	0.53	0.55	0.93	0.67	0.81	0.44	0.01	0.00	
X _{OH}	0.06	0.41	0.47	0.45	0.07	0.33	0.19	0.40	1.00	1.00	

* All Fe as Fe⁺³; OH= Al+Fe⁺³-F;

d.l.: detection limit

Table 4.2.5: Representative electron microprobe analysis of vesuvianite (stoichiometry calculated on the basis of 50 cations. Anions calculated after the procedure of Ketcham 2015). Oxide data are given in weight %.

Point	Vesuvianite-epidote veins										
	epidote-free									epidote-bearing	
	13/1 [#]	42/1 [#]	1/1.	6/1.	13/1.	19/1.	23/1.	33/1.	42/1.	61/1.	73/1.
SiO ₂	36.05	36.93	38.65	38.63	38.55	38.54	38.52	38.41	38.37	35.08	35.61
TiO ₂	1.26	1.58	0.93	1.44	1.06	1.76	0.99	1.24	1.00	1.22	1.82
Al ₂ O ₃	15.83	15.65	17.18	16.85	17.10	16.58	17.18	16.82	17.51	15.99	16.12
Cr ₂ O ₃	0.05	0.12	0.25	0.31	0.06	0.05	0.00	0.28	0.07	0.36	0.00
Fe ₂ O ₃	5.16	5.54	4.11	4.12	4.59	4.23	4.17	3.85	4.37	5.21	4.77
MnO	0.17	0.41	0.16	0.07	0.05	0.11	0.26	0.25	0.10	0.70	0.36
MgO	1.92	1.99	2.03	2.10	2.10	2.12	2.06	2.12	2.03	2.06	1.80
CaO	33.61	33.50	36.64	36.43	36.44	36.52	36.76	36.98	36.49	35.67	35.93
Na ₂ O	0.07	0.09	0.05	0.05	0.05	0.08	0.05	0.05	0.04	0.06	0.07
K ₂ O	<d.l.	<d.l.	0.00	0.00	0.00	0.00	0.01	0.00	0.01	0.01	0.01
F	2.47	1.50	1.97	1.8	1.83	1.52	1.79	1.64	1.87	<d.l.	<d.l.
Cl	<d.l.	0.09	<d.l.	0.06	0.01	0.04	0.02	0.05	0.01	0.05	0.06
Total	96.61	97.42	96.48	96.33	95.88	95.96	95.24	94.76	95.53	96.62	96.51
Si	17.98	18.19	18.43	18.35	18.43	18.42	18.39	18.22	18.31	17.32	17.59
Ti	0.47	0.59	0.33	0.32	0.37	0.63	0.34	0.41	0.36	0.45	0.67
Al	9.30	9.09	9.65	9.72	9.81	9.34	9.58	9.63	9.84	9.30	9.39
Cr ⁺³	0.02	0.05	0.10	0.08	0.01	0.02	0.08	0.08	0.03	0.14	0.00
Fe ^{+3*}	1.90	2.02	1.21	1.29	1.14	1.24	1.28	1.33	1.28	1.94	1.77
Fe ⁺²	0.00	0.00	0.00	0.00	0.00	0.00	0.00	0.00	0.00	0.00	0.00
Mn	0.81	0.83	0.06	0.09	0.06	0.04	0.06	0.05	0.04	0.29	0.15
Mg	1.43	1.46	1.45	1.47	1.50	1.51	1.53	1.51	1.44	1.52	1.33
Ca	17.96	17.68	18.72	18.65	18.61	18.70	18.67	18.73	18.65	18.87	19.02
Na	0.07	0.09	0.05	0.04	0.08	0.08	0.06	0.04	0.04	0.06	0.07
K	0.01	0.01	0.00	0.00	-0.01	0.00	0.00	0.01	0.01	0.00	0.00
Total	50.00	50.00	50.00	50.00	50.00	50.00	50.00	50.00	50.00	50.00	50.00
F	3.74	2.26	3.02	3.27	3.41	2.34	2.99	2.70	2.89	0.00	0.00
Cl	0.00	0.07	0.00	0.02	0.01	0.03	0.02	0.02	0.01	0.04	0.05
O	1.00	1.00	1.00	1.00	1.00	1.00	1.00	1.00	1.00	1.00	1.00
OH	5.26	6.67	5.99	5.71	5.58	6.63	5.99	6.27	6.10	8.96	8.95

* All Fe as Fe⁺³; d.l.: detection limit

Table 4.2.6: Representative electron microprobe analysis of garnet (stoichiometry calculated on the basis of 12 oxygens, oxide data are given in weight %).

Point	Vesuvianite-epidote veins							
	31 / 1	46 / 1	56	57	78	62 / 1.	66 / 1.	68 / 1.
Texture	coronal							
SiO ₂	38.58	38.49	38.96	38.64	38.71	38.96	38.94	38.99
TiO ₂	0.40	0.31	0.23	0.29	0.28	0.33	0.43	0.46
Al ₂ O ₃	19.75	20.53	20.49	19.28	20.41	19.77	19.79	19.51
Cr ₂ O ₃	0.46	0.21	0.01	0.45	0.29	0.57	0.51	0.51
FeO	9.52	7.76	7.75	9.58	7.40	5.53	5.70	5.38
MnO	1.49	1.11	0.83	1.96	0.94	1.21	1.24	1.52
MgO	0.41	0.48	0.47	0.36	0.42	0.22	0.22	0.19
CaO	28.69	29.45	29.82	27.43	29.33	32.80	32.57	32.95
Na ₂ O	<d.l.	0.12	<d.l.	0.07	<d.l.	0.00	0.01	0.00
K ₂ O	<d.l.	<d.l.	<d.l.	<d.l.	<d.l.	0.00	0.01	0.00
F	0.54	0.61	0.98	0.65	0.73	<d.l.	<d.l.	<d.l.
Total	99.85	99.11	99.58	98.73	98.55	99.39	99.43	99.50
Si	3.00	2.99	3.02	3.04	3.03	2.99	2.99	3.00
Ti	0.02	0.02	0.01	0.02	0.02	0.02	0.03	0.03
Al	1.81	1.88	1.87	1.79	1.88	1.79	1.79	1.77
Cr ⁺³	0.03	0.01	0.00	0.03	0.02	0.03	0.03	0.03
Fe ⁺³	0.13	0.12	0.07	0.08	0.02	0.15	0.14	0.16
Fe ⁺²	0.49	0.38	0.44	0.55	0.46	0.21	0.22	0.19
Mn	0.10	0.07	0.05	0.13	0.06	0.08	0.08	0.10
Mg	0.05	0.06	0.05	0.04	0.05	0.03	0.03	0.02
Ca	2.39	2.45	2.48	2.31	2.46	2.70	2.68	2.71
Na	0.00	0.02	0.00	0.01	0.00	0.00	0.00	0.00
K	0.00	0.00	0.00	0.00	0.00	0.00	0.00	0.00
Total	8.00	8.00	8.00	8.00	8.00	8.00	8.00	8.00
X _{Adr}	0.07	0.06	0.03	0.04	0.01	0.08	0.07	0.08
X _{Py}	0.01	0.02	0.02	0.01	0.02	0.01	0.01	0.01
X _{Alm}	0.15	0.12	0.14	0.17	0.15	0.06	0.07	0.06
X _{Grs}	0.73	0.77	0.79	0.73	0.80	0.80	0.80	0.80
X _{Sps}	0.03	0.02	0.02	0.04	0.02	0.02	0.02	0.03
X _{Mg}	0.09	0.13	0.11	0.07	0.10	0.11	0.10	0.10

d.l.: detection limit

Table 4.2.7: Representative electron microprobe analysis of epidote (stoichiometry calculated on the basis of 12.5 oxygens, oxide data are given in weight %).

Point	Vesuvianite-epidote veins					
	48 / 1 .	50 / 1 .	52 / 1 .	56 / 1 .	54 / 1 .	53 / 1 .
SiO ₂	37.46	37.03	37.36	36.83	37.44	38.13
TiO ₂	0.01	0.06	0.05	0.07	0.00	0.02
Al ₂ O ₃	26.43	26.95	27.21	26.19	28.77	29.60
Cr ₂ O ₃	0.05	0.26	0.20	0.26	0.02	0.00
FeO	7.98	7.72	7.43	8.80	5.35	4.24
MnO	0.00	0.25	0.26	0.06	0.24	0.26
MgO	0.00	0.05	0.10	0.08	0.07	0.09
CaO	24.80	24.24	24.35	24.48	25.17	24.69
Na ₂ O	0.03	0.00	0.07	0.00	0.01	0.01
K ₂ O	0.00	0.01	0.04	0.04	0.00	0.00
F	0.01	0.03	0.03	0.01	0.02	0.01
Total	96.76	96.56	97.23	96.82	97.26	97.04
Si	2.94	2.91	2.91	2.90	2.90	2.95
Ti	0.00	0.00	0.00	0.00	0.00	0.00
Al	2.44	2.50	2.50	2.43	2.63	2.70
Cr ⁺³	0.00	0.02	0.01	0.02	0.00	0.00
Fe ⁺³	0.52	0.51	0.48	0.58	0.35	0.27
Fe ⁺²	0.00	0.00	0.00	0.00	0.00	0.00
Mn	0.00	0.02	0.02	0.00	0.02	0.02
Mg	0.00	0.01	0.01	0.01	0.01	0.01
Ca	2.09	2.04	2.03	2.06	2.09	2.05
Na	0.00	0.00	0.01	0.00	0.00	0.00
K	0.00	0.00	0.00	0.00	0.00	0.00
Total	8.00	8.00	8.00	8.00	8.00	8.00
pistacite	0.18	0.17	0.16	0.19	0.12	0.09

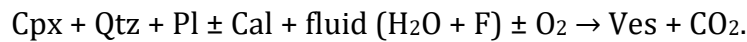
The *apatite* also contains ~5 wt% F in its structure.

The *calcite* is a pure phase.

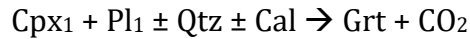
4.2.3. Formation of the vesuvianite-garnet-epidote mineral assemblage

Textural relations indicate early stabilized peak mineral assemblage of clinopyroxene + plagioclase + titanite ± quartz ± calcite ± apatite, in the host calc-silicate rock. Textural relations also suggest that vesuvianite-garnet-epidote formed subsequent to the peak assemblages via different reactions:

Presence of inclusions of clinopyroxene + plagioclase ± quartz ± calcite within vesuvianites signifies the formation of vesuvianite via the reaction,



Coronal garnet grows along the margins of clinopyroxene and plagioclase. Aggregates of coronal garnet also enclose the former two, in the clinopyroxene-rich bands. Therefore, it is inferred that in these domains, the coronal garnets formed via:



However, coronal garnets also form around vesuvianite grains. This opens up two possibilities: (a) coronal garnets form by breakdown of vesuvianite, along clinopyroxene and plagioclase, via: $\text{Cpx}_1 + \text{Pl}_1 + \text{Ves} \pm \text{Qtz} \rightarrow \text{Grt} + \text{CO}_2$; (b) garnet and vesuvianite forms simultaneously from the precursor minerals (clinopyroxene and plagioclase) via: $\text{Cpx}_1 + \text{Pl}_1 \pm \text{Qtz} + \text{fluid} \pm \text{Cal} \rightarrow \text{Ves} + \text{Grt} + \text{CO}_2$. Now a few features like: (i) the presence of pegmatitic veins intruding the rock, and signatures of fluid-rock interaction (formation of amphibole proximal to pegmatite and host calc-silicate contact), (ii) presence of variable amounts of F and H₂O in the structure of vesuvianite, titanite and epidote, all point towards an open system during the formation of these veins. In view of this, the Mg released by breakdown of vesuvianite (possibility 'a') possibly have been removed from the system. Hence, formation of garnet can be described by either or a combination of the two possibilities, 'a' and 'b'.

Additionally, epidote extensively replaces clinopyroxene and plagioclase: $\text{Cpx} + \text{Pl} \pm \text{Cal} + \text{H}_2\text{O} \pm \text{O}_2 \rightarrow \text{Ep} + \text{CO}_2$. In the domains where vesuvianite and garnet is present, epidote also partially encloses vesuvianite and garnet: $\text{Ves} + \text{Grt} + \text{Pl} = \text{Ep}$.

Therefore, the sequential evolution of the mineral assemblages that occurred in the studied rock: clinopyroxene + plagioclase + titanite \pm quartz \pm calcite \pm apatite (host calc-silicate) \rightarrow vesuvianite + garnet \rightarrow epidote.

4.2.4. P-T conditions of formation of vesuvianite-garnet-epidote assemblages:

Owing to the high Fe^{+3} content in garnet and clinopyroxene and high Ca content in garnet, conventional thermobarometers involving these minerals could not be applied to the studied rock. Nevertheless, considering the following observations and findings: (i) field features suggesting that these vesuvianite-garnet-epidote veins develop close to the pegmatitic veins; (ii) presence of F in vesuvianite, as well as in amphiboles within pegmatite, and (iii) amphiboles forming in proximity to the pegmatite veins; all signify that (i) the formation of the vesuvianite-garnet-epidote veins in connection with the intrusion of these pegmatites; (ii) the pegmatites served as the source of F and H_2O which stabilized the vesuvianite-garnet-epidote bearing assemblage.

Moreover, textural relations indicate the replacing plagioclases (Pl_2) to be in equilibrium with amphibole rim within the pegmatites. Therefore, these were used to determine the P-T conditions of formation of the vesuvianite-garnet-epidote assemblage. Conventional thermobarometry involving amphibole and plagioclase (Anderson and Smith, 1995; Holland and Blundy, 1994) were applied. These constrain a P-T range of 5.6-6.8 kbar and ~ 640 - 740°C . This estimated P-T matches well with the P-T conditions of the third major tectonothermal event (M3) in the CGGC. This implies that these vesuvianite-garnet-epidote bearing veins developed during this amphibolite facies

Table 4.2.8: Results using hornblende-plagioclase thermometer (Holland and Blundy, 1994) and Al in amphibole barometer (Anderson and Smith, 1995). All mineral abbreviations are after Kretz (1983).

Hornblende-plagioclase thermometry							Aluminium in amphibole barometry			
Am No.	43 / 1 .	43 / 1 .	23 / 1 .	23 / 1 .	25 / 1 .	25 / 1 .	Am No.	Al(total)	P(Kbar)	
XSi,T1	0.62	0.62	0.62	0.61	0.60	0.60	12 / 1 .	1.98	6.2	
XAl,T1	0.38	0.38	0.38	0.39	0.40	0.40	17 / 1 .	2.14	6.8	
XAl,M2	0.20	0.20	0.20	0.18	0.18	0.18	19 / 1 .	2.03	6.3	
Xvac,A	0.44	0.44	0.44	0.42	0.51	0.51	AS32Diii	23 / 1 .	1.91	5.8
XNa,A	0.21	0.21	0.21	0.26	0.17	0.17		25 / 1 .	1.97	6.0
XNa,M4	0.04	0.04	0.04	0.04	0.06	0.06		29 / 1 .	2.00	6.2
XCa,M4	0.97	0.97	0.97	0.98	1.00	1.00		31 / 1 .	2.08	6.5
XK,A	0.35	0.35	0.35	0.33	0.33	0.33		39 / 1 .	1.97	6.0
								43 / 1 .	1.92	5.8
PI No.	32 / 1 .	33 / 1 .	28 / 1 .	37 / 1 .	32 / 1 .	35 / 1 .	AS32Di	1 / 1 .	2.02	6.3
XAb	0.59	0.61	0.70	0.42	0.59	0.82		2 / 1 .	2.03	6.3
XAn	0.41	0.39	0.30	0.58	0.41	0.16		5 / 1 .	1.97	6.0
T (°C)	712	706	673	757	739	648		18 / 1 .	1.91	5.7

4.2.5. Petrogenetic grid for the studied calc-silicate rock

Textural and mineral reactions as described in section 4.2.2, point towards a sequential development of the minerals: Clinopyroxene+ plagioclase + titanite ± garnet ± calcite → Vesuvianite+ coronal garnet → epidote. Presence of clinopyroxene, garnet, amphibole and epidote demand involvement of non-CASV components (primarily MgO and FeO). On account of the highly magnesian composition of clinopyroxene, combined with the presence of hydrous phases (epidote), MgO and H₂O were also incorporated as system components. Hence, the mineral evolution in the studied calc-silicate rock has been described in the simple six- component system CaO-MgO-Al₂O₃-SiO₂-H₂O-CO₂ (CMASV). Since titanite is the only mineral having significant Ti component, and does not react to form any new Ti-bearing phase, Ti has not been included as a phase component in the present study. Topologies have been described in P-T (for fixed X_{CO2}) and isobaric T-X_{CO2} spaces, with nine phases, Mg-vesuvianite (Ves), diopside (Di), anorthite (An), grossular (Grs), clinozoisite (Cz), calcite (Cal), quartz (Qtz), wollastonite (Wo) and vapor (H₂O-CO₂). The stoichiometric composition of Mg-vesuvianite has been considered as Ca₁₉Mg₂Al₁₁Si₁₈O₆₉(OH)₉ (Holland and Powell, 1998; Valley et al., 1985). These topologies have been constructed using the Perple_X program (version

6.7.6, updated March 2017, Connolly, 2005) and the internally consistent thermodynamic dataset of (Holland and Powell, 1998 revised 2002).

4.2.5.1. Topology in P-T space for pure compositions in the CMASV system:

P-T topologies have been constructed at different X_{CO_2} sections (0.3, 0.15, 0.05, 0.001). Since the sections have been constructed at constant X_{CO_2} , the number of system component reduces to five. Therefore, for a five-component system with nine phases, number of phases present in each non-degenerate invariant points are six (+H₂O), with two absent phases in each. Now, from each invariant point, six non-degenerate univariant reactions emanate, each with five phases (three absent phases in each). Based on the stability of natural vesuvianite-bearing and epidote-bearing assemblages in metamorphosed rocks (Grapes and Hoskin, 2004; Poli and Schmidt, 1998; Schmidt and Thompson, 1996), a P-T window of 2-12 kbar and 300-900°C has been chosen. All mineral abbreviations used are after Kretz, (1983). Fig.4.2.4 depicts the characteristics of CMASV P-T topology with pure phases with the following features:

- (i) At $X_{CO_2}=0.3$, within the chosen P-T field, only one invariant point [Ves Cz] is stable (Fig.4.2.4).
- (ii) At $X_{CO_2}=0.3$, stability of wollastonite bearing assemblages are restricted to high temperatures (>700°C). On the other hand, clinozoisite is stable in the lower temperature, and over a wide range of pressure. Its stability increases towards high temperatures (up to ~720°C) with increase in pressure, bounded by the degenerate reaction $Cal An = Cz$. Grossular stability, on the other hand is restricted only to high temperature (>780°C) and moderate to high pressures (>6 kbar).
- (iii) Vesuvianite is not stable at $X_{CO_2}>0.2$, within the chosen P-T space.
- (iv) With slight decrease in $X_{CO_2}= 0.2-0.15$, [Ves Cz] invariant points shift to lower P-T. Additionally, [Ves Wo] invariant point becomes stable. Vesuvianite stability is limited to temperatures greater than ~700°C. Clinozoisite stability field increases towards slightly lower pressures and higher temperatures. In contrast grossular stability increases towards lower pressures. However, vesuvianite stability field does not overlap with that of clinozoisite. Vesuvianite+ grossular stability is

restricted to higher temperatures ($> 780^{\circ}\text{C}$) and pressures (>7 kbar). Wollastonite stability remains unchanged.

(v) At $X_{\text{CO}_2} = 0.05$, [Ves Cz] becomes unstable, and [Ves Wo] shifts towards very low temperatures. A new invariant point [Q Wo] stabilises. Vesuvianite stability field enlarges towards the lower temperatures, while that of clinozoisite enlarges towards higher temperatures.

(vi) At even lower $X_{\text{CO}_2} = 0.004-0.001$, two new invariant points become stable, [An Wo] and [An Cz]. With decrease in $X_{\text{CO}_2} = 0.001$, they shift towards higher pressures. These invariant points restrict the stability of vesuvianite+ quartz bearing assemblage at low temperatures ($330-480^{\circ}\text{C}$), between 3-9 kbar pressure (Fig.4.2.4). Wollastonite stability also shifts slightly towards lower temperatures. vesuvianite+ quartz association becomes unstable at $\geq 0.05 X_{\text{CO}_2}$.

At $X_{\text{CO}_2} \leq 0.05$, vesuvianite stability field overlaps with that of clinozoisite. The vesuvianite +clinozoisite is initially restricted to high pressures. At subsequently lower X_{CO_2} , their stability field enlarges ($360-740^{\circ}\text{C}$). Although a distinct pressure limit cannot be constrained, it is evident that their stability becomes restricted to lower temperatures with decreasing pressure.

Hence, Fig.4.2.4 depicts that the stability of vesuvianite is restricted to low $X_{\text{CO}_2} \leq 0.2$, while Ves+Qtz has more restricted stability below $X_{\text{CO}_2} < \sim 0.05$. This justifies the occurrence of Ves/ Ves+Qtz bearing assemblages in the presence of H_2O -rich fluids (e.g., Hochella et al. 1982; Valley et al. 1985; Bogoch et al. 1997). Fig.4.2.4 also demonstrates that Ves+Qtz has a restricted thermal stability between $330-480^{\circ}\text{C}$. Moreover, Fig.4.2.4 also demonstrates that the occurrence of vesuvianite + clinozoisite assemblage is restricted to lower temperatures with decrease in pressure, as well as to H_2O -rich conditions ($X_{\text{CO}_2} \leq 0.05$).

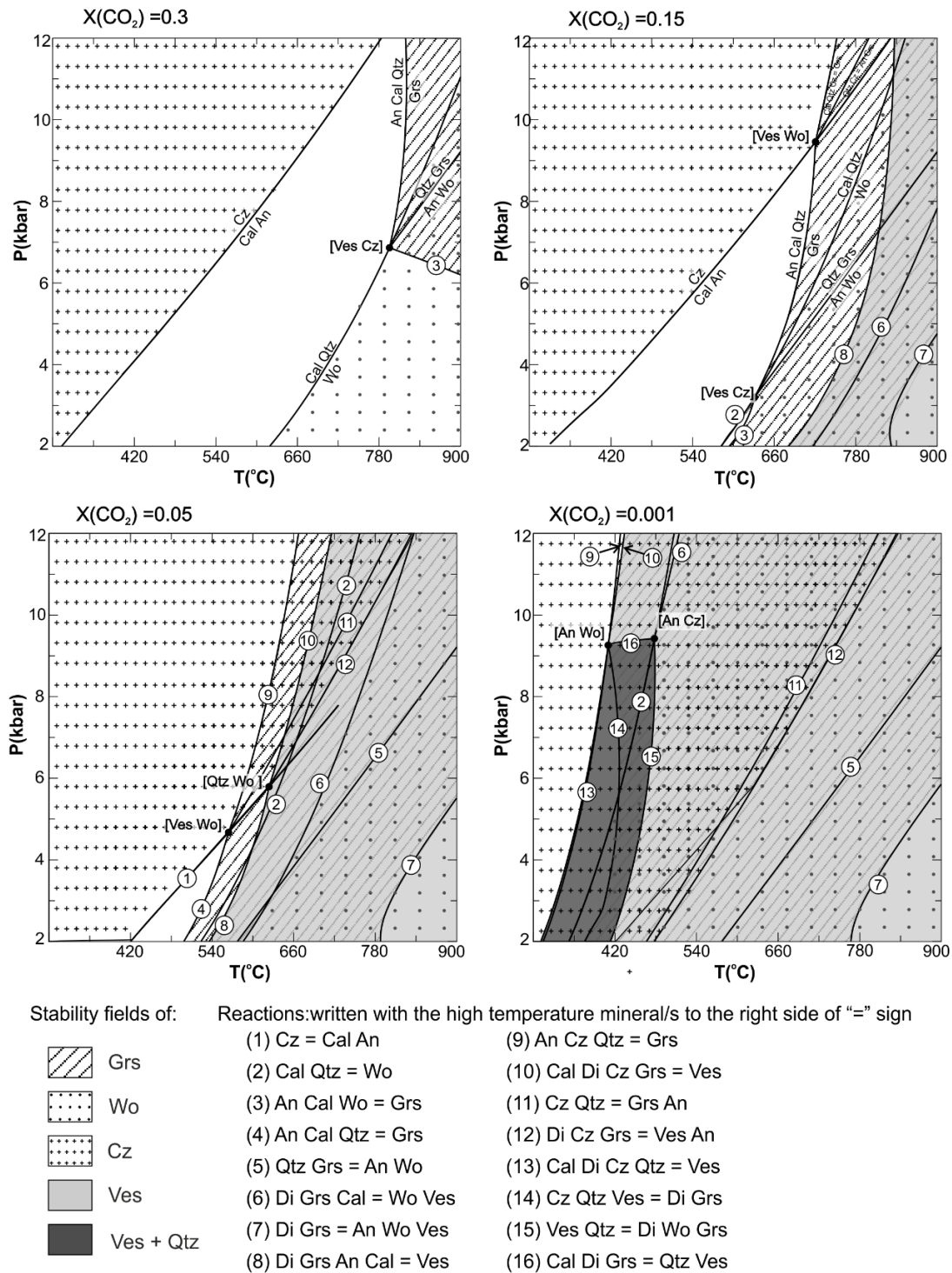


Fig.4.2.4: P-T topology in the CMASV system calculated at different X_{CO_2} conditions for pure compositions. All mineral abbreviations used are after Kretz, (1983)

4.2.5.2. Topology in isobaric T-X_{CO2} space for pure compositions in the CMASV system:

Isobaric T-X_{CO2} topologies involving vesuvianite-bearing assemblages have been constructed by several workers (Kerrick et al., 1973; Trommsdorff, 1968) in the CMASV system. Primarily two topologies (Top-I and Top-II) have been proposed (Kerrick et al., 1973). While Valley et al., (1985) proposed an exhaustive T-X_{CO2} topology (similar to Top-I) combining the experimental works of Hochella et al., (1982) with their own; few works on natural vesuvianite-bearing assemblages supported Top-II (Cartwright and Oliver, 1994; Hover Granath et al., 1983). In a multi-component system, all the invariant points and univariant reactions (as predicted by the phase rule) are not stable together (reviewed in Groppo et al., 2013; Robinson, 1991; Sengupta and Raith, 2002). The number of stable the invariant points and univariant reactions are rather determined/ guided/ controlled by one or a combination of the intensive parameters (e.g., P, T, fluid compositions (X), activity of minerals). In their extensive study, Dey et al., (2019a) demonstrated that Top-I and Top-II are alternate forms of each other, and also discussed the various factors controlling this topological inversion. They also showed that except few characteristic invariant points and reactions, most of the reactions and vesuvianite-bearing assemblages are common to both the topologies (Top-I and Top-II). Qualitative and quantitative grids involving epidote/ zoisite-bearing assemblages have previously been constructed by several workers mostly in CASV system (Grapes and Hoskin, 2004; Poli and Schmidt, 1998; Schmidt and Thompson, 1996). In the present study, these vesuvianite-bearing isobaric T-X_{CO2} topologies have been reconstructed in the CMASV system, with addition of clinozoisite (instead of epidote), to infer the P-T-X (fluid) conditions, and the stabilities of the different associations in the studied calc-silicate rock.

Isobaric T-X_{CO2} topology has been constructed over a temperature range of 300-800°C and 0-0.5 X_{CO2}, at different pressures (2, 4, 6 and 8 kbar). The following characteristics are illustrated by Fig.4.2.5.

i. At 2 kbar, Fig.4.2.5 is similar to the Top-I described by Kerrick et al., (1973), Dey et al., (2019a) and Valley et al., (1985). The stability of vesuvianite is restricted to low X_{CO2} (<~0.2) conditions. The stability of Ves+Qtz is further restricted to even

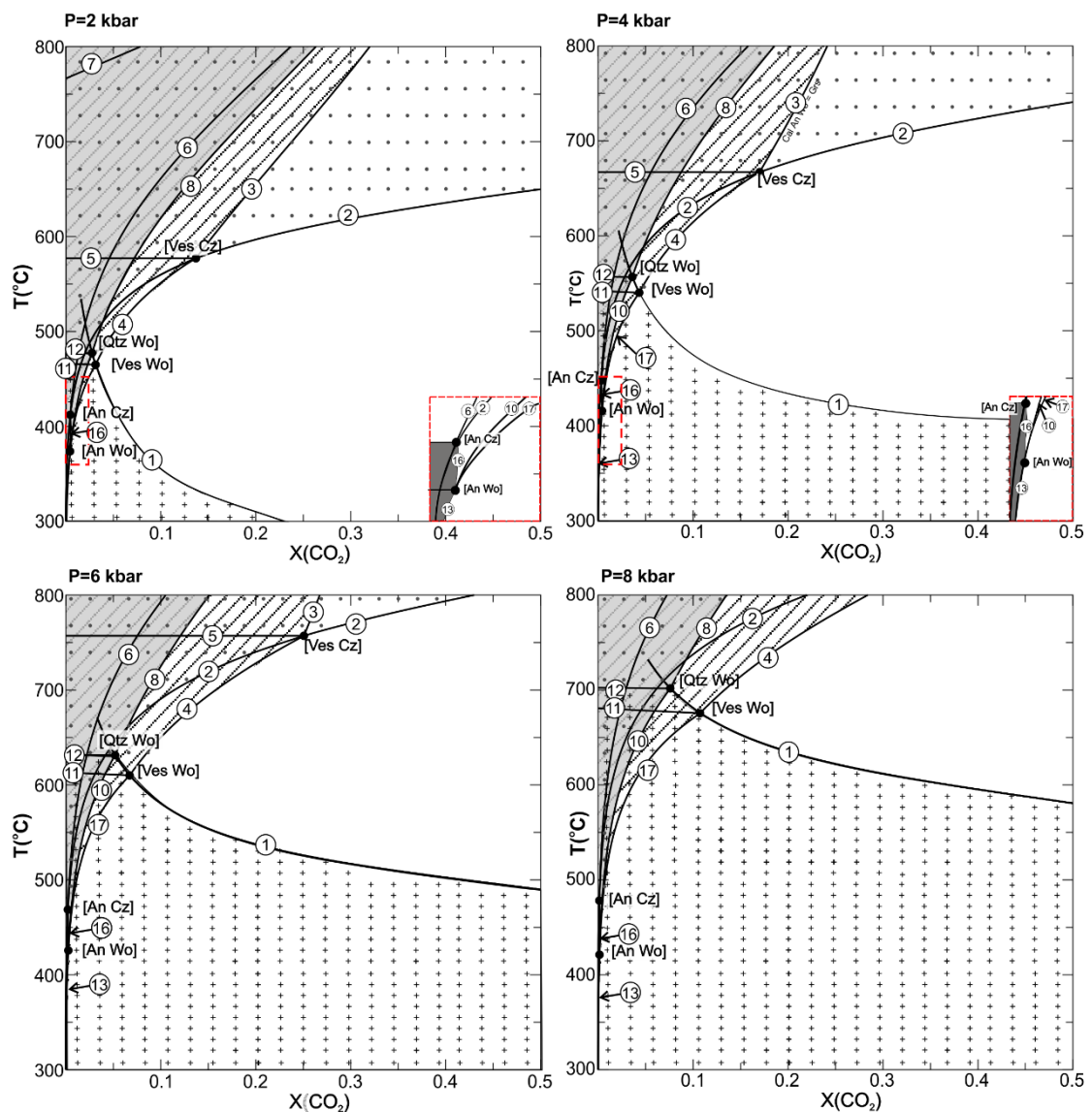
lower X_{CO_2} conditions, consistent with the observations from P-T topology. On the other hand, clinozoisite stability is confined to low temperatures ($< \sim 480^\circ\text{C}$) by the reaction: "Cz Di Grs = Ves An" (Fig.4.2.5). Its stability decreases, and extends towards higher X_{CO_2} conditions in the lower temperature portion. Wollastonite is stable at temperatures above $\sim 550^\circ\text{C}$.

- ii. With increasing pressure (Fig.4.2.5), stability of wollastonite and vesuvianite decreases, and shifts towards higher temperatures and lower X_{CO_2} conditions. In contrast, clinozoisite stability enlarge towards higher temperatures and X_{CO_2} conditions. However, the stabilities of Ves+ Qtz remains restricted to very low X_{CO_2} (Fig.4.2.5). Their stabilities decrease slightly towards more H_2O -rich conditions (see inset of Fig.4.2.5) with increase in pressure, on account of the slight shift of their bounding invariant points ([An Wo] and [An Cz]).
- iii. Vesuvianite +clinozoisite are also restricted to very low X_{CO_2} ($< \sim 0.05$). With increase in pressure, their stability fields slightly enlarge towards higher X_{CO_2} and slightly higher temperatures.

4.2.5.3. Effect of non-CMASV components on the CMASV P-T topology:

Natural calc-silicate rocks contain significant amount of non-CMASV components in the constituting minerals. Correspondingly, mineral compositions in the studied calc-silicate rocks also indicate presence of significant amount of non-CMASV components, which significantly determine the stabilities of the constituting minerals.

Amongst the minerals in the studied calc-silicate, vesuvianite incorporates the maximum number of non-CMASV components: Na, REE^{3+} , Bi^{3+} , Pb^{2+} , Th^{4+} , Sb^{3+} , Fe^{3+} , Fe^{2+} , Ti^{4+} , Cr^{3+} , Mn, Cu, Zn, B, F, Cl, S; Groat et al. 1992a, 1992b. Epidote also incorporates various components, the major component being Fe^{3+} . Other components include: Ce, Sr, Pb, La, Y, Th, F, Mn^{3+} , Mn^{2+} , Fe^{2+} , Cr, V and Ti. The pistacite component (up to ~ 19 mol%) of epidote in the studied samples indicates the presence of considerable amount of Fe^{3+} in epidote. However, in the studied rock, epidote has very low F contents depicting that the effect of F on epidote stability was not much. Garnet also contains considerable andradite component (up to ~ 7 mol%) along with Fe^{2+} and little Mn. Clinopyroxene and plagioclase also



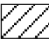
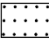



Stability fields of:	Reactions: written with the high temperature mineral/s to the right side of "=" sign		
 Grs	(1) Cz = Cal An	(7) Di Grs = An Wo Ves	(13) Cal Di Cz Qtz = Ves
 Wo	(2) Cal Qtz = Wo	(8) Di Grs An Cal = Ves	(14) Cz Qtz Ves = Di Grs
 Cz	(3) An Cal Wo = Grs	(9) An Cz Qtz = Grs	(15) Ves Qtz = Di Wo Grs
 Ves	(4) An Cal Qtz = Grs	(10) Cal Di Cz Grs = Ves	(16) Cal Di Grs = Qtz Ves
 Ves + Qtz	(5) Qtz Grs = An Wo	(11) Cz Qtz = Grs An	(17) Cz Cal Qtz = Grs
	(6) Di Grs Cal = Wo Ves	(12) Di Cz Grs = Ves An	

Fig.4.2.5: T-X topology in the CMASV system calculated at different X_{CO2} conditions for pure compositions. All mineral abbreviations used are after Kretz, (1983)

contain significant proportions of Fe^{2+} , Mn^{2+} , and Na^+ respectively. Non-CMASV components in fluid phase comprise F, Cl, B, S, etc.

Incorporation of these components within the respective minerals increases the stability of the minerals (by decreasing their activities). Consequently, the invariant points, along with the corresponding univariant reactions shift along the reaction lines in which that particular mineral is absent. For example, incorporation of F and other non-CMASV components in vesuvianite will shift the vesuvianite bearing invariant points and univariant reactions along vesuvianite absent reactions. The net displacement of the invariant points and univariant reactions is controlled by the equilibrium constants of the reactions in response to the various chemical substitutions. The final topology is determined by the net displacements of all the reactions corresponding to decrease in activities of all the constituting minerals. Hence, keeping in mind the the above discussion, evolution of mineral assemblages for the studied calc-silicates has been described using activity adjusted grids. The activities of anorthite, diopside, grossular and clinozoisite were calculated from the measured compositions using the a-X program (<https://www.esc.cam.ac.uk/research/research-groups/research-projects/timhollands-software-pages/ax>). In the constructed topologies, the epidote composition has been accommodated by correcting the activity of clinozoisite end member. Activity of vesuvianite was calculated according to the procedure followed in Dey et al., (2019a) (described in Hoisch, 1985). The activity corrected values of the minerals are: $a_{\text{Di}} = 0.68$, $a_{\text{Grs}} = 0.47$, $a_{\text{An}} = 0.96$, $a_{\text{Cz}} = 0.77$, $a_{\text{Ves}} = 0.0001$.

4.2.5.4. Activity adjusted topology in isobaric T- X_{CO_2} space:

In the present study, isobaric T- X_{CO_2} topology, has been constructed for the temperature range of 300-900°C and 0-0.5 X_{CO_2} , at different pressure sections (2, 5 and 8 kbar), consistent with the results of conventional barometry. Fig.4.2.6: shows the characteristics of activity corrected T- X_{CO_2} topology and its major differences with pure topology are:

- i. At 2 kbar, a completely different set of invariant points stabilize ([Cal Cz], [An Cz], [Wo Cz], [Di Wo] and [Grs Wo]). As discussed in section 4.2.3, inclusion assemblage in vesuvianite indicate its formation via the reaction: $\text{Di An Cal Qtz} = \text{Ves}$

(reaction 21; Fig.4.2.6:). On the other hand, development of coronal garnet at the margins of clinopyroxene, plagioclase and vesuvianite indicate its formation after the formation of vesuvianite, via the reaction: $An\ Ca\ Qtz = Grs$ (reaction 4; Fig.4.2.6), These vesuvianite and coronal garnet forming reactions (marked in blue colour) are bounded by the [Wo Cz], [Di Wo] and [Grs Wo] invariant points. Textural relations indicate that the above reactions (21 and 4) were driven with decrease in X_{CO_2} , with/without temperature change. The two reactions constrain the conditions of vesuvianite-coronal garnet formation at low X_{CO_2} ($< \sim 0.35$; Fig.4.2.6:).

ii. Textural relations indicate formation of epidote subsequent to vesuvianite and coronal garnet in the rock. The condition of formation of epidote is limited by the reactions $An\ Grs = Cz\ Qtz$ (reaction 11; marked in green colour; Fig.4.2.6:). This reaction emerges from the [Di Wo] invariant point. The T- X_{CO_2} topology indicate progress of the above reaction with further decrease in X_{CO_2} ($< \sim 0.05$), possibly accompanied by slight lowering of temperature.

iii. With increase in pressure (~ 5 kbar, Fig.4.2.6:), these for invariant points shift lightly towards higher temperatures and X_{CO_2} conditions, thereby enlarging the clinozoisite stability field, and decreasing the vesuvianite stability field. Therefore, from the different isobaric T- X_{CO_2} sections (at 2, 5 7 kbar; Fig.4.2.6:) these vesuvianite-garnet-epidote forming reactions constrain the fluid conditions of formation of vesuvianite-garnet and epidote between 0.05-0.4 X_{CO_2} and $< \sim 0.2 X_{CO_2}$ respectively. (Fig.4.2.6:).

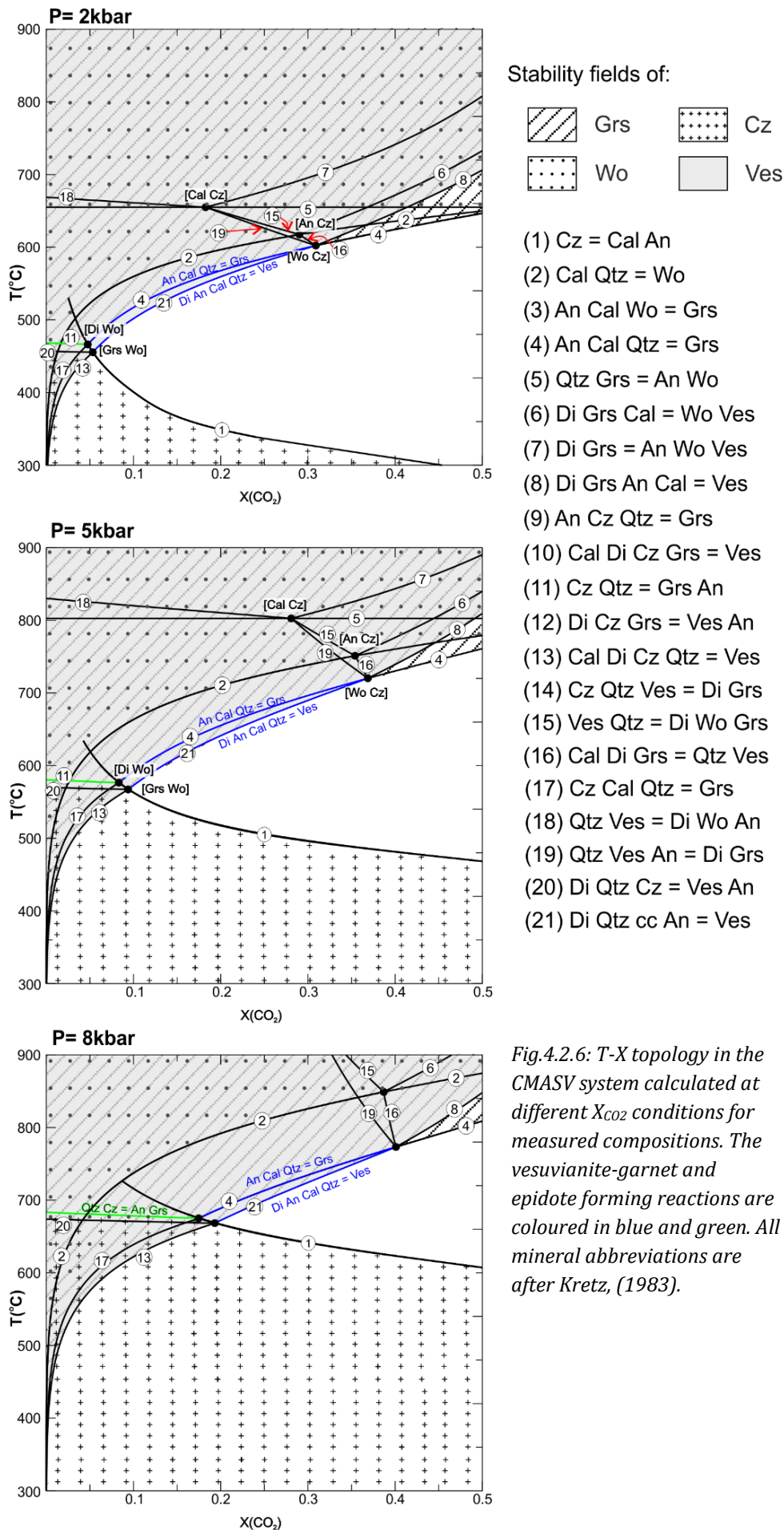


Fig.4.2.6: T-X topology in the CMASV system calculated at different X_{CO_2} conditions for measured compositions. The vesuvianite-garnet and epidote forming reactions are coloured in blue and green. All mineral abbreviations are after Kretz, (1983).

4.2.5.5. Application of quantitative T-X_{CO2} topology to mineral evolution in studied calc-silicate:

While using the activity corrected T-X_{CO2} topology for the studied rocks, the following characteristics were considered:

- i. The mineral assemblages stabilised in the wollastonite-free part of the topology.
- ii. A representative pressure section (at 6 kbar) has been chosen for the studied rock, based on the results of conventional thermobarometry.
- iii. A temperature range of 300-900°C has been chosen keeping in mind the stability of vesuvianite and epidote-bearing assemblages in natural calc-silicate rocks; and an X_{CO2} range=0-0.5 (based on the maximum stability of the concerned invariant points as evident from Fig.4.2.6:).

Fig.4.2.7 demonstrates the evolution of mineral assemblage/ vesuvianite-garnet-epidote veins in the studied rocks. As discussed earlier, the reactions 21 and 4 (limited by the invariant points ([Wo Cz], [Di Wo] and [Grs Wo]) constrain the conditions of formation vesuvianite-coronal garnets. These reactions and invariant point constrain a narrow temperature range of 600-740°C and fluid conditions between ~0.1-0.4 X_{CO2} for the stabilisation of vesuvianite and coronal garnet. Additionally, subsequent formation of epidote is depicted by the reaction 11, emerging from the invariant point [Di Wo]. The formation of epidote has been constrained at a temperature of <600°C and with the ambient fluid condition below ≤0.1 X_{CO2}.

Now, the sequential mineral evolution can be achieved via two paths (Path A and Path B; Fig.4.2.7). Path A involves influx of fluid (i.e., decrease in X_{CO2}), leading to vesuvianite-coronal garnet formation; followed by a cooling (during which epidote develops in the rock). Path B involves influx of fluid, with negligible temperature change (Fig.4.2.7). A few features: (a) extensive development (that is, high modal percentage) of epidote grains (in the epidote-present microdomains), combined with (b) large grain size of epidote, are not consistent with their development in a steep cooling path (Path A). Rather, Path B, that involves influx of a highly water-rich fluid, with a very small decrease in temperature, seems to be more probable. The small magnitude of temperature change, is also consistent

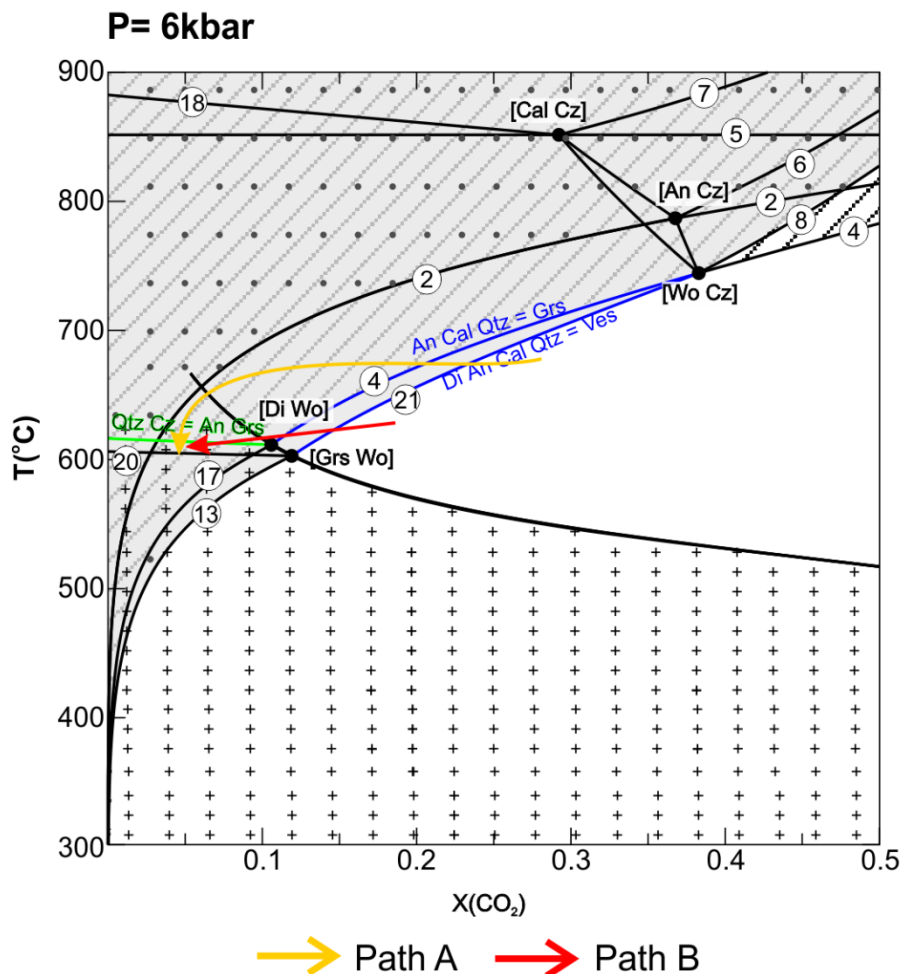


Fig.4.2.7: Activity corrected T-X topology in the CMASV system calculated at 6kbar. The vesuvianite-garnet and epidote forming reactions are coloured in blue and green. Two paths shown in different colours, that explain the observed textural features. All mineral abbreviations are after Kretz, (1983).

with Path B, that is close to the invariant point [Di Wo] (Fig.4.2.7). Therefore, it is inferred that the vesuvianite-garnet-epidote veins formed within a restricted P-T condition of ~6kbar and ~600-620°C.

Hence, it is inferred that the studied vesuvianite-garnet-epidote veins formed as a result of intrusion of a H₂O-rich fluid. The presence of F in the structure of vesuvianite in the epidote-free domains indicate that the infiltrated fluid was also F-rich. Moreover, (a) the close association of these veins with the pegmatites, (b) both these veins and pegmatites parallel (or locally intersect at low angles) the foliation of the host calc-silicate, signify that these are genetically linked. Consequently, these pegmatites seem to be the possible source of F and H₂O that led

to the development and stabilisation of these mineral associations. However, a few observations such as: (a) replacement of vesuvianite and coronal garnets by epidote, (b) predominance of H₂O (minor F content) in epidote structure, imply fluctuation of F content in the infiltrating fluid. That is, a F-rich fluid influx initially stabilised vesuvianite and garnet (M3). Subsequent to this, the infiltrating fluid became deficient in F, and more H₂O-rich, and stabilised epidote. Slight decrease in temperature associated with epidote formation is also consistent with its formation during the retrogressive phase of M3.

The epidote-free (vesuvianite-garnet bearing) system has been previously developed by Dey et al., 2019a from these calc-silicates. The following findings of the present study are consistent with the inferences of Dey et al., 2019a: (a) The formation of vesuvianite-garnet veins within the host calc-silicate rock occurred due to a fluid infiltration driven metamorphism, during the amphibolite facies M3 event; (b) the infiltrating fluid was water-rich, and was also fluorine bearing; (c) F in the fluid was possibly sourced from the undeformed pegmatites that also intruded the host calc-silicate rock. Apart from these, the present study also concludes that formation of epidote occurred subsequently, at more H₂O-rich conditions ($\leq 0.1 X_{CO_2}$ and lower X_F), combined with a slight cooling (at $< 600^\circ\text{C}$). This more H₂O-rich fluid conditions possibly may be related to fluctuation of F content in the fluid; or a later phase of another fluid influx during the tail end of the M3 event.

References

- Anderson, J.L., Smith, D.R., 1995. The effects of temperature and f_{O_2} on the Al-in-hornblende barometer. *Am. Mineral.* 80, 549–559.
- Cartwright, I., Oliver, N.H.S., 1994. Fluid flow during contact metamorphism at Mary Kathleen, Queensland, Australia. *J. Petrol.* 35, 1493–1519.
- Connolly, J.A.D., 2005. Computation of phase equilibria by linear programming: A tool for geodynamic modeling and its application to subduction zone decarbonation. <https://doi.org/10.1016/j.epsl.2005.04.033>
- Dey, A., Choudhury, S.R., Mukherjee, S., Sanyal, S., Sengupta, P., 2019a. Origin of vesuvianite-garnet veins in calc-silicate rocks from part of the Chotanagpur

- Granite Gneiss Complex, East Indian Shield: The quantitative PTX CO₂ topology in parts of the system CaO-MgO-Al₂O₃-SiO₂-H₂O-CO₂ (+ Fe₂O₃, F). *Am. Mineral. J* 104, 744–760.
- Dey, A., Karmakar, S., Ibanez-Mejia, M., Mukherjee, S., Sanyal, S., Sengupta, P., 2019b. Petrology and geochronology of a suite of pelitic granulites from parts of the Chotanagpur Granite Gneiss Complex, eastern India: Evidence for Stenian-Tonian reworking of a late Paleoproterozoic crust. *Geol. J.*
- Droop, G.T.R., 1987. A General Equation for Estimating Fe³⁺ Concentrations in Ferromagnesian Silicates and Oxides from Microprobe Analyses, Using Stoichiometric Criteria. *Mineral. Mag.* 51, 431–435. <https://doi.org/10.1180/minmag.1987.051.361.10>
- Grapes, R.H., Hoskin, P.W.O., 2004. Epidote group minerals in low–medium pressure metamorphic terranes. *Rev. Mineral. Geochemistry* 56, 301–345.
- Grew, E.S., Locock, A.J., Mills, S.J., Galuskina, I.O., Galuskin, E. V, Hålenius, U., 2013. Nomenclature of the garnet supergroup. *Am. Mineral.* 98, 785–811.
- Groppo, C., Rolfo, F., Castelli, D., Connolly, J.A.D., 2013. Metamorphic CO₂ production from calc-silicate rocks via garnet-forming reactions in the CFAS–H₂O–CO₂ system. *Contrib. to Mineral. Petrol.* 166, 1655–1675.
- Hawthorne, F.C., Oberti, R., Harlow, G.E., Maresch, W. V, Martin, R.F., Schumacher, J.C., Welch, M.D., 2012. Nomenclature of the amphibole supergroup. *Am. Mineral.* 97, 2031–2048.
- Hochella, M.F., Liou, J.G., Keskinen, M.J., Kim, H.S., 1982. Synthesis and Stability Relations of Magnesium Idocrase. *Econ. Geol.* 77, 798–808.
- Hoisch, T.D., 1985. The solid solution chemistry of vesuvianite. *Contrib. Mineral. Petrol.* 89, 205–214.
- Holland, T., Blundy, J., 1994. Non-ideal interactions in calcic amphiboles and their bearing on amphibole-plagioclase thermometry. *Contrib. to Mineral. Petrol.* 116, 433–447.

- Holland, T.J.B., Powell, R., 1998. An internally consistent thermodynamic data set for phases of petrological interest. *J. Metamorph. Geol.* 16, 309–343. <https://doi.org/10.1111/j.1525-1314.1998.00140.x>
- Hover Granath, V.C., Papike, J.J., Labotka, T.C., 1983. The Notch Peak contact metamorphic aureole, Utah: Petrology of the Big Horse limestone member of the Orr Formation. *Geol. Soc. Am. Bull.* 94, 889–906.
- Kerrick, D.M., Crawford, K.E., Randazzo, A.F., 1973. Metamorphism of calcareous rocks in three roof pendants in the Sierra Nevada, California. *J. Petrol.* 14, 303–325.
- Ketcham, R.A., 2015. Calculation of stoichiometry from EMP data for apatite and other phases with mixing on monovalent anion sites. *Am. Mineral.* 100, 1620–1623.
- Kretz, R., 1983. Symbols for rock-forming minerals. *Am. Mineral.* 68, 277–279. [https://doi.org/10.1016/0016-7037\(83\)90220-X](https://doi.org/10.1016/0016-7037(83)90220-X)
- Poli, S., Schmidt, M.W., 1998. The high-pressure stability of zoisite and phase relationships of zoisite-bearing assemblages. *Contrib. to Mineral. Petrol.* 130, 162–175.
- Robinson, P., 1991. The eye of the petrographer, the mind of the petrologist. *Am. Mineral.* 76, 1781–1810.
- Schmidt, M.W., Thompson, A.B., 1996. Epidote in calcalkaline magmas; an experimental study of stability, phase relationships, and the role of epidote in magmatic evolution. *Am. Mineral.* 81, 462–474.
- Sengupta, P., Raith, M.M., 2002. Garnet composition as a petrogenetic indicator: An example from a marble -calc-silicate granulite interface at kondapalle, Eastern Ghats Belt, India. *Am. J. Sci.* 302, 686–725. <https://doi.org/DOI.10.2475/ajs.302.8.686>

Trommsdorff, V., 1968. Mineralreaktionen mit Wollastonit und Vesuvian in einem Kalksilikatfels der alpinen Disthenzone (Claro , Tessin). Schweiz. miner. petrogr. Mitt. 48, 655–666.

Valley, J.W., Peacor, D.R., Essene, E.J., 1985. Crystal chemistry of a Mg-vesuvianite and implications of phase equilibria in the system CaO-MgO-Al₂O₃-SiO₂-H₂O-CO₂. J. Metamorph. Geol. 3, 137–153.

Chapter-4.3

Factors controlling the incorporation of aluminium within titanites

Chapter 4.3

Factors controlling the incorporation of aluminium within titanites

Titanite [Ca (Ti, Al, Fe³⁺) SiO₄ (O, OH, F)] is a common accessory mineral stabilised in metamorphosed and unmetamorphosed felsic, intermediate to mafic rocks, as well as in marble, calc-silicate rocks and placer deposits (Enami et al., 1993; Kohn 2017; Rapa et al., 2017; Storey and Smith, 2017; Pan et al., 2018). Titanite accommodates variable amounts of Al³⁺, Fe³⁺, U, Pb, Nb⁵⁺, Ta⁵⁺, REE³⁺, F⁻ and OH⁻ in its structure (Higgins and Ribbe, 1976; Oberti et al., 1991; Frost et al., 2001; Prowatke and Klemme, 2005; Kohn, 2017; Storey and Smith, 2017). The incorporation of (Al, Fe)³⁺ and (F-OH)⁻ in titanite occurs via the coupled substitution: Ti⁴⁺ + O²⁻ → (Al + Fe)³⁺ + (F + OH)⁻ (e.g., Ribbe, 1980; Oberti et al., 1991). Significant substitution leads to the formation of high aluminous titanite [X_{Al} (Al/(Al+Fe³⁺+Ti⁴⁺)) ≥ 0.25; Oberti et al., 1985]. Based on the extent of F vs. OH incorporation, high aluminous titanite is broadly divided into, fluoro-titanite (X_F > X_{OH}; where Ca(Al,Fe³⁺)FSiO₄ is the dominant member; hereafter 'Al-F titanite'), or hydrous-titanite (X_{OH} > X_F; where Ca(Al,Fe³⁺)OHSiO₄ is the dominant member; hereafter 'Al-OH titanite'). Although less common, experimental studies (Green and Pearson 1986; Cérny et al. 1995) demonstrated the following substitutions from natural titanites: Ca²⁺ + Ti⁴⁺ = REE³⁺ + Al³⁺ (Garber et al., 2017), 2 Ti⁴⁺ = (Ta, Nb)⁵⁺ + Al³⁺ (Green and Pearson, 1986; Cérny et al., 1995; Kohn, 2017) and Ti⁴⁺ + O²⁻ = Al³⁺ + OH⁻ (Harlov et al., 2006). The factors that control the absolute amount of Al, F and OH in titanite structure have been the subject of a number of studies (Smith 1980; Franz and Spear, 1985; Castelli and Rubatto, 2002; Sengupta et al., 2004; Troitzsch and Ellis, 2002; Tropper et al., 2002). The CaAlFSiO₄ end-member has ~7% less molar volume than its titanium analogue (CaTiOSiO₄; Troitzsch and Ellis, 1999). This then follows that, other compositional factors being constant, the entry of Al and F in the structure of titanite will be facilitated by high pressure (e.g., Carswell et al., 1996; Troitzsch and Ellis, 2002; Tropper et al., 2002). A number of experimental studies

(Smith, 1980; Troitzsch et al., 1999; Troitzsch and Ellis, 2002) and occurrence of natural Al-F titanites in the high-pressure rocks (e.g. in eclogites; Carswell et al., 1996) attest to the pressure sensitive nature of the Al-F substitution. Franz and Spear, (1985) also documented a positive correlation between peak metamorphic pressures and Al and F content in naturally occurring high Al-F titanites. Temperature has an opposite effect as it stabilizes the CaTiOSiO_4 end member more, which has higher molar volume than the CaAlFSiO_4 (Enami et al., 1993; Troitzsch et al., 1999; Troitzsch and Ellis, 2002). The experiment of Troitzsch et al., (1999) additionally showed complete solid solution along the CaTiOSiO_4 - CaAlFSiO_4 join. However, maximum X_{Al} content of natural titanites never exceeds 0.54 (Markl and Piazzolo, 1999). Analysing the crystal structure of titanite, Troitzsch and Ellis, (2002) argued that the structure of titanite (CaTiOSiO_4) is not suited to accommodate Al and F, such that an Al-F dominated composition actually reduces the stability of titanite. Consequently, several natural studies have demonstrated that Al and F within titanite are controlled by complex mineral-fluid equilibria (Franz and Spear, 1985; Sengupta et al., 2004). Moreover, abundance of high aluminous titanites from low pressure (≤ 7 kbar) rocks (Enami et al., 1993; Markl and Piazzolo, 1999; Rene, 2008; Vakh et al., 2012), and occurrence of low aluminous titanites ($X_{\text{Al}}=0.05-0.11$) from eclogitic-facies rocks (Ye et al., 2002), additionally pointed towards different factors (other than pressure) which controlled the incorporation of Al in titanite structure. The Ti/Al and F/OH ratios in the natural titanite become complex functions of associated solid solution phases, and the fugacities of different components in the coexisting fluids (e.g. f_{F_2} , $f_{\text{H}_2\text{O}}$, f_{CO_2} , f_{O_2} etc, Bohlen and Essene, 1978; Markl and Piazzolo, 1999; Sengupta et al., 2004; Harlov et al., 2006). Owing to these compositional effects of the associated mineralogy and fluid phases in equilibrium with natural titanite, Al-F titanite is found over a wide range of pressure and temperature (Carswell et al., 1996; Ye et al., 2002; Rene, 2008; Vakh et al., 2012). Supporting these natural observations, the experimental studies of Troitzsch and Ellis, (2002) demonstrated that X_{Al} value of titanite can increase (in presence of zoisite, anorthite and margarite) or decrease (in presence of lawsonite) with increasing pressure. The phase diagrams in the $\text{CaO-Al}_2\text{O}_3\text{-TiO}_2\text{-SiO}_2\text{-H}_2\text{O}$ system demonstrates that high Al-F titanites loses CaAlFSiO_4 component, i.e., Ti/Al ratio in titanite increases, to form Ca-Al-Si bearing minerals (zoisite, anorthite, lawsonite)

with high f_{H_2O} even at constant P-T condition. Corroborating the study of Bohlen and Essene, (1978), Troitzsch and Ellis, (2002) showed that an increased f_{F_2} facilitates the entry of Al and F in the structure of titanite. Experiment of Lucassen et al., (2010) demonstrate that even at low pressure the X_{Al} of titanite can increase from 0.25 to 0.50 with an increase in f_{F_2} . While a positive correlation is documented between F and Al from natural titanites (Castelli and Rubatto, 2002; Franz and Spear, 1985) as well as the experimental data (Tropper et al., 2002; Lucassen et al., 2010), a small amount of Al can be present in F poor titanite owing to the substitution $Ti^{4+}+O^{2-} = Al^{3+}+OH^-$ (Ye et al., 2002; Harlov et al., 2006; Rene, 2008). The F content and the F/OH ratio of titanite is shown to be positively correlated with F/Cl and F/OH ratio of the coexisting biotite (Graber et al., 2017). Additionally, the co-existing melt structure and the fluid environment also plays a major role in controlling the Al and REE substitution in titanites (Garber et al., 2017). The aforesaid observation supports the view that compositions of titanite are controlled by several factors including pressure, temperature and composition of the coexisting solid and fluid phases. Quantification of the control of coexisting solid and fluid phases on the Al_2O_3 and F/OH ratio in natural titanite requires identification of stoichiometrically balanced chemical reactions involving titanite. Such reactions, particularly in open system, are expected to provide the influencing factors that governs the Ti/Al and F/OH ratio in titanite in a specific rock under isothermal-isobaric condition. Similar studies are attempted only in a few areas (e.g., Bohlen and Essene, 1978; Sengupta et al., 2004).

4.3.1. Field Relations

The present study documents detailed textural relations and compositional variation of high aluminous titanites from a suite of partially metasomatized, calc-silicate granulite enclaves in the north-eastern part of the Chotanagpur Granite Gneiss Complex, East Indian shield (Fig. 3.1). The studied calc-silicate enclaves primarily occur as metre-scale, boulder-like exposures, within the country rock of migmatitic felsic orthogneiss. They generally show millimetre to centimetre thick, pervasive, leuco- melanocratic banding, which define a prominent N-S foliation. In mesoscopic scale, the studied calc-silicates comprise clinopyroxene + plagioclase ±

garnet ± amphibole ± vesuvianite. Clinopyroxene and plagioclase are common to all the studied calc-silicates, but based on the presence/ absence of garnet, amphibole and vesuvianite (evident in both meso- and micro-scale), these rocks have been classified into four associations, that are exposed in three different outcrops. They are:

(1) **Association 1: Amphibole bearing calc-silicate (Sample No. AS32H1):** This rock is alternately dominated by millimetre to centimetre thick clinopyroxene-rich and plagioclase-rich layers. Amphibole is dispersed throughout the rock (Fig.4.3.1a-d).

(2) **Association 2: Vesuvianite-garnet bearing calc-silicate (Sample No. D4):** This association develops as several centimetre-thick veins within *association 1*. They are mostly parallel to the foliation of *association 1*, but also locally intersect them at low angles (Fig. 4.3.1b-c). The mineralogy of this association includes vesuvianite and garnet, in addition to clinopyroxene and plagioclase. Within these veins, the proportion of vesuvianite and garnet varies (Fig. 4.3.1c). The boundary between *association 1* and *2* shows mineralogical gradation (see Dey et al., 2019a for detailed images).

Both *association1* and *2* are dissected by a number of pegmatitic quartzo-feldspathic veins with an amphibole rich black selvage at the boundary (Fig. 4.3.1b, d). The field features are consistent with fluid aided material transport between the pegmatites and the host rock.

(3) **Association 3: Amphibole-garnet bearing calc-silicate (Sample No. AS32B):** The outcrop of this litho-unit is exposed within ~300 metres from *association 1* and *2*, and comprises clinopyroxene + plagioclase + amphibole + garnet (Fig. 4.3.1e). The plagioclase and Fe-Mg minerals impart alternate light-dark banded appearance to the rock. Centimetres to a few decimetres thick pegmatitic veins are found to intrude this outcrop as well. Owing to lack of exposure due to the tropical weathering it is not known if the *association1*, *2* and *3* formed continuous exposures.(4) **Association 4: Garnet-bearing calc-silicate (Sample No. AS29/19C and D93):** This association is common to most of the calc-silicate rocks in the studied area. The nearest outcrop of this rock occurs within a few kilometres from the calc-silicates rocks where the *association 1-3* are developed, and consists of clinopyroxene + plagioclase + garnet in mesoscopic scale. The rock exhibits a

gneissic foliation, with alternate plagioclase- and garnet-clinopyroxene rich bands (Fig. 4.3.1f). This rock does not contain any hydrous minerals and is devoid of any intrusive veins.

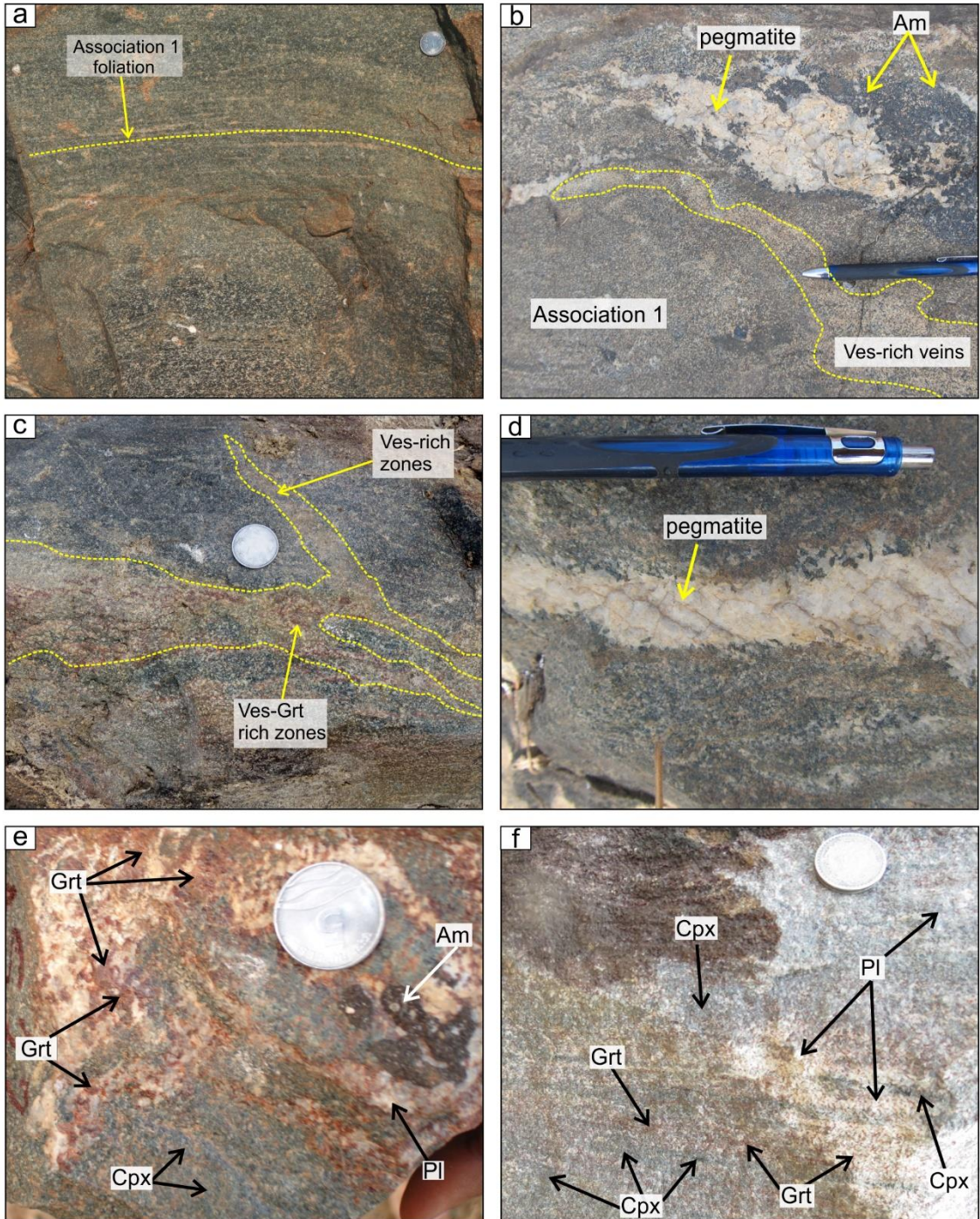


Fig. 4.3.1: (a) Alternate leuco- and melanocratic bands defining a foliation in association 1 rock. (b) Outcrop of association 1 calc-silicate, with vesuvianite-garnet bearing veins (association 2). Pegmatite veins intrude at low angles to the foliation of association 1, and show a prominent amphibole selvage at the interface of the pegmatite and host rock. (c) Figure taken from 'Fig. 2' (Dey et al., 2019a). Vesuvianite-garnet veins (association 2) parallel and at low angles to the foliation of association 1. Vesuvianite and garnet proportions vary within the veins. (d) Pegmatite veins intrude nearly parallel to the foliation of the association 1-2 rock outcrop. Note the thin amphibole selvage present at the interface. (e) Garnet and clinopyroxene rich portions of association 3. (f) Association 4 showing a crude foliation defined by alternate clinopyroxene and plagioclase-rich layers. Garnet is dispersed sporadically throughout the rock. All mineral abbreviations are after Kretz, (1983)

The field features are consistent with the fact that the calc-silicate rocks in *association 4* represent the host rock in which *association 1-3* developed, when it was dissected by pegmatitic quartzo-feldspathic veins. A summary of the different rock associations and their corresponding mineral assemblages and compositional variation have been provided in Table 4.3.1.

4.3.2. Mutual relations between mineral phases

Detailed petrographic study has been carried out from multiple thin sections from all the associations. The overall mutual textural relation amongst the minerals distinguishes two types of paragenetically different mineral assemblages: (1) a primary stabilized, anhydrous assemblage, and (2) a secondary hydrous and F bearing mineralogy (hereafter “secondary assemblage”), that formed subsequent to the primary anhydrous assemblage. Locally the secondary mineral assemblages in *association 1 and 3* include a second generation of plagioclase and garnet respectively. The secondary garnet and plagioclase will be marked with the suffix “2” to distinguish it from the primary assemblage (marked with suffix “1”). Detailed textural study indicates more or less similar primary stabilized mineral assemblage in all the four associations (and hence has been described together). However, considerable variation exists amongst the late-stage secondary minerals, and has been described separately below. All mineral abbreviations used are after Kretz, (1983).

Table 4.3.1: Table summarising the mineral assemblages and compositions of the minerals present in the four rock associations. Mineral abbreviations after Kretz, (1983).

Rock associations	Association 1	Association 2	Association 3	Association 4
Exposure	Foliated rock with alternate leuco- and melanocratic bands rich in clinopyroxene and plagioclase. Pegmatitic veins intrude rock outcrop.	Veins within <i>association 2</i> , comprising vesuvianite and garnet, in addition to clinopyroxene and plagioclase. Pegmatitic veins intrude rock outcrop.	Foliated rock with alternate leuco- and melanocratic bands rich in clinopyroxene and plagioclase. Garnet present throughout the rock. Pegmatitic veins intrude rock outcrop.	Foliated rock with alternate leuco- and melanocratic bands rich in plagioclase and clinopyroxene. Garnet present throughout the rock. No pegmatitic intrusions.
Mineral Assemblage	Clinopyroxene + plagioclase (primary Pl ₁ and replacing Pl ₂) + titanite + amphibole ± apatite ± calcite	Clinopyroxene + plagioclase + titanite + vesuvianite + coronal garnet (Gr ₂) ± apatite ± calcite	Clinopyroxene + plagioclase + titanite + garnet (both primary, Gr ₁ and coronal, Gr ₂) ± quartz	Garnet+ clinopyroxene + plagioclase + titanite
Mineral compositions of major minerals				
Titanite	Al ₂ O ₃ : ~6.8-9.6 wt%, X _{Al} = 0.26-0.36; F ~1.7-2.5 wt%	Al ₂ O ₃ : ~8-11.5 wt%; X _{Al} = 0.31-0.46; F: ~1.7-3.8 wt%	Al ₂ O ₃ : ~7.4-8.5 wt%, X _{Al} = 0.28-0.32; F: ~1.6-2.4 wt%	Al ₂ O ₃ : ~3.4-3.8 wt%, X _{Al} =~0.13-0.14
Clinopyroxene	X _{Mg} = 0.58-0.63	X _{Mg} = 0.54-0.58	X _{Mg} = 0.40-0.53	X _{Mg} = 0.15-0.56
Plagioclase	Less Anorthitic Pl ₁ : (X _{An} : 0.79-0.91); Pl ₂ : (X _{An} : 0.59-0.70)	Anorthitic (X _{An} : 0.94-0.97)	Anorthitic (X _{An} : 0.92-0.98)	Anorthitic (X _{An} : 0.93-0.95)
Garnet	-	Gr₂ : Gr _{S0.73-0.80} Alm _{0.12-0.17} Adr _{0.01-0.07}	Gr₁ : Gr _{S0.45-0.51} Alm _{0.39-0.48} Adr _{0.01-0.05} ; Gr₂ : Gr _{S0.42-0.49} Alm _{0.42-0.49} Adr _{0.02-0.04}	Gr₁ : Gr _{S0.66-0.76} Alm _{0.08-0.25} Adr _{0.07-0.15}
Vesuvianite	-	F: ~1.5-2.5 wt%	-	-
Amphibole	Potassic-pargasite; F: ~0.4-0.9 wt%	-	Ferro-pargasite; F: ~0.9-1.1 wt%	-

4.3.2.1. Primary anhydrous assemblage

Petrographic study of the four associations indicates more or less similar early stabilized, primary anhydrous mineral assemblage, comprising clinopyroxene (Cpx₁) + plagioclase (Pl₁) + titanite ± garnet (Grt₁) ± quartz ± calcite ± apatite. Under thin section, all the associations show leuco-melanocratic bandings, alternately rich in clinopyroxene (Cpx₁; ~60% volume of the bands) and plagioclase (Pl₁; >50% by volume of the bands) (Fig. 4.3.2a-b). Clinopyroxenes and plagioclase occur as medium to large sized, subidioblastic grains, that share straight equilibrium boundaries amongst them, defining a granoblastic texture (Fig. 4.3.2a-b). Locally, clinopyroxenes are slightly elongated and stretched, defining a crude foliation. Primary garnet (Grt₁) is present in *association 3* and *4* only. These medium to large sized garnet grains show straight and non-interfering grain boundaries with clinopyroxene and plagioclase (Fig. 4.3.2b). Titanite is associated with all the four rock associations. It varies in size from small, subrounded grains, to large (up to ~1 mm) subidioblastic ones (Fig. 4.3.2a-b). Titanite is dispersed in the matrix in association with the above minerals (e.g., Fig. 4.3.2a-c). Rarely do the titanite grains occur as inclusions in Cpx₁ (*association 1*) and Grt₁ (*association 3*). In *association 4* only, in addition to the coarse pyroxene Cpx₁ grains, a symplectic intergrowth of finger-like clinopyroxene (Cpx_s) and plagioclase develop by breakdown of garnets (Grt₁; Fig. 4.3.2b).

Calcite, apatite and quartz variably as accessory phases in *association 1-4*.

4.3.2.2. Secondary assemblage:

Association 1: Secondary minerals include medium sized amphiboles (up to ~20% by volume, hereafter abbreviated as 'Am' after Kretz, (1983), that replace clinopyroxenes (Cpx₁) and plagioclase (Pl₁) along their grain boundaries (Fig. 4.3.2c). Amphiboles share non-interfering boundary with titanites, and rarely also include the latter. Plagioclase in *association1* shows patchy zoning, in which Pl₁ (darker shades, Fig. 4.3.2d) seems to be replaced by the secondary plagioclases (Pl₂; lighter shades, Fig. 4.3.2d). Since both amphibole and plagioclase (Pl₂) replace the primary mineral assemblage, they both are considered to be in equilibrium with each other, and possibly formed via the (unbalanced) reaction: Cpx₁ + Pl₁ + H₂O → Am + Pl₂

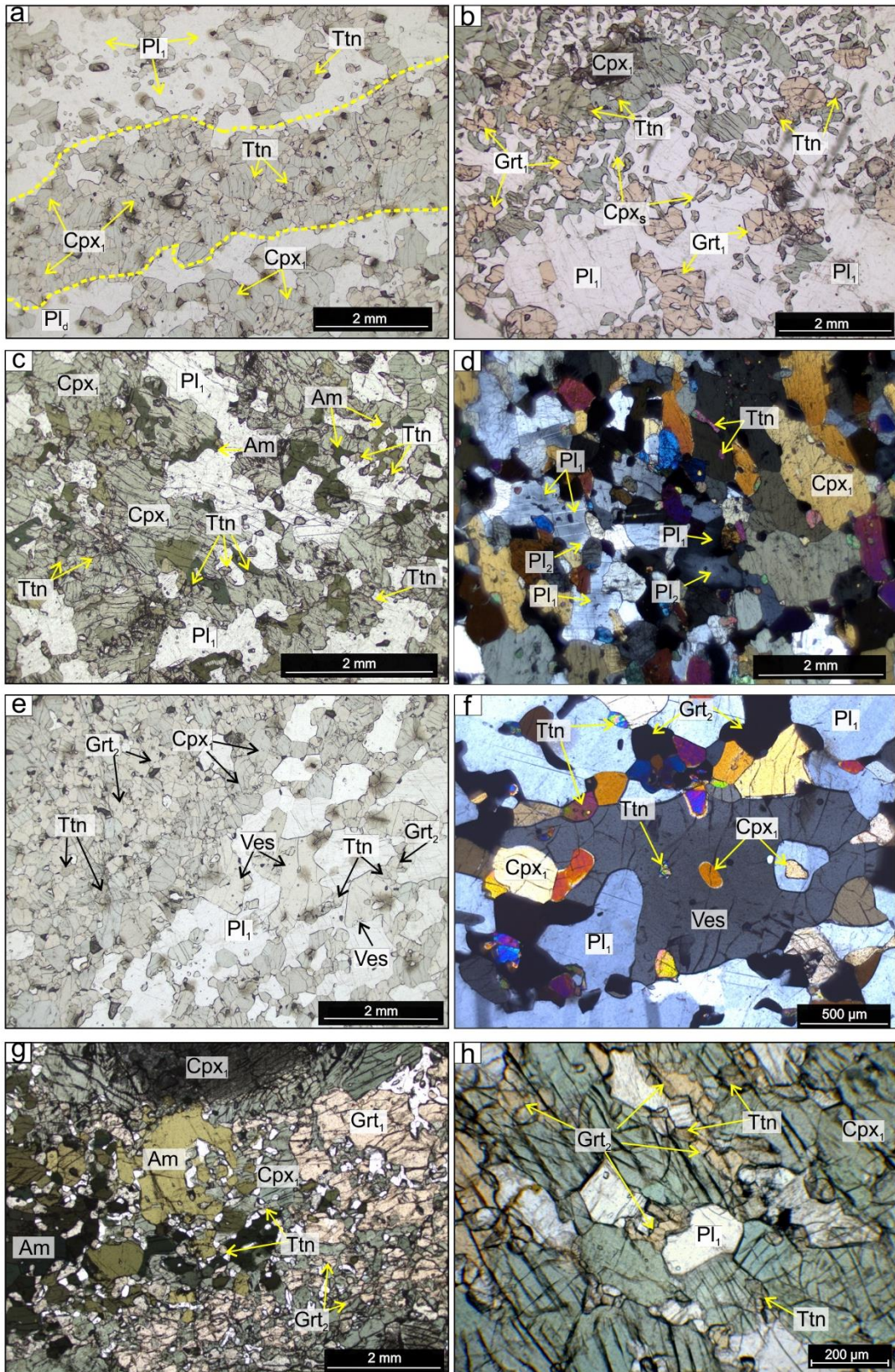


Fig. 4.3.2: Petrographic features of association 1-4. (a) Alternate primary clinopyroxenes and plagioclase rich bands in association 2, that share straight equilibrium boundaries, defining a granoblastic mosaic. Similar alternate banding is evident under thin section in all the other associations also. Titanites are dispersed sporadically in this granoblastic matrix. (b) Medium sized primary garnets showing equilibrium relations with primary clinopyroxene and plagioclase in association 4. Similar relations are shown by primary garnets in association 3. Garnets in association 4 are seen to break down into finger-like clinopyroxenes (Cpxs). (c) Primary clinopyroxenes (Cpx₁) replaced by amphiboles along their grain boundaries. Titanites are dispersed in this matrix of clinopyroxenes and plagioclases. Amphiboles mostly share straight boundaries with titanite, and locally, also surround them. (d) Darker primary plagioclase (Pl₁) replaced by later ones (lighter shade; Pl₂) in association 1. (e) Subidioblastic vesuvianite mostly disposed in the plagioclase-rich band (association 2). Small coronal garnet (Grt₂) form over clinopyroxene (Cpx₁) and plagioclase (Pl₁). Proportion of these coronal garnets increases in the clinopyroxene-rich bands. Note the matrix titanite grains dispersed along with these minerals in both the bands. (f) Inclusions of clinopyroxene and rare titanite in vesuvianite. Vesuvianite and coronal garnet grows along the margin of Cpx₁ and Pl₁ (association 2). (g) Amphiboles replacing the Cpx₁ and Pl₁ (association 3). Thin coronal garnets are also seen to form at the interface of Cpx₁ and Pl₁. (h) Coronal garnets (Grt₂) forming at the interface of Cpx₁ and Pl₁ (association 3). Cpx₁, Pl₁, Grt₁: primary anhydrous clinopyroxene, plagioclase and garnet. Pl₂, Grt₂: plagioclase and garnet associated with the late fluid-bearing secondary mineral assemblage. All mineral abbreviations are after Kretz, (1983).

Association 2: Clinopyroxene (Cpx₁) and plagioclase (Pl₁) are variably replaced by vesuvianite and coronal garnet (Grt₂). Subidioblastic vesuvianite grows preferentially more in the plagioclase rich domain, along the rims of plagioclase and clinopyroxene (Fig. 4.3.2e-f). Inclusions of clinopyroxene and quartz, along with rare apatite and calcite are also present in vesuvianite (Fig. 4.3.2f, see Dey et al., 2019a for more images). Small coronal garnets are present along with vesuvianite at the interface of clinopyroxene and plagioclase (Fig. 4.3.2e-f). In the clinopyroxene rich band, the proportion and thickness of these coronal garnet increases. In places, aggregates of coronal garnets coalesce to form a sieved garnet with numerous inclusions of primary clinopyroxene and plagioclase (Fig. 4.3.2e) within it. Subordinate amounts of vesuvianite are also present within this band. Titanites are present along the margins of vesuvianite and coronal garnet, as well as inclusions within them. (Fig. 4.3.2e-f). Textural relations suggest formation of vesuvianite + coronal garnet at the expense of the primary assemblage through progress of the (unbalanced) reaction: $Cpx_1 + Pl_1 \pm Qtz + fluid \pm Cal \rightarrow Ves + Grt_2 + CO_2$

Association 3: Medium sized amphiboles replace the primary clinopyroxene (Cpx₁). (Fig. 4.3.2g). Locally, the primary Cpx₁ and Pl₁ is also replaced by thin coronal garnets (Grt₂), forming at the interface of plagioclase (Pl₁) and

clinopyroxene (Cpx₁; Fig. 4.3.2g-h). Titanite grains are associated with Grt₂ as well as amphiboles. Textural relations indicate that both amphibole and coronal garnets formed at the expense of the primary clinopyroxene and plagioclase, via the (unbalanced) reaction: $Cpx_1 + Pl_1 + H_2O \rightarrow Am + Grt_2$

Association 4: No fluid-bearing minerals is developed in this rock association.

4.3.3. Mineral chemistry

The polished thin sections were carbon coated before the analysis to prevent charge localisation. Mineral compositions have been analyzed at the Central Research Facility of the Indian Institute of Technology (Indian School of Mines). Details of analytical techniques are described in Appendix. Fe⁺³ was calculated using the scheme of Droop, (1987) and Grew, (2013), during cation recalculation. Cation recalculation of amphibole was done using the scheme of Hawthorne et al., (2012) and references therein.

Mineral compositions were measured from a number of thin sections from each of associations. Representative compositions are presented in Table 4.3.2a-e. All mineral abbreviations used are after Kretz, (1983).

4.3.3.1. Clinopyroxene:

Clinopyroxenes in association 1 [$X_{Mg} (Mg/Mg+Fe^{+2}) = 0.58-0.63$], *association 2* ($X_{Mg} = 0.54-0.58$) and *association 3* ($X_{Mg} = 0.40-0.53$) shows a continuous, yet overlapping spread of X_{Mg} contents (Fig. 4.3.3a). Clinopyroxenes in *association 4* have a large range of X_{Mg} (0.15-0.56) varying from outcrop to outcrop. In *D93*, clinopyroxene is magnesian ($X_{Mg} = 0.51-0.56$; similar to *association 1-3*), with respect to *AS29/19C* ($X_{Mg} = 0.15-0.18$). Compositions of symplectic clinopyroxene (Cpx_s) are overlapping with that of larger, porphyroblastic ones (Cpx₁) (Fig. 4.3.3a, Table 4.3.2a) in *association 4*. All clinopyroxenes are low aluminous (Al₂O₃: ~0.9-2.9 wt%). The Al-Tschermak and essentite components vary randomly within the range of ~2-13 mol%. Acmite (NaFe⁺³Si₂O₆), jadeite (NaAl⁺³Si₂O₆), and donpeacorite [(Mn,Mg)⁺²MgSi₂O₆] components add up to a maximum of ~3 mol%.

4.3.3.2. Plagioclase:

Primary plagioclases (Pl₁) in *association 2-4* are highly anorthitic, having a very restricted composition of An_{0.92-0.98}Ab_{0.02-0.08} (Fig. 4.3.3b). Orthoclase component is negligible. In *association 1* however, the primary plagioclase (Pl₁) is slightly less anorthitic (An_{0.79-0.91}Ab_{0.9-0.20}Or_{0-0.01}), and are replaced by secondary, more albitic plagioclase (Pl₂: An_{0.59-0.70}Ab_{0.29-0.40}Or_{0.01}; Table 4.3.2b; Fig. 4.3.3b).

4.3.3.3. Garnet:

Grt₁ in the studied rocks (*association 3-4*) are dominantly a solid solution of grossular and almandine/ andradite (Fig. 4.3.3c). Only garnets in *D93* have marginally higher andradite content (up to ~15mol%). The garnets in *association 3* (Grs_{0.45-0.51}Alm_{0.39-0.48}Adr_{0.01-0.05}) have lower grossular content than *association 4* (Grs_{0.66-0.76}Alm_{0.08-0.25}Adr_{0.07-0.15}). All these garnets are highly Fe-rich (X_{Mg}: ~0.02-0.11), with variable content of almandine and andradite component. Pyrope and spessartine components together not exceeding ~6 mol% (Table 4.3.2c; Fig. 4.3.3c).

Coronal garnets are present in *association 2* and *3*. In *association 2*, these have very high grossular, and low almandine and andradite contents (Grs_{0.73-0.80}Alm_{0.12-0.17}Adr_{0.01-0.07}, X_{Mg}:0.07-0.13; Table 4.3.2c). Measurable amount of F is also present within its structure (~0.5 to 1 wt %; Table 4.3.2c). F-bearing garnets have also been previously reported (Valley et al., 1983; reviewed in Grew et al., 2013) from around the world. However, in *association 3*, compositions of coronal garnets (Table 4.3.2c, Fig. 4.3.3c). Pyrope and spessartine contents together vary between ~3-7 mol% in both associations. Fluorine contents (~0.02-0.23 wt%) in both these garnets (primary and coronal) in *association 3* suggest, slight compositional modification during this late-stage fluid driven metamorphism. Conversely, the primary garnets in *association 4* do not contain any F in their structures.

4.3.3.4. Titanite:

Except *association 4*, titanites in all the associations are high aluminous (X_{Al} (Al/(Al+Fe⁺³+Ti) ≥0.25; Oberti et al., 1985), containing significant amounts of Al₂O₃ (~6.8-11.5 wt%, X_{Al}=0.26-0.46), as well as F (~1.6-3.8 wt%) and OH (0.01-0.18 apfu; recalculated according to the method followed by Sengupta et al. 2004; Harlov et al., 2006) in their structures (Table 4.3.2d, Fig. 4.3.3d-e). Conversely, titanites in

association 4 contain very small amount Al in their structures ($\sim 3.4\text{-}3.8$ wt% Al_2O_3 , $X_{\text{Al}} = \sim 0.13\text{-}0.14$; Fig. 4.3.3d), with recalculated OH of $\sim 0.07\text{-}0.15$ apfu and practically negligible F ($0\text{-}0.8$ wt%; Fig. 4.3.3e). In the titanite stoichiometry, Ca p.f.u. are values close to 1 in titanites from all associations (Table 4.3.2d). This suggests that the studied titanite does not contain any significant actinides and REE that would replace Ca ions (Higgins and Ribbe, 1976). No compositional zoning was observed within individual titanite grains.

4.3.3.5. Vesuvianite:

Cation calculation of vesuvianite was done following the procedure in Dey et al., (2019a). Vesuvianites are compositionally homogenous with considerable proportion of F in their structures ($\sim 1.5\text{-}2.5$ wt%; Table 4.3.2e), and negligible Cl content. OH contents range between $\sim 5.1\text{-}6.1$ apfu. Mg content varies between $\sim 1.4\text{-}1.5$ apfu. These vesuvianites do not contain any Fe^{+2} (Dey et al., 2019a). They contain minor amount of sodium and are boron free (see Dey et al., 2019a for more details on vesuvianite composition).

4.3.3.6. Amphibole:

Amphibole is mainly ferro-pargasitic, while only few analyses fall into the potassic-pargasite category (Hawthorne et al., 2012 and references therein; Fig. 4.3.3f) in *association 1*. Moreover, amphiboles in *association 3* are more Fe-rich ($X_{\text{Mg}} = 0.34\text{-}0.38$) than in *association 1* ($X_{\text{Mg}}: 0.53\text{-}0.57$). However, amphiboles in both the rocks have considerable F ($\sim 0.4\text{-}1.1$ wt%) in their structure (Table 4.3.2e).

Apatite also contains ~ 5 wt% F in its structure.

Calcite and rare *quartz* are pure phases.

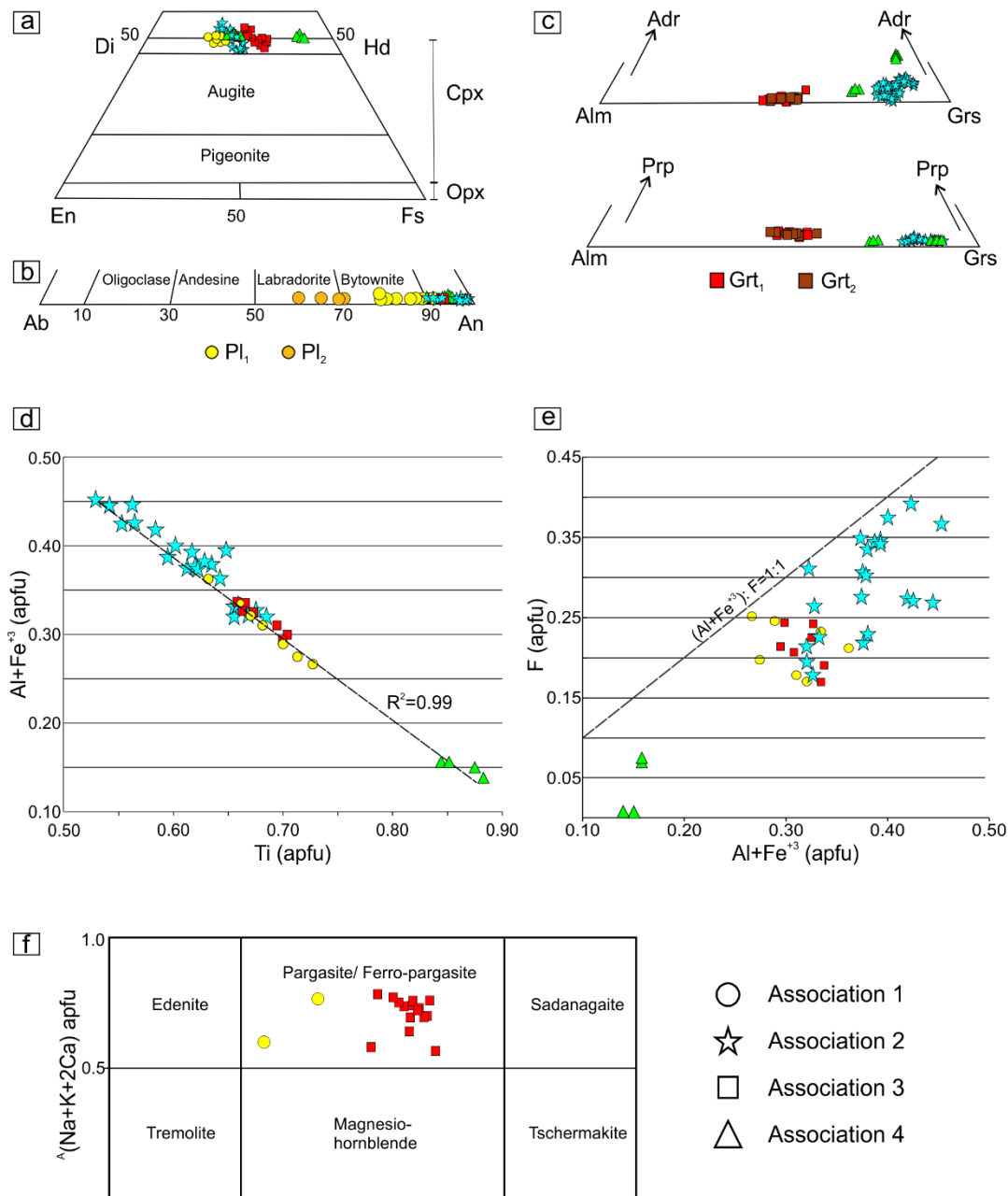


Fig. 4.3.3: (a) Representative clinopyroxene compositions from the calc-silicate associations plotted in pyroxene quadrilateral. (b) Composition of plagioclase from all associations plotted on albite-anorthite join. PI_2 in association 1 plots towards the more albitic side relative to primary plagioclase (PI_1). (c) Composition of garnets in association 2-4 plotted in andradite-almandine-grossular and pyrope-almandine-grossular triangles. The two generations of garnet (Grt_1 and Grt_2) in association 3 show overlapping compositions. (d) Negative correlation ($R^2=0.99$) between Ti and $(Al+Fe^{3+})$ content in titanites, showing that the highest substitution occurred in association 2, while that in association 1 and 3 were relatively lower. Note that titanites in association 4 contains negligible $Al+Fe^{3+}$ in its structure. (e) A plot of $(Al+Fe^{3+})$ and F (apfu) showing very high F and Al contents in association 2. Association 1 and 3 have slightly lower $Al+Fe^{3+}$ as well as F. Association 4 on the other hand, having negligible F, plot near the origin. The deviation from 1:1 line [$(Al+Fe^{3+}):F$] implies the presence of OH as the balancing substituent for $(Al+Fe^{3+})$ in addition to F. (f) Composition of amphiboles from association 1 and 3, presented in ${}^A(Na+K+2Ca)$ vs. ${}^C(Al+Fe+3+2Ti)$ (apfu) plot for calcic amphiboles after the classification scheme of Hawthorne et al. (2012). Grt_1 : primary garnet, Grt_2 : Coronal garnet, PI_1 : primary plagioclase, PI_2 : late-stage secondary plagioclase. All mineral abbreviations are after Kretz, (1983).

Table 4.3.2a: Representative electron microprobe analysis of clinopyroxene (stoichiometry calculated on the basis of 6 oxygens, oxide data are given in weight%).

Point	Association 1			Association 2		Association 3		Association 4			
	(AS32H1)			(D4)		(AS32B)		(AS29/19C)		(D93)	
	32/1	12/1 [#]	24/1	1 / 1	44 / 1	12 / 1	13 / 1	38 / 1	1 / 1	1/16	1/27
Texture	symplectic										
SiO ₂	52.94	52.64	52.79	51.88	49.45	48.89	49.09	48.34	48.19	50.18	49.37
TiO ₂	0.01	0.08	0.03	0.18	0.14	0.35	0.17	0.14	0.13	0.11	0.08
Al ₂ O ₃	0.86	1.27	1.28	1.89	2.17	2.91	1.68	1.72	1.34	1.88	1.25
Cr ₂ O ₃	0.11	0.19	0.18	<d.l.	0.04	0.19	0.22	<d.l.	<d.l.	0.02	0.00
FeO	12.03	11.87	12.46	13.71	13.25	17.06	15.89	25.10	25.25	14.92	15.06
MnO	0.28	0.37	0.36	0.42	0.40	<d.l.	<d.l.	<d.l.	<d.l.	0.31	0.27
MgO	10.63	10.78	9.80	9.04	9.05	7.37	8.37	2.86	2.43	8.00	8.26
CaO	23.93	24.22	23.87	23.77	23.49	23.40	23.31	22.35	22.27	24.30	24.49
Na ₂ O	0.20	0.23	0.24	0.19	0.22	0.17	0.14	0.16	0.14	0.18	0.20
K ₂ O	<d.l.	<d.l.	<d.l.	<d.l.	<d.l.	<d.l.	<d.l.	<d.l.	<d.l.	<d.l.	<d.l.
F	<d.l.	<d.l.	<d.l.	<d.l.	<d.l.	<d.l.	<d.l.	<d.l.	<d.l.	<d.l.	<d.l.
Cl	<d.l.	<d.l.	<d.l.	<d.l.	<d.l.	<d.l.	<d.l.	<d.l.	<d.l.	<d.l.	<d.l.
Total	101.00	101.67	101.04	101.11	98.22	100.38	99.02	100.91	99.91	99.90	98.99
Si	1.99	1.97	1.99	1.97	1.93	1.89	1.92	1.93	1.95	1.94	1.92
Ti	0.00	0.00	0.00	0.01	0.00	0.01	0.01	0.00	0.00	0.00	0.00
Al	0.04	0.06	0.06	0.08	0.10	0.13	0.08	0.08	0.06	0.09	0.06
Cr ⁺³	0.00	0.01	0.01	0.00	0.00	0.01	0.01	0.00	0.00	0.00	0.00
Fe ⁺³	0.00	0.02	0.00	0.00	0.05	0.07	0.09	0.06	0.04	0.04	0.11
Fe ⁺²	0.38	0.35	0.39	0.44	0.38	0.48	0.43	0.77	0.81	0.44	0.38
Mn	0.01	0.01	0.01	0.01	0.01	0.00	0.01	0.01	0.01	0.01	0.01
Mg	0.60	0.60	0.55	0.51	0.53	0.42	0.49	0.17	0.15	0.46	0.48
Ca	0.97	0.97	0.97	0.97	0.98	0.97	0.97	0.96	0.97	1.01	1.02
Na	0.01	0.02	0.02	0.01	0.02	0.01	0.01	0.01	0.01	0.01	0.02
K	0.00	0.00	0.00	0.00	0.00	0.00	0.00	0.00	0.00	0.00	0.00
Total	4.00	4.00	4.00	4.00	4.00	4.00	4.00	4.00	4.00	4.00	4.00
Di	0.59	0.60	0.55	0.51	0.53	0.42	0.48	0.17	0.14	0.48	0.49
Hd	0.39	0.35	0.43	0.45	0.39	0.48	0.43	0.76	0.80	0.45	0.40
Ac	0.00	0.00	0.00	0.00	0.00	0.00	0.01	0.00	0.00	0.00	0.02
Jd	0.01	0.02	0.02	0.01	0.02	0.01	0.00	0.01	0.01	0.01	0.00
Ess	0.00	0.02	0.00	0.00	0.05	0.07	0.08	0.06	0.04	0.04	0.09
crTs	0.00	0.01	0.01	0.00	0.00	0.01	0.01	0.00	0.00	0.00	0.00
AlTs	0.02	0.01	0.03	0.04	0.01	0.01	0.00	0.00	0.00	0.01	0.00
Wo	0.97	0.97	0.97	0.97	0.98	0.97	0.97	0.96	0.97	1.01	1.02
En	0.60	0.60	0.55	0.51	0.53	0.42	0.49	0.17	0.15	0.46	0.48
Fs	0.39	0.35	0.43	0.45	0.38	0.48	0.43	0.77	0.81	0.44	0.38
Don	0.01	0.01	0.01	0.01	0.01	0.00	0.01	0.01	0.01	0.01	0.01
X _{Mg}	0.61	0.63	0.58	0.54	0.58	0.40	0.53	0.18	0.15	0.51	0.56

Don: Donpeacorite; [#] Dey et al. (2019a); d.l.= detection limit; d.l.= detection limit

Table 4.3.2b: Representative electron microprobe analysis of plagioclase (stoichiometry calculated on the basis of 8 oxygens, oxide data are given in weight%).

Point	Association 1				Association 2		Association 3		Association 4			
	(AS32H1)				(D4)		(AS32B)		(AS29/19C)		(D93)	
	2 / 1	25/1 [#]	27/1 [#]	10 / 1	13 / 1	10 / 1	6 / 1	65 / 1	2 / 1	43 / 1	19	32
Texture	Pl _d	Pl _d	Pl _f	Pl _f								
SiO ₂	48.93	45.82	54.10	51.27	42.90	44.16	43.85	43.62	44.40	44.45	44.43	44.11
TiO ₂	<d.l.	<d.l.	<d.l.	0.06	<d.l.	0.08	<d.l.	0.05	<d.l.	<d.l.	0.00	0.00
Al ₂ O ₃	32.70	34.72	29.36	31.66	35.42	35.98	34.53	35.92	35.55	35.47	35.60	35.51
FeO	<d.l.	<d.l.	<d.l.	<d.l.	<d.l.	<d.l.	<d.l.	<d.l.	0.27	<d.l.	0.13	0.16
MnO	<d.l.	<d.l.	<d.l.	<d.l.	<d.l.	<d.l.	<d.l.	<d.l.	<d.l.	<d.l.	0.00	0.00
MgO	<d.l.	<d.l.	<d.l.	<d.l.	<d.l.	<d.l.	<d.l.	<d.l.	<d.l.	<d.l.	0.00	0.02
CaO	16.14	18.75	12.18	14.58	21.23	19.40	18.56	19.95	18.89	18.79	19.88	19.82
Na ₂ O	2.28	1.01	4.48	3.30	0.70	0.37	0.88	0.18	0.58	0.72	0.58	0.70
K ₂ O	0.09	<d.l.	0.18	0.14	<d.l.	<d.l.	<d.l.	<d.l.	<d.l.	<d.l.	0.02	0.03
Total	100.41	100.35	100.44	101.16	100.44	100.03	98.13	99.89	99.75	99.70	100.65	100.36
Si	2.23	2.10	2.44	2.31	1.97	2.04	2.06	2.02	2.06	2.06	2.04	2.04
Ti	0.00	0.00	0.00	0.00	0.00	0.00	0.00	0.00	0.00	0.00	0.00	0.00
Al	1.76	1.88	1.56	1.68	1.92	1.96	1.91	1.96	1.94	1.93	1.93	1.93
Fe ⁺³	0.00	0.00	0.00	0.00	0.00	0.00	0.00	0.00	0.00	0.00	0.00	0.00
Fe ⁺²	0.00	0.00	0.00	0.00	0.00	0.00	0.00	0.00	0.00	0.00	0.01	0.01
Mn	0.00	0.00	0.00	0.00	0.00	0.00	0.00	0.00	0.00	0.00	0.00	0.00
Mg	0.00	0.00	0.00	0.00	0.00	0.00	0.00	0.00	0.00	0.00	0.00	0.00
Ca	0.79	0.92	0.59	0.70	1.04	0.96	0.93	0.99	0.94	0.93	0.98	0.98
Na	0.20	0.09	0.39	0.29	0.06	0.03	0.08	0.02	0.05	0.06	0.05	0.06
K	0.01	0.00	0.01	0.01	0.00	0.00	0.00	0.00	0.00	0.00	0.00	0.00
Total	5.00	5.00	5.00	5.00	5.00	5.00	5.00	5.00	5.00	5.00	5.00	5.00
X _{An}	0.79	0.91	0.59	0.70	0.94	0.97	0.92	0.98	0.95	0.93	0.95	0.94
X _{Ab}	0.20	0.09	0.40	0.29	0.06	0.03	0.08	0.02	0.05	0.06	0.05	0.06
X _{Or}	0.01	0.00	0.01	0.01	0.00	0.00	0.00	0.00	0.00	0.00	0.00	0.00

[#] Dey et al. (2019a); Pl₁: Early plagioclase; Pl₂: late-stage replacing plagioclase

d.l.: detection limit

Table 4.3.2c: Representative electron microprobe analysis of garnet (stoichiometry calculated on the basis of 12 oxygens, oxide data are given in weight%).

Point	Association 2					Association 3						Association 4					
	(D4)					(AS32B)						(AS29_19C)			(D93)		
	31 / 1	46 / 1	56/1 [#]	57/1 [#]	78/1 [#]	15 / 1	2 / 1	44 / 1	46 / 1	29 / 1	61 / 1	46 / 1	47 / 1	12	15	37	
Texture	coronal					coronal											
SiO ₂	38.58	38.49	38.96	38.64	38.71	38.00	38.18	38.00	38.28	37.39	38.73	38.18	38.41	37.58	38.16	37.60	
TiO ₂	0.40	0.31	0.23	0.29	0.28	0.13	0.10	0.15	0.08	0.05	0.10	0.12	0.14	0.27	0.29	0.28	
Al ₂ O ₃	19.75	20.53	20.49	19.28	20.41	20.43	20.40	20.35	20.32	20.15	20.87	19.79	19.59	18.14	18.27	18.82	
Cr ₂ O ₃	0.46	0.21	0.01	0.45	0.29	0.23	0.25	0.39	0.78	0.93	0.28	<d.l.	<d.l.	0.23	0.10	0.00	
FeO	9.52	7.76	7.75	9.58	7.40	19.95	20.35	22.44	22.21	22.74	21.34	14.12	14.59	8.79	8.48	9.09	
MnO	1.49	1.11	0.83	1.96	0.94	0.71	0.71	1.01	1.14	1.45	0.65	0.78	0.42	0.22	0.28	0.25	
MgO	0.41	0.48	0.47	0.36	0.42	0.98	0.85	0.89	0.88	1.02	1.05	0.14	0.12	0.48	0.50	0.47	
CaO	28.69	29.45	29.82	27.43	29.33	18.89	19.19	16.27	17.20	15.02	18.34	25.84	25.75	32.67	32.23	32.63	
Na ₂ O	<d.l.	0.12	<d.l.	0.07	<d.l.	<d.l.	<d.l.	<d.l.	<d.l.	<d.l.	<d.l.	<d.l.	<d.l.	<d.l.	0.01	<d.l.	
K ₂ O	<d.l.	<d.l.	<d.l.	<d.l.	<d.l.	<d.l.	<d.l.	<d.l.	<d.l.	<d.l.	<d.l.	<d.l.	<d.l.	<d.l.	<d.l.	<d.l.	
F	0.54	0.61	0.98	0.65	0.73	0.03	0.02	<d.l.	0.23	n.m.	0.14	<d.l.	<d.l.	<d.l.	<d.l.	<d.l.	
Total	99.85	99.11	99.58	98.73	98.55	99.38	100.05	99.50	101.12	98.75	101.54	99.01	99.02	98.39	98.32	98.32	
Si	3.00	2.99	3.02	3.04	3.03	3.00	3.00	3.02	3.00	3.00	3.00	2.99	3.01	3.01	3.00	2.98	
Ti	0.02	0.02	0.01	0.02	0.02	0.01	0.01	0.01	0.00	0.00	0.01	0.01	0.01	0.02	0.02	0.02	
Al	1.81	1.88	1.87	1.79	1.88	1.90	1.89	1.90	1.88	1.90	1.90	1.83	1.81	1.65	1.67	1.69	
Cr ⁺³	0.03	0.01	0.00	0.03	0.02	0.01	0.02	0.02	0.05	0.06	0.02	0.00	0.00	0.01	0.01	0.00	
Fe ⁺³	0.13	0.12	0.07	0.08	0.02	0.08	0.10	0.02	0.07	0.03	0.07	0.17	0.14	0.29	0.28	0.31	
Fe ⁺²	0.49	0.38	0.44	0.55	0.46	1.24	1.24	1.47	1.38	1.49	1.31	0.76	0.82	0.27	0.27	0.27	
Mn	0.10	0.07	0.05	0.13	0.06	0.05	0.05	0.07	0.08	0.10	0.04	0.05	0.03	0.03	0.03	0.03	
Mg	0.05	0.06	0.05	0.04	0.05	0.12	0.10	0.11	0.10	0.12	0.12	0.02	0.01	0.03	0.03	0.03	
Ca	2.39	2.45	2.48	2.31	2.46	1.60	1.61	1.38	1.44	1.29	1.52	2.17	2.17	2.69	2.68	2.67	
Na	0.00	0.02	0.00	0.01	0.00	0.00	0.00	0.00	0.00	0.00	0.01	0.00	0.00	0.00	0.00	0.00	
K	0.00	0.00	0.00	0.00	0.00	0.00	0.00	0.00	0.00	0.00	0.00	0.00	0.00	0.00	0.00	0.00	
Total	8.00	8.00	8.00	8.00	8.00	8.00	8.00	8.00	8.00	8.00	8.00	8.00	8.00	8.00	8.00	8.00	
X _{Adr}	0.07	0.06	0.03	0.04	0.01	0.04	0.05	0.01	0.04	0.02	0.04	0.09	0.07	0.15	0.14	0.15	
X _{Py}	0.01	0.02	0.02	0.01	0.02	0.04	0.03	0.03	0.03	0.04	0.04	0.00	0.00	0.01	0.01	0.01	
X _{Alm}	0.15	0.12	0.14	0.17	0.15	0.40	0.39	0.48	0.44	0.49	0.42	0.23	0.25	0.08	0.08	0.08	
X _{Grs}	0.73	0.77	0.79	0.73	0.80	0.51	0.51	0.45	0.46	0.42	0.49	0.66	0.66	0.76	0.76	0.75	
X _{Sps}	0.03	0.02	0.02	0.04	0.02	0.02	0.01	0.02	0.02	0.03	0.01	0.02	0.01	0.01	0.01	0.01	
X _{Mg}	0.09	0.13	0.11	0.07	0.10	0.09	0.07	0.07	0.07	0.08	0.08	0.02	0.02	0.09	0.11	0.10	

[#] Dey et al. (2019a); d.l.: detection limit

Table 4.3.2d: Representative electron microprobe analysis of titanite (stoichiometry calculated on the basis of 5 oxygens, oxide data are given in weight%).

Point	Association 1 (AS32H1)				Association 2 (D4)				Association 3 (AS32B)				Association 4 (AS29/19C) (D93)				
	4/1 [#]	22/1 [#]	26/1	2/1	2/26	4/1	24/1	50/1	23/1	49/1	10	11	16	4 ^b	40	11/1	17/1
SiO ₂	31.45	31.54	31.18	30.49	30.23	31.80	30.34	30.86	31.13	29.95	31.06	31.02	30.73	30.35	30.27	30.54	30.31
TiO ₂	30.28	26.49	27.83	27.72	22.37	27.87	21.32	24.16	26.66	22.66	27.61	27.25	29.14	35.42	35.49	33.90	34.61
Al ₂ O ₃	6.77	9.55	8.31	8.33	10.74	8.27	11.53	10.92	8.00	11.29	8.47	8.49	7.40	3.36	3.56	3.71	3.76
Cr ₂ O ₃	0.22	0.43	0.30	<d.l.	<d.l.	<d.l.	0.05	0.11	0.07	0.04	0.21	0.19	0.29	<d.l.	<d.l.	0.13	0.00
Fe ₂ O ₃	0.50	0.21	0.29	0.38	0.30	0.44	0.24	0.24	0.60	0.23	0.66	0.64	0.76	0.38	0.58	0.56	0.46
MnO	<d.l.	<d.l.	<d.l.	<d.l.	<d.l.	<d.l.	<d.l.	0.03	<d.l.	0.04	<d.l.	<d.l.	<d.l.	<d.l.	<d.l.	0.13	0.00
MgO	0.09	0.09	0.08	<d.l.	<d.l.	<d.l.	<d.l.	0.08	<d.l.	0.03	0.07	<d.l.	0.08	<d.l.	<d.l.	0.04	0.01
CaO	28.91	29.14	28.94	28.98	29.24	29.14	28.81	28.77	28.59	28.05	28.93	29.11	29.03	28.02	28.19	28.06	0.02
Na ₂ O	<d.l.	<d.l.	<d.l.	<d.l.	<d.l.	<d.l.	<d.l.	0.13	0.07	0.07	<d.l.	<d.l.	<d.l.	<d.l.	<d.l.	0.00	27.92
K ₂ O	<d.l.	<d.l.	<d.l.	<d.l.	<d.l.	<d.l.	<d.l.	0.03	<d.l.	0.01	<d.l.	<d.l.	<d.l.	<d.l.	<d.l.	0.00	0.01
F	2.49	2.08	1.65	1.73	3.75	2.11	3.50	2.65	3.00	2.52	1.64	1.83	2.38	<d.l.	<d.l.	0.65	0.00
Cl	<d.l.	<d.l.	<d.l.	<d.l.	<d.l.	0.04	<d.l.	0.01	<d.l.	0.00	<d.l.	<d.l.	<d.l.	<d.l.	<d.l.	<d.l.	0.79
Total	100.84	99.58	98.68	97.78	96.69	99.85	95.87	97.98	98.17	95.10	98.82	98.61	99.83	97.60	98.18	97.72	97.89
Si	1.00	1.00	1.00	0.99	0.99	1.01	1.00	0.99	1.02	0.99	0.99	1.00	0.99	1.00	0.99	1.00	1.00
Ti	0.73	0.63	0.67	0.68	0.55	0.67	0.53	0.58	0.65	0.56	0.66	0.66	0.70	0.88	0.87	0.84	0.86
Al	0.25	0.36	0.31	0.32	0.42	0.31	0.45	0.41	0.31	0.44	0.32	0.32	0.28	0.13	0.14	0.14	0.15
Cr ⁺³	0.01	0.01	0.01	0.00	0.00	0.00	0.00	0.00	0.00	0.00	0.01	0.00	0.01	0.00	0.00	0.00	0.00
Fe ⁺³ *	0.01	0.00	0.01	0.01	0.01	0.01	0.01	0.01	0.01	0.01	0.02	0.02	0.02	0.01	0.01	0.01	0.01
Fe ⁺²	0.00	0.00	0.00	0.00	0.00	0.00	0.00	0.00	0.00	0.00	0.00	0.00	0.00	0.00	0.00	0.00	0.00
Mn	0.00	0.00	0.00	0.00	0.00	0.00	0.00	0.00	0.00	0.00	0.00	0.00	0.00	0.00	0.00	0.00	0.00
Mg	0.00	0.00	0.00	0.00	0.00	0.00	0.00	0.00	0.00	0.00	0.00	0.00	0.00	0.00	0.00	0.00	0.00
Ca	0.99	0.99	0.99	1.01	1.03	0.99	1.02	0.99	1.00	0.99	0.99	1.00	1.00	0.99	0.99	0.99	0.98
Na	0.00	0.00	0.00	0.00	0.00	0.00	0.00	0.01	0.00	0.00	0.00	0.00	0.00	0.00	0.00	0.00	0.00
K	0.00	0.00	0.00	0.00	0.00	0.00	0.00	0.00	0.00	0.00	0.00	0.00	0.00	0.00	0.00	0.00	0.00
Total	3.00	3.00	3.00	3.00	3.00	3.00	3.00	3.00	3.00	3.00	3.00	3.00	3.00	3.00	3.00	3.00	3.00
F	0.25	0.21	0.17	0.18	0.39	0.21	0.37	0.27	0.31	0.27	0.17	0.19	0.24	0.00	0.00	0.07	0.08
Cl	0.00	0.00	0.00	0.00	0.00	0.00	0.00	0.00	0.00	0.00	0.00	0.00	0.00	0.00	0.00	0.00	0.00
OH	0.01	0.15	0.15	0.15	0.03	0.11	0.08	0.15	0.01	0.18	0.17	0.15	0.06	0.14	0.15	0.09	0.07
X _{Al}	0.26	0.36	0.32	0.32	0.43	0.31	0.46	0.41	0.32	0.60	0.32	0.32	0.28	0.13	0.13	0.14	0.14
X _{Fe}	0.94	0.59	0.53	0.55	0.93	0.67	0.81	0.65	0.96	0.44	0.50	0.56	0.82	0.00	0.00	0.43	0.52
X _{OH}	0.06	0.41	0.47	0.45	0.07	0.33	0.19	0.35	0.04	0.40	0.50	0.44	0.18	1.00	1.00	0.57	0.48

* All Fe as Fe⁺³; OH= Al+Fe⁺³-F; [#] Dey et al. (2019a). ^btitanite data used in reaction modelling as a proxy for pristine titanite;

d.l.: detection limit

Table 4.3.2e: Representative electron microprobe analysis of vesuvianite (stoichiometry calculated on the basis of 50 cations. Anions calculated after Ketcham 2015 and amphibole (Hawthorne et. al. 2012); oxide data are given in weight %).

Vesuvianite			Amphibole						
Association 2			Association 1		Association 3				
(D4)			(AS32H1)		(AS32B)				
Point			Potassic-pargasite		Ferropargasite				
	13/1 [#]	42/1 [#]	Point	11/1 [#]	13/1 [#]	31	54	51	22
SiO ₂	36.05	36.93	SiO ₂	42.37	44.65	41.47	39.50	40.52	39.88
TiO ₂	1.26	1.58	TiO ₂	0.50	0.68	0.46	0.54	0.58	0.49
Al ₂ O ₃	15.83	15.65	Al ₂ O ₃	12.68	10.02	11.92	14.00	13.33	13.10
Cr ₂ O ₃	0.05	0.12	Cr ₂ O ₃	1.35	1.48	0.43	0.55	0.34	0.17
Fe ₂ O ₃	5.16	5.54	FeO	14.73	14.63	22.44	21.98	23.73	22.46
MnO	0.17	0.41	MnO	0.29	0.27	<d.l.	0.31	<d.l.	0.22
MgO	1.92	1.99	MgO	9.48	11.05	6.31	6.28	5.58	5.89
CaO	33.61	33.50	CaO	12.24	12.29	11.80	12	11.6	11.56
Na ₂ O	0.07	0.09	Na ₂ O	1.18	0.97	1.42	1.42	1.64	1.78
K ₂ O	<d.l.	<d.l.	K ₂ O	2.24	1.84	0.95	1.5	0.69	0.71
F	2.47	1.50	F	1.06	0.88	0.39	0.86	0.65	0.46
Cl	<d.l.	0.09	Cl	<d.l.	<d.l.	<d.l.	<d.l.	<d.l.	0.02
Total	96.61	97.42	Total	98.13	98.75	97.75	98.89	98.70	96.72
Si	17.98	18.19	Si	6.42	6.67	6.39	6.21	6.06	6.22
Ti	0.47	0.59	Al	1.58	1.33	1.61	1.79	1.94	1.78
Al	9.30	9.09	Ti	0.00	0.00	0.00	0.00	0.00	0.00
Cr ⁺³	0.02	0.05	Fe ³⁺	0.00	0.00	0.00	0.00	0.00	0.00
Fe ^{+3*}	1.90	2.02	T subtotal	8.00	8.00	8.00	8.00	8.00	8.00
Fe ⁺²	0.00	0.00	Ti	0.06	0.08	0.05	0.07	0.06	0.06
Mn	0.81	0.83	Al	0.68	0.43	0.56	0.62	0.59	0.63
Mg	1.43	1.46	Cr	0.16	0.18	0.05	0.04	0.07	0.02
Ca	17.96	17.68	Mn ³⁺	0.00	0.00	0.00	0.00	0.00	0.00
Na	0.07	0.09	Fe ³⁺	0.00	0.01	0.33	0.49	0.48	0.40
K	0.01	0.01	Mn ²⁺	0.04	0.03	0.00	0.00	0.02	0.00
Total	50.00	50.00	Fe ²⁺	1.87	1.82	2.56	2.52	2.34	2.53
F	3.74	2.26	Mg	2.14	2.46	1.45	1.27	1.44	1.37
Cl	0.00	0.07	Li	0.00	0.00	0.00	0.00	0.00	0.00
O	1.00	1.00	C subtotal	4.94	5.00	5.00	5.00	5.00	5.00
OH	5.26	6.67	Mn ²⁺	0.00	0.00	0.02	0.01	0.02	0.03
			Fe ²⁺	0.00	0.00	0.00	0.04	0.00	0.00
			Mg	0.00	0.00	0.00	0.00	0.00	0.00
			Li	0.00	0.00	0.00	0.00	0.00	0.00
			Ca	1.99	1.97	1.95	1.90	1.96	1.93
			Na	0.01	0.03	0.03	0.05	0.02	0.04
			B subtotal	2.00	2.00	2.00	2.00	2.00	2.00
			Ca	0.00	0.00	0.00	0.00	0.00	0.00
			Li	0.00	0.00	0.00	0.00	0.00	0.00
			Na	0.33	0.25	0.40	0.43	0.40	0.50
			K	0.43	0.35	0.19	0.14	0.29	0.14
			A subtotal	0.77	0.60	0.58	0.57	0.70	0.64
			O (non-W)	22.00	22.00	22.00	22.00	22.00	22.00
			OH	1.49	1.58	1.81	1.69	1.58	1.77
			F	0.51	0.42	0.19	0.32	0.42	0.23
			Cl	0.00	0.00	0.00	0.00	0.00	0.01
			W subtot	2.00	2.00	2.00	2.00	2.00	2.00
			Sum T, C, B,	15.71	15.60	15.58	15.57	15.70	15.64
			X _{Mg}	0.53	0.57	0.36	0.34	0.38	0.35

T: Tetrahedral site; B,C: Octahedral sites; A: Alkali site; W: Anion site;

* All Fe as Fe⁺³; # Dey et al. (2019a)

d.l.: detection limit

4.3.4. Discussion

4.3.4.1. Formation of high aluminous titanites in the studied calc-silicate granulites

The field features, mutual textural relations and composition of minerals in the four associations are consistent with the fact that the hydrous and F-bearing secondary minerals developed proximal to the intruded pegmatitic quartzo-feldspathic veins, and dissected the granulite facies assemblage ($Cpx_1+Pl_1 \pm Grt_1+low\ Al\ titanite$) of the calc-silicate rocks. The comparable primary mineralogy and their compositions of *association 4*, with that of *association 1-3*, and the vestiges of these primary minerals in *association 1-3* are consistent with this observation. The presence of Al-F titanite, restricted only within *association 1-3*, signify that the Al-rich titanite was also formed along with the secondary minerals. An infiltration driven process, with F-bearing aqueous fluid (presumably derived from the pegmatitic veins) seems to be the triggering factor, that stabilized vesuvianite (in *association 2*) or amphibole (in *association 1 and 3*) and high Al-F titanite (in *association 1-3*: 6.8-11.5wt % Al_2O_3 , Fig. 4.3.3d-e; Table 4.3.2d) along with Grt_2 and Pl_2 , after the primary assemblage ($Cpx_1+Pl_1 \pm Grt_1+low\ Al\ titanite$).

Absence of any infiltration driven process in *association 4*, away (>5 km) from the pegmatite veins, preserved the primary anhydrous mineralogy of the calc-silicate rocks, along with the low aluminous titanite (3.4-3.8 wt% Al_2O_3 , Fig. 4.3.3d-e, Table 4.3.2d).

4.3.4.2. Physical conditions of formation of high aluminous titanites

The primary mineral assemblage in all the four rock associations (clinopyroxene + plagioclase + low Al titanite \pm garnet) represent a granulite facies calc-silicate assemblage (Maki et al., 2009), which is consistent with the high-grade metamorphic event (M2) that affected the CGGC. Evidence of this metamorphism is preserved in the other lithounits of the study area, including the pelitic and mafic granulites, as well as the migmatitic felsic orthogneiss (Mukherjee et al., 2017; Dey et al., 2019b, c). Some of these studies (Dey et al., 2019b; Karmakar et al., 2011) also reported the breakdown of garnet into clinopyroxene during the weaning part of M2, similar to that observed in *association 4*. Several rock-types from different parts

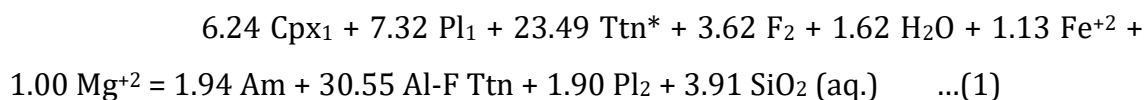
of the CGGC (Domain IB, Mukherjee et al., 2019) also bears evidence of extensive fluid rock interaction processes during the amphibolite facies M3 metamorphism (Ray et al., 2011; Mukherjee et al., 2018b; Dey et al., 2019a). Development of fluid-bearing low temperature mineral assemblages in the studied rock associations at the expense of the primary granulite-facies minerals, is hence consistent with this phase of metamorphism (M3). The study of Dey et al., (2019a) on the vesuvianite-garnet bearing association (*association 2*) also established that, infiltration of F-rich fluid within the studied calc-silicate rock occurred during this amphibolite-facies M3 event. Therefore, the incorporation of Al and F within titanite structure of *association 1-3*, is also possibly related to this metamorphic event (M3). In contrast, preservation of the primary anhydrous mineralogy, absence of any fluid-bearing minerals and veining features in the outcrop of *association 4*, suggests that M3 metamorphism did not leave any major imprints in this rock, possibly due to the unavailability of fluid. The prevailing P-T conditions for M3 were estimated to be ~5.5-6.5 kbar and ~650-750°C (Dey et al., 2019a). Hence, it can be inferred that the fluid influx and the formation of the high Al-F titanites in the studied rock associations, occurred under moderate to low pressures.

4.3.4.3. Reactions and effect of fluid

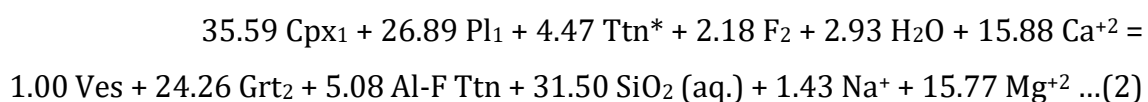
Mass balance calculations were done (using C-Space software) to chemically model the observed possible reaction textures. Details of this methodology has been described in the previous section ('Sample materials and analytical techniques'). Since titanites from *association 1-3* preserve only secondary high Al-F titanites, it is not possible to identify the exact compositions of the primary titanites in these rocks. However, the composition of titanites in *association 4* is most likely to represent the composition of titanite prior to the infiltration of the F-bearing aqueous fluid. Based on this presumption, 'Ttn*' (titanite having the least Al content and devoid of any F; Table 4.3.2d) have been used as proxy for the composition of primary titanites, in modelling the reaction textures. Ttn* compositions, combined with the measured compositions of other minerals from the respective associations, were used to calculate all plausible balanced mineral reactions for the formation of high Al-F titanites and the secondary fluid-bearing minerals in the three rock associations (*association 1-3*). Out of the reactions

generated, the ones that satisfy the textural relations observed in each association, were chosen (i.e., the chosen reactions must have predicted reactants and products on opposite sides, and the volume proportions of the products in the equation must fairly correspond to that observed within the rock textures). A number of studies have demonstrated that Ti and Al are nominally soluble in crustal fluids (Audétat and Keppler, 2005; Tropper and Manning, 2005; Lucassen et al., 2010). Consequently, Al and Ti remain virtually immobile (beyond the grain scale of a few mm) during fluid rock interactions in most of the geological situations (Abart et al., 2012; Chowdhury et al., 2013; Remmert et al., 2018). For this reason, Al and Ti are treated as immobile components during the textural modelling studies. Development of Al-bearing secondary minerals (amphibole, garnet, vesuvianite and Al-rich titanite) in the presence of primary plagioclase and low aluminous titanite are consistent with the above assumption, and suggest local redistribution of Al and Ti at the site of nucleation only. The modelled reactions that can explain the formation of Al-rich titanite in the studied rocks are shown below. All mineral abbreviations used in the reactions are after Kretz, (1983).

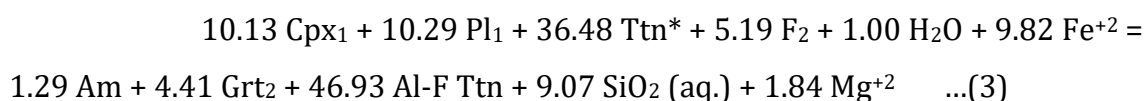
Association 1:



Association 2:



Association 3:



Since the actual volume of titanite in the rocks are low, the volume ratio of the above reactions indicates, correspondingly low proportions of the other fluid-bearing products formed by these reactions. However, it is to be noted that the reactions presented here are not the dominant reactions by which these fluid-bearing minerals form. Rather, these are sub-reactions that occur in local micro-domains associated with the pristine titanite and plagioclase grains (contributing to

the incorporation of Al in titanite structure) simultaneously with many other reactions occurring within the rock volume (Lasaga and Kirkpatrick, 1981). Hence, the actual volume ratio of the fluid-bearing secondary products observed in the rock, are a combined manifestation of all these reactions.

All the above three modelled reactions require destabilization of primary plagioclase and clinopyroxene, and conversion of primary low Al-titanite to Al-F rich titanite along with the formation of secondary hydrous and anhydrous minerals in the *association 1-3*. The modelled mass balanced reactions suggest that a number of species including Fe^{+2} , Mg^{+2} , SiO_2 , Na^+ , Ca^{+2} , F^- and H_2O , behaved as mobile components during the reaction progress. F and H_2O occur on the reactant side of the secondary Al-F rich titanite producing reactions, and petrological attributes suggest that they were sourced from the pegmatite veins.

Experimental studies of Tropper and Manning, (2007) have demonstrated that solubility of CaF_2 and hence F-carrying capacity of aqueous fluid increases with temperature. Presence of NaCl dramatically enhances the solubility of CaF_2 by driving the reaction: $\text{CaF}_2 + \text{NaCl} = \text{CaClF} + \text{NaF}$. Studies have shown that aqueous fluids that are expelled from acid pegmatite can be rich in NaCl and F (Gagnon et al., 2004). In view of these studies, it seems likely that the hot F-bearing aqueous fluid from the pegmatite veins infiltrated the calc-silicate rocks in the study area. Interaction with this fluid can drive the amphibole/ vesuvianite forming reactions (1-3) to the right, and can potentially facilitate the growth of Al-F rich titanite through the coupled substitution $\text{Ti}^{4+} + \text{O}^{2-} \rightarrow \text{Al}^{+3} + (\text{F}^- + \text{OH}^-)$ under virtually isothermal-isobaric condition. Our study therefore, demonstrate that the Ti/Al and F/OH ratios of titanite are not only dependent on the physical conditions of formation, but are complex functions of the fugacities of different components in the coexisting fluid phase, and the mineral assemblage in which the titanite grows.

4.3.4.4. Chemical substitutions in the titanites

Fig.4.3.3d shows a well-defined negative correlation ($R^2=0.99$) between Ti and $(\text{Al}+\text{Fe}^{3+})$ content, which points towards the prevalence of the coupled substitution $\text{Ti}^{4+} + \text{O}^{2-} = (\text{Al}^{3+} + \text{Fe}^{3+}) + (\text{F}^- + \text{OH}^-)$ (Ribbe, 1980; Oberti et al., 1991 and references therein). The extent of substitution is highest in titanites of the

association 2 (Al_2O_3 : ~8-11.5 wt%; $X_{\text{Al}} = [\text{Al}^{+3}/(\text{Al}^{+3} + \text{Fe}^{+3} + \text{Ti}^{+4})] = 0.31-0.46$), whereas *association 1* (Al_2O_3 : ~6.8-9.6 wt%, $X_{\text{Al}} = 0.26-0.36$) and *association 3* (Al_2O_3 : ~7.4-8.5 wt%, $X_{\text{Al}} = 0.28-0.32$) have relatively lower Al_2O_3 (Fig. 4.3.3d, Table 4.3.2d). Titanites in *association 4* shows the least Al_2O_3 (~3.4-3.8 wt% Al_2O_3 , $X_{\text{Al}} = \sim 0.13-0.14$; Fig. 4.3.3d). Al_2O_3 (or X_{Al}) and F in titanite show sympathetic variation in all the associations. Highest F contents are recorded in *association 2* (~1.7-3.8 wt%), followed by *association 1* (~1.7-2.5 wt%) and *association 3* (~1.6-2.4 wt%) (Fig. 4.3.3e, Table 4.3.2d). Notably, the maximum Al contents in titanites from the present study (X_{Al} ranging up to ~0.46, in *association 2*) is the third highest (along with titanites reported by Vakh et al., 2012), and are marginally below the highest reported X_{Al} values in titanites (~0.54: Markl and Piazzolo, 1999; and ~0.53: Granitoids and skarn from SW Japan, Enami et al., 1993), from low to medium pressure rocks till date. Maximum OH contents in titanites of *association 2* (~0.01-0.18 apfu) are also slightly higher than the other two associations (~0.01-0.17 apfu). However, the X_{F} [$\text{F}/(\text{F} + \text{OH})$] ratio in almost all titanites is high (~0.55-0.96: *association 2*, ~0.50-0.94: *association 1 and 3*), suggesting the dominance of Al-F end member in them (Table 4.3.2d). The dashed lines in Fig. a-b depicts the X_{F} contents in titanites. The deviation from 1:1 line in the $(\text{Al} + \text{Fe}^{3+})$ vs F diagram (Fig. 4.3.3e and Fig. 4.3.4a-b) implies the presence of OH as the balancing substituent for $(\text{Al} + \text{Fe}^{3+})$ in addition to F. This feature can be explained by either or combination of the following processes:

- A. Operation of the exchange vector $\text{Ti}^{4+} + \text{O}^{2-} = (\text{Al}, \text{Fe})^{3+} + \text{OH}^-$ (Harlov et al. 2006)
- B. Change of initial F/OH ratio of titanites by re-equilibration with a H_2O -rich fluid.

Fig. 4.3.4a-b compiles and compares the aluminium ($\text{Al} + \text{Fe}^{3+}$) and F contents in natural titanites reported from high-pressure (Fig. 4.3.4a) and low to medium-pressure (≤ 7 kbar) rocks (Fig. 4.3.4b) along with the present study. While high Al-F titanites ($\text{Al} + \text{Fe}^{3+}$ up to 0.53 apfu, F up to 0.55 apfu; Franz and Spear, 1985) were recorded from ultra-high pressure (UHP) rocks (Fig. 4.3.4a), Enami et al. (1993), Markl and Piazzolo (1999) and several others, reported high Al-F titanites, with even higher Al and F contents ($\text{Al} + \text{Fe}^{3+}$ up to 0.55 apfu: Markl and Piazzolo 1999; Enami et al., 1993; F up to 0.58 apfu: Vakh et al., 2012; Fig. 4.3.4b) from low to

medium pressure assemblages. Rare occurrence of high Al-F titanite within natural assemblages is also consistent with the experimental/thermodynamic analyses of Troitzsch and Ellis, (2002) that the species $\text{CaAl}(\text{F}/\text{OH})\text{SiO}_4$ is thermodynamically less stable compared to other natural commonly occurring end member.

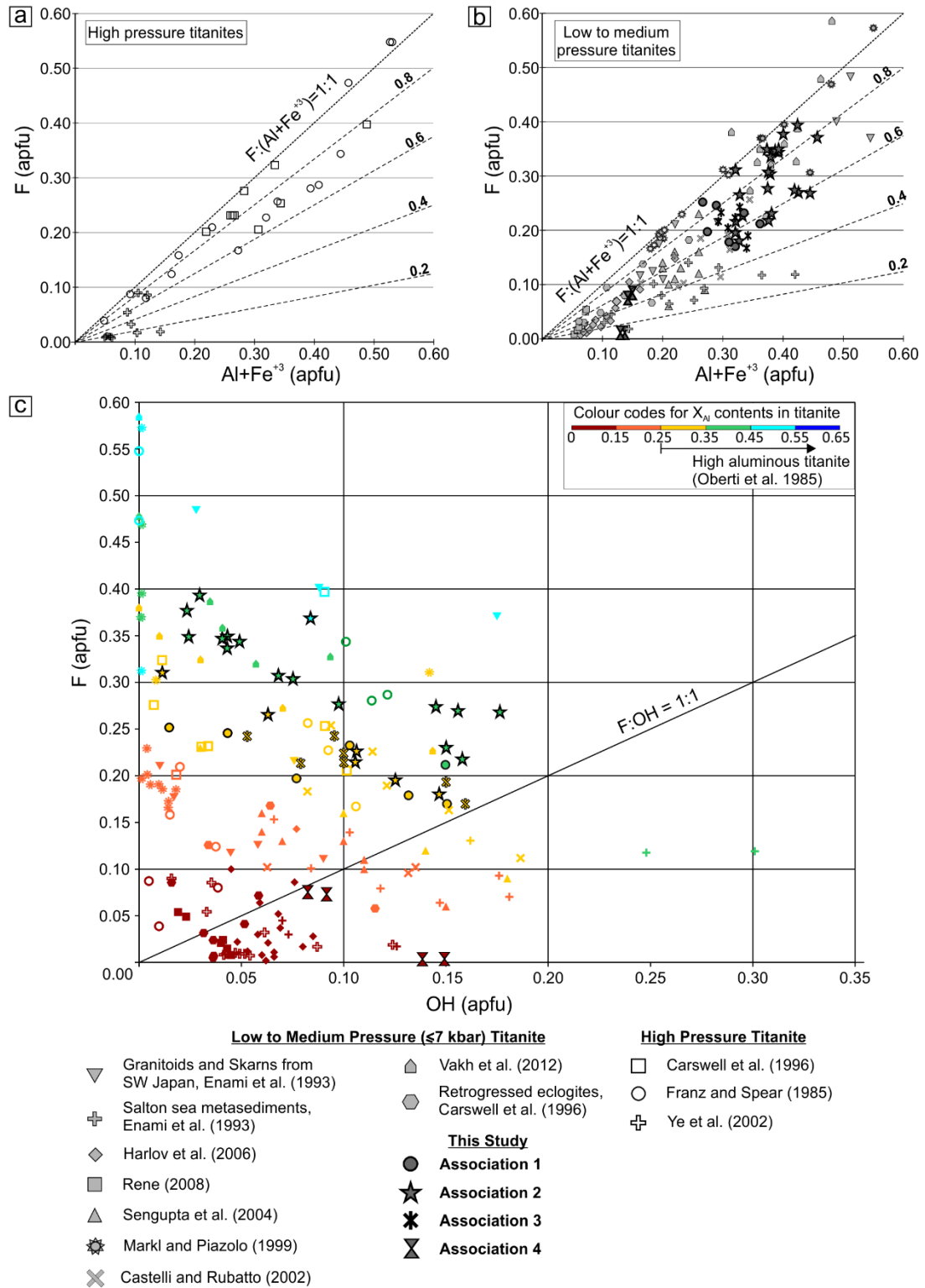


Fig. 4.3.4(a-b) A plot of $(Al+Fe^{3+})$ and $F(apfu)$ showing compilation of titanite data reported in several works (including this study) from (a) high pressure rocks and (b) low to medium pressure rocks. Note that maximum Al and F contents reported are higher in low to medium pressures rocks, than the high-pressure ones. The dashed lines indicate X_F contents in titanites. The deviation from 1:1 line in the $(Al+Fe^{3+})$ vs F diagram (Fig. 5a-b) implies the presence of OH as the balancing substituent for $(Al+Fe^{3+})$ in addition to F. (c) A plot of $F(apfu)$ and $OH(apfu)$, of the above reported titanites (including this study), colour coded for their X_{Al} [$Al^{+3}/(Ti^{+4}+Al^{+3}+Fe^{+3})$] contents (colour code index given inside figure) is presented. The symbols used to represent titanite data from other reports (and the different associations in this study) in figures 5a-c, have been described in index below. Titanite data from our study is given in bold outlines in all the figures.

Fig. 4.3.4c compiles the F and OH content of natural titanites with respect to their X_{Al} contents, reported from various rock assemblages across the globe, including this study. Following observations can be made from the figure:

i) Al-F titanites ($X_F > X_{OH}$; above the 1:1 line) are far more common in nature than Al-OH titanites ($X_{OH} > X_F$; below the 1:1 line).

ii) Titanites with very low Al ($X_{Al} < 0.15$, coloured in deep brown) dominantly belong to the OH-rich end member, and plot below the 1:1 line.

iii) Al-F titanites (i.e., $X_F > X_{OH}$) have variable OH, ranging from OH-free ones (e.g., Franz and Spear, 1985; Markl and Piazzolo, 1999) to having a considerable amount of OH (up to ~ 0.18 apfu; Enami et al., 1993; This study).

iv) It is intriguing to note that, while Al-F titanites with very high Al content (having X_{Al} between 0.45 to 0.54) may be completely devoid of OH (marked in light blue colour, like Franz and Spear, 1985; Markl and Piazzolo, 1999; Vakh et al., 2012), there is no occurrence where Al-OH titanites, with high Al, is devoid of F. Majority of the Al-OH titanites, with $X_{Al} \geq 0.25$, also contain a certain amount of F ($F > 0.10$ apfu) in their structure (data in yellow and green, below 1:1 line; e.g., few titanites from Salton Sea samples, Enami et al., 1993; Castelli and Rubatto, 2002, Sengupta et al., 2004). On the other hand, Al-OH titanites with minor F, dominantly contain negligible Al ($X_{Al} < 0.15$, brown data; e.g., retrogressed eclogites of Carswell et al., 1996; Harlov et al., 2006; Rene, 2008; part of *association 4* of this study).

The presence of significant F even in Al-OH titanites with high Al, raises the possibility that formation of Al-OH titanite results from the interaction of a precursor Al-F titanite with H_2O -bearing fluids. This interaction decreases the F/OH ratio and shifts the composition towards Al-OH titanites. This possibility explains well why Al-OH titanites are rare in nature in spite of the wide availability of hydrous

fluid and low Al titanites in crustal rocks. These observations from natural titanites are also supported by the experimental findings of Lucassen et al., (2010), who recorded greater Al content in titanites when F is present in the system. This, then follows that fugacity of F (F/OH ratio) and availability of Al (Ti/Al ratio) in the bulk composition (which is a function of the mineral and fluid phases in equilibrium with the titanite) seems to be the main regulating factor behind the extent of substitution and incorporation of a significant amount of aluminium ($X_{Al} \geq 0.25$) in titanite structure.

In the studied rocks, the compositional variation of titanites follow the global trend with regard to the relation between the Ti/Al and F/OH ratios in titanite. Titanites in *association 2* exhibit the maximum extent of substitution leading to some of the highest reported Al contents (~8-11.5 wt% Al_2O_3 , $X_{Al} = \sim 0.31-0.46$), accompanied by high F (~1.7-3.8 wt%, ~0.18-0.39 apfu) and variable OH (OH: ~0.01-0.18 apfu). On the other hand, *association 2 and 3* having lower F (~1.6-2.5 wt%, ~0.17-0.25 apfu) but similar OH contents (~0.01-0.17 apfu), correspondingly has lower Al (~6.8-9.6 wt%; $X_{Al} = 0.26-0.36$; Fig. 4.3.4c) contents. Moreover, substitution of Al is not very significant due to the absence/ minimal presence of F in *association 4*. Existing studies (Alaminia et al., 2020) show that, vesuvianite stabilise under relatively higher F-fugacity than amphiboles, implying a variation of f_{F2} within the infiltrated fluid, between *association 1-3*. This is consistent with the findings of Dey et al., (2019a), who also predicted fluctuating F contents, within the fluid infiltrating the studied calc-silicate rocks.

Our study, therefore, demonstrates that the Ti/Al and F/OH ratios in titanite (that depicts the extent of Al incorporation) are complex functions of fugacities of the different components in the coexisting fluid phase and the mineral assemblage in which the titanite grows, even when P-T conditions are held constant. Whether or not the effect of these two parameters can offset the effect of physical conditions needs to be evaluated in future studies. Our study, when combined with global data also infer that variation of f_{F2} within the infiltrated fluid plays the dominant role in regulating the different mineral reactions and controlling the Al incorporation in titanites in the different associations.

References

- Abart R, Petrishcheva E, Joachim B, (2012) Thermodynamic model for growth of reaction rims with lamellar microstructure. *Am. Mineral.* 97: 231–240
- Alaminia Z, Mehrabi B, Razavi S M H, Tecce F, (2020) Mineral chemistry, petrogenesis and evolution of the Ghorveh-Seranji skarn, Northern Sanandaj Sirjan Zone, Iran. *Mineral Petrol.* 114:15–38. [https://doi.org/10.1134/S0016702912040027](https://doi.org/10.1007/s00710-019-00688-Avchenko O V, Vakh A S, Chudnenko K V, Sharova O I, (2012) Physicochemical crystallization conditions of Al-F sphene in metasomatic rocks with ore mineralization at the Berezitovoe Deposit. <i>Geochemistry Int.</i> 50:409–424. <a href=)
- Audétat A, Keppler H, (2005) Solubility of rutile in subduction zone fluids, as determined by experiments in the hydrothermal diamond anvil cell. *Earth Planet. Sci. Lett.* 232: 393–402.
- Bohlen S R, Essene E J, (1978) The significance of metamorphic fluorite in the Adirondacks. *Geochim. Cosmochim. Acta* 42: 1669–1678
- Banerjee M, Dutta U, Anand R, Atlas Z D, (2019) Insights on the process of two-stage coronae formation at olivine-plagioclase contact in mafic dyke from Palghat Cauvery Shear Zone, southern India. *Mineral. Petrol.* 113, 625–649. <https://doi.org/10.1007/s00710-019-00674-y>
- Carswell D A, Wilson R N, Zhai M, (1996) Ultra-high pressure aluminous titanites in carbonate-bearing eclogites at Shuanghe in Dabieshan, central China. *Mineral Mag* 60: 461–471. [10.1180/minmag.1996.060.400.07](https://doi.org/10.1180/minmag.1996.060.400.07)
- Castelli D, Rubatto D, (2002) Stability of Al- and F-rich titanite in metacarbonate: petrologic and isotopic constraints from a polymetamorphic eclogitic marble of the internal Sesia Zone (Western Alps). *Contrib Mineral Petrol* 142:627–639. <https://doi.org/10.1007/s00410-001-0317-6>
- Černý P, Novák M, Chapman R, (1995) The Al (Nb, Ta) Ti (in- 2) substitution in titanite: the emergence of a new species? *Mineral. Petrol.* 52: 61–73
- Dey A, Mukherjee S, Sanyal S, Ibanez-Mejia M, Sengupta P, (2017) Deciphering sedimentary provenance and timing of sedimentation from a suite of metapelites from the Chotanagpur Granite Gneissic Complex, India:

- Implications for Proterozoic Tectonics in the East-Central Part of the Indian Shield, in: *Sediment Provenance*. Elsevier: 453–486
- Dey A, Choudhury SR, Mukherjee S, Sanyal S, Sengupta P, (2019a) Origin of vesuvianite-garnet veins in calc-silicate rocks from part of the Chotanagpur Granite Gneiss Complex, East Indian Shield: The quantitative PTX CO₂ topology in parts of the system CaO-MgO-Al₂O₃-SiO₂-H₂O-CO₂ (+Fe₂O₃, F). *Am Mineral* 104: 744–760. <https://doi.org/10.2138/am-2019-6811>
- Dey A, Karmakar S, Ibanez-Mejia M, Mukherjee S, Sanyal S, Sengupta P, (2019b) Petrology and geochronology of a suite of pelitic granulites from parts of the Chotanagpur Granite Gneiss Complex, eastern India: Evidence for Stenian-Tonian reworking of a late Paleoproterozoic crust. *Geol. J.* 2019:1–30. <https://doi.org/10.1002/gj.3552>
- Dey A, Karmakar S, Mukherjee S, Sanyal S, Dutta U, Sengupta P, (2019c) High pressure metamorphism of mafic granulites from the Chotanagpur Granite Gneiss Complex, India: Evidence for collisional tectonics during assembly of Rodinia. *J. Geodyn* 129: 24–43. <https://doi.org/10.1016/j.jog.2019.03.005>
- Droop G T R, (1987) A General Equation for Estimating Fe³⁺ Concentrations in Ferromagnesian Silicates and Oxides from Microprobe Analyses, Using Stoichiometric Criteria. *Mineral Mag* 51:431–435. <https://doi.org/10.1180/minmag.1987.051.361.10>
- Enami M, Suzuki K, Liou J G, Bird D K, (1993) Al-Fe³⁺ and F-OH substitutions in titanite and constraints on their PT dependence. *Eur J Mineral* 5: 219–232. <https://doi.org/10.1127/ejm/5/2/0219>
- Franz G, Spear F S, (1985) Aluminous titanite (sphene) from the eclogite zone, south-central Tauern Window, Austria. *Chem Geol* 50: 33–46. [https://doi.org/10.1016/0009-2541\(85\)90110-X](https://doi.org/10.1016/0009-2541(85)90110-X)
- Frost B R, Chamberlain K R, Schumacher J C, (2001) Sphene (titanite): phase relations and role as a geochronometer. *Chem. Geol.* 172: 131–148
- Gagnon J E, Samson I M, Fryer B J, Williams-Jones A E, (2004) The composition and origin of hydrothermal fluids in a NYF-type granitic pegmatite, South Platte District, Colorado: evidence from LA-ICP-MS analysis of fluorite-and quartz-

- hosted fluid inclusions. *Can. Mineral.* 42: 1331–1355
- Garber J M, Hacker B R, Kylander-Clark A R C, Stearns M, Seward G, (2017) Controls on trace element uptake in metamorphic titanite: Implications for petrochronology. *J. Petrol.* 58: 1031–1057
- Green T H, Pearson N J, (1986) Rare-earth element partitioning between sphene and coexisting silicate liquid at high pressure and temperature. *Chem. Geol.* 55: 105–119
- Grew E S, Locock A J, Mills S J, Galuskina I O, Galuskin E V, Hålenius U, (2013) Nomenclature of the garnet supergroup. *Am Mineral* 98: 785–811
- Harlov D, Tropper P, Seifert W, Nijland T, Förster H J, (2006) Formation of Al-rich titanite (CaTiSiO₄O–CaAlSiO₄OH) reaction rims on ilmenite in metamorphic rocks as a function of fH₂O and fO₂. *Lithos* 88:72–84. <https://doi.org/10.1016/j.lithos.2005.08.005>
- Hawthorne F C, Oberti R, Harlow G E, Maresch W V, Martin R F, Schumacher J C, Welch M D, (2012). Nomenclature of the amphibole supergroup. *Am. Mineral.* 97: 2031–2048.
- Higgins J B, Ribbe P H, (1976) The crystal chemistry and space groups of natural and synthetic titanites. *Am Mineral* 61:878–888.
- Karmakar S, Bose S, Sarbadhikari A B, Das K, (2011) Evolution of granulite enclaves and associated gneisses from Purulia, Chhotanagpur Granite Gneiss Complex, India: evidence for 990–940 Ma tectonothermal event (s) at the eastern India cratonic fringe zone. *J Asian Earth Sci* 41: 69–88. <https://doi.org/10.1016/j.jseaes.2010.12.006>
- Karmakar S, Mukherjee S, Sanyal S, Sengupta P, (2017) Origin of peraluminous minerals (corundum, spinel, and sapphirine) in a highly calcic anorthosite from the Sittampundi Layered Complex, Tamil Nadu, India. *Contrib Mineral Petrol* 172:1–23. <https://doi.org/10.1007/s00410-017-1383-8>
- Kohn M J, (2017) Titanite petrochronology. *Rev. Mineral. Geochemistry* 83: 419–441
- Lasaga A C, Kirkpatrick R J, (1981) Rate laws of chemical reactions, in *Reviews in Mineral, Volume 8: Kinetics in Geochemical Processes* (ed):pp 1-68. <https://doi.org/10.1515/9781501508233>

- Lucassen F, Franz G, Rhede D, Wirth R, (2010) Ti-Al zoning of experimentally grown titanite in the system CaO-Al₂O₃-TiO₂-SiO₂-NaCl-H₂O-(F): Evidence for small-scale fluid heterogeneity. *Am Mineral* 95: 1365–1378. <https://doi.org/10.2138/am.2010.3518>
- Maki K, Fukunaga Y, Nishiyama T, Mori Y, (2009) Prograde P–T path of medium-pressure granulite facies calc-silicate rocks, Higo metamorphic terrane, central Kyushu, Japan. *J Metamorph Geol* 27: 107–124. <https://doi.org/10.1111/j.1525-1314.2008.00808.x>
- Markl G, Piazzolo S, (1999) Stability of high-Al titanite from low-pressure calcsilicates in light of fluid and host-rock composition. *Am Mineral* 84:37–47. <https://doi.org/10.2138/am-1999-1-204>
- Mukherjee S, Dey A, Sanyal S, Ibanez-Mejia M, Dutta U, Sengupta P, (2017) Petrology and U–Pb geochronology of zircon in a suite of charnockitic gneisses from parts of the Chotanagpur Granite Gneiss Complex (CGGC): evidence for the reworking of a Mesoproterozoic basement during the formation of the Rodinia supercontinent. *Geol. Soc. London, Spec. Publ.* 457: 197–231. <https://doi.org/10.1144/SP457.6>
- Mukherjee S, Dey A, Ibanez-Mejia M, Sanyal S, Sengupta P, (2018a) Geochemistry, U–Pb geochronology and Lu–Hf isotope systematics of a suite of ferroan (A-type) granitoids from the CGGC: Evidence for Mesoproterozoic crustal extension in the east Indian shield. *Precambrian Res* 305:40–63. <https://doi.org/10.1016/j.precamres.2017.11.018>
- Mukherjee S, Dey A, Sanyal S, Sengupta P, (2018b) Tectonothermal imprints in a suite of mafic dykes from the Chotanagpur Granite Gneissic complex (CGGC), Jharkhand, India: Evidence for late Tonian reworking of an early Tonian continental crust. *Lithos* 320–321:490–514. <https://doi.org/10.1016/j.lithos.2018.09.014>
- Mukherjee S, Dey A, Sanyal S, Sengupta P, (2019) Proterozoic crustal evolution of the Chotanagpur Granite Gneissic complex, Jharkhand-Bihar-West Bengal, India: current status and future prospect. In: Mukherjee S (ed) *Tectonics and Structural Geology: Indian Context*. Springer Nature, Switzerland: pp 7–54

- Oberti R, Rossi G, Smith D C, (1985) X-ray crystal structure refinement studies of the TiO \rightarrow Al (OH, F) exchange in high-aluminum sphenes. *Terra Cogn.* 5, 428
- Oberti R, Smith D C, Rossi G, Caucia F, (1991) The crystal-chemistry of high-aluminium titanites. *Eur J Mineral* 3: 777–792.
<https://doi.org/10.1127/ejm/3/5/0777>
- Pan L C, Hu R Z, Bi X W, Li C, Wang X S, Zhu J J, (2018) Titanite major and trace element compositions as petrogenetic and metallogenic indicators of Mo ore deposits: Examples from four granite plutons in the southern Yidun arc, SW China. *Am. Mineral. J. Earth Planet. Mater.* 103: 1417–1434
- Prowatke S, Klemme S, (2005) Effect of melt composition on the partitioning of trace elements between titanite and silicate melt. *Geochim. Cosmochim. Acta* 69: 695–709
- Ray S, Sanyal S, Sengupta P, (2011) Mineralogical control on rheological inversion of a suite of deformed mafic dykes from parts of the Chottanagpur Granite Gneiss Complex of eastern India, in: *Dyke Swarms: Keys for Geodynamic Interpretation.* Springer-Verlag, Berlin Heidelberg: 263–276.
<https://doi.org/10.1007/978-3-642-12496-9>
- Rapa G, Groppo C, Rolfo F, Petrelli M, Mosca P, Perugini D, (2017) Titanite-bearing calc-silicate rocks constrain timing, duration and magnitude of metamorphic CO₂ degassing in the Himalayan belt. *Lithos* 292: 364–378
- Remmert P, Heinrich W, Wunder B, Morales L, Wirth R, Rhede D, Abart R, (2018) Synthesis of monticellite–forsterite and merwinite–forsterite symplectites in the CaO–MgO–SiO₂ model system: influence of temperature and water content on microstructure evolution. *Contrib. to Mineral. Petrol.* 173: 1–17
- Rene M, (2008) Titanite-ilmenite-magnetite phase relations in amphibolites of the Chynov area (Bohemian massif, Czech Republic). *Acta Geodyn. Geomaterialia* 5:239–246
- Ribbe PH (1980): Titanite (sphene). In: Ribbe PH (editor): *Orthosilicates*, Volume 5, 2nd edition. *Reviews in Mineral* (5): 137–154.
<https://doi.org/doi:10.1515/9781501508622-010>

- Sanyal S, Sengupta P, & Goswami R, (2007) Evidence of Mesoproterozoic ultra-high temperature meta-morphism from parts of CGGC, Jharkhand, India. In Abstract volume of the International Conference on Precambrian Sedimentation and Tectonics and Second GPSS Meeting, pp. 62–63, Bombay: Indian Institute of Technology
- Sengupta P, Raith M M, Datta A, (2004) Stability of fluorite and titanite in a calc-silicate rock from the Vizianagaram area, Eastern Ghats Belt, India. *J Metamorph Geol* 22: 345–359. <https://doi.org/10.1111/j.1525-1314.2004.00518.x>
- Singh R N, Thorpe R, Kristic D, (2001) Galena Pb isotope data of base metal occurrences in the Hesatu-Belbathan belt, eastern Precambrian shield, Bihar. *J. Geol. Soc. India (Online Arch. from Vol 1 to Vol 78)* 57: 535–538
- Smith D C, (1980) Highly aluminous sphene (titanite) in natural high-pressure hydrous-eclogite facies rocks from Norway and Italy, and in experimental runs at high pressure. *Congres Geologique International*. 26/1980/Paris; FRA; Orleans: B.R.G.M.; DA. 1: 145
- Storey C D, Smith M P, (2017) Metal source and tectonic setting of iron oxide-copper-gold (IOCG) deposits: Evidence from an in situ Nd isotope study of titanite from Norrbotten, Sweden. *Ore Geol. Rev.* 81: 1287–1302
- Troitzsch U, Ellis D J, (2002) Thermodynamic properties and stability of AlF-bearing titanite $\text{CaTiOSiO}_4\text{-CaAlFSiO}_4$. *Contrib. to Mineral. Petrol.* 142: 543–563
- Troitzsch U, Ellis D J, (1999) The synthesis and crystal structure of CaAlFSiO_4 , the Al-F analog of titanite. *Am. Mineral.* 84:1162–1169
- Troitzsch U, Ellis D J, Thompson J, Fitz Gerald J, (1999) Crystal structure changes in titanite along the join TiO-AlF. *Eur. J. Mineral.* 11: 955–965
- Tropper P, Manning C E, (2007) The solubility of fluorite in H_2O and $\text{H}_2\text{O-NaCl}$ at high pressure and temperature. *Chem. Geol.* 242: 299–306
- Tropper P, Manning C E, (2005) Very low solubility of rutile in H_2O at high pressure and temperature, and its implications for Ti mobility in subduction zones. *Am. Mineral.* 90: 502–505
- Tropper P, Manning C E, Essene E J, (2002) The substitution of Al and F in titanite at

high pressure and temperature: experimental constraints on phase relations and solid solution properties. *J. Petrol.* 43: 1787–1814

Vakh A S, Avchenko O V, Karabtsov A A, Stepanov V A, (2012) High-alumina titanite in mineral assemblages of the Berezitovy gold-base-metal deposit, Upper Amur Region. *Geol. Ore Depos* 54: 580–588. <https://doi.org/10.1134/S1075701511080162>

Valley J W, Essene E J, Peacor D R, (1983) Fluorine-bearing garnets in Adirondack calc-silicates. *Am. Mineral.* 68: 444–448

Ye K, Liu J B, Cong B L, Ye D N, Xu P, Omori S, Maruyama S, (2002) Ultrahigh-pressure (UHP) low-Al titanites from carbonate-bearing rocks in Dabieshan-Sulu UHP terrane, eastern China. *Am Mineral* 87: 875–881. <https://doi.org/10.2138/am-2002-0710>

Whitney D L, Evans B W, (2010). Abbreviations for names of rock-forming minerals. *Am. Mineral.* 95, 185–187. <https://doi.org/10.2138/am.2010.3371>

Chapter-5

Metamorphic evolution of the pelitic granulite

Chapter 5

Metamorphic evolution of pelitic granulite

The pelitic granulites are the most abundant amongst the meta-sedimentary enclaves in the study area. Moreover, these rocks preserve multiple metamorphic and deformation histories. Owing to its bulk composition, these rocks develop distinct mineral assemblages that help trace multiple metamorphic events. Moreover, zircon and monazite are common accessory minerals in pelitic bulk, which makes these rocks very useful for geochronologic studies. This chapter deals with the field relations, petrographic study, mineral compositional variation and P-T conditions of metamorphism of some selected pelitic granulites from the study area. The studied sample locations have been shown in Fig. 3.1.

5.1. Field Observation

The pelitic granulites occur as several meter to kilometre long enclaves within the migmatitic felsic gneiss country rock. These rocks show prominent migmatitic bandings, with alternate leucosomal and melanosomal segregations (Fig. 5.1a). These migmatitic fabric has a general N-S trend. Two generations of leucosome-melanosomes (S1 and S2) are present. The S1 leucosomes, the earliest fabric that could be discerned from the study area, are thick, constituting >30% of the total rock volume (Fig. 5.1b). The S1 leucosomes show tight to isoclinal folds, and S2 fabric develops axial planar to these folds (Fig. 5.1c-d). S1 and S2 intersect each other at high angles only at the hinges, and become parallel (trending N-S) at the limbs, indicating transposition of the S1 fabric. S1 leucosomes comprise quartz + K-feldspar \pm plagioclase, along with large garnets (Fig. 5.1b). Thin, discontinuous leucosomes (varying between few millimetres, comprising \sim 10% by volume of the rock) are also associated with the S2 foliation (Fig. 5.1d). These S2 leucosomes also show folding, but on a larger scale. S2 foliation is defined primarily by oriented sillimanite-biotite grains. Small garnets are also associated with the S2 fabric (Fig. 5.1d). Extent of development of S2 foliation varies in different outcrops. The S2

foliation is dominant in certain outcrops (AS1, AS17). Previous studies (Dey et al., 2019a) have inferred that the S1 foliation developed during the earliest metamorphic event (~1680-1580 Ma, M1), while folding of S1, and development of S2 has been attributed to the second major tectonic event (M2) that affected the CGGC during the early Neoproterozoic. In the following sections the petrological evolution of the pelitic granulites (AS1 and AS17) will be presented with the emphasis on the Neoproterozoic metamorphic imprints.

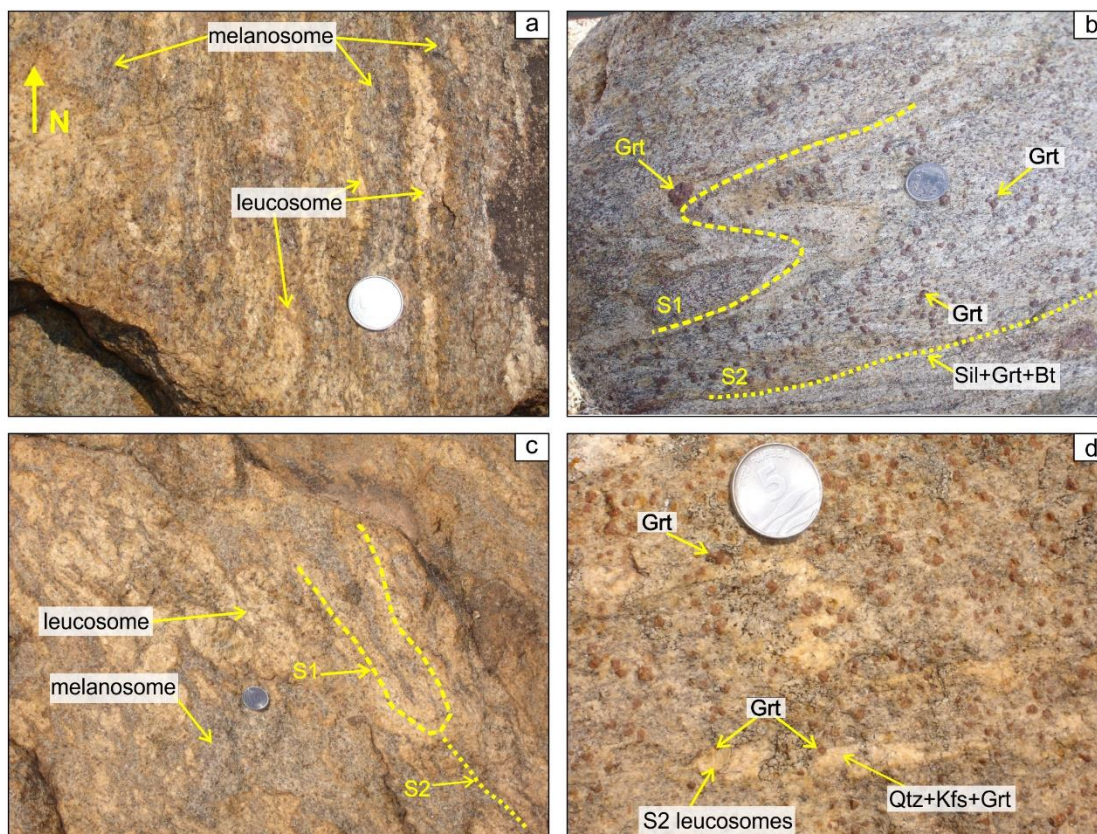


Fig. 5.1(a-d): Field features of the metapelitic enclaves. (a) Leucosomal and melanosomal segregations within the metapelitic enclaves. (b-c) Thick S1 leucosomes showing tight to isoclinal folds. Note that S1 and S2 are parallel at the limbs. Large garnets present within S1 leucosomes. S1 folding with axial planar S2 foliation (c). (d) Thin S2 leucosomal segregations comprising garnet. All mineral abbreviations are after Kretz, (1983).

5.2. Petrography

Detailed petrography from a number of thin sections were done from both the samples (AS1 and AS17). The overall textural relations are same in the two studied samples, and hence are described together.

The S2 leucosomal and melanosomal segregations are very thin. The overall mineral assemblage of the S2 melanosomes is dominated by biotite, sillimanite, garnet, ilmenite \pm rutile, with small amount of quartz, alkali feldspar (some perthite grains are also present) and plagioclase. These quartzo-feldspathic minerals define a granoblastic mosaic. The S2 foliation is defined by euhedral prismatic sillimanite and prismatic biotite (Fig. 5.2a). Medium-to large sized garnet porphyroblasts are associated with this S2 foliation. These garnet porphyroblasts are idioblastic to subidioblastic in shape. These garnets are distinctly different in appearance, than those associated with S1 fabric. S1 garnets have abundant inclusions within them, along with an inclusion free rim (S2 garnet; Fig. 5.2b see Dey et. al., 2019 for details). In contrast to S1 garnets, these S2 garnets are nearly inclusion free. Of the few inclusions present, quartz and rare rutile and biotite are the constituting minerals (Fig.5.2c). Although not found in this sample, kyanite inclusions are present within porphyroblasts of garnet associated with S2 in other samples (Dey et al., 2019a). The garnet porphyroblasts share straight equilibrium boundaries with the euhedral to slightly elongated sillimanites and matrix biotites (Fig. 5.2c-d). Garnet, prismatic biotite and sillimanite, along with K-feldspar, plagioclase and quartz (in the melanosome matrix) define a granoblastic texture.

Apart from rare inclusions in garnet, rutile is also present in matrix, associated with the sillimanite-biotite aggregates. These matrix rutile grains are mostly replaced partially by matrix ilmenite grains (Fig. 5.2e). Locally, a thin quartzo-feldspathic rim develops around the garnet porphyroblasts, suggesting crystallised melt. Less commonly, however, these garnet porphyroblasts are also replaced by biotite with fibrolitic sillimanite aggregates. (Fig.5.2f-g). These fibrolites also replace euhedral stumpy sillimanites and the matrix biotite, K-feldspar grains (Fig.5.2h-i). Ilmenite is also associated with these fibrolitic sillimanite-biotite intergrowths (Fig.5.2h).

On the other hand, the thin S2 leucosomes are dominated by K-feldspar, quartz, along with a subordinate amount of biotite, and minor garnet, sillimanite and plagioclase.

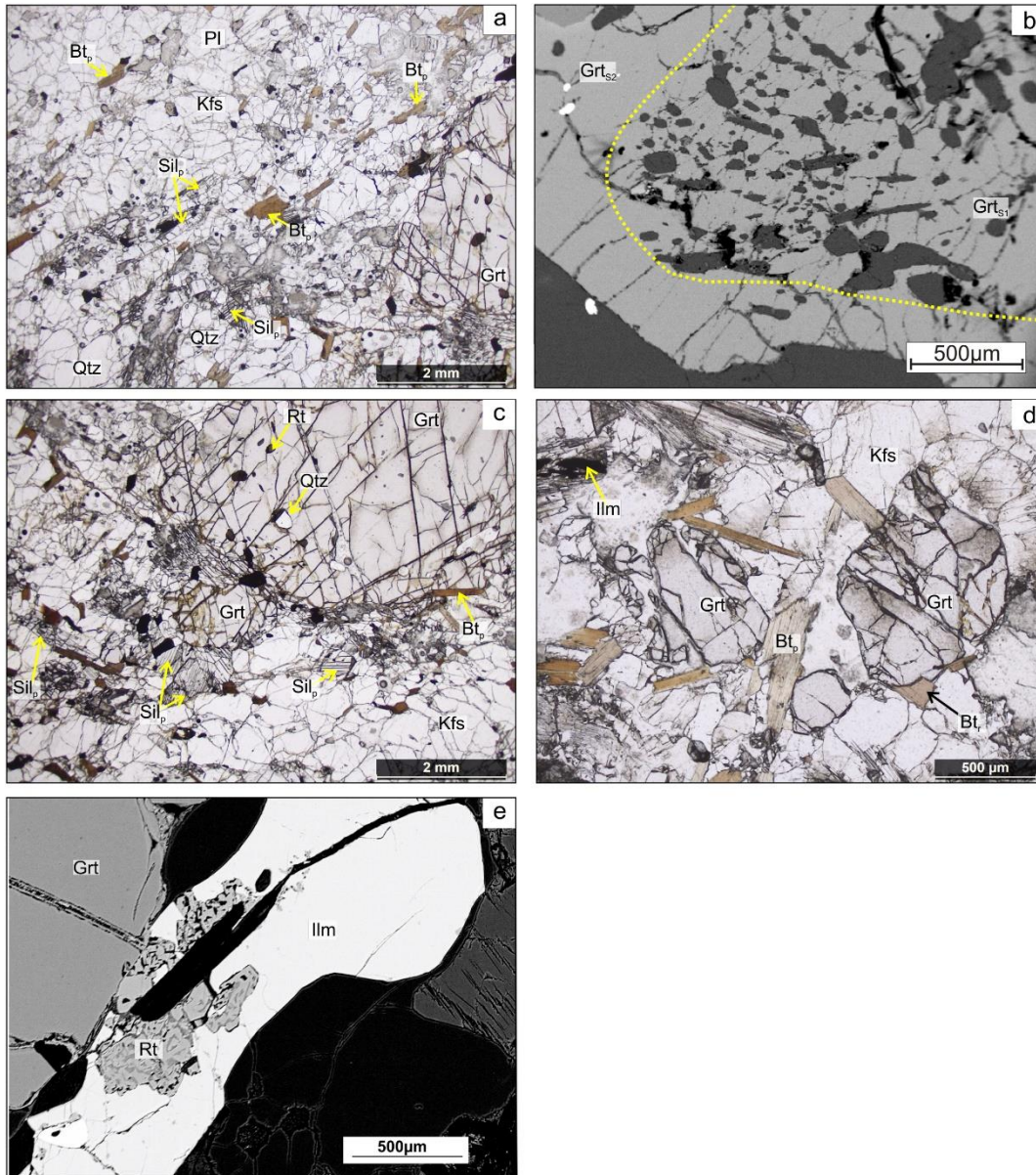


Fig. 5.2: (a) Prismatic sillimanite and biotite defining S2 foliation. (b) S1 garnet with numerous inclusions, and rimmed by S2 garnet. Figure taken from Dey et al., 2019a. (c-d) S2 Garnet porphyroblasts with rare inclusions of rutile and quartz. Prismatic biotite and sillimanite share straight margin with garnet. (e) Rutile grains partially replaced by ilmenite in matrix. Sil_p, Sil_f: Prismatic and fibrolitic sillimanite, Bt_p, Bt_r: Prismatic and replacing biotite respectively. All mineral abbreviations are after Kretz, (1983).

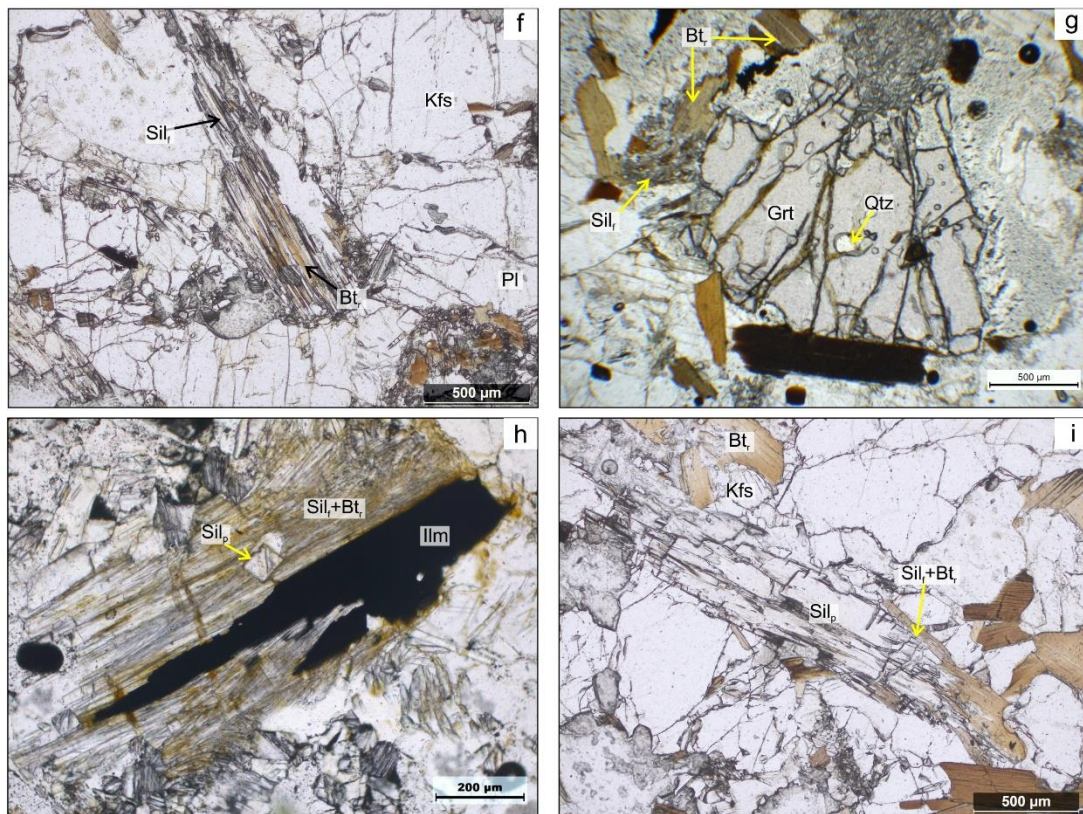


Fig. 5.2(f-i): Fibrolitic sillimanite and biotite replaces garnet and prismatic sillimanite. Ilmenite is locally associated with these fibrolites. Sil_p , Sil_f : Prismatic and fibrolitic sillimanite, Bt_p , Bt_r : Prismatic and replacing biotite respectively. All mineral abbreviations are after Kretz, (1983).

5.3. Mineral Chemistry

Mineral compositions were measured using a Cameca SX100 Electron Probe Micro Analyzer (EPMA) at the Department of Geology and Geophysics, Indian Institute of Technology, Kharagpur. All points were analyzed with an acceleration voltage of 15 kV, a beam current of 20 nA and a beam size of 1-3 μm . Dwell time for the measured elements was set as 10 sec at peak and 5 sec at background. Natural and synthetic samples were used for standards. The representative mineral analyses are presented in Table 5.1-5.4. Abbreviations for the mineral names in the figures and tables have been used after Kretz, (1983).

5.3.1. Garnet

Garnet is a solid solution of pyrope and almandine, with minor grossular and spessartine components. There is small variation in garnet composition between the two samples (AS1 and AS17). In AS1, the garnet core ($X_{Mg}:0.15-0.16$; $Alm_{0.77-0.79}Prp_{0.14-0.15}Grs_{0.02-0.03}Sps_{0.03}$) compositions are slightly more magnesian than rim ($X_{Mg}:0.12-0.14$; $Alm_{0.80-0.81}Prp_{0.11-0.13}Grs_{0.03-0.04}Sps_{0.03}$; Table 5.1). However, garnet grains have slightly higher magnesium content in AS17 than AS1. The garnet core ($X_{Mg}:0.20-0.21$; $Alm_{0.75-0.77}Prp_{0.18-0.20}Grs_{0.02-0.03}Sps_{0.01}$) compositions have slightly higher magnesian content than its rim ($X_{Mg}:0.14-0.17$; $Alm_{0.79-0.81}Prp_{0.13-0.16}Grs_{0.02}Sps_{0.01}$; Table 5.1). Fig. 5.3 depicts the change in garnet composition from a magnesian core to a relatively less magnesian rim adjacent to biotite in sample AS17.

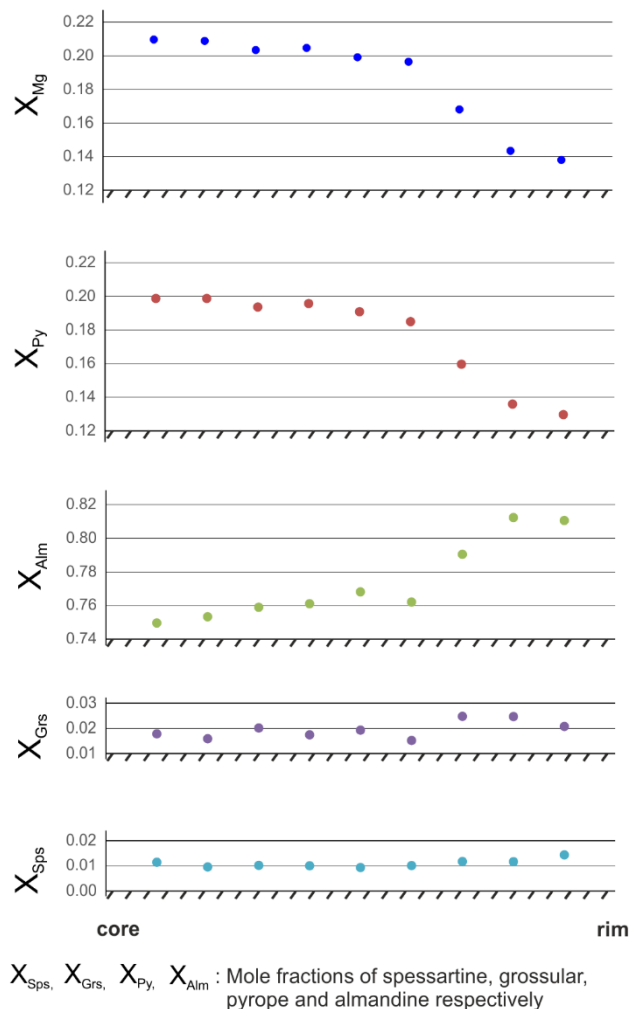


Fig. 5.3:
Representative
compositional
zoning profiles of
garnet in sample
AS17. The
profiles extend
from core to rim.
All mineral
abbreviations
are after Kretz,
(1983).

5.3.2. Biotite

In AS1, the biotite included in garnet porphyroblasts are the most magnesian (X_{Mg} :0.53; Table 5.2). The matrix biotites (defining the S2 foliation) are slightly less magnesian (X_{Mg} :0.44-0.46) relative to those adjacent to garnet porphyroblasts (X_{Mg} : 0.48-0.49). However, biotites in AS17 are slightly less magnesian than AS1. The biotites adjacent to garnet (X_{Mg} : 0.45-0.48; Table 5.2) have higher magnesian content than the matrix ones (X_{Mg} : 0.41-0.45; Table 5.2).

5.3.3. Feldspar

Plagioclase is albite rich ($Or_{0.01}Ab_{0.64}An_{0.35-0.36}$; Table 5.3). K-feldspar is dominated by orthoclase ($KAlSi_3O_8$) component, with minor albite ($Or_{0.86-0.91}Ab_{0.09-0.14}An_{0.0}$; Table 5.3). On the other hand, albitic lamellae exsolved within K-feldspar host are nearly pure albite (~97 mol% albite component), with minor orthoclase (~2mol%) and anorthite content (~1 mol%; Table 5.3).

5.3.4. Ilmenite

Ilmenites are nearly pure. MgO and MnO contents vary up to 1wt% and 0.2 wt% respectively (Table 5.4).

Other phases

Rutile, sillimanite and quartz are pure phases.

Table 5.1: Representative electron microprobe analysis of garnet (stoichiometry calculated on the basis of 12 oxygens, oxide data are given in weight %).

Texture	AS1				AS17																		
	Point No. 62/1.79/1.81/1.63/1.		7/1.14/1.8/1.8/2.8/3.8/4.8/5.8/6.8/8.8/9.8/10.23/1.		garnet profile data																		
	core	rim	core	rim	core	core	core	core	core	core	core	core	core	core	core	core	core	core	core	core	rim	rim	
SiO ₂	37.61	37.54	37.26	37.41	38.06	38.20	37.51	37.96	37.53	37.98	38.16	37.99	37.70	37.76	37.41	37.66							
TiO ₂	0.00	0.00	0.05	0.05	0.00	0.03	0.04	0.00	0.00	0.07	0.00	0.04	0.00	0.00	0.00	0.01							
Al ₂ O ₃	20.83	20.76	20.83	21.32	21.19	21.33	20.99	21.27	21.03	21.08	21.37	20.95	21.09	21.19	20.75	20.73							
Cr ₂ O ₃	0.00	0.00	0.03	0.00	0.00	0.00	0.00	0.00	0.00	0.00	0.00	0.00	0.00	0.00	0.00	0.00							
FeO	36.07	36.53	37.07	35.87	35.52	35.64	34.67	35.22	34.97	35.35	35.63	36.16	36.28	37.53	37.55	36.86							
MnO	1.16	1.29	1.10	1.31	0.50	0.47	0.51	0.43	0.46	0.45	0.42	0.46	0.53	0.52	0.64	0.62							
MgO	3.81	3.50	2.90	3.26	5.06	4.98	5.06	5.11	4.93	5.03	4.92	4.82	4.07	3.48	3.30	3.95							
CaO	1.17	1.21	1.30	1.32	0.92	1.00	0.89	0.84	0.91	0.81	0.84	0.94	1.04	1.06	1.02	1.11							
Na ₂ O	0.05	0.02	0.00	0.02	0.03	0.00	0.03	0.02	0.00	0.00	0.01	0.01	0.02	0.00	0.00	0.01							
K ₂ O	0.02	0.00	0.01	0.00	0.01	0.00	0.00	0.00	0.00	0.00	0.00	0.00	0.00	0.00	0.00	0.00							
Total	100.71	100.85	100.57	100.61	101.30	101.78	99.78	101.03	99.84	100.92	101.42	101.37	100.73	101.54	100.76	100.95							
Si	3.00	3.00	2.99	2.99	2.99	2.99	2.99	2.99	2.99	2.99	3.00	2.99	3.00	2.99	3.00	3.00							
Ti	0.00	0.00	0.00	0.00	0.00	0.00	0.00	0.00	0.00	0.00	0.00	0.00	0.00	0.00	0.00	0.00							
Al	1.96	1.95	1.97	2.01	1.96	1.97	1.97	1.98	1.98	1.96	1.98	1.95	1.98	1.98	1.96	1.94							
Cr ⁺³	0.00	0.00	0.00	0.00	0.00	0.00	0.00	0.00	0.00	0.00	0.00	0.00	0.00	0.00	0.00	0.00							
Fe ⁺³	0.06	0.05	0.03	0.00	0.06	0.04	0.05	0.05	0.03	0.03	0.02	0.07	0.03	0.03	0.05	0.06							
Fe ⁺²	2.35	2.39	2.46	2.39	2.28	2.29	2.27	2.28	2.30	2.30	2.32	2.32	2.39	2.46	2.47	2.39							
Mn	0.08	0.09	0.08	0.09	0.03	0.03	0.03	0.03	0.03	0.03	0.03	0.03	0.04	0.04	0.04	0.04							
Mg	0.45	0.42	0.35	0.39	0.59	0.58	0.60	0.60	0.59	0.59	0.58	0.57	0.48	0.41	0.39	0.47							
Ca	0.10	0.10	0.11	0.11	0.08	0.08	0.08	0.07	0.08	0.07	0.07	0.08	0.09	0.09	0.09	0.09							
Na	0.01	0.00	0.00	0.00	0.00	0.00	0.00	0.00	0.00	0.00	0.00	0.00	0.00	0.00	0.00	0.00							
K	0.00	0.00	0.00	0.00	0.00	0.00	0.00	0.00	0.00	0.00	0.00	0.00	0.00	0.00	0.00	0.00							
Total	8.00	8.00	8.00	8.00	8.00	8.00	8.00	8.00	8.00	8.00	8.00	8.00	8.00	8.00	8.00	8.00							
X _{Adr}	0.03	0.03	0.02	0.00	0.03	0.02	0.02	0.02	0.02	0.02	0.01	0.03	0.01	0.02	0.02	0.03							
X _{Py}	0.15	0.14	0.11	0.13	0.20	0.19	0.20	0.20	0.19	0.20	0.19	0.18	0.16	0.14	0.13	0.15							
X _{Alm}	0.77	0.78	0.81	0.80	0.75	0.76	0.75	0.75	0.76	0.76	0.77	0.76	0.79	0.81	0.81	0.78							
X _{Grs}	0.02	0.03	0.03	0.04	0.02	0.02	0.02	0.02	0.02	0.02	0.02	0.02	0.02	0.02	0.02	0.02							
X _{Sps}	0.03	0.03	0.02	0.03	0.01	0.01	0.01	0.01	0.01	0.01	0.01	0.01	0.01	0.01	0.01	0.01							
X _{Mg}	0.16	0.15	0.12	0.14	0.21	0.20	0.21	0.21	0.20	0.20	0.20	0.20	0.17	0.14	0.14	0.16							

Table 5.2: Representative electron microprobe analysis of biotite (stoichiometry calculated on the basis of 11 oxygens, oxide data are given in weight %).

Point No.	AS1					AS17			
	76 / 1 .	66 / 1 .	78 / 1 .	64 / 1 .	82 / 1 .	9 / 1 .	24 / 1 .	26 / 1 .	27 / 1 .
Texture	matrix		matrix	rim	rim	matrix	matrix	rim	rim
SiO ₂	34.52	35.07	35.78	35.58	35.67	36.55	36.98	36.15	36.34
TiO ₂	4.91	5.17	5.05	4.50	3.97	4.32	4.46	5.38	3.93
Al ₂ O ₃	17.20	17.11	17.29	17.42	17.04	15.89	15.98	15.84	15.89
FeO	16.30	19.79	19.04	18.73	18.73	17.14	15.82	17.64	17.93
MnO	0.00	0.06	0.00	0.00	0.01	0.07	0.00	0.00	0.00
MgO	10.27	8.69	8.98	9.72	10.29	11.75	12.68	10.70	12.05
CaO	0.05	0.00	0.00	0.00	0.00	0.03	0.00	0.07	0.00
Na ₂ O	0.26	0.05	0.14	0.11	0.09	0.09	0.10	0.14	0.11
K ₂ O	9.97	10.37	10.26	10.70	10.70	9.61	9.56	9.51	9.72
Total	93.53	96.34	96.56	96.80	96.54	96.05	96.08	95.77	96.24
Si	2.74	2.75	2.79	2.75	2.75	2.83	2.85	2.83	2.81
Ti	0.29	0.30	0.30	0.26	0.23	0.25	0.26	0.32	0.23
Al	1.61	1.58	1.59	1.59	1.55	1.45	1.45	1.46	1.45
Fe ⁺³	0.00	0.00	0.00	0.00	0.00	0.00	0.00	0.00	0.00
Fe ⁺²	1.08	1.30	1.24	1.21	1.21	1.11	1.02	1.16	1.16
Mn	0.00	0.00	0.00	0.00	0.00	0.00	0.00	0.00	0.00
Mg	1.22	1.02	1.04	1.12	1.18	1.36	1.46	1.25	1.39
Ca	0.00	0.00	0.00	0.00	0.00	0.00	0.00	0.01	0.00
Na	0.04	0.01	0.02	0.02	0.01	0.01	0.02	0.02	0.02
K	1.01	1.04	1.02	1.05	1.05	0.95	0.94	0.95	0.96
Total	8.00	8.00	8.00	8.00	8.00	8.00	8.00	8.00	8.00
X _{Mg}	0.53	0.44	0.46	0.48	0.49	0.45	0.41	0.48	0.45

Table 5.3: Representative electron microprobe analysis of feldspar (stoichiometry calculated on the basis of 8 oxygens, oxide data are given in weight %).

Point No.	AS1				AS17		
	Plagioclase		K-feldspar		Albite lamellae	K-feldspar	
	30/1	31/1	83/1.	84/1.	12/1.	11/1.	25/1.
SiO ₂	58.64	58.84	64.30	64.14	70.40	64.88	64.80
TiO ₂	0.00	0.00	0.00	0.00	0.00	0.00	0.05
Al ₂ O ₃	25.73	25.36	18.84	18.58	20.09	18.75	18.53
FeO	0.00	0.02	0.00	0.02	0.14	0.00	0.00
MnO	0.01	0.00	0.00	0.01	0.02	0.00	0.00
MgO	0.02	0.00	0.00	0.00	0.00	0.00	0.01
CaO	7.44	7.40	0.00	0.00	0.25	0.04	0.00
Na ₂ O	7.58	7.27	1.01	1.62	11.55	1.17	1.01
K ₂ O	0.10	0.12	16.52	15.36	0.28	15.01	14.99
Total	99.54	99.01	100.68	99.73	102.79	100.15	99.76
Si	2.62	2.65	2.94	2.95	3.00	2.99	3.01
Ti	0.00	0.00	0.00	0.00	0.00	0.00	0.00
Al	1.36	1.35	1.01	1.01	1.01	1.02	1.01
Fe ⁺³	0.00	0.00	0.00	0.00	0.00	0.00	0.00
Fe ⁺²	0.00	0.00	0.00	0.00	0.00	0.00	0.00
Mn	0.00	0.00	0.00	0.00	0.00	0.00	0.00
Mg	0.00	0.00	0.00	0.00	0.00	0.00	0.00
Ca	0.36	0.36	0.00	0.00	0.01	0.00	0.00
Na	0.66	0.64	0.09	0.14	0.96	0.10	0.09
K	0.01	0.01	0.96	0.90	0.02	0.88	0.89
Total	5.00	5.00	5.00	5.00	5.00	5.00	5.00
X _{Or}	0.01	0.01	0.91	0.86	0.02	0.89	0.91
X _{Ab}	0.64	0.64	0.09	0.14	0.97	0.11	0.09
X _{An}	0.35	0.36	0.00	0.00	0.01	0.00	0.00

Table 5.4: Representative electron microprobe analysis of ilmenite, rutile and sillimanite (stoichiometry calculated on the basis of 3. 5 and 2 oxygens respectively, oxide data are given in weight %).

Point No.	Ilmenite			Rutile		Sillimanite
	5 / 1 .	17 / 1 .	20 / 1 .	15 / 1 .	21 / 1 .	71 / 1 .
Texture	Inc in Grt	replacin g Ilm	matrix	Inc in Grt	matrix replaced by Ilm	
SiO ₂	0.04	0.01	0.01	0.00	0.00	36.60
TiO ₂	53.04	53.17	53.70	97.53	99.25	0.00
Al ₂ O ₃	0.19	0.16	0.20	0.30	0.29	63.04
FeO	45.27	44.89	45.67	0.31	0.30	0.00
MnO	0.09	0.00	0.16	0.05	0.03	0.00
MgO	0.72	0.97	0.64	0.00	0.01	0.00
CaO	0.04	0.00	0.02	0.01	0.03	0.00
Na ₂ O	0.01	0.00	0.00	0.01	0.04	0.03
K ₂ O	0.00	0.00	0.00	0.01	0.00	0.04
BaO	1.09	1.08	1.02	2.03	1.87	0.00
Total	100.80	100.36	101.49	100.25	101.91	99.78
Si	0.00	0.00	0.00	0.00	0.00	0.99
Ti	1.00	1.01	1.01	0.99	0.99	0.00
Al	0.01	0.00	0.01	0.00	0.00	2.01
Fe ⁺³	0.00	0.00	0.00	0.00	0.00	0.00
Fe ⁺²	0.95	0.95	0.95	0.00	0.00	0.00
Mn	0.00	0.00	0.00	0.00	0.00	0.00
Mg	0.03	0.04	0.02	0.00	0.00	0.00
Ca	0.00	0.00	0.00	0.00	0.00	0.00
Na	0.00	0.00	0.00	0.00	0.00	0.00
K	0.00	0.00	0.00	0.00	0.00	0.00
Total	2.00	2.00	2.00	1.00	1.00	3.00

5.4. Evolution of mineral assemblages

As discussed above, the S2 assemblage comprises euhedral to slightly elongated sillimanite, prismatic biotite and small garnets. Textural relations indicate sillimanite + prismatic biotite + garnet + plagioclase +K-feldspar + quartz constitute the peak assemblage. Presence of rutile in matrix additionally imply that rutile also stabilised during peak conditions of metamorphism along with the other minerals. Rare inclusions of rutile in garnet (coupled with presence of kyanite inclusions in

other metapelite samples) indicates that the prograde assemblage stabilised at high pressures (within the stability field of rutile \pm kyanite).

Subsequent to peak conditions, garnet has been variously replaced by intergrowths of biotite and fibrolitic sillimanite. These fibrolitic sillimanite and biotite also replaces the euhedral, prismatic sillimanite, prismatic biotite, K-feldspar that stabilised at peak conditions.

5.5. P-T conditions of metamorphism

Quantitative P-T estimates of peak metamorphism associated with formation of S2 mineral assemblage was done using phase equilibria modelling techniques. P-T pseudosection for a representative sample AS17, have been constructed using the *Perple_X* program, version 6.8.0 (Connolly, 2005 updated December 2017) with the internally consistent thermodynamic dataset of Holland and Powell, (2011) in the system NCKFMASHT (Na₂O-CaO-K₂O-FeO-MgO-Al₂O₃-SiO₂-TiO₂-H₂O). The pseudosection involves the following phases: garnet, biotite, K-feldspar, quartz, plagioclase, rutile, ilmenite, sillimanite, kyanite, andalusite, orthopyroxene, muscovite, cordierite, spinel, sapphirine, staurolite, chlorite, chloritoid, corundum, and melt. The chosen thermodynamic models and a-X relationships for most of the solid solution minerals are from (White et al., 2014a, 2014b) except plagioclase, sapphirine, spinel and ilmenite, for which the models of (Holland and Powell, 2003), Taylor-Jones and Powell, (2010), White et al., (2002) and White et al., (2000) modified by White et al., (2014b) were used, respectively. Since, none of the minerals contain any significant amount of MnO and ZnO, these were excluded from the system components. Moreover, as garnet, biotite and ilmenite do not contain any Fe⁺³ component, and absence of ferric oxide minerals indicate that the minerals did not stabilise under free oxygenated environment.

P-T pseudosections are constructed using the composition of the rock volume in chemical equilibrium. However, as the rock becomes extremely dry under high grade conditions, diffusivity of elements is greatly reduced, and the rock equilibrates within a small volume. In such cases, bulk rock compositions reflect a much larger volume than the actual equilibrated one. Hence, effective bulk compositions, calculated from the mineral modes and the respective measured

compositions has been used for constructing the pseudosection of the studied samples.

Estimation of water content in the bulk is challenging. At high grade granulite-facies conditions, the porosity of the rock is highly minimised (Clemens and Vielzeuf, 1987). Therefore, the amount of water available in the system is that trapped within the structure of the hydrous phases. Hence, the amount of H₂O has been estimated from the amount of biotite in the rock.

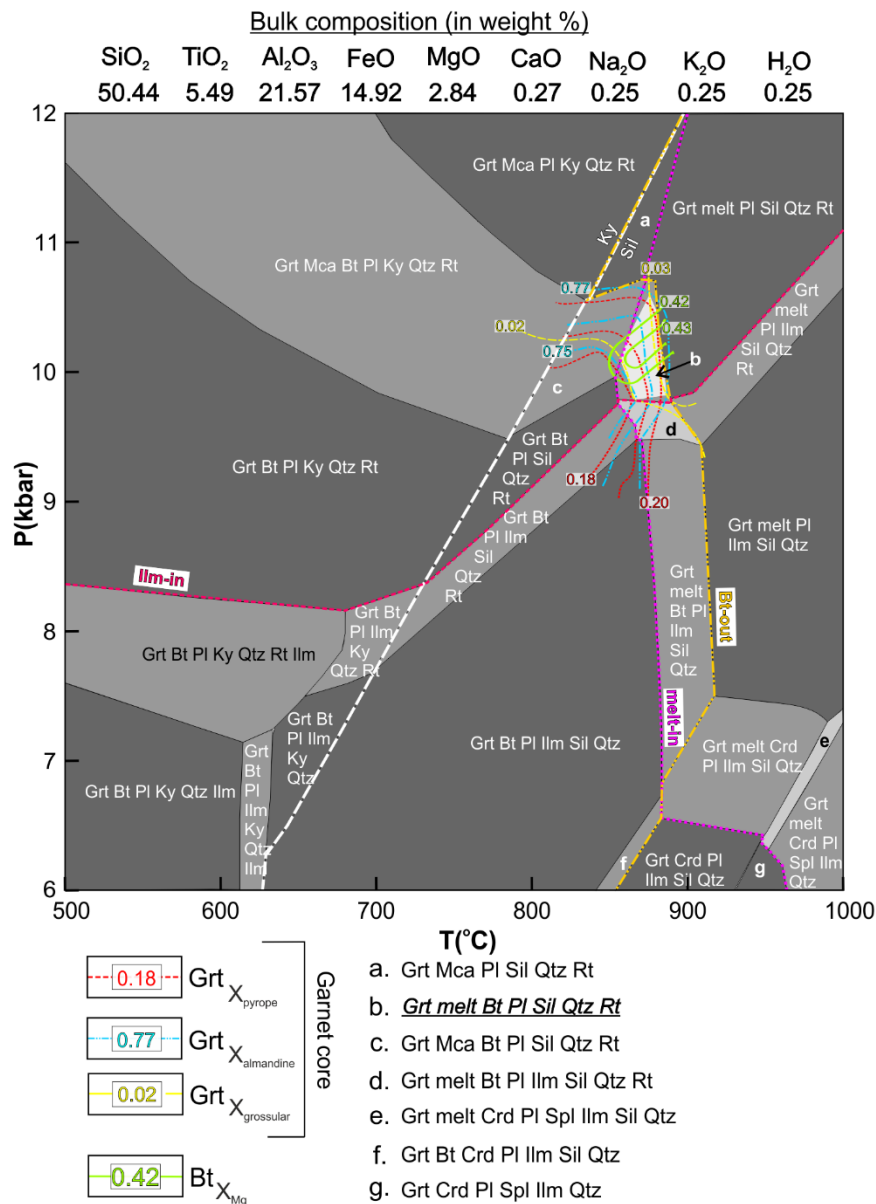


Fig. 5.4: P-T pseudosection for the sample number AS17. The used bulk composition has been given as weight% of the oxides at the top of the pseudosection. The peak M2 metamorphic assemblage is given in bold and underlined. All mineral abbreviations are after Kretz, (1983).

As discussed in section 5.4, the textural relations indicate sillimanite + prismatic biotite + garnet + plagioclase + K-feldspar + quartz + rutile to be the peak assemblage. Presence of small amount of leucosomal segregations associated with S2, combined with the presence of recrystallised melt along the margins of the peak minerals suggest that melting occurred during this peak metamorphism. Presence of rutile inclusions in S2 garnet porphyroblasts (in the studied samples) and rare kyanite inclusions (in other samples) signify that the prograde assemblage was in the stability field of rutile and kyanite. In the constructed pseudosection, the field representing the peak assemblage of the studied rock (garnet+ biotite+ sillimanite+ plagioclase + quartz+ rutile+ melt) covers a small P-T range. Isopleths of garnet core (X_{Py} , X_{Alm} and X_{Grs}) and X_{Mg} isopleths of matrix biotite (away from garnet) further constrain the peak P-T conditions between 9.8-10.5 kbar and 850-880°C (Fig. 5.4). Additionally, replacement of matrix rutile by ilmenite, association of ilmenite with the intergrowths of biotite and fibrolitic sillimanite which replaces garnet porphyroblasts (as well as other peak minerals) signify that these minerals stabilised after peak conditions, possibly after a pressure drop (where the ilmenite-in line was intersected) and cooling path (intersection of the melt-in reaction line, and formation of replacing biotite) (Fig. 5.4).

5.6. Nature and timing of metamorphism

The studied pelitic granulites record peak conditions of metamorphism at 9.8-10.5 kbar and 850-880°C, defining an apparent geothermal gradient of ~26°C/km, corresponding to the development of S2. Although the prograde conditions cannot be constrained, the presence of rare rutile inclusions in garnet, and rare kyanite inclusions in other samples of the pelitic granulite enclaves (Dey et al., 2019a) indicate high pressures experienced by the rock in the prograde path. The transformation of kyanite (prograde) to sillimanite (in peak assemblage) may have occurred via drop in pressure, or increase in temperature, or a combination of the two. However, melting and formation of large grains in the rock are consistent with increase in temperature, with/ without pressure drop. Additionally, the formation of ilmenite and replacing biotite suggest pressure drop associated with cooling. Hence, the high-pressure peak, this inferred nature of the P-T path along with the geothermal gradient all point towards a clockwise P-T path (Harley, 1989)

experienced by the rocks. The P-T conditions constrained from other pelitic granulite exposures in the study area by Dey et al., (2019a) also inferred similar clockwise P-T path culminating at (≥ 10 kbar, ~ 760 – 850°C), followed by a steeply decompressive retrograde P-T path, and subsequent cooling up to ~ 4.3 – 6.5 kbar ~ 530 – 700°C . Similar clockwise P-T paths (with high pressure, moderate temperature peak: ~ 750 – 870°C and ~ 9 – 12 kbar), has also been constrained from different lithounits of the study area (Dey et al., 2019b; Mukherjee et al., 2017) as well as other parts of the CGGC (Chatterjee, 2018; Karmakar et al., 2011). All these studies have related this high-pressure, moderate temperature metamorphism to the second major metamorphic event in the CGGC (M2).

Dey et al., (2019a) also constrained the timing of this peak metamorphism (M2) using U-Pb zircon dating of metamorphic zircons, and in-situ U-Th-Pb chemical dating of monazite between ~ 1050 – 920 Ma (Dey et al., 2019a). Hence, it is inferred that the studied pelitic granulite enclaves experienced the peak metamorphism during the late Stenian-early Tonian time, in response to the second major tectonothermal event (M2) in the CGGC.

References

- Chatterjee, N., 2018. An assembly of the Indian Shield at c. 1.0 Ga and shearing at c. 876–784 Ma in Eastern India: insights from contrasting PT paths, and burial and exhumation rates of metapelitic granulites. *Precambrian Res.* 317, 117–136.
- Clemens, J.D., Vielzeuf, D., 1987. Constraints on melting and magma production in the crust. *Earth Planet. Sci. Lett.* 86, 287–306.
- Connolly, J.A.D., 2005. Computation of phase equilibria by linear programming: A tool for geodynamic modeling and its application to subduction zone decarbonation. <https://doi.org/10.1016/j.epsl.2005.04.033>
- Dey, A., Karmakar, S., Ibanez-Mejia, M., Mukherjee, S., Sanyal, S., Sengupta, P., 2019a. Petrology and geochronology of a suite of pelitic granulites from parts of the Chotanagpur Granite Gneiss Complex, eastern India: Evidence for Stenian-

- Tonian reworking of a late Paleoproterozoic crust. *Geol. J.*
- Dey, A., Karmakar, S., Mukherjee, S., Sanyal, S., Dutta, U., Sengupta, P., 2019b. High pressure metamorphism of mafic granulites from the Chotanagpur Granite Gneiss Complex, India: Evidence for collisional tectonics during assembly of Rodinia. *J. Geodyn.* 129, 24–43.
- Harley, S.L., 1989. The origins of granulites: a metamorphic perspective. *Geol. Mag.* 126, 215–247.
- Holland, T., Powell, R., 2003. Activity–composition relations for phases in petrological calculations: an asymmetric multicomponent formulation. *Contrib. to Mineral. Petrol.* 145, 492–501.
- Holland, T.J.B., Powell, R., 2011. An improved and extended internally consistent thermodynamic dataset for phases of petrological interest, involving a new equation of state for solids. *J. Metamorph. Geol.* 29, 333–383.
- Karmakar, S., Bose, S., Sarbadhikari, A.B., Das, K., 2011. Evolution of granulite enclaves and associated gneisses from Purulia, Chhotanagpur Granite Gneiss Complex, India: evidence for 990–940 Ma tectonothermal event (s) at the eastern India cratonic fringe zone. *J. Asian Earth Sci.* 41, 69–88.
- Kretz, R., 1983. Symbols for rock-forming minerals. *Am. Mineral.* 68, 277–279. [https://doi.org/10.1016/0016-7037\(83\)90220-X](https://doi.org/10.1016/0016-7037(83)90220-X)
- Mukherjee, S., Dey, A., Sanyal, S., Ibanez-Mejia, M., Dutta, U., Sengupta, P., 2017. Petrology and U–Pb geochronology of zircon in a suite of charnockitic gneisses from parts of the Chotanagpur Granite Gneiss Complex (CGGC): evidence for the reworking of a Mesoproterozoic basement during the formation of the Rodinia supercontinent. *Geol. Soc. London, Spec. Publ.* 457, 197–231.
- Taylor-Jones, K., Powell, R., 2010. The stability of sapphirine+ quartz: calculated phase equilibria in FeO–MgO–Al₂O₃–SiO₂–TiO₂–O. *J. Metamorph. Geol.* 28, 615–633.
- White, R., Powell, R., Holland, T.J.B., Worley, B.A., 2000. The effect of TiO₂ and Fe₂O₃ on metapelitic assemblages at greenschist and amphibolite facies conditions: mineral equilibria calculations in the system K₂O–FeO–MgO–Al₂O₃–SiO₂–H₂O–TiO₂–Fe₂O₃. *J. Metamorph. Geol.* 18, 497–511.

- White, R.W., Powell, R., Clarke, G.L., 2002. The interpretation of reaction textures in Fe-rich metapelitic granulites of the Musgrave Block, central Australia: constraints from mineral equilibria calculations in the system $K_2O-FeO-MgO-Al_2O_3-SiO_2-H_2O-TiO_2-Fe_2O_3$. *J. Metamorph. Geol.* 20, 41–55.
- White, R.W., Powell, R., Holland, T.J.B., Johnson, T.E., Green, E.C.R., 2014a. New mineral activity–composition relations for thermodynamic calculations in metapelitic systems. *J. Metamorph. Geol.* 32, 261–286.
- White, R.W., Powell, R., Johnson, T.E., 2014b. The effect of Mn on mineral stability in metapelites revisited: New $a-x$ relations for manganese-bearing minerals. *J. Metamorph. Geol.* 32, 809–828.

PART-II

The Granulite Terrane of South India

Chapter-6

Metamorphic evolution pelitic granulite from Madukkarai Supracrustal Unit

Chapter 6

Metamorphic evolution of pelitic granulite from the Madukkarai Supracrustal Unit

In this chapter, the field observations, petrological and geochronological data (LA-ICP-MS U–Pb zircon and in-situ EPMA chemical age of monazite) from the pelitic granulites of the Madukkarai supracrustal unit (MSU) within the PCSZ (Fig. 2.2a) have been presented. This chapter focuses primarily on a suite of pelitic granulites complemented by a sample of garnet-orthopyroxene bearing meta-psammite (for U–Pb zircon dating, due to the scarcity of zircon in the pelitic granulites), interlayered and co-metamorphosed with the pelitic granulites. Detailed field features, petrography, phase equilibria modelling, combined with zircon and monazite dating constrain the nature and timing of metamorphism and deformation, and record an orogenic event, which occurred in a continent-continent collision setting during the Ediacaran- Cambrian time.

6.1. Field features

Two types of pelitic granulites, viz. garnet-biotite-sillimanite gneisses ('Grt-Bt-Sil gneiss') and very rare garnet-cordierite-biotite-sillimanite gneisses ('Grt-Crd-Bt-Sil gneiss') were distinguished in the MSU based on field observations (sample locations given in Table 6.1 and Fig. 2.2b). These meta-supracrustals overlie migmatitic enderbitic gneisses (Fig. 6.1a) that were widely retrogressed to hornblende-biotite gneisses. The Grt-Bt-Sil gneisses consists of melanosomal and local leucosomal portions (S1, Fig. 6.1b). The leucosomes are garnetiferous, constituting ~10% of the total rock volume, and form centimetre-thick discontinuous layers (S1) or nebular patches (Fig. 6.1b). These discontinuous S1 leucosomes exhibit tight isoclinal folds with an E-W trending axial planar foliation (S2) (Fig. 6.1b). Garnet-sillimanite-K-feldspar-biotite constitutes the S1 melanosomes. Centimetre-sized kyanite grains, pseudomorphically replaced by sillimanite, were also identified in the outcrop within the S1 melanosomes (Fig. 6.1c-

d). The K-feldspar porphyroblasts enclose garnet and abundant biotite (Fig. 6.1d). The S2 foliation is pervasive throughout the outcrops and imparts a thinly banded gneissic appearance to the rocks (Fig. 6.1b). The S2 foliation is dominantly defined by oriented crystals of biotite and sillimanites (Fig. 6.1b). No leucosomal segregations are observed along S2 in the studied samples. Grt-Crd-Bt-Sil gneisses are massive in nature consisting of garnet, biotite, cordierite, aluminosilicates, quartz, K-feldspar and plagioclase (Fig. 6.1e-f). Locally, quartzo-feldspathic leucosomes (S1) with garnet, occur as nebular patches. The S1 melanosome contains

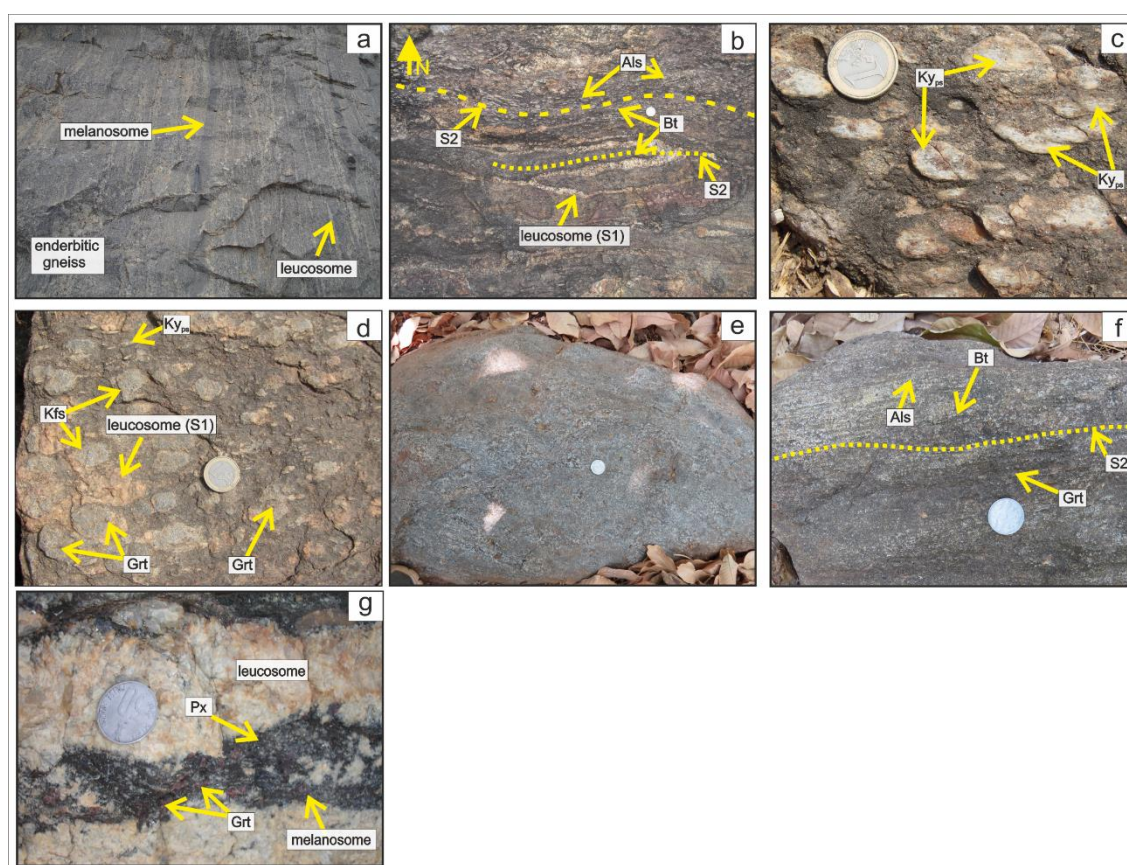


Fig. 6.1: Photographs showing field features of the studied pelitic granulites (b-f) and intercalated Grt-Opx bearing meta-psammite (g): (a) Enderbitic gneissic basement having prominent leucosomal and melanosomal bands. (b) Local discontinuous leucosomal bands (S1) in Grt-Bt-Sil gneiss showing tight isoclinal folding with E-W axial planar foliation (S2). S2 foliation is defined by oriented grains of biotite and aluminosilicates. (c) Large kyanite grains pseudomorphed by fibrolitic sillimanite (also seen in 'd'). (d) Large K-feldspar porphyroblasts with inclusions of biotite and few garnets. (e) Massive nature of the Grt-Crd-Bt-Sil gneiss rock. (f) Cordierite free zones within Grt-Crd-Bt-Sil gneiss showing crude E-W trending foliation (S2). (g) Thin layers of garnet-orthopyroxene dominated melanosomes alternating with leucosomes, which are dominated by recrystallized quartz along with variable amounts of feldspar. Als: Aluminosilicate, Kyps: kyanite pseudomorphed by sillimanite. Mineral abbreviations after Kretz, (1983).

anhedral cordierite porphyroblasts that encloses fine garnet and biotite grains imparting the massive appearance to the rock. The S2 foliation is not prominent in this rock, except for a few cordierite-free patches which exhibit a crude E-W trending foliation (S2) defined by biotite and sillimanite (Fig. 6.1f). These cordierite free zones are mineralogically similar to the Grt-Bt-Sil gneisses. Garnet-orthopyroxene bearing meta-psammite (“Grt-Opx-bearing meta-psammite”) occur intercalated with the pelitic granulite units. The rock comprises thin layers of garnet + orthopyroxene ± biotite dominated melanosomes, associated with leucosomes (Fig. 6.1g). The leucosomes are primarily dominated by recrystallized quartz along with some feldspar. Some feldspar free, garnet-orthopyroxene rich bands are also present where quartz is the only felsic mineral. In addition to the pelitic granulites, one sample of this rock was also chosen for geochronological analysis, as it contains abundant zircon, unlike the pelitic granulites, where zircon is very rare and very fine-grained.

6.2. Petrography

The Grt-Bt-Sil gneiss is more abundant within the MSU and shows no significant textural variation in meso- or microscopic scale. A number of samples from different outcrops were studied (locations given in Table 6.1 and shown in map, Fig. 2.2b) and few representative samples were chosen for detailed analyses. The Grt-Crd-Bt-Sil gneiss is very rare and only one sample was suitable for detailed study (shown in map, Fig. 2.2b). Multiple thin sections have been prepared separately from the leucosomal and melanosomal bands from each of the samples and are described below.

6.2.1. *Grt-Bt-Sil gneiss*

The rocks are dominantly composed of garnet, sillimanite, kyanite, K-feldspar, quartz, biotite, and plagioclase along with minor amounts of ilmenite. Rutile, monazite and zircon occur as accessory phases (Table 6.1). Within the S1 melanosomes, garnets form medium to coarse grained, hypidioblastic porphyroblasts that are distributed in a granoblastic matrix of quartz, K-feldspar, plagioclase and randomly dispersed biotite grains (Fig. 6.2a). Medium- to coarse-

grained stumpy kyanite blades (now replaced by sillimanite) are also present in the matrix. Matrix biotite grains majorly occur as medium grained crystals that share straight equilibrium boundaries with garnet porphyroblasts (Fig. 6.2a). Garnet shows poikiloblastic cores that are surrounded by almost inclusion free mantles (Fig. 6.2a-b). Apart from numerous quartz inclusions within garnet cores, minor inclusions of plagioclase, biotite, K-feldspar and rutile are also present (Fig. 6.2b-c). Rutile inclusions are partially replaced by ilmenite (Fig. 6.2d). In contrast to rutile, ilmenite is present in the matrix (Fig. 6.2a, e, i). Rarely, thin rims of K-feldspar and quartz are observed around garnet porphyroblasts (Fig. 6.2c), probably representing crystallised anatectic melt. Sillimanite also occurs as small prismatic grains in the matrix, concentrated within definite zones (Fig. 6.2e). Sillimanite inclusions in the inclusion-poor mantles of garnet show the same orientation as those in matrix (Fig. 6.2f), indicating growth of the garnet mantles in equilibrium with sillimanite. The K-feldspar porphyroblasts that were macroscopically recognized in S1 melanosomes (Fig. 6.2d) preserve abundant inclusions of biotite, plagioclase and quartz (Fig. 6.2g) as well as rare small garnet grains. The S1 melanosomes exhibit overprinting of the pervasive S2 foliation as well. The S2 foliation is defined by aligned biotite and fibrolitic sillimanite (Fig. 6.2a, e). Along grain margins and fissures, garnet porphyroblasts are locally replaced by biotite (Fig. 6.2h), or intergrowths of biotite and fibrolitic sillimanite. Less commonly, intergrowths of biotite, plagioclase and quartz occur (Fig. 6.2h). Fibrolitic sillimanite also replaces prismatic sillimanites (Fig. 6.2e). The kyanite blades of the S1 melanosome are partially to completely pseudomorphed by fibrolitic sillimanite (Fig. 6.2i). Quartz, K-feldspar and plagioclase of the matrix are flattened and stretched along the S2 foliation (Fig. 6.2e). The small amount of S1 leucosomes (~10 vol%) suggests a low extent of partial melting. The leucosomes are dominated by quartz, K-feldspar and plagioclase, which together constitute up to 90 vol% of the leucosomes and define an interlocking texture suggesting their crystallisation from melt (Fig. 6.2j). Garnets are scattered within the quartzo-feldspathic matrix (Fig. 6.2j) with rare biotite.

Table 6.1: Sample numbers, locations and mineral modes of the studied rocks in Madukkarai supracrustal unit.

Rock Type	Sample Locations	Latitudes	Longitudes	Mineral modal percentages														
				Major minerals							Accessory minerals							
				Grt	Crd	Bt	Sil	Ky	Pl	Kfs	Qtz	Ilm	Opx	Rt	Spl	Mnz	Zrn	Mag
	B117	10°55.935'N	76°57.445'E	18	-	15	20	ps	8	11	23	4	-	1	-	Y	-	-
	B152B	10°54.241'N	76°56.489'E	16	-	14	18	ps	10	15	25	2	-	Y	-	Y	-	-
Grt-Bt-Sil	I-235-1-07	10°53.507'N	76°52.650'E	20	-	14	16	ps	8	13	25	4	-	Y	-	-	Y	-
gneiss	I-236-1-07	10°53.109'N	76°52.050'E	22	-	21	12	ps	6	4	33	2	-	-	-	-	-	-
	I-349-1-10	10°54.206'N	76°56.236'E	15	-	14	12	ps	7	15	35	2	-	-	-	-	-	-
	I-262-1-07	10°56.377' N	76°41.886' E	4	-	31	9	ps	3	4	48	1	-	-	-	-	-	-
Grt-Crd-																		
Bt-Sil	I-353-1-10	10°51.496'N	76°43.185'E	7	34	17	12	ps	9	4	15	2	-	Y	Y	Y	-	-
gneiss																		
Grt-Opx																		
bearing	I-353-10-10	10°51.513'N	76°43.163'E	15	-	5	-	-	5	13	45	-	17	-	-	-	Y	Y
meta-																		
psammite																		

(ps): Ky pseudomorphed by Sil Mineral abbreviations after (Kretz, 1983)

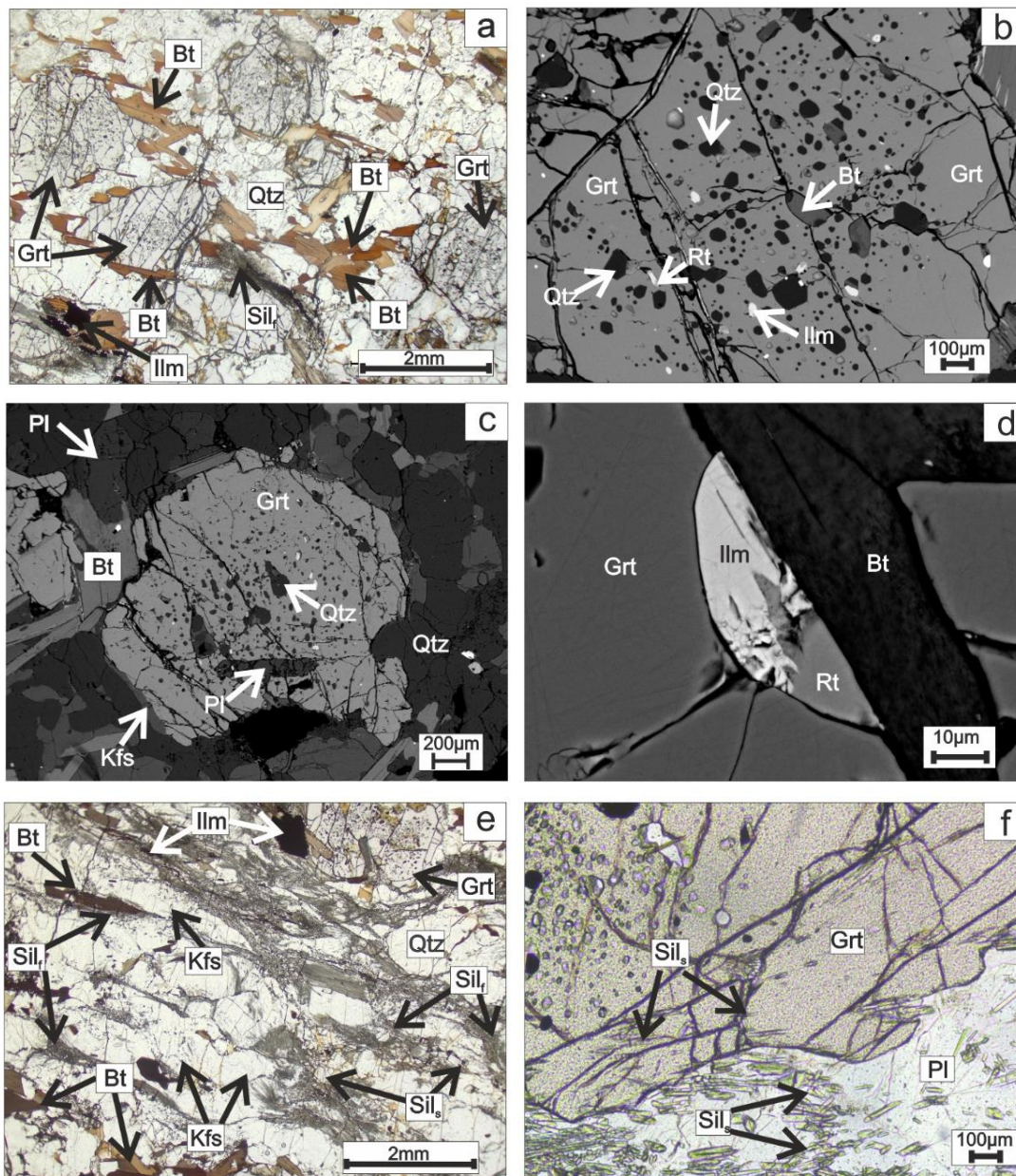


Fig. 6.2: Photomicrographs and BSE images of Grt-Bt-Sil gneiss (a-j), Grt-Crd-Bt-Sil gneiss (k-p) and Grt-Opx bearing meta-psammite (q-r) (a) Porphyroblastic garnet with poikiloblastic cores and inclusion free rims dispersed within a matrix of quartz, K-feldspar, plagioclase and prismatic biotites. These biotites show straight grain boundaries with garnet porphyroblasts. (b) Garnet porphyroblast with inclusions of quartz, biotite, ilmenite and rutile. (c) Garnet porphyroblast containing plagioclase and quartz inclusions. Note the thin rim of K-feldspar around garnet porphyroblasts indicating late-stage melt crystallisation. (d) Rutile inclusions in garnet partially replaced by ilmenite. (e) Pervasive foliation (S_2) defined by fibrolitic sillimanite-biotite. Idioblastic sillimanite grains, dispersed in matrix, are replaced by fibrolitic ones. Ilmenite grains are dispersed in the matrix. Stretched K-feldspar and quartz grains are interlayered with the fibrolites. (f) Sillimanite inclusions present in the inclusion poor rims of garnet. Mineral abbreviations after Kretz, (1983).

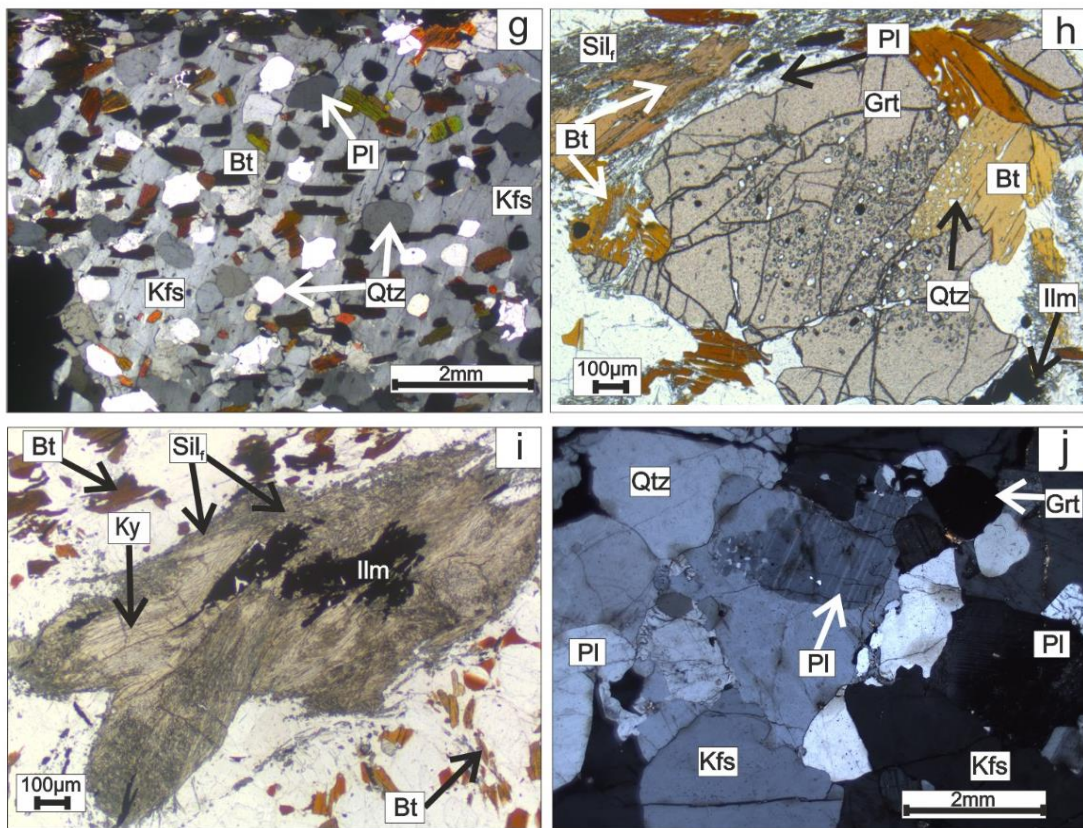


Fig. 6.2: (g) K-feldspar porphyroblasts with abundant inclusions of biotite, plagioclase and quartz. (h) Garnet porphyroblasts replaced by intergrowth of fibrolitic biotite and sillimanite (left). Prismatic biotite having corroded margins with garnet indicates replacement of garnet by the former. Plagioclase is also associated with these intergrowths. These biotites overgrow quartz inclusions in poikilitic garnet (right). (i) Kyanite pseudomorphed by fibrolitic sillimanite. (j) Leucosomal segregations comprising quartz, plagioclase, K-feldspar and minor amounts garnet. Mineral abbreviations after Kretz, (1983).

6.2.2. Grt-Crd-Bt-Sil gneiss

The Grt-Crd-Bt-Sil gneisses are essentially composed of garnet, cordierite, sillimanite, biotite, quartz, plagioclase, kyanite, K-feldspar, ilmenite, with minor amounts of monazite, spinel and rutile (Table 6.1). Quartz, plagioclase and K-feldspar with small anhedral garnets constitute the scarce S1 leucosomes. The minerals exhibit an interlocking mosaic. Within the S1 melanosomes, medium to fine-grained (~500 μm diameter) xenoblastic garnets are scattered within a matrix mainly composed of cordierite along with lesser amounts of quartz, aluminosilicates, K-feldspar, plagioclase, biotite and ilmenite (Fig. 6.2k-p). Except rare quartz inclusions, garnets are generally inclusion free. Prismatic sillimanite

forms idioblastic grains that are often concentrated in clusters within the matrix (Fig. 6.2l) and preserve rare inclusions of biotite and rutile. Locally, tabular crystals of kyanite (now replaced by fibrolitic sillimanite) are also preserved (Fig. 6.2m). Cordierite occurs as large (~2–5 mm) grains in the matrix and often engulfs matrix biotites and prismatic sillimanites (Fig. 6.2n-o). However, garnets share straight boundaries with cordierite grains (Fig. 6.2o). Rare inclusions of spinel are also present within cordierite (Fig. 6.2n). Thin rims of feldspar occur along the grain boundary of cordierites (Fig. 6.2p) and are interpreted as crystallised anatectic

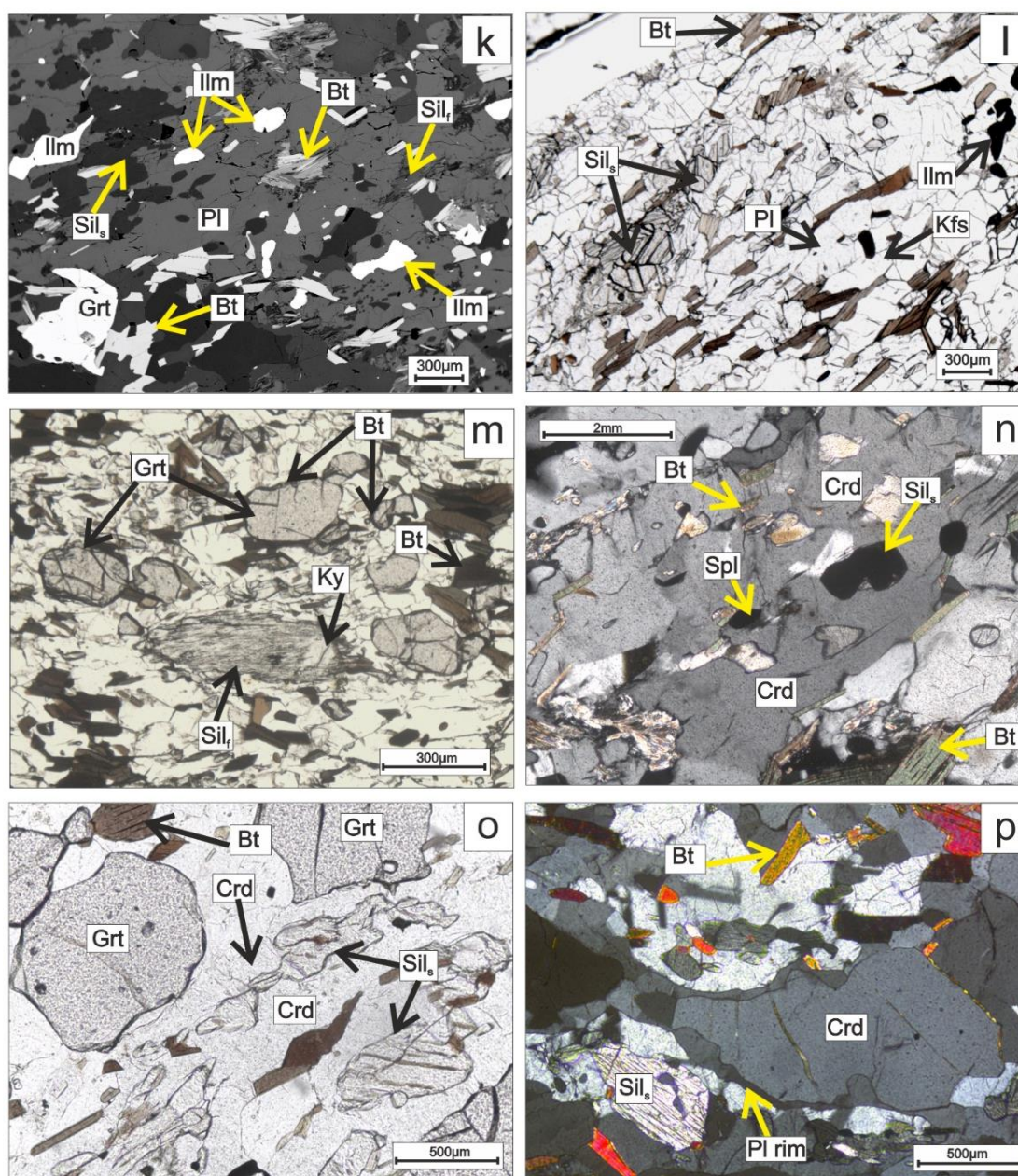


Fig. 6.2 contd.: (k) Inclusion free garnet porphyroblasts dispersed in a matrix of quartz, plagioclase, K-feldspar, biotite and sillimanite (both idioblastic and fibrolitic). (l) Large porphyroblastic aggregates formed by idioblastic sillimanites and stretched along S2 foliation. (m) Kyanite porphyroblasts pseudomorphed by fibrolitic sillimanites, and prismatic biotites dispersed in matrix. Few garnets are replaced by fine biotite-quartz intergrowths. (n) Biotite, sillimanite and spinel included within matrix cordierite. (o) Cordierite present at the interface of garnet and sillimanite. Note the straight margins between garnet and cordierite. (p) Thin plagioclase rims (crystallised melt) around matrix cordierite grains. Mineral abbreviations after Kretz, (1983).

melt. Locally, cordierite is replaced by very fine-grained muscovite and chlorite while the xenoblastic garnets are replaced by fine biotite-quartz intergrowths. However, no fibrolitic sillimanites are associated with the replacement of garnet porphyroblasts and cordierite. The S1 melanosomes bears the imprint of the S2 foliation as well; which is defined by aligned crystals of biotite and stretched sillimanite clusters (Fig. 6.2k-l). The mineralogy of the cordierite free zones in the Grt-Crd-Bt-Sil gneiss resembles that of the Grt-Bt-Sil gneisses.

6.2.3. Grt-Opx bearing meta-psammites

The melanosomes of Grt-Opx bearing meta-psammites, are composed of garnet, orthopyroxene, biotite, quartz and variable amounts of feldspar (Fig. 6.2q). Locally, in garnet-orthopyroxene-rich bands, feldspar is completely absent, leaving quartz as the sole felsic mineral within the matrix of the melanosomes (Fig. 6.2r). Garnet and orthopyroxenes occur as medium to large sized subidioblastic porphyroblasts. These are mostly inclusion free, with the exception of few quartz in some garnet and orthopyroxene porphyroblasts (Fig. 6.2q-r). Straight grain boundaries suggest contemporaneous formation of garnet and orthopyroxene, with that of matrix quartz and K-feldspar. Together they define a recrystallized granoblastic mosaic. A weak banding that parallels the foliation of the pelitic granulites is defined by orthopyroxene-garnet-rich layers. Locally, fine grained biotites replaces orthopyroxene and garnet along their margins and fractures. However, subidioblastic, medium grained, matrix biotites are also present. Rare magnetite grains are observed in the matrix of the feldspar free melanosomal segregations. The associated leucosomal portions comprises primarily quartz, along

with some K-feldspar and few plagioclases. Abundant zircon and apatite occur as accessory phases.

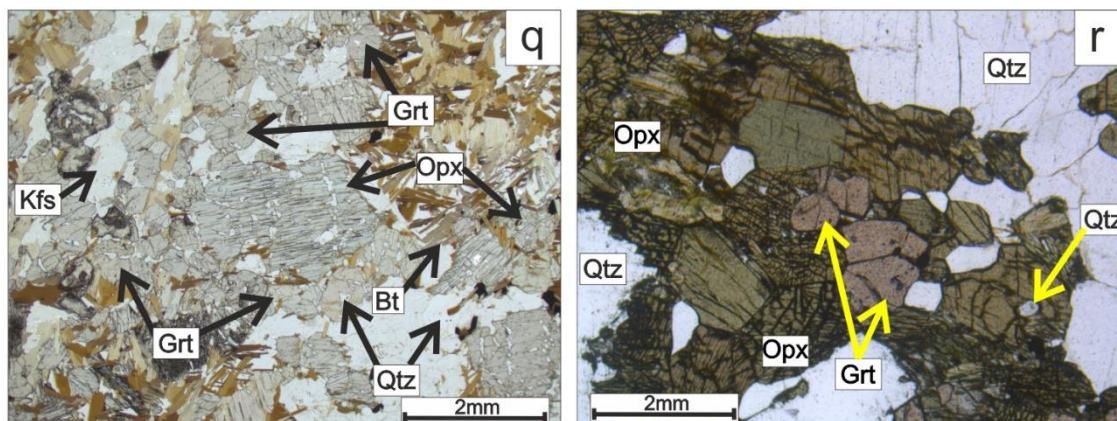


Fig. 6.2 contd.:(q) Garnet-orthopyroxene porphyroblast dominated melanosomes, showing straight equilibrium boundaries with each other as well as with quartz and K-feldspar in the matrix. Fine grained biotite replaces these porphyroblasts along their margins and fractures. (r) Feldspar-free melanosomal portions, containing medium grained garnet and orthopyroxene porphyroblasts with quartz as the sole felsic mineral in the matrix. Rare inclusions of quartz observed in orthopyroxene. Note the recrystallized granoblastic mosaic defined by these three minerals. (Silf and Sils: fibrolitic and idioblastic sillimanite respectively). Mineral abbreviations after Kretz, (1983).

6.3. Mineral Chemistry

Two representative samples (B117 and I-236-1-07) from the Grt-Bt- Sil gneiss and the Grt-Crd-Bt-Sil gneiss sample, I-353-1-10 were selected for mineral compositional analysis. Mineral compositions of B117 were analysed at the Central Petrological Laboratory of Geological Survey of India, Kolkata, India with CAMECA SX100 electron microprobe. Natural standards were used for all elements except for Mn and Ti, for which, synthetic standards were used. The diameter of the electron beam was 1–3 μm , and voltage and beam current were 15 kV and 12 nA respectively. Mineral compositions of samples I-236-1-07 and I-353-1-10 were analysed at the Institute of Geosciences of the University Kiel, Germany with a JEOL Superprobe JXA 8900R. The beam size was 5 μm and the analyses were performed under 15 kV accelerating voltage and a beam current of 15 nA. Mineral abbreviations mentioned below are after (Kretz, 1983).

6.3.1. Garnet

Garnets in the Grt-Bt-Sil gneisses are essentially Fe-rich almandine-pyrope solid solutions with minor grossular and spessartine components ($\text{Alm}_{0.69-0.78}\text{Prp}_{0.17-0.25}\text{Grs}_{0.03-0.04}\text{Sps}_{0.02-0.03}$). Garnet of the two samples show slight chemical variation. Moderate zoning with the X_{Mg} decreasing from core (X_{Mg} : 0.25–0.26; $\text{Alm}_{0.69-0.71}\text{Prp}_{0.24-0.25}$ in B117 and X_{Mg} : 0.23–0.24 $\text{Alm}_{0.71-0.73}\text{Prp}_{0.22-0.23}$ in I-236-1-07) towards rim (X_{Mg} : 0.18–0.24; $\text{Alm}_{0.72-0.78}\text{Prp}_{0.17-0.23}$ in B117 and X_{Mg} : 0.20–0.22; $\text{Alm}_{0.74-0.76}\text{Prp}_{0.19-0.21}$ in I-236-1-07) is observed. Rims at the contact of biotites in B117 have the highest Fe-rich compositions (X_{Mg} : 0.18–0.21; $\text{Alm}_{0.75-0.78}\text{Prp}_{0.17-0.20}$), suggesting diffusional Fe–Mg re-equilibration during retrogression. Grossular and spessartine components show no systematic zoning (Table 6.2a).

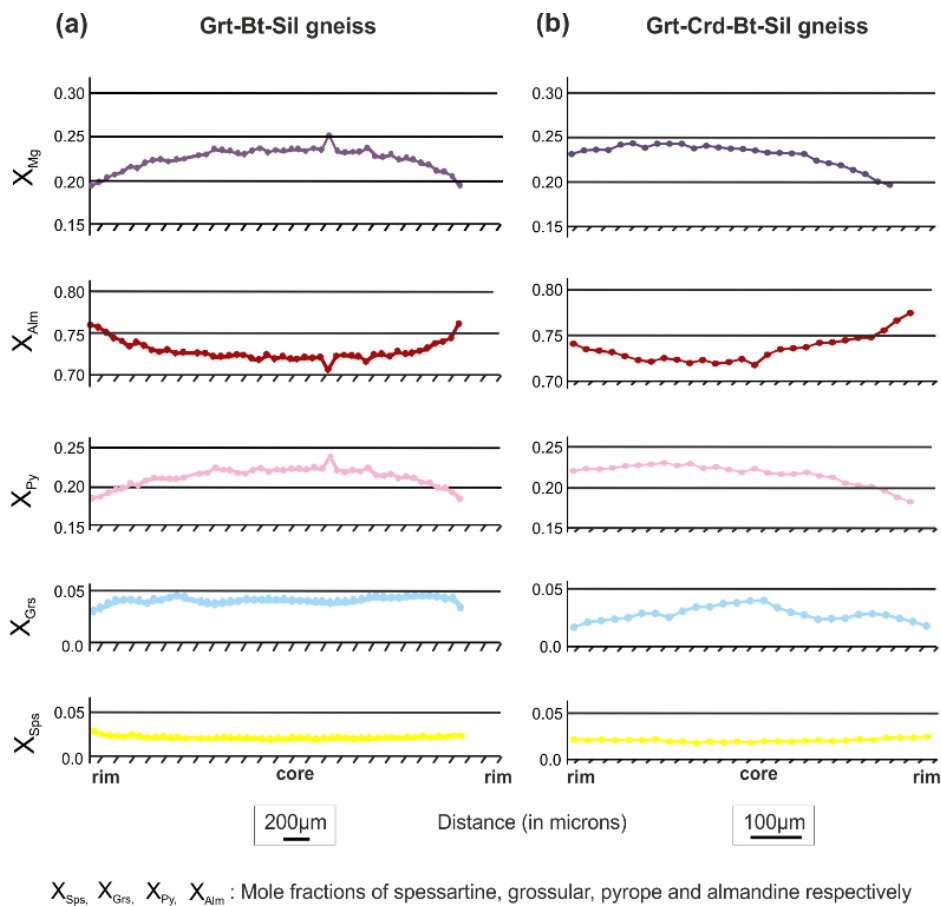


Fig. 6.3: Representative compositional zoning profiles of garnet in (a) Grt-Bt-Sil gneiss (I-236-1-07) and (b) Grt-Crd-Bt-Sil gneiss (I-353-1-10). The profiles extend from rim to rim through the core of the grains. Mineral abbreviations are after Kretz, (1983).

Fig. 6.3a depicts the representative compositional zoning profile for sample I-236-1-07. Garnet of the Grt-Crd-Bt-Sil gneiss (Fig. 6.3b) has a similar Fe-rich composition ($\text{Alm}_{0.72-0.79}\text{Prp}_{0.17-0.23}\text{Grs}_{0.02-0.04}\text{Sps}_{0.02}$) with similar zoning pattern as garnet of Grt-Bt-Sil gneisses. The X_{Mg} decreases from cores (X_{Mg} : 0.23–0.25, $\text{Alm}_{0.72-0.75}\text{Prp}_{0.22-0.23}$) to rims (X_{Mg} : 0.18–0.22, $\text{Alm}_{0.76-0.79}\text{Prp}_{0.17-0.21}$), suggesting Fe–Mg re-equilibration during retrogression. Grossular and spessartine contents show no systematic zoning (Fig. 6.3b; Table 6.2a).

6.3.2. Biotite

Biotites in the two samples (B117 and I-236-1-07) have slight variation in their compositional ranges, but show systematic chemical variations related to their textural position (Table 6.2b). Inclusions within garnet of sample B117 are more magnesian (X_{Mg} : 0.62–0.66, TiO_2 : 3.4–3.6 wt%) than matrix biotites (X_{Mg} : 0.49–0.53), with garnet have intermediate magnesium (X_{Mg} : 0.54–0.55) and titanium (4.1–5.4 wt% TiO_2) contents. Biotite of sample I-236-1-07 is less magnesian. Biotite inclusions in garnet record the highest X_{Mg} values (0.49–0.52, TiO_2 : 4–4.4 wt%, Table 6.2b). Matrix grains are less magnesian (X_{Mg} : 0.43–0.45) and Ti-rich (4.2–5.1 wt% TiO_2). Biotites adjacent to garnet are slightly more magnesian (X_{Mg} : 0.46–0.47) and less titaniferous (3.8–4.4 wt% TiO_2) than the matrix grains. Matrix biotites of the Grt-Crd-Bt-Sil gneiss have a similar composition (X_{Mg} : 0.46–0.48; 4.2–5.3 wt% TiO_2) as that of the Grt-Bt-Sil gneiss sample I-236-1-07. Biotite in contact with garnet is slightly more magnesian (X_{Mg} : 0.49–0.50) whereas the TiO_2 content is similar (4.5–5 wt%, Table 6.2b) irrespective of their textural positions. Biotite of the Grt-Crd-Bt-Sil gneiss contains significant Cr_2O_3 (up to 0.84 wt%).

6.3.3. Plagioclase

Plagioclase of the Grt-Bt-Sil gneisses is mainly unzoned oligoclase. Composition of matrix plagioclase grains varies from $\text{An}_{23}\text{Ab}_{76}\text{Or}_1$ to $\text{An}_{29}\text{Ab}_{70}\text{Or}_1$, while that of small plagioclases in biotite-quartz-plagioclase intergrowths replacing garnet porphyroblasts, range from $\text{An}_{0.28}\text{Ab}_{0.71}\text{Or}_{0.01}$ to $\text{An}_{0.30}\text{Ab}_{0.68}\text{Or}_{0.02}$ (Table 6.2c). In contrast, plagioclase inclusions in garnet of sample I-236-1-07 are slightly more calcium-rich and are classified as andesine ($\text{An}_{0.37-0.39}\text{Ab}_{0.59-0.60}\text{Or}_{0.02}$) (Table

6.2c). Matrix plagioclase of the Grt-Crd-Bt-Sil gneiss is unzoned oligoclase ($An_{0.17}Ab_{0.82}Or_{0.01}$ to $An_{0.24}Ab_{0.75}Or_{0.01}$) as well, whereas rare plagioclases that are adjacent to garnet and biotite are slightly more calcic ($An_{0.20}Ab_{0.79}Or_{0.01}$ to $An_{0.31}Ab_{0.68}Or_{0.01}$) (Table 6.2c).

6.3.4. K-feldspar

K-feldspar of the Grt-Bt-Sil gneisses occurring as matrix grains and as inclusions in garnet has similar compositions ($Or_{0.82-0.88}Ab_{0.18-0.12}An_0$) in both the samples (Table 6.2d). K-feldspar of the Grt-Crd-Bt-Sil gneiss, however, shows more restricted composition ($Or_{0.87}Ab_{0.13}An_0$) (Table 6.2d).

6.3.5. Ilmenite

Ilmenites in both rocks have almost pure composition with minor MgO (~0.6–1.1 wt%) and negligible MnO (~0.2–0.3 wt%) content. They do not contain any Fe^{+3} component as calculated from ideal stoichiometry (Table 6.2d). Rutile and aluminosilicates occur as pure phases in both the rocks (Table 6.2d).

6.3.6. Cordierite

The X_{Mg} of cordierite in the Grt-Crd-Bt-Sil gneiss varies within a restricted range of 0.68 to 0.72. The compositions of matrix cordierite and those adjacent to garnet, both fall within this range. The low analytical totals (~97–98 wt%) suggest the presence of H_2O within the structural channels (Table 6.2e).

6.3.7. Spinel

Spinel in the Grt-Crd-Bt-Sil gneiss is hercynite-rich (X_{Mg} calculated as $[Mg/(Mg + Fe^{+2})]:0.17$), with significant gahnite and chromite component ($Hc_{61}Gh_{15}Spl_{13}Chr_{10}Mag_1$) (Table 6.2e). While Zn-rich spinel are common in metapelites, presence of ~10 mol% chromite end-member is rarely reported.

Table 6.2a: Representative chemical analyses of garnet (stoichiometry calculated on the basis of 12 oxygens, oxide data are given in weight%).

Point No.	B117			Grt-Bt-Sil gneiss I-236-1-07			Grt-Crd-Bt-Sil gneiss I-353-1-10								
	core		rim adjacent to biotite	core		rim	core		rim						
	22	14 / 1.	10	2	11 / 1.	281	288	390	259	257	164	31	174	363	235
SiO ₂	37.54	37.86	37.29	37.69	37.57	37.90	38.05	37.93	37.54	37.78	38.39	38.48	38.80	37.69	38.51
TiO ₂	0.06	0.00	0.01	0.00	0.03	0.03	0.01	0.04	0.03	0.03	0.00	0.05	0.00	0.00	0.01
Al ₂ O ₃	20.89	21.52	20.58	21.14	21.58	21.54	21.48	21.53	21.63	21.65	21.74	21.73	21.75	21.22	21.93
Cr ₂ O ₃	0.01	0.00	0.02	0.00	0.04	0.00	0.00	0.00	0.01	0.01	0.00	0.00	0.00	0.00	0.00
FeO	31.92	31.95	33.03	34.18	33.14	33.51	33.55	34.44	34.49	34.69	33.62	32.65	32.69	34.35	33.85
MnO	0.85	0.94	0.92	0.91	1.11	0.84	0.83	0.88	0.97	1.20	0.78	0.84	0.78	1.11	0.82
MgO	6.21	6.06	5.80	5.02	4.25	5.80	5.67	5.31	4.94	4.72	5.59	5.82	6.03	4.23	5.33
CaO	1.40	1.14	0.99	1.11	1.02	1.47	1.10	1.14	1.29	1.03	0.66	1.33	0.74	0.64	0.72
Na ₂ O	0.00	0.04	0.00	0.04	0.00	0.00	0.00	0.00	0.00	0.00	0.00	0.00	0.00	0.00	0.00
K ₂ O	0.02	0.00	0.02	0.01	0.01	0.00	0.00	0.00	0.00	0.00	0.00	0.00	0.00	0.00	0.00
Total	98.91	99.68	98.68	100.10	98.75	101.09	100.69	101.26	100.89	101.12	100.78	100.90	100.78	99.24	101.17
Si	2.99	2.99	2.99	2.99	3.03	2.96	2.99	2.97	2.96	2.98	3.02	3.01	3.04	3.03	3.02
Ti	0.00	0.00	0.00	0.00	0.00	0.00	0.00	0.00	0.00	0.00	0.00	0.00	0.00	0.00	0.00
Al	1.96	2.01	1.95	1.98	2.05	1.99	1.99	1.99	2.01	2.01	2.01	2.00	2.01	2.01	2.03
Cr	0.00	0.00	0.00	0.00	0.00	0.00	0.00	0.00	0.00	0.00	0.00	0.00	0.00	0.00	0.00
Fe ^{+3*}	0.05	0.01	0.07	0.04	0.00	0.08	0.03	0.06	0.07	0.03	0.00	0.00	0.00	0.00	0.00
Fe ⁺²	2.08	2.10	2.15	2.23	2.24	2.11	2.18	2.20	2.21	2.26	2.21	2.14	2.14	2.31	2.22
Mn	0.06	0.06	0.06	0.06	0.08	0.06	0.06	0.06	0.06	0.08	0.05	0.06	0.05	0.08	0.05
Mg	0.74	0.71	0.69	0.59	0.51	0.68	0.66	0.62	0.58	0.55	0.65	0.68	0.70	0.51	0.62
Ca	0.12	0.10	0.09	0.09	0.09	0.12	0.09	0.10	0.11	0.09	0.06	0.11	0.06	0.06	0.06
Na	0.00	0.01	0.00	0.01	0.00	0.00	0.00	0.00	0.00	0.00	0.00	0.00	0.00	0.00	0.00
K	0.00	0.00	0.00	0.00	0.00	0.00	0.00	0.00	0.00	0.00	0.00	0.00	0.00	0.00	0.00
Total	8.00	8.00	8.00	8.00	8.00	8.00	8.00	8.00	8.00	8.00	8.00	8.00	8.00	8.00	8.00
X _{py}	0.25	0.24	0.23	0.20	0.17	0.23	0.22	0.21	0.20	0.19	0.22	0.23	0.23	0.17	0.21
X _{Alm}	0.69	0.71	0.72	0.75	0.78	0.71	0.73	0.74	0.75	0.76	0.75	0.72	0.73	0.79	0.76
X _{Grs}	0.04	0.03	0.03	0.03	0.03	0.04	0.03	0.03	0.04	0.03	0.02	0.04	0.02	0.02	0.02
X _{Sps}	0.02	0.02	0.02	0.02	0.02	0.02	0.02	0.02	0.02	0.03	0.02	0.02	0.02	0.02	0.02
X _{Mg}	0.26	0.25	0.24	0.21	0.18	0.24	0.23	0.22	0.21	0.20	0.23	0.24	0.25	0.18	0.22

*Fe⁺³ recalculated according to the scheme of Droop (1987)

Table 6.2b: Representative chemical analyses of biotite (stoichiometry calculated on the basis of 11 oxygens, oxide data are given in weight%).

Point No	B117											Grt-Bt-Sil gneiss						Grt-Crd-Bt-Sil gneiss						
	matrix			replacing			inclusion			matrix			replacing			inclusion			matrix			replacing		
	14	6/1	9/1	9	10/2	12	19/1	2/1	2/1	443	352	441	342	347	340	368	377	377	70	88	332	74	318	316
SiO ₂	33.42	35.58	35.24	34.50	35.99	33.43	37.18	37.60	35.03	35.04	35.06	35.36	35.33	35.50	35.75	35.30	34.99	34.92	35.07	34.92	35.04	35.11		
TiO ₂	5.63	4.80	4.36	6.09	4.05	5.39	3.62	3.42	4.25	5.05	4.16	4.08	4.39	3.79	4.38	3.95	4.74	4.19	5.30	4.60	4.54	5.00		
Al ₂ O ₃	16.13	16.98	17.34	17.11	17.76	16.03	19.34	19.22	18.27	17.62	18.35	18.39	18.50	18.21	18.02	18.22	16.85	17.40	16.98	16.86	17.33	17.02		
Cr ₂ O ₃	0.02	0.01	0.05	0.07	0.11	0.03	0.14	0.05	0.05	0.07	0.04	0.02	0.06	0.05	0.04	0.03	0.73	0.72	0.49	0.84	0.67	0.59		
FeO	16.71	18.59	18.28	17.88	16.90	17.22	14.34	12.49	19.57	20.15	19.00	18.90	19.13	19.03	17.45	18.39	18.69	18.17	18.10	18.55	17.66	17.22		
MnO	0.01	0.00	0.01	0.05	0.05	0.00	0.00	0.04	0.05	0.08	0.05	0.03	0.05	0.05	0.01	0.02	0.03	0.04	0.02	0.04	0.05	0.11		
MgO	10.58	9.87	10.55	10.50	11.63	11.31	13.16	13.90	8.43	8.88	8.69	9.41	9.15	9.27	10.51	9.82	9.00	8.98	9.33	9.36	9.53	9.81		
CaO	0.09	0.00	0.00	0.00	0.02	0.06	0.07	0.00	0.00	0.03	0.01	0.02	0.04	0.01	0.01	0.00	0.03	0.02	0.00	0.02	0.00	0.00		
Na ₂ O	0.13	0.21	0.18	0.16	0.16	0.12	0.24	0.18	0.13	0.22	0.18	0.16	0.19	0.20	0.17	0.18	0.25	0.27	0.16	0.24	0.17	0.21		
K ₂ O	11.07	9.40	9.65	11.25	9.40	11.07	9.29	9.16	9.76	9.65	9.63	9.55	9.64	9.62	9.87	9.79	9.46	9.51	9.50	9.48	9.39	9.60		
Total	93.80	95.44	95.69	97.60	96.16	94.66	97.37	96.11	95.54	96.79	95.17	95.91	96.47	95.73	96.20	95.70	94.76	94.21	94.95	94.91	94.37	94.67		
Si	2.65	2.79	2.74	2.64	2.77	2.62	2.79	2.83	2.76	2.73	2.77	2.76	2.75	2.78	2.76	2.75	2.78	2.78	2.78	2.77	2.78	2.78		
Ti	0.34	0.28	0.26	0.35	0.23	0.32	0.20	0.19	0.25	0.30	0.25	0.24	0.26	0.22	0.25	0.23	0.28	0.25	0.32	0.27	0.27	0.30		
Al	1.51	1.57	1.59	1.54	1.61	1.48	1.71	1.71	1.70	1.62	1.71	1.69	1.70	1.68	1.64	1.67	1.58	1.63	1.59	1.57	1.62	1.59		
Cr	0.00	0.00	0.00	0.00	0.01	0.00	0.01	0.00	0.00	0.00	0.00	0.00	0.00	0.00	0.00	0.00	0.05	0.05	0.03	0.05	0.04	0.04		
Fe ^{+3*}	0.00	0.00	0.00	0.00	0.00	0.00	0.00	0.00	0.00	0.00	0.00	0.00	0.00	0.00	0.00	0.00	0.00	0.00	0.00	0.00	0.00	0.00		
Fe ⁺²	1.11	1.22	1.19	1.14	1.09	1.13	0.90	0.79	1.29	1.31	1.25	1.23	1.24	1.24	1.13	1.20	1.24	1.21	1.20	1.23	1.17	1.14		
Mn	0.00	0.00	0.00	0.00	0.00	0.00	0.00	0.00	0.00	0.01	0.00	0.00	0.00	0.00	0.00	0.00	0.00	0.00	0.00	0.00	0.00	0.01		
Mg	1.25	1.16	1.23	1.20	1.33	1.32	1.47	1.56	0.99	1.03	1.02	1.09	1.06	1.08	1.21	1.14	1.07	1.07	1.10	1.11	1.13	1.16		
Ca	0.01	0.00	0.00	0.00	0.00	0.01	0.01	0.00	0.00	0.00	0.00	0.00	0.00	0.00	0.00	0.00	0.00	0.00	0.00	0.00	0.00	0.00		
Na	0.02	0.03	0.03	0.02	0.02	0.02	0.04	0.03	0.02	0.03	0.03	0.02	0.03	0.03	0.03	0.03	0.04	0.04	0.02	0.04	0.03	0.03		
K	1.12	0.94	0.96	1.10	0.92	1.11	0.89	0.88	0.98	0.96	0.97	0.95	0.96	0.96	0.97	0.97	0.96	0.97	0.96	0.96	0.95	0.97		
Total	8.00	8.00	8.00	8.00	8.00	8.00	8.00	8.00	8.00	8.00	8.00	8.00	8.00	8.00	8.00	8.00	8.00	8.00	8.00	8.00	8.00	8.00		
X _{Mg}	0.53	0.49	0.51	0.51	0.55	0.54	0.62	0.66	0.43	0.44	0.45	0.47	0.46	0.46	0.52	0.49	0.46	0.47	0.48	0.47	0.49	0.50		

*Fe⁺³ recalculated according to the scheme of Droop, (1987)

Table 6.2c: Representative chemical analyses of plagioclase (stoichiometry calculated on the basis of 8 oxygens, oxide data are given in weight%).

Point No.	Grt-Bt-Sil gneiss						Grt-Crd-Bt-Sil gneiss			
	B117	I-236-1-07	I-236-1-07	B117	I-236-1-07		I-353-1-10			
	Matrix		Adj to Grt		Inclusions in Grt		Matrix		Adj to Grt	
	4 / 1	471	379	27 / 1	308	328	129	385	153	377
SiO ₂	62.00	60.27	60.29	60.39	57.84	57.92	64.46	61.90	63.29	60.51
TiO ₂	0.00	0.00	0.00	0.00	0.03	0.01	0.00	0.00	0.00	25.02
Al ₂ O ₃	23.35	24.53	24.24	24.82	25.71	26.20	22.66	24.05	22.92	0.00
FeO	0.00	0.07	0.16	0.03	0.23	0.24	0.09	0.05	0.08	0.00
MnO	0.00	0.04	0.00	0.00	0.00	0.04	0.00	0.00	0.00	0.00
MgO	0.00	0.00	0.01	0.01	0.01	0.02	0.00	0.00	0.00	0.00
CaO	4.88	5.86	5.87	6.50	7.89	7.94	3.34	4.75	4.14	6.22
Na ₂ O	9.07	7.96	8.19	8.10	7.00	6.71	9.11	8.17	8.84	7.54
K ₂ O	0.17	0.23	0.16	0.43	0.41	0.33	0.15	0.18	0.14	0.15
Total	99.50	98.97	98.91	100.27	99.16	99.41	99.81	99.10	99.41	99.50
Si	2.75	2.71	2.71	2.67	2.61	2.61	2.86	2.78	2.82	3.00
Ti	0.00	0.00	0.00	0.00	0.00	0.00	0.00	0.00	0.00	0.93
Al	1.22	1.30	1.28	1.30	1.37	1.39	1.19	1.27	1.20	0.00
Fe ^{+3*}	0.00	0.00	0.03	0.00	0.05	0.00	0.00	0.00	0.00	0.00
Fe ⁺²	0.00	0.01	0.00	0.00	0.00	0.01	0.12	0.11	0.08	0.00
Mn	0.00	0.00	0.00	0.00	0.00	0.00	0.00	0.00	0.00	0.00
Mg	0.00	0.00	0.00	0.00	0.00	0.00	0.00	0.00	0.00	0.00
Ca	0.23	0.28	0.28	0.31	0.38	0.38	0.16	0.23	0.20	0.33
Na	0.78	0.69	0.71	0.70	0.61	0.59	0.78	0.71	0.76	0.73
K	0.01	0.01	0.01	0.02	0.02	0.02	0.01	0.01	0.01	0.01
Total	5.00	5.00	5.00	5.00	5.00	5.00	5.00	5.00	5.00	5.00
X _{An}	0.23	0.29	0.28	0.30	0.37	0.39	0.17	0.24	0.20	0.31
X _{Ab}	0.76	0.70	0.71	0.68	0.60	0.59	0.82	0.75	0.79	0.68
X _{Or}	0.01	0.01	0.01	0.02	0.02	0.02	0.01	0.01	0.01	0.01

*Fe⁺³ recalculated according to the scheme of Droop (1987)

Table 6.2d: Representative chemical analyses of K-feldspar, ilmenite, rutile and sillimanite (stoichiometry calculated on the basis of 8, 3, 2 and 5 oxygens respectively, oxide data are given in weight %).

Point No.	K-feldspar			Ilmenite		Rutile	Sillimanite/ Kyanite
	Grt-Bt-Sil gneiss		Grt-Crd-Bt- Sil gneiss	7	7 / 1	4 / 1	12 / 1
	B117	I-236-1-07	I-353-1-10				
	29 / 1	26 / 1	12 / 1				
SiO ₂	65.09	65.13	64.40	0.00	0.03	0.03	37.03
TiO ₂	0.00	0.00	0.03	55.20	54.56	99.00	0.00
Al ₂ O ₃	18.61	18.52	18.43	0.01	0.18	0.29	62.85
Cr ₂ O ₃	0.06	0.00	0.00	0.02	0.00	0.21	0.10
FeO	0.07	0.26	0.00	43.31	44.07	0.55	0.18
MnO	0.02	0.01	0.00	0.30	0.23	0.00	0.00
MgO	0.01	0.00	0.00	1.12	0.55	0.04	0.00
NiO	0.00	0.00	0.00	0.00	0.00	0.00	0.00
ZnO	0.00	0.00	0.00	0.00	0.18	0.01	0.00
CaO	0.07	0.00	0.00	0.00	0.00	0.03	0.00
Na ₂ O	2.00	1.32	1.48	0.01	0.05	0.00	0.01
K ₂ O	14.22	15.36	14.86	0.00	0.00	0.00	0.00
Total	100.15	100.61	99.20	99.97	99.86	100.16	100.16
Si	2.98	2.98	2.98	0.00	0.00	0.00	1.00
Ti	0.00	0.00	0.00	1.04	1.03	0.99	0.00
Al	1.00	1.00	1.01	0.00	0.01	0.00	2.00
Cr	0.00	0.00	0.00	0.00	0.00	0.00	0.00
Fe ^{+3*}	0.00	0.01	0.04	0.00	0.00	0.02	0.00
Fe ⁺²	0.00	0.00	0.00	0.99	1.00	0.00	0.00
Mn	0.00	0.00	0.00	0.01	0.00	0.00	0.00
Mg	0.00	0.00	0.00	0.04	0.02	0.00	0.00
Ni	0.00	0.00	0.00	0.00	0.00	0.00	0.00
Zn	0.00	0.00	0.00	0.00	0.00	0.00	0.00
Ca	0.00	0.00	0.00	0.00	0.00	0.00	0.00
Na	0.18	0.12	0.13	0.00	0.00	0.00	0.00
K	0.83	0.90	0.88	0.00	0.00	0.00	0.00
Total	5.00	5.00	5.00	2.00	2.00	1.00	3.00
X _{An}	0.00	0.00	0.00				
X _{Ab}	0.18	0.12	0.13				
X _{Or}	0.82	0.88	0.87				

*Fe⁺³ recalculated according to the scheme of Droop, (1987)

Table 6.2e: Representative chemical analyses of cordierite and spinel (stoichiometry calculated on the basis of 18 and 4 oxygens respectively, oxide data are given in weight %).

Grt-Crd-Bt-Sil gneiss						
I-353-1-10						
Point No.	Cordierite				Point No.	Spinel
	108	323	396	202		97
SiO ₂	49.14	48.71	48.49	49.03	SiO ₂	0.03
TiO ₂	0.00	0.02	0.00	0.03	TiO ₂	0.20
Al ₂ O ₃	32.07	32.70	32.40	32.93	Al ₂ O ₃	50.71
Cr ₂ O ₃	0.01	0.00	0.01	0.00	Cr ₂ O ₃	8.70
FeO	7.28	6.99	6.90	6.37	FeO	29.45
MnO	0.10	0.05	0.06	0.07	MnO	0.07
MgO	8.76	8.92	8.85	9.37	MgO	3.27
NiO	0.00	0.00	0.00	0.00	NiO	0.00
ZnO	0.00	0.00	0.00	0.00	ZnO	7.64
CaO	0.02	0.01	0.01	0.00	CaO	0.01
Na ₂ O	0.16	0.10	0.15	0.09	Na ₂ O	0.00
K ₂ O	0.03	0.00	0.00	0.00	K ₂ O	0.00
Total	97.57	97.50	96.87	97.89	Total	100.08
Si	5.07	5.02	5.03	5.02	Si	0.00
Ti	0.00	0.00	0.00	0.00	Ti	0.00
Al	3.90	3.97	3.96	3.98	Al	1.76
Cr	0.00	0.00	0.00	0.00	Cr	0.20
Fe ^{+3*}	0.00	0.00	0.00	0.00	Fe ^{+3*}	0.03
Fe ⁺²	0.64	0.61	0.60	0.55	Fe ⁺²	0.69
Mn	0.01	0.00	0.00	0.01	Mn	0.00
Mg	1.35	1.37	1.37	1.43	Mg	0.14
Ni	0.00	0.00	0.00	0.00	Ni	0.00
Zn	0.00	0.00	0.00	0.00	Zn	0.17
Ca	0.00	0.00	0.00	0.00	Ca	0.00
Na	0.03	0.02	0.03	0.02	Na	0.00
K	0.00	0.00	0.00	0.00	K	0.00
Total	11.00	11.00	11.00	11.00	Total	3.00
X _{Mg}	0.68	0.69	0.70	0.72	X _{Mag}	0.01
					X _{Spl}	0.13
					X _{Hc}	0.61
					X _{Gh}	0.15
					X _{Chr}	0.10
					X _{Mg}	0.17

*Fe⁺³ recalculated according to the scheme of Droop (1987). Gh:Gahnite, Chr:Chromite components in spinel.

6.4. PT conditions and evolution of mineral assemblage

Based on the observed sequence of mineral assemblages combined with mineral compositions, the P-T evolution of the two pelitic granulites types was reconstructed using thermobarometric calculations and P-T pseudosection modelling.

6.4.1. Thermobarometry

Methodologies

Temperatures achieved by the studied rocks were calculated from the garnet-biotite (GB) (Bhattacharya et al., 1992; Holdaway and Lee, 1977; Perchuk et al., 1985), garnet-cordierite (GCrd) (Bhattacharya et al., 1988; Holdaway and Lee, 1977; Perchuk et al., 1985) Fe–Mg exchange thermometers, and the Ti in biotite (Henry et al., 2005) thermometer, while pressures from garnet–aluminosilicate-quartz-plagioclase (GASP) (Ganguly and Saxena, 1984; Hodges and Crowley, 1985; Newton and Haselton, 1981) barometers. As garnet zoning documents post-peak Fe–Mg re-equilibration with adjacent biotite, peak conditions were calculated by combining analyses of garnet cores/ mantles with that of Fe-rich matrix biotite and matrix plagioclases (peak pressures). Post peak conditions were calculated by combining compositions of garnet rims with replacing biotites. The very restricted composition of cordierite even at the contact of compositionally zoned garnet has been reported from other high-grade rocks (Ellis et al., 1980 and some others). One of the plausible explanations of such phenomenon could be faster diffusion of Fe–Mg in cordierite relative to garnet (Chakraborty and Ganguly, 1991). The post peak temperatures for Grt- Crd-Bt-Sil gneiss was therefore also constrained by garnet rim-adjacent cordierite compositions. P-T conditions for the Grt-Bt-Sil gneiss were calculated from two samples B117 and I-236-1-07, while that for the Grt- Crd-Bt-Sil gneiss was calculated from sample I-353-1-10. Lack of sillimanite associated with post peak replacement of garnet as well as cordierite restricts the use of GASP and GCrdAS (garnet-cordierite-aluminosilicate-quartz) barometers to constrain post peak pressures in Grt-Crd-Bt-Sil gneiss. Ti in biotite thermometer was applied for different compositions of biotite from varied textural occurrences. However,

composition of matrix biotites, yield abnormally low temperature ranges implying that the Ti content in the matrix biotites might have undergone local and partial re-equilibration (Henry et al., 2005). Hence, this thermometer has been efficiently used to constrain the post peak conditions only.

Results

The spread of the respective thermobarometric results for each sample have been represented by the mean value calculated with the standard deviation (excluding the uncertainties related to analysis and formulations). The reference pressure/temperatures used for these calculations are those obtained from pseudosection modelling.

6.4.1.1. *Grt-Bt-Sil gneiss*

Results of thermobarometric calculations for both samples (B117 and I-236-1-07) are represented in Table 6.3a. GB thermometry using garnet core and matrix biotite compositions yields peak temperatures that cluster at $\sim 756 \pm 37^\circ\text{C}$. GASP barometry calculated with matrix plagioclase yields peak pressures of $\sim 6.4 \pm 0.7$ kbar (Table 6.3a). A distinctly lower temperature was calculated with GB thermometry using the rim compositions of garnet and adjacent biotite. Compositions of plagioclase in biotite-quartz intergrowths resorbing garnet were used for GASP calculations. P-T conditions during the post peak garnet replacement cluster at $\sim 651 \pm 29^\circ\text{C}$ and $\sim 4.1 \pm 0.7$ kbar (Table 6.3a). Ti in biotite thermometry also constrains similar post peak temperatures of $\sim 634 \pm 20^\circ\text{C}$ (Table 6.3a).

6.4.1.2. *Grt-Crd-Bt-Sil gneiss*

GB thermometry and GASP barometry for Grt-Crd-Bt-Sil gneiss (sample I-353-1-10) yielded peak temperatures and pressures of $\sim 750 \pm 32^\circ\text{C}$ (Table 6.3b) and $\sim 6.3 \pm 0.8$ kbar (Table 6.3b). Rim compositions of garnet and replacing biotites record the retrogression temperature conditions of $\sim 662 \pm 39^\circ\text{C}$ (Table 6.3b). Post peak temperatures constrained from garnet rim and adjacent cordierite yields slightly lower values of $\sim 643 \pm 36^\circ\text{C}$ (Table 6.3b). Ti in biotite thermometry constrains post peak temperatures around $\sim 649 \pm 12^\circ\text{C}$ (Table 6.3b).

Table 6.3a: *P–T estimates of Grt-Bt-Sil gneiss (B117 and I-236-1-07) obtained using various conventional thermobarometers (T: °C, P: kbar).*

Peak	Conventional Thermometry					Conventional Barometry				
	Assemblage used for calculation	P _{ref} [*]	Results ^{a,b,c}			Assemblage used for calculation	T _{ref} [*]	Results ^{d,e,f}		
			B117	I-236-1-07	Mean			B117	I-236-1-07	Mean
Peak	Grt [C]– Bt [M]	6.5	738 ± 32	775 ± 42	756 ± 37	Grt [C]– Pl– Als–Qtz	780	6.7 ± 0.6	6 ± 0.8	6.4 ± 0.7
	Retrogression Grt [R]– Bt [R]	5	603 ± 29	698 ± 29	651 ± 29	Grt [R]– Pl– Als–Qtz	670	3.9 ± 0.7	4.3 ± 0.8	4.1 ± 0.7
	Biotite	5	653±28	615±13	634±20 ^g	–	–	–	–	–

Grt: Garnet, Bt: Biotite, Pl: Plagioclase, Als: Aluminosilicate, Qtz: Quartz, [C]: core, [R]: rim, [M]: matrix.

Grt–Bt thermometers: ^a Bhattacharya et al. (1992), ^b Holdaway and Lee (1977), ^c Perchuk et al. (1985).

Grt–Als–Pl–Qtz barometers: ^d Newton and Haselton (1981), ^e Hodges and Crowley (1985),

^f Ganguly and Saxena (1984), **Ti in biotite:** ^g Henry et al. (2005).

* obtained from pseudosection modelling.

Table 6.3b: *P–T estimates of Grt-Crd-Bt-Sil gneiss (I-353-1-10) obtained using various conventional thermobarometers (T: °C, P: kbar).*

Peak	Conventional Thermometry			Conventional Barometry		
	Assemblage used for calculation	P _{ref} [*]	Results	Assemblage used for calculation	T _{ref} [*]	Results
Peak	Grt [C]– Bt [M]	5.8	750 ± 32 ^{a,b,c}	Grt [C]– Pl– Als–Qtz	760	6.3 ± 0.8 ^{d,e,f}
Retrogression	Grt [R]– Bt [R]	5	662 ± 39 ^{a,b,c}	–	–	–
	Grt [R]– Crd [R]		643 ± 36 ^{b,c,g}	–	–	–
	Biotite	5	649±12 ^h	–	–	–

Grt: Garnet, Bt: Biotite, Pl: Plagioclase, Als: Aluminosilicate, Qtz: Quartz, [C]: core, [R]: rim,

[M]: matrix. **Grt–Bt thermometers:** ^a Bhattacharya et al. (1992), ^b Holdaway and Lee (1977),

^c Perchuk et al. (1985). **Grt–Als–Pl–Qtz barometers:** ^d Newton and Haselton (1981),

^e Hodges and Crowley (1985), ^f Ganguly and Saxena (1984). **Grt–Crd thermometers:** ^b Holdaway

and Lee (1977), ^c Perchuk et al. (1985), ^g Bhattacharya et al. (1988).

Ti in biotite: ^h Henry et al. (2005).

* obtained from pseudosection modelling.

6.4.2. Pseudosection modelling

Pseudosection for the two studied pelitic granulites (Grt-Bt-Sil gneiss: B117 and Grt-Crd-Bt-Sil gneiss: I-353-1-10) were constructed using the *Perple_X* program, version 6.8.0 (Connolly, 2005 updated December 2017) with the internally consistent thermodynamic dataset of Holland and Powell (2011) in the system NCKFMASHTO (Na₂O-CaO-K₂O-FeO-MgO-Al₂O₃-SiO₂-TiO₂-H₂O-O₂). The pseudosection modelling of these two pelitic granulite assemblages involve the minerals garnet, orthopyroxene, biotite, cordierite, plagioclase, K-feldspar, quartz, rutile, ilmenite, sillimanite, kyanite, andalusite, muscovite, spinel, sapphirine, staurolite, corundum, chlorite, chloritoid and melt. The chosen thermodynamic models and *a-X* relationships for most of the solid solution minerals are from White et al. (2014a, 2014b) except plagioclase, sapphirine, spinel and ilmenite for which the models of Holland and Powell (2003), Taylor-Jones and Powell (2010), White et al. (2002), and White et al. (2000) modified by White et al. (2014b) were used, respectively. In view of the insignificant concentration of MnO in garnet and ZnO in spinel along with absence of any other MnO and ZnO bearing minerals in the two samples, these were not considered as system components. In oxide-poor silicate rocks, chemical potential of oxygen (and hence the f_{O_2}) is buffered by mineral/ fluid composition with which oxygen was in equilibrium (Frost, 1991). The studied rocks do not contain any known oxygen buffer. However, natural observations show that the crustal rocks are commonly buffered at f_{O_2} values close to NNO buffer (Frost, 1991; Sengupta et al., 1991) at which the pseudosections for the studied rocks were constructed. P-T pseudosections are calculated using the composition of a rock volume that was in chemical equilibrium. Identification of such an equilibrated domain is very difficult in granulite facies rocks as the rock becomes extremely dry at high-grade conditions (because of the partitioning of water preferentially to the segregated leucosomes). It greatly decreases the diffusivity of the elements and thus puts a kinetic hindrance to the element transport process. Consequently, the minerals equilibrate within a much smaller volume (may be in microscopic scale) rather than the hand specimen scale (Palin et al., 2016). In such cases, the bulk rock XRF composition data may reflect the composition of a much larger rock volume than the actual equilibration volume. Additionally, presence of cordierite-free

patches (mineralogically similar to Grt-Bt-Sil gneiss) within Grt-Crd-Bt-Sil gneisses also suggests heterogeneity of the bulk composition in mesoscopic scale. Calculation of the effective bulk composition is thus more appropriate for the studied high-grade rocks. Effective bulk compositions for the two studied assemblages were calculated by combining the modal proportions of the minerals with their respective measured chemical compositions. Details of the methodology have been provided in the Appendix. Since, at high grade conditions, the porosity of rocks become very low, the rock becomes practically devoid of any free fluid (Clemens and Vielzeuf, 1987). The only fluid available to the system is that within the structure of the minerals. Fixing of H₂O for the pseudosection study is not straightforward, as the amount of hydrous minerals (biotite, cordierite) prior to the onset of high-grade metamorphism cannot be predicted accurately. Nevertheless, following the procedure described in Mukherjee et al., (2018), an attempt has been made to estimate the amount of H₂O from T-X_{H₂O} sections (constructed at ~7 kbar, the average pressure constrained from conventional barometry) for the two pelitic granulites separately. Garnet composition, and melt volume isopleths (as observed from volume of leucosomes in rock) were used to constrain the H₂O content. The T-X_{H₂O} sections have been provided in Supplementary Material 1.

6.4.2.1. Metamorphic evolution of the Grt-Bt-Sil gneiss

Based on the compositional similarity between the different samples, phase equilibria modelling for the sample B117 is being presented here (Fig. 6.4a-b) as a representative for all the studied Grt-Bt-Sil gneisses. Inclusions in the cores of garnet porphyroblasts indicate an early stabilised prograde assemblage comprising biotite, quartz, plagioclase, K-feldspar and rutile. Additionally, the presence of relict kyanite in the matrix indicates that it was also part of the prograde assemblage (garnet-biotite-kyanite-rutile-plagioclase-quartz-K-feldspar). The presence of rutile and kyanite implies that the prograde assemblage had witnessed elevated pressures. The garnet porphyroblasts, dispersed within a matrix defined by recrystallized well-grown grains of plagioclase, K-feldspar, quartz and biotite suggests that all matrix minerals survived through prograde metamorphism and were in equilibrium during peak metamorphic conditions. Partial replacement of rutile inclusions by ilmenite indicates that garnet growth persisted from the rutile-present field during the early

stage of the prograde path to the ilmenite-present field during heating (associated with slight pressure decrease) to peak metamorphic conditions (Fig. 6.4b). Heating, associated with drop in pressures, led to crossing of the kyanite-sillimanite reaction, resulting in the formation of sillimanite grains in the matrix and the pseudomorphic replacement of kyanite by sillimanite. Inclusions of sillimanite in the garnet mantle also document the continued growth of garnet in the sillimanite stability field, leading to the peak temperature assemblage of garnet-biotite-sillimanite-K-feldspar-plagioclase-ilmenite-quartz-melt after crossing of the solidus at $\sim 750^{\circ}\text{C}$ (Fig. 6.4a-b). Many experimental studies (e.g., Gardien et al., 1995) have constrained similar temperature ranges, for the initiation of the biotite dehydration melting reaction (biotite + sillimanite + plagioclase + quartz = garnet + K-feldspar + melt). The volume of anatectic melt (<10 vol%) constrained from the presence of scarce garnet-bearing leucosomes in the outcrop, and the presence of abundant primary biotites, suggest limited dehydration melting of biotite in the studied rocks. In the calculated pseudosection, the field representing the peak temperature assemblage garnet-biotite-sillimanite-K-feldspar-plagioclase-ilmenite-quartz-melt is stable over a P-T range of ~ 750 – 820°C and ~ 5.4 – 9.5 kbar (Fig. 6.4a-b). The isopleths representing compositions of garnet core/mantle (X_{Py} , X_{Alm} and X_{Grs}) and matrix biotite (X_{Mg} : 0.49–0.52) further refine the peak P-T conditions to ~ 5.8 – 7.1 kbar and ~ 760 – 790°C (Fig. 6.4a). The volume isopleths of melt passing through this peak metamorphic field (up to a maximum 10%) are also consistent with the amount of leucosomes observed in the rock. The peak P-T conditions constrained from the pseudosection modelling are in good agreement with those estimated from geothermobarometry ($756 \pm 37^{\circ}\text{C}$, 6.4 ± 0.7 kbar; Fig. 6.4b, Table 6.3a). Breakdown of garnet porphyroblasts to biotite-quartz intergrowth, with additional fibrolitic sillimanite and/or plagioclase (through the GASP reaction and the reverse biotite dehydration melting reaction: garnet + K-feldspar + melt = biotite + sillimanite + plagioclase + quartz) documents post-peak retrogression. The stability field of the retrograde subsolidus assemblage garnet-biotite-plagioclase-sillimanite-ilmenite-quartz-K-feldspar is large (~ 3.4 – 8.6 kbar and ~ 530 – 770°C , Fig. 6.4a-b). Compositions of garnet rims (X_{Py} and X_{Alm}) adjacent to the replacing biotites, along with compositions of plagioclase (X_{An}) were used to tightly bracket the P-T

conditions achieved during retrograde metamorphism at ~630–700°C, ~4.2–5.4 kbar (Fig. 6.4a).

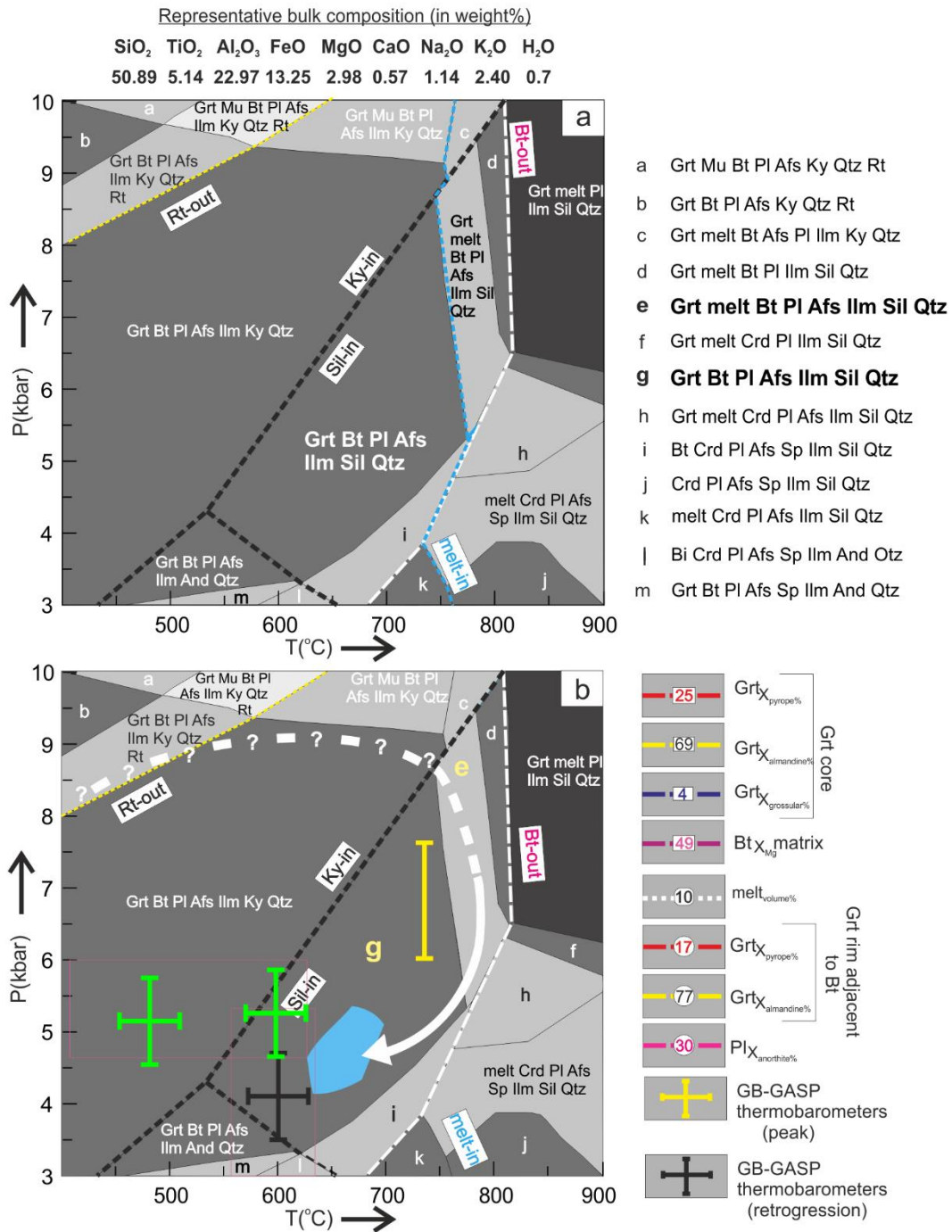


Fig. 6.4. (a-b): P-T pseudosections constructed in the system NCKFMASHTO for Grt-Bt-Sil gneiss (B117). The peak (green) and post peak (blue) field are represented by 'e' and 'g' respectively (bold in the index). (a) Intersecting isopleths constraining the peak and post peak P-T ranges. (b) Peak and post peak fields shown along with the results of conventional thermobarometry. The overall P-T path is shown with a white arrow. GB: Garnet-Biotite thermometry, GASP: Garnet-Aluminosilicate-Plagioclase-Quartz barometry. Mineral abbreviations after Kretz, (1983).

6.4.2.2. Metamorphic evolution of the Grt-Crd-Bt-Sil gneiss

Textural relations showing xenoblastic garnets in equilibrium with ilmenite suggests that garnet along with these minerals stabilised during peak metamorphic conditions. The straight grain boundaries between garnet and cordierite imply that cordierite also formed during peak metamorphism. Thin rim of melt crystallised around large matrix cordierite (Fig. 6.2p), indicate minor amount of partial melting during peak metamorphism, through the reaction $\text{biotite} + \text{sillimanite} + \text{quartz} \pm \text{plagioclase} = \text{garnet} + \text{cordierite} + \text{melt}$. Several studies that have experimentally constrained this reaction (Ward et al., 2008 and some others), estimated melting temperatures comparable with that obtained from our pseudosection modelling ($\sim 700\text{--}750^\circ\text{C}$, Fig. 6.4c-d). The presence of matrix biotite in equilibrium with garnet indicates that garnet-biotite-cordierite-sillimanite-plagioclase-K-feldspar-quartz-ilmenite and melt constitute the peak metamorphic assemblage. Presence of relict kyanite in the matrix and inclusions of rutile in sillimanite, points towards their stability as a prograde mineral at elevated pressure conditions. In the calculated pseudosection, this peak assemblage is stable over a wide P-T range of $\sim 730\text{--}840^\circ\text{C}$ and $\sim 5.3\text{--}7.1$ kbar (Fig. 6.4c-d). The melt volume isopleths in the pseudosection, passing through this field predicts a maximum of $\sim 3\text{--}8\%$ melt in equilibrium with the peak assemblage. This is in accordance with the scarce amount of leucosomal segregations observed in the outcrops and the narrow melt rims around cordierite. To further concise the P-T range for the formation of the peak assemblage, garnet core compositions (X_{Py} , X_{Alm} and X_{Grs}) and X_{Mg} isopleths of matrix biotites were plotted. They refine the peak P-T conditions to $\sim 730\text{--}790^\circ\text{C}$ and $\sim 5.5\text{--}6.1$ kbar (Fig. 6.4c). The peak P-T data constrained from the pseudosection is in good agreement with the P-T conditions estimated from geothermobarometry ($750 \pm 32^\circ\text{C}$, 6.3 ± 0.8 kbar; Fig. 6.4d, Table 6.3b) and with the P-T data for the Grt-Bt-Sil gneiss. Breakdown of garnet into biotite-quartz intergrowths (and diffusive re-equilibration of garnet-biotite rims) marks the terminal phase of the retrogressive path (Fig. 6.4d). Peak conditions are also succeeded by complete compositional re-equilibration of cordierite by Fe-Mg diffusive exchange between adjacent garnet and cordierite. Hence, in the modelled pseudosection, the stability field of garnet-biotite-cordierite-plagioclase-K-feldspar-sillimanite-quartz-ilmenite is presumed

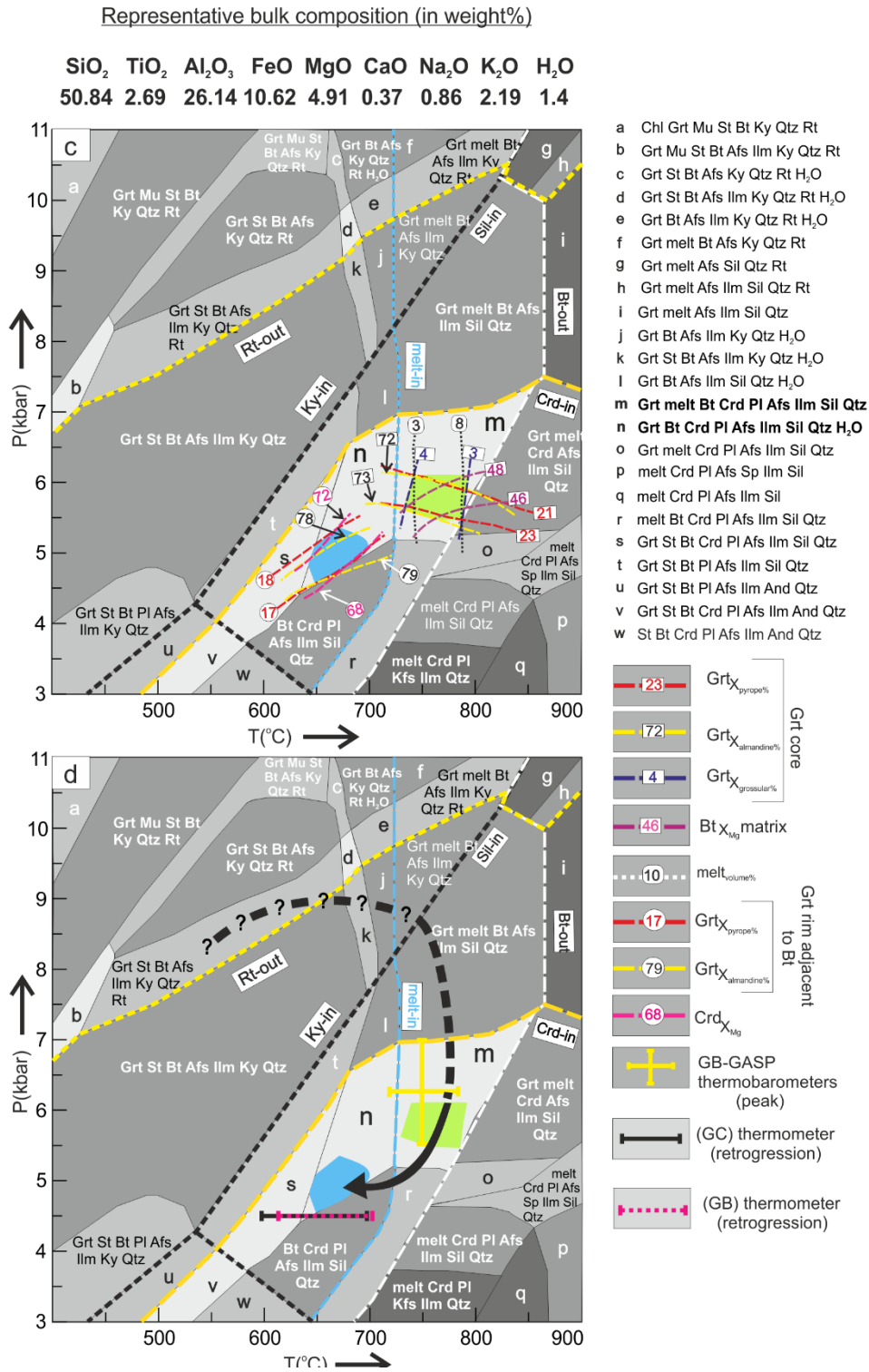


Fig. 6.4(c-d): P-T pseudosections constructed in the system NCKFMASHTO for Grt-Crd-Bt-Sil gneiss. The peak (green) and post peak (blue) field is represented by 'm' and 'n' respectively (bold in the index). (c) Intersecting isopleths constrain the peak and post peak P-T ranges. (d) Peak and post peak fields shown along with the results of conventional thermobarometry. The overall P-T path is shown with a black arrow; GB: Garnet-Biotite thermometry, GASP: Garnet-Aluminosilicate-Plagioclase-Quartz barometry, GC: Garnet-Cordierite thermometry. Mineral abbreviations after Kretz, (1983).

to represent the latest recorded retrograde assemblage. Isopleths representing the compositions of garnet rim and X_{Mg} of cordierite bracket the P-T conditions attained during retrogression between $\sim 640\text{--}700^\circ\text{C}$ and $\sim 4.6\text{--}5.3$ kbar (Fig. 6.4c). The results of phase equilibria modelling and conventional thermobarometric calculations for each stage of metamorphism lie roughly within the uncertainty limits of ~ 1.0 kbar and $\sim 50^\circ\text{C}$ (references cited in Palin et al., 2016) and hence are considered well in accordance with each other (Fig. 6.4b, d). After combining the P-T calculations from the two pelitic granulite assemblages it is evident that the P-T path of the studied rocks passed through $\sim 730\text{--}790^\circ\text{C}$, $\sim 5.5\text{--}7$ kbar and $\sim 630\text{--}700^\circ\text{C}$, $\sim 4\text{--}5.4$ kbar clusters, thus defining a CW P-T path. However, the presence of kyanite (now pseudomorphed by sillimanite) and rutile in the assemblage suggest that the studied rocks must have experienced higher pressures during the prograde evolution (≥ 8 kbar, Fig. 6.4b, d). The bulk compositions indicate that the formation of cordierite is mainly related to the more magnesian composition of the Grt-Crd-Bt-Sil gneiss ($X_{Mg}=0.45$) compared to Grt-Bt-Sil gneiss ($X_{Mg}=0.29$) that enlarges the stability of cordierite towards higher pressures.

6.5. Geochronology

6.5.1. U-Pb Zircon dating

Proper detrital zircon with datable size is less common in the pelitic granulites, owing to the likely deposition of their probable protolith, shale, under tranquil water conditions (Kooijman et al., 2011). However, detrital zircon grains are common in psammitic rocks that are deposited under high energy condition. These detrital grains, in turn, act as nuclei of metamorphic overgrowth. The studied pelitic granulites do not contain adequate number of zircons with datable size (only two grains could be separated from the analysed Grt-Bt-Sil gneiss, 'I-235-1-07', Table 6.4). Hence, we complemented the geochronological study by the zircon data from an associated meta-psammite sample, 'I-353-10-10', which contains abundant detrital and metamorphic zircons (Table 6.4). As the chosen Grt-Opx bearing meta-psammite is intercalated with the studied pelitic granulites in field, they are presumed to share the same metamorphic evolutionary history. U-Pb spot analysis of zircon grains were carried out by Laser Ablation Inductively Coupled Plasma Mass

Spectrometry (LA-ICP-MS) at Frankfurt University. Details of the analytical techniques for U–Pb zircon dating are given in Appendix.

6.5.1.1. Morphology and age data of Grt-Bt-Sil gneiss (I-235-1-07)

The two separated grains are anhedral in shape and very small (60–70 μm in length) (Fig. 6.5a-b). The zircons either show patchy zoning without distinct cores (Fig. 6.5a), or contain a very small, highly luminescent core, surrounded by a broad sector-zoned rim (Fig. 6.5b). The anhedral shape and the patchy or sector zoning strongly suggest new growth of the zircons during metamorphism, preferably in absence of any melt phase (Corfu et al., 2003). The metamorphic growth of the grains is corroborated by the very low Th/U ratios (0.01–0.08; Table 6.4), that is typical for metamorphic zircons (e.g., Rubatto, 2002). A total of five spots were analysed. All the analysed points show less than 4% discordance with $^{207}\text{Pb}/^{206}\text{Pb}$ ages ranging from 578 ± 34 to 533 ± 36 Ma (Table 6.4). The data define a concordia age of 553 ± 4 Ma (MSWD = 1.5) (Fig. 6.6a).

6.5.1.2. Morphology and age data Grt-Opx bearing meta-psammite (I-353-10-10)

The Grt-Opx bearing meta-psammite contains abundant zircon grains (<150 μm in size). Most of the anhedral to subhedral grains contain a small but distinct core that is surrounded by a broad rim (Fig. 6.5c-d). The cores are usually rounded and have irregular, often resorbed margins, suggesting a detrital origin. Both the cores and rims are weakly luminescent and unzoned (Fig. 6.5c & d). Zircons without core are weakly luminescent, small, subhedral and homogenous (Fig. 6.5e). The homogenous rims around the detrital cores and the individual subhedral to anhedral homogenous grains suggest their metamorphic growth (Corfu et al., 2003). Low Th/U ratios obtained from these zircons (\sim 0.01–0.18; Table 6.4) also support their metamorphic origin (e.g., Rubatto, 2002). A total of fifty-two spots were analysed from both cores and rims. The cores, rims and homogenous grains define a discordia with an early Palaeoproterozoic upper intercept age of 2433 ± 10 Ma and an early Cambrian lower intercept age of 536 ± 17 Ma (MSWD = 8.7) (Fig. 6.6b). Nine near-concordant analyses from the detrital cores (with \geq 90% concordance) yield a $^{207}\text{Pb}/^{206}\text{Pb}$ age range between 2450 ± 16 to 2361 ± 14 Ma

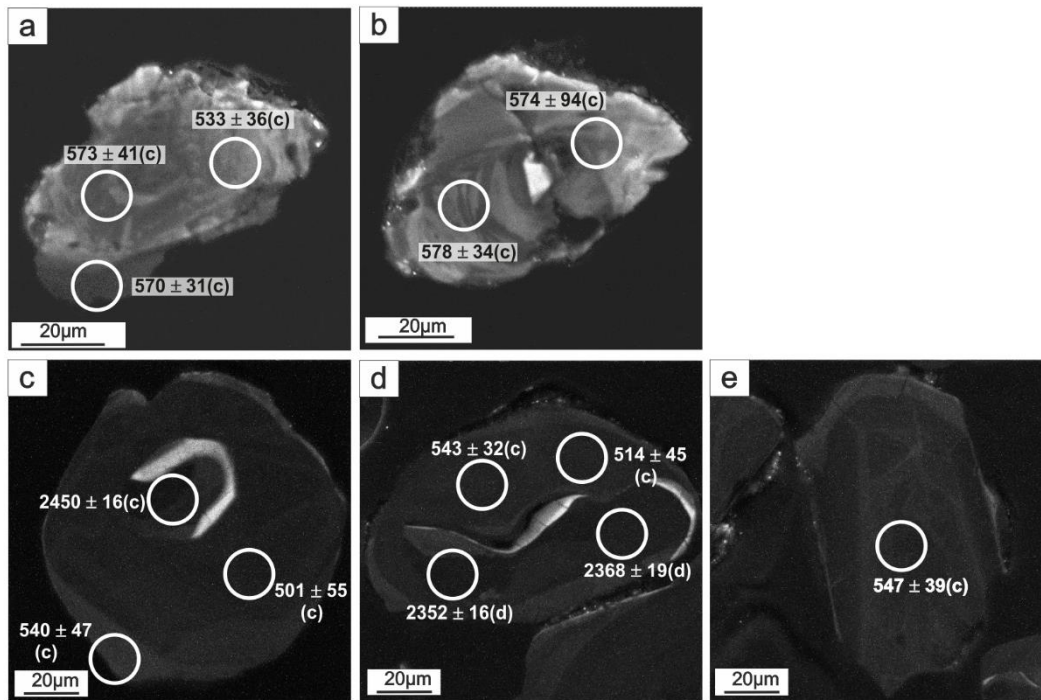


Fig. 6.5: Cathodoluminescence (CL) images of selected zircon grains from (a-b) Grt-Bt-Sil gneiss (I-235-1-07) and (c-e) Grt-Opx bearing meta-psammite (I-353-10-10). (a-b) Zircon grains showing patchy zoning without any distinct cores. (c-d) Zircon grains containing small unzoned detrital cores with irregular margins. These are rimmed by broad unzoned metamorphic overgrowths. (e) Unzoned metamorphic zircon grain without any distinct cores. White circles mark the position of the laser spots. The dates indicate $^{207}\text{Pb}/^{206}\text{Pb}$ ages of the spots in 'Ma'. 'c': concordant age data (for ages with $\geq 90\%$ concordance), 'd': discordant age data (for ages with $< 90\%$ concordance).

that is consistent with the upper-intercept age. Moderate to low Th/U ratios ranging from 0.16 to 0.34 suggest the metamorphic growth of these cores and their later reworking into the sedimentary protolith of the Grt-Opx bearing meta-psammite (Table 6.4). The remaining 27 spot analyses from the cores yield discordant dates (< 90 to 50% concordance; Table 7.4). 12 concordant analyses ($\geq 90\%$ concordance) of the broad unzoned rims and the homogenous grains yield a concordia age of 530 ± 3 Ma (MSWD = 1.9) (Fig. 6.6b) that is in good agreement with the ~ 536 Ma lower-intercept age, documenting lead loss of all zircons during the Ediacaran-Cambrian metamorphism.

Table 6.4: Results of U-Th-Pb LA-ICP-MS analyses of zircon.

Grain	Texture	Radiogenic isotopes										Apparent age (Ma)								
		$^{207}\text{Pb}^a$ (cps)	U^b (ppm)	Pb^b (ppm)	Th^b U	$\frac{^{206}\text{Pb}}{^{204}\text{Pb}}$	$\frac{^{206}\text{Pb}^c}{^{238}\text{U}}$	$\pm 2s$ (%)	$\frac{^{207}\text{Pb}^c}{^{235}\text{U}}$	$\pm 2s$ (%)	Rho^d	$\frac{^{206}\text{Pb}}{^{238}\text{U}}$	$\pm 2s$	$\frac{^{207}\text{Pb}}{^{235}\text{U}}$	$\pm 2s$	$\frac{^{207}\text{Pb}^c}{^{206}\text{Pb}}$	$\pm 2s$	conc. ^e (%)		
Sample No.: I-235-1-07																				
c1	Metamorphic	9683	284	24	0.01	6097	0.0909	2.43	0.7430	2.88	0.0593	1.54	0.84	561	13	564	13	578	34	97
c2	Metamorphic	16058	218	25	0.08	10719	0.0897	2.05	0.7317	4.77	0.0592	4.31	0.43	554	11	558	21	574	94	97
c3	Metamorphic	8115	241	20	0.04	1433	0.0881	2.11	0.7053	2.67	0.0581	1.64	0.79	544	11	542	11	533	36	102
c4	Metamorphic	10398	324	27	0.02	644	0.0888	2.08	0.7239	2.80	0.0592	1.88	0.74	548	11	553	12	573	41	96
c5	Metamorphic	7458	214	18	0.07	1751	0.0900	1.45	0.7331	2.02	0.0591	1.40	0.72	555	8	558	9	570	31	97
Sample No.: I353-10-10																				
A479	Metamorphic	6378	1270	102	0.04	2589	0.0866	1.57	0.6837	2.94	0.0572	2.48	0.54	536	8	529	12	501	55	107
A477	Metamorphic	7318	1354	109	0.01	b.d.	0.0868	1.41	0.6857	2.42	0.0573	1.96	0.58	537	7	530	10	503	43	107
A499	Metamorphic	7486	1401	110	0.01	b.d.	0.0850	1.50	0.6750	2.54	0.0576	2.05	0.59	526	8	524	10	514	45	102
A489	Metamorphic	7627	1479	116	0.04	23187	0.0845	1.45	0.6754	2.14	0.0580	1.57	0.68	523	7	524	9	529	34	99
A528	Metamorphic	6567	1296	102	0.03	2104	0.0853	1.45	0.6827	2.87	0.0581	2.48	0.50	527	7	528	12	532	54	99
A476	Metamorphic	5829	1141	88	0.03	3414	0.0839	1.48	0.6729	2.69	0.0582	2.24	0.55	519	7	522	11	537	49	97
A481	Metamorphic	6286	1265	97	0.03	6288	0.0831	1.51	0.6681	2.62	0.0583	2.14	0.58	515	7	520	11	540	47	95
A500	Metamorphic	6978	1309	105	0.01	30558	0.0877	1.51	0.7055	2.11	0.0584	1.48	0.72	542	8	542	9	543	32	100
A492	Metamorphic	7595	1442	114	0.03	19714	0.0853	1.52	0.6878	2.34	0.0585	1.78	0.65	528	8	532	10	547	39	97
A525	Metamorphic	14854	1753	142	0.08	b.d.	0.0868	2.44	0.6994	2.79	0.0585	1.36	0.87	536	13	538	12	547	30	98
A504	Metamorphic	7626	1573	125	0.02	9042	0.0860	1.44	0.6939	2.43	0.0585	1.95	0.59	532	7	535	10	549	43	97
A482	Metamorphic	4055	682	53	0.02	7645	0.0831	3.20	0.6754	4.68	0.0590	3.42	0.68	514	16	524	19	566	74	91
A486	Metamorphic	2190	355	30	0.18	1072	0.0864	2.98	0.7047	6.42	0.0592	5.69	0.46	534	15	542	27	573	124	93
A517	Metamorphic	6772	1109	87	0.02	14104	0.0847	1.95	0.6925	2.64	0.0593	1.77	0.74	524	10	534	11	578	39	91
A511	Metamorphic	21594	343	77	0.10	47	0.0921	8.46	0.7742	19.95	0.0610	18.07	0.42	568	46	582	92	638	389	89
A475	Detrital	19533	746	112	0.05	1622	0.1515	1.51	2.3480	2.33	0.1124	1.78	0.65	910	13	1227	17	1838	32	49
A509	Detrital	22194	1568	200	0.17	b.d.	0.1285	1.54	1.7240	2.08	0.0973	1.40	0.74	779	11	1018	13	1573	26	50
A515	Detrital	21351	1206	183	0.04	b.d.	0.1533	2.37	2.1810	2.74	0.1032	1.37	0.87	919	20	1175	19	1682	25	55
A521	Detrital	90532	2271	476	0.16	32474	0.2039	1.62	3.5430	1.98	0.1260	1.13	0.82	1196	18	1537	16	2043	20	59
A531	Detrital	63470	1098	261	0.12	9939	0.2302	2.38	4.4860	2.75	0.1413	1.39	0.86	1336	29	1728	23	2243	24	60
A505	Detrital	11849	1443	137	0.02	5341	0.0996	2.49	0.9681	3.15	0.0705	1.92	0.79	612	15	687	16	943	39	65
A518	Detrital	52931	1500	396	0.25	1153	0.2545	1.64	4.8480	3.34	0.1382	2.91	0.49	1461	21	1793	28	2204	50	66
A523	Detrital	56586	1350	357	0.22	7473	0.2548	1.72	4.8130	2.07	0.1370	1.16	0.83	1463	23	1787	18	2190	20	67
A508	Detrital	49926	1255	343	0.28	74574	0.2602	1.61	4.9500	1.81	0.1380	0.83	0.89	1491	22	1811	15	2202	14	68
A484	Detrital	84103	1721	495	0.25	15867	0.2718	2.23	5.4050	2.61	0.1442	1.35	0.86	1550	31	1886	23	2278	23	68
A502	Detrital	95146	2032	596	0.32	2101	0.2697	1.44	5.1770	1.88	0.1392	1.21	0.76	1539	20	1849	16	2217	21	69

Table 6.4 contd.: Results of U-Th-Pb LA-ICP-MS analyses of zircon.

Grain	Texture	$^{207}\text{Pb}^a$ (cps)	U^b (ppm)	Pb^b (ppm)	$\frac{\text{Th}^b}{\text{U}}$	Radiogenic isotopes				Apparent age (Ma)				concentration (%)						
						$\frac{^{206}\text{Pb}}{^{204}\text{Pb}}$	$\frac{^{206}\text{Pb}^c}{^{238}\text{U}}$	$\pm 2s$ (%)	$\frac{^{207}\text{Pb}^c}{^{235}\text{U}}$	$\pm 2s$ (%)	$\frac{^{207}\text{Pb}^c}{^{206}\text{Pb}}$	$\pm 2s$ (%)	$\frac{^{206}\text{Pb}}{^{238}\text{U}}$		$\pm 2s$ (%)	$\frac{^{207}\text{Pb}}{^{235}\text{U}}$	$\pm 2s$ (%)			
A483	Detrital	63219	1664	458	0.18	3536	0.2686	2.13	5.0990	2.36	0.1377	1.01	0.90	1534	29	1836	20	2199	18	70
A501	Detrital	88351	1622	525	0.17	5511	0.3106	1.68	6.4480	1.92	0.1506	0.93	0.87	1744	26	2039	17	2352	16	74
A491	Detrital	83572	1595	537	0.29	153788	0.3167	1.69	6.5220	1.87	0.1493	0.81	0.90	1774	26	2049	17	2338	14	76
A522	Detrital	73528	1509	506	0.15	b.d.	0.3248	1.55	6.6390	1.87	0.1482	1.05	0.83	1813	24	2065	17	2326	18	78
A514	Detrital	78237	1526	536	0.37	21539	0.3252	1.57	6.6320	1.80	0.1479	0.87	0.87	1815	25	2064	16	2322	15	78
A503	Detrital	161073	2699	1011	0.41	2477	0.3389	1.90	7.1970	2.12	0.1540	0.94	0.90	1881	31	2136	19	2391	16	79
A527	Detrital	70845	1471	507	0.26	5173	0.3291	1.66	6.6090	1.96	0.1456	1.03	0.85	1834	27	2061	17	2295	18	80
A478	Detrital	80822	1460	514	0.21	b.d.	0.3374	2.38	6.9600	2.57	0.1496	0.96	0.93	1874	39	2106	23	2342	16	80
A513	Detrital	89635	1806	649	0.16	24731	0.3495	1.87	7.1860	2.04	0.1491	0.81	0.92	1932	31	2135	18	2336	14	83
A507	Detrital	85353	1568	581	0.14	b.d.	0.3620	1.66	7.5200	1.90	0.1507	0.92	0.87	1992	29	2175	17	2353	16	85
A516	Detrital	73322	1310	492	0.19	15431	0.3623	2.06	7.4290	2.30	0.1487	1.01	0.90	1993	35	2165	21	2331	17	85
A524	Detrital	64061	1158	459	0.16	8695	0.3842	1.74	8.2550	1.99	0.1559	0.97	0.87	2096	31	2259	18	2411	16	87
A520	Detrital	115859	1642	662	0.18	64144	0.3860	1.55	8.3270	1.86	0.1565	1.02	0.84	2104	28	2267	17	2418	17	87
A493	Detrital	86400	1738	684	0.16	b.d.	0.3822	1.99	8.0050	2.28	0.1519	1.10	0.87	2086	36	2232	21	2368	19	88
A512	Detrital	63527	1054	416	0.11	9487	0.3858	1.50	8.1690	1.83	0.1536	1.04	0.82	2103	27	2250	17	2386	18	88
A526	Detrital	100833	1550	631	0.19	3070	0.3909	1.93	8.3540	2.15	0.1550	0.94	0.90	2127	35	2270	20	2402	16	89
A488	Detrital	73090	1293	527	0.30	2395	0.3857	1.69	8.0440	1.97	0.1513	1.02	0.86	2103	30	2236	18	2360	17	89
A487	Detrital	87333	1407	591	0.22	b.d.	0.4014	1.47	8.6100	1.77	0.1556	0.98	0.83	2176	27	2298	16	2408	17	90
A485	Detrital	182118	3016	1296	0.34	b.d.	0.4024	1.37	8.6520	1.55	0.1559	0.73	0.88	2180	25	2302	14	2412	12	90
A530	Detrital	146694	2396	986	0.23	6188	0.3933	1.59	8.2060	1.79	0.1513	0.83	0.89	2138	29	2254	16	2361	14	91
A490	Detrital	86123	1397	596	0.30	27739	0.4024	2.11	8.5980	2.25	0.1549	0.79	0.94	2180	39	2296	21	2401	13	91
A480	Detrital	107504	1633	703	0.18	b.d.	0.4127	1.66	9.0760	1.92	0.1595	0.96	0.86	2227	31	2346	18	2450	16	91
A510	Detrital	102570	1763	732	0.16	11781	0.4026	2.17	8.4390	2.33	0.1520	0.83	0.93	2181	40	2279	21	2369	14	92
A529	Detrital	87848	1507	626	0.17	10688	0.4033	1.60	8.4500	1.83	0.1520	0.89	0.87	2184	30	2281	17	2368	15	92
A506	Detrital	165051	2614	1151	0.20	5546	0.4231	1.79	9.0960	1.96	0.1559	0.78	0.92	2275	34	2348	18	2412	13	94
A519	Detrital	104824	1509	681	0.16	4996	0.4355	1.49	9.4730	1.79	0.1577	0.98	0.83	2331	29	2385	17	2432	17	96

Diameter of laser spot = 20 and 30 μm , respectively; depth of crater 10–15 μm . ^a Within run background-corrected mean ^{207}Pb signal. ^b U and Pb content and Th/U ratio were calculated relative to Plesovice reference zircon. ^c corrected for background, common Pb and within-run Pb/U fractionation and subsequently normalised to GJ-1 (ID-TIMS value/measured value). ^d $^{207}\text{Pb}/^{235}\text{U}$ calculated using $^{207}\text{Pb}/^{206}\text{Pb}/(^{238}\text{U}/^{206}\text{Pb} \times 1/137.88)$. Uncertainties propagated following Gerdes & Zeh (2006, 2008). ^e rho is the error correlation defined as $\text{err}(^{206}\text{Pb}/^{238}\text{U})/\text{err}(^{207}\text{Pb}/^{235}\text{U})$. ^f degree of discordance = $(^{206}\text{Pb}/^{238}\text{U} / ^{207}\text{Pb}/^{235}\text{U}) \times 100$.
b.d. : below detection limit.

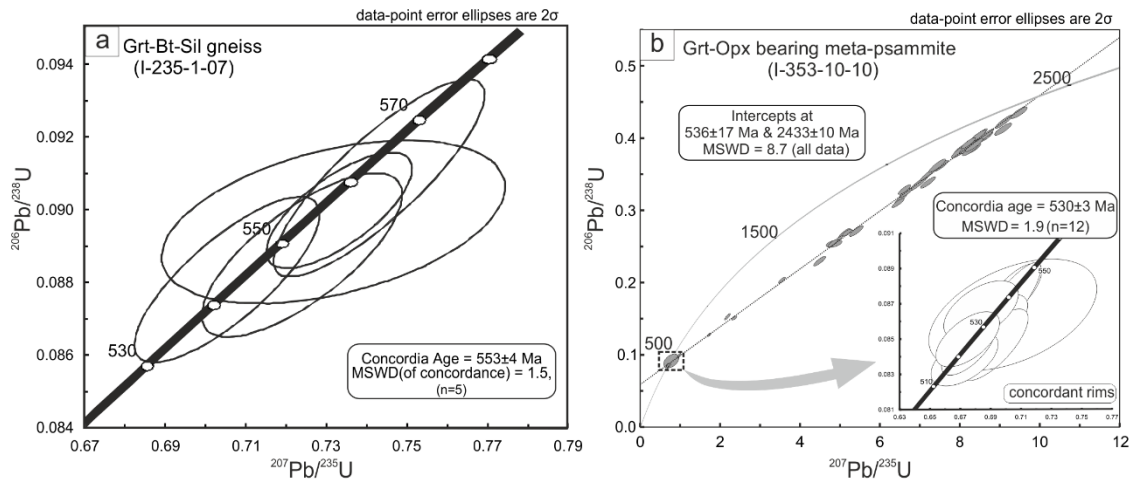


Fig. 6.6: (a) Concordia age cluster for the zircons in Grt-Bt-Sil gneiss and (b) U-Pb concordia diagram with all the data from the Grt-Opx bearing meta-psammite defining an upper-intercept age of ~2433 Ma and a lower-intercept age of ~536 Ma. The concordia age cluster using the age data of the broad overgrowths and homogenous subhedral metamorphic zircons is shown in the inset.

6.5.2. Th-U-total-Pb in situ monazite dating

Monazite grains were analysed from both Grt-Bt-Sil gneiss and Grt-Crd-Bt-Sil gneiss. Analytical techniques are given in details in Appendix.

6.5.2.1. Morphology and age data

Grt-Bt-Sil gneiss

Monazite of Grt-Bt-Sil gneiss was analysed from the sample B117. These monazites mostly occur as matrix grains and rarely as inclusions in garnet porphyroblasts. They are subhedral to anhedral and range from 60 to 100 μm in length. Most of the grains show patchy zoning, while few are completely homogenous (Fig. 6.7a-d). Twenty-one spots were analysed from eight monazite grains, which yielded ages ranging from 599 ± 53 Ma to 524 ± 40 Ma (Table 6.5a). The spots define a probability density peak at 553 ± 16 Ma (relative misfit = 1; Fig. 6.8a, Table 6.5a) that is interpreted to date the timing of peak metamorphism experienced by these pelitic granulites.

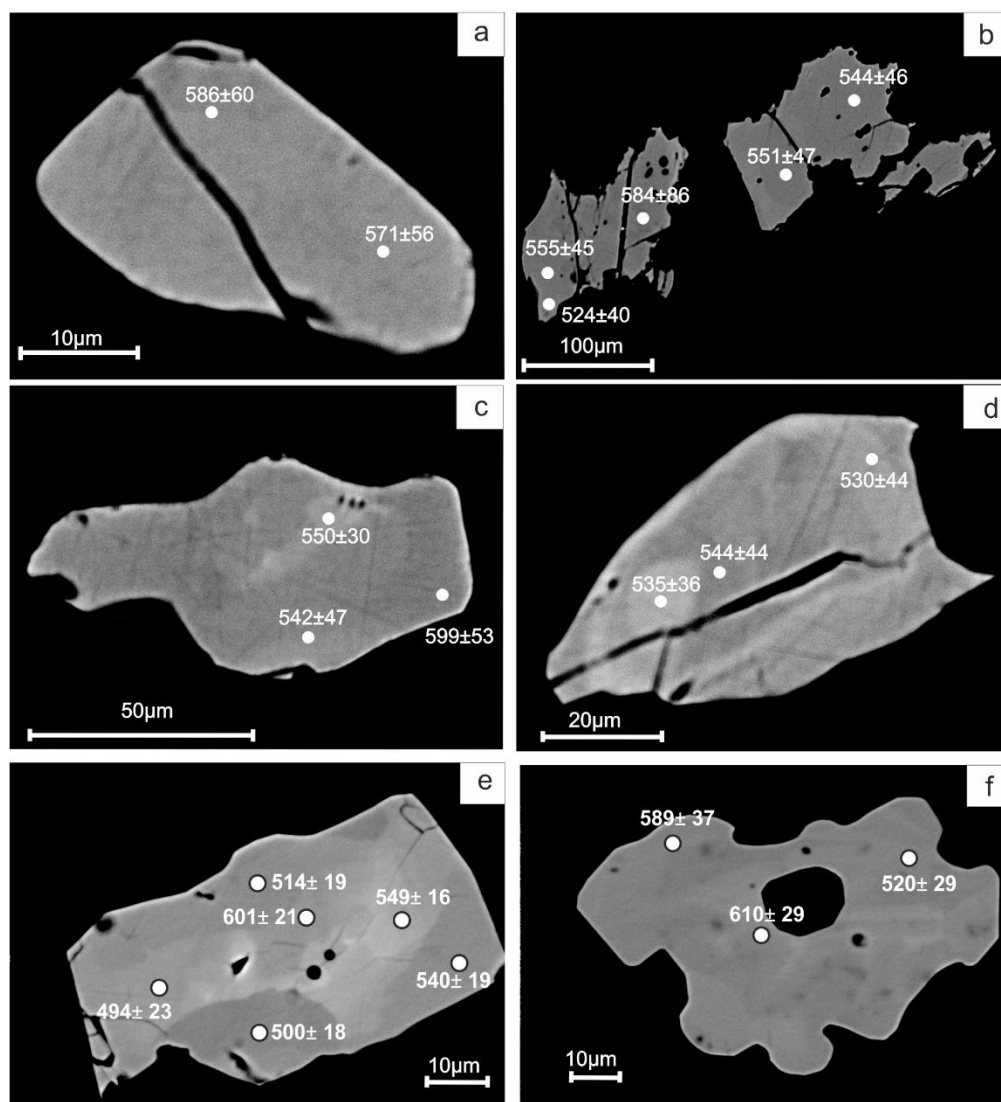


Fig. 6.7: BSE images of monazite grains showing patchy zoning patterns. The numbers on the images indicate apparent ages in Ma of (a-d) Grt-Bt-Sil gneiss (B117) (e-f) Grt-Crd-Bt-Sil gneiss (I-353-1-10). (a) Monazite inclusion in garnet porphyroblast (Grt-Bt-Sil gneiss). (b-d) Matrix monazite grains in Grt-Bt-Sil gneiss. (e) Matrix monazite grains in Grt-Crd-Bt-Sil gneiss. (f) Monazite included in cordierite (Grt-Crd-Bt-Sil gneiss).

Grt-Crd-Bt-Sil gneiss

The monazite grains in sample I-353-1-10 occur primarily in the matrix and scarcely as inclusions in cordierite. They are mostly anhedral and range from 40 to 100 μm in length (Fig. 6.7e-f), with a few having slightly irregular margins (Fig. 6.7f). Most of the monazite grains, particularly those included in cordierite is unzoned. Few shows patchy irregular zoning with no definite core to rim variation pattern

(Fig. 6.7e-f). No compositional variation is observed between the matrix grains and monazite inclusions in cordierite. A total of nineteen spots were analysed from five monazite grains (Table 6.5b). Spot ages from all monazite grains range from 610 ± 29 to 477 ± 22 Ma (Table 6.5b), with one prominent and one subordinate age peak at $\sim 520 \pm 6$ Ma and $\sim 600 \pm 14$ Ma, respectively, as evident from the probability density curve and ThO₂*vs PbO isochron diagram (Fig. 6.8b).

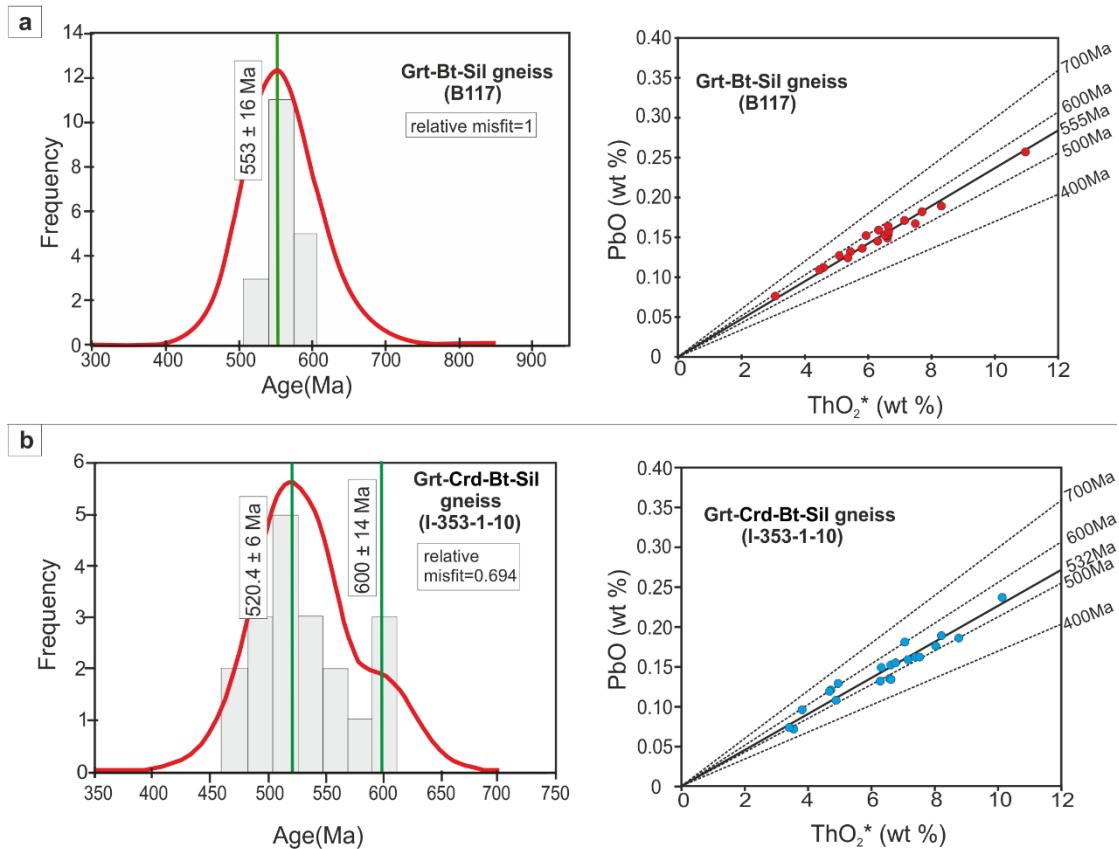


Fig. 6.8: Frequency histogram and cumulative probability density distribution curve representing apparent ages for all analysed spots of monazite grains and PbO-ThO₂* isochron diagram for the analysed samples from (a) Grt-Bt-Sil gneiss and (b) Grt-Crd-Bt-Sil gneiss. Age populations are shown with 2σ error.

Table 6.5a: Representative U-Th-total Pb electron microprobe analyses of monazite grains in Grt-Bt-Sil gneiss with calculated ages and +2s error.

Grain No.	Texture	Point No.	Y ₂ O ₃ (wt.%)	PbO (wt.%)	ThO ₂ (wt.%)	UO ₂ (wt.%)	ThO ₂ * (wt.%)	Age (Ma)	Age error (Ma)
Sample No.: B117									
1	Inclusion in Grt	1	0.07	0.13	4.04	0.42	5.45	571	56
		2	0.05	0.13	3.66	0.43	5.09	586	60
2	Matrix	3	0.00	0.17	7.19	0.09	7.50	524	40
		4	0.00	0.15	5.82	0.21	6.52	551	47
		5	0.00	0.15	5.67	0.28	6.59	544	46
		6	1.15	0.08	1.70	0.41	3.07	584	86
		7	0.83	0.16	4.82	0.55	6.66	555	45
3	Matrix	8	0.38	0.26	9.46	0.46	10.98	550	30
		9	0.00	0.15	5.12	0.25	5.94	599	53
		10	0.00	0.15	6.03	0.08	6.31	542	47
4	Matrix	11	0.00	0.11	3.69	0.27	4.59	574	65
		12	0.00	0.12	4.38	0.30	5.36	545	56
5	Matrix	13	0.00	0.16	5.82	0.15	6.33	591	49
		14	0.92	0.11	2.29	0.65	4.47	577	64
6	Matrix	15	0.00	0.18	7.37	0.10	7.71	555	40
		16	0.00	0.16	6.32	0.09	6.63	580	46
7	Matrix	17	0.00	0.17	6.24	0.28	7.15	562	43
		18	0.75	0.14	4.16	0.50	5.82	551	50
8	Matrix	19	0.00	0.19	8.08	0.07	8.32	535	36
		20	1.14	0.15	5.04	0.48	6.63	544	44
		21	0.00	0.15	6.33	0.09	6.62	530	44

Table 6.5b: Representative U-Th-total Pb electron microprobe analyses of monazite grains in Grt-Crd-Bt-Sil gneiss with calculated ages and +2s error.

Grain No.	Texture	Point No.	Y ₂ O ₃ (wt.%)	PbO (wt.%)	ThO ₂ (wt.%)	UO ₂ (wt.%)	ThO ₂ * (wt.%)	Age (Ma)	Age error (Ma)
Sample No.: I-353-1-10									
1	matrix	1	2.11	0.13	4.28	0.71	6.63	477	22
		2	2.27	0.16	5.30	0.67	7.52	508	20
		3	2.14	0.15	3.86	0.74	6.33	554	24
2	matrix	4	2.16	0.16	5.15	0.69	7.41	513	20
		5	1.94	0.16	4.95	0.67	7.16	521	21
		6	2.40	0.15	4.41	0.68	6.66	535	22
		7	3.19	0.16	4.96	0.54	6.75	540	22
3	matrix	8	0.20	0.07	2.00	0.47	3.54	480	40
		9	0.18	0.07	2.00	0.43	3.44	501	41
		10	0.16	0.12	2.90	0.54	4.69	595	31
4	in Crd	11	0.21	0.10	2.23	0.48	3.83	589	37
		12	0.17	0.13	3.42	0.46	4.96	610	29
		13	0.22	0.11	3.51	0.42	4.90	520	29
5	matrix	14	0.11	0.13	5.22	0.32	6.29	494	23
		15	3.19	0.19	6.40	0.71	8.77	500	18
		16	2.08	0.18	5.61	0.74	8.04	514	19
		17	2.42	0.19	5.51	0.82	8.22	540	19
		18	0.10	0.24	8.70	0.43	10.14	549	16
		19	0.11	0.18	5.82	0.38	7.07	601	21

6.6. Tectonothermal evolution of the Madukkarai supracrustal unit

6.6.1. Formation of the protoliths of the meta-supracrustal rocks

The studied meta-supracrustal rocks are an integral part of a large sequence of pelitic granulites - meta-psammite-marble-calc-silicate-quartzite, that constitute the MSU (Fig. 2.2b Meißner et al., 2002; Naha et al., 1997). The protoliths of this supracrustal package were presumably sandstone-shale-limestone-(marl) that were deposited in a shallow marine condition on a stable continental shelf (c.f. Kooijman et al., 2011; Raith et al., 2016, 2010; Sengupta et al., 2015). Similar meta-supracrustal rocks of Ediacaran-Cambrian age and containing Archaean/ early Palaeoproterozoic detrital zircon ages are reported from within and from both sides of the PCSZ (Fig. 6.9). Detail studies on the detrital zircon grains and its metamorphic overgrowths from these meta-supracrustal rocks bracket the timing of deposition of their sedimentary protoliths between ~1750–1020 Ma (Fig. 6.9, Kooijman et al., 2011; Li et al., 2017; Plavsa et al., 2014; Raith et al., 2010; Sengupta et al., 2015; Teale et al., 2011).

In the present study, the limited U–Pb ages of the detrital zircons and their metamorphic rims from the Grt-Opx bearing meta-psammite yield larger, but overlapping time span for basin formation of the studied meta-supracrustal rocks (~2360–578 Ma, determined on the basis of the time gap between the youngest near-concordant detrital core age and oldest metamorphic zircon overgrowth on the detrital cores; Table 6.4, Grain No. A530 and Grain No. A517 respectively). If the chemical age of monazite grains is considered, the lower limit of this time span becomes ~610 Ma (Table 6.5b, Point No. 12). The U–Pb age population from the detrital zircons in this study is not sufficiently robust. Nevertheless, this range overlaps well with the timing of basin formation (~1900–610 Ma) established by Meißner et al., (2002) for the protoliths of the MSU, as well as with the late Palaeo to Mesoproterozoic (~1750–1020 Ma) sedimentary cover across the GTSI.

6.6.2. P-T evolution of the Madukkarai supracrustal unit

The constrained P-T path shows that the studied rocks attained the measured 'peak' P-T conditions at $\sim 730\text{--}790^\circ\text{C}$, $\sim 5.5\text{--}7$ kbar, followed by decompression and cooling that can be recorded till $\sim 630^\circ\text{C}$, ~ 4 kbar. The presence of relict kyanite however, suggests that the studied rocks experienced higher pressures (≥ 8 kbar at $\sim 730\text{--}790^\circ\text{C}$, Fig. 6.4b, d), than that recorded by the mineralogical geothermobarometers and phase equilibria. The estimated pressure maxima, therefore, corresponds to a minimum depth of ~ 25 km at which the metamorphosed sedimentary protoliths of the studied rocks resided during metamorphism and deformation (i.e. >25 km). The most plausible tectonic setting that can explain the burial of continental shelf sediments to a depth > 25 km is a continent-continent collision zone (e.g., Harley, 1989). The typical metamorphic P-T path expected in a continent-continent collision zone is a CW P-T path (e.g., England and Thompson, 1984; Harley, 1989). That the studied meta-supracrustal rocks evolved along a CW metamorphic P-T path is consistent with (a) the pseudomorphic replacement of kyanite by fibrous sillimanite and (b) the shape of the construed segment of the retrograde P-T path connecting the estimated two clusters of P-T arrays (Fig. 6.4 b, d).

6.6.3. Timing of metamorphism and deformation

The concordia ages obtained from the metamorphic zircon grains and overgrowths in the Grt-Bt-Sil gneiss and the Grt-Opx bearing meta-psammite constrain the timing of metamorphism of the studied meta-supracrustal packet within a narrow span of $\sim 550\text{--}530$ Ma (Fig. 6.5). Notwithstanding the uncertainties of the analyses, bulk of the monazite dates ($\sim 550\text{--}520$ Ma; Fig. 6.7) obtained from the studied rocks overlap with the metamorphic zircon dates. Deformation in the pelitic granulites is evident from the isoclinal folding of garnetiferous leucosomes (S1). Detailed structural work by Naha et al., (1997) indicates superposed folds of at least two generations (D1-D2), which are coaxial, producing hook shaped outcrops in the MSU. The growth of garnet porphyroblasts in the pelitic granulites was related to the first folding event by Naha et al., (1997). The formation of garnetiferous leucosomes in the studied pelitic granulites during D1 and its subsequent coaxial

folding during D2 suggest that D1 and D2 occurred in continuum and was syn-metamorphic. Occasional presence of thin leucosomes axial planar to the D2 folds encountered in the MSU (not in the studied samples) also indicates that the leucosome formation (i.e., metamorphism) and deformation are coeval. Meißner et al., (2002) attributed this coaxial deformation to have occurred under the 'Pan-African' orogeny, and inferred its timing to be between $\sim 610 \pm 60$ to 560 ± 17 Ma. Combining all this information, the narrow age span of ~ 550 – 520 Ma, obtained in this study, is interpreted to date the timing of granulite facies metamorphism and the accompanied deformation in the studied area. The lack of sector-zoning and the low Th/U ratios of the zircon grains, and overgrowths around detrital cores indicate the origin of these zircons during high-grade metamorphism at ~ 550 – 520 Ma. The discordia defined by the zircons from the Grt-Opx bearing meta-psammite shows upper and lower intercepts at ~ 2433 Ma and ~ 536 Ma respectively (Fig. 6.6b). This observation, and the presence of concordant zircon age clusters at ~ 2450 – 2361 Ma and ~ 578 – 514 Ma (Table 6.4) is consistent with the resetting of the U–Pb systematics of the late Neoproterozoic to early Palaeoproterozoic detrital zircon grains during the Ediacaran-Cambrian tectonothermal event. Similar observations are documented from other parts of the GTSI as well (Brandt et al., 2011; Plavsa et al., 2014; Raith et al., 2016, 2010; Sengupta et al., 2015). The older age population (~ 600 Ma) as revealed by the chemical dates of monazite grains, opens up two possibilities: (a) it records an early stage of the same Ediacaran-Cambrian metamorphism, or (b) it represents the imprints of an independent thermal event prior to the main metamorphic event. A distinct ~ 600 Ma event, recorded sporadically in different studies from the GTSI (Collins et al., 2007; Raith et al., 2010), supports option 'b'. However, the following observations and information are consistent with the first possibility: (i) field as well as petrographic observations of the studied rocks do not provide any evidence for the presence of a separate metamorphic event prior to the main granulite facies metamorphism; and, (ii) Meißner et al., (2002) dated the core of individual garnet porphyroblasts (that grew during peak metamorphism), and obtained similar ~ 610 Ma old age, which they linked with the 'Pan-African' collision event. Therefore, it is possible that this ~ 600 Ma age cluster (obtained by Meißner et al., 2002 as well as in the present study).

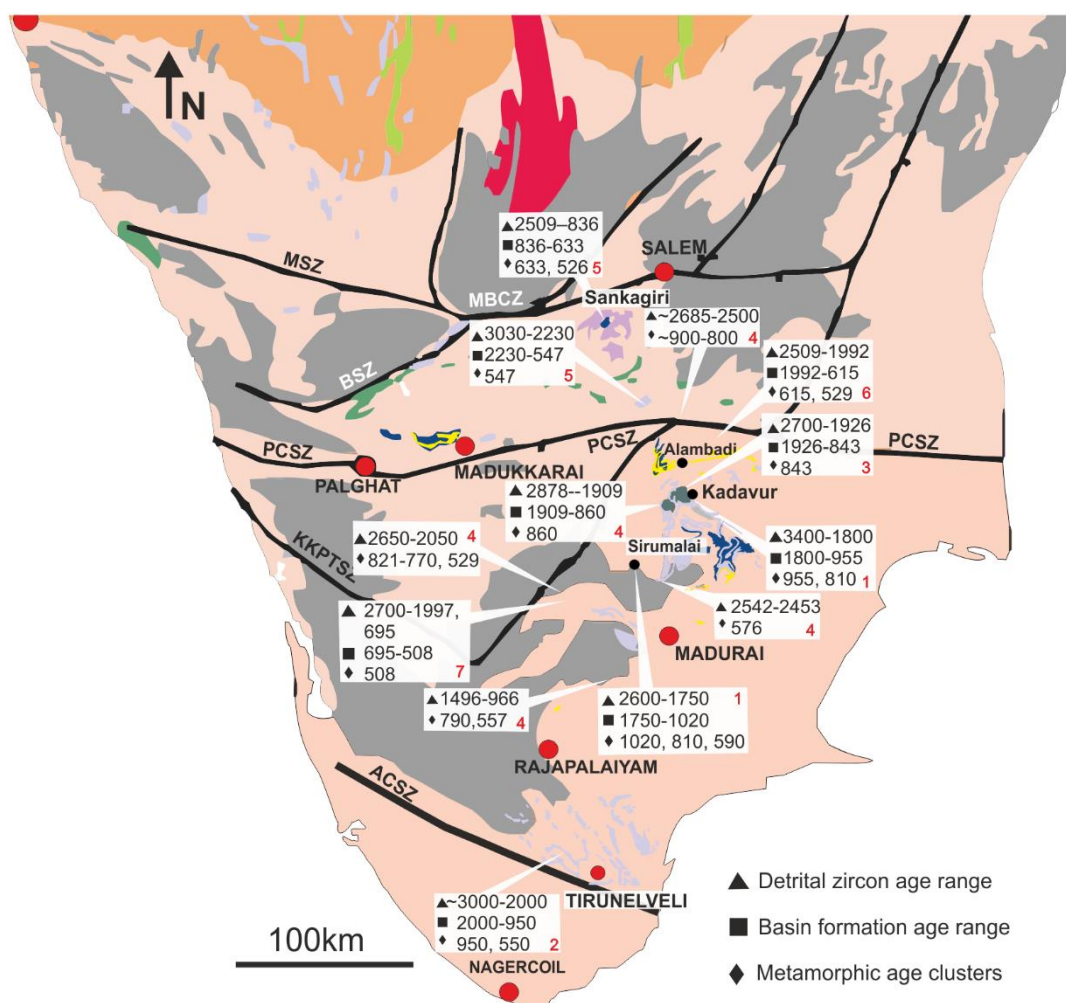


Fig. 6.9: Figure showing the geochronological attributes of the sedimentary cover reported from various areas of the GTSI. References: (1) Kooijman et al., 2011, (2) Li et al., 2017, (3) Teale et al., 2011, (4) Plavsa et al., 2014, (5) Sengupta et al., 2015, (6) Raith et al., 2010, (7) Collins et al., 2007b.

References

- Bhattacharya, A., Mazumdar, A.C., Sen, S.K., 1988. Fe-Mg mixing in cordierite; constraints from natural data and implications for cordierite-garnet geothermometry in granulites. *Am. Mineral.* 73, 338–344.
- Bhattacharya, A., Mohanty, L., Maji, A., Sen, S.K., Raith, M., 1992. Non-ideal mixing in the phlogopite-annite binary: constraints from experimental data on Mg–Fe partitioning and a reformulation of the biotite-garnet geothermometer.

- Contrib. to Mineral. Petrol. 111, 87–93.
- Brandt, S., Schenk, V., Raith, M.M., Appel, P., Gerdes, A., Srikantappa, C., 2011. Late Neoproterozoic PT evolution of HP-UHT granulites from the Palni Hills (South India): New constraints from phase diagram modelling, LA-ICP-MS zircon dating and in-situ EMP monazite dating. *J. Petrol.* 52, 1813–1856.
- Chakraborty, S., Ganguly, J., 1991. Compositional zoning and cation diffusion in garnets, in: *Diffusion, Atomic Ordering, and Mass Transport*. Springer, pp. 120–175.
- Clemens, J.D., Vielzeuf, D., 1987. Constraints on melting and magma production in the crust. *Earth Planet. Sci. Lett.* 86, 287–306.
- Collins, A.S., Santosh, M., Braun, I., Clark, C., 2007. Age and sedimentary provenance of the Southern Granulites, South India: U-Th-Pb SHRIMP secondary ion mass spectrometry. *Precambrian Res.* 155, 125–138.
- Corfu, F., Hanchar, J.M., Hoskin, P.W.O., Kinny, P., 2003. Atlas of zircon textures. *Rev. Mineral. geochemistry* 53, 469–500.
- Ellis, D.J., Sheraton, J.W., England, R.N., Dallwitz, W.B., 1980. Osumilite-sapphirine-quartz granulites from Enderby Land Antarctica—mineral assemblages and reactions. *Contrib. to Mineral. Petrol.* 72, 123–143.
- England, P.C., Thompson, A.B., 1984. Pressure—temperature—time paths of regional metamorphism I. Heat transfer during the evolution of regions of thickened continental crust. *J. Petrol.* 25, 894–928.
- Frost, B.R., 1991. Introduction to oxygen fugacity and its petrologic importance. *Rev. Mineral. Geochemistry* 25, 1–9.
- Ganguly, J., Saxena, S.K., 1984. Mixing properties of aluminosilicate garnets: constraints from natural and experimental data, and applications to geothermo-barometry. *Am. Mineral.* 69, 88–97.
- Gardien, V., Thompson, A.B., Grujic, D., Ulmer, P., 1995. Experimental melting of biotite+ plagioclase+ quartz±muscovite assemblages and implications for crustal melting. *J. Geophys. Res. Solid Earth* 100, 15581–15591.
- Harley, S.L., 1989. The origins of granulites: a metamorphic perspective. *Geol. Mag.*

126, 215–247.

- Henry, D.J., Guidotti, C. V, Thomson, J.A., 2005. The Ti-saturation surface for low-to-medium pressure metapelitic biotites: Implications for geothermometry and Ti-substitution mechanisms. *Am. Mineral.* 90, 316–328.
- Hodges, K. V, Crowley, P.D. t, 1985. Error estimation and empirical geothermobarometry for pelitic systems. *Am. Mineral.* 70, 702–709.
- Holdaway, M.J., Lee, S.M., 1977. Fe-Mg cordierite stability in high-grade pelitic rocks based on experimental, theoretical, and natural observations. *Contrib. to Mineral. Petrol.* 63, 175–198.
- Holland, T., Powell, R., 2003. Activity–composition relations for phases in petrological calculations: an asymmetric multicomponent formulation. *Contrib. to Mineral. Petrol.* 145, 492–501.
- Holland, T.J.B., Powell, R., 2011. An improved and extended internally consistent thermodynamic dataset for phases of petrological interest, involving a new equation of state for solids. *J. Metamorph. Geol.* 29, 333–383.
- Kooijman, E., Upadhyay, D., Mezger, K., Raith, M.M., Berndt, J., Srikantappa, C., 2011. Response of the U–Pb chronometer and trace elements in zircon to ultrahigh-temperature metamorphism: the Kadavur anorthosite complex, southern India. *Chem. Geol.* 290, 177–188.
- Kretz, R., 1983. Symbols for rock-forming minerals. *Am. Mineral.* 68, 277–279. [https://doi.org/10.1016/0016-7037\(83\)90220-X](https://doi.org/10.1016/0016-7037(83)90220-X)
- Li, S.-S., Santosh, M., Indu, G., Shaji, E., Tsunogae, T., 2017. Detrital zircon geochronology of quartzites from the southern Madurai Block, India: Implications for Gondwana reconstruction. *Geosci. Front.* 8, 851–867.
- Meißner, B., Deters, P., Srikantappa, C., Köhler, H., 2002. Geochronological evolution of the Moyar, Bhavani and Palghat shear zones of southern India: implications for east Gondwana correlations. *Precambrian Res.* 114, 149–175.
- Mukherjee, S., Dey, A., Sanyal, S., Sengupta, P., 2018. Tectonothermal imprints in a suite of mafic dykes from the Chotanagpur Granite Gneissic complex (CGGC), Jharkhand, India: Evidence for late Tonian reworking of an early Tonian continental crust. *Lithos* 320–321.

<https://doi.org/10.1016/j.lithos.2018.09.014>

- Naha, K., Srinivasan, R., Deb, G.K., 1997. Structural geometry of the early Precambrian terrane south of Coimbatore in the “Palghat Gap”, southern India. *Proc. Indian Acad. Sci. Planet. Sci.* 106, 237–247.
- Newton, R.C., Haselton, H.T., 1981. Thermodynamics of the garnet—plagioclase—Al₂SiO₅—quartz geobarometer, in: *Thermodynamics of Minerals and Melts*. Springer, pp. 131–147.
- Palin, R.M., Weller, O.M., Waters, D.J., Dyck, B., 2016. Quantifying geological uncertainty in metamorphic phase equilibria modelling; a Monte Carlo assessment and implications for tectonic interpretations. *Geosci. Front.* 7, 591–607.
- Perchuk, L.L., Aranovich, L.Y., Podlesskii, K.K., LAVRANT’EvA, I. V., Gerasimov, V.Y., Fed’Kin, V. V., Kitsul, V.I., Karsakov, L.P., Berdnikov, N. V., 1985. Precambrian granulites of the Aldan shield, eastern Siberia, USSR. *J. Metamorph. Geol.* 3, 265–310.
- Plavsa, D., Collins, A.S., Payne, J.L., Foden, J.D., Clark, C., Santosh, M., 2014. Detrital zircons in basement metasedimentary protoliths unveil the origins of southern India. *GSA Bull.* 126, 791–811.
- Raith, M.M., Brandt, S., Sengupta, P., Berndt, J., John, T., Srikantappa, C., 2016. Element mobility and behaviour of zircon during HT metasomatism of ferroan basic granulite at Ayyarmalai, South India: Evidence for polyphase Neoproterozoic crustal growth and multiple metamorphism in the Northeastern Madurai Province. *J. Petrol.* 57, 1729–1774.
- Raith, M.M., Sengupta, P., Kooijman, E., Upadhyay, D., Srikantappa, C., 2010. Corundum–leucosome-bearing aluminous gneiss from Ayyarmalai, Southern Granulite Terrain, India: A textbook example of vapor phase-absent muscovite-melting in silica-undersaturated aluminous rocks. *Am. Mineral.* 95, 897–907.
- Rubatto, D., 2002. Zircon trace element geochemistry: partitioning with garnet and the link between U–Pb ages and metamorphism. *Chem. Geol.* 184, 123–138.
- Sengupta, P., Karmakar, S., Dasgupta, S., Fukuoka, M., 1991. Petrology of spinel granulites from Araku, Eastern Ghats, India, and a petrogenetic grid for

- sapphirine-free rocks in the system FMAS. *J. Metamorph. Geol.* 9, 451–459.
- Sengupta, P., Raith, M.M., Kooijman, E., Talukdar, M., Chowdhury, P., Sanyal, S., Mezger, K., Mukhopadhyay, D., 2015. Chapter 20 Provenance, timing of sedimentation and metamorphism of metasedimentary rock suites from the Southern Granulite Terrane, India. *Geol. Soc. London, Mem.* 43, 297–308. <https://doi.org/10.1144/m43.20>
- Taylor-Jones, K., Powell, R., 2010. The stability of sapphirine+ quartz: calculated phase equilibria in FeO–MgO–Al₂O₃–SiO₂–TiO₂–O. *J. Metamorph. Geol.* 28, 615–633.
- Teale, W., Collins, A.S., Foden, J., Payne, J.L., Plavsa, D., Chetty, T.R.K., Santosh, M., Fanning, M., 2011. Cryogenian (~ 830 Ma) mafic magmatism and metamorphism in the northern Madurai Block, southern India: A magmatic link between Sri Lanka and Madagascar? *J. Asian Earth Sci.* 42, 223–233.
- Ward, R., Stevens, G., Kisters, A., 2008. Fluid and deformation induced partial melting and melt volumes in low-temperature granulite-facies metasediments, Damara Belt, Namibia. *Lithos* 105, 253–271.
- White, R., Powell, R., Holland, T.J.B., Worley, B.A., 2000. The effect of TiO₂ and Fe₂O₃ on metapelitic assemblages at greenschist and amphibolite facies conditions: mineral equilibria calculations in the system K₂O–FeO–MgO–Al₂O₃–SiO₂–H₂O–TiO₂–Fe₂O₃. *J. Metamorph. Geol.* 18, 497–511.
- White, R.W., Powell, R., Clarke, G.L., 2002. The interpretation of reaction textures in Fe-rich metapelitic granulites of the Musgrave Block, central Australia: constraints from mineral equilibria calculations in the system K₂O–FeO–MgO–Al₂O₃–SiO₂–H₂O–TiO₂–Fe₂O₃. *J. Metamorph. Geol.* 20, 41–55.
- White, R.W., Powell, R., Holland, T.J.B., Johnson, T.E., Green, E.C.R., 2014a. New mineral activity–composition relations for thermodynamic calculations in metapelitic systems. *J. Metamorph. Geol.* 32, 261–286.
- White, R.W., Powell, R., Johnson, T.E., 2014b. The effect of Mn on mineral stability in metapelites revisited: New a–x relations for manganese-bearing minerals. *J. Metamorph. Geol.* 32, 809–828.

Chapter-7

Metamorphic evolution calc-silicate granulite from Madukkarai Supracrustal Unit

Chapter 7

Metamorphic evolution of calc-silicate granulite from the Madukkarai Supracrustal Unit

Mineral reaction textures form very useful ways in identifying and establishing the P-T conditions under which they develop. Wollastonite, scapolite, garnet, clinopyroxene, calcite bearing calc-silicates commonly preserve important mineral reactions used to trace the P-T evolutionary histories as well as fluid-rock interactions, and have been increasingly studied in the last two decades (Buick et al., 1994; Ferry and Burt, 1982; Fitzsimons and Harley, 1994; Harley et al., 1994; Sengupta et al., 1997). Initially, semi-qualitative grids were constructed; later activity corrected quantitative topologies, mostly in the CASV system were used to explain the textures in wollastonite scapolite bearing calc-silicates.

Granulite facies wollastonite-scapolite assemblage is commonly associated with garnet (grossular rich) via CASV reactions (Buick et al., 1993; Dasgupta, 1993; Dasgupta and Pal, 2005; Fitzsimons and Harley, 1994; Harley and Buick, 1992; Sengupta et al., 1997; Sengupta and Raith, 2002; Stephenson and Cook, 1997). Moreover, a considerable amount of andradite component (varying up to pure granditic compositions) has also been reported to be also associated (e.g., Buick et al., 1994). Origin of grandite garnet has been variously attributed to non-pervasive H₂O-rich fluid infiltration from adjacent granitic or pelitic sources (Buick et al., 1994, 1993), or a result of vapor-deficient metamorphism during near isobaric cooling (Sengupta et al., 1997). Sengupta et al., (1997) and Sengupta and Raith, (2002) discussed the role of clinopyroxene in the formation of grandite garnet in the system CFS-O₂-CO₂ and CFAS-O₂-CO₂ respectively. Dasgupta and Pal, (2005) also demonstrated the influence of temperature and fO₂ in the formation of grandite garnet. Later Groppo et al., (2013) extended the topology to the hydrous system (CFAS-H₂O-CO₂), and demonstrated the involvement of zoisite in garnet formation.

Calc-silicates in and around PCSZ have been rarely studied. Of the few records available, mineralogical evolution of a grandite ±wollastonite ± scapolite

bearing skarn within marble from Sittampundi, has been estimated at $\sim 750 \pm 30^\circ\text{C}$, 7-9 kbar, and $< 0.35 X_{\text{CO}_2}$ conditions, along a clockwise P-T path characterized by a steep decompression followed by cooling (Sengupta et al., 2009). In this backdrop, the present study reports the occurrence of a wollastonite-free, scapolite-clinopyroxene-calcite- garnet-amphibole-epidote bearing calc-silicate granulite from the Madukkarai Supracrustal Unit (MSU). The meta-supracrustal rocks of the MSU expose an interlayered platformal sequence of metapelites, marbles, calc-silicates, meta-psammites and quartzites (Raith et al., 2010; Roy Choudhury et al., 2021). Previously, Naha et al., (1997) worked extensively on the structural aspect of a few “calc-gneisses” in this area, while Meißner et al., (2002) constrained the age of deposition and metamorphism of this unit. However, the evolution of mineral assemblage and metamorphic characterization of the calc-silicates are lacking. The calc-silicates of MSU preserve grandite garnet, along with scapolite-clinopyroxene-amphibole-epidote and calcite. Using the internally consistent thermodynamic dataset, quantitative topologies in P-T (for fixed X_{CO_2}) and isobaric T- X_{CO_2} sections, within the CMASV system were constructed, in order to trace the P-T, and fluid evolutionary history of the studied calc-silicate granulites of the MSU. Integrating the textural relations and the findings from the activity corrected topologies, with the P-T evolutionary history of the adjacent, intercalated pelitic granulites, it is inferred that the grandite garnet- formed during an extended cooling phase (subsequent to post-peak decompression, but possibly concomitant with, or following the retrogressive phase in the pelitic granulites). Clinopyroxene acted as the source of Fe^{+3} for grandite formation. Additionally, the inferred fluid conditions demand intermittent influx of (H_2O -rich) fluid, in stabilizing the observed mineralogy in the studied calc-silicates.

7.1 Field features

As discussed in the previous chapter, these calc-silicate granulites form a part of the platformal sediments, that overlie the migmatitic enderbitic gneissic basement, intercalated with the marbles, metapelites, meta-psammites and quartzites. The calc-silicates occur as decimeter to a few meter scale boulders, and have a distinct banded appearance, showing prominent ridge and furrows. Calc-

silicates show intercalation of marble and calc-silicate layers. Locally, within the outcrop, intercalated pelitic layers, now rich in biotite are present. These calc-silicates consists of light, and dark coloured bands, alternately rich in plagioclase (\pm scapolite) and clinopyroxene (\pm amphibole) respectively (Fig. 7.1a). Locally, one outcrop of the calc-silicate also contains garnet in certain layers. Epidote is also present in these calc-silicates in certain, discontinuous layers/ patches. These layers are folded into near isoclinal folds in response to two sets of syn-metamorphic

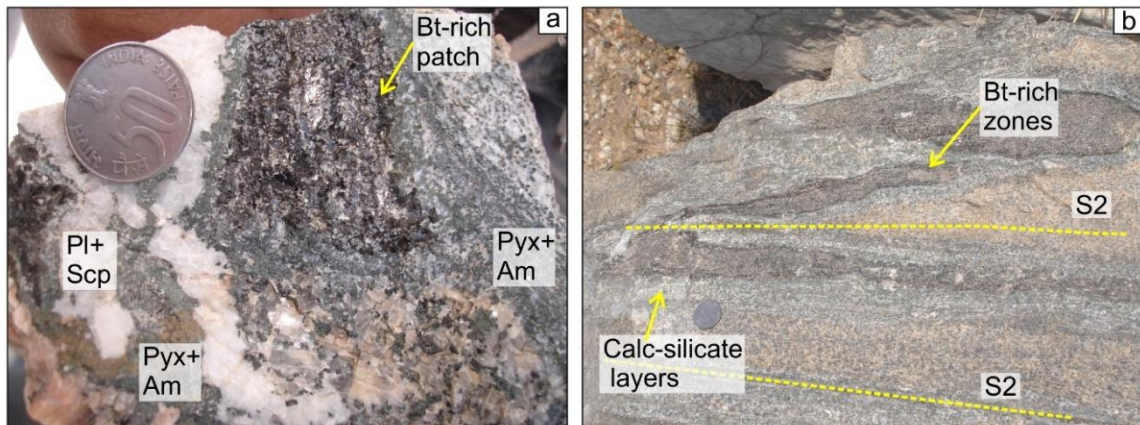


Fig. 7.1: Field features of the studied calc-silicate. (a) Alternate bandings defined by plagioclase (\pm scapolite) and clinopyroxene (\pm amphibole). Few biotite-rich pelitic patches are intercalated also. (b) Isoclinal folding defined by calc-silicate and biotite rich layers, with E-W axial planar foliation. All mineral abbreviations used are after Kretz (1983).

coaxial deformation (see chapter 6, section 6.5.3), with E-W trending axial planar S2 foliation (mostly defined by biotite in intercalated pelitic layers, and amphibole in the calc-silicates) (Fig. 7.1b). Undeformed pegmatitic veins (comprising primarily pink feldspar and quartz) are also associated with the calc-silicate-marble intercalations. For this study, we have concentrated on the calc-silicate layers only.

7.2. Petrography

The overall mineralogy of the calc-silicate granulite include plagioclase, clinopyroxene, amphibole, garnet, titanite, calcite and epidote. These rocks show variation in grain size shape and distribution of minerals. The overall mineralogy includes clinopyroxene (~15%), plagioclase (25%), calcite (~5%), titanite (5%), scapolite (~8%), K-feldspar (5%), garnet (~8%), amphibole (~18%), epidote (~8%) and magnetite (3%).

Clinopyroxenes and plagioclase occur as medium to large sized subidioblastic grains, showing polygonal granoblastic texture (Fig. 7.2a). Titanite, with variable grain sizes, share sharp equilibrium boundaries, and are dispersed in the aggregates of clinopyroxene, scapolite and feldspar (Fig. 7.2b). Few K-feldspar (microcline) are also observed within this granoblastic mosaic (Fig. 7.2a). Magnetite is sporadically dispersed in the granoblastic mosaic, and less commonly occurs as

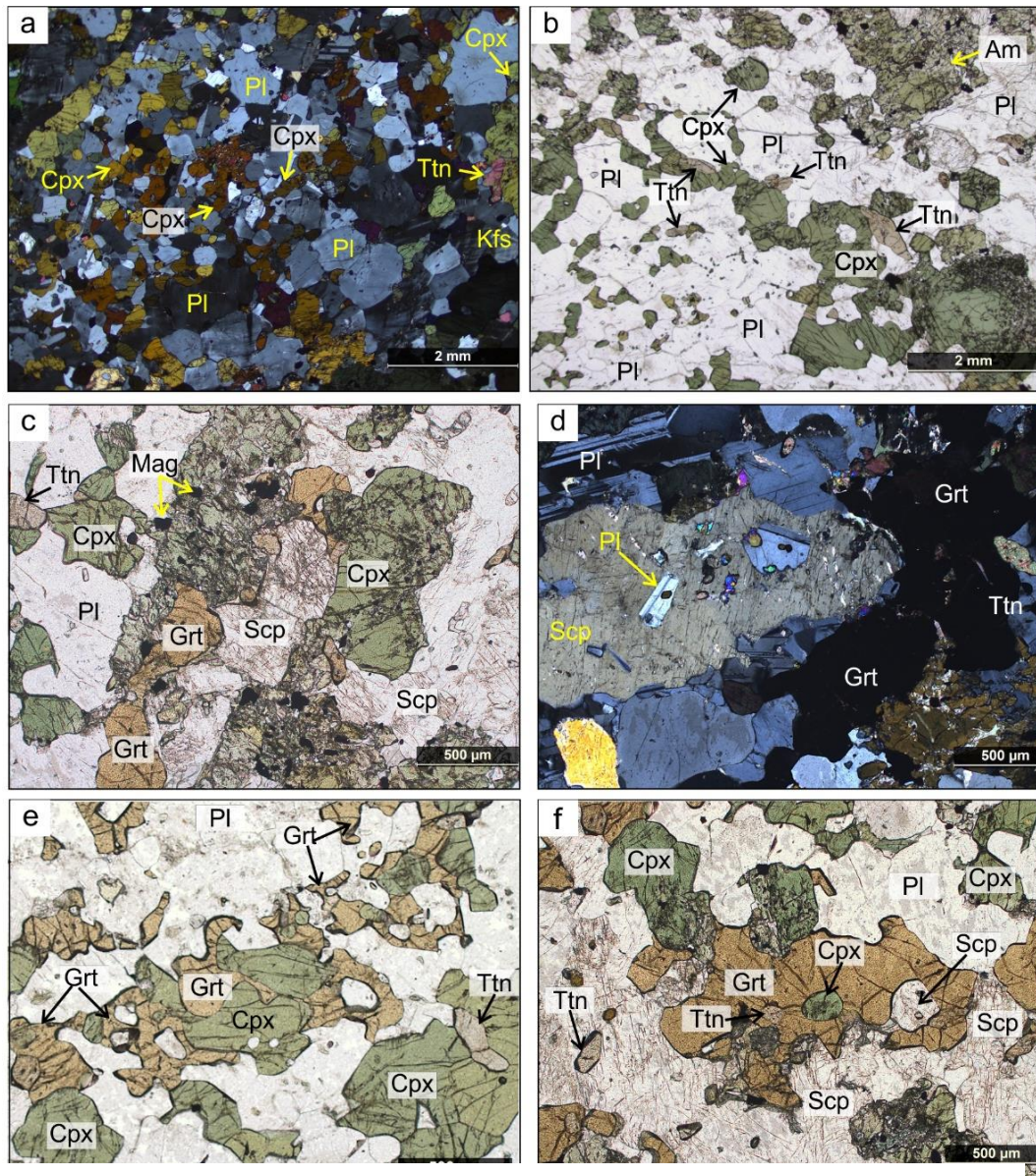


Fig. 7.2: Petrographic features of the studied calc-silicate. (a-b) Clinopyroxene, plagioclase and titanite defining a recrystallized granoblastic texture. (c) Clinopyroxene and scapolite share straight equilibrium boundaries. (d) Plagioclase inclusion in scapolite. (e-f) Garnet partially or fully engulfing clinopyroxene and scapolite. All mineral abbreviations used are after Kretz, (1983).

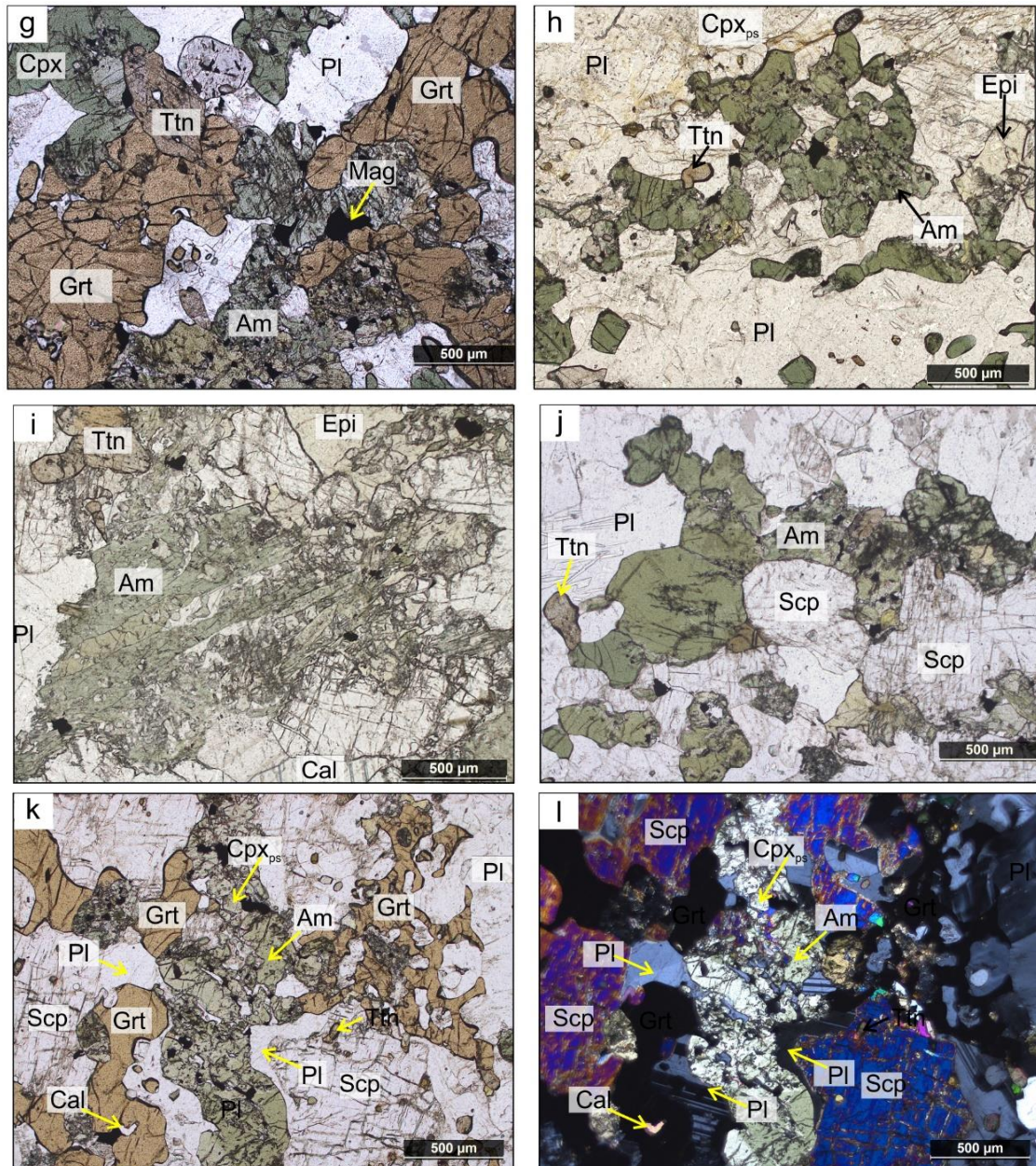


Fig. 7.2 contd: (g-h) Amphiboles occurring as medium to large subidioblastic grains. They share straight boundaries with garnet, but also show interfingering relationship. (h) Amphiboles pseudomorphically replace clinopyroxene. (i) Amphiboles also occur as needle shaped grains without any particular orientation. (j) Amphiboles partially engulfing scapolite. (k-l) a thin rim of plagioclase forms along the grain boundary of scapolite and clinopyroxene, along with garnet and amphibole. Note the small inclusion of calcite in garnet. All mineral abbreviations used are after Kretz, (1983).

inclusion in clinopyroxene (Fig. 7.2c, g). Calcite mostly occur as medium sized grains in this mosaic, and share straight margins with clinopyroxenes and plagioclase. Scapolite occurs in a particular zone only. Clinopyroxenes in general share straight equilibrium boundaries with scapolite (Fig. 7.2c), however, rare clinopyroxene

inclusions are also observed within scapolite. Inclusions of plagioclase in scapolite are also observed (Fig. 7.2d).

Volumetrically minor garnet forms in the scapolite-bearing zones, and occurs as corona of variable thickness around clinopyroxene grains, and separate them from scapolite, plagioclase and titanite (Fig. 7.2e-g). Rare calcite inclusions are also present within garnet (Fig. 7.2k). Locally aggregates of garnets form a network around the clinopyroxene, scapolite and plagioclase, and simulate porphyroblastic garnet (Fig. 7.2e-f). Amphiboles occur in various forms: as medium to large sized subidioblastic grains, or as millimeter-thick, needle shaped grains, without any

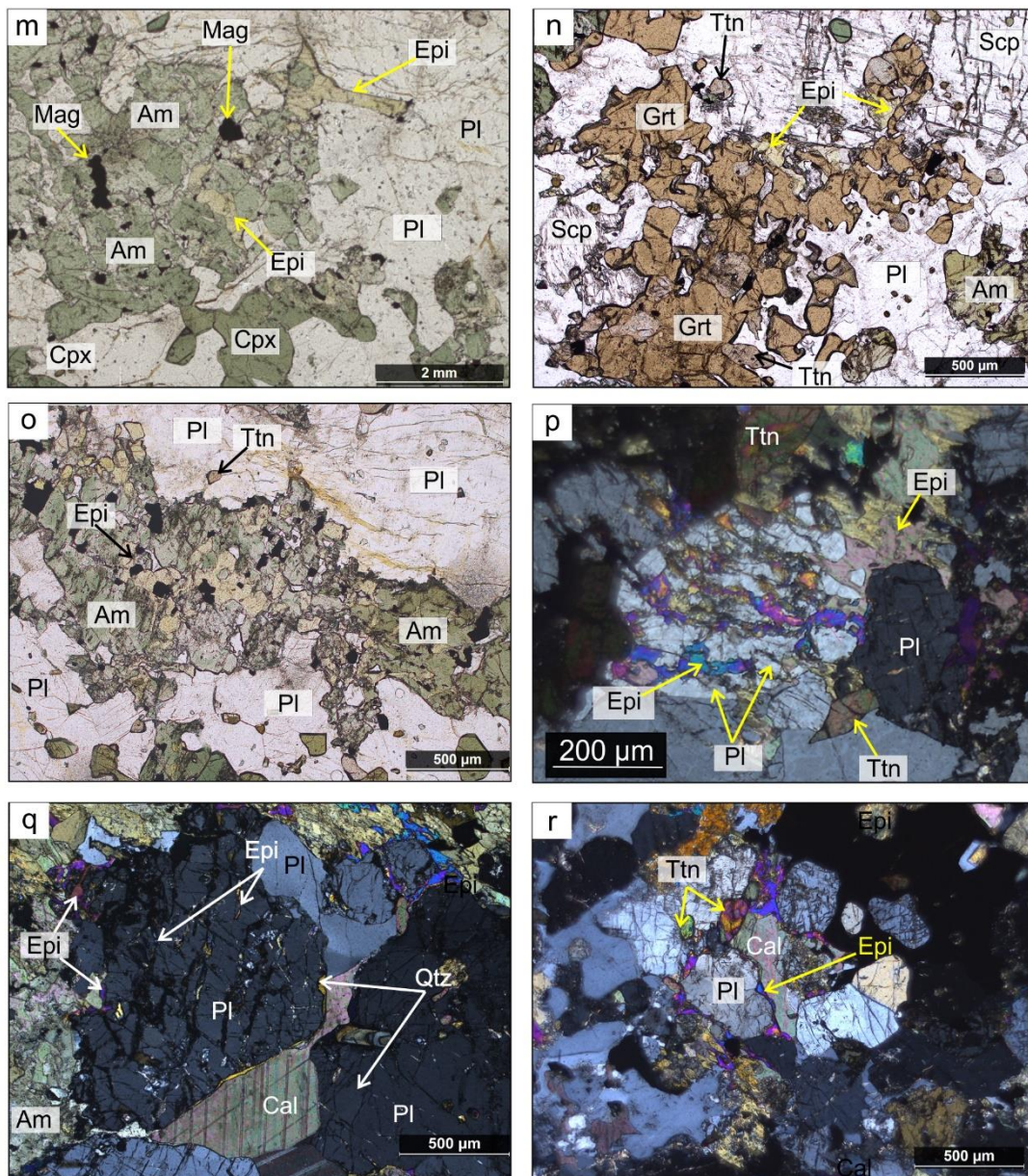
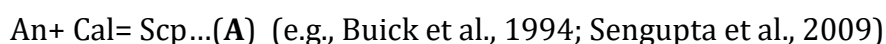


Fig. 7.2 contd: (m-o) Epidote replacing amphibole and garnet, along their margins. (p-q) Multiple veins of epidote cut across plagioclase. Occasionally, a thin rim of quartz also forms at the interface of these plagioclase grains and calcite. (r) Epidote encloses matrix calcite. All mineral abbreviations used are after Kretz, (1983). Cpx_{ps}: Clinopyroxene pseudomorphed by amphibole.

particular orientation; and are also closely associated with garnets (Fig. 7.2g-i). They mostly share straight boundaries with garnet, with rare interfingering relationship (Fig. 7.2g). Amphibole extensively replaces clinopyroxenes (both small and large ones) throughout the thin section. The replacement is commonly pseudomorphic (Fig. 7.2h). Amphiboles are also seen to grow on scapolite (Fig. 7.2j). Locally, both garnet and amphibole form at the interface of scapolite and clinopyroxene. Additionally, a thin rim of plagioclase forms along the grain boundary of scapolite and clinopyroxene (Fig. 7.2k-l). Epidote extensively replaces amphibole and garnet, along their grain margins (Fig. 7.2m-o). Commonly, multiple veins of epidote cut across plagioclase grains (Fig. 7.2p-q). Rarely, along with epidote veins, a thin rim of quartz also forms at the interface of these plagioclase grains and calcite (Fig. 7.2q). Epidote is also seen to partially enclose matrix calcite grains (Fig. 7.2r). Individual grains of epidote are not observed in the rock. Moreover, these epidote veins do not show any orientation or alignment, indicating their development after deformation.

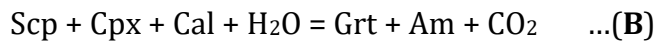
7.3. Reaction textures and evolution of mineral assemblage

In this section, the textural relations that are described in the previous section (section 7.2) are used to identify the probable reactions that occurred in the rock. All mineral abbreviations used are after Kretz, (1983). The above textural features indicate that clinopyroxene, plagioclase, calcite and titanite, were the early stabilized mineral assemblage. Inclusion of plagioclase in scapolite combined with the growth of scapolite over calcite advocates that scapolite formed subsequent to this early assemblage, via the reaction:

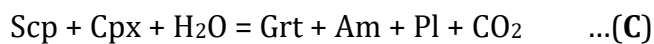


Presence of garnet along grain boundaries of clinopyroxene and scapolite suggest garnet formation at the expense of the latter two. Moreover, rare inclusion of calcite within garnet point towards its participation in garnet forming reaction.

Interestingly, textural observations (predominance of straight equilibrium margins) advocate for the stabilization of amphibole along with garnet. Since amphibole replaces clinopyroxene extensively and also overgrows on scapolite, it is evident that both garnet and amphibole grew at the expense of the same reactant phases via reaction:

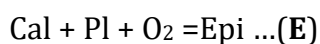
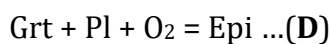


Additionally, the local development of a thin rim of plagioclase (in addition to garnet and amphibole) along the interface of scapolite and clinopyroxene suggest the reaction:



However, reaction (B) and (C) might have progressed separately, or in combination with each other.

Development of epidote marks the final stage of mineral evolution. Epidote replaces nearly all the previously stabilized phases, including garnet, amphibole, plagioclase, calcite. Formation of epidote can be explained via multiple reactions:



7.4. Mineral Chemistry

Mineral compositions were measured at the Central Petrological Laboratory of Geological Survey of India, Kolkata, India with CAMECA SX100. The diameter of the electron beam was 1–3 μm , and voltage and beam current were 15 kV and 12 nA respectively. Natural standards were used for all elements (Si, Al, Cr, Fe, Mg, Ca, Na, K) except for Mn and Ti, for which, synthetic standards were used. Fe^{+3} was calculated using the scheme of Droop, (1987), during cation recalculation. Cation recalculation of amphibole was done using the scheme of Hawthorne et al., (2012). All mineral abbreviations used are after Kretz, (1983). Representative compositions of the minerals have been provided in Table 7.

7.4.1. Clinopyroxene:

Clinopyroxenes are highly magnesian and have a large range of X_{Mg} [$Mg^{+2}/(Mg^{+2}+Fe^{+2})= 0.56-0.80$]. The cores have overlapping but slightly lower magnesian content (X_{Mg} : 0.56-0.77) than the rims (X_{Mg} : 0.65-0.80) (Table 7.1). They have low Al_2O_3 content, ranging between $\sim 1.1-5.5$ wt%. However, no zoning with respect to aluminium is present. The clinopyroxenes also have considerable amount of Fe^{+3} , ranging up to $\sim 0.04-0.26$ apfu. Acmite and essonite components vary between 1-6 mol% and 3-21 mol% respectively. Jadeite and CaTs components together add up to ~ 2 mol%. The small clinopyroxenes have identical compositions as the larger ones. Individual grains do not show any significant compositional zoning.

7.4.2. Plagioclase:

The compositions of plagioclases show a considerable variation. Plagioclase in the matrix is primarily andesine. They consist of a more albitic core ($An_{0.42-0.45}Ab_{0.53-0.56}Or_{0.01-0.02}$), but have relatively higher anorthite in the rim ($An_{0.45-0.49}Ab_{0.50-0.54}Or_{0.01}$) (Table 7.2). Few large plagioclases however are more anorthitic: $An_{0.81-0.82}Ab_{0.18-0.19}$ (Table 7.2). However, plagioclases adjacent to scapolite show overlapping anorthite content, varying between andesine to labradorite (and very few bytownite) (cores: $An_{0.46}Ab_{0.53}Or_{0.01}$ and rim: $An_{0.55-0.71}Ab_{0.28-0.44}Or_{0.01}$) (Table 7.2).

7.4.3. K-feldspar:

There is no compositional variation within K-feldspar grains. They show a very restricted composition between $Or_{0.90-0.92}Ab_{0.08-0.10}An_0$ (Table 7.2).

7.4.4. Scapolite:

Scapolite shows restricted compositional spread. Compositionally they are meionite. Equivalent anorthite ($Eq.An=(Al-3)/3$) of scapolite ranges from 0.60 to 0.69, which is a characteristic feature of calcic scapolites formed by CO_3^{2-} bearing solution ($Eq_{an} \geq 0.6$) (Rebbert and Rice 1997). Scapolite does not have any significant amount of 'S' and 'Cl' in the anion site, and therefore, this anion site is practically occupied by $(CO_3)^{2-}$ (Table 7.3). No zoning was observed in individual grains.

7.4.5. Garnet:

Garnet is typically grandite (grossular + andradite = ~95-96 mol%, Table 7.4). Pyrope, almandine and spessartine components add up to ~4 mol%. No significant compositional variations were observed between core ($\text{Adr}_{0.73-0.75}\text{Grs}_{0.21-0.22}\text{Alm}_{0.01-0.02}\text{Prp}_0\text{Sps}_{0.01}$; X_{Mg} : 0.11-0.19) and rim ($\text{Adr}_{0.70-0.74}\text{Alm}_{0.01-0.02}\text{Prp}_0\text{Grs}_{0.22-0.25}\text{Sps}_{0.02-0.03}$; X_{Mg} : 0.11-0.16) of garnet irrespective of its thickness (Table 7.4).

7.4.6. Amphibole:

Amphibole has a restricted composition, and is magnesium rich (X_{Mg} =0.68-0.74). The amphiboles compositionally magnesio-hornblende (Fig. 7.3; Hawthorne et al., 2012). The Al_2O_3 content of amphiboles ranges between 7.2-8.9 wt%. They also have a considerable Fe^{+3} (0.5-0.6 apfu) and Na^+ (0.25-0.28 apfu) (Table 7.5).

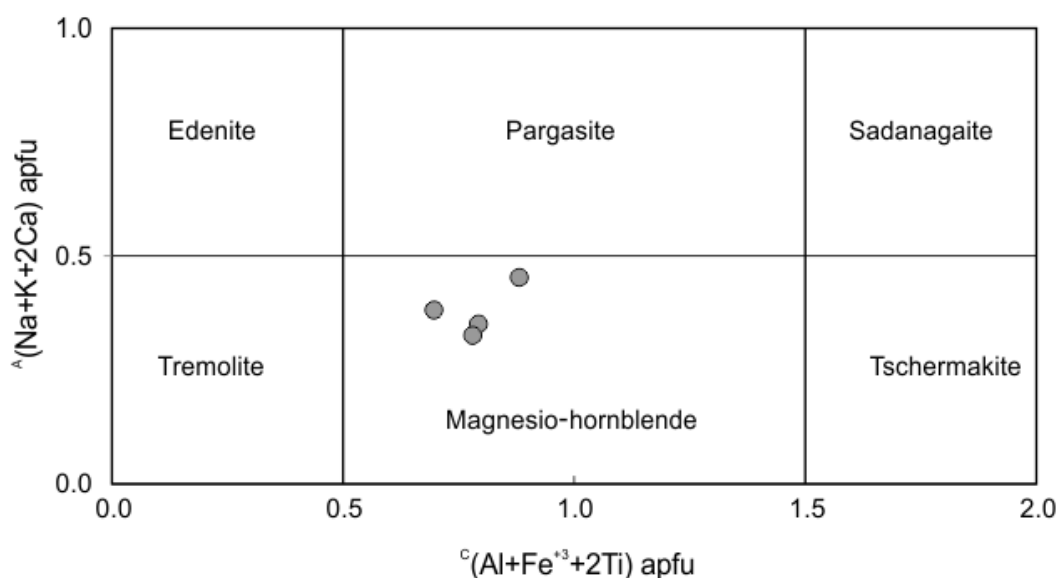


Fig. 7.3: Composition of amphiboles presented in a $^a(\text{Na}+\text{K}+2\text{Ca})$ vs. $^c(\text{Al}+\text{Fe}^{+3}+2\text{Ti})$ (apfu) plot for calcic amphiboles after the classification scheme of Hawthorne et al., (2012)

7.4.7. Epidote:

Epidote shows restricted compositional ranges. Not much variation observed from core to rim. Pistacite [$\text{Fe}^{+3}/(\text{Fe}^{+3}+\text{Al})$] component of epidote varies between 0.29-0.33 (Table 7.6).

Table 7.1: Representative electron microprobe analysis of clinopyroxene (stoichiometry calculated on the basis of 6 oxygens, oxide data are given in weight %).

Point No.	3 / 1 .	45	32 / 1 .	36 / 1 .	9 / 1 .	11 / 1 .	28 / 1 .	46	24
Texture	core	core	small grain		rim	rim	rim	medium sized grain	small grain
								rim	rim
SiO ₂	44.91	49.21	52.11	50.83	48.08	52.83	52.55	47.03	47.34
TiO ₂	0.31	0.19	0.04	0.01	0.18	0.00	0.01	0.28	0.20
Al ₂ O ₃	5.53	2.99	1.16	2.04	3.71	1.03	1.05	4.16	3.83
Cr ₂ O ₃	0.22	0.10	0.32	0.04	0.06	0.01	0.04	0.04	0.03
FeO	17.11	13.52	8.30	11.39	14.28	7.46	9.11	14.78	14.09
MnO	0.71	0.92	0.92	0.97	0.87	1.21	1.05	0.98	0.82
MgO	6.76	9.09	12.48	10.83	8.70	13.42	12.78	8.41	8.94
CaO	22.08	22.89	23.64	23.72	22.72	23.78	23.92	22.46	23.19
Na ₂ O	0.75	0.62	0.47	0.62	0.84	0.32	0.46	0.83	0.80
K ₂ O	0.01	0.04	0.00	0.01	0.02	0.00	0.03	0.01	0.00
Total	98.49	99.57	99.45	100.60	99.46	100.08	101.01	98.98	99.24
Si	1.76	1.89	1.96	1.91	1.84	1.97	1.95	1.82	1.82
Ti	0.01	0.01	0.00	0.00	0.01	0.00	0.00	0.01	0.01
Al	0.26	0.14	0.05	0.09	0.17	0.05	0.05	0.19	0.17
Cr ⁺³	0.01	0.00	0.01	0.00	0.00	0.00	0.00	0.00	0.00
Fe ^{+3*}	0.26	0.13	0.05	0.14	0.20	0.04	0.09	0.22	0.24
Fe ⁺²	0.31	0.31	0.21	0.22	0.26	0.19	0.19	0.25	0.21
Mn	0.02	0.03	0.03	0.03	0.03	0.04	0.03	0.03	0.03
Mg	0.40	0.52	0.70	0.61	0.50	0.74	0.71	0.48	0.51
Ca	0.93	0.94	0.95	0.95	0.93	0.95	0.95	0.93	0.95
Na	0.06	0.05	0.03	0.05	0.06	0.02	0.03	0.06	0.06
K	0.00	0.00	0.00	0.00	0.00	0.00	0.00	0.00	0.00
Total	4.00	4.00	4.00	4.00	4.00	4.00	4.00	4.00	4.00
X _{Mg}	0.56	0.63	0.77	0.73	0.65	0.80	0.79	0.66	0.71
Di	0.41	0.53	0.72	0.63	0.51	0.75	0.71	0.50	0.53
Hd	0.31	0.31	0.22	0.23	0.27	0.19	0.19	0.26	0.22
Ac	0.04	0.02	0.02	0.05	0.05	0.01	0.03	0.06	0.06
Jd	0.02	0.02	0.01	0.00	0.01	0.01	0.00	0.01	0.00
Ess	0.21	0.10	0.03	0.09	0.14	0.03	0.06	0.17	0.18
crTs	0.01	0.00	0.01	0.00	0.00	0.00	0.00	0.00	0.00
AlTs	0.00	0.00	0.00	0.00	0.00	0.00	0.00	0.00	0.00
Wo	0.93	0.94	0.95	0.95	0.93	0.95	0.95	0.93	0.95
En	0.40	0.52	0.70	0.61	0.50	0.74	0.71	0.48	0.51
Fs	0.31	0.31	0.21	0.22	0.26	0.19	0.19	0.25	0.21
Don	0.02	0.03	0.03	0.03	0.03	0.04	0.03	0.03	0.03

Table 7.2: Representative electron microprobe analysis of plagioclase (stoichiometry calculated on the basis of 8 oxygens, oxide data are given in weight %).

Point No.	30 / 1 .	29 / 1 .	14 / 1 .	15 / 1 .	16 / 1 .	17 / 1 .	42	28 / 1 .	26 / 1 .	9
Texture	rim	core	core	rim	core	rim	rim	rim	core	core
	matrix plagioclases						adjacent to scapolite			
SiO ₂	47.31	47.61	57.29	56.37	57.71	57.15	56.344	50.24	54.31	55.82
TiO ₂	0.03	0.00	0.00	0.01	0.00	0.00	0.004	0.00	0.03	0.00
Al ₂ O ₃	33.10	32.79	26.98	27.45	26.36	27.42	27.167	31.05	28.54	26.57
FeO	0.58	0.64	0.43	0.16	0.38	0.22	0.297	0.51	0.42	0.30
MnO	0.00	0.00	0.00	0.00	0.00	0.00	0.010	0.00	0.02	0.00
MgO	0.04	0.00	0.00	0.04	0.00	0.01	0.009	0.00	0.01	0.00
CaO	16.77	16.38	9.42	9.97	8.94	9.52	10.478	14.45	11.40	9.83
Na ₂ O	2.13	1.99	6.14	6.10	6.58	6.28	6.008	3.16	5.02	6.31
K ₂ O	0.04	0.06	0.25	0.18	0.27	0.14	0.156	0.09	0.18	0.27
Total	100.05	99.56	100.58	100.29	100.24	100.76	100.476	99.50	99.93	99.13
Si	2.17	2.20	2.56	2.52	2.58	2.55	2.52	2.30	2.46	2.53
Ti	0.00	0.00	0.00	0.00	0.00	0.00	0.00	0.00	0.00	0.00
Al	1.79	1.78	1.42	1.45	1.39	1.44	1.43	1.68	1.52	1.42
Fe ^{+3*}	0.02	0.00	0.00	0.00	0.00	0.00	0.01	0.00	0.01	0.01
Fe ⁺²	0.00	0.02	0.02	0.00	0.00	0.00	0.00	0.02	0.00	0.00
Mn	0.00	0.00	0.00	0.00	0.00	0.00	0.00	0.00	0.00	0.00
Mg	0.00	0.00	0.00	0.00	0.00	0.00	0.00	0.00	0.00	0.00
Ca	0.82	0.81	0.45	0.48	0.43	0.45	0.50	0.71	0.55	0.48
Na	0.19	0.18	0.53	0.53	0.57	0.54	0.52	0.28	0.44	0.55
K	0.00	0.00	0.01	0.01	0.02	0.01	0.01	0.01	0.01	0.02
Total	5.00	5.00	5.00	5.00	5.00	5.00	5.00	5.00	5.00	5.00
X _{An}	0.81	0.82	0.45	0.47	0.42	0.45	0.49	0.71	0.55	0.46
X _{Ab}	0.19	0.18	0.53	0.52	0.56	0.54	0.50	0.28	0.44	0.53
X _{Or}	0.00	0.00	0.01	0.01	0.02	0.01	0.01	0.01	0.01	0.01

7.4.8. Titanite:

Titanites are nearly pure, and contains a very small amount aluminium in their structures (~1.9-4 wt% Al₂O₃). X_{Al} of titanites varies between 0.07 to 0.14 apfu (Table 7.6).

Calcite is nearly pure, up to 1.4 wt% MgO (Table 7.6). **Quartz** and **magnetite** are nearly pure phases (Table 7.6).

Table 7.3: Representative electron microprobe analysis of scapolite (stoichiometry calculated on the basis of 25 oxygens, oxide data are given in weight %).

Point No.	25 / 1 .	12	30	40	24 / 1 .	13
Texture	core	core	core	rim	rim	rim
SiO ₂	45.55	44.60	43.99	45.96	45.62	45.28
TiO ₂	0.00	0.01	0.06	0.04	0.00	0.00
Al ₂ O ₃	27.23	27.11	26.27	26.18	27.44	27.33
FeO	0.13	0.19	0.57	0.05	0.15	0.03
MnO	0.02	0.04	0.14	0.04	0.04	0.02
MgO	0.02	0.02	0.37	0.02	0.04	0.02
CaO	18.31	18.29	14.75	18.05	18.21	18.30
Na ₂ O	3.24	3.37	2.64	3.41	3.39	3.27
K ₂ O	0.18	0.23	0.49	0.12	0.20	0.20
Total	94.74	93.86	89.31	93.87	95.09	94.45
Si	7.01	6.91	7.20	7.14	6.98	6.98
Ti	0.00	0.00	0.01	0.00	0.00	0.00
Al	4.94	4.95	5.07	4.79	4.95	4.97
Fe ^{+3*}	0.02	0.02	0.00	0.00	0.02	0.00
Fe ⁺²	0.00	0.00	0.08	0.01	0.00	0.00
Mn	0.00	0.00	0.02	0.01	0.01	0.00
Mg	0.00	0.00	0.09	0.00	0.01	0.00
Ca	3.02	3.04	2.59	3.00	2.99	3.02
Na	0.97	1.01	0.84	1.03	1.01	0.98
K	0.04	0.05	0.10	0.02	0.04	0.04
Total	16.00	16.00	16.00	16.00	16.00	16.00
Eq An	0.65	0.65	0.69	0.60	0.65	0.66

Table 7.4: Representative electron microprobe analysis of garnet (stoichiometry calculated on the basis of 12 oxygens, oxide data are given in weight %).

Point No.	1 / 1 .	18	49	2 / 1 .	4	7	17
Texture	core	core	core	rim	rim	rim	rim
SiO ₂	36.27	36.11	35.43	36.42	35.53	35.84	35.66
TiO ₂	0.82	0.85	0.88	0.76	0.85	0.90	0.85
Al ₂ O ₃	4.92	5.20	4.77	5.03	4.98	5.68	5.30
Cr ₂ O ₃	0.02	0.04	0.08	0.06	0.10	0.07	0.05
FeO	23.25	23.25	22.92	23.23	23.22	21.92	22.78
MnO	1.92	2.21	2.06	2.07	1.85	2.05	2.09
MgO	0.31	0.21	0.27	0.25	0.25	0.30	0.24
CaO	30.33	29.68	29.55	30.39	29.18	29.69	29.36
Na ₂ O	0.07	0.01	0.00	0.03	0.00	0.02	0.02
K ₂ O	0.00	0.02	0.00	0.00	0.02	0.02	0.01
Total	97.93	97.58	95.97	98.32	95.99	96.47	96.37
Si	2.99	3.00	2.99	3.00	3.00	3.00	2.99
Ti	0.05	0.05	0.06	0.05	0.05	0.06	0.05
Al	0.48	0.51	0.47	0.49	0.50	0.56	0.52
Cr ⁺³	0.00	0.00	0.01	0.00	0.01	0.00	0.00
Fe ⁺³	1.44	1.39	1.43	1.42	1.39	1.33	1.38
Fe ⁺²	0.17	0.22	0.19	0.17	0.25	0.20	0.22
Mn	0.13	0.16	0.15	0.14	0.13	0.14	0.15
Mg	0.04	0.03	0.03	0.03	0.03	0.04	0.03
Ca	2.68	2.64	2.67	2.68	2.64	2.66	2.64
Na	0.01	0.00	0.00	0.00	0.00	0.00	0.00
K	0.00	0.00	0.00	0.00	0.00	0.00	0.00
Total	8.00	8.00	8.00	8.00	8.00	8.00	8.00
X _{Adr}	0.75	0.73	0.75	0.74	0.74	0.70	0.72
X _{Py}	0.00	0.00	0.00	0.00	0.00	0.00	0.00
X _{Alm}	0.01	0.02	0.02	0.01	0.02	0.02	0.02
X _{Grs}	0.21	0.22	0.21	0.22	0.22	0.25	0.23
X _{Sps}	0.01	0.01	0.01	0.01	0.01	0.01	0.01
X _{Mg}	0.19	0.11	0.15	0.15	0.11	0.16	0.12

Table 7.5: Representative electron microprobe analysis of amphibole (stoichiometry calculated on the basis of 23 oxygens, oxide data are given in weight %).

Point No.	33 / 1 .	35 / 1 .	37 / 1 .
Magnesiohornblende			
Na ₂ O	0.88	1.00	0.96
MgO	12.86	14.51	12.83
Al ₂ O ₃	7.37	7.16	8.89
SiO ₂	47.20	48.09	45.20
K ₂ O	0.57	0.80	1.21
CaO	12.34	12.30	11.92
TiO ₂	0.24	0.24	0.18
Cr ₂ O ₃	0.03	0.00	0.00
MnO	1.06	1.11	0.83
FeO	15.09	12.79	14.48
Total	97.64	98.00	96.50
Si	6.93	6.97	6.72
Al (IV)	1.07	1.03	1.28
Ti	0.00	0.00	0.00
Sum T	8.00	8.00	8.00
Al (VI)	0.20	0.19	0.28
Ti	0.03	0.03	0.02
Cr +3	0.00	0.00	0.00
Fe +3	0.52	0.45	0.56
Mg	2.81	3.13	2.84
Fe +2	1.33	1.10	1.24
Mn	0.10	0.09	0.06
Li	0.00	0.00	0.00
Sum C	5.00	5.00	5.00
Mg	0.00	0.00	0.00
Fe +2	0.00	0.00	0.00
Mn	0.03	0.04	0.05
Li	0.00	0.00	0.00
Ca	1.94	1.91	1.90
Na	0.03	0.05	0.05
Sum B	2.00	2.00	2.00
Ca	0.00	0.00	0.00
Na	0.22	0.23	0.22
K	0.11	0.15	0.23
Sum A	0.33	0.38	0.45
TOTAL	15.33	15.38	15.45
X _{Mg}	0.68	0.74	0.70

Table 7.6: Representative electron microprobe analysis of epidote, K-feldspar, titanite, calcite, quartz and magnetite (stoichiometry calculated on the basis of 12.5, 8, 5, 3, 2, 4 oxygens respectively, oxide data are given in weight %).

Mineral	Epidote			K-feldspar		Titanite		Calcite	Quartz	Magnetite	
	Point No.	3 / 1 .	4 / 1 .	52	39	43	19 / 1 .	22 / 1 .	50	32	5
Texture	rim	core									
SiO ₂	37.31	37.34	36.61	64.90	63.73	30.48	30.02	0.00	97.42	0.03	
TiO ₂	0.09	0.12	0.16	0.01	0.00	32.77	35.87	0.01	0.00	0.00	
Al ₂ O ₃	21.58	21.59	21.74	18.53	18.39	3.76	1.95	0.02	0.00	0.04	
Cr ₂ O ₃	0.00	0.00	0.01	0.02	0.03	0.04	0.00	0.00	0.03	0.03	
FeO	14.81	14.18	12.42	0.11	0.05	2.61	2.00	0.34	0.09	93.93	
MnO	0.21	0.31	0.51	0.04	0.04	0.03	0.10	0.28	0.00	0.21	
MgO	0.06	0.06	0.04	0.00	0.01	0.00	0.03	1.44	0.01	0.00	
CaO	23.41	22.81	23.30	0.04	0.05	28.53	28.34	54.67	0.02	0.42	
Na ₂ O	0.00	0.00	0.00	0.98	1.14	0.02	0.00	0.03	0.01	0.00	
K ₂ O	0.00	0.00	0.00	16.47	16.68	0.00	0.00	0.00	0.03	0.00	
Total	97.70	96.46	94.80	101.10	100.12	98.24	98.31	56.79	97.61	94.66	
Si	2.96	3.00	2.98	2.95	2.92	0.99	0.98	0.00	1.00	0.00	
Ti	0.01	0.01	0.01	0.00	0.00	0.80	0.89	0.00	0.00	0.00	
Al	2.02	2.04	2.09	0.99	0.99	0.14	0.08	0.00	0.00	0.00	
Cr ⁺³	0.00	0.00	0.00	0.00	0.00	0.00	0.00	0.00	0.00	0.00	
Fe ⁺³	0.98	0.94	0.85	0.00	0.00	0.07	0.05	0.00	0.00	2.00	
Fe ⁺²	0.00	0.01	0.00	0.00	0.00	0.00	0.00	0.00	0.00	0.98	
Mn	0.01	0.02	0.04	0.00	0.00	0.00	0.00	0.01	0.00	0.01	
Mg	0.01	0.01	0.00	0.00	0.00	0.00	0.00	0.07	0.00	0.00	
Ca	1.99	1.96	2.03	0.00	0.00	0.99	1.00	1.91	0.00	0.02	
Na	0.00	0.00	0.00	0.09	0.10	0.00	0.00	0.00	0.00	0.00	
K	0.00	0.00	0.00	0.96	0.98	0.00	0.00	0.00	0.00	0.00	
Total	8.00	8.00	8.00	5.00	5.00	3.00	3.00	2.00	1.00	3.00	
Pistacite	0.33	0.32	0.29								
X _{An}				0.00	0.00						
X _{Ab}				0.08	0.09						
X _{Or}				0.92	0.90						
X _{Al}						0.14	0.07				

7.5. Petrogenetic grid for the studied calc-silicate granulite

Owing to the high andradite content and high Fe^{+3} in garnet and clinopyroxene respectively, conventional garnet-clinopyroxene Fe^{+2} -Mg exchange geothermometers and garnet-clinopyroxene-plagioclase-quartz barometers could not be applied to the studied assemblage. The textural relations and mineral reaction as described in sections 7.2 and 7.3, point towards a sequential development of the minerals: Clinopyroxene+ plagioclase+ calcite +titanite \pm magnetite \rightarrow Scapolite \rightarrow Garnet + amphibole \rightarrow Epidote. As evident from the textural relations, formation of scapolite also involves a simple CASV (+Na) reaction (A). However, presence of clinopyroxene, garnet, amphibole and epidote demand involvement of other non-CASV components (primarily MgO and FeO). On account of the highly magnesian composition of clinopyroxene and amphibole, combined with the presence of hydrous phases (amphibole and epidote), MgO and H_2O were also incorporated as system components. Hence, the mineral evolution in the studied calc-silicate granulite has been described in the simple six-component system $\text{CaO-MgO-Al}_2\text{O}_3\text{-SiO}_2\text{-H}_2\text{O-CO}_2$ (CMASV). Since titanite is the only mineral having significant Ti component, and does not react to form any new Ti-bearing phase, Ti has not been included as a phase component in the present study. To study the influence of P-T-fluid compositions, topologies have been described in P-T (for fixed X_{CO_2}) and isobaric T- X_{CO_2} space, with ten phases: diopside (Di), anorthite (An), scapolite (Me), grossular (Grs), tremolite (Tr), clinozoisite (Cz), calcite (Cal), quartz (Qtz), wollastonite (Wo) and vapor ($\text{H}_2\text{O-CO}_2$). These topologies have been constructed using the *Perple_X* program (version 6.9.1, updated February, 2021, Connolly, 2005) and the internally consistent thermodynamic dataset of Holland and Powell, (2011).

7.5.1. Topology in P-T space for pure compositions:

P-T topologies have been constructed at fixed X_{CO_2} (molar $\text{CO}_2/\text{CO}_2+\text{H}_2\text{O}$) that are set at X_{CO_2} of 0.2, 0.35, 0.5 and 0.9. As X_{CO_2} is kept constant, the number of system component reduces to five. Therefore, for a five-component system with ten phases, the number of phases present in each non-degenerate invariant points is six (+ H_2O), with three absent phases in each. From each invariant point, six non-degenerate univariant reactions emanate, each with five phases (four absent phases in each line). A P-T window of 3-10 kbar and 400-1000°C has been chosen to (a)

cover the wide range of physical conditions, and (b) make it compatible with the P-T conditions recorded from the adjoining meta-sedimentary units in and around the study area (PCSZ) (Raith et al., 2010; Roy Choudhury et al., 2021; Sengupta et al., 2009). All mineral abbreviations used are after Kretz, (1983). Fig. 7.4 depicts the characteristics of CMASV P-T topology with pure phases with the following features:

- (i) In the chosen P-T space, at low X_{CO_2} (~ 0.2), three invariant points, ([Wo Me Tr], [Wo Me Gr], [Tr Me Cz]) are stable (Fig. 7.4a).
- (ii) At lower X_{CO_2} (~ 0.2), stability of wollastonite bearing mineral assemblages is restricted to temperatures $>650^\circ\text{C}$ (higher temperature side of reaction: $\text{Cal Qtz} = \text{Wo}$), while clinozoisite stability (demarcated by the degenerate reaction $\text{Cal An} = \text{Cz}$) is restricted to increasingly higher temperatures with increasing pressure. Grossular and meionite stability fields are limited to higher pressures (>5 kbar) and temperatures ($>850^\circ\text{C}$).
- (iii) With a marginal increase in X_{CO_2} ($0.35 X_{\text{CO}_2}$), the invariant point [Wo Me Tr] disappear, and the invariant points [Tr Me Cz], [Tr Qtz Cz] and [Tr Cal Cz] shift towards each other. The stability of wollastonite decreases and becomes more restricted towards higher temperatures (and relatively lower pressures) (Fig. 7.4b). The degenerate reaction $\text{Cal An} = \text{Cz}$ progressively shifts towards lower temperatures and higher pressures, thereby decreasing the clinozoisite stability field, which ultimately becomes unstable at $>0.8 X_{\text{CO}_2}$. The stability of grossular also becomes restricted to high pressures. The decrease in stability of these minerals is accompanied by an increase in the stability of tremolite. The assemblage $\text{Cal} + \text{An} + \text{Qtz} + \text{Di}$ also becomes increasingly stable (Fig. 7.4b).

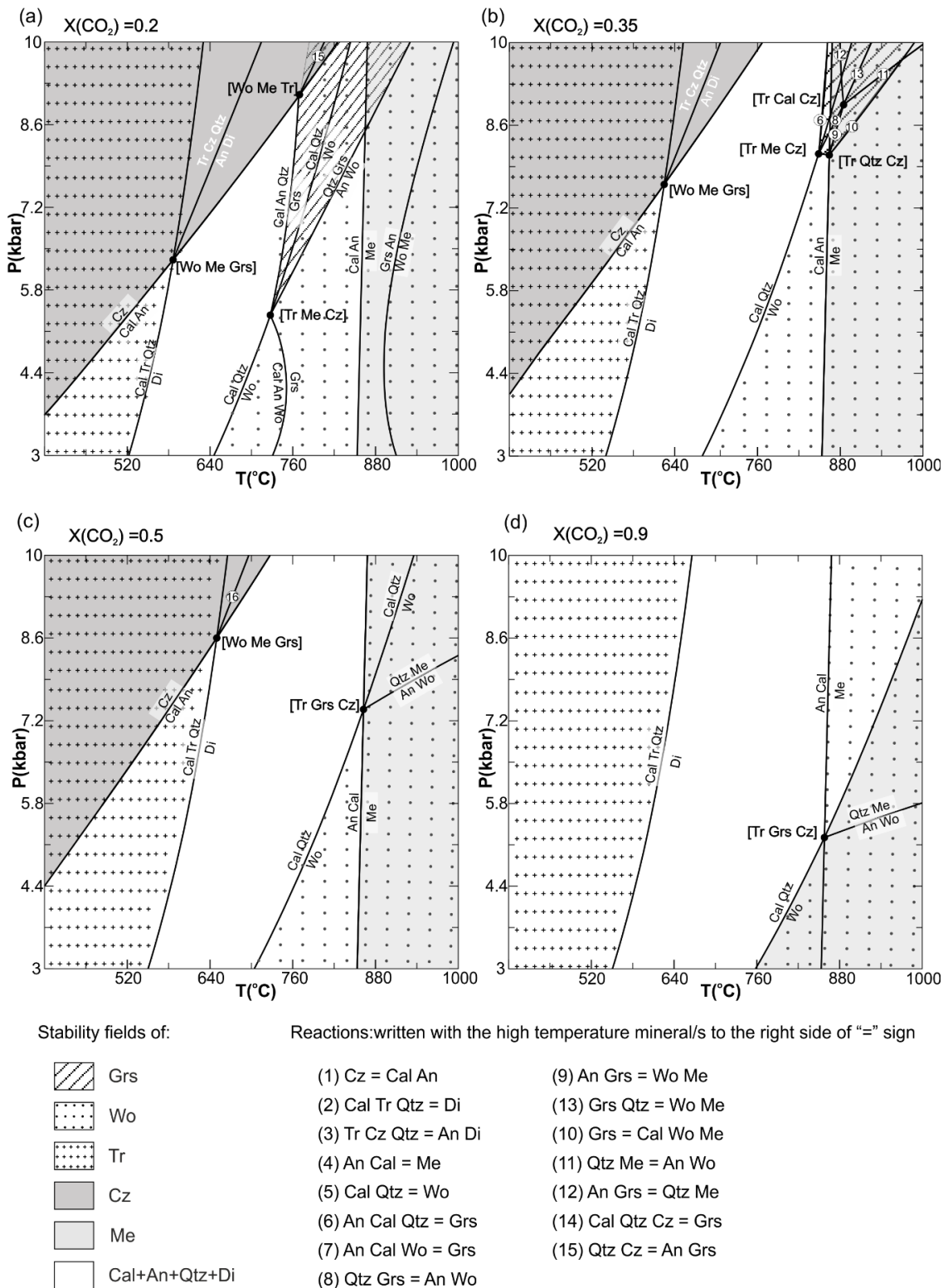


Fig. 7.4: P-T topology (for pure phases) of the CMASV system calculated at different X_{CO_2} conditions. The reaction numbers are consistent throughout the figures a-d. All abbreviations are after Kretz, (1983).

- (iv) At $X_{\text{CO}_2} > 0.4$, [Tr Qtz Cz], [Tr Me Cz] and [Tr Cal Cz] disappear, and an alternate topology stabilises instead (Fig. 7.4c), with a new grossular absent invariant point ([Tr Grs Cz]), thereby restricting the stability of pure grossular below 0.4 X_{CO_2} . Instead, wollastonite free, meionite + quartz + calcite assemblage become stable.
- (v) At $X_{\text{CO}_2} = 0.9$ (Fig. 7.4d), clinozoisite becomes unstable, while wollastonite field is more restricted towards higher temperatures. Stability of tremolite, Cal + An + Qtz + Di and meionite + quartz + calcite, on the other hand is further enlarged.

Fig. 7.4 shows that for CMASV system, garnet and tremolite do not coexist together.

7.5.2. Effect of non-CMASV components on the CMASV P-T topology:

The mineral compositions of the studied calc-silicate compositions are complex, and cannot be defined by this simple CMASV system. The measured mineral compositions indicate the presence of a considerable number of non-CMASV components (Fe^{+2} , Fe^{+3} , Na) in the minerals of the studied calc-silicate. These components are expected to significantly control the stability of the minerals, and must be taken into account.

As evident from the measured compositions, garnet is compositionally “grandite” (with higher proportion of andradite to grossular). Amphibole also contains significant amount of Fe^{+3} component. Although clinopyroxenes are highly magnesian, they also contain a considerable amount of essenite (Fe^{+3}) and acmite (Na^+ and Fe^{+3}) component. The growth of garnet as well as amphibole (often pseudomorphically) on clinopyroxene is consistent with the latter being the source of Fe^{+3} for andradite. Fe^{+3} also forms a major component of epidote. The extensive replacement of garnet and amphibole by epidote points towards the former being source of Fe^{+3} for epidote. Owing to very low almandine content in garnet, Fe^{+2} seems to be partitioned primarily in clinopyroxene and amphibole. Apart from clinopyroxene (acmite component), Na is also incorporated in plagioclase, and to some extent, in scapolite. As scapolite does not contain any appreciable amount of SO_4 and Cl, their effect on scapolite is negligible. Since there is no significant amount of MnO within the structure of any of the minerals, its effect has been neglected.

Incorporation of these non-CMASV components results in increase in stability of the minerals. Therefore, the invariant points shift along univariant reactions, in the direction in which the phase/s incorporating these components are absent (see Dey et al., 2019; Sengupta and Raith, 2002 for details). Hence, keeping in mind the predominance of these non-CMASV components in the measured mineral compositions, evolution of the mineral assemblages for the studied calc-silicate has been described using activity adjusted grids.

7.5.3. Activity adjusted P-T topology:

The P-T topology discussed above (Fig. 7.4) is adjusted for measured compositions to portray the P-T conditions of formation of garnet-amphibole and epidote in the studied calc-silicate. Activities for measured compositions were calculated using the a-X program (<https://www.esc.cam.ac.uk/research/research-groups/research-projects/tim-hollands-software-pages/ax>). Fig. 7.5 shows a series of activity corrected P-T grids (400-800°C, 3-10 kbar) constructed at different X_{CO_2} sections (0.7, 0.5, 0.3). The corrected activities of the minerals used for constructing these topologies are: scapolite ($a_{\text{Me}}=0.3$), plagioclase ($a_{\text{Pl}}=0.78$), garnet ($a_{\text{Grs}}=0.024$), clinopyroxene ($a_{\text{Di}}=0.6$), amphibole ($a_{\text{Tr}}=0.134$) and epidote (corrected activity of clinozoisite: $a_{\text{Cz}}=0.23$). The major differences with pure topology of the activity corrected grid (Fig. 7.5) include:

- (i) A completely different set of invariant points (amphibole present and wollastonite absent) stabilise here. At 0.7 X_{CO_2} (Fig. 7.5a), [Qtz Wo Cz], [Cal Wo Cz], [Di Wo Cz], [Di Grs Wo] invariant points are stable. At higher X_{CO_2} (>0.8) conditions, the topology inverts to give to a new set of invariant points ([Tr Wo Cz], [Gr Wo Cz], [An Wo Cz]). Scapolite has a large stability field (>~520°C) demarcated by the reaction $\text{Di Cal Me} = \text{Grs Tr (An Wo Cz Qtz)}$.
- (ii) Epidote is stable only below $\leq 0.5 X_{\text{CO}_2}$, and at low temperature ($T < 460^\circ\text{C}$; Fig. 7.5b-c). With decrease in X_{CO_2} (≤ 0.5 ; Fig. 7.5b), [Cal Wo Cz] and [Di Wo Cz] shift towards higher pressures, while [Qtz Wo Cz] and [Di Grs Wo] shift towards lower pressures. As a consequence, the epidote and grossular stability fields also expand slightly at the expense of scapolite bearing field, which shifts towards higher temperatures (>640°C).

(iii) Below $X_{CO_2} \sim 0.45/0.5$, the topology inverses again (Fig. 7.5c). Invariant points [Di Wo Cz] and [Di Grs Wo] disappears to give rise to a new set of points ([Wo Di Me], [Wo Di Qtz], [Wo Di Cal] and [Wo Di An]). Stability of epidote and grossular further enlarges.

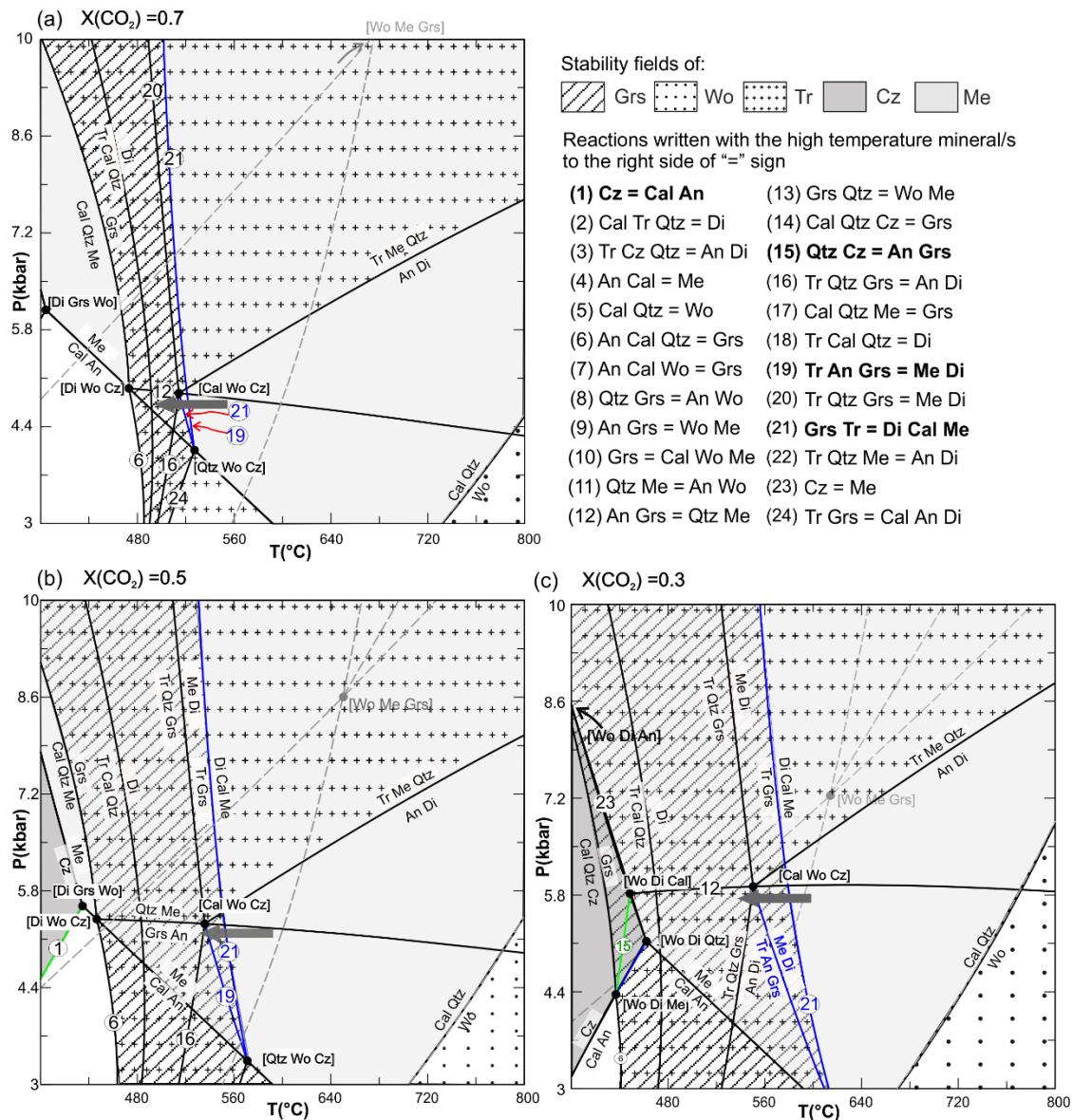


Fig. 7.5: P-T topology (activity corrected) of the CMASV system calculated at different X_{CO_2} conditions. The reaction numbers are consistent throughout the figures a-c. The garnet-amphibole and epidote forming reactions have been marked in blue and green colours in the topology and in bold in the index. The grey circle and grey dashed lines represent position of invariant point and corresponding reactions for pure compositions within this P-T range, and has been added for comparison with the activity corrected topology.

- (iv) Garnet and amphibole stability fields overlap. Formation of garnet on scapolite and clinopyroxene, combined with the pseudomorphic replacement of clinopyroxene by amphibole is consistent with the reactions: $\text{Me Di} = \text{Grs An Tr (Cal Wo Cz Qtz)}$ and $\text{Di Cal Me} = \text{Grs Tr (An Wo Cz Qtz)}$ (coloured in blue in Fig. 7.5 and 7.7). These reactions originate from [Cal Wo Cz] and [Qtz Wo Cz] invariant points, and are extremely temperature sensitive. Pressure-temperature conditions for the formation of garnet and amphibole are estimated from the stability ranges of these two reactions, and the invariant point [Cal Wo Cz]. At high X_{CO_2} ($=0.7$), the temperature range varies between 520-530°C. With decreasing X_{CO_2} , the [Cal Wo Cz] and [Qtz Wo Cz] invariant points move away from each other, thereby increasing the P-T range of the above reactions (Fig. 7.5b-c). Therefore, combining the P-T ranges obtained from various isobaric X_{CO_2} sections (Fig. 7.5a-c), a maximum temperature range of 520-640°C can be estimated for garnet-amphibole formation in the studied calc-silicate granulite. Additionally, a maximum pressure constraint of ~4.7-6 kbar can also be inferred from this activity corrected P-T topology.
- (v) The highly temperature sensitive slope of the reactions (Cal Wo Cz Qtz) and (An Wo Cz Qtz) implies that the textural progress is driven by slight decrease in temperature from 640°C to 520°C, within a pressure window of ~4.7-6 kbar. Moreover, the stability of these two reactions (at $<0.7 X_{\text{CO}_2}$) demands the presence of fluid within the system (discussed later).
- (vi) On the other hand, the formation of epidote extensively at the expense of garnet, plagioclase and calcite advocates for the degenerate reactions $\text{Cz} = \text{Cal An}$ and $\text{Qtz Cz} = \text{An Grs}$ (coloured in green in Fig. 7.5 and 7.7). While $\text{Cz} = \text{Cal An}$ is stable from $<\sim 0.7 X_{\text{CO}_2}$ (emerging from [Di Grs Wo] in Fig. 7.5b, and from [Wo Di Qtz] in the alternate topology below $0.4 X_{\text{CO}_2}$, Fig. 7.5c); the reaction $\text{Qtz Cz} = \text{An Grs}$ (emerging from [Wo Di Cal] invariant point) is stabilised only in the alternate topology, at low X_{CO_2} (<0.4) conditions. The stability of these two reactions constrains the P-T conditions of epidote formation between 430-500°C, roughly within a pressure range of ~4.5-6 kbar.

7.5.4. Topology in T - X_{CO_2} space for pure compositions in the CMASV system:

Fig. 7.6 depicts the isobaric T - X_{CO_2} topology constructed for different pressure sections (2, 5 and 8 kbar). Within the given temperature range (400–1000°C) the constructed topology is similar to the qualitative CASV topology of Buick et al., (1994). Fig. 7.6 illustrates the following characteristics:

- (i) In the chosen T - X_{CO_2} range, five invariant points are stable ([Tr Grs Cz], [Tr Qtz Cz], [Tr Me Cz], [Wo Me Tr], [Wo Me Grs]). At pressures lower than 5 kbar, however, [Tr Grs Cz] invariant point is unstable (Fig. 7.6a).

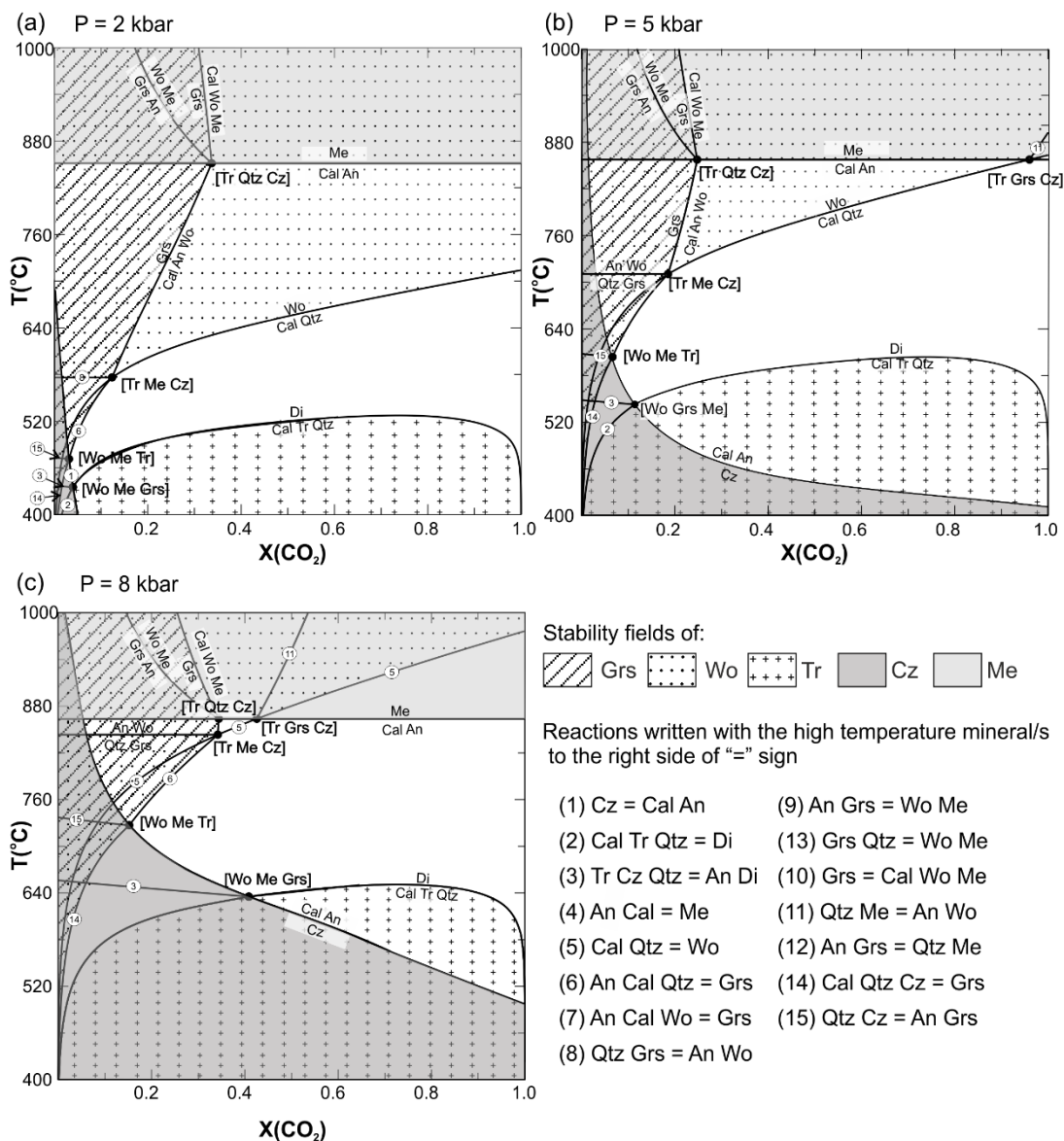


Fig. 7.6: Isobaric T - X_{CO_2} topology (for pure phases) of the CMASV system calculated at different pressures. The reaction numbers are consistent throughout the figures a–c.

- (ii) At low pressures (2 kbar, Fig. 7.6a), wollastonite has a large stability field, which extends up to very low temperatures, at extremely high H₂O-rich conditions (<0.1 X_{CO2}). With increase in pressure, stability of wollastonite is increasingly restricted to much higher temperatures. Stability of scapolite, however, remains constant (> ~850°C).
- (iii) Stability of grossular is also limited to low X_{CO2} conditions, that widens slightly with increase in pressure, but never exceeds beyond 0.4 X_{CO2} (consistent with the observations from P-T topology) (Fig. 7.6a-c).
- (iv) Tremolite stability is controlled by the temperature insensitive reaction Tr Qtz Cal = Di, and enlarges with increase in pressure, corresponding to the shift of the above reaction towards higher temperature (Fig. 7.6a-c).
- (v) At low pressures (2 kbar), clinozoisite is restricted to extremely low X_{CO2} conditions (Fig. 7.6a). Its stability field enlarges towards higher temperatures and X_{CO2} conditions with increase in pressure (Fig. 7.6b-c).

However, as also observed in P-T topology, here also grossular and tremolite stability fields do not overlap in the chosen T-X_{CO2} space.

7.5.5. Activity adjusted topology in isobaric T-X_{CO2} space:

T-X_{CO2} topology has been used widely to estimate the fluid conditions during the development of calc-silicate assemblages (Buick et al., 1994; e.g., Dey et al., 2019; Groppo et al., 2013; Kerrick, 1974). In the present study, isobaric T-X_{CO2} topology, has been constructed for the temperature range of 400-800°C and 0-1 X_{CO2}. Owing to the temperature sensitive nature of the garnet- amphibole and epidote forming reactions, it is very hard to provide an accurate estimation of pressure conditions. Considering the approximate pressure window (~4.5-6 kbar) constrained from the P-T topology (see section 7.5.3) for both garnet and epidote formation, the T-X_{CO2} sections have been described at two representative pressures: 5 and 6 kbar (Fig. 7.7a-b). The major differences with pure grid are as follows:

- (i) At 6 kbar, six new invariant points ([Cal Wo Cz], [An Wo Cz], [Cal Wo Di], [An Wo Di], [Grs Wo Di] and [Grs Wo Cz]) stabilise (which were not stable in pure grid). The garnet-amphibole forming reactions (Cal Wo Cz Qtz) and (An Wo Cz Qtz) and the invariant point [Cal Wo Cz] constrain low X_{CO2} conditions (~0.25) for their formation (Fig. 7.7a).

- (ii) With decrease in pressure (at ~5 kbar), [Cal Wo Di], [An Wo Di], [Grs Wo Di] and [Grs Wo Cz] disappear, and the topology inverts to stabilise a new set of invariant points ([Qtz Wo Di], [Me Wo Di] and [Di Wo Cz]) (Fig. 7.7b).
- (iii) [Cal Wo Cz] and [An Wo Cz] invariant points, on the other hand remain stable, but shift towards higher X_{CO_2} conditions, expanding the amphibole-garnet stability field towards higher X_{CO_2} and slightly higher temperature conditions (Fig. 7.7b). The reactions (Cal Wo Cz Qtz) and (An Wo Cz Qtz) constrain the fluid conditions of stability of garnet + amphibole between ~0.25-0.6 X_{CO_2} . Therefore, it is suggested that formation of garnet and amphibole at the expense of scapolite and clinopyroxene proceeds with lowering of temperature as well as X_{CO_2} conditions.
- (iv) Epidote forming reaction (Grs An=Cz Qtz), emerging from [Cal Wo Di] invariant point, limits its stability to low X_{CO_2} (~0.2, Fig. 7.7a) and low temperatures (~450°C) relative to garnet forming reactions (Fig. 7.7a). In the inverted topology (Fig. 7.7b), this Grs An=Cz Qtz reaction emerges from a new [Me Wo Di] invariant point. Additionally, another epidote forming reaction "An Cal=Cz", stabilises in this inverted topology, bounded by the invariant points [Qtz Wo Di] and [Me Wo Di] (Fig. 7.7b). These two reactions limit the T and X_{CO_2} conditions of epidote formation between ~440-460°C and ~0.25-0.4 (Fig. 7.7a-b).
- (v) Textural features indicate that these two reactions proceed to the right (that is, epidote forms) with decreasing temperature, with/ without decrease in X_{CO_2} . These two reactions constrain the fluid conditions of epidote formation below 0.4 X_{CO_2} . Fig. 7.7 also puts a tighter constrain on the epidote forming temperature between 440-460°C within a pressure of ~5-6 kbar.

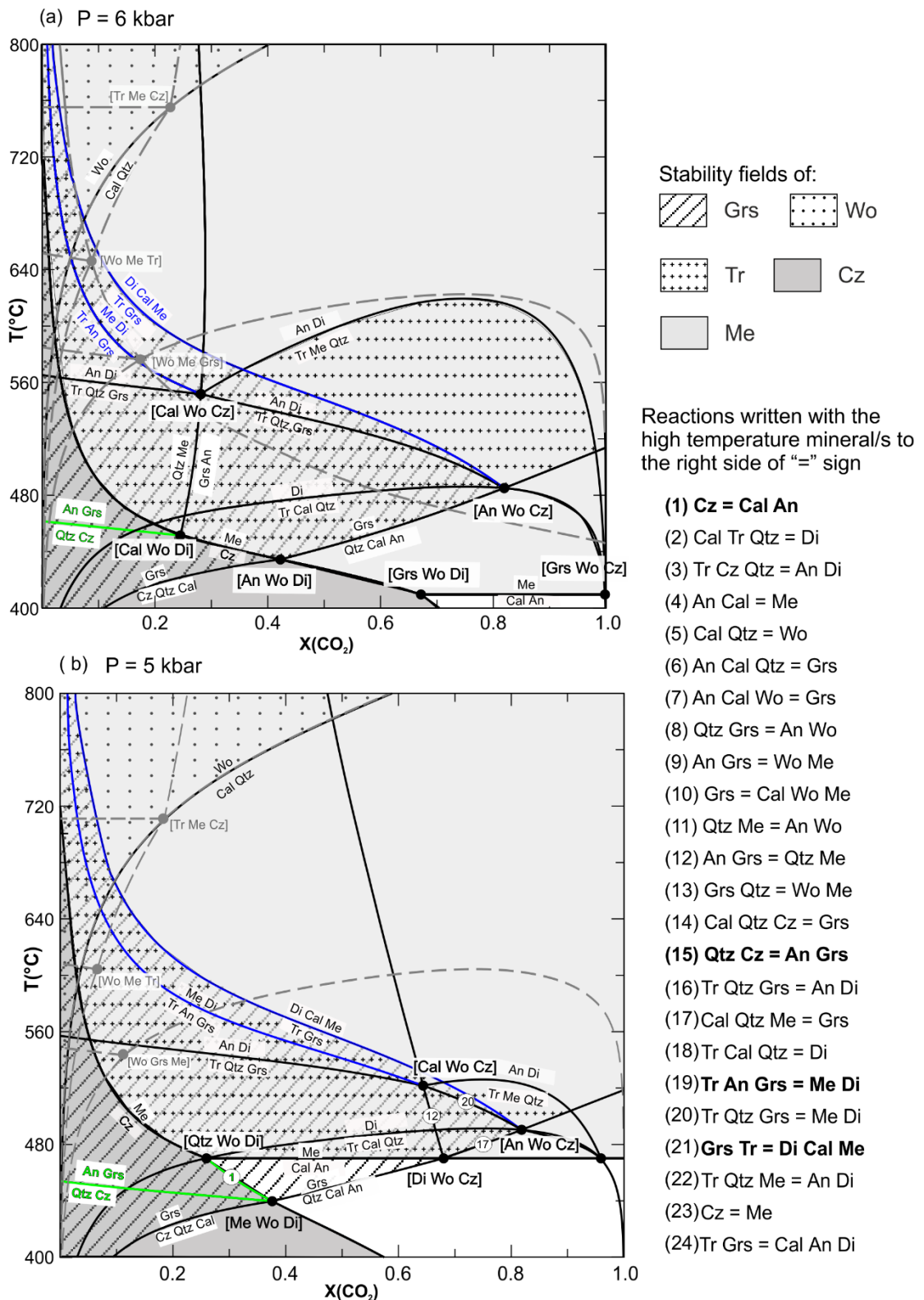


Fig. 7.7: Isobaric T-XCO₂ topology (activity corrected) in the CMASV system calculated at different pressures. The reaction numbers are consistent throughout the figures a-b. The garnet-amphibole and epidote forming reactions have been marked in blue and green colours in the topology and in bold in the index.

7.5.6. Mineral evolution in studied calc-silicate of MSU

Representative activity corrected P-T (at 0.3 X_{CO_2} ; Fig. 7.8a) and T- X_{CO_2} (at 5 kbar; Fig. 7.8b) have been chosen for the following discussion, as all the concerned reactions are well depicted. From the above discussion, it is evident that clinopyroxene, plagioclase and scapolite (\pm titanite \pm magnetite) were the early stabilised minerals (possibly at peak conditions). Subsequently, garnet-amphibole formed at the expense of these minerals. Now, activity corrected P-T topology constrains the temperature of garnet-amphibole formation between 520-640°C, while the maximum pressure limit ranges between \sim 4.7-6 kbar. A detailed study of evolution of the adjacent metapelitic rocks of the MSU have been previously carried out by Roy Choudhury et al., (2021). The workers recorded a clockwise P-T path, that culminated at \sim 730-790°C and 5.5-7 kbar, followed by a moderately steep decompressive path and subsequent cooling to the final retrograde conditions (\sim 630°C and \sim 4 kbar). The constrained pressure range from the calc-silicate granulites (\sim 4.7-6 kbar), overlaps with that constrained for the retrogressive phase of the pelitic granulites (\sim 4-5.4 kbar). However, the temperature is slightly lower than that estimated for the retrograde biotite formation in the pelitic granulites (\sim 630-700°C). Hence, it suffices that formation of garnet and amphibole occurred during near isobaric cooling, subsequent to decompression as well as retrograde biotite formation (Fig. 7.8a), as recorded from the adjacent pelitic granulites. Formation of garnet (coronal) during cooling (with or without pressure drop) has been previously reported in different calc-silicate rocks by various workers (Fitzsimons and Harley, 1994; Sengupta et al., 1997, etc. and references therein). Subsequent conditions of epidote formation have been constrained between 440-460°C (Fig. 7.7; for a pressure range of \sim 4.5-6 kbar). The approximate pressure window (\sim 4.5-6 kbar) constrained for both garnet and epidote formation suggests that there was little or no change in pressure conditions, and that temperature and ambient fluid conditions actually controlled the stability of garnet-amphibole and epidote.

The activity adjusted P-T and T- X_{CO_2} topologies put a broad constrain on the fluid conditions of garnet-amphibole formation between \sim 0.25-0.6 X_{CO_2} (Fig. 7.7). Moreover, the abundance of amphibole, combined with their large sizes is indicative of the presence of hydrous fluid in the system. On the other hand, the epidote

forming reactions limit the fluid conditions of epidote stability below $\sim 0.4 X_{\text{CO}_2}$. However, the modal percentage of epidote is low, and has smaller grain size with respect to amphibole.

Combining the above information, it is inferred that the studied calc-silicates of the MSU stabilised garnet and amphibole on account of near isobaric cooling in the presence of a hydrous fluid, during the late stages of metamorphic evolution of the metasedimentary package of Madukkarai. Additionally, continued cooling (with/without hydrous fluid influx) led to the stabilisation of epidote subsequent to garnet formation. However, as evident from the T- X_{CO_2} sections (Fig. 7.7a-b), the fluid conditions prevalent during these two stages might have varied slightly. Fig. 7.8b shows three possible paths in T- X_{CO_2} section that could explain the mineral evolution in the studied calc-silicates:

Path A: (Red path) Formation of garnet-amphibole and epidote occurs along a cooling path, without any fluid influx.

Path B: (Blue path) Garnet-amphibole formed during cooling combined with influx of water-rich fluid (i.e., decrease in X_{CO_2}); epidote formed during subsequent and continued cooling at similar fluid conditions.

Path C: (Green line) Garnet- amphibole as well as epidote formed during cooling associated with influx of H_2O bearing fluid

Path A is not a feasible option as a simple temperature decrease is not sufficient to explain the modal percentage of amphibole observed in the rock. It demands infiltration of water-rich fluid. However, the lower modal percentage of epidote (along with its small size) indicates that not much fluid infiltration occurred subsequent to garnet and amphibole formation (as should have been the case for Path C, Fig. 7.8b). This indicates that epidote primarily formed as a consequence of a continued temperature drop subsequent to garnet-amphibole formation. Therefore, near isobaric temperature decrease (subsequent to decompression) with the influx of moderately water-rich fluid, followed by continued isobaric cooling (Path B; Fig. 7.8b), seems to be most appropriate in explaining the T- X_{fluid} conditions of formation of the calc-silicate mineralogy.

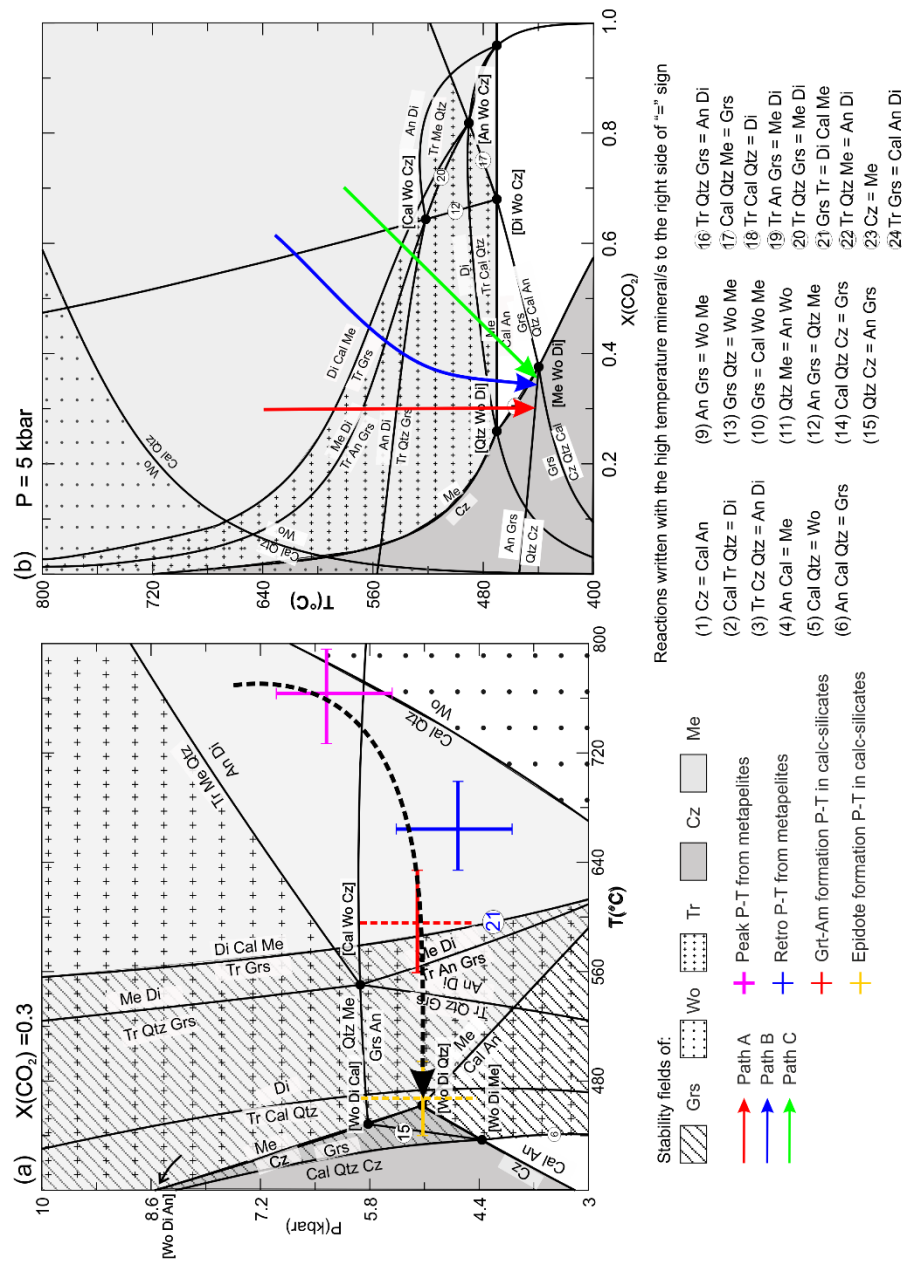


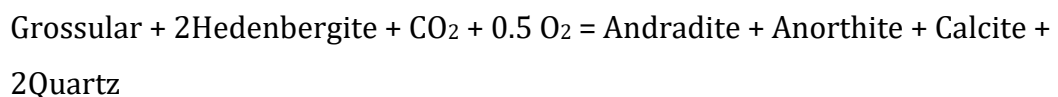
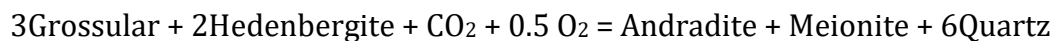
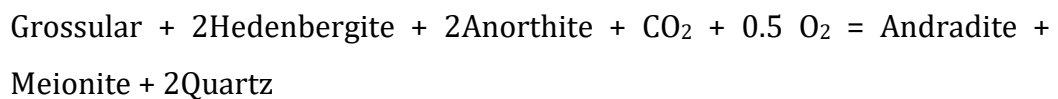
Fig. 7.8: (a) P-T conditions of adjacent pelitic granulites and those estimated from the calc-silicates of this study plotted in an activity corrected P-T topology at 0.3 X_{CO_2} . Since a broad pressure range for formation of garnet-amphibole and epidote has been constrained, it has been given in dotted line. (b) Isobaric T- X_{CO_2} topology (activity corrected at 5 kbar) showing the three possibilities of the path followed by the studied calc-silicates. The reaction numbers are consistent throughout the figures a-b.

7.5.7. Formation of andradite component in garnet

Garnets with considerable amount of andradite component have been variously inferred to be the result of Fe-metasomatism (Buick et al., 1994, 1993), or as a consequence of complex mineral equilibria (Sengupta et al., 1997). Fe-metasomatism is typically characterised by garnets forming in layers (both in meso- and microscopic scale), a high modal percentage of garnet, and very high andradite content. Although the andradite component is high in the studied garnets (~70-75 mol%), their modal amount does not exceed ~8%. Moreover, garnets do not occur in layers or zones in mesoscopic scale, contrary to the view of Fe-metasomatism. However, the high proportion of andradite demands an explanation. The constructed CMASV topology cannot explain the andradite forming reactions. Growth of garnet preferentially over clinopyroxene suggests the later mineral (CaFe³⁺Si₂O₆ component) to be the source of andradite (also see Buick et al., 1993; Harley and Buick, 1992; Sengupta et al., 1997; Sengupta and Raith, 2002). Formation of andraditic garnet at the expense of Fe³⁺ in clinopyroxene has also been previously described from the calc-silicates of Anakapalle, eastern ghats (Sengupta et al., 1997, Harley and Buick, 1992, Fitzsimons and Harley, 1994). Andradite can form from clinopyroxene via the following reactions:

$$2\text{Essenite} + 4\text{Calcite} + 4\text{Quartz} = \text{Andradite} + \text{Grossular} + 4\text{CO}_2 \text{ (Sengupta et al., 1997)}$$

and by the following oxidation reactions (Sengupta and Raith, 2002),



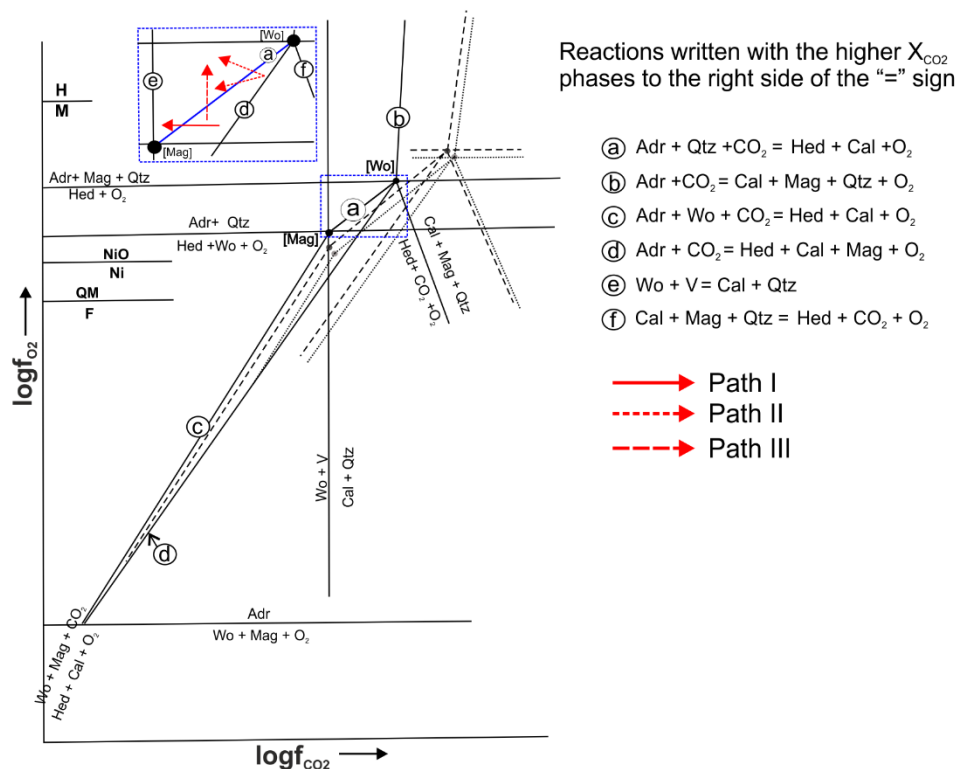


Fig. 7.9: Qualitative $\log f_{\text{O}_2}$ vs $\log f_{\text{CO}_2}$ topology in the system $\text{SiO}_2\text{-FeO-CaO-CO}_2\text{-O}_2$ (SFC- $\text{CO}_2\text{-O}_2$) modified after Sengupta et al., 1997, showing andradite formation at the expense of hedenbergite. The dashed and dotted lines, and the semi-transparent invariant points depict the progressive shift due to the effects of non-SFC- $\text{CO}_2\text{-O}_2$. The inset shows the different paths that may lead to formation of andradite at the expense of hedenbergite.

A considerable amount of essonite component (up to ~21 mol%) is consistent with the occurrence of the above reaction. However, the measured compositions of garnet depict that the andradite/ grossular ratio is around 3:1. This poses an additional requirement for the involvement of hedenbergite component in clinopyroxene in order to balance the higher andradite. Involvement of hedenbergite component can be qualitatively explained in the $\log f_{\text{O}_2}$ vs $\log f_{\text{CO}_2}$ topology constructed by Sengupta et al., 1997 (Fig. 7.9). The authors computed a $\log f_{\text{O}_2}$ vs $\log f_{\text{CO}_2}$ topology in the system $\text{SiO}_2\text{-FeO-CaO-CO}_2\text{-O}_2$ (SFC- $\text{CO}_2\text{-O}_2$). In the constructed topology, [Wo], [Qtz] and [Mag] invariant points are stable (Fig. 7.9). The univariant reactions were plotted by calculating their slopes, using the relation: $d(\log f_{\text{CO}_2})/d(\log f_{\text{O}_2}) = m_1/m_2$; where m_1 and m_2 are coefficients of O_2 and CO_2 respectively. Effects of non-SFC- $\text{CO}_2\text{-O}_2$ components (activity corrected for

measured compositions) results in shift of the andradite forming reactions. In the studied calc-silicate, the andradite forming reaction is depicted by the wollastonite absent univariant reaction: $4\text{Hedenbergite} + 2\text{Calcite} + \text{O}_2 = 2\text{Andradite} + 2\text{Quartz} + 2\text{CO}_2$ (Sengupta et al., 1997; Fig. 7.9). For the measured compositions of the studied calc-silicate, the above reaction shifts. The slope of the above reaction indicates that the reaction progresses in either of the three ways (see inset of Fig. 7.9): (I) influx of H₂O rich fluid, (II) influx of H₂O rich fluid coupled with change in $f\text{O}_2$ conditions (increase or decrease); and (III) increase in $f\text{O}_2$ conditions without any fluid conditions. Now, a slight increase in $f\text{O}_2$ should be accompanied by oxidation of all the Fe⁺² bearing silicates present in the rock (Frost, 1991). However, the oxide poor nature of the studied rocks (only accessory magnetite present) implies that the reaction progressed at nearly constant $f\text{O}_2$ conditions. Hence, the influx of hydrous fluid (without change in ambient $f\text{O}_2$ conditions, Path I, see inset of Fig. 7.9), is inferred to have driven the formation of andradite from hedenbergite in the studied rocks. This is also consistent with the findings of the constructed P-T and T-X_{CO2} topologies. Additionally, the absence of wollastonite, and coexistence of calcite and quartz in the rock indicates that the reaction conditions remained at the higher X_{CO2} side of $\text{Cal} + \text{Qtz} = \text{Wo} + \text{V}$ (Fig. 7.9).

References

- Buick, I.S., Cartwright, I., Hand, M., Powell, R., 1994. Evidence for pre-regional metamorphic fluid infiltration of the Lower Calcsilicate Unit, Reynolds Range Group (central Australia). *J. Metamorph. Geol.* 12, 789–810.
- Buick, I.S., Harley, S.L., Cartwright, I.C., 1993. Granulite facies metasomatism: zoned calc-silicate boudins from the Rauer Group, East Antarctica. *Contrib. to Mineral. Petrol.* 113, 557–571.
- Connolly, J.A.D., 2005. Computation of phase equilibria by linear programming: A tool for geodynamic modeling and its application to subduction zone decarbonation. <https://doi.org/10.1016/j.epsl.2005.04.033>
- Dasgupta, S., 1993. Contrasting mineral parageneses in high-temperature calc-silicate granulites: examples from the Eastern Ghats, India. *J. Metamorph. Geol.*

11, 193–202.

Dasgupta, S., Pal, S., 2005. Origin of grandite garnet in calc-silicate granulites: mineral–fluid equilibria and petrogenetic grids. *J. Petrol.* 46, 1045–1076.

Dey, A., Choudhury, S.R., Mukherjee, S., Sanyal, S., Sengupta, P., 2019. Origin of vesuvianite-garnet veins in calc-silicate rocks from part of the Chotanagpur Granite Gneiss Complex, East Indian Shield: The quantitative PTX CO₂ topology in parts of the system CaO-MgO-Al₂O₃-SiO₂-H₂O-CO₂ (+ Fe₂O₃, F). *Am. Mineral. J.* 104, 744–760.

Droop, G.T.R., 1987. A General Equation for Estimating Fe³⁺ Concentrations in Ferromagnesian Silicates and Oxides from Microprobe Analyses, Using Stoichiometric Criteria. *Mineral. Mag.* 51, 431–435. <https://doi.org/10.1180/minmag.1987.051.361.10>

Ferry, J.M., Burt, D., 1982. Characterization of metamorphic fluid composition through mineral equilibria., in: *Characterization of Metamorphism through Mineral Equilibria*. Mineralogical Society of America: Reviews in Mineralogy, 10, pp. 207–262.

Fitzsimons, I.C.W., Harley, S.L., 1994. Garnet coronas in scapolite-wollastonite calc-silicates from East Antarctica: the application and limitations of activity-corrected grids. *J. Metamorph. Geol.* 12, 761–777.

Frost, B.R., 1991. Introduction to oxygen fugacity and its petrologic importance. *Rev. Mineral. Geochemistry* 25, 1–9.

Groppo, C., Rolfo, F., Castelli, D., Connolly, J.A.D., 2013. Metamorphic CO₂ production from calc-silicate rocks via garnet-forming reactions in the CFAS–H₂O–CO₂ system. *Contrib. to Mineral. Petrol.* 166, 1655–1675.

Harley, S.L., Buick, I.A.N.S., 1992. Wollastonite—Scapolite assemblages as indicators of granulite pressure-temperature-fluid histories: The Rauer group, East Antarctica. *J. Petrol.* 33, 693–728.

Harley, S.L., Fitzsimons, I.C.W., Buick, I.S., 1994. Reactions and textures in wollastonite-scapolite granulites and their significance for pressure-temperature-fluid histories of high-grade terranes. *Precambrian Res.* 66, 309–323.

- Hawthorne, F.C., Oberti, R., Harlow, G.E., Maresch, W. V, Martin, R.F., Schumacher, J.C., Welch, M.D., 2012. Nomenclature of the amphibole supergroup. *Am. Mineral.* 97, 2031–2048.
- Holland, T.J.B., Powell, R., 2011. An improved and extended internally consistent thermodynamic dataset for phases of petrological interest, involving a new equation of state for solids. *J. Metamorph. Geol.* 29, 333–383.
- Holland, T.J.B., Powell, R., 1998. An internally consistent thermodynamic data set for phases of petrological interest. *J. Metamorph. Geol.* 16, 309–343. <https://doi.org/10.1111/j.1525-1314.1998.00140.x>
- Kerrick, D.M., 1974. Review of metamorphic mixed-volatile (H₂O-CO₂) equilibria. *Am. Mineral. J. Earth Planet. Mater.* 59, 729–762.
- Kretz, R., 1983. Symbols for rock-forming minerals. *Am. Mineral.* 68, 277–279. [https://doi.org/10.1016/0016-7037\(83\)90220-X](https://doi.org/10.1016/0016-7037(83)90220-X)
- Meißner, B., Deters, P., Srikantappa, C., Köhler, H., 2002. Geochronological evolution of the Moyar, Bhavani and Palghat shear zones of southern India: implications for east Gondwana correlations. *Precambrian Res.* 114, 149–175.
- Naha, K., Srinivasan, R., Deb, G.K., 1997. Structural geometry of the early Precambrian terrane south of Coimbatore in the “Palghat Gap”, southern India. *Proc. Indian Acad. Sci. Planet. Sci.* 106, 237–247.
- Raith, M.M., Sengupta, P., Kooijman, E., Upadhyay, D., Srikantappa, C., 2010. Corundum–leucosome-bearing aluminous gneiss from Ayyarmalai, Southern Granulite Terrain, India: A textbook example of vapor phase-absent muscovite-melting in silica-undersaturated aluminous rocks. *Am. Mineral.* 95, 897–907.
- Roy Choudhury, S., Dey, A., Brandt, S., Sanyal, S., Sengupta, P., 2021. Petrology and geochronology of a suite of meta-supracrustal rocks from Madukkarai, Tamil Nadu: Implications for the Ediacaran-Cambrian orogenesis of the Granulite Terrane of South India. *Lithos* 400, 106347.
- Sengupta, P., Dutta, U., Bhui, U.K., Mukhopadhyay, D., 2009. Genesis of wollastonite- and grandite-rich skarns in a suite of marble-calc-silicate rocks from Sittampundi, Tamil Nadu: constraints on the P–T–fluid regime in parts of the Pan-African mobile belt of South India. *Mineral. Petrol.* 95, 179.

-
- Sengupta, P., Raith, M.M., 2002. Garnet composition as a petrogenetic indicator: An example from a marble -calc-silicate granulite interface at kondapalle, Eastern Ghats Belt, India. *Am. J. Sci.* 302, 686–725. <https://doi.org/DOI.10.2475/ajs.302.8.686>
- Sengupta, P., Sanyal, S., Dasgupta, S., Fukuoka, M., Ehl, J., 1997. Controls of mineral reactions in high-grade garnet-wollastonite-scapolite-bearing calcsilicate rocks: an example from Anakapalle, Eastern Ghats, India. *J. Metamorph. Geol.* 15, 551–564.
- Stephenson, N.C.N., Cook, N.D.J., 1997. Metamorphic evolution of calcsilicate granulites near Battye Glacier, northern Prince Charles Mountains, East Antarctica. *J. Metamorph. Geol.* 15, 361–378.

Chapter-8

Discussion

Chapter 8

Discussion

In polymetamorphic terranes, the complete evolutionary history is generally not preserved in any single lithological unit. Rather, each lithounit records different segments of metamorphism and deformation, in response to the difference in mineral associations and compositions stabilised in the respective rock types, in course of the evolution of the terrane. Compilation of all these signatures from all the lithounits therefore gives a complete picture of the tectonothermal history of the terrane. This is also evident from the present study, where the various litho-types preserved different segments of the evolutionary history of the two studied terranes, the CGGC and the GTSI. In the previous chapters, field features, textural relations, mineral evolution, and P-T-X_{CO2} conditions of formation of these mineral assemblages have been described separately for the different meta-supracrustal rocks from both the CGGC and the GTSI. On the basis of these findings, the individual P-T evolutionary paths of these meta-supracrustal rocks have been discussed. Additionally, geochronological studies using U-Pb zircon dating and U-Th-total Pb monazite dating has been done from selected rocks to provide a time constraint of these events. In this chapter, these findings will be integrated with the available published information for the CGGC and GTSI separately, to reconstruct their respective evolutionary history, and finally to decipher the status of Indian subcontinent through the Neoproterozoic time.

8.1. Neoproterozoic evolution of the Indian subcontinent

8.1.1. The CGGC

8.1.1.1. Late Stenian-early Tonian metamorphic event (M2_{CGGC})

The second tectonothermal event (M2_{CGGC}) is the most pervasive metamorphism in the study area, as well as in the other parts of the CGGC. All the

meta-supracrustal, and mafic granulite enclaves, as well as the migmatitic felsic gneiss country rock preserve strong evidence of M2_{CGGC} metamorphism. Except local preservation of M1_{CGGC} mineralogy and fabric (S1) in the pelitic granulites, this high-grade pervasive event (M2_{CGGC}) has obliterated the imprints of M1_{CGGC} from all the other meta-sedimentary and mafic granulite enclaves in the study area.

Detailed textural study reveals that the studied meta-supracrustal rocks (calc-silicate granulites and pelitic granulites) also developed their dominant mineralogies during M2_{CGGC}. Oxygen isotope analysis from the high aluminous clinopyroxene, spinel, ilmenite bearing calc-silicate granulite, signifies that the protolith of this rock was altered by interaction with meteoric water at surficial conditions. Subsequent high-grade metamorphism led to the development of this unusual symplectic assemblage. Phase equilibria modelling categorises this M2_{CGGC} as a high-pressure, moderate to high temperature metamorphism, that culminated at ~8.4-9.5 kbar and ~790-890°C, followed by a near isothermal decompression up to ~5-5.8 kbar and ~780-860°C during which the symplectic assemblage developed. Although the prograde path could not be constrained from the existing mineral assemblage, this moderate to high pressure, moderate temperature peak, followed by a steep decompression point towards a clockwise P-T path (England and Thompson, 1984; Harley, 1989) experienced by the rocks. Additionally, P-T conditions constrained from the adjoining pelitic granulites also records similar high pressure, moderate temperature peak conditions (~8.4-9.5 kbar and ~850-880°C) for the M2_{CGGC} event. Dey et al., (2019a) also inferred similar conditions (≥ 10 kbar, ~760–850°C), followed by a steeply decompressive retrograde P-T path, and subsequent cooling up to ~530-700°C and ~4.3-6.5 kbar, from other pelitic granulite exposures in the study area (Fig. 8.1). Presence of rutile inclusions (this study, Dey et al., 2019a), as well as rare kyanite inclusions in garnet porphyroblasts (Dey et al., 2019a) within few pelitic granulite enclaves, point towards a high-pressure prograde assemblage, consistent with the clockwise nature of the P-T path.

The mafic granulite enclaves in the study area record the highest P-T conditions, yielding 12 ± 1 kbar and 800 ± 50 °C (Dey et al., 2019b), while the felsic gneiss recorded slightly lower pressures (~9 kbar and ~850°C; Mukherjee et al., 2017) (Fig. 8.1). All these lithounits also document a near isothermal decompression

(of ~5-6 kbar) subsequent to peak. Similar clockwise P-T paths (with high pressure, moderate temperature peak: ~700-870°C and ~9-12 kbar, succeeded by a steep decompressive path) have also been recorded from other parts of the CGGC (Fig. 8.1; Chatterjee, 2018; Karmakar et al., 2011). Owing to the difference in mineral assemblage, this high-grade event led to the development of prominent leucosomes and melanosomes (S2) in the migmatitic felsic gneiss and the pelitic granulites (as also evident in the present study). In contrast, dearth of fertile mineral assemblages hinders prominent melting features in the mafic and calc-silicate granulites. However, crude N-S trending S2 foliation developed in these rocks (see previous chapters), parallel to the S2 of the host felsic gneiss.

U-Pb zircon dating identifies early Neoproterozoic/late Stenian-early Tonian ages (~970 Ma and ~1060 Ma) to be the predominant concordia age clusters preserved in the zircons of the studied calc-silicate granulites. These ages were obtained from unzoned metamorphic grains, or few overgrowths on small detrital cores and hence are interpreted as the timing of peak metamorphism and symplectite formation in the studied calc-silicate granulite. Studies have

shown that Zr-rich mineral phases (e.g., amphibole, titanite, garnet) may act as a source of Zr for new zircon growth, during solid-state mineral reactions. It has been demonstrated that amphibole has a higher concentration of Zr than garnet, as well

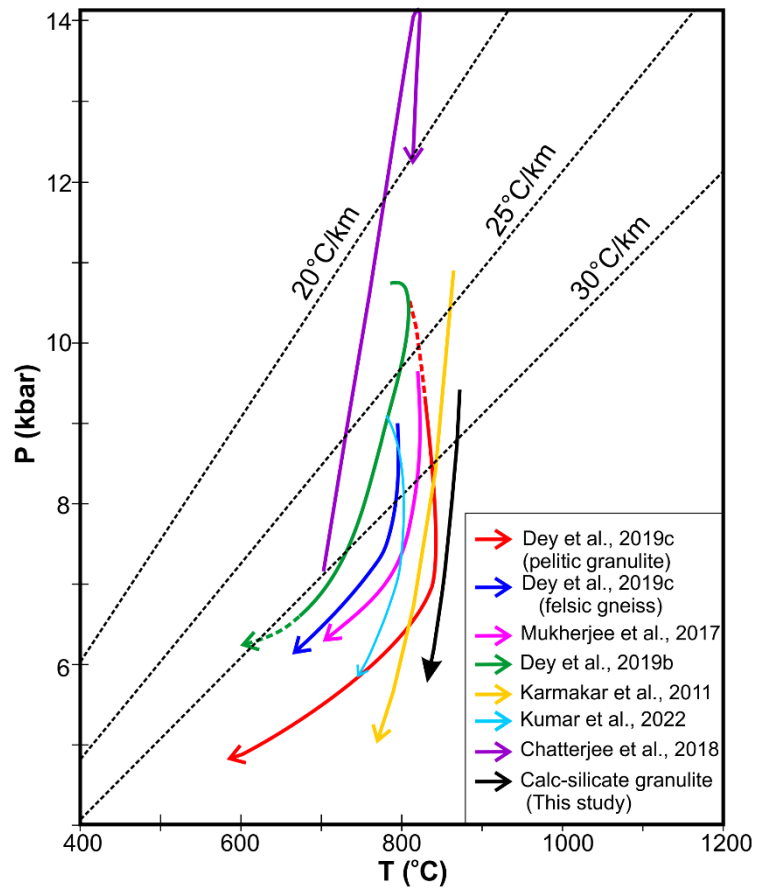


Fig. 8.1: Compilation of P-T path for M2_{CGGC} metamorphic event, obtained from the various lithounits in the study area (including this study). Apparent geothermal gradients are

as clinopyroxene, ilmenite and plagioclase, while titanite also has higher Zr than ilmenite (Kohn et al., 2015; Raith et al., 2016; Sláma et al., 2007). Between amphibole and titanite, the former takes higher Zr. Therefore, progress of both reaction prograde and symplectite forming reactions in the studied calc-silicate granulite (see chapter 4.1), that involves break down of amphibole, could release Zr and trigger the growth of metamorphic zircon. In addition to this process, part of the detrital zircon could recrystallize and can contribute to the formation of metamorphic zircon.

In the pelitic granulites also, the metamorphic zircons depicted prominent age clusters at ~970-950 Ma and ~1050-1040 Ma (Dey et al., 2019a), while ~943 Ma was estimated for the peak M2 metamorphism from the migmatitic felsic gneiss (Mukherjee et al., 2017). Comparable Stenian-Tonian ages, ranging between ~910-1190 Ma have also been reported from the CGGC by various studies (Chatterjee, 2018; Chatterjee et al., 2010; Chatterjee and Ghose, 2011; Karmakar et al., 2011; Maji et al., 2008; Mukherjee et al., 2017; Rekha et al., 2011; Sequeira et al., 2020). This age range have been unanimously interpreted to be the timing of the pervasive granulite facies metamorphism (M2), with the major peak between ~990-940 Ma; and two subordinate peaks at ~930-910 Ma and ~1190-1000 Ma (summarized in Dey et al., 2019a). In view of the above discussion, it is inferred that the peak metamorphism was experienced by the studied calc-silicate granulites, as well as the other lithounits, during this Late Stenian- early Tonian time span (~1060-970 Ma), corresponding to the M2 event.

The peak P-T conditions as constrained from the studied calc-silicate granulite define an apparent geothermal gradient of ~28°C/km. Comparable gradients (~20-26°C/km) have also been constrained from the other lithounits (Dey et al., 2019a, 2019b; Karmakar et al., 2011; Kumar et al., 2022; Mukherjee et al., 2017)(Dey et al., 2019a, 2019b; Karmakar et al., 2011; Kumar et al., 2021; Mukherjee et al., 2017). The clockwise P-T path that culminated at a high pressure, signifies crustal thickening, and burial of this litho-package to mid/lower-crustal depths, during this metamorphic event. Hence, all these observations point towards a continental collisional setting (Brown, 2008; Harley, 1989) prevalent during M2 (Dey et al., 2019a; Karmakar et al., 2011; Mukherjee et al., 2017; Sanyal and

Sengupta, 2012)(e.g., Dey et al., 2019a; Mukherjee et al., 2017; Sanyal and Sengupta, 2012).

The subsequent near-isothermal decompression, recorded in all the lithounits therefore represents post collisional extension (England and Thompson, 1984), that brought the litho-package to shallower depths (of at least ~23 km; corresponding to minimum recorded pressure drop of ~7 kbar). A suite of mafic dykes which intruded the country rock in the study area (Mukherjee et al., 2018b), subsequent to M2_{CGGC}, is possibly related to this post collisional extension and continental rifting.

8.1.1.2. Late Tonian metamorphic event (M3_{CGGC})

This is the third and the last recorded major tectonothermal event in the study area, as well as in the CGGC. Detailed petrological study of the various lithounits (including this study) indicate this to be an amphibolite facies event. Deformation associated with this event led to the tight folding of the S2 leuco- and melanosomes in the migmatitic felsic gneiss and the pelitic granulites, and development of N-S axial planar foliation (S3). Moreover, the intruded mafic dykes also got folded with N-S axial planes. In the studied calc-silicate granulites, this deformation event developed the prominent, pervasive N-S foliation evident in the present day.

In the studied calc-silicate granulites, M3_{CGGC} is characterised by, (i) development of amphibole, that replaces the early mineralogy of the host calc-silicate rock (consisting of clinopyroxene +plagioclase +titanite+/ garnet, the assemblage stabilised at peak conditions of M2_{CGGC} metamorphism); (ii) development of vesuvianite-garnet-epidote; (iii) intrusion of pegmatitic veins within the host calc-silicate rocks parallel to / at a low angle to the S3 foliation of the host calc-silicate rock; (iv) incorporation of Al and F in the pre-existing titanites. As discussed in chapter 4.2, the stabilisation of amphibole and vesuvianite-garnet-epidote occurred corresponding to influx of F and H₂O bearing fluid. The most plausible source of this fluid has been inferred to be the intruded pegmatitic veins. Development of amphibole selvage at the contact of pegmatites and host calc-silicate

rock attest to fluid-rock exchange. P-T estimates obtained using conventional thermobarometry from these intruded pegmatites range between ~5.6-6.8 kbar and ~640-740°C for the M3_{CGGC} event. Application of petrogenetic grids to the studied calc-silicate rocks also provides an estimate of the P-T- X_{fluid} conditions of formation of these vesuvianite-garnet-epidote bearing association. The P-T conditions of this fluid infiltration driven M3_{CGGC} metamorphism has been constrained to be ~6 kbar and ~620-600°C. Fluid compositions of vesuvianite-garnet formation were constrained to be between ~0.1-0.4 X_{CO_2} . However, epidote formed subsequent to vesuvianite and garnet, at more H₂O-rich conditions ($\leq 0.1 X_{\text{CO}_2}$ and lower X_{F}), combined with a slight cooling (at <600°C). This slight decrease in temperature points towards the formation of epidote during the retrogressive phase of this M3_{CGGC} event. However, it may also be related to another separate fluid infiltration event, subsequent to/ in continuation with M3_{CGGC}. Further detailed study is required to comment on this problem.

As evident from chapter 4.3, detailed petrological and compositional study, combined with reaction modelling demonstrate destabilization of peak plagioclase and clinopyroxene, and conversion of peak low Al-titanite to Al-F rich titanite, along with the formation of fluid bearing secondary minerals (amphibole, vesuvianite and garnet) corresponding to this fluid infiltration during M3_{CGGC}. Our study, when combined with the global data, also demonstrates that the presence of F in the infiltrating fluid plays a very crucial role (in combination with the coexisting mineral assemblage), if not the most important, in regulating the incorporation of a significant amount of Al in titanite structure. Of the very few reports that contain high aluminous titanites [$\text{Al}/(\text{Al}+\text{Fe}^{+3}+\text{Ti}^{+4}) \geq 0.25$; Oberti et al., 1985], with OH as the dominant anion (i.e., $X_{\text{F}} < X_{\text{OH}}$; Enami et al., 1993), can be possibly be explained by the replacement of F by OH in titanite structure during later fluid influx, that left the titanites aluminous, but deficient in F. This can also explain the absence of F in vesuvianites of the epidote-bearing domains, unlike those in the epidote-free domains. That is, influx of more H₂O-rich, F-deficient fluid, which was possibly related to the development of epidote (see chapter 4.2), might have replaced the F in the vesuvianite structure. Nevertheless, it is evident from these two case studies

that the rocks witnessed a late-stage fluorine bearing fluid infiltration driven metamorphism at the tail end of M3_{CGGC} event.

Apart from the studied calc-silicate rocks, M3_{CGGC} metamorphism has also been recorded from the mafic dykes, felsic orthogneiss and mafic granulite enclaves in and around the study area (Dey et al., 2019b, 2019a; Mukherjee et al., 2019b; Ray et al., 2011). These studies constrain the P-T conditions of this event between $\sim 7.5 \pm 1$ kbar and $\sim 700^\circ\text{C}$, corresponding to an apparent geothermal gradient of $\sim 25\text{-}30^\circ\text{C}/\text{km}$. Das et al., (2019) also constrained the P-t conditions of the M3_{CGGC} event from alkaline rocks in the Santuri-Kankarkhari area of Purulia between $\sim 9\text{-}10$ kbar $\sim 690\text{-}770^\circ\text{C}$.

Monazite dating constrain the timing of this amphibolite facies metamorphism (M3_{CGGC}) at ~ 902 Ma from the migmatitic felsic gneiss (Mukherjee et al., 2017). A younger age cluster was also obtained from the U-Pb zircon dating in pelitic granulites (~ 880 Ma; Dey et al., 2019a) in the study area. Similar metamorphic ages (~ 850 Ma) were also obtained from few mafic dykes in the south western part of the CGGC (Kumar et al., 2022). Karmakar et al., (2011), also reported the $\sim 850\text{-}775$ Ma age cluster from the southern part of CGGC. Late Tonian ($\sim 870\text{-}780$ Ma) ages were also constrained from the eastern margin of the CGGC, (Chatterjee, 2018; Chatterjee et al., 2010). They attributed this age cluster to be a separate event (EITZ) restricted to the eastern margin of the CGGC only. The predominance of compressional structures (like superposed folding) in all the lithounits, combined with the apparent geothermal gradients ($\sim 25\text{-}30^\circ\text{C}/\text{km}$), led Mukherjee et al., (2018) to associate the M3_{CGGC} to a continent-continent collision event (Brown, 2007; Condie, 2021).

8.1.2. The GTSI

8.1.2.1. Late Neoproterozoic/ Ediacaran-Cambrian metamorphic event (M2_{GTSI})

After the early Palaeoproterozoic orogenic event (M1_{GTSI}), the major metamorphic event recorded from various the parts of the GTSI is during the late Neoproterozoic or Ediacaran-Cambrian time (M2_{GTSI}). This event, although abundant in the Madurai Block, is also recorded from parts of the CSS (north of

PCSZ), as well as in the studied meta-supracrustal unit in Madukkarai. In the MSU, two sets of coaxial deformation were associated with this late Neoproterozoic metamorphism (Naha et al., 1997; Roy Choudhury et al., 2021) and led to the folding of leucosomal segregates in the metapelites (Roy Choudhury et al., 2021), and formation of tight isoclinal folds in the adjoining studied calc-silicate rocks (Naha et al., 1997).

Textural relations, phase equilibria modelling and conventional thermobarometry from the studied metapelites of the MSU indicate 'peak' P-T conditions at $\sim 730\text{--}790^\circ\text{C}$, $\sim 5.5\text{--}7$ kbar, followed by decompression and cooling recorded till $\sim 630^\circ\text{C}$, ~ 4 kbar (Fig. 6.4). Relict kyanite in matrix signifies that the studied rocks experienced even higher pressures (≥ 8 kbar at $\sim 730\text{--}790^\circ\text{C}$, corresponding to a minimum depth of about ~ 25 km), than that recorded by the mineralogical geothermobarometers and phase equilibria modelling. The only process that can bury these surface sediments to such lower crustal depths is a continent-continent collision. The attainment of high-pressure conditions prior to peak metamorphism, and the nature of the retrograde P-T path, all indicate a clockwise P-T path (England and Thompson, 1984; Harley, 1989) experienced by the rocks, corresponding to crustal thickening during continental collision. This was followed by post thickening crustal extension, represented by the decompressive arm of the P-T path, during which these rocks were exhumed to shallower depths. Additionally, application of petrogenetic grids to the calc-silicate granulites of the MSU constrain the P-T- X_{fluid} conditions of formation of garnet-amphibole during a near isobaric temperature decrease ($\sim 520\text{--}640^\circ\text{C}$, and $\sim 4.7\text{--}6$ kbar; subsequent to decompression), along with the influx of moderately water-rich fluid ($\sim 0.25\text{--}0.6 X_{\text{CO}_2}$). This was followed by continued isobaric cooling (up to $\sim 440^\circ\text{C}$, $\leq 0.4 X_{\text{CO}_2}$) at the tail end of the retrogressive path, during which epidote formed. A common source of such aqueous fluid has been linked to the prograde metamorphism of adjacent metapelitic units (Ague, 2000; Buick et al., 1994). However, as discussed in the previous sections, the formation of garnet-amphibole-epidote is related to post-peak, post decompression, retrogression event. Although the exact source of fluid cannot be traced, the most plausible source seems to be the late-stage fluids from adjacent migmatized granitic/enderbitic rocks, which infiltrated both the

metapelitic and calc-silicate gneisses. Formation of biotites in the adjacent metapelites, and phlogopite in the calc gneisses studied by Naha et al., (1997), are consistent with the above inference. Alternative source may be pegmatitic veins, present nearby a few calc-silicate exposures. However, further detailed study is required to comment conclusively on this.

Clockwise P-T paths have been also reported from Ediacaran-Cambrian meta-supracrustal rocks as well as other lithounits (e.g., mafic granulites and granite gneisses) in and around the PCSZ (~730-800°C, ~7.5-12 kbar: Lal et al., 1984; Raith et al., 2010; Sengupta et al., 2009; Simmat and Raith, 2008).

U-Pb isotopic dating of metamorphic zircons from Grt-Bt-Sil gneiss and Grt-Opx bearing meta-psammite constrain the timing of this metamorphism and coeval deformation of the studied meta-supracrustal packet within a narrow span of ~550–530 Ma. Chemical dating of monazite also restricts the timing of this metamorphic event at ~550-520 Ma. Discordia defined by the zircons from the Grt-Opx bearing meta-psammite, estimates upper and lower intercepts at ~2433 Ma and ~ 536 Ma respectively. This indicates that the U-Pb isotopic system of the late Neoproterozoic to early Palaeoproterozoic detrital zircon grains were reset during the Ediacaran-Cambrian tectonothermal event. Meißner et al., (2002) also inferred the timing of this coaxial deformation between $\sim 610 \pm 60$ to 560 ± 17 Ma from the metapelitic rocks, and ~490 Ma from the calc-granulites of the MSU.

8.2. The significance of the CGGC and the GTSI in the evolution of the Indian shield

Indian subcontinent in its present form is believed to have formed by juxtaposition/ suturing of several crustal blocks. The most important ones being the northern Indian block (NIB; consisting of the Bundelkhand craton) and the southern Indian block (SIB; comprising the Singhbhum, Bastar and Dharwar cratons) (Acharyya, 2003), that has been fused along the polymetamorphosed zone, the Central Indian Tectonic Zone (CITZ, Sausar, Mahakoshal, Son-Narmada Fault system, Makrohar, Betul, Balaghat-Bhandara, Ramakona-Katangi and Gavilgarh-Tan Shear Zone belts being its major components) (Bhowmik, 2019). This

transcontinental tectonic zone is inferred to extend through the CGGC, up to the Shillong Meghalaya Gneissic Complex (SMGC) in the north-east (Acharyya, 2003), forming a “composite CITZ orogenic belt” (Acharyya, 2003; Bhowmik et al., 2012). The GTSI that is located in the SIB and south of the Meso- to Neoproterozoic Dharwar Craton, consists of the Northern Granulite Block (NGT) and the Madurai Block (MB). However, recent studies have demonstrated that the Neoproterozoic GTSI forms a part of the Eastern and western Dharwar craton (reviewed in Talukdar et al., 2022). NGT and MB separated by the Cauvery shear System (CSS) (with the Palghat Cauvery shear Zone (PCSZ)). The timing and position of amalgamation of these blocks (the northern and southern Indian blocks; and the NGT and MB) have been a matter of debate over decades (e.g., Bhowmik et al., 2012; Brandt et al., 2014; Clark et al., 2009; Collins et al., 2003b; Dey et al., 2019a; Santosh, 2020; Sengupta et al., 2015). Position of the Indian shield in the during the formation and breakup of the different supercontinents has been a subject of considerable debate (Buchan et al., 2001; Rogers and Santosh, 2004). Detail analyses on this aspect are beyond the purview of this study. In the following sections Proterozoic history of the CGGC and the GTSI will be reviewed with emphasis on the Neoproterozoic events. The information thus obtained will be linked to the evolution of the adjoining crustal blocks of the Indian shield. Finally, significance of Neoproterozoic CGGC (in Indo-Antarctic connection) and the GTSI (in Indo-Madagascar connection) will be briefly discussed.

8.2.1. Imprints of early Neoproterozoic orogeny in the CGGC and other adjacent terranes: implications for reconstruction of Rodinia

8.2.1.1. Pre-Neoproterozoic evolution of the CGGC and adjacent terranes

The studied meta-supracrustal enclaves (pelitic granulites and calc-silicate granulites) represent the metamorphosed counterpart of an old sandstone-shale-limestone shelf sedimentary sequence (Basu and Bickford, 2014; Sengupta et al., 2015). Timing of sedimentation of these sediments were constrained between ~1760-1650 Ma (Dey et al., 2017; Rekha et al., 2011; Singh et al., 2001) indicating extension of the existing continental crust during the late Palaeoproterozoic (~1700-1650 Ma). The present study also constrains a broad, but overlapping basin formation age of ~1790-1486 Ma from the studied calc-silicate granulites. The

plausible provenance of these sediments have been inferred to be Proterozoic enclaves in the lesser Himalaya, the Aravalli and/or Bastar craton, the Sausar and Mahakoshal belts within the CITZ, or the Singhbhum craton (Dey et al., 2017).

In the northern and central parts of the CGGC, Palaeoproterozoic arc magmatism (~1750-1640 Ma; Chatterjee and Ghose, 2011; Mukherjee et al., 2019a; Ray Barman et al., 1994; Saikia et al., 2017), and high-grade metamorphic imprints (~1680-1520 Ma; Dey et al., 2019a; Kumar and Dwivedi, 2021; Rekha et al., 2011; Sanyal et al., 2007) although scarce, have been recorded and related to a continental collision event during the amalgamation of Columbia supercontinent (Dey et al., 2019a). Contemporaneous metamorphic events are also reported from the Balaghat-Bhandara Granulite Belt (~1600 Ma; Bhandari et al., 2011; Bhowmik et al., 2005) and Mahakoshal belt (~1800-1600 Ma; Deshmukh et al., 2017) within the CITZ, in addition to a ~1700 Ma arc magmatism (Bora et al., 2013; Deshmukh et al., 2017). In the Ongole domain within the Eastern Ghats Mobile Belt (EGMB), arc magmatism (~1790-1710 Ma) was accompanied by UHT metamorphism (~1750-1610 Ma) attests to an orogenic setting (*sensu lato*; Dasgupta et al., 2017, 2013; Sarkar et al., 2015; Sarkar and Schenk, 2014; Vadlamani et al., 2013). Palaeoproterozoic imprints have been also preserved as far as the ADFB in the west (~1740-1580 Ma; Buick et al., 2010; ~1860-1810 Ma arc type felsic magmatism: Kaur et al., 2017, 2011; Roy et al., 2005), and the Shillong-Meghalaya Gneissic Complex in the north-east (intrusion of ~1780-1630 Ma granitoids in “syn-collisional settings”). These similar timing and tectonic setting in the above-mentioned terranes conform with the view that the northern and southern Indian blocks got amalgamated, and became the unified ‘Greater Indian Landmass’ at least from the late Palaeoproterozoic/ Mesoproterozoic (~1700-1600 Ma) along this trans-continental tectonic zone. Subsequent evidences of crustal extension (e.g., emplacement of A-type granites and alkaline rocks) during the Mesoproterozoic recorded in the different terranes (~1590-1350 Ma; Dobmeier et al., 2006; Upadhyay et al. 2006; Vijaya Kumar et al. 2007; ~1450-1350 Ma in the CGGC; Mukherjee et al., 2017; Sequeira et al., 2022), has been correlated with the breakdown of Columbia supercontinent (e.g., Mukherjee et al., 2018a). An older zircon growth (~1260 Ma) over the detrital zircon core has also been recorded from

the studied calc-silicate granulite. Zircon growth of similar ages (clustered around ~1200 Ma) have been reported from the CGGC (Chatterjee et al., 2010, 2008; Chatterjee and Ghose, 2011; Karmakar et al., 2011; Maji et al., 2008; Mukherjee et al., 2017; Rekha et al., 2011), as well as from the other adjoining Proterozoic terranes (Central Indian Tectonic Zone: Chattopadhyay et al., 2017; Das et al., 2017; e.g., Eastern ghats: belt Dasgupta et al., 2017). However, it is not yet clear whether this zircon growth (~1200 Ma) represents a thermal imprint or another tectonothermal event that shaped the Indian shield across the Meso- to Neoproterozoic time (Chatterjee et al., 2010; Chatterjee and Ghose, 2011; Karmakar et al., 2011; Maji et al., 2008)(Chatterjee et al., 2010; Chatterjee and Ghose, 2011; Karmakar et al., 2011; Maji et al., 2008).

8.2.1.2. Neoproterozoic evolution of the CGGC and adjacent terranes

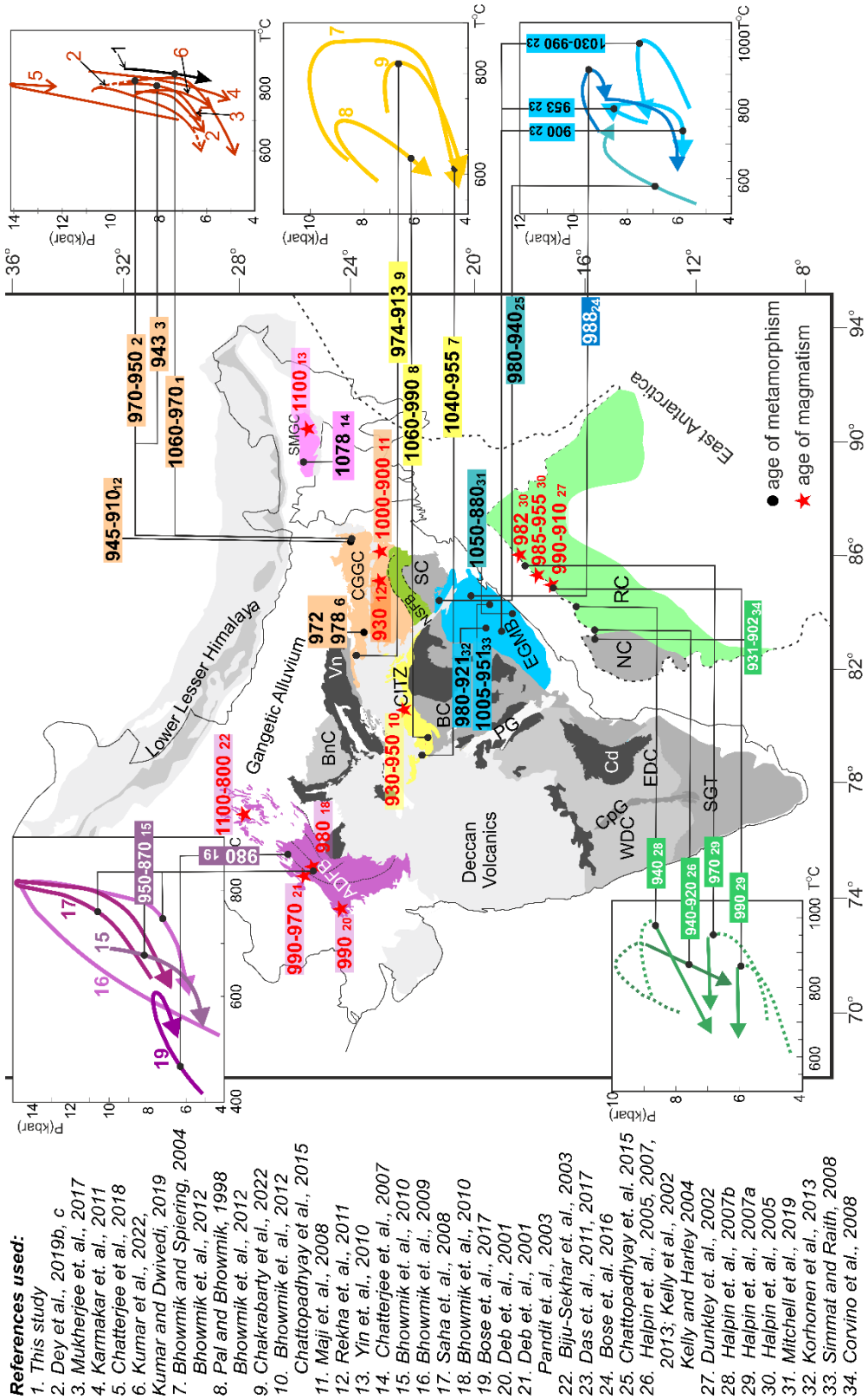
The present study characterises a clockwise P-T path for the M2_{CGGC} event, with a high pressure, moderate to high temperature peak metamorphism followed by a steeply decompressive retrograde arm. The nature of P-T path combined with the apparent geothermal gradient all point towards a continental collisional setting, associated with this event. The timing of this M2_{CGGC} tectonothermal event, as inferred in this study is late Stenian- early Tonian. Other workers constrain similar clockwise P-T paths and timing of this M2_{CGGC} event (Fig. 8.1), with major peak between ~990-940 Ma; and two subordinate peaks at ~930-910 Ma and ~1190-1000 Ma (Chatterjee et al., 2010; Chatterjee and Ghose, 2011; Dey et al., 2019a; Karmakar et al., 2011; Kumar et al., 2022; Mukherjee et al., 2017; Rekha et al., 2011)(summarized in Dey et al., 2019a), from the various parts of the CGGC. This continent-continent collisional event, unambiguously correlates with the Grenvillian orogeny, corresponding to the assembly of Rodinia supercontinent as also inferred by other workers ((e.g., Dey et al., 2019a; Mukherjee et al., 2017; Rekha et al., 2011; Sequeira et al., 2020).

Early Neoproterozoic orogenic imprints are widely preserved not only in the CGGC, but also in the adjacent terranes of CITZ, SMGC, EGMB and North Singhbhum Fold Belt (NSFB) (Fig. 8.2). Coeval events are also preserved in the southern parts of the CGGC (~1000-920 Ma; Karmakar et al., 2011; Maji et al., 2008;

Rekha et al., 2011), as well as the northern parts of the NSFB (~1000-950 Ma; Pal and Rhede, 2013; Rekha et al., 2011). Similar clockwise P-T path within a continent-continent collisional setting, having a high-pressure amphibolite to granulite facies peak has been recorded in the different components of the CITZ, viz.: the Sausar mobile belt, the Ramakona-Katangi granulite belt, the Gavligarh–Tan Shear Zone, as well as the Makrohar Granulite Belt, during ~1060-940 Ma, ~1040-940 Ma, ~1000-950 Ma and ~974-913 Ma respectively (Bhandari et al., 2011; Bhowmik et al., 2012; Chakrabarty et al., 2022; Chattopadhyay et al., 2015; Deshmukh and Prabhakar, 2020; Mukherjee et al., 2019b). Moreover, similar early Neoproterozoic, high-pressure granulite facies metamorphism has been documented in a continental collisional setting in the EGMB (~1000-900; Das et al., 2017, 2011; Korhonen et al., 2013; Mitchell et al., 2019).

A slightly younger orogenic event (M3_{CGGC}) is evident from different lithounits in the CGGC. The calc-silicate granulites of the present study records the tail end/ retrogressive and cooling phase of this M3_{CGGC} event, corresponding to the formation of vesuvianite and epidote. However, imprints of this M3_{CGGC} event are well preserved in the mafic dykes (emplaced after M2_{CGGC}, but before M3_{CGGC} metamorphic event), as well as the migmatitic felsic gneiss of the area, and is characterised as an amphibolite facies metamorphic event, within a continent-continent collision setting. This metamorphic imprint (M3_{CGGC}) has been dated to be late Tonian (~920-880 Ma; Dey et al., 2019a; Mukherjee et al., 2017) from the study area. Chatterjee et al., (2010) also constrained a ~870-780 Ma event, that is characterised by high-pressure metamorphism, and formation of pervasive N-S foliation along a linear belt along the eastern margin of the CGGC and NSFB. This perceived zone, was termed as the “Eastern Indian Tectonic Zone” (EITZ), (Chatterjee, 2018; Chatterjee et al., 2010). Kumar et al., (2022) also constrained coeval age metamorphism (~850 Ma) from the mafic dykes in south-western CGGC (Fig. 8.3).

Fig. 8.2: Diagram illustrating the relative positions of the Indian and East Antarctic land masses prior to Gondwana break-up (modified after Fitzsimons, 2003), and summarizing relevant 1100-900 Ma old metamorphic and magmatic history with published geochronology and available P-T paths. Terranes that contain imprint of 1100-900 Ma events are highlighted with colours. All the dates are in Ma. The alphabets beside dates represent the references. NC: Napier Complex; RC: Rayner Complex; Other abbreviations are same as in the text



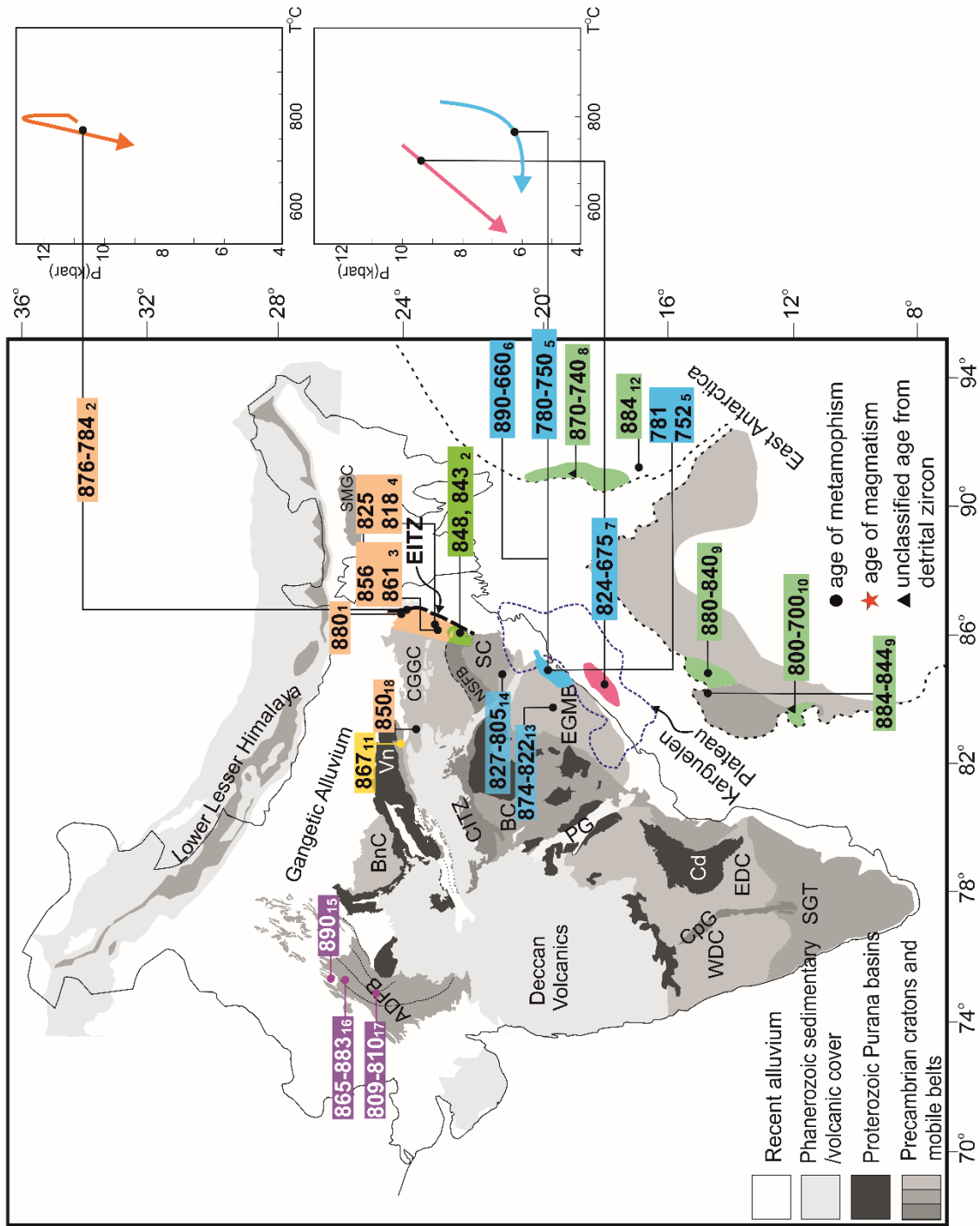


Fig. 8.3: Diagram illustrating the relative positions of the India, East Antarctica (modified after Fitzsimons, 2003) and Karguelen plateau (after Chatterjee et al., 2012) prior to Gondwana break-up, and summarizing relevant late Tertiary tectono-thermal imprints with published geochronology and available P-T paths. All the dates are in Ma. The alphabets beside dates represent the references.

References used:

1. Dey et al., 2019b
2. Chatterjee et al., 2010, 2018
3. Karmakar et al., 2011
4. Maji et al., 2008
5. Bose et al., 2016
6. Kovach et al., 2001
Dobmeier & Simmat, 2002
Simmat & Raith, 2008
7. Chatterjee et al., 2008b
8. Wang et al., 2008
9. Kelly et al., 2002
10. Asami et al., 2005
11. Deshmukh et al., 2017
12. Liu et al., 2013
13. Korhonen et al., 2013
14. Chattopadhyay et al., 2015
15. Bose et al., 2017
16. Bhowmik et al., 2010
17. Chatterjee et al., 2017
18. Kumar et al., 2022

Contemporaneous late Tonian (~900-800 Ma; Chattopadhyay et al., 2015; Dobmeier and Simmat, 2002; Korhonen et al., 2013; Simmat and Raith, 2008) collisional imprints are also reported from the EGMB. Few workers have also reported a ~910-810 Ma event from the Aravalli-Delhi fold Belt (ADFB) (Bhowmik et al., 2010; Chattopadhyay et al., 2017; Dasgupta et al., 2017) (Fig. 8.3).

Integrating all the available information, it is evident that this Stenian-Tonian orogenic imprint was spatially widespread, encompassing the Proterozoic terranes of, ADFB, EGMB, CITZ and CGGC, which acted as zones of accretion, during which the final amalgamation of the northern and southern Indian blocks, as a consequence of formation of Rodinia supercontinent. Moreover, the emplacement of dykes in between M2_{CGGC} and M3_{CGGC} imply that the early and late Tonian continental collisional events were punctuated by a period of extension, during which the mafic dykes in the CGGC were emplaced. Emplacement of late Tonian alkaline rocks, in the southern parts of the CGGC and their subsequent metamorphism during M3_{CGGC} (Das et al., 2019), are also consistent with the above statement. Therefore, it stands to reason that the late Tonian collisional event marks the timing of the final amalgamation of Rodinia supercontinent in India.

8.2.1.3. The CGGC in the context of Indo-Antarctic correlation

The early Neoproterozoic orogenic imprints that are widespread in the CGGC and adjacent terrane of CITZ, SMGC, EGMB are also preserved widely in the eastern parts of Antarctica (Fig. 8.2-8.3). Early Tonian records are evident extensively in the Rayner Complex, East Antarctica (~930-900 Ma; Halpin et al., 2013, 2007a, 2007b; Kelly et al., 2002; Kelly and Harley, 2004; Morrissey et al., 2015). Moreover, the late Tonian metamorphism (~800-700 Ma) and other tectonothermal (~880-840 Ma) imprints are also present in the Rayner Complex and Kemp Land in East Antarctica (Asami et al., 2005; Kelly et al., 2002; Shiraishi et al., 2008).

Furthermore, the published P-T paths in the crustal segments of Indian shield and the east Antarctica show remarkable similarity (Fig. 8.2-8.3; also see Mukherjee et al., 2019b). These features support the view that with the Neoproterozoic granulites of east Antarctica and the Indian shield with the CGGC,

CITZ, SMGC and EGMB formed a coherent landmass at least before the Neoproterozoic time (Dasgupta et al., 2017; Mukherjee et al., 2019b).

8.2.2. Imprints of late Neoproterozoic orogeny in the GTSI and other adjacent terranes: implications for reconstruction of Gondwanaland

8.2.2.1. Pre-Ediacaran-Cambrian evolution of the GTSI and adjacent terranes

The GTSI has a complex geological history of magmatism, sedimentation and metamorphism that span over 2 billion years (reviewed in Talukdar et al. 2022). Detail discussion on the geological evolution in the GTSI is beyond the purview of this work and the same has been the subject of a number of recent reviews (Brandt et al., 2014; Plavsa et al., 2014; Raith et al., 2016; Talukdar et al., 2022). In this section only the main pre-Ediacaran history of the GTSI will be presented.

The Pre-Ediacaran history includes ~3200-2520 Ma mafic-ultramafic – anorthosite-chromitite (only in places) association, locally with presence of BIF. This ensemble that is interpreted to be remnants of fossil oceanic crust occurs as map scale enclaves within felsic magma (~3300-2500Ma) whose compositions resemble the felsic magma of continental arc (reviewed in Brandt et al., 2014; Talukdar et al., 2022). Soon after the felsic magmatism, the Neoproterozoic crust of the GTSI, along with the other lithounits, was extensively reworked by high pressure granulite facies metamorphism at the dawn of Palaeoproterozoic ($M1_{GTSI}$; ~2570-2430 Ma, reviewed in Brandt et al., 2014; Roy Choudhury et al., 2021; Talukdar et al., 2022). Though late Palaeoproterozoic felsic magmatism are sporadically reported (1740-1620 Ma; Brandt et al., 2014 and references therein), the most conspicuous pre-Ediacaran events include extensive sedimentation of stable continental self-affinity during ~1750-1020 Ma (Fig. 8.4; Kooijman et al., 2011; Li et al., 2017; Meißner et al., 2002; Plavsa et al., 2014; Raith et al., 2010; Roy Choudhury

et al., 2021; Sengupta et al., 2015; Teale et al., 2011). The studied area MSU belongs to this shelf sedimentary unit.

A number of studies considered that the roughly E-W perceived shear zone PCSZ define the northern limit of this stable shelf deposit (reviewed in Sengupta et al., 2015). This observation led to the conclusion that the PCSZ represent a

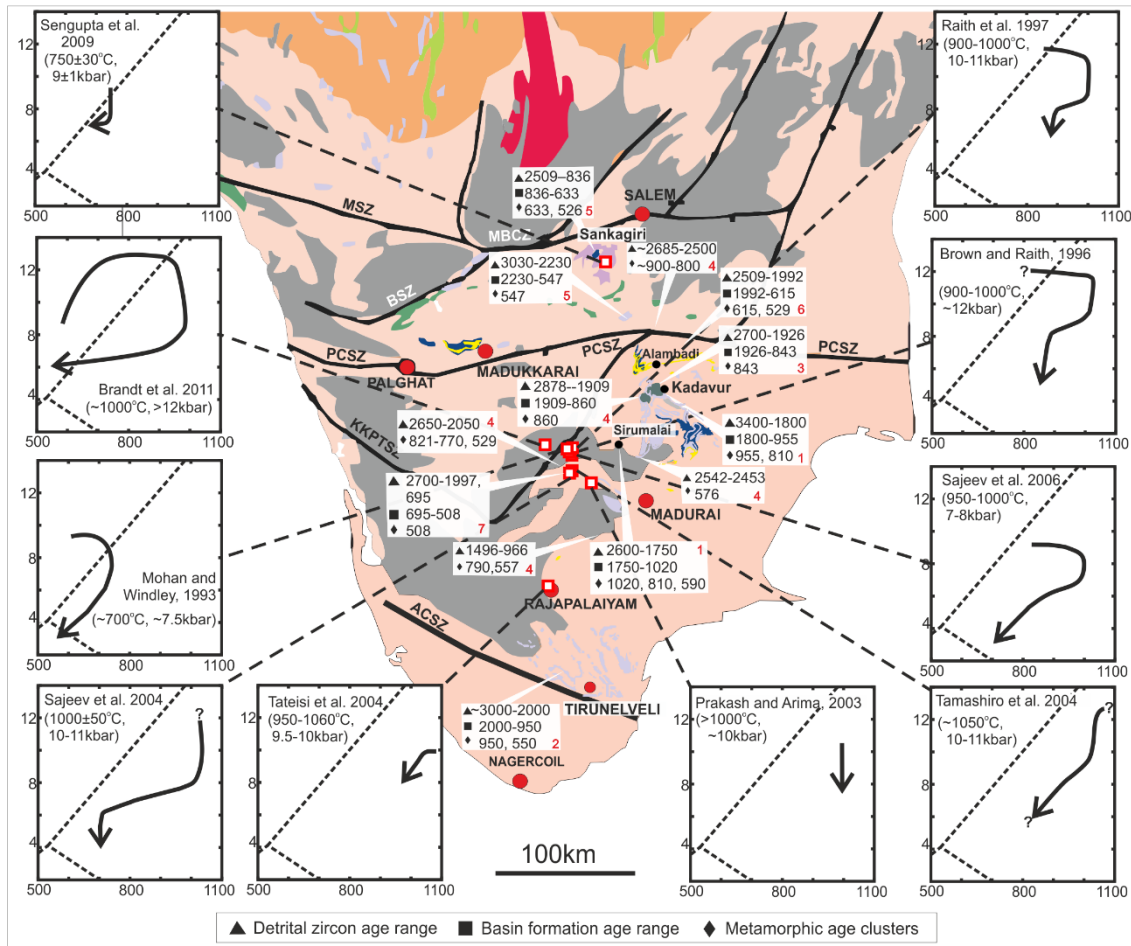


Fig. 8.4: P-T paths of the meta-supracrustal units from various parts of the GTSI (north and south of PCSZ) as reported by different workers including this study. The peak P-T conditions recorded in these reports is given in brackets in the respective boxes. Also added in the figure are the geochronological attributes of the sedimentary cover reported from various areas of the GTSI. References: (1) Kooijman et al., 2011, (2) Li et al., 2017, (3) Teale et al., 2011, (4) Plavsa et al., 2014, (5) Sengupta et al., 2015, (6) Raith et al., 2010, (7) Collins et al., 2007b.

continental suture along which the Mozambique ocean was closed (Collins et al., 2003a, 2003b). This then followed that the southern part of the GTSI that lie south of the PCSZ is an 'exotic' crustal block that was fused to the northern part of the GTSI only during Ediacaran-Cambrian orogenesis (reviewed in Roy Choudhury et al., 2021, Talukdar et al., 2022). Occurrence of metamorphosed continental shelf sediments at MSU and a few localities lying north of the PCSZ are in complete

disagreement with the idea that PCSZ is the loci of the strand line of the “Mozambique Ocean” (reviewed in Talukdar et al.2022). Along with the published information (Kooijman et al., 2011, Sengupta et al., 2015), this study at the MSU is in good agreement with the observations that ~2500 Ma old crust of the northern GTSI continues south of the PCSZ (reviewed in Sengupta et al., 2015). Mid-Neoproterozoic A-type granitoids and massif type anorthositic magmatism that occur on both sides of the perceived PCSZ (~720-840 Ma; Brandt et al., 2014; Ghosh et al., 2004; Santosh et al., 2012; Sato et al., 2011; Teale et al., 2011) also speaks against the PCSZ being a Ediacaran-Cambrian suture.

8.2.2.2. Neoproterozoic evolution of the GTSI and adjacent terranes

In this section, metamorphic signatures of the Ediacaran-Cambrian tectonothermal event (M_{2GTSI}) in the studied rocks of the MSU, will be compared with its counterparts lying within and on both sides of the PCSZ. The present study documents a clockwise P-T path, culminating in a moderate pressure and moderate temperature peak, followed by a decompression. The timing of this M_{2GTSI} event has been constrained between ~550-520 Ma. All the findings of this study therefore, point towards a continental collision setting during this Ediacaran-Cambrian time. This late Neoproterozoic metamorphic event has been widely recorded in the northern and southern parts of the perceived PCSZ. Timing of this late Neoproterozoic metamorphic event has been constrained by other workers from the north of the PCSZ (~529 Ma: Raith et al., 2010; ~610-520 Ma: Raith et al., 2016; ~522 Ma: Ghosh et al., 2004), as well as the MB, south of PCSZ (~600–500 Ma: Brandt et al., 2011; Collins et al., 2007b; Li et al., 2017; Plavsa et al., 2014; Sengupta et al., 2015) (Fig. 8.4).

Fig. 8.4 depicts that these meta-supracrustal rocks across the PCSZ shows CW P-T paths, with post peak near-isothermal decompression followed by near isobaric cooling segments. While some areas record two stages of near-isothermal decompression history separated by a cooling event (e.g., Brown and Raith, 1996; Raith et al., 1997; Sajeev et al., 2004; Fig. 8.4), others record only a single-phase decompressive event following the pressure maxima (e.g., Mohan and Windley, 1993; Sengupta et al., 2015 Fig. 8.4). At the present information level, it is not

possible to choose either of the following two options: (A) The two-stage decompression is the general case, and due to their inability to preserve finer details, few rocks have recorded a P-T path with single-phase decompression; (B) Some parts of the Ediacaran-Cambrian rocks in the GTSI had different upliftment history. Nevertheless, the CW geometry of the retrograde P-T paths obtained from the Ediacaran-Cambrian meta-supracrustal rocks on both sides of the PCSZ (including the MSU), seems to support crustal thickening within a compressional setting, followed by post thickening orogenic collapse, as obtained in the present study. The compressional regime is also consistent with the folding and deformation associated with this metamorphism. The steep decompressive arm, recorded in almost all the instances suggests an episode of crustal extension/ crustal thinning that allowed the deep crustal rocks to be exhumed to shallower depths in order to achieve post-collisional isostatic equilibrium (e.g., Rey et al., 2001). Additionally, geochemical proxies of post-collisional extension, like emplacement of A-type granites/ alkali granites and alkaline rocks during the late Ediacaran- Cambrian time have been reported in several studies in and around PCSZ and from other parts of the GTSI as well (e.g., Glorie et al., 2014; Plavsa et al., 2015; Renjith et al., 2016 and several others). Structural evidences in support of the post-orogenic collapse (e.g., steep exhumation fabrics, and shallow to sub-horizontal mineral lineation indicating lateral escape) for the Ediacaran-Cambrian metamorphites, have also been reported by Plavsa et al., (2015) from parts of the PCSZ and regions south of it.

Variation in recorded 'peak' pressure-temperatures

While all the published information suggests an overall CW P-T path (discussed in previous section; Fig. 8.4), a feature consistent with metamorphism in a continent-continent collision setting, their intensity of metamorphism (recorded thermal maxima; Fig. 8.4, 8.5a) varies spatially from upper amphibolite to UHT granulite (represented by data clusters under yellow and blue rectangular bars respectively in Fig. 8.5a). The most plausible explanation of this variation of metamorphic intensities recorded in meta-supracrustal rocks having similar protoliths and timing of metamorphism could be the exposure of different crustal sections in different places (Fig. 8.6). Shallower and deeper crustal sections record lower and higher temperatures respectively. Several studies employing robust

geochronometers have demonstrated that the Indian shield was differentially uplifted due to neotectonic activities (e.g. Chamyal et al., 2002). This explains the southward increase in metamorphic grade of the greenstone belts of the DC (Gopalakrishna et al., 1986 and several others). This process might have been operative in the GTSI, and may also explain why the Ediacaran-Cambrian meta-supracrustal cover rocks occur as detached outcrops on the Archaean/ early Palaeoproterozoic basement of the GTSI.

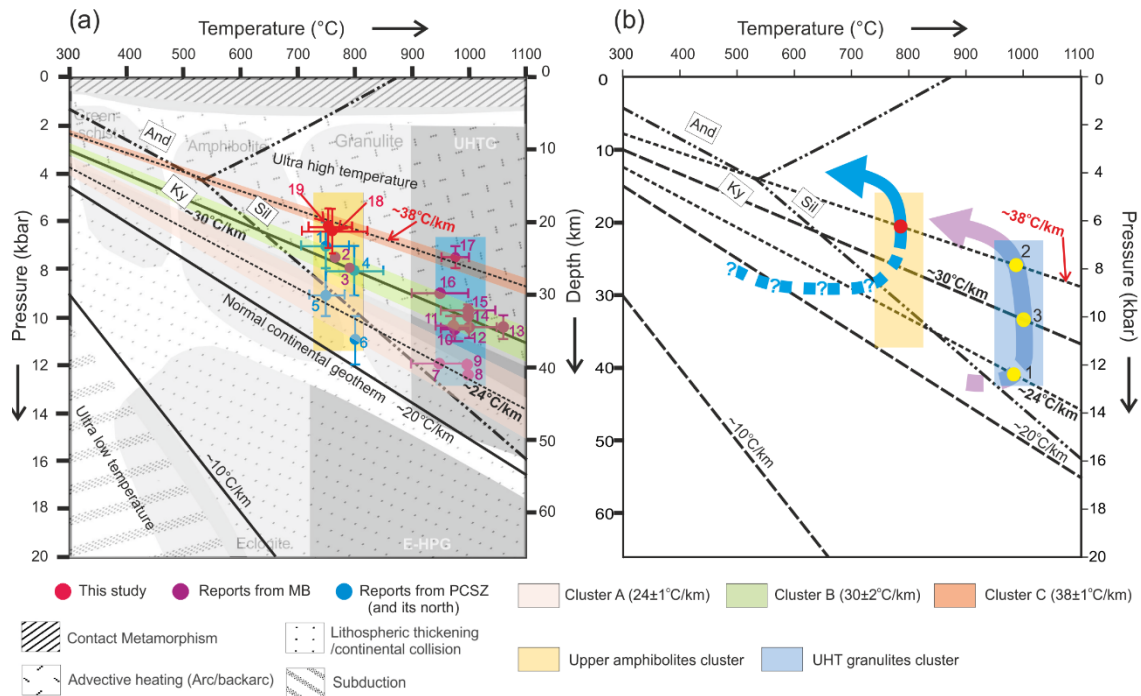


Fig. 8.5: (a) P-T conditions of metamorphism (the bars indicate uncertainty of calculations) as reported from the Ediacaran-Cambrian meta-supracrustal rocks from different parts of the GTSI (and this study). Also included in the diagram are some typical geothermal gradients found in different tectonic settings and the P-T field of some key metamorphic domains (after Brown, 2008). The published P-T data from these meta-supracrustal rocks are spread along three reference geothermal gradients (Clusters A, B and C). The two shaded rectangular bars depict the large variation in pressure, against a very restricted temperature variation recorded by these reports. This indicates that the recorded P-T conditions could be frozen at different points on a steeply decompressive retrograde P-T path (explained in 'b'). (b) Different P-T points are recorded during intersection of the steeply decompressive retrograde P-T path from Palni Hills (Brandt et al., 2011; purple path with yellow circles 1, 2 and 3) with progressively hotter geothermal gradients. The P-T path constrained from this study (blue path) is also shown. Owing to lack of suitable markers, the P-T conditions that prevailed during the stability of kyanite in the studied rocks could not be determined. The very warm geothermal gradient (~37°C/km) as deduced on a clockwise P-T path from the studied rocks points to the equilibration of mineral assemblages at or close to the terminal part of the steeply decompressive P-T path (red circle). UHTG: Ultra High Temperature Granulite metamorphism; E-HPG: Eclogite High Pressure Granulite metamorphism. References: 1) Lal et al., 1984, 2) Mohan and Windley, 1993, 3) Mohan et al., 1996, 4) Raith and Srikanthappa, 2008, 5) Sengupta et al. 2009, 6) Raith et al. 2010, 7) Brown and Raith, 1996, 8) Brandt et al. 2010, 9) Brandt et al. 2011, 10) Raith et al., 1997, 11) Tiwari and Sarkar, 2020, 12) Sajeev et al., 2004, 13) Tamashiro et al., 2004, 14) Prakash and Arima, 2003, 15) Tateishi et al., 2004, 16) Prakash et al., 2006, 17) Sajeev et al., 2006, 18) Grt-Bt-Sil gneiss (this study), 19) Grt-Crd-Bt-Sil gneiss (this study).

Fig. 8.5a shows the published P-T conditions (recorded P-T maxima) for the Ediacaran-Cambrian metamorphism of the supracrustal rocks across the GTSI. Also included in Fig. 8.5a are the reference transient geothermal gradients observed in metamorphic rocks from different tectonic settings (Brown, 2008). The published P-T data are spread along three transient geothermal gradients $\sim 24(\pm 2)^\circ\text{C}/\text{km}$ (A), $\sim 30(\pm 2)^\circ\text{C}/\text{km}$ (B) and $\sim 38(\pm 1)^\circ\text{C}/\text{km}$ (C) (Fig. 8.5), with most of the data-points spread along the geothermal gradients A and B (Fig. 8.5a). The geothermal gradient A, overlaps with the gradients expected from rocks of typical continent-continent collision zone (Fig. 8.5a). The MSU, however, records a geothermal gradient ($\sim 37^\circ\text{C}/\text{km}$, cluster C, Fig. 8.5a) hotter than the typical collision zone transient geothermal gradients (Fig. 8.5a). Two models may explain the variation in the transient geothermal gradients recorded by the Ediacaran-Cambrian meta-supracrustal rocks of the GTSI.

Model-I: It is a common observation that the retrograde P-T path of the metamorphic rocks in a typical continent-continent collision setting is characterized by a steeply decompressive P-T segment after the attainment of peak pressure (Brandt et al., 2011; England and Thompson, 1984; Harley, 1989; Sengupta et al., 2009). During decompression, the metamorphic rocks traverse progressively hotter geothermal gradients as pressure drops significantly against a smaller temperature drop (Fig. 8.5a-b). A significant decrease in pressure against a small drop in temperature enlarges the stability of melt, owing to its higher volume, and facilitates melting and/or growth of porphyroblastic phases (e.g., Harris and Massey, 1994). The P-T conditions of the metamorphic rocks, and the transient geothermal gradient calculated therefrom, would thus record a 'snap shot' on the retrograde decompressive P-T trajectory at which the melting and/or growth of porphyroblasts occur (shown in Fig. 8.5b). As a consequence, different parts of a same collisional orogen may record different geothermal gradients depending upon the time when the corresponding 'peak' metamorphic assemblages were stabilised, while the rock traversed a steeply decompressive P-T path (Fig. 8.5b).

Model-II: Concentration of the heat producing radioactive elements in the thickened crust has also been considered to be an important source of heat in a continent-continent collision zone (England and Thompson, 1984; Kelsey and Hand,

2015 and references cited therein). The heat thus generated from the radioactive decay may result in hotter geothermal gradients, that intersect the melting reactions.

Combination of these two models may also be responsible for the obtained trend of geothermal gradients recorded in the GTSI.

A number of the reported meta-supracrustal rocks from the GTSI that experienced Ediacaran-Cambrian metamorphism, show that the estimated maximum temperature was reached at or close to the pressure maxima (points 5–9 in Fig. 8.5a). Mineral assemblages in the MSU, however, do not allow calculation of metamorphic temperature at or close to the maximum pressure (≥ 8 kbar, Fig. 6.4b, d), when kyanite transformed to sillimanite. In a detailed study, Brandt et al. (2011) documented that different sets of mineral assemblages were developed when the rocks of the Palni Hills traversed the steeply decompressive retrograde P-T path, intersecting progressively hotter geothermal gradients (purple arrow in Fig. 8.5b). Moreover, the recorded P-T conditions of the Ediacaran-Cambrian meta-supracrustal rocks of the GTSI show large variation of estimated pressure against limited variation in temperature (shown by rectangular colour bars, Fig. 8.5a), which is consistent with Model-I. Collating all the observations from the studied rocks, it seems likely that the mineral assemblage of the MSU, recording the estimated 'peak' metamorphism ($\sim 730\text{--}790$ °C, $\sim 5.5\text{--}7$ kbar), may have equilibrated after a pressure drop from the maximum pressure actually witnessed by the studied rocks during continent-continent collision (Model-I). The absence of extensive granitic crust of Ediacaran-Cambrian age (source of radioactive heat for metamorphism) in the GTSI (especially in the MB, where UHT meta-supracrustal rocks of similar age are dominantly exposed) also supports Model-I. However, more studies are required to negate completely the option presented in Model-II.

Therefore, all the above discussion is consistent with the following information:

(a) occurrence of meta-supracrustal rocks on both sides of the perceived 'PCSZ' having similar protoliths, timing of sedimentation (late Palaeoproterozoic to

late Mesoproterozoic, ~1750–1020 Ma; Kooijman et al., 2011; Sengupta et al., 2015; Fig. 8.4);

(b) Similar detrital age populations and similar sources of detrital zircon for these meta-supracrustal rocks, lying far north of the perceived PCSZ (Sengupta et al., 2015).

(c) Preservation of early Palaeoproterozoic metamorphism (from basement gneisses, mafic granulites, and rarely from a few meta-supracrustal rocks also, (Brandt et al., 2011)) across the GTSI, in the MB as well as the CSS (north of PCSZ) (Fig. 8.7);

(d) Ediacaran-Cambrian deformation and metamorphism of these supracrustal rocks, and other lithounits across the PCSZ (Fig. 8.4 and 8.7);

Hence, it is inferred that (a) the GTSI behaved as a coherent landmass at least before ~1020 Ma (the minimum timing of shelf sedimentation on the Archaean/ early Palaeoproterozoic basement, Sengupta et al., 2015), (b) a vast expanse of late Palaeoproterozoic to late Mesoproterozoic (~1750–1020 Ma) shallow marine shelf sediments (shale-sandstone-limestone), the likely protoliths of the meta-supracrustal rocks of GTSI (including the MSU), were deposited on the a unified, continuous Archaean/ early Palaeoproterozoic crust of the GTSI across the perceived location of the PCSZ, (Fig. 8.6, Stage I; Kooijman et al., 2011; Sengupta et al., 2015); and (c) this sedimentary packet was reworked in a continent-continent collision in the Ediacaran-Cambrian period (Fig. 8.6, Stage II). Hence, these meta-supracrustal rocks mark a flip from a passive continental setting (marked by formation of stable sediments of sandstone-shale-limestone, Raith et al., 2016, Raith et al., 2010) to an orogenic setting during Ediacaran-Cambrian time.

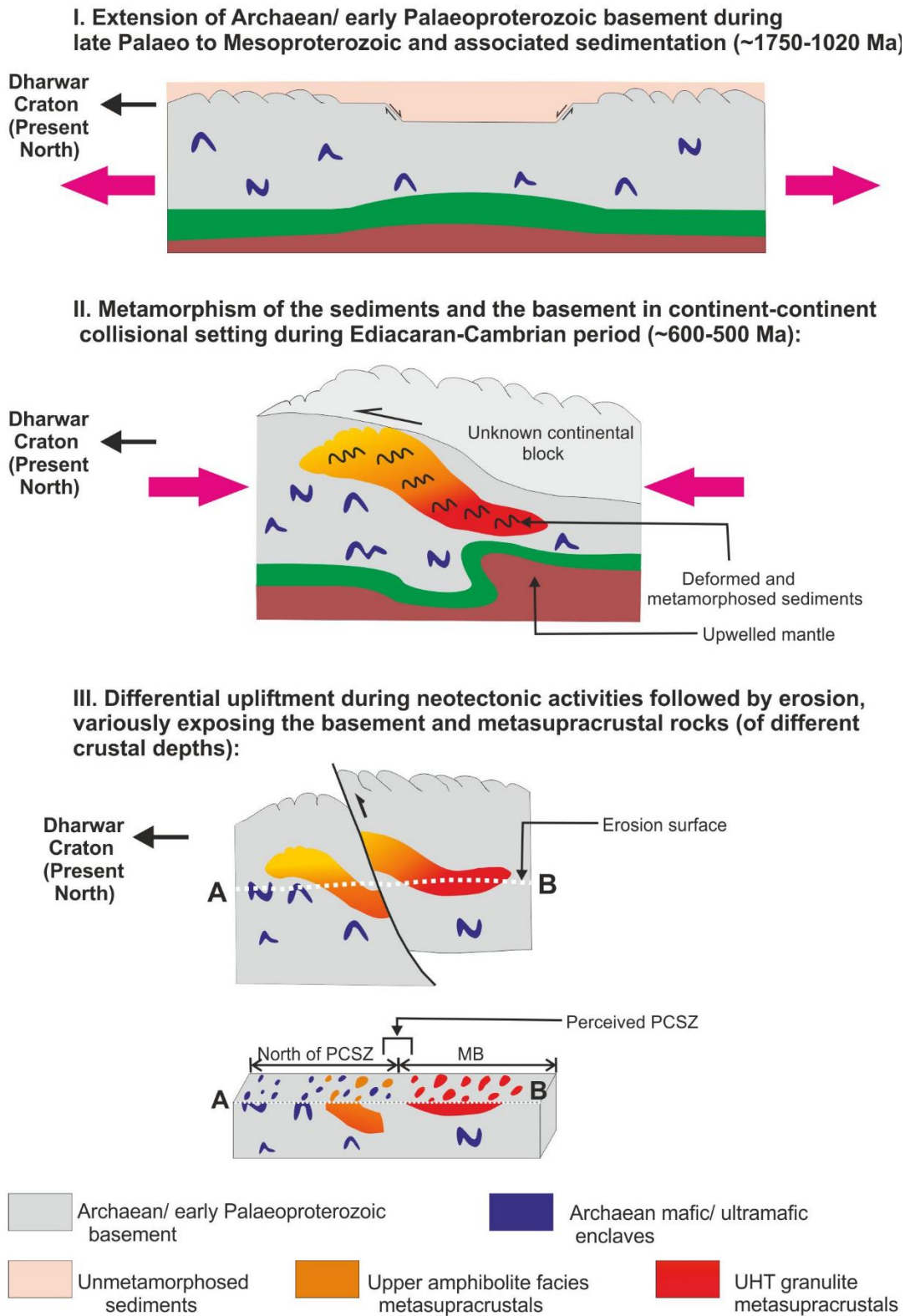


Fig. 8.6: Schematic model showing the possible stages of tectonic evolution of the GTSI since the late Palaeoproterozoic. PCSZ: Palghat Cauvery Shear Zone, MB: Madurai Block.

Consequently, it is evident that the coherent land mass of the GTSI acted as the lower plate during the global continent-continent collision associated with the formation of the Ediacaran-Cambrian supercontinent Gondwanaland during the 'Pan-African' orogenesis. Additionally, (a) absence of any field evidences supporting the presence of a crustal scale shear zone in the eastern part of the PCSZ (Mukhopadhyay et al., 2003), and (b) recent geophysical data which convincingly demonstrates uniform depth of Moho and occurrence of a dominant felsic crust across the 'PCSZ' (Prathigadapa et al., 2020), further corroborates our view that the PCSZ is not an Ediacaran- Cambrian terrane boundary, and that, the GTSI behaved as a coherent landmass at least from the late Mesoproterozoic (~1020 Ma; Brandt et al., 2014 ; Kooijman et al., 2011 ; Sengupta et al., 2015).

8.2.2.3. The GTSI in the context of Link with Madagascar

Reconstruction of Gondwanaland juxtaposed the Precambrian basement of Madagascar with the GTSI (Fig. 8.7). Three major Archaean-early Palaeoproterozoic units are identified from the northern and central Madagascar. These are Antongil and Masora block to the northeast and Antananarivo block to the central part of the Madagascar (Fig. 8.7; reviewed in Tucker et al., 2014). Similar to the western Dharwar, the two north-eastern block bears the impress of crust formation at >3000 Ma whereas the Antananarivo unit is younger and show crust formation at ~2500 Ma (reviewed in Talukdar et al.2022, Sengupta et al. 2015, Tucker et al., 2014). A strong early Palaeoproterozoic metamorphism (>2400 Ma) are recorded in all the three units (De Waele et al., 2011; e.g., Fitzsimons, 2016; Tucker et al., 2011). In view of the remarkable similarity in geological history, >3000 Ma old Antongil and Masora units are correlated with the western Dharwar Craton and the Antananarivo unit with the southern part of the GTSI, lying south of the Moyar-Bhawani Shear zone. The Archaean-early Palaeoproterozoic crust of the Madagascar received sedimentation during Palaeo- to Meso- to Neoproterozoic time (~1722-810 Ma, Fig. 8.7). The MSU and the other metasedimentary units in the GTSI show similar basin formation age (~1750-1020 Ma; Kooijmaan et al., 2011; reviewed in Sengupta et al., 2015, Roy Choudhury et al., 2021). Much similar to the metasedimentary unit of north eastern and central Madagascar, Archaean (>3000Ma) and Neo- to early Palaeoproterozoic detrital zircon has been reported from the metasedimentary

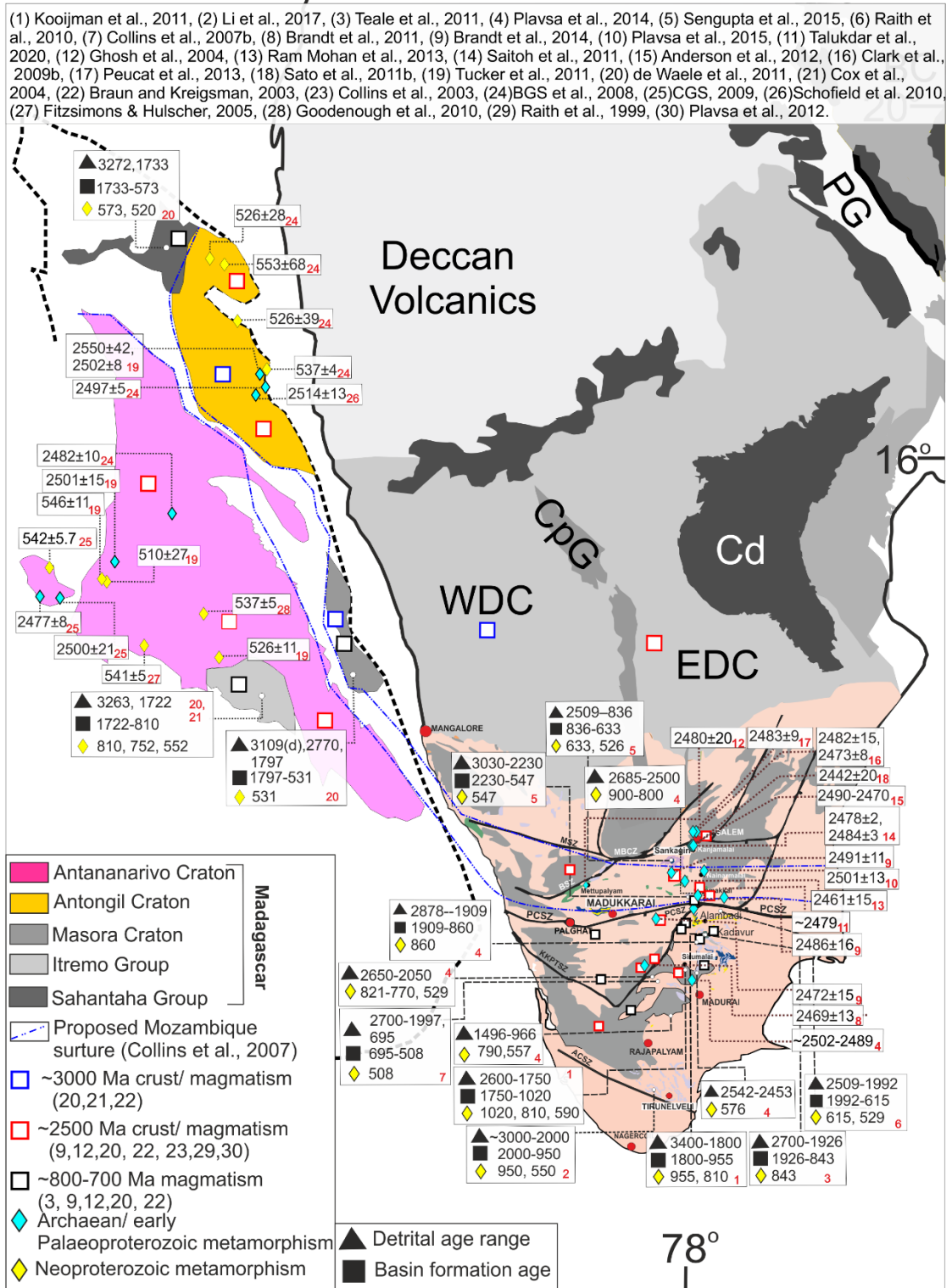


Fig. 8.7: Diagram illustrating the relative positions of the India and east and central Madagascar (modified after Sengupta et al., 2015) summarizing relevant late Neoproterozoic tectono-thermal imprints from published geochronology, along with representative Archaean and Palaeoproterozoic metamorphic and magmatic imprints. All the dates are in Ma. The alphabets beside dates represent the references.

units of the GTSI (Fig. 8.4 and 8.7). The Palaeo- to Meso- to Neoproterozoic sedimentary rocks from both the GTSI (including the MSU) and the north-eastern to central Madagascar were extensively reworked during the Ediacaran-Cambrian orogenesis, presumably in a continent-continent collision setting (Fig. 8.7). In view of all the information, it seems logical to infer a combined Indo-Madagascar land mass that existed at least from 2400 Ma. This unified landmass received sedimentation over a protracted period (~1800-550 Ma) and participated in the globally extensive Pan-African orogenesis during formation of the Gondwanaland. Along with published information, the observation from the MSU supports the view that PCSZ and Betsimisaraka Shear Zone (presumed to separate Antananarivo unit from the >3000 Ma old NE unit of Madagascar), cannot be the loci along which the “Mozambique Ocean” was closed during the Ediacaran-Cambrian time (Collins et al., 2007a, 2003a, 2003b; Kroener et al., 2000).

8.3. Summary

Integrating all the findings of the present study with the extant available geological and geochronological information, it stands to reason that the Indian subcontinent evolved through multiple orogenic cycles during the Neoproterozoic. The geochronologic evidences preserved in the CGGC, and the surrounding terranes all indicate that the northern and southern Indian blocks were amalgamated at least before the Neoproterozoic (possibly in the late-Palaeo to Mesoproterozoic). Additionally, evidences from the northern and southern parts of the PCSZ, as well as the parts of Madagascar signify that the Northern Granulite Terrane and the Madurai Block (at least north of the Trivandrum block) got amalgamated much before the Neoproterozoic, possibly during the Palaeoproterozoic. Additionally, this observation is also consistent with the view that Antananarivo and Antongil–Masora blocks of Madagascar was joined with the Indian subcontinent long before Neoproterozoic, in contrast with the view of Collins et al., (2003) and Kröner et al. (2000), who suggested late Neoproterozoic suturing of the Antananarivo and Antongil–Masora blocks of Madagascar (corresponding to closure of the Mozambique Ocean) during Pan-African Orogeny. Subsequently, this continuous crustal landmass experienced extension in the NIB, as recorded in the CGGC and

adjoining areas during Mesoproterozoic, before they participated in the Grenvillian Orogeny in the early Neoproterozoic (late Stenian- early Tonian time; M2_{CGGC}), corresponding to the formation of Rodinia supercontinent. Punctuated by a short extensional phase, the CGGC and its the adjacent terranes experienced another collision event (M3_{CGGC}) during the late Tonian, corresponding to the final amalgamation of Rodinia supercontinent. Late Tonian extensional granites in some parts of the GTSI (as well as Madagascar) attest to a period of extension in these terranes. Subsequently, during the late Neoproterozoic (Ediacaran-Cambrian, M2_{GTSI}), the continuous crust of GTSI in the southern part of the Indian peninsula, evidenced another continental collisional event corresponding to the formation of Gondwanaland, during Pan-African orogeny.

8.4. Concluding remarks

- The studied calc-silicate and pelitic granulite enclaves in the CGGC together preserve evidences of two major tectonothermal events (M2_{CGGC}-M3_{CGGC}) in the early Neoproterozoic time.
- The present study provides an age constraint from the calc-silicate granulites in the CGGC for the first time. Sedimentation age of the protolith of these enclave suite rocks obtained from the calc-silicate granulites ranges between ~1790-1486 Ma. These rocks record M2_{CGGC} event as a high pressure, moderate to high temperature granulite facies metamorphism, that culminated at ~790-890°C and ~8.4-10.5 kbar, followed by a near isothermal, decompression of ~4 kbar, along a clockwise P-T path. The timing of this event has been estimated to be late Stenian-early Tonian (~1060-970 Ma).
- The rare association of aluminous clinopyroxene-ilmenite-spinel symplectites, preserved in one of the calc-silicate granulites, was inferred to be derived from a mixed protolith (carbonate + Al rich sediments or mafic+ carbonate sediments). These sediments were enriched in aluminium and depleted in calcium via interaction with meteoric fluid at surficial conditions. Subsequent metamorphism (related to M2_{CGGC} event) led to the formation of such a unique mineral assemblage. Formation of symplectic texture, by the breakdown of the peak metamorphic minerals: garnet, amphibole and titanite, occurred during the subsequent near isothermal decompressive phase.

- The third metamorphism (M3_{CGGC}) has been characterised as an amphibolite facies tectono-thermal event. Fluid infiltration driven metamorphism, resulting in formation of amphibole, vesuvianite and epidote is associated with this M3_{CGGC} event. P-T conditions of this fluid infiltration driven M3_{CGGC} metamorphism has been constrained to be ~5.6-6.8 kbar and 600-740°C. Formation of vesuvianite was inferred to have occurred due to influx of aqueous (~0.1-0.4 X_{CO2}) at ~600-620°C and ~6kbar, and fluorine rich fluid, while epidote formed subsequently, at more H₂O-rich conditions (≤ 0.1 X_{CO2} and lower X_F), combined with a slight cooling (at <600°C).
- The incorporation of Al and F/ OH in titanites (within the studied calc-silicate granulites) occurred as a consequence of the formation of the fluid-bearing minerals (amphibole, vesuvianite), in response to F-bearing fluid induced metamorphism during M3_{CGGC}. This study demonstrates that presence of F plays a very crucial role, in regulating the extent of Al substitution in titanites, relative to pressure and temperature.
- The findings of this study, when combined with the available geochronological information, is consistent with fact that the Indian shield with the CGGC, along with the composite CITZ belt, EGMB and east Antarctica, formed a coherent landmass at least before the Neoproterozoic time. This coherent landmass was reworked in a continent-continent collision during the early Neoproterozoic, corresponding to the amalgamation of Rodinia supercontinent.
- In the GTSI, the sedimentary protoliths of the studied MSU are akin to the late Palaeoproterozoic to late Mesoproterozoic (~1750–1020 Ma) sedimentary cover, deposited in a stable continental shelf across the GTSI.
- The studied metapelites of the MSU constrain the peak temperature and pressure of metamorphism (M2_{GTSI}) in the range of ~730–790°C, ~5.5–7 kbar, followed by a decompressive retrograde P-T path recorded till ~630°C and ~4 kbar.
- The findings of the present study shows that the variation in the metamorphic grade of the meta-supracrustal rocks is possibly due to exposure of different crustal sections in different places. Additionally, the variation in the recorded ‘peak’ metamorphic conditions (and corresponding transient geotherm gradient) has been attributed to be dependent on the time when the corresponding ‘peak’ metamorphic assemblages were stabilised, while the rock traversed a steeply decompressive P-T path.

- The studied calc-silicate granulites of the MSU constrain the P-T- X_{fluid} conditions of formation of garnet-amphibole during a near isobaric temperature decrease (~520-640°C, and ~4.7-6 kbar; subsequent to decompression), along with the influx of moderately water-rich fluid (~0.25-0.6 X_{CO_2}). This was followed by continued isobaric cooling (up to ~440-460°C, $\leq 0.4 X_{\text{CO}_2}$) at the tail end of the retrogressive path, during which epidote formed.
- This tectonothermal event of the MSU ($M2_{\text{GTSI}}$) occurred in a continent-continent collisional setting, during the late Neoproterozoic (~550–520 Ma).
- The evolutionary history of the MSU shows remarkable similarity with that of the Ediacaran-Cambrian meta-supracrustal rocks on both side of the so called ‘PCSZ’. This together with the occurrence of Archaean/ early Palaeoproterozoic crust further south of PCSZ, and the recent geophysical investigation, support the view that the PCSZ should not be considered as an Ediacaran-Cambrian terrane boundary.
- The observations of the present study and extant information on the meta-supracrustal rocks across the GTSI are consistent with the view that the GTSI with its Archaean/ early Palaeoproterozoic crust and late Palaeoproterozoic to late Mesoproterozoic (~1750–1020 Ma) stable continental shelf deposits, behaved as a coherent lower plate during Ediacaran-Cambrian ‘Pan-African’ orogenesis corresponding to formation of Gondwanaland.
- The present study from the MSU when integrated with existing geological information from Madagascar, seems also consistent with the existence of a combined Indo-Madagascar landmass at least from the Palaeoproterozoic, and therefore contradicts the view that the ‘Betsimisaraka Shear Zone’ is the loci along which the “Mozambique Ocean” closed during Ediacaran-Cambrian time.
- The present study on meta-supracrustal rocks in two different terranes (CGGC and GTSI) therefore, demonstrates the whole spectrum of the crustal evolution of the Indian subcontinent through the Neoproterozoic time.

References

- Acharyya, S.K., 2003. The nature of Mesoproterozoic Central Indian Tectonic Zone with exhumed and reworked older granulites. *Gondwana Res.* 6, 197–214.

- Ague, J.J., 2000. Release of CO₂ from carbonate rocks during regional metamorphism of lithologically heterogeneous crust. *Geology* 28, 1123–1126.
- Anderson, J.R., Payne, J.L., Kelsey, D.E., Hand, M., Collins, A.S., Santosh, M., 2012. High-pressure granulites at the dawn of the Proterozoic. *Geology* 40, 431–434.
- Asami, M., Suzuki, K., Grew, E.S., 2005. Monazite and zircon dating by the chemical Th-U-total Pb isochron method (CHIME) from Alasheyev Bight to the Sør Rondane Mountains, East Antarctica: a reconnaissance study of the Mozambique Suture in eastern Queen Maud Land. *J. Geol.* 113, 59–82.
- Basu, A., Bickford, M.E., 2014. Contributions of zircon U–Pb geochronology to understanding the volcanic and sedimentary history of some Purāna basins, India. *J. Asian Earth Sci.* 91, 252–262.
- BGS (British Geological Survey), USGS (U.S. Geological Survey), GLW (GLW Conseil), 2008. Final Report: Révision de la cartographie géologique et minière des zones Nord et Centre de Madagascar (Zones A, B et D). République de Madagascar, Ministère de l’Energie et des Mines (MEM/SG/DG/UCP/PGRM), 1049 pp, and Appendix.
- CGS (Council for Geoscience, South Africa), 2009a. Map Explanation of 1:100 000 scale (Zone E) Sheets I46 – Ambararata, J46 – Beopoaka, 47 – Itondy, J47 – Belobaka, K47 – Ambatofotsy, I48 – Miandrivazo, J48 – Betrondro, K48 – Ambatondradama, I49 – Ankotrofotsy, J49 – Dabolava, K49 – Anjoma-Ramartina, L49 – Vasiana, M49 – Ankazomiriotra, N49 – Antsirabe. République de Madagascar, Ministère de l’Energie et des Mines – Project de Gouvernance des Ressources Minérales, Antananarivo, Madagascar and Council for Géoscience, Pretoria, South Africa.
- Bhandari, A., Chandra Pant, N., Bhowmik, S.K., Goswami, S., 2011. ~ 1.6 Ga ultrahigh-temperature granulite metamorphism in the Central Indian Tectonic Zone: insights from metamorphic reaction history, geothermobarometry and monazite chemical ages. *Geol. J.* 46, 198–216.
- Bhowmik, S.K., 2019. The current status of orogenesis in the Central Indian Tectonic

Zone: A view from its Southern Margin. *Geol. J.* 54, 2912–2934.

Bhowmik, S.K., Bernhardt, H.-J., Dasgupta, S., 2010. Grenvillian age high-pressure upper amphibolite-granulite metamorphism in the Aravalli-Delhi Mobile Belt, Northwestern India: New evidence from monazite chemical age and its implication. *Precambrian Res.* 178, 168–184.

Bhowmik, S.K., Saha, L., Dasgupta, S., Fukuoka, M., 2009. Metamorphic phase relations in orthopyroxene-bearing granitoids: Implication for high-pressure metamorphism and prograde melting in the continental crust. *J. Metamorph. Geol.* 27, 295–315.

Bhowmik, S.K., Sarbadhikari, A.B., Spiering, B., Raith, M.M., 2005. Mesoproterozoic reworking of Palaeoproterozoic ultrahigh-temperature granulites in the Central Indian Tectonic Zone and its implications. *J. Petrol.* 46, 1085–1119.

Bhowmik, S.K., Wilde, S.A., Bhandari, A., Pal, T., Pant, N.C., 2012. Growth of the Greater Indian Landmass and its assembly in Rodinia: geochronological evidence from the Central Indian Tectonic Zone. *Gondwana Res.* 22, 54–72.

Biju-Sekhar, S., Yokoyama, K., Pandit, M.K., Okudaira, T., Yoshida, M., Santosh, M., 2003. Late Paleoproterozoic magmatism in Delhi Fold Belt, NW India and its implication: evidence from EPMA chemical ages of zircons. *J. Asian Earth Sci.* 22, 189–207. doi:10.1016/S1367-9120(02)00188-8

Bora, S., Kumar, S., Yi, K., Kim, N., Lee, T.H., 2013. Geochemistry and U–Pb SHRIMP zircon chronology of granitoids and microgranular enclaves from Jhircadandi pluton of Mahakoshal Belt, Central India Tectonic Zone, India. *J. Asian Earth Sci.* 70, 99–114.

Bose, S., Das, K., Torimoto, J., Arima, M., Dunkley, D.J., 2016. Evolution of the Chilka Lake granulite complex, northern Eastern Ghats Belt, India: First evidence of ~780Ma decompression of the deep crust and its implication on the India–Antarctica correlation. *Lithos* 263, 161–189.

Bose, S., Seth, P., Dasgupta, N., 2017. Meso-Neoproterozoic mid-crustal metamorphic

record from the Ajmer–Shrinagar section, Rajasthan, India and its implication to the assembly of the Greater Indian Landmass during the Grenvillian-age orogenesis. *Geol. Soc. London, Spec. Publ.* 457, SP457-7.

Brandt, S., Raith, M.M., Schenk, V., Sengupta, P., Srikantappa, C., Gerdes, A., 2014. Crustal evolution of the Southern Granulite Terrane, south India: New geochronological and geochemical data for felsic orthogneisses and granites. *Precambrian Res.* 246, 91–122. <https://doi.org/10.1016/j.precamres.2014.01.007>

Brandt, S., Schenk, V., Raith, M.M., Appel, P., Gerdes, A., Srikantappa, C., 2011. Late Neoproterozoic PT evolution of HP-UHT granulites from the Palni Hills (South India): New constraints from phase diagram modelling, LA-ICP-MS zircon dating and in-situ EMP monazite dating. *J. Petrol.* 52, 1813–1856.

Braun, I., Kriegsman, L.M., 2003. Proterozoic crustal evolution of southernmost India and Sri Lanka. *Geol. Soc. London, Spec. Publ.* 206, 169–202.

Brown, M., 2008. Characteristic thermal regimes of plate tectonics and their metamorphic imprint throughout Earth history: When did Earth first adopt a plate tectonics mode of behavior? When did plate tectonics begin planet Earth? 440, 97.

Brown, M., 2007. Metamorphic conditions in orogenic belts: a record of secular change. *Int. Geol. Rev.* 49, 193–234.

Brown, M., Raith, M., 1996. First evidence of ultrahigh-temperature decompression from the granulite province of southern India. *J. Geol. Soc. London.* 153, 819–822.

Buchan, K.L., Ernst, R.E., Hamilton, M.A., Mertanen, S., Pesonen, L.J., Elming, S.-Å., 2001. Rodinia: the evidence from integrated palaeomagnetism and U–Pb geochronology. *Precambrian Res.* 110, 9–32.

Buick, I.S., Cartwright, I., Hand, M., Powell, R., 1994. Evidence for pre-regional metamorphic fluid infiltration of the Lower Calcisilicate Unit, Reynolds Range

- Group (central Australia). *J. Metamorph. Geol.* 12, 789–810.
- Buick, I.S., Clark, C., Rubatto, D., Hermann, J., Pandit, M., Hand, M., 2010. Constraints on the Proterozoic evolution of the Aravalli–Delhi Orogenic belt (NW India) from monazite geochronology and mineral trace element geochemistry. *Lithos* 120, 511–528.
- Chakrabarty, A., Karmakar, S., Mukherjee, S., Choudhury, S.R., Maiti, P., Sanyal, S., Sengupta, P., 2022. Neoproterozoic reworking of a Mesoproterozoic magmatic arc from the north-eastern part of the Central Indian Tectonic Zone: Implication for the growth and disintegration of the Indian shield in the Proterozoic supercontinental cycles. *Precambrian Res.* 378, 106758.
- Chamyal, L.S., Maurya, D.M., Bhandari, S., Raj, R., 2002. Late Quaternary geomorphic evolution of the lower Narmada valley, Western India: implications for neotectonic activity along the Narmada–Son Fault. *Geomorphology* 46, 177–202.
- Chatterjee, N., 2018. An assembly of the Indian Shield at c. 1.0 Ga and shearing at c. 876–784 Ma in Eastern India: insights from contrasting PT paths, and burial and exhumation rates of metapelitic granulites. *Precambrian Res.* 317, 117–136.
- Chatterjee, N., Banerjee, M., Bhattacharya, A., Maji, A.K., 2010. Monazite chronology, metamorphism–anatexis and tectonic relevance of the mid-Neoproterozoic Eastern Indian Tectonic Zone. *Precambrian Res.* 179, 99–120.
- Chatterjee, N., Crowley, J.L., Ghose, N.C., 2008a. Geochronology of the 1.55 Ga Bengal anorthosite and Grenvillian metamorphism in the Chotanagpur gneissic complex, eastern India. *Precambrian Res.* 161, 303–316.
- Chatterjee, N., Crowley, J.L., Mukherjee, A., Das, S., 2008b. Geochronology of the 983-Ma Chilka Lake Anorthosite, Eastern Ghats Belt, India: Implications for Pre-Gondwana Tectonics. *J. Geol.* 116, 105–118.
- Chatterjee, N., Ghose, N.C., 2011. Extensive early Neoproterozoic high-grade

metamorphism in north Chotanagpur gneissic complex of the Central Indian tectonic zone. *Gondwana Res.* 20, 362–379.

Chatterjee, N., Mazumdar, A. C., Bhattacharya, A., Saikia, R.R., 2007. Mesoproterozoic granulites of the Shillong-Meghalaya Plateau: Evidence of westward continuation of the Prydz Bay Pan-African suture into Northeastern India. *Precambrian Res.* 152, 1–26. doi:10.1016/j.precamres.2006.08.011

Chatterjee, N., Nicolaysen, K., 2012. An intercontinental correlation of the mid-Neoproterozoic Eastern Indian tectonic zone: evidence from the gneissic clasts in Elan Bank conglomerate, Kerguelen Plateau. *Contrib. to Mineral. Petrol.* 163, 789–806.

Chattopadhyay, A., Chatterjee, A., Das, K., Sarkar, A., 2017. Neoproterozoic transpression and granite magmatism in the Gavilgarh-Tan Shear Zone, central India: Tectonic significance of U-Pb zircon and U-Th-total Pb monazite ages. *J. Asian Earth Sci.* 147, 485–501.

Chattopadhyay, S., Upadhyay, D., Nanda, J.K., Mezger, K., Pruseth, K.L., Berndt, J., 2015. Proto-India was a part of Rodinia: Evidence from Grenville-age suturing of the Eastern Ghats Province with the Paleoproterozoic Singhbhum Craton. *Precambrian Res.* 266. <https://doi.org/10.1016/j.precamres.2015.05.030>

Clark, C., Collins, A.S., Santosh, M., Taylor, R., Wade, B.P., 2009. The PTt architecture of a Gondwanan suture: REE, U-Pb and Ti-in-zircon thermometric constraints from the Palghat Cauvery shear system, South India. *Precambrian Res.* 174, 129–144.

Collins, A.S., Clark, C., Sajeev, K., Santosh, M., Kelsey, D.E., Hand, M., 2007a. Passage through India: the Mozambique Ocean suture, high-pressure granulites and the Palghat-Cauvery shear zone system. *Terra Nov.* 19, 141–147.

Collins, A.S., Fitzsimons, I.C.W., Hulscher, B., Razakamanana, T., 2003a. Structure of the eastern margin of the East African Orogen in central Madagascar. *Precambrian Res.* 123, 111–133.

- Collins, A.S., Kröner, A., Fitzsimons, I.C.W., Razakamanana, T., 2003b. Detrital footprint of the Mozambique ocean: U–Pb SHRIMP and Pb evaporation zircon geochronology of metasedimentary gneisses in eastern Madagascar. *Tectonophysics* 375, 77–99.
- Collins, A.S., Santosh, M., Braun, I., Clark, C., 2007b. Age and sedimentary provenance of the Southern Granulites, South India: U–Th–Pb SHRIMP secondary ion mass spectrometry. *Precambrian Res.* 155, 125–138.
- Condie, K.C., 2021. *Earth as an evolving planetary system*. Academic Press.
- Corvino, A.F., Boger, S.D., Henjes-Kunst, F., Wilson, C.J.L., Fitzsimons, I.C.W., 2008. Superimposed tectonic events at 2450 Ma, 2100 Ma, 900 Ma and 500 Ma in the North Mawson Escarpment, Antarctic Prince Charles Mountains. *Precambrian Res.* 167, 281–302.
- Cox, R., Fernandez, A., Schreurs, G., 2004. Discussion on tectonic evolution of the Proterozoic Itremo Group metasediments in Central Madagascar Special Publication 206, 2003, 381–399. *J. Geol. Soc. London.* 161, 539–541.
- Das, E., Karmakar, Subrata, Dey, A., Karmakar, Shreya, Sengupta, P., 2017. Reaction textures, pressure–temperature paths and chemical dates of monazite from a new suite of sapphirine–spinel granulites from parts of the Eastern Ghats Province, India: insights into the final amalgamation of India and East Antarctica during the for. *Geol. Soc. London, Spec. Publ.* 457, 141–170.
- Das, K., Bose, S., Karmakar, S., Dunkley, D.J., Dasgupta, S., 2011. Multiple tectonometamorphic imprints in the lower crust: first evidence of ca. 950 Ma (zircon U–Pb SHRIMP) compressional reworking of UHT aluminous granulites from the Eastern Ghats Belt, India. *Geol. J.* 46, 217–239.
- Das, S., Sanyal, S., Karmakar, S., Sengupta, S., Sengupta, P., 2019. Do the deformed alkaline rocks always serve as a marker of continental suture zone? A case study from parts of the Chotanagpur Granite Gneissic complex, India. *J. Geodyn.* 129, 59–79.

- Dasgupta, S., Bose, S., Bhowmik, S.K., Sengupta, P., 2017. The Eastern Ghats Belt, India, in the context of supercontinent assembly. *Geol. Soc. London, Spec. Publ.* 457, 87–104.
- Dasgupta, S., Bose, S., Das, K., 2013. Tectonic evolution of the Eastern Ghats belt, India. *Precambrian Res.* 227, 247–258.
- Deb, M., Thorpe, R., Krstic, D., 2002. Hindoli Group of Rocks in the Eastern Fringe of the Aravalli-elhi Orogenic Belt-Archean Secondary Greenstone Belt or Proterozoic Supracrustals? *Gondwana Res.* 5, 879–883.
- Deshmukh, T., Prabhakar, N., 2020. Linking collision, slab break-off and subduction polarity reversal in the evolution of the Central Indian Tectonic Zone. *Geol. Mag.* 157, 340–350.
- Deshmukh, T., Prabhakar, N., Bhattacharya, A., Madhavan, K., 2017. Late Paleoproterozoic clockwise P–T history in the Mahakoshal Belt, Central Indian Tectonic zone: implications for Columbia supercontinent assembly. *Precambrian Res.* 298, 56–78.
- Dey, A., Karmakar, S., Ibanez-Mejia, M., Mukherjee, S., Sanyal, S., Sengupta, P., 2019a. Petrology and geochronology of a suite of pelitic granulites from parts of the Chotanagpur Granite Gneiss Complex, eastern India: Evidence for Stenian-Tonian reworking of a late Paleoproterozoic crust. *Geol. J.*
- Dey, A., Karmakar, S., Mukherjee, S., Sanyal, S., Dutta, U., Sengupta, P., 2019b. High pressure metamorphism of mafic granulites from the Chotanagpur Granite Gneiss Complex, India: Evidence for collisional tectonics during assembly of Rodinia. *J. Geodyn.* 129, 24–43.
- Dey, A., Mukherjee, S., Sanyal, S., Ibanez-Mejia, M., Sengupta, P., 2017. Deciphering sedimentary provenance and timing of sedimentation from a suite of metapelites from the Chotanagpur Granite Gneissic Complex, India: Implications for Proterozoic Tectonics in the East-Central Part of the Indian Shield, in: *Sediment Provenance*. Elsevier, pp. 453–486.

- De Waele, B., Thomas, R.J., Macey, P.H., Horstwood, M.S.A., Tucker, R.D., Pitfield, P.E.J., Schofield, D.I., Goodenough, K.M., Bauer, W., Key, R.M., 2011. Provenance and tectonic significance of the Palaeoproterozoic metasedimentary successions of central and northern Madagascar. *Precambrian Res.* 189, 18–42.
- Dobmeier, C., Lütke, S., Hammerschmidt, K., Mezger, K., 2006. Emplacement and deformation of the Vinukonda meta-granite (Eastern Ghats, India)—Implications for the geological evolution of peninsular India and for Rodinia reconstructions. *Precambrian Res.* 146, 165–178.
- Dobmeier, C., Simmat, R., 2002. Post-Grenvillean transpression in the Chilka Lake area, Eastern Ghats Belt—implications for the geological evolution of peninsular India. *Precambrian Res.* 113, 243–268.
- Dunkley, D.J., Clarke, G.L., White, R.W., 2002. Structural and metamorphic evolution of the mid-late Proterozoic Rayner Complex, Cape Bruce, east Antarctica, in: *Antarctica at the Close of a Millennium: Proceedings of the 8th International Symposium on Antarctic Earth Sciences, Wellington 1999.*
- Enami, M., Suzuki, K., Liou, J.G., Bird, D.K., 1993. Al-Fe³⁺ and F-OH substitutions in titanite and constraints on their PT dependence. *Eur. J. Mineral.* 219–232.
- England, P.C., Thompson, A.B., 1984. Pressure—temperature—time paths of regional metamorphism I. Heat transfer during the evolution of regions of thickened continental crust. *J. Petrol.* 25, 894–928.
- Fitzsimons, I.C.W., 2016. Pan-African granulites of Madagascar and southern India: Gondwana assembly and parallels with modern Tibet. *J. Mineral. Petrol. Sci.* 111, 73–88.
- Fitzsimons, I.C.W., Hulscher, B., 2005. Out of Africa: detrital zircon provenance of central Madagascar and Neoproterozoic terrane transfer across the Mozambique Ocean. *Terra Nov.* 17, 224–235.
- Goodenough, K.M., Thomas, R.J., De Waele, B., Key, R.M., Schofield, D.I., Bauer, W., Tucker, R.D., Rafahatelo, J.-M., Rabarimanana, M., Ralison, A. V., 2010. Post-

- collisional magmatism in the central East African Orogen: the Maevarano Suite of north Madagascar. *Lithos* 116, 18–34.
- Ghosh, J.G., de Wit, M.J., Zartman, R.E., 2004. Age and tectonic evolution of Neoproterozoic ductile shear zones in the Southern Granulite Terrain of India, with implications for Gondwana studies. *Tectonics* 23.
- Glorie, S., De Grave, J., Singh, T., Payne, J.L., Collins, A.S., 2014. Crustal root of the Eastern Dharwar Craton: zircon U–Pb age and Lu–Hf isotopic evolution of the East Salem Block, southeast India. *Precambrian Res.* 249, 229–246.
- Gopalakrishna, D., Hansen, E.C., Janardhan, A.S., Newton, R.C., 1986. The southern high-grade margin of the Dharwar Craton. *J. Geol.* 94, 247–260.
- Halpin, J.A., Clarke, G.L., White, R.W., Kelsey, D.E., 2007a. Contrasting P–T–t paths for Neoproterozoic metamorphism in MacRobertson and Kemp Lands, east Antarctica. *J. Metamorph. Geol.* 25, 683–701.
- Halpin, J.A., Daczko, N.R., Clarke, G.L., Murray, K.R., 2013. Basin analysis in polymetamorphic terranes: An example from east Antarctica. *Precambrian Res.* 231, 78–97.
- Halpin, J.A., White, R.W., Clarke, G.L., Kelsey, D.E., 2007b. The Proterozoic P–T–t evolution of the Kemp Land coast, East Antarctica; Constraints from Si-saturated and Si-undersaturated metapelites. *J. Petrol.* 48, 1321–1349.
- Halpin, J.A., Gerakiteys, C.L., Clarke, G.L., Belousova, E.A., Griffin, W.L., 2005. In-situ U – Pb geochronology and Hf isotope analyses of the Rayner Complex, east Antarctica. *Contrib. to Mineral. Petrol.* 148, 689–706. doi:10.1007/s00410-004-0627-6
- Harley, S.L., 1989. The origins of granulites: a metamorphic perspective. *Geol. Mag.* 126, 215–247.
- Karmakar, S., Bose, S., Sarbadhikari, A.B., Das, K., 2011. Evolution of granulite enclaves and associated gneisses from Purulia, Chhotanagpur Granite Gneiss Complex, India: evidence for 990–940 Ma tectonothermal event (s) at the

- eastern India cratonic fringe zone. *J. Asian Earth Sci.* 41, 69–88.
- Kaur, P., Zeh, A., Chaudhri, N., Eliyas, N., 2017. Two distinct sources of 1.73–1.70 Ga A-type granites from the northern Aravalli orogen, NW India: Constraints from in situ zircon U-Pb ages and Lu-Hf isotopes. *Gondwana Res.* 49, 164–181.
- Kaur, P., Zeh, A., Chaudhri, N., Gerdes, A., Okrusch, M., 2011. Archaean to Palaeoproterozoic crustal evolution of the Aravalli mountain range, NW India, and its hinterland: the U-Pb and Hf isotope record of detrital zircon. *Precambrian Res.* 187, 155–164.
- Kelly, N.M., Clarke, G.L., Fanning, C.M., 2002. A two-stage evolution of the Neoproterozoic Rayner Structural Episode: new U-Pb sensitive high resolution ion microprobe constraints from the Oygarden Group, Kemp Land, East Antarctica. *Precambrian Res.* 116, 307–330.
- Kelly, N.M., Harley, S.L., 2004. Orthopyroxene–corundum in Mg–Al-rich granulites from the Oygarden Islands, east Antarctica. *J. Petrol.* 45, 1481–1512.
- Kohn, M.J., Corrie, S.L., Markley, C., 2015. The fall and rise of metamorphic zircon. *Am. Mineral.* 100, 897–908.
- Kooijman, E., Upadhyay, D., Mezger, K., Raith, M.M., Berndt, J., Srikantappa, C., 2011. Response of the U-Pb chronometer and trace elements in zircon to ultrahigh-temperature metamorphism: the Kadavur anorthosite complex, southern India. *Chem. Geol.* 290, 177–188.
- Korhonen, F.J., Clark, C., Brown, M., Bhattacharya, S., Taylor, R., 2013. How long-lived is ultrahigh temperature (UHT) metamorphism? Constraints from zircon and monazite geochronology in the Eastern Ghats orogenic belt, India. *Precambrian Res.* 234, 322–350.
- Kovach, V.P., Simmat, R., Rickers, K., Berezhnaya, N.G., Salnikova, E.B., Dobmeier, C., Raith, M.M., Yakovleva, S.Z., Kotov, A.B., 2001. The Western Charnockite Zone of the Eastern Ghats Belt, India—An Independent Crustal Province of Late Archaean (2.8 Ga) and Palaeoproterozoic (1.7–1.6 Ga) Terrains. *Gondwana*

Res. 4, 666–667.

Kroener, A., Hegner, E., Collins, A.S., Windley, B.F., Brewer, T.S., Razakamanana, T., Pidgeon, R.T., 2000. Age and magmatic history of the Antananarivo Block, central Madagascar, as derived from zircon geochronology and Nd isotopic systematics. *Am. J. Sci.* 300, 251–288.

Kumar, R.R., Dwivedi, S.B., 2021. Exsolution intergrowth of cpx-opx and pseudosection modelling of two-pyroxene mafic granulite from Daltonganj of Chhotanagpur Granite Gneiss Complex, Eastern India. *Arab. J. Geosci.* 14, 1–16.

Kumar, R.R., Dwivedi, S.B., Pathak, P., 2022. Phase equilibria modelling and geochemistry of high-grade gneiss from the Chhotanagpur Granite Gneiss Complex, eastern India: Implications for tectono-metamorphic evolution. *Geosystems and Geoenvironment* 100082.

Kumar, R.R., Kawaguchi, K., Dwivedi, S.B., Das, K., 2021. Metamorphic evolution of the pelitic and mafic granulites from Daltonganj, Chhotanagpur Granite Gneiss Complex, India: Constraints from zircon U–Pb age and phase equilibria modelling. *Geol. J.* 57, 1284–1310.

Lal, R.K., Ackermann, D., Raith, M., Raase, P., Seifert, F., 1984. Sapphirinebearing assemblages from Kiranur, Southern India: A study of chemographic relationships in the Na₂O-FeO-MgO-Al₂O₃-SiO₂-H₂O system. *Neues Jahrb. für Mineral. Abhandlungen* 150, 121–152.

Li, S.-S., Santosh, M., Indu, G., Shaji, E., Tsunogae, T., 2017. Detrital zircon geochronology of quartzites from the southern Madurai Block, India: Implications for Gondwana reconstruction. *Geosci. Front.* 8, 851–867.

Liu, X., Zhao, Y., Hu, J., 2013. The c. 1000–900 Ma and c. 550–500 Ma tectonothermal events in the Prince Charles Mountains–Prydz Bay region, East Antarctica, and their relations to supercontinent evolution. *Geol. Soc. London, Spec. Publ.* 383, 95–112.

Maji, A.K., Goon, S., Bhattacharya, A., Mishra, B., Mahato, S., Bernhardt, H.-J., 2008.

- Proterozoic polyphase metamorphism in the Chhotanagpur Gneissic Complex (India), and implication for trans-continental Gondwanaland correlation. *Precambrian Res.* 162, 385–402.
- Meißner, B., Deters, P., Srikantappa, C., Köhler, H., 2002. Geochronological evolution of the Moyar, Bhavani and Palghat shear zones of southern India: implications for east Gondwana correlations. *Precambrian Res.* 114, 149–175.
- Mitchell, R.J., Johnson, T.E., Clark, C., Gupta, S., Brown, M., Harley, S.L., Taylor, R., 2019. Neoproterozoic evolution and Cambrian reworking of ultrahigh temperature granulites in the Eastern Ghats Province, India. *J. Metamorph. Geol.* 37, 977–1006.
- Mohan, A., Prakash, D., Motoyoshi, Y., 1996. Decompressional PT history in sapphirine-bearing granulites from Kodaikanal, southern India. *J. Southeast Asian Earth Sci.* 14, 231–243.
- Mohan, A., Windley, B.F., 1993. Crustal trajectory of sapphirine-bearing granulites from Ganguvarpatti, South India: evidence for an isothermal decompression path. *J. Metamorph. Geol.* 11, 867–878.
- Morrissey, L.J., Hand, M., Kelsey, D.E., 2015. Multi-stage metamorphism in the Rayner–Eastern Ghats Terrane: P–T–t constraints from the northern Prince Charles Mountains, east Antarctica. *Precambrian Res.* 267, 137–163.
- Mukherjee, S., Dey, A., Ibanez-Mejia, M., Sanyal, S., Sengupta, P., 2018a. Geochemistry, U–Pb geochronology and Lu–Hf isotope systematics of a suite of ferroan (A-type) granitoids from the CGGC: Evidence for Mesoproterozoic crustal extension in the east Indian shield. *Precambrian Res.* 305, 40–63.
- Mukherjee, S., Dey, A., Sanyal, S., Ibanez-Mejia, M., Dutta, U., Sengupta, P., 2017. Petrology and U–Pb geochronology of zircon in a suite of charnockitic gneisses from parts of the Chotanagpur Granite Gneiss Complex (CGGC): evidence for the reworking of a Mesoproterozoic basement during the formation of the Rodinia supercontinent. *Geol. Soc. London, Spec. Publ.* 457, 197–231.

- Mukherjee, S., Dey, A., Sanyal, S., Ibanez-Mejia, M., Sengupta, P., 2019a. Bulk rock and zircon geochemistry of granitoids from the Chotanagpur Granite Gneissic Complex (CGGC): implications for the late Paleoproterozoic continental arc magmatism in the East Indian Shield. *Contrib. to Mineral. Petrol.* 174, 1–17.
- Mukherjee, S., Dey, A., Sanyal, S., Sengupta, P., 2019b. Proterozoic crustal evolution of the Chotanagpur Granite Gneissic complex, Jharkhand-Bihar-West Bengal, India: current status and future prospect, in: *Tectonics and Structural Geology: Indian Context*. Springer, pp. 7–54.
- Mukherjee, S., Dey, A., Sanyal, S., Sengupta, P., 2018b. Tectonothermal imprints in a suite of mafic dykes from the Chotanagpur Granite Gneissic complex (CGGC), Jharkhand, India: Evidence for late Tonian reworking of an early Tonian continental crust. *Lithos* 320–321. <https://doi.org/10.1016/j.lithos.2018.09.014>
- Naha, K., Srinivasan, R., Deb, G.K., 1997. Structural geometry of the early Precambrian terrane south of Coimbatore in the “Palghat Gap”, southern India. *Proc. Indian Acad. Sci. Planet. Sci.* 106, 237–247.
- Pal, D.C., Rhede, D., 2013. Geochemistry and chemical dating of uraninite in the Jaduguda Uranium Deposit, Singhbhum Shear Zone, India—Implications for uranium mineralization and geochemical evolution of uraninite. *Econ. Geol.* 108, 1499–1515.
- Pal, T., Bhowmik, S.K., 1998. Metamorphic history of Sausar Group of rocks. *Geol. Surv. India Unpubl. Rep*
- Peucat, J.-J., Jayananda, M., Chardon, D., Capdevila, R., Fanning, C.M., Paquette, J.-L., 2013. The lower crust of the Dharwar Craton, Southern India: Patchwork of Archean granulitic domains. *Precambrian Res.* 227, 4–28.
- Plavsa, D., Collins, A.S., Foden, J.D., Clark, C., 2015. The evolution of a Gondwanan collisional orogen: A structural and geochronological appraisal from the Southern Granulite Terrane, South India. *Tectonics* 34, 820–857.

- Plavsa, D., Collins, A.S., Payne, J.L., Foden, J.D., Clark, C., Santosh, M., 2014. Detrital zircons in basement metasedimentary protoliths unveil the origins of southern India. *GSA Bull.* 126, 791–811.
- Plavsa, D., Collins, A.S., Foden, J.F., Kropinski, L., Santosh, M., Chetty, T.R.K., Clark, C., 2012. Delineating crustal domains in Peninsular India: age and chemistry of orthopyroxene-bearing felsic gneisses in the Madurai Block. *Precambrian Res.* 198, 77–93.
- Prakash, D., Arima, M., 2003. High-temperature dehydration melting and decompressive textures in Mg-Al granulites from the Palni hills, South India. *Polar Geosci.* 16, 149–175.
- Prakash, D., Arima, M., Mohan, A., 2006. Ultrahigh-temperature metamorphism in the Palni Hills, South India: insights from feldspar thermometry and phase equilibria. *Int. Geol. Rev.* 48, 619–638.
- Prathigadapa, R., Das Sharma, S., Ramesh Sai, D., 2020. Seismic Evidence for Proterozoic Collisional Episodes along Two Geosutures within the Southern Granulite Province of India. *Geosci. Lithosph. Volume 202*. <https://doi.org/https://doi.org/10.2113/2020/8861007>
- Ram Mohan, M., Satyanarayanan, M., Santosh, M., Sylvester, P.J., Tubrett, M., Lam, R., 2013. Neoproterozoic suprasubduction zone arc magmatism in southern India: Geochemistry, zircon U-Pb geochronology and Hf isotopes of the Sittampundi Anorthosite Complex. *Gondwana Res.* 23, 539–557.
- Raith, M.M., Brandt, S., Sengupta, P., Berndt, J., John, T., Srikantappa, C., 2016. Element mobility and behaviour of zircon during HT metasomatism of ferroan basic granulite at Ayyarmalai, South India: Evidence for polyphase Neoproterozoic crustal growth and multiple metamorphism in the Northeastern Madurai Province. *J. Petrol.* 57, 1729–1774.
- Raith, M.M., Karmakar, S., Brown, M., 1997. Ultra-high-temperature metamorphism and multistage decompressional evolution of sapphirine granulites from the Palni Hill Ranges, southern India. *J. Metamorph. Geol.* 15, 379–399.

- Raith, M.M., Sengupta, P., Kooijman, E., Upadhyay, D., Srikantappa, C., 2010. Corundum–leucosome-bearing aluminous gneiss from Ayyarmalai, Southern Granulite Terrain, India: A textbook example of vapor phase-absent muscovite-melting in silica-undersaturated aluminous rocks. *Am. Mineral.* 95, 897–907.
- Raith, M.M., Srikantappa, C., 2008. Corundum–leucosome-bearing aluminous gneiss from Ayyarmalai, Southern Granulite Terrain, India: a textbook example of vapour phase-absent muscovite melting in silica-undersaturated pelitic rocks. 86th Meet. Ger. Mineral. Assoc. Berlin, Abstr. Vol.
- Raith, M.M., Srikantappa, C., Buhl, D., Koehler, H., 1999. The Nilgiri enderbites, South India: nature and age constraints on protolith formation, high-grade metamorphism and cooling history. *Precambrian Res.* 98, 129–150.
- Ray Barman, T., Bishui, P.K., Mukhopadhyay, K., Ray, J.N., 1994. Rb-Sr geochronology of the high-grade rocks from Purulia, West Bengal and Jamua-Dumka sector, Bihar. *Indian Miner.* 48, 45–60.
- Ray, S., Sanyal, S., Sengupta, P., 2011. Mineralogical control on rheological inversion of a suite of deformed mafic dykes from parts of the Chottanagpur Granite Gneiss Complex of eastern India, in: *Dyke Swarms: Keys for Geodynamic Interpretation*. Springer, pp. 263–276.
- Rekha, S., Upadhyay, D., Bhattacharya, A., Kooijman, E., Goon, S., Mahato, S., Pant, N.C., 2011. Lithostructural and chronological constraints for tectonic restoration of Proterozoic accretion in the Eastern Indian Precambrian shield. *Precambrian Res.* 187, 313–333.
- Renjith, M.L., Santosh, M., Satyanarayanan, M., Rao, D.V.S., Tang, L., 2016. Multiple rifting and alkaline magmatism in southern India during Paleoproterozoic and Neoproterozoic. *Tectonophysics* 680, 233–253.
- Rey, P., Vanderhaeghe, O., Teyssier, C., 2001. Gravitational collapse of the continental crust: definition, regimes and modes. *Tectonophysics* 342, 435–449.
- Rogers, J.J.W., Santosh, M., 2004. *Continents and supercontinents*. Oxford University

Press.

- Roy, A.B., KRÖNER, A., Bhattachaya, P.K., Rathore, S., 2005. Metamorphic evolution and zircon geochronology of early Proterozoic granulites in the Aravalli Mountains of northwestern India. *Geol. Mag.* 142, 287–302.
- Roy Choudhury, S., Dey, A., Brandt, S., Sanyal, S., Sengupta, P., 2021. Petrology and geochronology of a suite of meta-supracrustal rocks from Madukkarai, Tamil Nadu: Implications for the Ediacaran-Cambrian orogenesis of the Granulite Terrane of South India. *Lithos* 400, 106347.
- Saha, L., Bhowmik, S.K., Fukuoka, M., Dasgupta, S., 2008. Contrasting episodes of regional granulite-facies metamorphism in enclaves and host gneisses from the Aravalli–Delhi mobile belt, NW India. *J. Petrol.* 49, 107–128.
- Saikia, A., Gogoi, B., Kaulina, T., Lialina, L., Bayanova, T., Ahmad, M., 2017. Geochemical and U–Pb zircon age characterization of granites of the Bathani Volcano Sedimentary sequence, Chotanagpur Granite Gneiss Complex, eastern India: vestiges of the Nuna supercontinent in the Central Indian Tectonic Zone. *Geol. Soc. London, Spec. Publ.* 457, 233–252.
- Saitoh, Y., Tsunogae, T., Santosh, M., Chetty, T.R.K., Horie, K., 2011. Neoproterozoic high-pressure metamorphism from the northern margin of the Palghat–Cauvery Suture Zone, southern India: Petrology and zircon SHRIMP geochronology. *J. Asian Earth Sci.* 42, 268–285.
- Sajeev, K., Osanai, Y., Santosh, M., 2004. Ultrahigh-temperature metamorphism followed by two-stage decompression of garnet–orthopyroxene–sillimanite granulites from Ganguvarpatti, Madurai block, southern India. *Contrib. to Mineral. Petrol.* 148, 29–46.
- Sajeev, K., Santosh, M., Kim, H.S., 2006. Partial melting and P–T evolution of the Kodaikanal Metapelite Belt, southern India. *Lithos* 92, 465–483.
- Santosh, M., 2020. The Southern Granulite Terrane: A synopsis. *Episodes J. Int. Geosci.* 43, 109–123.

- Santosh, M., Xiao, W.J., Tsunogae, T., Chetty, T.R.K., Yellappa, T., 2012. The Neoproterozoic subduction complex in southern India: SIMS zircon U–Pb ages and implications for Gondwana assembly. *Precambrian Res.* 192, 190–208.
- Sanyal, S., Sengupta, P., 2012. Metamorphic evolution of the Chotanagpur granite gneiss complex of the east Indian shield: current status. *Geol. Soc. London, Spec. Publ.* 365, 117–145.
- Sarkar, T., Schenk, V., 2014. Two-stage granulite formation in a Proterozoic magmatic arc (Ongole domain of the Eastern Ghats Belt, India): Part 1. Petrology and pressure–temperature evolution. *Precambrian Res.* 255, 485–509.
- Sarkar, T., Schenk, V., Berndt, J., 2015. Formation and evolution of a Proterozoic magmatic arc: geochemical and geochronological constraints from meta-igneous rocks of the Ongole domain, Eastern Ghats Belt, India. *Contrib. to Mineral. Petrol.* 169. <https://doi.org/10.1007/s00410-014-1096-1>
- Sato, K., Santosh, M., Tsunogae, T., Chetty, T.R.K., Hirata, T., 2011. Laser ablation ICP mass spectrometry for zircon U–Pb geochronology of metamorphosed granite from the Salem Block: Implication for Neoproterozoic crustal evolution in southern India. *J. Mineral. Petrol. Sci.* 106, 1–12.
- Schofield, D.I., Thomas, R.J., Goodenough, K.M., De Waele, B., Pitfield, P.E.J., Key, R.M., Bauer, W., Walsh, G.J., Lidke, D.J., Ralison, A. V., 2010. Geological evolution of the Antongil craton, NE Madagascar. *Precambrian Res.* 182, 187–203.
- Sengupta, P., Dutta, U., Bhui, U.K., Mukhopadhyay, D., 2009. Genesis of wollastonite- and grandite-rich skarns in a suite of marble-calc-silicate rocks from Sittampundi, Tamil Nadu: constraints on the P–T–fluid regime in parts of the Pan-African mobile belt of South India. *Mineral. Petrol.* 95, 179.
- Sengupta, P., Raith, M.M., Kooijman, E., Talukdar, M., Chowdhury, P., Sanyal, S., Mezger, K., Mukhopadhyay, D., 2015. Chapter 20 Provenance, timing of sedimentation and metamorphism of metasedimentary rock suites from the Southern Granulite Terrane, India. *Geol. Soc. London, Mem.* 43, 297–308.

<https://doi.org/10.1144/m43.20>

- Sequeira, N., Bhattacharya, A., Bell, E., 2022. The ~ 1.4 Ga A-type granitoids in the “Chottanagpur crustal block”(India), and its relocation from Columbia to Rodinia? *Geosci. Front.* 13, 101138.
- Sequeira, N., Bhattacharya, A., Nance, D., 2020. Early Neoproterozoic deformation kinematics in the Chottanagpur gneiss complex (eastern India): evidence from the curvilinear Hundru falls shear Zone Analysis. *Lithosphere* 2020.
- Shiraishi, K., Dunkley, D.J., Hokada, T., Fanning, C.M., Kagami, H., Hamamoto, T., 2008. Geochronological constraints on the Late Proterozoic to Cambrian crustal evolution of eastern Dronning Maud Land, East Antarctica: a synthesis of SHRIMP U-Pb age and Nd model age data. *Geol. Soc. London, Spec. Publ.* 308, 21–67.
- Simmat, R., Raith, M.M., 2008. U–Th–Pb monazite geochronometry of the Eastern Ghats Belt, India: timing and spatial disposition of poly-metamorphism. *Precambrian Res.* 162, 16–39.
- Singh, R.N., Thorpe, R., Kristic, D., 2001. Galena Pb isotope data of base metal occurrences in the Hesatu-Belbathan belt, eastern Precambrian shield, Bihar. *J. Geol. Soc. India (Online Arch. from Vol 1 to Vol 78)* 57, 535–538.
- Sláma, J., Košler, J., Pedersen, R.B., 2007. Behaviour of zircon in high-grade metamorphic rocks: evidence from Hf isotopes, trace elements and textural studies. *Contrib. to Mineral. Petrol.* 154, 335–356.
- Talukdar, M., Sarkar, T., Sengupta, P., Mukhopadhyay, D., 2022. The Southern Granulite Terrane, India: The saga of over 2 billion years of Earth’s history. *Earth-Science Rev.* 104157.
- Talukdar, M., Mukhopadhyay, D., Sanyal, S., Sengupta, P., 2020. Early Palaeoproterozoic structural reconstitution of a suite of rocks from the Mahadevi Layered Complex, Tamil Nadu, India. *Geol. J.*
- Tamashiro, I., Santosh, M., Sajeev, K., Morimoto, T., Tsunogae, T., 2004. Multistage

- orthopyroxene formation in ultrahigh-temperature granulites of Ganguvarpatti, southern India: implications for complex metamorphic evolution during Gondwana assembly. *J. Mineral. Petrol. Sci.* 99, 279–297.
- Tateishi, K., Tsunogae, T., Santosh, M., Janardhan, A.S., 2004. First report of sapphirine+ quartz assemblage from southern India: implications for ultrahigh-temperature metamorphism. *Gondwana Res.* 7, 899–912.
- Teale, W., Collins, A.S., Foden, J., Payne, J.L., Plavsa, D., Chetty, T.R.K., Santosh, M., Fanning, M., 2011. Cryogenian (~ 830 Ma) mafic magmatism and metamorphism in the northern Madurai Block, southern India: A magmatic link between Sri Lanka and Madagascar? *J. Asian Earth Sci.* 42, 223–233.
- Tiwari, A.K., Sarkar, T., 2020. PTt evolution of sapphirine-bearing semipelitic granulites from Vadkampatti in Eastern Madurai Domain, southern India: Insights from petrography, pseudosection modelling and in-situ monazite geochronology. *Precambrian Res.* 348, 105866.
- Tucker, R.D., Roig, J.-Y., Delor, C., Amelin, Y., Goncalves, P., Rabarimanana, M.H., Ralison, A. V, Belcher, R.W., 2011. Neoproterozoic extension in the Greater Dharwar Craton: a reevaluation of the “Betsimisaraka suture” in Madagascar. *Can. J. Earth Sci.* 48, 389–417.
- Tucker, R.D., Roig, J.-Y., Moine, B., Delor, C., Peters, S.G., 2014. A geological synthesis of the Precambrian shield in Madagascar. *J. African Earth Sci.* 94, 9–30.
- Vadlamani, R., Kröner, A., Vasudevan, D., Wendt, I., Tobschall, H., Chatterjee, C., 2013. Zircon evaporation ages and geochemistry of metamorphosed volcanic rocks from the Vinjamuru domain, Krishna Province: evidence for 1.78 Ga convergent tectonics along the southeastern margin of the Eastern Dharwar Craton. *Geol. J.* 48, 293–309.
- Wang, Y., Liu, D., Chung, S.-L., Tong, L., Ren, L., 2008. SHRIMP zircon age constraints from the Larsemann Hills region, Prydz Bay, for a late Mesoproterozoic to early Neoproterozoic tectono-thermal event in East Antarctica. *Am. J. Sci.* 308, 573–617.

Appendix

Appendix

1. Methodology for calculation of effective bulk

Effective bulks were calculated for the studied Grt-Bt-Sil gneiss and the Grt-Crd-Bt-Sil gneiss by combining the modal proportions of minerals in each rock with their corresponding analysed compositions.

Step 1: The average compositions of each mineral in wt% and in apfu are calculated. The moles of each cation per formula unit are multiplied with the respective molecular weights of cation oxides to get the molecular weight of unit mineral formula.

Step 2: The number of mole% of each mineral present in the rock were calculated by dividing the volume proportions of each mineral present in the rock by their respective molar volumes. The volume proportions of each mineral (given in Table. 1) are estimated by point counting method under microscope. The thermodynamic data of Holland and Powell, (2011) and the computer program of PERPLEX (Connolly, 2005) are used to obtain the molar volumes of the minerals.

Step 3: Combining the results obtained from Step 1 and 2, the volume percentage of minerals present in the rock is converted to weight percentage.

Step 4: Weight percentage of each mineral can again be distributed in terms of the weight of their respective cation-oxides. Similar cation-oxides for all the minerals are added together and recalculated in 100 to give the effective bulk composition.

2. Analytical techniques for zircon and monazite dating

2.1. U-Pb Zircon dating:

(a) U-Pb zircon geochronology in the calc-silicate granulite in the CGGC

Uranium-lead (U-Pb) isotope dating of in-situ zircon was carried out at the Radiogenic Isotope Facility in the Department of Geology and Geophysics, Indian

Institute of Technology (IIT), Kharagpur. Back Scattered Electron (BSE) and Cathodo-luminescence (CL) images have been taken using ZEISS EVO 18 Scanning Electron Microscope at the Department of Geological Sciences, Jadavpur University, Kolkata and JEOL JSA 6490 Scanning Electron Microscope at the Department of Geology and Geophysics, IIT Kharagpur respectively. BSE images helped to identify the morphology and viable spots for dating of the zircon grains, while CL images helped in understanding zoning and grain interiors. Detailed methodology and handling of the analyzed data are discussed in (Chakrabarty et al., 2022; Chakraborty et al., 2019). Uncertainties of the analyzed data are reported in 2σ and the standard deviation of isotopic ratios and U content have been calculated using GJ-1 reference zircon. The U–Pb isotope analysis were done using a Thermo-Fisher Scientific iCAP-Q quadrupole ICP-MS attached to a New Wave 193 ArF Excimer laser ablation system. The laser was operated at ~ 5 J/cm² beam energy density at 5 Hz repetition rate. Depending on the thickness of the zones within the zircon grains the spot sizes has been fixed at 25–40 μm . For maximum sensitivity on Pb, Th, and U, the ICPMS was optimized using the NIST 612 reference glass. The oxide production rate monitored on ²³²Th/¹⁶⁰ was varying between 0.6–0.8%. External standardization method has been described in Jackson et al. (2004). The concordia ages and discordia diagrams were plotted using the Isoplot software.

(b) U-Pb zircon geochronology in the meta-supracrustal rocks of the MSU, GTSI

Zircon separation for both Grt-Bt-Sil gneiss (I-235-1-07) and Grt-Opx bearing meta-psammite (I-353-10-10) was done using heavy mineral separation techniques at Kiel University, Germany. Cathodoluminescence (CL) image of zircons were taken by JEOLJSM-6400 electron microprobe at the Institute of Geosciences, Frankfurt University. U-Pb spot analysis of zircon grains were carried out by Laser Ablation Inductively Coupled Plasma Mass Spectrometry (LA-ICP-MS) at Frankfurt University using a Thermo-Finnigan Element II sector field ICP-MS system coupled to a New Wave UP213 ultraviolet laser system. The diameter of the laser spot was 20 and 30 μm . The analytical details are summarized in (Zeh et al., 2007). The apparent ages have been presented with 2σ

error. The program Isoplot-4.15 (Ludwig, 2003) has been used for statistical analysis of these data. Data with $\geq 90\%$ concordance is considered as concordant. Additionally, the reversely discordant data that overlap concordia within uncertainty are also considered as concordant ages.

2.2. Th-U-total-Pb in situ monazite dating:

Monazite grains from Grt-Bt-Sil gneisses (B117) in the MSU were analysed in-situ at Indian Institute of Technology, Kharagpur with Cameca SX100 Electron Probe Micro Analyser. The points were analysed with a 20 kV voltage, 150 nA beam current and 1 μm beam diameter. Monazite analyses of this samples also included the REE (La, Ce, Pr, Nd, Sm, Gd, Dy), P, Fe, Ca, Si and Al. Well-characterized natural and synthetic standards were used for calibration. The standards used for monazite calibration were: UO_2 for U; pyromorphite for Pb; ThO_2 for Th and Yttrium aluminium garnet (YAG) for Y; synthetic silica-aluminium glass containing 4% REE for La, Ce, Nd, Pr, Sm, Ho, Dy and Gd; apatite for P and Ca; corundum for Al; hematite for Fe; Th-glass for Si. The monazite age used as standard in this study is from Moacyr pegmatite from Brazil that yielded a TIMS age of 487 ± 1 Ma (Crowley et al., 2005) and EPMA age of 497 ± 10 Ma (Spear et al., 2009). The age of each spot was calculated by the equation given by Montel et al. (1996) with in-built Age quant software of CAMECA SX-100. The error associated with the spot age depends on the propagation of errors during the calibration using the standard (Montel et al., 1996; Williams et al., 1999). The procedures of computation of errors associated with the element analysis from standard deviation of the measurements on standard and on peak and background counts are outlined in CAMECA SX-100 manual (Steiger and Jäger, 1977). Although the analyses of Pb, U and Th were used to calculate the apparent ages, the remaining elements allowed a more accurate X-PHI matrix reduction of the data. Further details have been presented in (Bhowmik et al., 2014). The apparent ages have been presented with 2σ error. The monazites from Grt-Crd-Bt-Sil gneiss (I-353-1-10) were analysed by EPMA on a JEOL Superprobe JXA 8900R at the Institute of Geosciences, University Kiel, following the analytical

protocol given by (Jöns et al., 2006). The program Isoplot-4.15 (Ludwig, 2003) has been used for statistical analysis of these data.

3.Textural modelling technique

Mass balance calculations were done to chemically model the observed possible reaction textures using an algebraic analysis process based on measured mineral compositions. This algebraic process can be used to obtain balanced mineral reactions and to infer whether the reactions occurred in a closed or an open system (Chowdhury et al. 2013 and references therein). Singular value decomposition (SVD) is a widely used technique in textural modelling and chemical modelling (Rice 1985; Lang et al. 2004; Sengupta et al. 2009a; Chowdhury et al. 2013; Karmakar et al. 2017, Banerjee et al. 2019). The SVD method uses a compositional matrix 'M' of 'm' minerals having 'n' components, where $(M=m \times n)$ (Lang et al. 2004). The chemical species that are added or removed from the system during the reactions are considered mobile (phases) during this matrix operation. Here, we used the C-Space software (published by Torres-Roldan et. al. (2000) to perform the matrix operation required for the SVD method. It generates all possible balanced chemical reactions involving a given set of mineral compositions or chemical species.

References

- Bhowmik, S.K., Wilde, S.A., Bhandari, A., Basu Sarbadhikari, A., 2014. Zoned monazite and zircon as monitors for the thermal history of granulite terranes: an example from the Central Indian Tectonic Zone. *J. Petrol.* 55, 585–621.
- Chakrabarty, A., Karmakar, S., Mukherjee, S., Choudhury, S.R., Maiti, P., Sanyal, S., Sengupta, P., 2022. Neoproterozoic reworking of a Mesoproterozoic magmatic arc from the north-eastern part of the Central Indian Tectonic Zone: Implication for the growth and disintegration of the Indian shield in the Proterozoic supercontinental cycles. *Precambrian Res.* 378, 106758.
- Chakraborty, T., Upadhyay, D., Ranjan, S., Pruseth, K.L., Nanda, J.K., 2019. The geological evolution of the Gangpur Schist Belt , eastern India : Constraints on

- the formation of the Greater Indian Landmass in the Proterozoic. *J. Metamorph. Geol.* 37, 113–151. <https://doi.org/10.1111/jmg.12452>
- Connolly, J.A.D., 2005. Computation of phase equilibria by linear programming: A tool for geodynamic modeling and its application to subduction zone decarbonation. <https://doi.org/10.1016/j.epsl.2005.04.033>
- Crowley, J.L., Chatterjee, N., Bowring, S.A., Sylvester, P.J., Myers, J.S., Searle, M.P., 2005. U-(Th)-Pb dating of monazite and xenotime by EMPA, LA-ICPMS, and IDTIMS: examples from the Yilgarn Craton and Himalayas.
- Dey, A., Choudhury, S.R., Mukherjee, S., Sanyal, S., Sengupta, P., 2019. Origin of vesuvianite-garnet veins in calc-silicate rocks from part of the Chotanagpur Granite Gneiss Complex, East Indian Shield: The quantitative PTX CO₂ topology in parts of the system CaO-MgO-Al₂O₃-SiO₂-H₂O-CO₂ (+ Fe₂O₃, F). *Am. Mineral. J.* 104, 744–760.
- Holland, T.J.B., Powell, R., 2011. An improved and extended internally consistent thermodynamic dataset for phases of petrological interest, involving a new equation of state for solids. *J. Metamorph. Geol.* 29, 333–383.
- Jackson, S.E., Pearson, N.J., Griffin, W.L., Belousova, E.A., 2004. The application of laser ablation-inductively coupled plasma-mass spectrometry to in situ U-Pb zircon geochronology. *Chem. Geol.* 211, 47–69. <https://doi.org/10.1016/j.chemgeo.2004.06.017>
- Jöns, N., Schenk, V., Appel, P., Razakamanana, T., 2006. Two-stage metamorphic evolution of the Bemarivo Belt of northern Madagascar: constraints from reaction textures and in situ monazite dating. *J. Metamorph. Geol.* 24, 329–347.
- Ludwig, K.R., 2003. User's manual for a geochronological toolkit for Microsoft Excel (Isoplot/Ex version 3.0). Berkeley Geochronol. Center, Spec. Publ. 4, 1–71.
- Montel, J.-M., Foret, S., Veschambre, M., Nicollet, C., Provost, A., 1996. Electron microprobe dating of monazite. *Chem. Geol.* 131, 37–53.
- Spear, F.S., Pyle, J.M., Cherniak, D., 2009. Limitations of chemical dating of monazite. *Chem. Geol.* 266, 218–230.

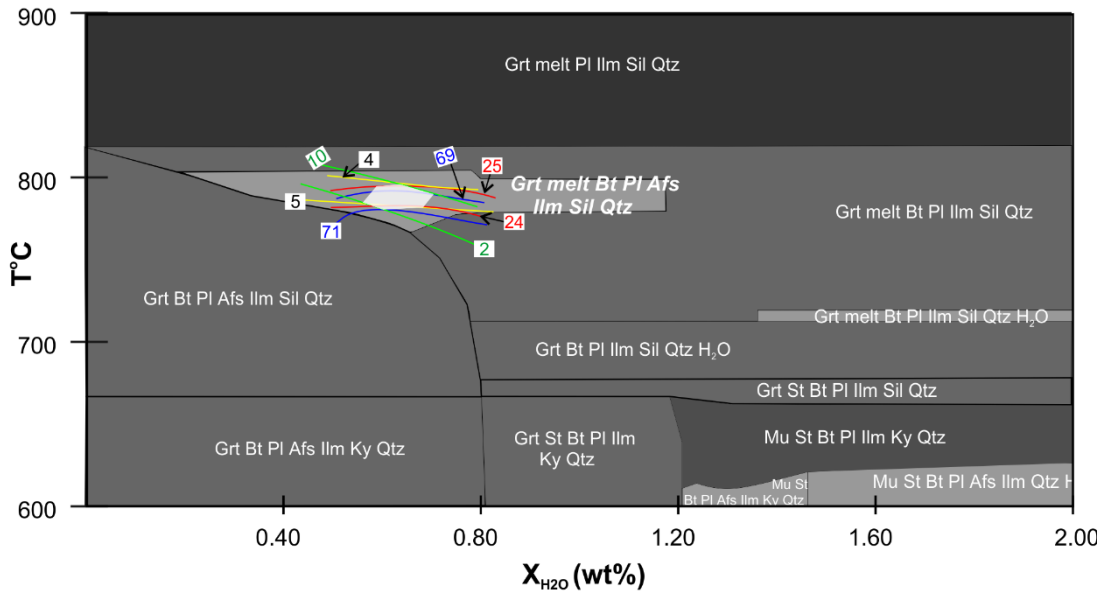
- Steiger, R., Jäger, E., 1977. Subcommittee on geochronology: convention on the use of decay constants in geo- and cosmochemistry. *Earth Planet. Sci. Lett.* 36, 359–362.
- Williams, M.L., Jercinovic, M.J., Terry, M.P., 1999. Age mapping and dating of monazite on the electron microprobe: Deconvoluting multistage tectonic histories. *Geology* 27, 1023–1026.
- Zeh, A., Gerdes, A., Klemd, R., Barton Jr, J.M., 2007. Archaean to Proterozoic crustal evolution in the central zone of the Limpopo Belt (South Africa–Botswana): constraints from combined U–Pb and Lu–Hf isotope analyses of zircon. *J. Petrol.* 48, 1605–1639.

Supplementary Material 1

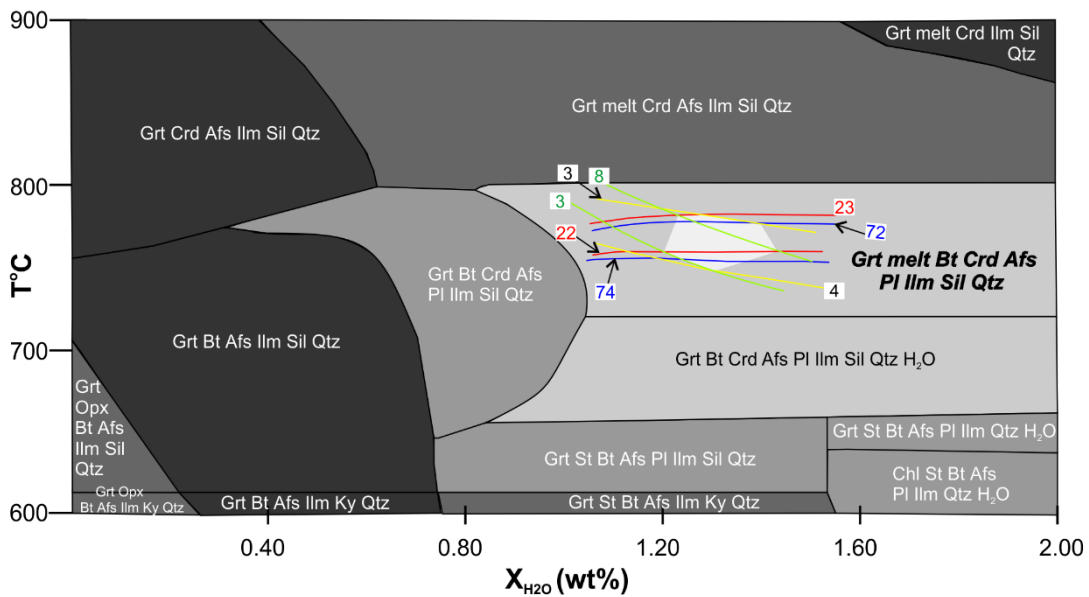
Supplementary Table: Bulk compositions of the studied calc-silicate granulite in the CGGC (AS29) showing the dissimilarities with the adjacent calc-silicate granulite (AS29X) of the area

Bulk composition	AS29	AS29X
SiO ₂	37.03	44.38
TiO ₂	3.56	1.90
Al ₂ O ₃	19.74	16.58
FeO	16.69	12.49
MgO	3.87	0.75
CaO	18.86	23.63
Na ₂ O	0.17	0.27
H ₂ O	0.08	0.00

a) Grt-Bt-Sil gneiss (B117):



b) Grt-Crd-Bt-Sil gneiss (I-353-1-10):



Supplementary Figure: T - X_{H_2O} sections constructed at 7 kbar pressure in NCKFMASHTO system for the two studied pelitic granulites from the MSU. Mineral abbreviations after Kretz, (1983).

Publications

Published Papers

Roy Choudhury, Sirina, Dey, Anindita, Brandt, Sönke, Sanyal, Sanjoy, & Sengupta, Pulak. (2021). Petrology and geochronology of a suite of meta-supracrustal rocks from Madukkarai, Tamil Nadu: Implications for the Ediacaran-Cambrian orogenesis of the Granulite Terrane of South India. *Lithos*, 400-401, 106347. <https://doi.org/10.1016/j.lithos.2021.106347>.

Dey, Anindita, **Roy Choudhury, Sirina**, Mukherjee, Subham, Sanyal, Sanjoy, & Sengupta, Pulak. (2019). Origin of vesuvianite-garnet veins in calc-silicate rocks from part of the Chotanagpur Granite Gneiss Complex, East Indian Shield: The quantitative P-T-XCO₂ topology in parts of the system CaO-MgO-Al₂O₃-SiO₂-H₂O-CO₂ (+Fe₂O₃, F). *American Mineralogist*, 104(5), 744–760. <http://doi.org/10.2138/am-2019-6811>

Das Satabdi, Sinha Deepak K, Sanyal Sanjoy, Karmakar Subrata, Panigrahi Biswajit, **Roy Choudhury, Sirina**, Sengupta Shyamal and Sengupta Pulak (2022); Petrogenesis of a nepheline syenite from parts of the Chotanagpur Granite Gneissic Complex: implications for Neoproterozoic crustal extension in the East Indian Shield. *Geological Magazine*; <https://doi.org/10.1017/S0016756822000140>.

Chakrabarty Arimita, Karmakar Shreya, Mukherjee Subham, **Roy Choudhury, Sirina**, Maiti Prithwiraj, Sanyal Sanjoy, Sengupta Pulak (2022). Neoproterozoic reworking of a Mesoproterozoic magmatic arc from the north-eastern part of the Central Indian Tectonic Zone: Implication for the growth and disintegration of the Indian shield in the Proterozoic supercontinental cycles. *Precambrian Research*; 106758.

Mukherjee Subham, Dey, Anindita, **Roy Choudhury, Sirina**, Mayne, Matthew J. (2022). Effect of source heterogeneity, melt extraction and crystal separation

on the composition of a suite of ferroan (A-type) granites from parts of the Chotanagpur Granite Gneissic Complex (CGGC), India. *Lithos*, 430-431, 1-18.

Publications under review

Roy Choudhury, Sirina, Dey, Anindita, Mukherjee, Subham, Sanyal, Sanjoy, Karmakar, Subrata, Sengupta, Pulak (2022). On the factors controlling the incorporation of aluminium within titanites: a case study from medium pressure calc silicate granulites in parts of the East Indian shield. *Mineralogy and Petrology*. MIPE-D-22-00011R1.

Roy Choudhury, Sirina, Dey, Anindita, Mukherjee, Subham, Sanyal, Sanjoy, Karmakar, Subrata, Sengupta, Pulak (2022). Formation of aluminous clinopyroxene-ilmenite-spinel symplectic assemblage in a regionally metamorphosed calc-silicate granulite from the Chotanagpur Granite Gneiss Complex, East Indian shield. *Lithos*. LITHOS10845.

Abstracts In International Conferences

Sanyal, Sanjoy, **Roy Choudhury, Sirina**, Sinha, D.K., Panigrahi, B., Das, Satabdi, Sengupta, Pulak. (2020). On the formation of REE-bearing minerals associated with carbonatite from parts of the North Purulia Shear Zone (NPSZ), East Indian Shield, 36th International Geological Congress, India. Abs no. XXXX.

Roy Choudhury, Sirina, Dey, Anindita, Mukherjee, Subham, Sanyal, Sanjoy, Sengupta, Pulak. (2020). Petrological evolution of clinopyroxene-ilmenite symplectites in a calc silicate rock from parts of Chotanagpur Granite Gneissic Complex (CGGC), East Indian shield. International Symposium on Food, Livelihood, Opportunity & Wood (FLOW), Raichak, India. Pg 72-73.

Das, Satabdi, Dasgupta, Nandini, **Roy Choudhury, Sirina**, Paul, M., Sanyal, Sanjoy, Karmakar, Subrata, Sengupta, Shyamal, Sengupta, Pulak. (2020). Formation of Pyroxene-Barite veins adjacent to carbonatite in southern parts of

Publications

Chotanagpur Granite Gneissic Complex: Implications for late stage fluid-rock interaction. International Symposium on Food, Livelihood, Opportunity & Wood (FLOW), Raichak, India. Pg 67-68.

Roy Choudhury, Sirina, Dey, Anindita, Mukherjee, Subham, Sanyal, Sanjoy, Sengupta, Pulak, (2017). Occurrence of fluoro-vesuvianite and fluoro-titanite in a suite of calc silicate rocks: evidence of fluorine rich aqueous fluid metasomatism from north eastern parts of Chotanagpur Gneissic Complex, India. Humboldt Kolleg 'Earth and Material Sciences for Sustainable Societal Developments' (13 – 15 January), Raichak, India, Abstract Volume- pp. 44-45, ISBN-978-93- 82549-29- 1

Roy Choudhury, Sirina, Mukherjee, Subham, Dey, Anindita, Sanyal, Sanjoy, Sengupta, Pulak, (2016). Reaction textures in some calc-silicate enclaves from the Chotanagpur granite gneissic complex, and their implications. International conference on Electron Microscopy & XXXVII Annual Meeting of EMSI (2-4 June), Varanasi, India. P:84-85.